CRANFIELD UNIVERSITY

WALEED K. Al-BUSAIDI

TECHNO-ECONOMIC ASSESSMENT OF RADIAL TURBOMACHINERY IN PROCESS GAS APPLICATIONS

SCHOOL OF AEROSPACE, TRANSPORT AND MANUFACTURING

PhD Full Time

Academic Year: 2015 - 2016

Supervisor: Professor. Pericles Pilidis
February 2016

CRANFIELD UNIVERSITY

SCHOOL OF AEROSPACE, TRANSPORT AND MANUFACTURING

PhD Full Time

Academic Year 2015 - 2016

WALEED K. Al-BUSAIDI

TECHNO-ECONOMIC ASSESSMENT OF RADIAL TURBOMACHINERY IN PROCESS GAS APPLICATIONS

Supervisor: Professor. Pericles Pilidis
February 2016

ABSTRACT

This research aims to assess the causes of inefficient and unstable operation of centrifugal compressors and turboexpanders in process gas applications in order to provide a solution for performance restoration and enhancement. It encompasses thermodynamic and flow evaluations to examine the efficiency and operating range improvement options of new units. Besides, this work is complemented by a techno-economic analysis to provide a rounded outcome from these studies. In order to achieve the desired objectives, a novel integrated approach has been developed to assess the design and performance of multi-stage centrifugal compressors. The proposed systematic methodology involves five basic elements including evaluation of compressor selection, compressor sizing and casing structure, performance prediction at the design and off-design conditions, modelling of efficiency and head deterioration causes; and stage design evaluation. This will contribute towards evaluating the geometrical parameters of the new units' designs at the early preliminary design phase, and thus, will be useful to identify the options for efficiency and operating range enhancements. For installed units, this approach can be implemented to assess the cause of inefficient and unstable operation by assessing the available operation data.

A method was developed to predict the performance curve of multi-stage centrifugal compressor based on a stage stacking technique. This approach considers the advantages of Lüdtke and Casey-Robinson methods with an incorporation of a methodology for compressor selection and sizing to generate more accurate results. To emphasize the validity of the developed model, it has been evaluated for both low and high flow coefficient applications. The obtained results show a significant improvement in the estimated efficiency, pressure ratio, shaft power and operating range as compared with the existing methods.

The centrifugal compressor is designed to run under various operating conditions and different gas compositions with the primary objective of high efficiency and reliability. Therefore, a new iterative method has been developed to predict the equivalent compressor performance at off-design conditions. This technique uses the performance parameters at design conditions as a reference point to derive the corresponding performance characteristics at numerous suction conditions with less dependency on the geometrical features. Through a case study on a gas transport centrifugal compressor, it was found that the developed approach can be applied for design evaluation on the expected variation of working conditions, and for the operation diagnosis of installed units as well. Furthermore, a parametric study has been conducted to investigate the effect of gas properties on the stage efficiency, surge margin, and compressor structure. The obtained results support the need for considering the gas properties variation when the off-design performance is derived.

To evaluate the impact of internal blockage on the performance parameters, this study proposed an approach to model the effect of non-reactive deposits, which has been qualified using four operation cases and the obtained results are compared with the internal inspection findings from the stage overhauling process. This also covers the influential aspects of flow blockage on the technical and economic values. Since the main challenge here is to analyze the process gas composition in real time, the influences of the non-reactive deposits have been compared with the effect of the unanticipated gas composition change. Subsequently, it has turned out that the pressure ratio parameter is not enough to assess the possibility of flow blockage and unexpected gas properties change. Moreover, it was observed that the stage discharge pressure was more sensitive to the fouled aftercooler comparing with suction and internal blockage. However, the effect of contaminated aftercooler on the surge point and discharge pressure and temperature of the upstream stage was found greater than its impact on the shaft power. Thus, a substantial surge margin reduction was detected when the first stage was operating with a fouled aftercooler comparing with the measured reduction as a result of unanticipated gas properties change. Furthermore, a larger pressure ratio drop was measured in the case of liquid carryover which revealed a more significant impact of the two phases densities difference comparing with the gas volume fraction (GVF) effect. The possibility of hydrate formation has been assessed using hydrate formation temperature (HFT) criteria.

Additionally, this research highlights a number of challenges facing the selection of typical centrifugal stage design by assessing the contribution of design characteristics on the operating efficiency and stable flow range. Besides, an empirical-based-model was established to select the optimum impeller and diffuser configurations in order to make a compromise decision based on technical and economic perspective. It was concluded that there is no absolute answer to the question of optimum rotor and stator configuration. The preliminary aerothermodynamic evaluation exposed that the selection of the optimum impeller structure is governed by several variables: stage efficiency, pressure loss coefficient, manufacturing cost, required power cost, resonance frequency and stable operating range. Hence, an evaluation is required to compromise between these parameters to ensure better performance. Furthermore, it was argued throughout this study that the decision-making process of the typical stage geometrical features has to be based upon the long-term economic performance optimization. Thus, for higher long-term economic performance, it is not sufficient to select the characteristics of the impeller and diffuser geometry based on the low manufacturing cost or efficiency improvement criterion only.

For turboexpanders, a simple and low cost tool has been developed to determine the optimum turboexpander characteristics by analysing the generated design alternatives. This approach was used in designing a turboexpander for hydrocarbon liquefaction process. Moreover, since the turboexpanders are expected to run continuously at severe gas conditions, the performance of the selected turboexpander was evaluated at different inlet flow rates and gas temperatures. It has turned out that designing a turboexpander with the maximum isentropic efficiency is not always possible due to the limitations of the aerodynamic parameters for each component. Therefore, it is necessary to assess the stage geometrical features prior the construction process to compromise between the high capital cost and the high energetic efficiency.

****

Keywords:

Centrifugal compressor, turboexpander, efficiency, operating range, design conditions, off-design, deterioration, flow blockage, design evaluation, operation diagnosis, geometrical parameters, gas compositions.

ACKNOWLEDGEMENTS

All my praise and gratitude belong to Allah for all the uncountable bounties. He is most merciful and gracious who is one in his in His Essence.

This thesis is dedicated to the soul of my grandpa and my aunt who passed away during this study, May Allah forgive them and grant them the highest of paradise (Ameen).

I would like to express my sincere gratitude to my supervisor professor Pericles Pilidis for his guidance, help and encouragement throughout my study.

My profound appreciation to my parents who motivated me to acquire knowledge. Special thanks also to my brothers and sisters and all my family members for their unlimited support and understanding.

Finally, I’m also grateful to the following people for their valuable technical support despite their busy schedules:

- Mr. Abdulrahman Al-Mutairi (Ph.D. Student, Cranfield University)
- Mr. Abdulaziz Al-Wardi (Senior Rotating Equipment Engineer, PDO)
- Mr. Saif Al-Farsi (Company Subject Matter Expert and Rotating Equipment Lead (FEED), PDO)
- Mr. Mohammed Al-Brashdi (Rotating Equipment Engineer, PDO)
- Mr. Leonardo Baldassarre (Compressors Expanders & Electrical Systems Engineering Executive Leader at GE O&G)
- Mr. Mohammed Al-Busaidi (Condition Monitoring Supervisor, PDO)
- Mr. Avinash Godbole (Expert in design of Centrifugal Compressors for Fertilizer and Refinery)
- Dr. Bader Al-Abri (Senior Project Engineer, PDO)
- Dr. Mohammed Al-Yahyai (Rotating Equipment Engineer, PDO)
- Prof. Michael Casey (Institute of Thermal Turbomachinery, University of Stuttgart, Germany)
- Mr. Andriy Skoryk (Technical Thermophysics Department, Sumy State University, Ukraine)

TABLE OF CONTENTS

LIST OF FIGURES

LIST OF TABLES

LIST OF ABBREVIATIONS

AFT	Afterward
BHP	Brake Horsepower
BL	Blade Loading Coefficient
BRG	Bearings
CR	Casey-Robinson
CVD	Conventional Vaned Diffuser
EOS	Equation of State
FC	Flow Coefficient
FWD	Forward
g	Gauge
GHP	Gas Horsepower
HC	Head Coefficient
HP	High Pressure
kSCMD	10^3 × Standard Cubic Meter per Day
LP	Low Pressure
LSVD	Low Solidity Vaned Diffuser
MAWP	Maximum Allowed Working Pressure
ML	Mechanical Losses
MMSCMD	Million Standard Cubic Meter per Day
MP	Medium Pressure
MW	Molecular Weight
OECD	Organisation for Economic Cooperation and Development
OEM	Original Equipment Manufacture
OR	Operating Range
OVLD	Overload Margin
PP	Pinched Percentage
PR	Pressure Ratio
PRC	Pressure Recovery Coefficient
Re	Reynolds Number
RR	Radius Ratio
SRE	Single Relative Eddy
VIGV	Variable Inlet Guide Vanes
VLD	Vaneless Diffuser
VS	Variable Speed
BP	Blockage Percentage
HFT	Hydrate Formation Temperature
SM	Surge Margin $\left(\mathrm{SM} = \frac{\varphi_d - \varphi_{surge}}{\varphi_d}\right)$
SP	Shrouded Percentage

LIST OF NOMENCLATURE

a	Speed of Sound
$\mathrm{A}, \mathrm{B}, D, G, H, \mathrm{C}, k_s$ K_{rc}, K_{df}, K_{BL}	Correlation coefficients
b	Blade Width
$\vec{C}$	Absolute Velocity (Turboexpander)
$CPVAPA, CPVAPB,$ $CPVAPC, CPVAPD$	Heat Capacity Equation Coefficients
C_o	Spouting Velocity
C_s	Slip Velocity
C_P	Specific Heat at Constant Pressure
C_T	Throttling coefficient
D	Diameter
D_f	Diffusion Factor
D_s	Specific Diameter
f	Shultz Correction Factor
h	Enthalpy/ Blade Height
Δh	Enthalpy Drop
H_p	Polytropic Head
H_s, f_s	Boundary Layer Shape Parameters
k	Specific Heat Ratio
k_{df}	Disc Friction Coefficient
L_{θ}	Impeller Meridional Length
N_s	Specific Speed
$\dot{m}$	Mass Flow Rate
Mu	Mach Number
n	Polytropic Exponent
N	Rotational Speed
P	Pressure
ρ	Density
Δp_{cl}	Pressure Drop Across Tip Clearance
PR_{fd}	Total Single Stage Pressure Ratio (Suction Flange to Discharge)
Pr	Prandtl Number
Q	Flow Capacity
R_D, R_L, R_S	Correlation coefficients
Ra	Arithmetic Average Roughness

Re	Reynolds Number
s	Entropy
S_w	Power Coefficient
T	Temperature
U	Tip Blade Velocity
V	Absolute Velocity (Centrifugal Compressor)
v	Specific Volume
$\dot{V}$	Volumetric Flow Rate
W	Relative Flow Velocity
X, Y	Compressibility Functions
y_r	Isentropic Head Increase
Z	Compressibility Factor
Z_b, Z_v	Number of Blades/ Number of Vanes

GREEK SYMBOLS

σ_{max}	Maximum Solidity
τ	Vaned Diffuser Throat Blockage Factor
τ_{IEB}	Impeller Exit Blockage Factor
β	Absolute Blade Angle
ε_c	Clearance Gap
ψ_h	Head Coefficient
ψ_l	Pressure Loss Coefficient due to Tip Clearance
ψ_w	Work Coefficient
α	Absolute Flow Angle from Tangential Direction
γ_D	Degree of Reaction
η	Polytropic Efficiency
η_{t-s}	Total-to-Static Polytropic Efficiency
λ	Friction Factor
ξ	Loss Coefficient
ζ	Tip Clearance Ratio (c/b_2)
φ	Flow Coefficient
μ	Viscosity / Slip Factor
$\sum \delta^*$	Total Displacement Thickness of Boundary Layers
δ	Blade/Vane Thickness
$\varepsilon(\eta)$	Gas Dynamic Functions of Density
$\pi(\eta)$	Gas Dynamic Functions of Pressure

LIST OF SUBSCRIPTS

0	Total or stagnation flow conditions

1	Centrifugal Impeller Inlet/ Turboexpander Nozzle inlet
2	Centrifugal Impeller Exit/ Turboexpander Nozzle Exit
3	Compressor Vaneless Space Exit / Turboexpander Impeller Exit
4	Diffuser Exit
5	Volute Exit
abs	Absolute
act	Actual Conditions
b	Basic
bld	Blade Loading
c	Choke
cl	Clearance
cr	Critical Property
d	Design Condition
DD	Diffuser Diameter Ratio Correction
df	Disc Friction
DS	Dry Seals
E	Effective
h	Impeller Hub
i	Different Rotational Speed
ic	Inlet Nozzle Loss Correction
inc	Incidence
lk	Leakage
m	Radial Direction
mix	Mixing
p	Peak/ Polytropic
r	Rated Point/ Reduced
rc	Recirculation
ref	Reference Test Conditions
rel	Relative
s	Surge/ Impeller Shroud
sc	Size Correction
std	Standard
T	Temperature
t	Total Property/ Impeller Tip
v	Volume
vld	Vaneless Diffuser
WS	Wet Seals
θ	Tangential Direction

CHAPTER 1: SCOPE OF RESEARCH

1.1 Motivation

The growing demand for natural gas as an energy source leads to place more focus on improving the efficiency and reliability of the gas industry equipment. Figure 1-1 demonstrates that the proven reserves in the Middle East and Europe account for about 75% of the whole world's reserves. In fact, around 40% of the total world natural gas reserves are still unproduced. However, over 2600 trillion cubic feet (tcf) from this percentage are sour gases (Duissenov, 2013). Moreover, the demand for natural gas is anticipated to rise by almost 43% in 2035 over the current demand as illustrated in figure 1-2 driven mainly by around 4.6% and 3.9% growth in the compressed gas demand of non-OECD Asia and the Middle East, respectively. Figure 1-3 illustrates a continuous rise in Oman's gas production and consumption over the last two decades as reported by EIA (2015). It is clear that the natural gas throughput increased strongly from 2000-2005.

Turboexpanders and radial compressors have been employed in gas industry since the mid-1950s and early 1900s, respectively. The turboexpanders are used vastly for hydrocarbon liquefaction, power recovery and refrigerant source in process gas applications. Furthermore, the broad operating flow range of the radial compressor makes it one of the fundamental components for the purpose of gas lift and transport. Several studies have been conducted with an attempt to improve the efficiency and aerodynamic stability of centrifugal compressors and turboexpanders by evaluating the geometrical parameters of each single component. A remarkable improvement in the compressor efficiency with relatively wider operating envelope has been accomplished over the years as shown in figure 1-4. The plotted trend is based on the obtained efficiencies values by Sorokes et al. (2010). The slope of the efficiency change is clearly greater in the early years, and it is decreasing gradually as it is approaching the asymptotic efficiency limit. This upward trend was achievable by improving the material capability and the design features of the compressor component. However, raising both parameters is still a challenge for the manufacturer since each one is attained in expenses of the other. Therefore, it is important to investigate the contribution of design characteristics on stage efficiency and operating flow range.

The operation parameters of radial turbomachinery are highly subjected to variation due to the fluctuation in the environmental conditions and process requirement. As this will affect on machine availability and efficiency, there is a need for evaluating the design and performance of radial compressor and turboexpander over different working conditions. Focusing on centrifugal compressors, this research aims to assess the causes of inefficient and unstable operation of both new and aged centrifugal compressors units. This includes a multi-decision evaluation for the design options and an evaluation of different performance parameters and various working scenarios from aerothermodynamic perspective. One of the primary outcomes of this study is to develop a sequential approach which can be used for new design evaluation and existing machines operation diagnosis. Hence, this will help to provide alternatives to improve the geometrical features of the compression stage in the early preliminary design process and to propose an operation and maintenance plan for the installed units.

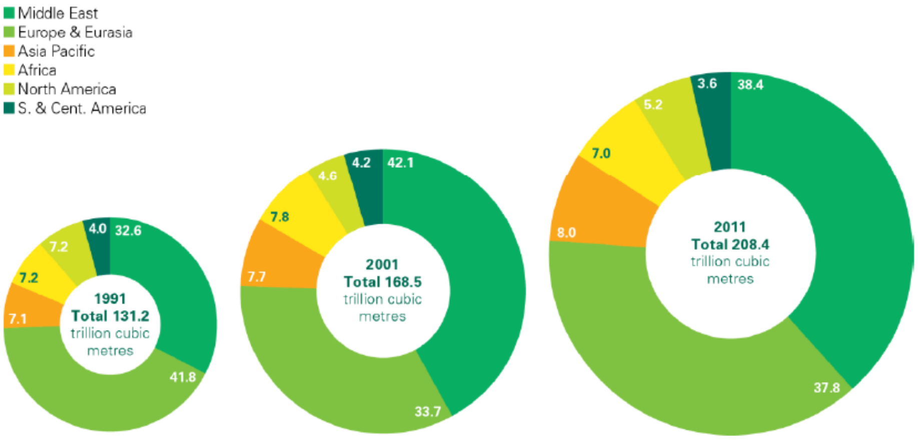

Figure 1- 1: Distribution of Proven Reserves of Natural Gas (BP, 2012)

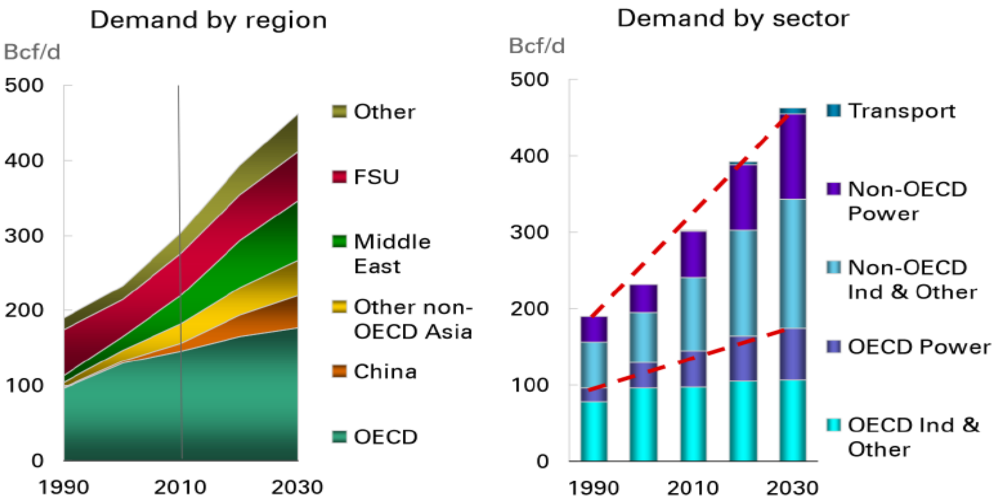

Figure 1- 2: Worldwide Gas Demand (BP, 2011)

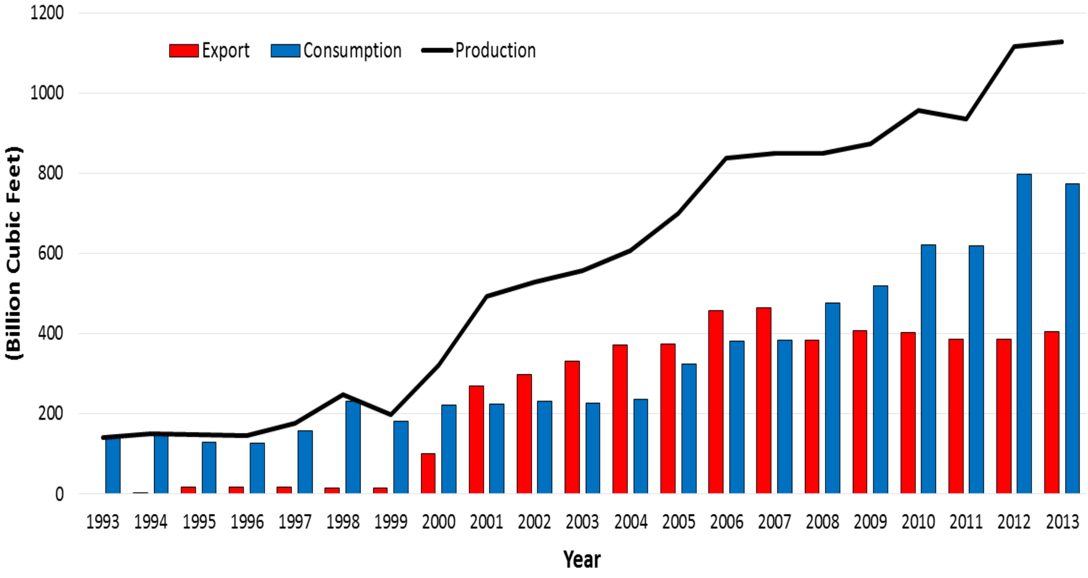

Figure 1- 3: Natural Gas Production and Consumption of Oman Based on Published Statistics by Energy Information Administration (Accessed on: 23/12/2015)

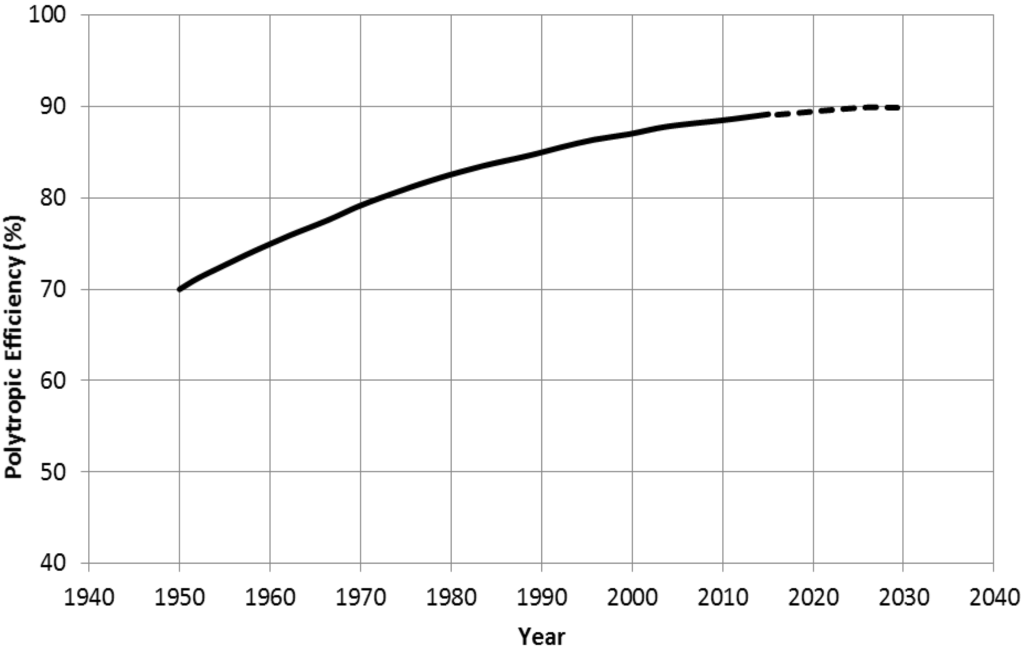

Figure 1- 4: Derived Centrifugal Compressor Efficiency Trend over the Years with Flow Coefficient Greater than 0.08 Based on Published Data by Sorokes et al. (2010)

Furthermore, this study will introduce an empirical one-dimensional design approach for the turboexpanders. This model becomes useful to generate different design options and to evaluate the proposed stage design based on aerothermodynamic evaluation.

1.2 Fundamentals of Natural Gas Classification

When the natural gas is dissolved in the oil in the reservoir, it is called “associated gas”. As the oil is extracted to the surface, the associated petroleum gas (APG) is separated from the crude oil prior the transmission of oil via pipeline. This process is performed in oil-gas separation plants (OGSP) which are often located near the drilling sites within the oil field. On the other hand, the non-associated gas is extracted from the reservoir without the link with other products. Therefore, this kind of fields is not constructed with the OGSP.

Natural gas (NG) is a mixture of various hydrocarbons which have different molecular weight values and with some acid gases. However, it frequently comes with impurities, and it is essential to remove them prior thermal decomposition process to meet the quality standards as shown in figure 1-5. Besides, the presence of these hydrocarbons with the natural gas can cause fire and explosion hazards in burners, and it might lead to pipe corrosion in the low areas. For the purpose of high-density storage and long-distance transport, the clean natural gas is liquefied to extract the hydrocarbon liquids from natural gas (NGL). There are two main methods are applied for NGL recovery, which are absorption and cryogenics process. For ethane-plus recovery applications, the cryogenic process can be considered as a more efficient process and it can recover up to 60-85% (Mehra and Thomas, 1999). The cryogenic process plants incorporate turboexpander as a source of refrigeration for the extraction of condensations from the natural gas with less energy demand.

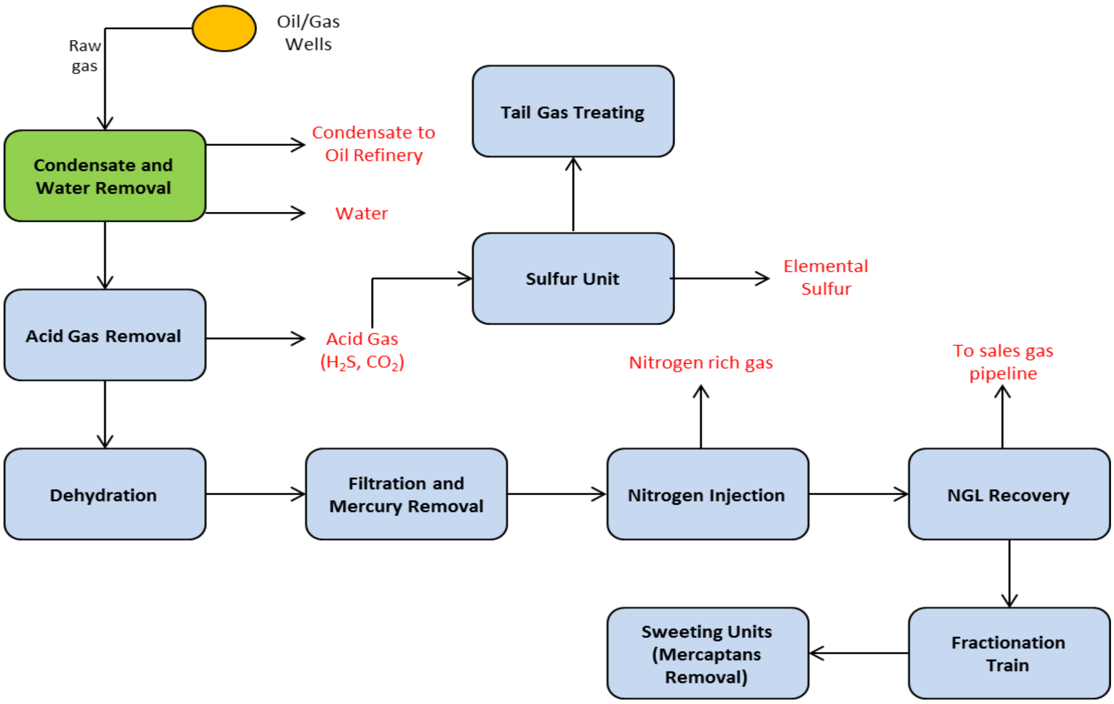

Figure 1- 5: Schematic Flow Diagram of Gas Processing Plant

Based on the amount of sulfur compounds in the natural gas, it can be also classified as sweet and sour gas as demonstrated in table 1-1.

Table 1- 1: Classification of Natural Gas (Rojey and Jaffret., 1997)

Category	**1**	**2**	**3**	**4**
Classification	sweet dry gas (non-associated)	sour dry gas (non-associated)	sweet wet gas (associated)	sour wet gas (associated)
Ethane and Higher Hydrocarbons (Volume %)	<15	<15	>15	>15
Hydrogen Sulfide (Volume %)	<0.5	>0.5	<0.5	>0.5
Carbon Dioxide (Volume %)	<2	>2	<2	>2

When selecting a gas compressor, it is important to determine whether it is a sweet or sour crude oil application since the compressors in sour gas services are manufactured from a different material to prevent sulfide stress cracking. Sour gas contains higher than 0.5% of hydrogen sulfide (H_2S). As this gas is a colorless, flammable and toxic gas; the excess H_2S must be separated from the sour gas before it can be utilized as shown in figure 1-5. There are different types of sweetening processes; however, the selection of the typical process is influenced by the concentration of H_2S, design flow rate, inlet gas inlet pressure and the requirement for sulfur recovery.

Based on the gas composition, the gas can be also categorized into wet and dry gas as shown in table 1-1. The wet gas contains less than 85% methane and a high percentage of liquid natural gasses (LNG's) such as ethane, propane and butane (U.S. Energy Development Corporation, 2013). However, this percentage of heavy hydrocarbons varies between 10-15% as there is no fixed measure to classify wet gas. These heavy hydrocarbons are condensed at a higher temperature, and they are separated and sold as individuals which are called NGL's (Natural Gas Liquids).

1.3 Anatomy of Turboexpander

The turboexpander is a radial reaction turbine, and it was initially used to replace a Joule-Thompson (JT) valve in order to enhance the overall efficiency of air separation plants (Byrne and Mariotti, 2010). The concept of using an expansion turbine for liquefaction of gases was introduced in 1898 instead of piston expander (Sixsmith, 1984). Nowadays, the turboexpander is used as a key component in a hydrocarbon gas separation plant for a more efficient ethylene recovery. Ghosh (2002) stated that the use of radial inflow expansion turbines added a fourth attractive feature to the cryogenic processing plants by improving the efficiency, reliability and operating range of the overall plant. This definitely affects the economic value of the process plants.

The turboexpander consists mainly of three fundamental components enclosed by the outer casing as illustrated in figure 1-6. Using the VIGVs is also essential to ensure a uniform inlet flow to the impeller leading edge by reducing the relative Mach number and flow incidence angle with minimal total pressure loss. The gas pressure is reduced through the inlet guide vanes, and it is used to accelerate the gas prior reaching to the rotor. The gas is then turned to the axial direction while it flows inward the impeller. This gas enters the rotor with a high relative velocity, and it forces the turbine impeller to rotate; thus, its velocity is reduced gradually. Consequently, the gas leaves the impeller at lower pressure and temperature due to the increase in the volume flow rate. However, less than about 10% of the gas energy remains when the gas reaches the impeller exit, and a part of it recovered in the diffuser. A portion of the liquid hydrocarbons condenses as it passes through the turboexpander, but they don't cause any damage to the turboexpander under normal operating conditions. The advantages and disadvantages of both configurations are shown in table 1-2.

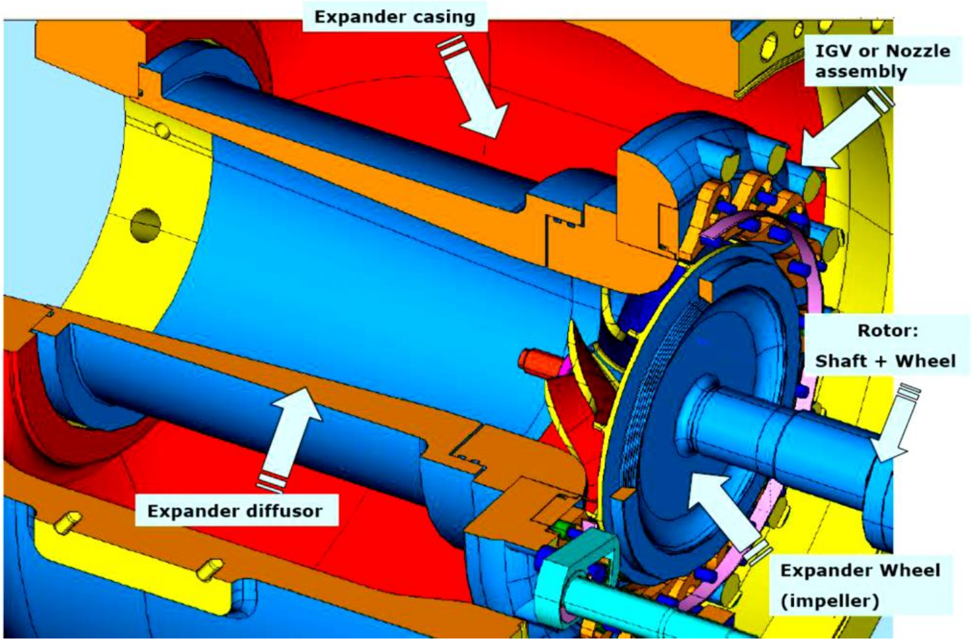

Figure 1- 6: Basic Turboexpander Components (Petrofac, 2009)

Table 1- 2: Comparison of Turboexpander Machinery Configurations (Based on: Byrne and Mariotti, 2010)

Configuration	Advantages	Disadvantages
Turboexpander-Generator	• High efficiency can be achieved since the rotating speed is changed freely without other machines constraints. • The re-compressor unit is designed independently from the turboexpander which allows merging more stages into a single machine with higher efficiency. • Simpler control system • A fixed speed machine can typically perform better in off-design condition when the enthalpy drop is maintained constant with process controls	• The machine tends to speed up in the case of electric load rejection. So, the maximum allowed tip speed of the wheel has to be limited. • More Tripping devices are needed for safety reasons. • The machine is typically more complicated than a turboexpander compressor due to the presence of a gearbox, generator, and other auxiliaries. • Cost per unit is higher and oil free solutions are not yet economically feasible.
Turboexpander-Compressor	• Very robust and simple machine. • Typical for oil free applications with the use of active magnetic bearings. • The stiff shaft design improves the operating range and the capability to withstand excessive imbalances. • The supplied labyrinth, seals and the pressurized auxiliaries system reduce the chance of gas leakage from the machine in case of failure. • The linked flow between the turboexpander and re-compressor reduces the size of required anti-surge systems.	• Efficiencies are sometimes lower than turboexpander-generator due to the mechanical limitations of both turboexpander and re-compressor. • At constant pressure ratio, the machine speed will reduce with the plant flow reduction but with a significant loss in efficiency. • The series arrangement of the units increases the complexity and tuning of the control system.

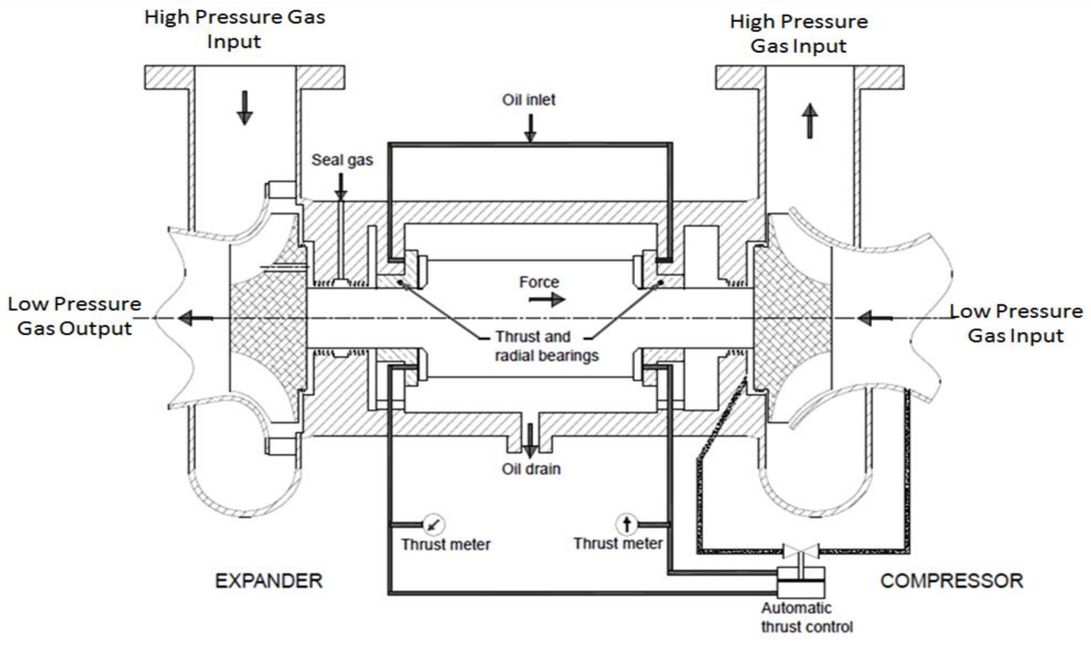

Figure 1- 7: Turboexpander-Compressor Cross Section (API617, 2002)

The generated mechanical power by gas expansion in the radial turbine can be recovered or dissipated in three main forms based on the required service:

- Electrical power through a reduction gear and a generator
- Mechanical drive via boost compressor coupling
- Dissipated through oil brake if it is not economical to convert the excess power.

The turboexpander-compressor machine consists of two basic components, which are the radial expansion turbine (power unit) and the centrifugal compressor (driven unit) connected on a single shaft as illustrated in figure 1-7. The high suction pressure of the natural gas stream is used to drive the turboexpander impeller, and the recovered work is used to drive the connected centrifugal compressor. As a result of work extraction, the gas pressure is reduced yields a lower the stream temperature.

The use of the turbo-expander has grown rapidly over the years due to the increased demand for higher ethane and propane recovery levels with low cost. This leads to improve the technology, design, and material selection with a broad range of flexibility. Although the isentropic efficiency of turboexpander alone can reach about 90%, the interaction with the coupled compressor has to be taken into account since the turboexpander efficiency is restricted by the mechanical limitations of each machine. Moreover, it should be noted that the location of this machine should be studied carefully in order to optimize the power generation potential and operating efficiency. However, there are other applications for turboexpanders such as:

- Energy extraction applications such as refrigeration.
- Recovery of power from high-pressure wellhead natural gas.
- Geothermal heat power cycles.
- Organic Rankine cycle (ORC).
- Freezing or condensing of impurities in gas streams.

1.4 Basic Components of Centrifugal Compressor

The centrifugal compressor is used widely in oil and gas industry to elevate the gas pressure for different purposes including upstream and midstream sectors such as LNG compression, pipeline compression, gas injection, gas lift, gas gathering and export compression (Rasmussen and Kurz, 2009). Unlike the axial compressor, the flow leaves the impeller radially due to the centrifugal and Coriolis forces within the impeller. The centrifugal compressor consists of three basic sections as illustrated in figure 1-8 which are inlet section, impeller section and diffuser section. When the gas enters the nozzle, it is accelerated by reducing the flow area and then, it is directed to the inlet section axially. In this section, the exit gas from the convergence nozzle flows toward the impeller eye, whereupon it meets the leading edge of the inducer blades. The inducer is essential to change the tangential motion of the fluid to radial direction to ensure a smooth inlet flow to the impeller section. The absence of inducer might lead to fluid separation and turbulent mixing near the leading edge of the impeller vane which in turn can be very noisy. In addition, the inlet section may consist of suction elbow and guide vanes prior the inducer to provide the working fluid with some degree of prerotation and to control the direction of the inlet inducer flow.

The impeller is a very critical component to achieve high operating efficiency over a wide flow range. The rotational speed of the impeller blades provides the required kinetic energy to the working fluid, and a part of this energy is converted to pressure. There are various geometries and types of impeller vanes and each has different performance characteristics. The fluid leaves the tip of the impeller at high velocity, and it is directed to the diffuser section where its velocity is reduced and its pressure increases. The gas then passes through the return channel to the inlet of the next impeller in the case of multi-stage compressor or to the volute if it is the last stage where a further increase in static pressure occurs.

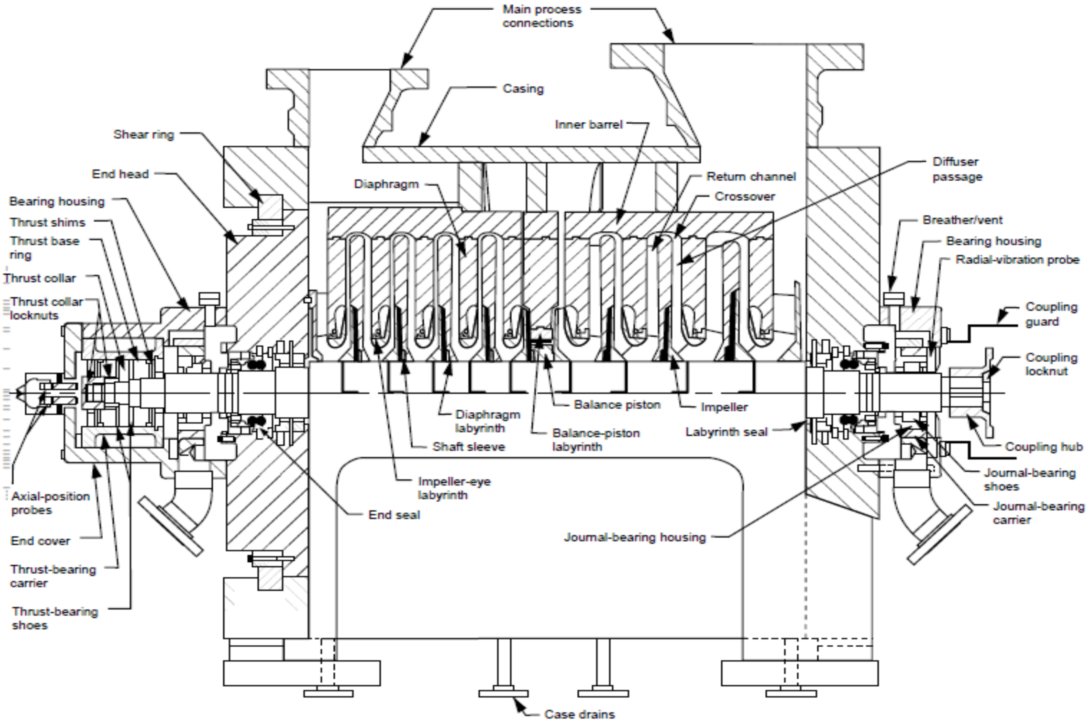

Figure 1- 8: Sectional view of centrifugal compressor schematic API617 (2002)

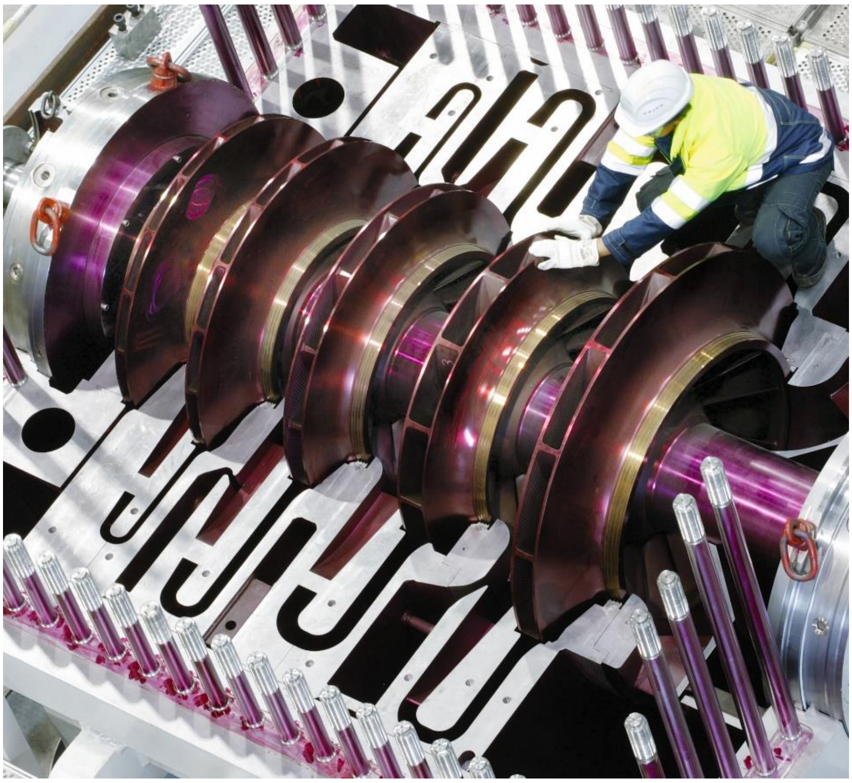

Figure 1- 9: Horizontal Split Centrifugal Compressor (Siemens, 2016)

There are several configurations for centrifugal compressor as will be explained later in this thesis. However, dealing with compressible fluids necessitates the need for different impeller sizes as shown in figure 1-9. Moreover, the large and complicated compression system makes the performance prediction of such machines quite difficult.

Furthermore, it is important to improve the system stability in order to avoid the high vibration at high rotational speed operation.

1.5 Research Methodology

As aforementioned, the main challenge of designing the turboexpanders and centrifugal compressors is to achieve both a broad operating range and to maintain high efficiencies throughout the operating envelope. Moreover, the variation in the suction parameters and operating circumstances makes the testing of the acceptability of any compressor unit to deal with these variables essential during the preliminary design stage. The performance of the new compressor has to be reliable and able to develop the required polytropic head at the expected efficiency within the stable region and by using the specified speed range and input shaft power. Furthermore, inefficient and unstable operating mode costs the user an enormous amount of money in the form of greater power consumption and lower gas production.

Thus, it is imperative to evaluate the design based on the environmental and operating conditions prior the construction process and to develop an approach for operation diagnosis of the aged units. Therefore, this study aims to assess the causes of inefficient and unstable operation of centrifugal compressors and turboexpanders and to propose a solution to avoid their catastrophic consequences.

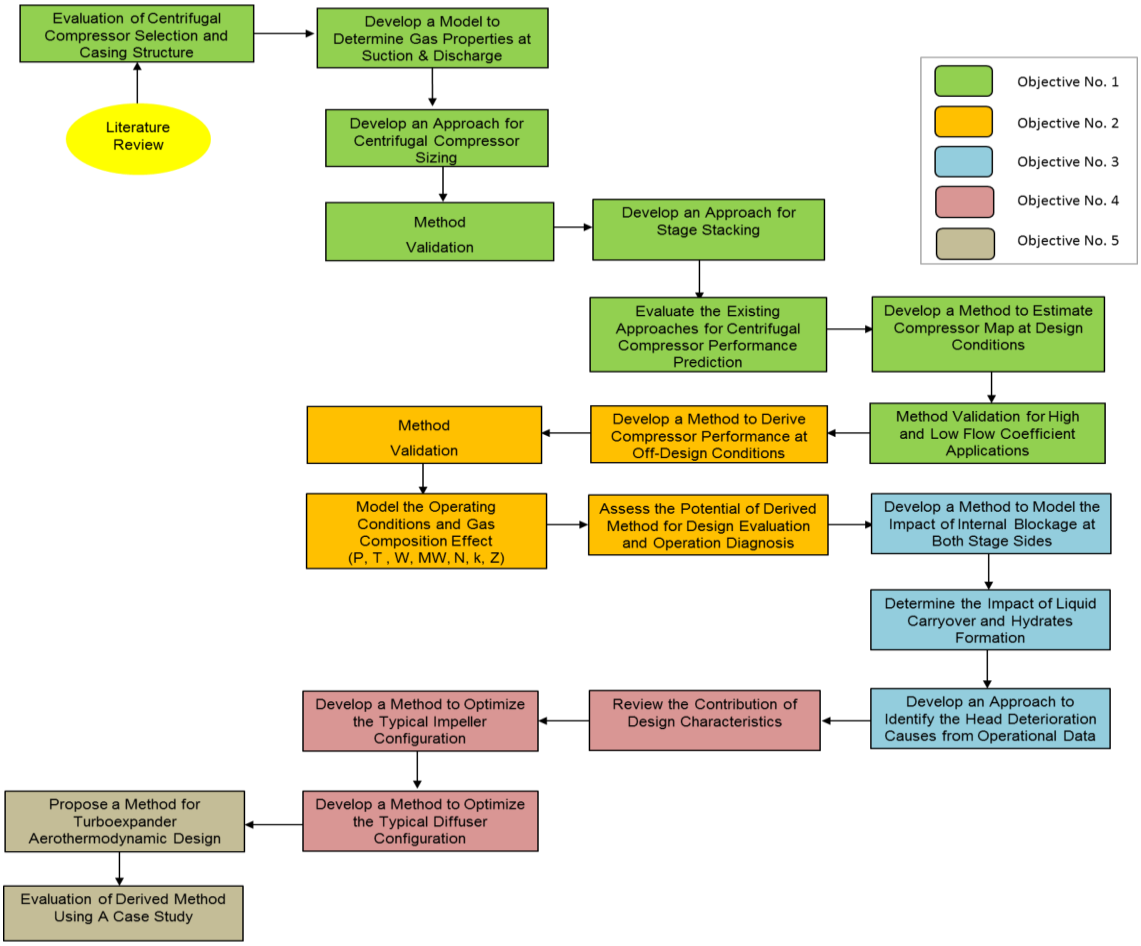

Figure 1- 10: Developed Methodology to Achieve the Research Aim

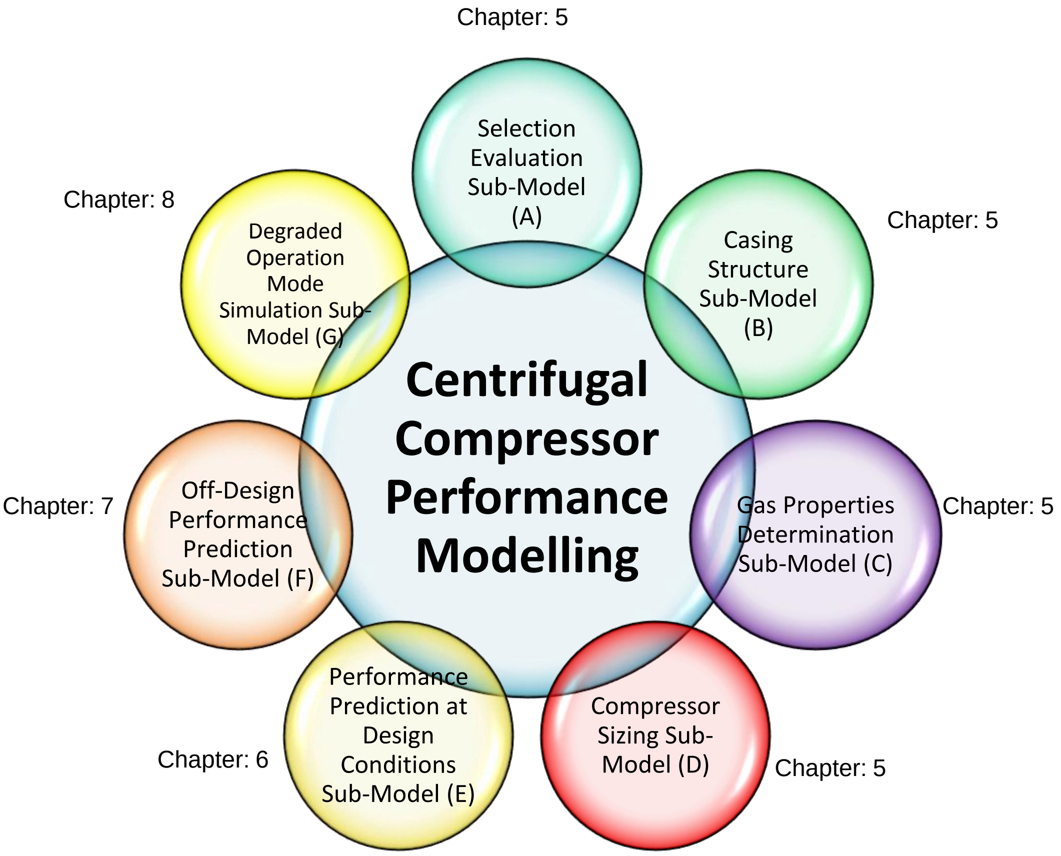

Figure 1- 11: Developed Integrated Model for Performance Prediction of Centrifugal Compressor

This will cover both the new and aged units, and it is expected to contribute in:

- Sustaining the gas throughput of production station by improving the machine efficiency and availability.
- Solving some of the existed operating issues related to the aerodynamic stability leading to reduce the downtime due to breakdowns and unnecessary overhauls.

To accomplish this aim, five main objectives have been specified as demonstrated in figure 1-10:

1. Construct and develop an integrated model for centrifugal compressor performance modelling at design conditions.

In order to predict the performance map of the multi-stage centrifugal compressor, an integrated approach has been developed to deal with the selection, sizing and aerothermodynamic modelling of designed centrifugal compressor unit as shown in figure 1-11. Based on the required duty, the selection of the centrifugal compressor is evaluated to consider the process requirements, initial capital cost, operation cost and logistics aspects. As the variation in the gas properties has a significant impact on compressor operation, a tool has been created namely “GasProp” to estimate the gas properties of each single mechanical stage throughout the compression process. The obtained properties are compared with the experimental measurements in order to check the uncertainty of the calculated values.

For more precise estimation, this study introduces a new method to predict the performance curve of multi-stage centrifugal compressor based on stage stacking technique. This method considers the advantages of two most recent available approaches in the literature to generate more accurate results. This model is incorporated with a unique sizing methodology to specify the optimum compressor structure. The developed model has been evaluated for both low and high flow coefficient applications, and the obtained parameters are compared with the existing methods results and measured data.

2. Derive a new methodology to predict the overall efficiency and operating range of a centrifugal compressor in order to model its performance at different off-design conditions.

Since the centrifugal compressor is designed to operate under various working conditions and different gas compositions, a new iterative method has been developed to predict the equivalent compressor performance at off-design conditions. This technique uses the performance parameters at design conditions as a reference point to derive the corresponding performance characteristics at various suction conditions with less dependency on the geometrical features. Unlike the correction method, one of the unique advantages of this model is the fact that it considers the variation in working fluid properties and stage efficiency to predict the new operating envelope. This method has been validated and tested to estimate the compressor performance at different operating modes. A parametric study has also been conducted to verify the suitability of this approach for the compressor design evaluation based on the expected variation in suction parameters and gas properties. Moreover, a case study is presented to emphasize the potential of this method for operation diagnosis of the installed units.

3. Develop an approach to assess the causes of inefficient and unstable operation of aged centrifugal compressor units.

As the centrifugal compressor is subjected to work under severe operating modes, this study proposes an approach to assess the causes of inefficient and unstable operation including the effect of flow blockage. This will contribute to identify the root causes of the abnormal performance by evaluating the obtained operational data from the monitoring system. In order to emphasize the validity of the new method, it has been qualified using four operation cases and the obtained results were compared with the discharge parameters and the observations from the stage overhauling process. Moreover, the conducted evaluation for the three phases of fouling has well defined the trends of flow, pressure and temperature in both normal and degraded operating modes. Besides, the influences of the non-reactive deposits have been compared with the effect of the unanticipated gas composition change.

4. Represent the opportunities of efficiency and operating range improvement of new centrifugal compressor units.

The high efficiency and the wide stable operating range are two fundamental criteria of the selected centrifugal compressor. Over the years, more advanced technologies and materials have been introduced in centrifugal compressor design to improve its full load and partload efficiencies and to maintain it over a wide operating range. However, the trade-off between these two features makes raising both parameters as challenging work. Thus, this research will review the options for efficiency and operating range improvement of new centrifugal compressor units. Besides, an empirical-based-model has been established to assess the typical impeller and diffuser configurations in order to make a compromise decision based on the required duty. This method has been examined at high and very low flow coefficients and Mach numbers operating conditions, and the obtained parameters are compared with the CFD simulation results and the recorded measured data.

5. Develop an approach for turboexpander design using N_s-D_s method and based on the aerothermodynamic parameters constraints.

This study introduced a simple and low cost tool to determine the optimum turboexpander design by evaluating the generated alternatives from an aerodynamic perspective. This method depends on the certain aerothermodynamic limitations to evaluate the available stage design. The physical properties have been estimated using the developed gas properties estimation tool (GasProp) while the thermodynamic properties are calculated by IPSEpro software. Moreover, the impact of flow and gas temperature variation was studied using the correction factors technique.

1.6 Thesis Structure

This study contributes in assessing and modelling the causes of inefficient and unstable operation of centrifugal compressor and turboexpander in order to provide a solution for performance enhancement. It also includes thermodynamic and flow evaluations to examine the options for efficiency and operating range enhancement of both new and aged units. The main outcomes of this study have been published in several research papers as shown in Appendix (A). In order to cover the basic elements of this research steadily, this thesis is organized into 12 chapters as following:

CHAPTER 1: This chapter introduces the research scope and the developed methodology to achieve the desired objectives. The significance of this research and thesis structure have been also summarized to highlight the contribution of this study. Moreover, the fundamentals of the natural gas classifications have been covered briefly to define some of the important concepts related to natural gas processing. Furthermore, this chapter describes the key components of centrifugal compressor and turboexpander and range of applications of such machines.

CHAPTER 2: Focusing on the centrifugal compressor, this chapter provides an insight into the aerodynamic and thermodynamic basics of the compression process. This includes a brief discussion of thermodynamic and physical gas properties, aerodynamic principles, major enthalpy losses and the key non-dimensional parameters which are used commonly to present the compressor performance.

CHAPTER 3: This chapter expounds the influences of aerodynamic instability on the compressor operation including stall and surge phenomena. Furthermore, it reviews the opportunities for efficiency and stable operating range enhancement. This includes a discussion of the numerical investigation findings and the experimental observation made on the centrifugal compressor performance. Besides, it outlines the development trend of the aerodynamic design of the centrifugal compressors components over the decades driven by the high stage efficiency and wide stable operating range.

CHAPTER 4: This part of the thesis describes the main methods to estimate the performance of the centrifugal compressor. The advantages and disadvantages of each capacity control method have been also demonstrated. Finally, a brief discussion of the significance of compressor fouling and the cleaning methods has been included.

CHAPTER 5: The purpose of this chapter is to derive an integrated scheme for the centrifugal compressor selection and sizing based on the process requirements. The developed approach is implemented to estimate the aero-thermodynamic performance of the simulated compressor based on some stated assumptions and by considering the thermodynamic and aerodynamic limitations. As the variation in the gas properties has a significant impact on compressor operation, a tool has been created namely "GasProp" to obtain the gas properties of each single mechanical stage throughout the compression process. In order to validate this approach, the obtained parameters are compared with the OEM estimated values and measured discharge parameters.

CHAPTER 6: This chapter outlines a new systematic method to predict the performance curve of the multi-stage centrifugal compressor based on stage stacking technique. First of all, Lüdtke and Casey-Robinson models are adapted to be valid for industrial centrifugal compressors, and the predicted characteristics are evaluated against measured data. Based on the conducted evaluation, a new model is derived from incorporating the advantages of both approaches with more accurate prediction. To emphasize the validity of the new method, it has been examined for high and low flow coefficients applications and the obtained parameters have been compared with the obtained results using the existing approaches and measured data.

CHAPTER 7: This chapter explores the centrifugal compressor performance under different off-design conditions. For this purpose, a new iterative method has been developed to predict the equivalent compressor performance at various suction conditions and gas compositions. This method has been qualified through two gas transport multi-stage centrifugal compressors, and the estimated characteristics are evaluated against the measured data. A parametric study has also been conducted to verify the validity of this approach for the compressor design evaluation based on the expected variation in suction parameters and physical gas properties. Furthermore, a case study is presented to emphasize the potential of this method for operation diagnosis of the installed units.

CHAPTER 8: This chapter aims to develop an approach to assess the inefficient and unstable operation by evaluating the possible causes of head deterioration in centrifugal compressor operation. In order to emphasize the validity of the new method, it has been used for two operation cases, and the obtained results were compared with the internal inspection findings from the stage overhauling process. This covers the effect of internal blockage, fouled aftercooler, multi-phase flow and hydrate formation. In addition, the impact of the non-reactive deposits on the stage performance has been also compared with the effect of the gas composition change.

CHAPTER 9: There are several factors influence the stage efficiency in the operating environment leading to a deterioration in the compressor efficiency. The determination of the root cause will help for a proper maintenance plan and to reduce the machine downtime. Accordingly, this chapter focuses on the possible causes of efficiency degradation and way of evaluating the contribution of each cause to the inefficient operation. The investigated case is a three-stage gas transport centrifugal compressor driven by 2.9 MW two-shaft gas turbine. Unlike the previous chapter, this compressor is running in the stable operating region but with a substantial drop in the efficiency. The outcomes from the conducted evaluation are compared with the measured discharge parameters and the findings from the internal inspection observation.

CHAPTER 10: This chapter evaluates the impact of design characteristics of centrifugal compressor aerodynamic components on stage efficiency and stable operating range. A new approach is derived to assess the typical shrouded percentage and blade exit angle of the impeller by compromising the effect on stage efficiency and stable operating range. Focusing on the geometrical parameters of the diffuser, an empirical method has been derived to evaluate the effect of diffuser characteristics on the static pressure recovery, energy parameters, stage efficiency, flow range and power loss cost.

CHAPTER 11: This chapter discusses the basics of turboexpander function, design, types and performance. Furthermore, one-dimensional design approach is introduced as a low cost tool to evaluate the optimum turboexpander design by evaluating the generated alternatives from an aerodynamic perspective. This method depends on the stated aerothermodynamic limitations to evaluate the available stage design. As the turboexpander is expected to run continuously at severe gas conditions, the performance of the selected turboexpander design is evaluated under different inlet flow rates and various gas temperatures.

CHAPTER 12: The last chapter of this thesis draws conclusions on the conducted work and summarizes the obtained results while succinctly stating the gap in knowledge which has been bridged. The chapter also ends with recommendations for future work.

CHAPTER 2: THERMODYNAMIC AND AERODYNAMIC FUNDAMENTALS OF COMPRESSION PROCESS

2.1 Ideal and Real Gas Laws

The ideal gas law estimates the change in the temperature and volume of the gas as a result of the compression process, and it can be written in a simple form as following.

$$Pv = RT \tag{2-1}$$

where:
P : Pressure
v : Specific volume
T : Absolute temperature
R : Gas constant which is a function of the gas molecular weight

Based on this equation and at constant gas volume, the absolute temperature of the gas increases proportionally with the pressure rise. Moreover, the change in the pressure is inversely proportional to the change in the gas volume if the gas temperature is held constant. However, this equation can be applied accurately only if the gas temperature is greater than the critical temperature while the gas pressure has to be lower than the critical value.

Despite that this equation is used for ideal gases merely, the actual change direction in any of these parameters is still the same as the ideal gas law implies. At the same time, all gases approach the ideal gas behavior at high elevated temperatures and very low pressures. For more accurate estimation of gas properties, the ideal gas law is modified by introducing a new empirical value which is called compressibility factor (Z). The compressibility factor (Z) can be defined as the ratio between the actual and ideal gas volumes (Savidge, 2000). So, the equation (2-1) is rewritten in a new expression to be used for all real gases.

$$Pv = ZRT \tag{2-2}$$

This equation can be considered as the basis of the most widely used approaches to estimate the compressor performance. As it is clear from the real gas law, it is important to calculate the compressibility factor (Z) in order to obtain the rest of gas properties. However, it can be said that still there is no universal method to determine this parameter, but the most common way is by using the generalized compressibility charts. These charts estimate the compressibility value with respect to the reduced pressure (P_r) and reduced temperature (T_r) for a pure gas or even hydrocarbon mixture. These two non-dimensional numbers can be derived by dividing the exact pressure and temperature by their corresponding critical values (P_{cr} , T_{cr}).

$$Z = f\ (P_r\ , T_r) = f\ \left(\frac{P}{P_{cr}}\ , \frac{T}{T_{cr}}\right) \tag{2-3}$$

The compressibility charts have been obtained based on the law of corresponding states. Thus, they can be used to obtain an approximated value to the actual behavior (Hanlon, 2001). As the compression ratio increases, the occupied volume by the real gas relative to the ideal gas volume decreases due to the molecular effects leading to a lower compressibility factor. In general, the amount of compression in the volume is governed by several factors including chemical components of the substance, pressure and temperature. However, the further increase in the pressure yields a reversal impact on the compressibility factor leading to higher values. This behavior refers to repulsive forces between the gas molecules so that at high elevated pressure values, these forces begin to dominate. This sort of behavior can be found in the most chemical components of natural gas mixtures including methane. Different behavior is shown in figure 2-1(b) which illustrates the compressibility factor of pure hydrogen at the same range of pressure and temperature.

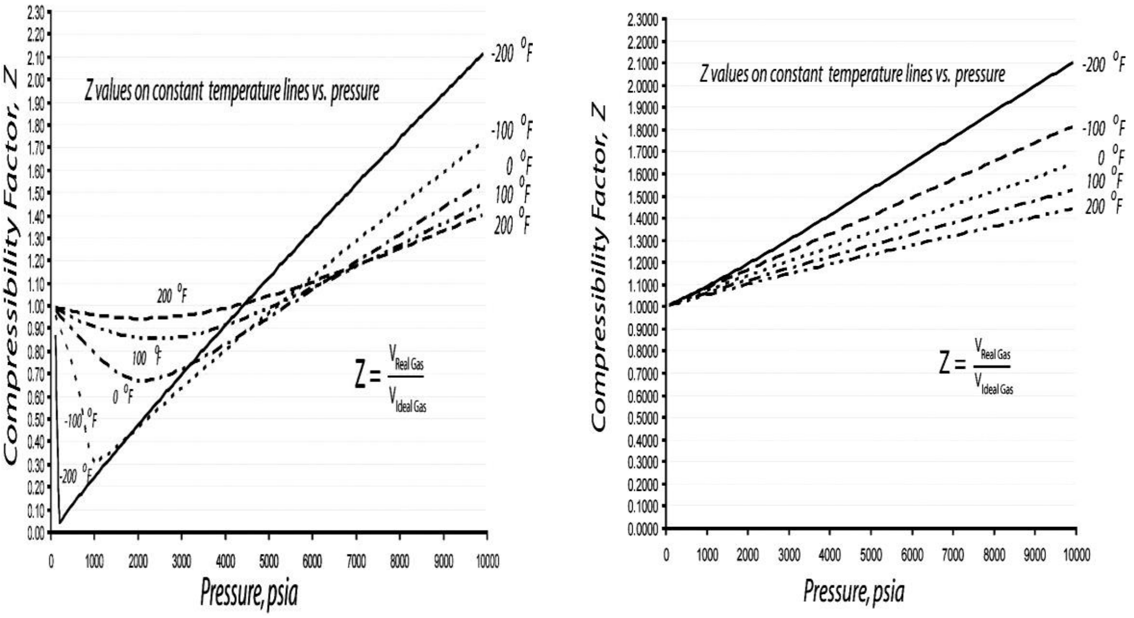

(a) Methane (CH_4) **(b) Hydrogen (H_2)**

Figure 2- 1: Compressibility Chart of CH_4 and H_2 (Savidge, 2000)

As the changes in the gas pressure, temperature and composition during the compression process lead to vary the Z factor and gas density, it is important to consider these changes throughout the gas compression process. In most cases, the compressibility factor is measured at the inlet and the outlet of the compressor, and the average value is taken.

Another way to predict the Z factor numerically is by using the equations of state (EOS). There are several equations of state available in the literature, but all of them are in the same classical form as Van der Waals equation of state. The ideal gas law assumes that the collisions between the gas molecules are perfectly elastic which is not in reality. The interaction forces cannot be neglected especially at low molar volumes or at high pressure. This equation has been modified by Van der Waals (1873) by taking into the consideration the molecular size and molecular interaction forces.

$$Z = \frac{v}{v - B} - \frac{A}{RTv} \tag{2-4}$$

where:

$A = \frac{27\,R^2T_{cr}^2}{64\,P_{cr}}$ $\qquad$ $B = \frac{RT_{cr}}{8P_{cr}}$

This form was modified further by Redlich and Kwong (1949), and a new cubic equation of state was introduced in a more complex form. This equation is the most widely used in the literature due to its simplicity and relatively accurate results comparing with the previous equation (2-4).

$$Z^3 - Z^2 - (B^2 + B - A)Z - AB = 0 \tag{2-5}$$

where:

$A = 0.42747\left[\frac{P_R}{{T_R}^{2.5}}\right]$ $\qquad$ $B = 0.08664\left[\frac{P_R}{T_R}\right]$

Soave (1972) expanded the dependency of the attractive parameter to be a function of temperature and molecules shape by introducing Pitzer's acentric factor (ω). This factor measures the deformity of the molecule, and this equation is known by Soave-Redlich-Kwong EOS.

$$Z^3 - Z^2 - (B^2 + B - A)Z - AB = 0 \tag{2-6}$$

where:

$A = \frac{0.42747P}{T^2}\left(\frac{{T_{cr}}^2}{P_{cr}}\right)\left[1 + (0.48 + 1.574\omega - 0.176\omega^2)\left(1 - \sqrt{\frac{T}{T_{cr}}}\right)\right]^2$ $\qquad$ $B = \frac{0.08664P}{T}\left(\frac{T_{cr}}{P_{cr}}\right)$

Another equation of state was developed by Peng-Robinson (1975).

$$Z^3 - (1 - B)Z^2 + (A - 2B - 3B^2)Z - (AB - B^2 - B^3) = 0 \tag{2-7}$$

where:

$A = \frac{0.45724 \propto P}{T^2}\left(\frac{{T_{cr}}^2}{P_{cr}}\right)$ $\qquad$ $B = \frac{0.0778P}{T}\left(\frac{T_{cr}}{P_{cr}}\right)$

However, there are other available equations in the literature which can be used to predict compressibility factor. These might be more accurate than the presented equations over a wider range of gases and conditions, but they are more complex such as Benedict-Webb-Rubin equation, Han-Starling equation and Lee-Kesler equation.

2.2 Thermodynamic Properties of Process Gas

There are three important concepts used frequently to describe the process in any thermo-system which are adiabatic, isentropic and polytropic processes.

$$Pv^n = constant \tag{2-8}$$

where:

$n = k$ for isentropic process (adiabatic and reversible)

$n = \frac{k}{k-1}\eta_p$ for polytropic process

Under ideal conditions, the compressor work is performed at constant entropy as demonstrated in figure 2-2. The isentropic efficiency can be written as a ratio between the isentropic work to the actual work. The adiabatic process also assumes that there is no heat transferred into or out of the control system.

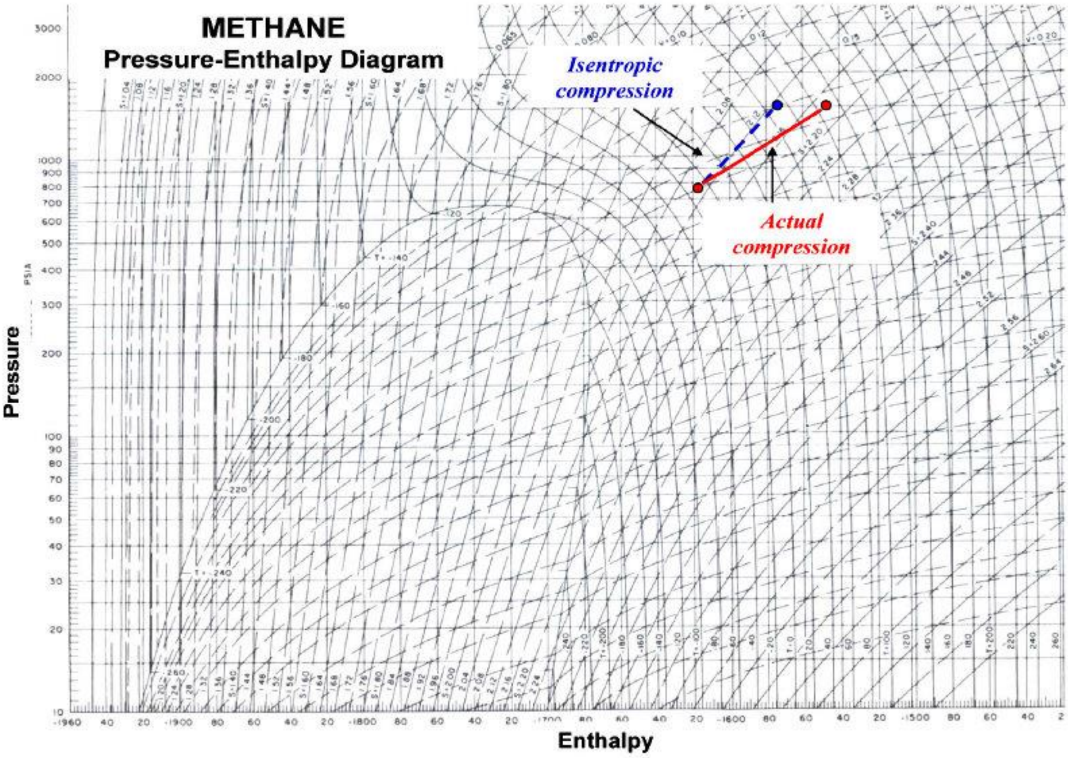

Figure 2- 2: Compression Process in a Mollier Diagram for Methane (Rasmussen, 2009)

Using the polytropic approach for the compressors has its advantages over the isentropic approach. The polytropic efficiency (η_p) is fixed and does not affected by the thermodynamic state of the compressed gas while the adiabatic efficiency (η_{ad}) is a function of the compression pressure ratio (PR) as can be seen from equations (2-9) and (2-10).

$$\eta_p = \frac{\frac{n}{n-1}}{\frac{k}{k-1}} \tag{2-9}$$

$$\eta_{ad} = \frac{PR^{(k-1)/k} - 1}{PR^{(n-1)/n} - 1} \tag{2-10}$$

One important factor which limits the stage compression ratio is the discharge temperature, and it should be kept under the maximum allowed value. The discharge temperature in both isentropic and polytropic processes is a function of the pressure ratio, suction temperature and process exponent.

$$T_2 = T_1 \left(\frac{P_2}{P_2}\right)^{(n-1)/n} = \frac{T_1 \left(\frac{P_2}{P_2}\right)^{(n-1)/n}}{\eta_{ad}} + T_1 \tag{2-11}$$

The isentropic head represents the required input energy to achieve the reversible (isentropic) compression process. Practically, the required input power (enthalpy) is relatively greater as shown in figure 2-2. The general head equation for polytropic process can be expressed as a function of inlet temperature, pressure ratio, compressibility factor and molecular weight as following:

$$H_{ad} = Z_{avg} \times \frac{8.314}{MW} T_1 \left(\frac{k}{k-1}\right) \left[PR^{(k-1)/k} - 1\right] \quad \textbf{(2-12)}$$

$$H_p = Z_{avg} \times \frac{8.314}{MW} T_1 \left(\frac{n}{n-1}\right) \left[PR^{(n-1)/n} - 1\right] \quad \textbf{(2-13)}$$

Thus, the required head for compression is increasing proportionally with the inlet temperature and compressibility factor and inversely with the molecular weight. The inlet and outlet pressures and temperatures are received from the process engineers, but the rest of parameters in equation (2-13) should be calculated. In general, the molecular weight tends to be constant throughout the compression process unless there is a formation of liquid knockout as a result of inter-stage cooling.

It should be noted that the above equation (2-13) is based on the assumption that the polytropic exponent (n) remains constant throughout the compression process. However, this is not always the case; thus, Shultz (1962) developed another model to compensate for this assumption by introducing a polytropic head correction factor (f).

$$H_p = f \times \left(\frac{n}{n-1}\right) \times (p_2 v_2 - p_1 v_1) \quad \textbf{(2-14)}$$

where:
f: Polytropic head correction factor
v: Specific volume considering isentropic process

This equation is recommended by ASME Power Test Code PTC10 (1997) which demonstrates the testing standards for compressors and exhausters.

2.3 Centrifugal Compressor System Analysis

The general principles of energy transfer in centrifugal compressor and turboexpander are governed by the basic thermodynamic equations: equation of state, conservation of energy, conservation of mass and conservation of momentum. In order to analyze the thermodynamics of centrifugal compressor, the stagnation properties will be used. These properties consider the kinetic energy of the flowing gas through the compressors which is important due to the very high velocities of gases encountered in centrifugal compressors. Figure 2-3(a) shows the *T-S* diagram of the centrifugal compressor. The gas enters the casing nozzle at inlet pressure and temperature of P_{00} and T_{00}, respectively. Due to the pressure loss in the inlet nozzle, the stagnation pressure will drop slightly to P_{01}. As the gas flows through the nozzle, the kinetic energy increases in the form of velocity rise as a result of static pressure drop which reaches to P_1 at the nozzle exit. The pressure drop in the inlet nozzle is denoted by $(P_{01} - P_1)$ in the isentropic process and by $(P_{00} - P_1)$ for polytropic process. However, the stagnation temperature is same in both isentropic and polytropic processes. The kinetic energy rise per mass unit of fluid is given by:

$$E_{K,0-1} = \frac{V_1^2}{2} - \frac{V_0^2}{2} \tag{2-15}$$

The gas then enters the impeller at condition “1” with an absolute velocity of V_1 and the isentropic and polytropic process in the impeller are indicated by (1-2) and (1-2′), respectively. The imposed kinetic energy by the impeller leads to increase the exit velocity of the process gas which reaches to V_2, as demonstrated in figure 2-3(b).

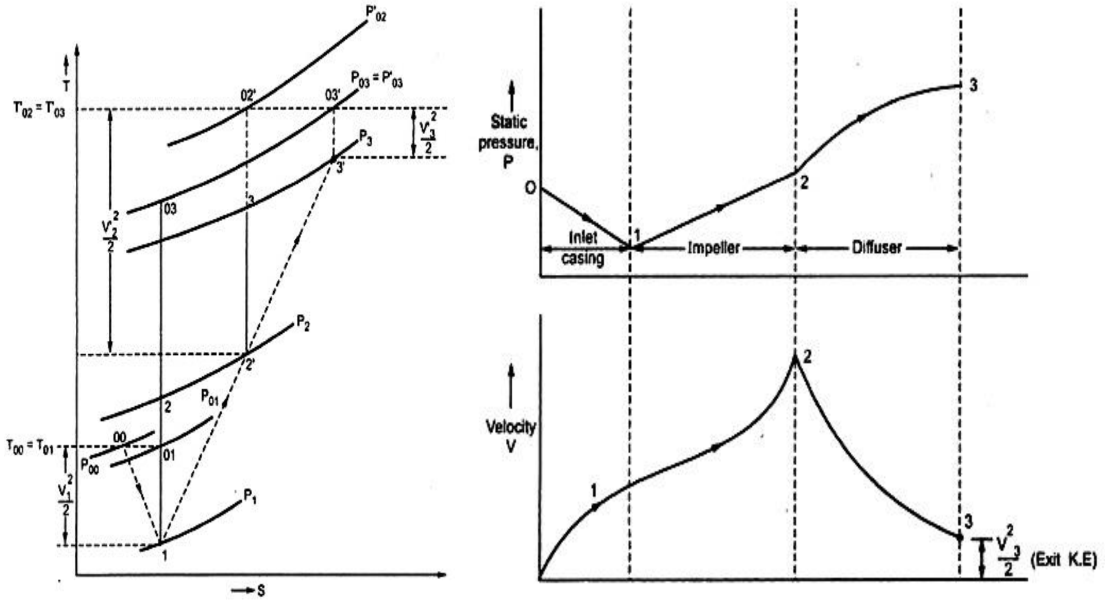

(a) (b)

Figure 2- 3: Variation in Aerodynamic and Thermodynamic Parameters: (a) T-S diagram for a Centrifugal Compressor (b) Static Pressure and Velocity in the Compressor Stage (Sable, 2006)

Furthermore, a part of the pressure rise is accomplished by the impeller while the remaining part is achieved in the diffuser. Comparing with the isentropic process, the discharge temperature at impeller exit is greater in the polytropic process. Hence, the provided work by the impeller is higher in this case at constant discharge pressure. The stagnation pressure at the impeller exit is P'_{02} while the stagnation temperature can be determined simply by adding the static temperature with the kinetic energy $\left(T'_{02} = T'_2 + \frac{V{\prime_2}^2}{2C_p}\right)$ as illustrated in figure 2-3(a). The actual process in the diffuser and volute is denoted by (2′-3′) while the isentropic process is represented by (2′-3). The deceleration in the compressor diffuser causes the gas pressure to increase to P_3 at the volute exit as shown in figure 2-3. At fully isentropic compression, the whole process from the impeller inlet to volute exit can be represented by a straight line (1-03). Despite that the exit pressure of both polytropic and isentropic processes are equal, the stagnation discharge temperature (T_{03}, and T_{03}) and enthalpy difference are greater in the polytropic process.

There are three common methods used to estimate the performance of centrifugal compressor which are: adiabatic method, N- method and Mollier method. The adiabatic method is used assuming that the compression process is a reversible adiabatic process (isentropic). So, that the power input is considered entirely converted to pressure energy without any heat loss. As it was discussed in section 2.2, the adiabatic process uses k exponent to derive the discharge conditions including the temperature and pressure and stage head as demonstrated in equation (2-11).

The N-method is named based on the polytropic exponent (n) which is used to calculate the polytrophic head and discharge temperature. The exponent value is derived from the k value and the polytropic efficiency as shown in equation (2-9). Unlike the adiabatic method, this process is variable entropy process so that the heat transfer can take place. However, the work input is same for both process whatever the method is used. The adiabatic approach is relatively simpler and quicker. On the other hand, using the N-method has two main advantages over the adiabatic method as aforementioned in the previous section. The polytropic approach is independent of the thermodynamic state of the compressed gas which is not the case in the adiabatic efficiency. The other advantage of using N-method is that the total polytropic head can be determined easily as the sum of each stage head which is not true for adiabatic head.

The third method uses a Mollier chart to calculate the head and discharge temperature, and it is primarily used for pure gases due to the availability of Mollier chart for such gases. However, the Mollier charts can also be constructed for gas mixtures if the diagram of each single compound is available. To calculate the adiabatic head, the inlet and exit enthalpies are used as shown in figure 2-2. The polytropic head is then derived by the ratio of polytropic and adiabatic efficiencies.

$$H_p = H_{ad}\left(\frac{\eta_p}{\eta_{ad}}\right) = (h_2 - h_1) \times \left(\frac{\eta_p}{\eta_{ad}}\right) \tag{2-16}$$

This approach is quite often used for side-load compressor where there is an additional gas injected through the intermediate nozzle after partial compression, so the mixture enthalpy has to be determined.

$$h_{mix} = \frac{m_1 h_2 + m_{SL} h_{2'}}{m_1 + m_{SL}} \tag{2-17}$$

where
m_1: Upstream section mass flow
h_2: Upstream section actual discharge enthalpy.
m_{SL}: Side-load mass flow
$h_{2'}$: Enthalpy of incoming side load

2.4 Aerodynamic Principles of Impellers

The impeller is responsible for imposing the whole required kinetic energy to the working fluid and for generating about 70% of the total stage pressure rise (Sorokes, 2013). Sable (2006) stated that an approximately the half of compressor pressure rise is achieved by the impeller in practice. The results of the experimental studies on the impeller flow demonstrate that the velocity distribution on the blade surfaces is different from the predicted flow profile theoretically (Boyce, 2003). This is actually due to the created secondary flows by the pressure losses and boundary layer separation in the impeller blade passages. The viscous shearing forces in the centrifugal impeller form a boundary layer when the kinetic energy is reduced. Hence, the reduced kinetic energy should be kept higher than a certain limit to avoid the stagnant and reverse flow.

2.4.1 Velocity Triangles

The gas enters the impeller vanes at the inlet diameter (D_1) axially with an absolute velocity of (V_1). The direction of the process gas is turned to radial direction when it approaches the impeller vane. The inlet velocity of the impeller leading edge is represented by (U_1) and the net velocity of both absolute gas and impeller tip velocities is called relative velocity W_1 (Vr_1 in figure 2-4).

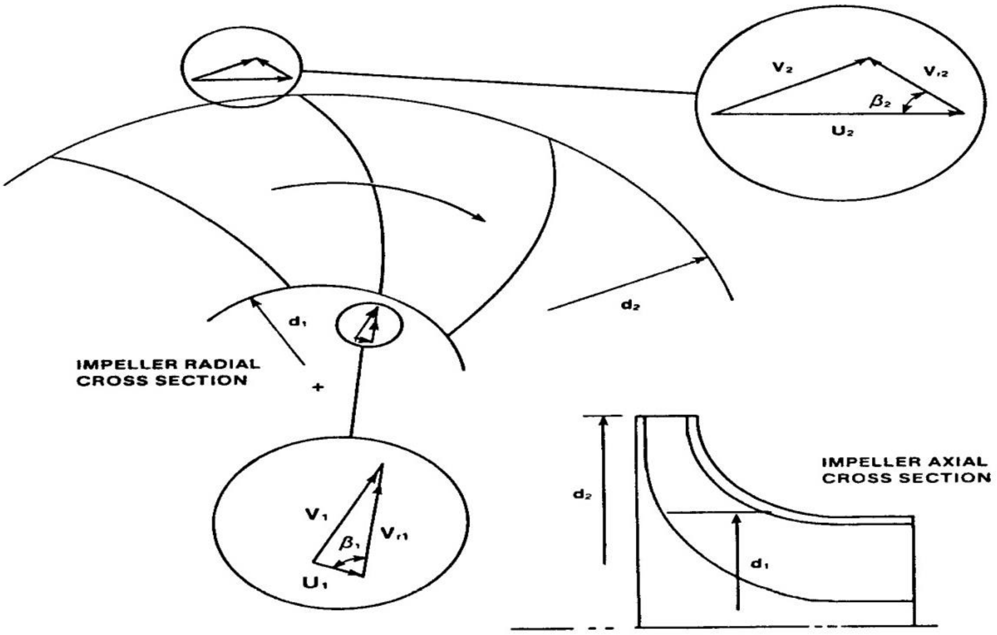

Figure 2- 4: Impeller Inlet and Exit Velocity Triangles (Brown, 2005)

The relative velocity is influenced by the inlet flow rate, rotational speed and impeller diameter. So, the increase in any of these parameters leads to raise the relative velocity. The theoretical amount of work that imported by the impeller (H) can be obtained using the basic Euler equation as a function of the inlet and exit velocities assuming simple one-dimensional flow theory.

$$H = U_1 V_{\theta 1} - U_2 V_{\theta 2} \tag{2-18}$$

2.4.2 Slip Factor (μ)

The flow at the impeller exit is not perfectly guided by the impeller blades so; the outlet flow angle does not exactly match the blade exit angle. This flow deviation is represented by "slip factor (μ)" and it can be defined as a ratio between the exit tangential absolute velocity ($V_{\theta 2}$) and the exit tip velocity (U_2).

$$\mu = \frac{V_{\theta 2}}{U_2} \tag{2-19}$$

Busemann (1928) proposed a unique slip factor prediction method by solving the inviscid flow field equations analytically. In this study, the maps of slip factor were generated as a function of impeller radius ratio, blade sweep angle and blade number. Unfortunately, this study did not give any correlation to obtain the slip factor; therefore, this method is very rarely used in the literature due to its complexity and dependency on figures. Stodola's theory (1927) assumes that the slip occurs as a result of relative eddy which is considered as a cylinder of fluid rotating with an angular velocity of (ω) about its own axis at the end of the blade passage.

$$\mu = 1 - \frac{\pi}{Z_b}\left[1 - \frac{\sin\beta_2}{\frac{V_{m2}}{U_2}\cot\beta_2}\right] \qquad \textbf{(2-20)}$$

Comparing with the experimental data, the obtained slip value using this equation was found lower than the experimental values. Stanitz (1952) developed a new equation based on inviscid flow numerical modeling. However, the predicted results using this equation agree well with the experimental data for radial blades.

$$\mu = 1 - \frac{0.63\pi}{Z_b}\left[1 - \frac{1}{\frac{W_{m2}}{U_2}\cot\beta_2}\right] \qquad \textbf{(2-21)}$$

Dixon (1998) recommended this equation for blade angle (β_2) less than 30° while he suggested Stodola equation for blade angle between 60° and 70°. At recommended range of the blade angle, the Stodola and Stanitz results are close to the Busemann results as demonstrated in figure 2-5(a) for blades number higher than 8.

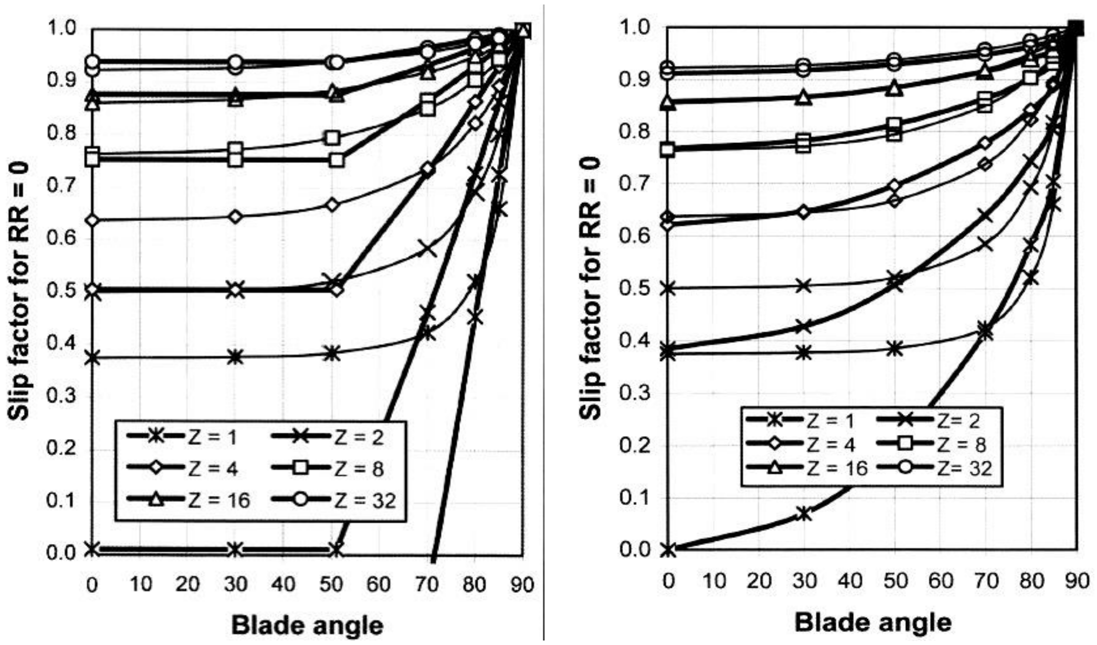

(a) **(b)**

Figure 2- 5: Stanitz-Stodola Slip Factor (a) and Wiesner Slip Factor (b) Compared to Busemann Results (Von Backström, 2006)

However, both these two models don't consider the radius ratio. Wiesner (1967) proposed an empirical equation for slip factor, but it is valid only for radius ratio less than a particular value.

$$\mu = 1 - \frac{\sqrt{\cos\beta_2}}{{Z_b}^{0.7}} \qquad \textbf{(2-22)}$$

Figure 2-5(b) compares between the obtained results by Wiesner model (Eqn. 2-22) with the derived data by Busemann (1928) at radius ratio less than the maximum limit. There is a good agreement for higher than 16 blades impeller for blade angle less than 80°, but it is hard to find a contiguous region of a very good matching.

Von Backström (2006) has recently derived a new method to determine the slip factor, which is known by single relative eddy (SRE) method.

$$\mu = 1 - \frac{1}{1 + \left[(2 + 3\cos\beta_2)\frac{(1-RR)\,Z_b}{2\pi\,(cos\beta_2)}\right]} \qquad \textbf{(2-23)}$$

where: *RR* is radius ratio, and it is taken as 0.5 when RR < 0.5.

The SRE approach matches the analytical method of Busemann very well, and the predicted values are close to the experimental slip factors over a broad range as the method of Wiesner.

2.5 Aerodynamic Loss in Centrifugal Compressor Stages

There are different sources of losses in the centrifugal compressor and their contribution to the overall performance is fluctuated over the operating range. Figure 2-6 demonstrates the variation in the summation of aerodynamic losses with flow rate as a ratio of design mass flow. However, the determination of these losses is quite complicated since they are a function of different parameters such as inlet conditions, pressure ratio, flow rate and blade angle.

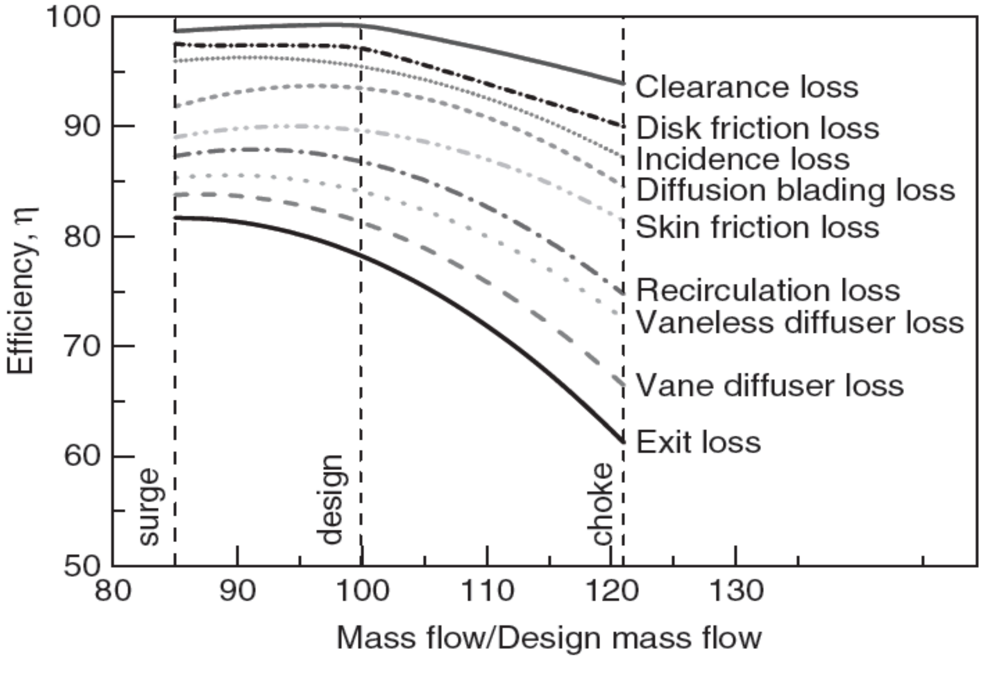

Figure 2- 6: Sum of Losses in Centrifugal Compressor (Holloway et al., 2012)

Hence, this section will describe the developed models to estimate some of the critical aerodynamic losses in a centrifugal compressor.

2.5.1 Disc Friction Loss

This type of losses is induced due to the adhesive forces between the rotating disk and the surrounding fluid. When the disc is rotating in a fluid, there is a resistive torque induced on the back surface of the impeller, and a part of the input power is used to overcome the friction of the external surfaces of rotating impeller. Several researches were conducted to estimate this disc power based on the resistive power of plane disc enclosed in casings such as Daily and Nece (1960). Shepherd (1956) developed a new model to estimate the enthalpy drop of centrifugal compressors as a result of disc friction (Δh_{df}).

$$\Delta h_{df} = K_{df}\ \frac{(\rho_1 + \rho_2) D_2^2 U_2^3}{2\dot{m} Re^{0.2}} \tag{2-24}$$

$$\text{where: } K_{df} = \begin{Bmatrix} \frac{2.67}{Re_2^{0.5}} & \text{for } Re_2 < 3 \times 10^5 \\ \frac{0.0622}{Re_2^{0.2}} & \text{for } Re_2 \geq 3 \times 10^5 \end{Bmatrix}$$

Based on equation (2-24), the disc friction loss is influenced by the speed difference between the disc and fluid and by the contact area size as well (exit impeller radius). Thus, this loss increases with the rise in rotational speed and impeller exit radius.

2.5.2 Leakage Loss

Another source of enthalpy drop in the centrifugal compressor is the secondary flow. As a result of pressure gradient throughout the compression process, a part of the main stream tends to leak to the suction side through the clearance gap and labyrinth seals causing the leakage loss. Aungier's model (1995) is used to predict the enthalpy loss due to the flow leakage (Δh_{leak}) which includes the disk/housing gap for covered impellers and the blade/housing gap for open impellers.

$$\Delta h_{leak} = \frac{\dot{m}_{cl} \times\ U_{cl} \times U_2}{2\dot{m}} \tag{2-25}$$

2.5.3 Diffuser Losses

Stanitz (1952) conducted one-dimensional analysis for the vaneless space loss (Δh_{vls}) assuming a compressible flow with friction and heat transfer but without considering the mixing losses. However, the primary cause of this loss is the fluid friction with the diffuser surface so that the higher flow velocity or the longer flow surface leads to greater loss.

$$\Delta h_{vls} = C_p T_{02}\left[\left(\frac{P_3}{P_{03}}\right)^{(\gamma-1)/\gamma} - \left(\frac{P_3}{P_{02}}\right)^{(\gamma-1)/\gamma}\right] \tag{2-26}$$

Although that the increase in the exit diffuser radius reduces the flow velocity, it also yields a higher flow length which is one of the contributed factors to the diffuser loss.

2.5.4 Recirculation Loss

The recirculation loss is associated with the work done to overcome the backflow into the impeller section when the flow leaves the impeller at a large absolute flow angle from the meridional direction. Oh (1997) developed a correlation to calculate the recirculation loss as a function of the flow angle (equation 2-27). This model has been derived based on the Coppage' model (1956) which is also a function of the same parameters as equation (2-28) demonstrates.

$$\Delta h_{rc} = 8 \times 10^{-5}\, sinch\, (3.5\alpha_2^3)\, D_f^2 {U_2}^2 \tag{2-27}$$

$$\Delta h_{rc} = 0.02 \sqrt{tan\, \alpha_2}\;\, D_f^2 {U_2}^2 \tag{2-28}$$

where:
Δh_{rc}: Enthalpy drop due to recirculation loss
D_f: Diffusion factor

The absolute exit flow angle (α_2) has a significant proportional impact on the recirculation loss. This angle can be minimized by either raising the inlet flow or by reducing the rotational speed.

2.5.5 Incidence Loss

The deviation between the relative inlet angle of the gas and the actual blade angle pushes the gas to change its direction. Consequently, this creates an incidence loss and it might lead to a significant drop in the input energy, and it raises as the difference between the two inlet angles increases. However, this loss can be minimised through the entire operating range by installing the VIGVs to ensure that the flow angle is corresponding to the blade angle over a wide range of flow rates.

Different models have been developed to calculate the incidence losses. Oh (1997) concluded that the Conrad model (1980) yields the most accurate results for the incidence loss. According to Oh study (1997), the incidence loss is resulted from the change in momentum due to the blade thickness and the deflection in the blades direction.

$$\Delta h_{inc} = f_{inc} \frac{W_{\theta i}^2}{2} \tag{2-29}$$

where:
Δh_{inc}: Enthalpy drop due to incidence loss
f_{inc}: Energy loss coefficient
W_{ui}: Tangential difference between ideal and actual relative inlet flow

Although that the energy loss coefficient is obtained experimentally, Conrad et al. (1980) suggested using a value between 0.5 and 0.7.

2.5.6 Blade Loading Loss

Boundary layer growth on the blade surfaces basically depends on the diffusion of the internal working fluid to the impeller. This leads to momentum loss and it is represented by blade loading loss.

$$\Delta h_{bld} = 0.05\;\, D_f^2 {U_2}^2 \tag{2-30}$$

Coppage et al. model (1956) demonstrated that the blade loading loss is a function of the diffusion factor and the tangential impeller velocity. Based on this model, the blade loading can be reduced by increasing the relative flow velocity. This, in fact, can be accomplished either by increasing the impeller rotational speed or by increasing the flow rate.

2.6 Dimensionless Parameters

The behavior of centrifugal compressor can be characterized in terms of dimensionless quantities. One main advantage of using this way of representation is to define the compressor performance in more general form with disregard of actual machine dimensions and the real operating conditions. The group of dimensionless quantities which used to describe the characteristics of the centrifugal compressor can be specified by Buckingham's theorem, and this section will discuss the most common parameters.

2.6.1 Flow Coefficient

The flow coefficient (φ) is the ratio of the actual volumetric flow rate ($\dot{V}$) and the hypothetical flow rate which passes through a pipe with a diameter (D) and velocity (U); thus, it is always well below unity for centrifugal compressor.

$$\varphi = \frac{\dot{V}}{\frac{\pi}{4}\, D^2 U} \tag{2-31}$$

Typically, the flow coefficient measures the flow handling capability of the centrifugal compressor which directly varies with the tip speed and the square of the impeller diameter. Therefore, it is a critical parameter to determine the impeller geometry and configuration. The global flow coefficient is usually used to describe the overall stage performance as a correlation between the inlet volume flow rate ($\dot{V}_1$) and the exit impeller diameter (D_2) and tip speed (U_2).

2.6.2 Head Coefficient (ψ_h)

The head coefficient (ψ_h) is dimensionless parameter which measures the actual developed head (H_p) with relative to the maximum theoretical value at zero flow and specified impeller tip speed. Theoretically, the maximum head is obtained with radial inlet impellers at zero tangential inlet velocity component and it equals to ($\mathrm{U}^2/2g$). The deviation from the maximum head value is increasing due to the eddy and separation losses at the inlet and exit of the impeller.

$$\psi_h = \frac{H_p}{(U^2/2g)} \tag{2-32}$$

The head coefficient is also called pressure coefficient. In multi-stage machines, the developed polytropic head can be considered for the entire compressor while the tip speed can be related to either the first stage for suction conditions or to the last stage for the discharge conditions.

$$\psi_w = \frac{\psi_h}{2\eta_p} \tag{2-33}$$

The work coefficient (ψ_w) is obtained by dividing the head coefficient (ψ_h) by the polytropic efficiency (η_p). This measures the developed work by the impeller as the ratio between the enthalpy rise through the compression process to the square of the tip speed.

2.6.3 Tip Speed Mach Number (*Mu*)

The Mach number (*Mu*) represents the ratio between the compressor tip speed (U) and the speed of sound (a) at the reference conditions. This parameter is usually calculated at the inlet and outlet of the compressor due to the variation in sonic speed. Besides, the global Mach number can be used to describe the stage performance as a relation between the exit tip speed and the inlet speed of sound.

$$Mu = \frac{U}{a} = \frac{U}{\sqrt{kRTZ}} \tag{2-34}$$

Approaching sonic velocity leads to high shock losses in the flow channel which might cause a compressor choke. Based on equation (2-34), the speed of sound is expected to be low at the compressor inlet due to the low inlet temperature. Furthermore, the Mach number is responsible for the gas compressibility as the high Mach number leads to greater variation in the gas density. Additionally, the greater Mach number raises the stage pressure ratio due to higher generated kinetic energy by the impeller and the increased pressure recovery in the diffuser. However, the large associated losses at high Mach number value reduces the stable flow range and stage efficiency (peak and part-load).

2.6.4 Reynolds Number (Re)

Another non-dimensional parameter which used to describe the centrifugal compressor characteristics is Reynolds number (Re). In a simplified form, it is defined as the ratio between inertial forces and viscous forces at reference conditions.

$$Re = \frac{U \times D}{(\mu/\rho)} \tag{2-35}$$

This parameter is used to characterize different fluid regimes such as laminar and turbulent fluid. The laminar flow occurs at low Reynolds number where the viscous forces are dominant. On the other hand, the fluid is described by turbulent when the inertial forces are dominant, and high separation and vortices are taking place. Besides, the machine Reynolds number is also responsible for the friction at the compressor flow channel in addition to the relative surface roughness.

CHAPTER 3: REVIEW OF EFFICIENCY AND STABLE OPERATING RANGE ENHANCEMENTS OPTIONS OF CENTRIFUGAL COMPRESSORS

This chapter demonstrates the influence of compressor aerodynamic instability on the performance parameters of centrifugal compressors. Besides, it outlines the development trend of the aerodynamic design over the decades driven by high stage efficiency and wide stable operating range. This will contribute to review the options for efficiency and operating range enhancements of new centrifugal compressor units. The conducted discussion covers the numerical investigation findings and the experimental observations made on the centrifugal compressor performance.

3.1 Aerodynamic Instability in Centrifugal Compressors

3.1.1 Surge Phenomenon

There are two kinds of stability related to the radial compressor performance which are operational stability and aerodynamic stability. The operational stability is associated with the performance characteristics matching between the compressor and the downstream system. On the other hand, the aerodynamic stability is concerned with the steady state operation. The operating envelope of the centrifugal compressor is bounded by two lines as illustrated in figure 3-1. At very low flow conditions, the generated pressure will not be sufficient to deliver a continuous flow to the downstream system which results in intense flow oscillation and pressure fluctuation.

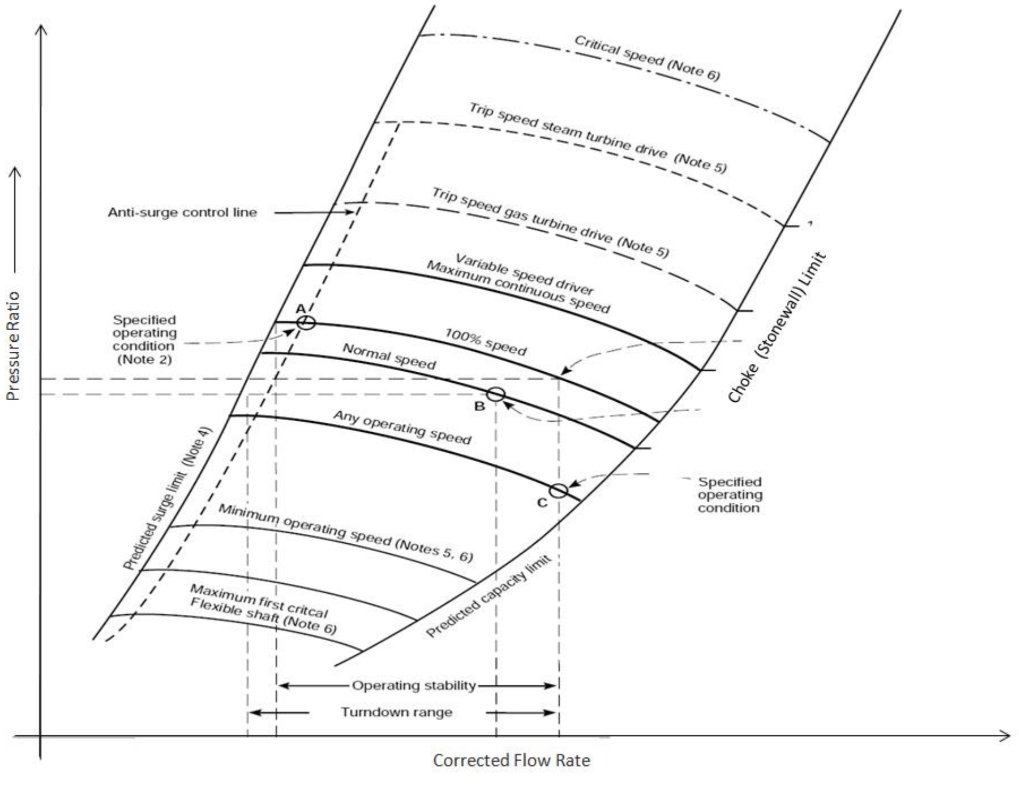

Figure 3- 1: Centrifugal Compressor Performance Map-Modified (API617, 2002)

The flow reversal and separation disturb the circumferential flow pattern and lead to increase the incidence angle of the impeller blade excessively. In consequence, this blade will stall, and it will not be able to produce an adequate pressure rise to maintain the sufficient flow around its geometry. Consequently, this will lead to form an effective flow blockage or reduced flow zone as shown in figure 3-2. By rotating this stalled blade, the breakdown flow will divert the flow around the blade and, in turn, increases the incidence angle of the neighboring blade while it is decreased for the above blade. Therefore, the blades below the retarded flow zone are expected to stall while the above blades are not. The stall is propagating in the direction of impeller rotation with a speed of 40-75% of rotor speed, so they might cover one or more adjacent blades (Boyce, 2003).

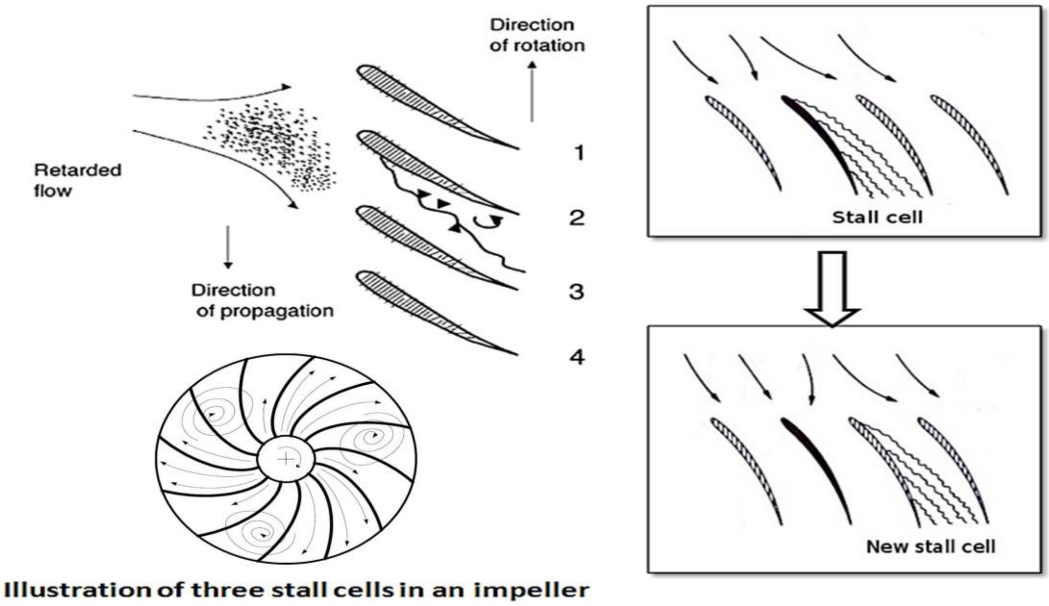

Figure 3- 2: Incidence and Stall Propagation in Centrifugal Compressor Blades- (Adapted from: Boyce, 2003 and Helvoirt, 2007)

All the compressor components may run into stall conditions including the impeller, diffuser and volute, particularly at the positive pressure gradient. The stall in one of these parts not necessary causes the whole a stage instability, but a strong stall in one or more of stage elements is enough to cause a stall in the pertinent stage. As a result of flow distortion, the rotating stall deteriorates the performance and efficiency of centrifugal compressor significantly (De Jager, 1995). Also, the stall cells reduce or completely block the flow channel which excites the resonant frequency of the inducer and resulted in high thermal and mechanical loads on the compressor components. Upon the rotating stall initiation, the stall cell rotates circumferentially. In surge, the entire compression system performance becomes unstable and the mass flow rate oscillates violently. Ljevar (2007) investigated the stall characteristics in a vaneless diffuser. Moreover, Paduano et al. (2001) explained the rotating stall from a system stability perspective. It is important to mention here that it is difficult to determine where the stall initiated at the beginning. However, it was found in the most of the recorded cases of low-pressure compressors that the stall starts at the diffuser part while it initiates in the inducer for a single stage centrifugal compressor with a pressure ratio higher than 3.0 (Boyce, 2003).

The conducted studies in the centrifugal compressors stall are significantly less than those of axial compressors. The surge phenomenon is not fully understood, but extensive investigations have been carried out in order to avoid the resulted catastrophic failure of the compressor. When this stall spread to the entire compressor stage, the compressor starts to surge. The surge is a periodic and unstable phenomenon; and due to its unsteadiness, it affects the whole compression system. In general, the experimental evidence shows that the stall is responsible for the flow pattern distortion, and in some cases it leads to high mechanical and thermal stresses on the internal components. Additionally, the following impacts were observed in the previous studies:

- A large drop in compressor performance and efficiency (De Jager, 1995)
- A gradual or abrupt reduction in the pressure ratio (Helvoirt, 2007)
- Hysteresis into the system (Greitzer, 1981).

Emmons (1955) detected the rotating stall at two different flow rates during constant speed operation. That was not observed at all speed lines as shown in figure 3-3. However, it is noticed that the compressor operation was stable between these two surge points, but the turbulence level becomes intensive prior the violent surge. It is important to mention here that the surge can also occur as a result of speed increase at constant flow rate. The mild surge is accompanied with slight oscillation and without any net back-flow. By looking to the surge cycle, it was an important observation that the reduction in pressure ratio relative to the value before the surge is followed by a period of recovery which pulls the compressor again to the stable state. So, if there is no change in the downstream parameters, perhaps the surge cycle is repeating itself. Besides, the surge has a significant effect on the blade vibration which creates a fluctuated stress on the impeller blade in respond to the static pressure characteristics which in turn has an impact on the fatigue life. However, the inducer stall can be detected using two ways. The first method is by measuring the inlet temperature at the inducer tip using thermocouples. The other way is less common, and it depends on the observation of the change in static pressure near the shroud.

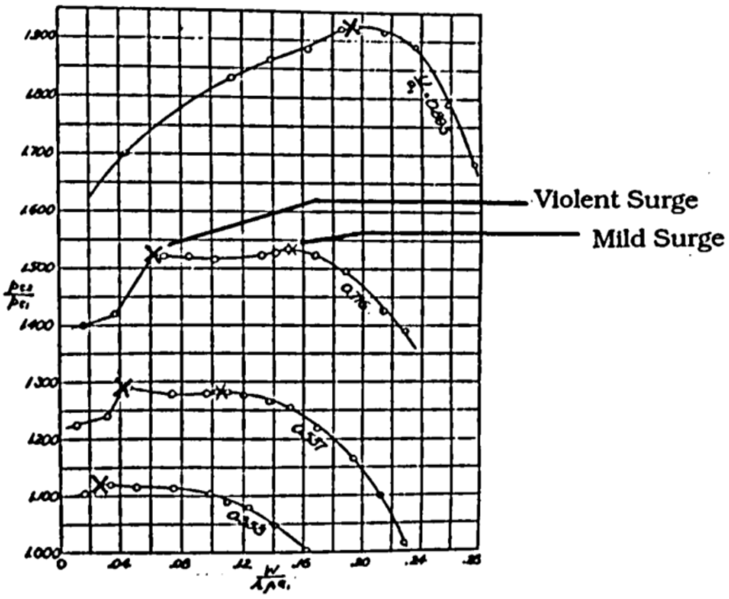

Figure 3- 3: Two Surge Points on Same Constant Speed Running Line of Centrifugal Compressor (Emmons, 1955)

The compressor is designed to work at operating line, and it is separated from surge line by a safety margin as shown in figure 3-1. However, it is important to mention here that the term “surge margin (SM) in this thesis refers to the deviation of the design flow coefficient from the surge flow coefficient as indicated in equation (3-1).

$$\mathrm{SM} = \frac{\varphi_d - \varphi_{surge}}{\varphi_d} \tag{3-1}$$

The surge line in performance curve separates the stable and unstable operating regions. In many cases, the surge can be indicated by excessive vibration and an audible sound but not always. In addition to the loss of performance and efficiency, the surge also excites the impeller and diffuser vanes and causes severe mechanical damages to the internal components of the centrifugal compressor and the connected piping systems due to the thrust reversal. Besides, it is essential to provide a proper anti-surge control system to avoid running at these conditions.

3.1.2 Operating at Choke

From the aerodynamic standpoint, the choke phenomenon is referring to the situation where flow passages (impeller inlet or diffuser vane inlet) are blocked due to the compression shocks or massive flow separation. In theory, the compressor runs in stonewall when the Mach number equals one at which the flow passage is choked, and no more flow can be passed. To avoid this, the inlet Mach number at deign point is limited to be less than 0.90. When Mach number is unity, the ratio of static temperature to total temperature can be obtained using equation (3-2).

$$\frac{T}{T_0} = \frac{2}{k+1} \tag{3-2}$$

As the machine inlet Mach number increases, the choke flow decreases while the surge point moves to lower flow regions. For the compressor inlet and by assuming an isentropic flow, the choking mass flow rate per unit area can be expressed purely as a function of inlet stagnation density (ρ_0) and speed of sound (a_0).

$$\frac{\dot{m}}{A} = \rho_0 a_0 \left(\frac{2}{k+1}\right)^{(k+1)/2(k-1)} \tag{3-3}$$

This means that the compressor is possible to be operated at higher flow rates than the choking mass flow when the impeller rotational speed increases. So it is important to make sure that the other components will not choke when the compressor operates at a higher rotational speed. Moving to the diffuser, the choking mass flow in the diffuser can be expressed in a similar formula as the compressor inlet in which the choking flow rate is only a function of the inlet diffuser conditions. However, since the choking mass flow of the diffuser is a function of the stagnation conditions at the impeller exit, it can be related to the rotational speed of the impeller.

$$\frac{\dot{m}}{A} = \rho_{02} a_{02} \left(\frac{2}{k+1}\right)^{(k+1)/2(k-1)} \tag{3-4}$$

In addition to the inlet gas Mach number, there is another important factor has a major contribution in the centrifugal compressor choke which is the inlet incidence angle. As the flow increases, the incidence angle of the relative inlet gas becomes negative which leads to reduce the flow area effectively and causes a gas impingement on the blade trailing edge. Reducing the flow area and the gas impingement both contribute to flow separation and compressor choke.

Despite that operating the compressor at high flow rates is not recommended due to the associated drop in efficiency, there are several operational cases where it can be encountered such as:

- When the recycle valve is fully opened during start-up (Kurz et al., 2011).
- Performance degradation due to fouling (Kurz et al., 2011).
- Process upsets: such as when one of the two compressors operate in parallel has to be shut down.

3.2 Investigation of Impeller Design Influences

Three fundamental characteristics will be considered regarding impeller design which are the presence of shroud, blade exit angle and impeller arrangement.

The shroud on centrifugal compressor impeller has a significant effect on the internal flow of the impeller. The absence of cover allows the unshrouded impellers to operate at higher rotational speed and to generate a greater pressure ratio relative to the shrouded impellers, reaching to 4:1 based on the gas conditions and impeller tip speed. Moreover, the rotating stall is taking place at higher flow rates in the case of shroud impellers which leads having a narrower stable range (Harada, 1985). However, based on the efficiency view, the open un-shrouded impellers are suffering from the tip leakage loss which makes them less efficient than the covered impellers. Figure 3-4 demonstrates that the trends of isentropic efficiency and pressure ratio are increasing non-linearly with the shrouded percentage rise.

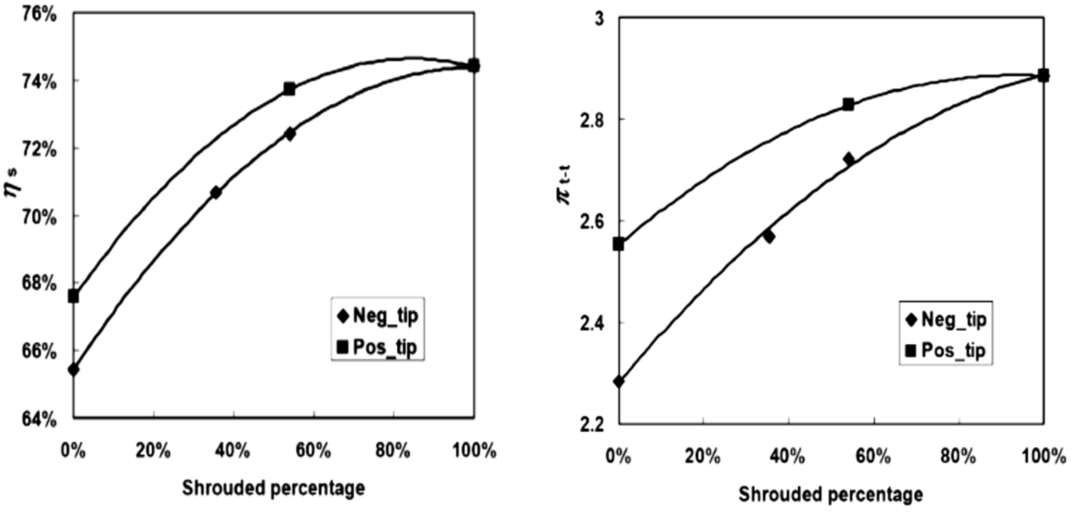

(a) Isentropic efficiency (b) Total pressure rise

Figure 3- 4: Effect of Shrouded Percentage on (a) Isentropic Efficiency (b) Pressure Rise (Tang et al., 2008)

So, the selected shrouded percentage should be optimized to compromise between the cost and performance. Tang et al. (2008) investigated the effect of using partially shrouded impellers on the compressor performance. This study reported an improvement in the tested compressor performance with partially shrouded impeller than when the unshrouded impeller is used, and the flow uniformity becomes better at the exit of the impeller.

To be capable of dealing with higher flow coefficient, the three-dimensional (3D) shrouded impellers have been designed. Based on the aerodynamic perspective, the impeller flow coefficient is one of the most important criteria which affects the selected impeller type. The low flow coefficient impellers are designed with 2D structure and with long and narrow passages as shown in figure 3-5.

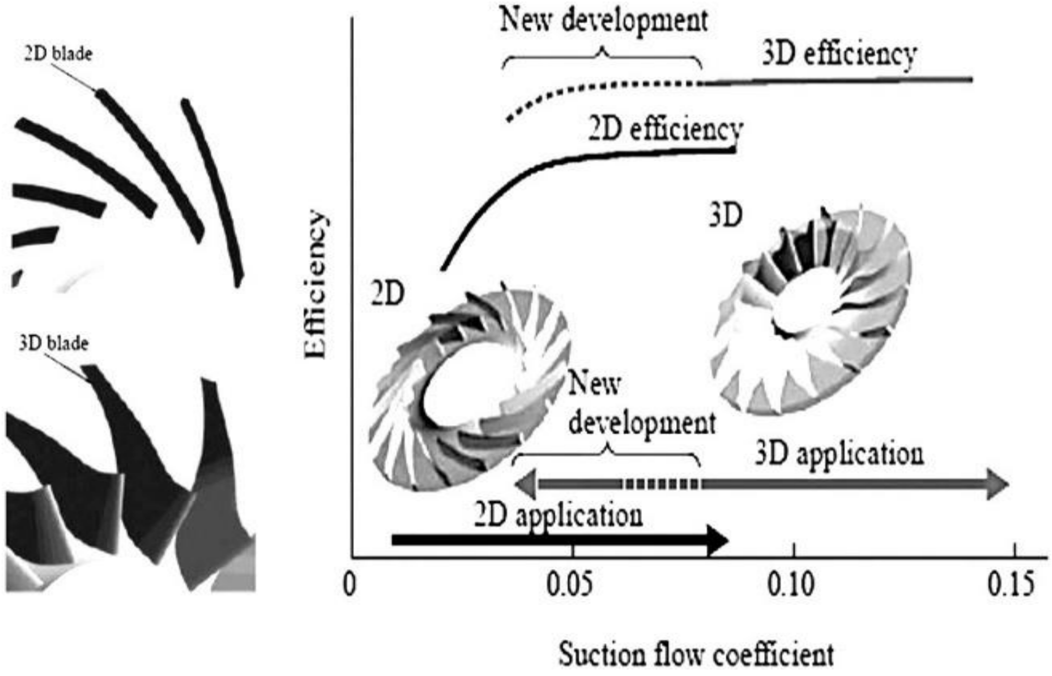

Figure 3- 5: Effect of Impeller Structure on Stage Efficiency and Operating Flow Coefficient (Adapted from: Fukushima et al., 2009)

Besides, they are used mostly in the later compressor stages where the pressure ratio is higher and the volumetric flow rate is lower. On the other hand, the impellers with high flow coefficient have more complex structures (3D) with wider passages to accommodate the higher flow rates. Despite this complexity in the structure, the 3D-impeller delivers a higher efficiency at wide operating range with greater rotational speed comparing with the previous type. Therefore, several researches are taken place to extend the flow range of the 3D-impeller structure to cover lower flow coefficient region.

To avoid the choking conditions in the inducer, many compressors incorporate splitter vanes. The adiabatic efficiency and stage pressure ratio can be improved significantly as shown in figure 3-6 due to the reduction in boundary layer separation and total pressure loss. However, a noticeable drop in the surge margin was observed with splitter vanes. Moreover, the use of the splitter blade is expected to rectify the flow at the impeller discharge outlet yielding a higher absolute velocity. This consequently induces a larger pressure loss by wall friction at diffuser inlet comparing with the conventional blades. Therefore, it is necessary to consider the integrated aerodynamic performance of impeller-diffuser interaction.

The traditional method to position the impellers on the shaft is by placing them one after the other, and this arrangement is called by in-line impeller arrangement as illustrated in figure 3-7. The amount of the power loss as a result of flow recirculation in the balance piston is relatively high for this type of arrangement, and it roughly fluctuates between 1% and 3.5 % based on the flow coefficient and pressure ratio.

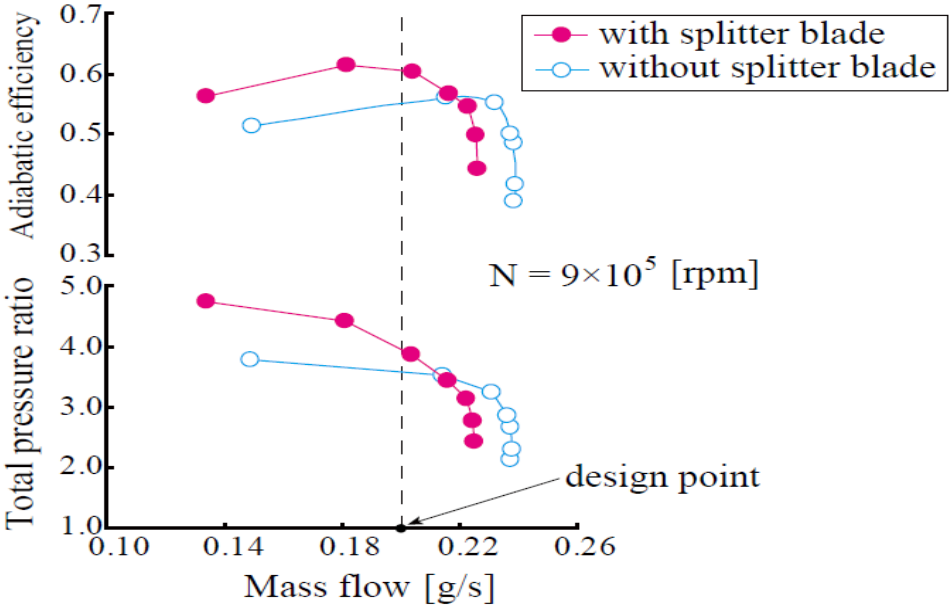

Figure 3- 6: Comparison Between the Performance of Splitter and Conventional Blades (Miwa et al., 2009)

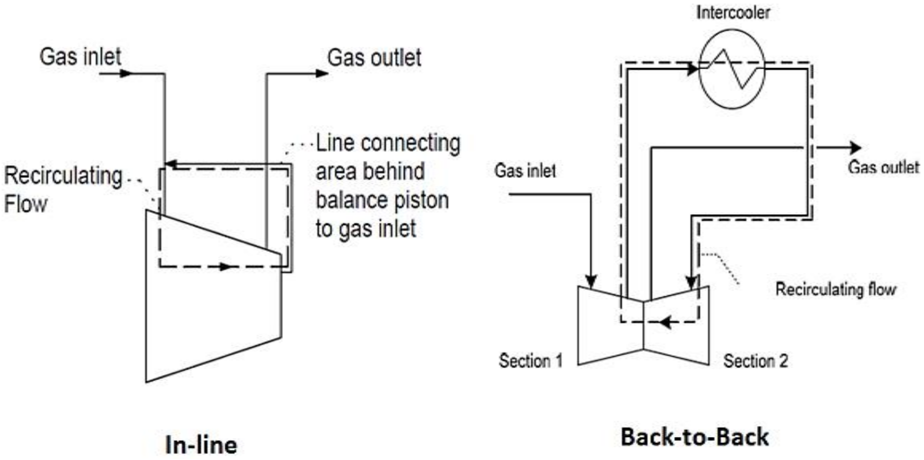

Figure 3- 7: Types of Impeller Arrangement (Hansen, 2008)

To reduce this power loss, another method of impeller arrangement was developed by placing two sections with one common casing so that the two outlets adjacent to each other, and it is called back-to-back arrangement. The advantage of this kind of configuration is that the balance piston has been replaced by a rudimentary labyrinth seal between the outlet stages of each section; thus, the leakage flow is re-circulated only through the latter section as shown in figure 3-7. This leads to reduce the resulted power loss due to flow recirculation to about one-third of that in the straight-through impeller configuration, which is very significant especially for high-pressure ratio applications. Sood (1979) estimated the total save in horsepower by using back-to-back arrangement to approximately 4-6% lower than that of series arrangement.

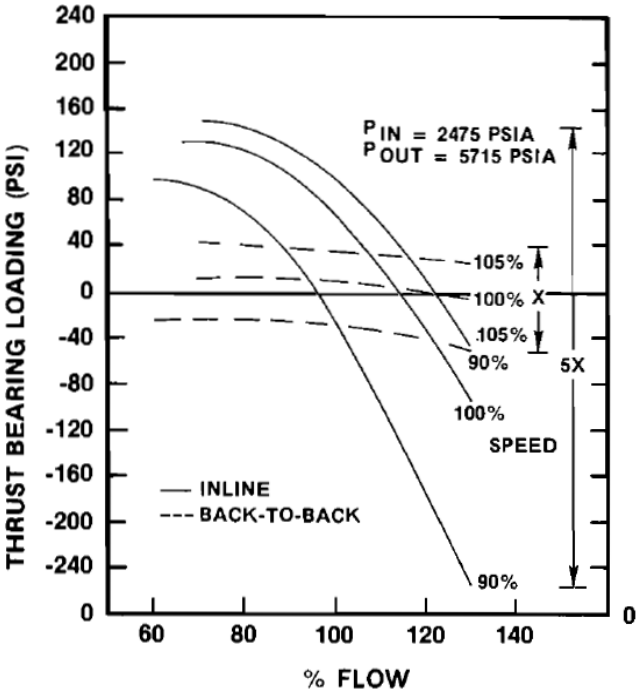

Figure 3- 8: Effect of Impeller Arrangement on Thrust Bearing Loading Variation (Sood, 1979)

Figure 3-8 illustrates the resulted variation in the axial thrust bearing loading due to the speed change in both types of arrangement. It is clear that the encountered variation in the back-to-back arrangement is about five times less than that of series arrangement. Furthermore, this arrangement is ideal to reduce the net unbalance thrust caused by the increase in the labyrinth clearance

3.3 Effect of Diffuser Configurations and Design Characteristics

An efficient diffusion system at the impeller exit is a crucial requirement for high performance centrifugal compressors to achieve the highest possible static pressure recovery over a wide range of incident flow conditions. However, there are some limitations have been set for the diffusion process to avoid the chance of the stall occurrence. Based on the impeller design and its matching with the diffuser component, the diffuser characteristics can greatly influence the location of stability limit of the centrifugal compressor. A higher operation efficiency of a centrifugal compressor can be achieved by improving the pressure recovery characteristics of the diffuser.

It is generally found that a well-designed vaned diffuser has a higher static pressure recovery coefficient leading to greater stage efficiency and higher head coefficient as shown in figure 3-9. This is in fact due to the long logarithmic particle spiral path in the vaneless diffuser leading to greater frictional loss. On the other hand, the absence of a throat in vaneless diffuser makes this configuration ideal for wider operating range applications. However, the vaneless diffuser has a simpler geometry; therefore, it is easier for manufacturing and less exposed to erosion and fouling than the vaned diffusers. There are different types of vaneless diffusers which can be classified based on the cross-sectional shapes and wall configurations. This makes the selection of the optimum diffuser geometry more complicated.

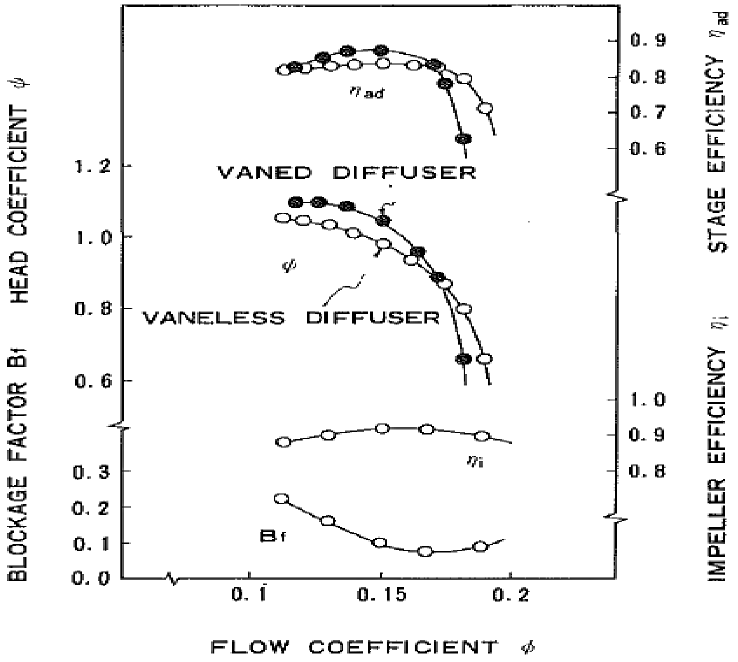

Figure 3- 9: Performance Characteristics of Vaneless and Vaned Diffusers (Yoshinaga et al., 1980)

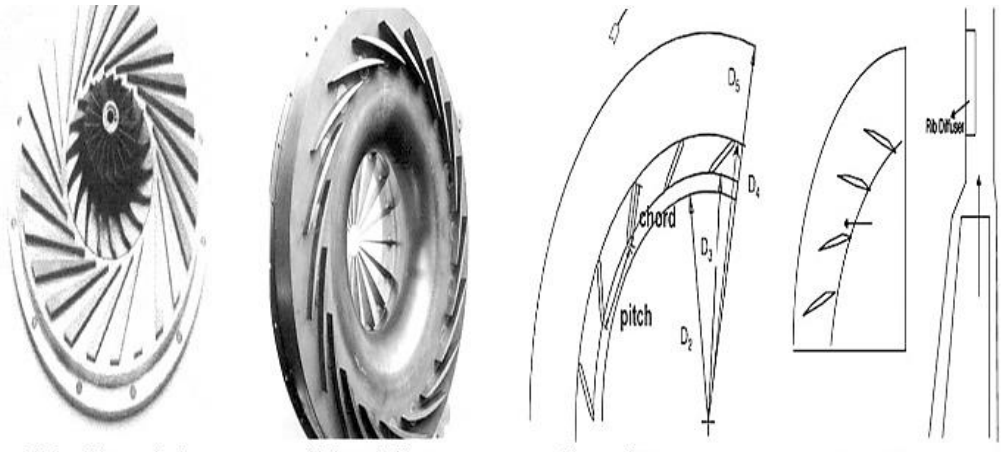

(a) Adjustable air-Foil Style Diffuser
(b) Channel Diffuser
(c) LSV Diffuser
(d) Rib Diffuser

Figure 3- 10: Types of Vaned Diffuser (Adapted from: Boyce, 2003)

The vaned diffusers are classified into four main categories as illustrated in figure 3-10:

- Airfoil style diffuser which is the most common type, and it is based on conventional standard cascade technology where the swirl velocity component is reduced by the turning vanes.

- Channel diffuser at which the passage area is controlled by increasing the vane thickness with radius.
- Low solidity vaned diffuser where there is no throat area.
- Rib diffuser which is a low solidity set of diffuser vanes attached to the shroud surface, so they extend over 25% to 60% of the diffuser passage.

However, there are three main disadvantages of vaned diffuser:

1. The mechanical complexity of vaned diffuser raises the manufacturing cost leading to higher capital cost.
2. The presence of vanes limits the available flow area and causes significant changes in the steady flow field yielding a shorter operating margin.
3. The excessive fluctuation in the process gas molecular weight causes a high incidence angle to the entry of the vaned diffuser.

Figure 3-11 demonstrates the strain level during the compressor surge of different diffuser structures with alternating blade stress of about 106 N/mm^2. The acting strain on the cambered diffuser vanes is the highest among the studied configuration, so it is important to consider a sufficient surge margin in order to avoid the high fatigue and stress loads on the mechanical integrity of the blades.

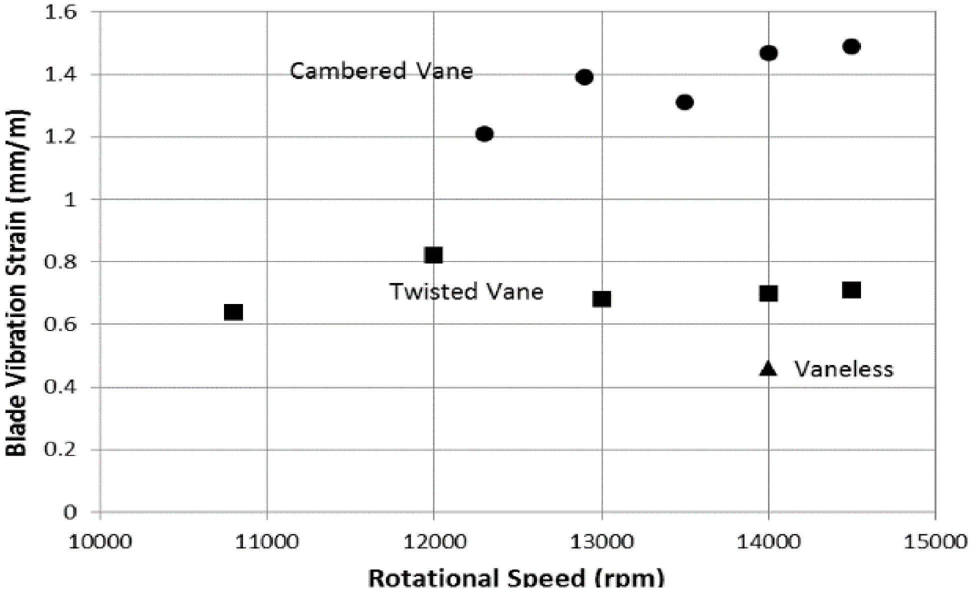

Figure 3- 11: Blade Vibration Strain of Different Diffuser Configurations (Derived from the obtained results by: Jin et al., 1992)

There are five major design parameters affect the overall performance of the diffuser as illustrated in figure 3-12 which are the diffuser width, radius ratio, chord length, vane number and inlet vane angle. One way to delay stage stall is by increasing the inlet flow angle at lower flow rates which can be accomplished by several techniques. The simplest way is by reducing the axial width of the diffuser, and this type of diffuser geometry is called pinched diffuser. The pinched shape of the diffuser has been designed to improve the inlet flow. This might be made to the shroud inlet or hub inlet or both of them as shown in figure 3-13.

The conducted study by Jaatinen et al. (2011) on the effect of vaneless diffuser width revealed a possible chance to improve the compressor efficiency by reducing the diffuser width. Ferrara et al. (2002), Engeda (2003) and Cellai et al. (2003) reported that by reducing the diffuser width, the stall inception shifted towards lower flow rates.

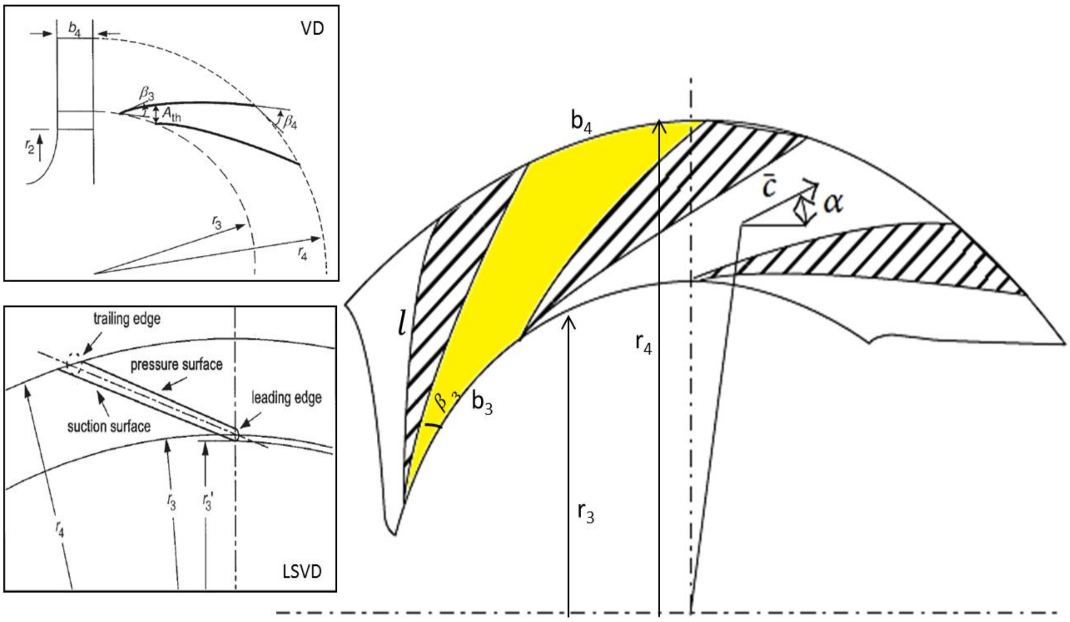

Figure 3- 12: Diffuser Design Characteristics (Adapted from: Kim et al., 2002 and Kalinkevych and Skoryk, 2013)

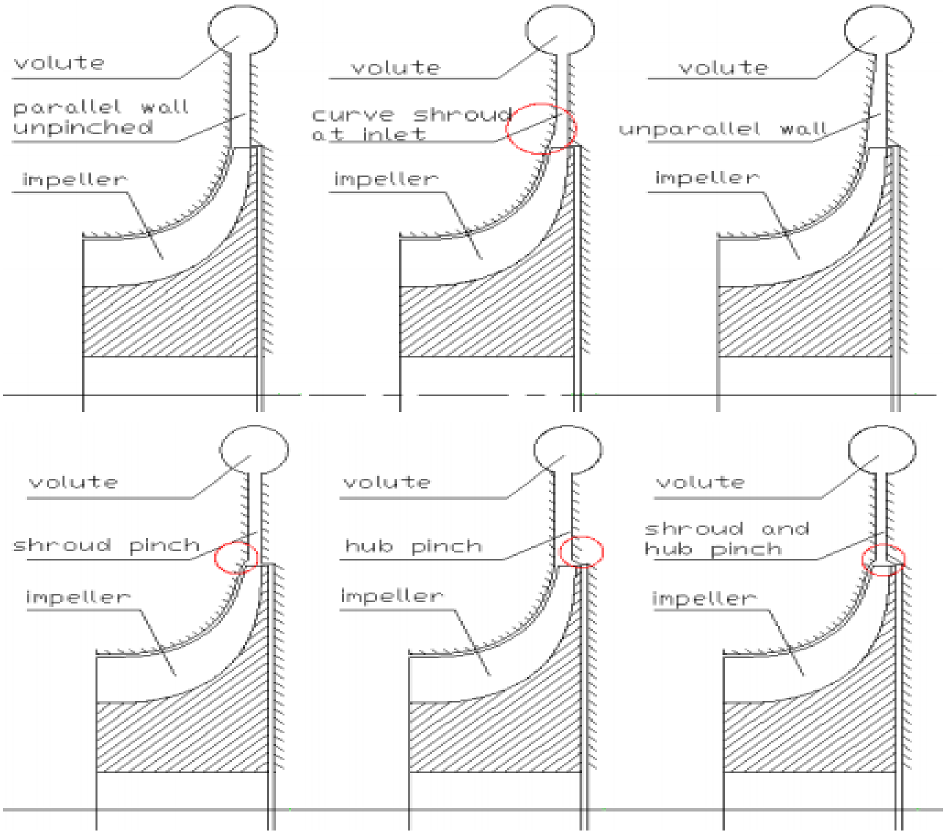

Figure 3- 13: Vaneless Diffuser Inlet Geometries (Wu, 2010)

Turunen-Saaresti et al. (2009) recorded an increase in the stage static-total pressure ratio of the pinched vaneless diffuser at all mass flows and the largest increment was observed at high flow as illustrated in figure 3-14. The pinch also increases the isentropic efficiency of the rotor and diffuser at design flow while there was a reduction in the volute isentropic efficiency. The flow rate is constant throughout the studied cases; thus, the radial velocity is higher at lower diffuser height. On the other hand, this increases the flow swirl in the volute which makes the flow path longer. This decrement was not observed in Case 2 most probably due to an insignificant change in the effective diffuser height.

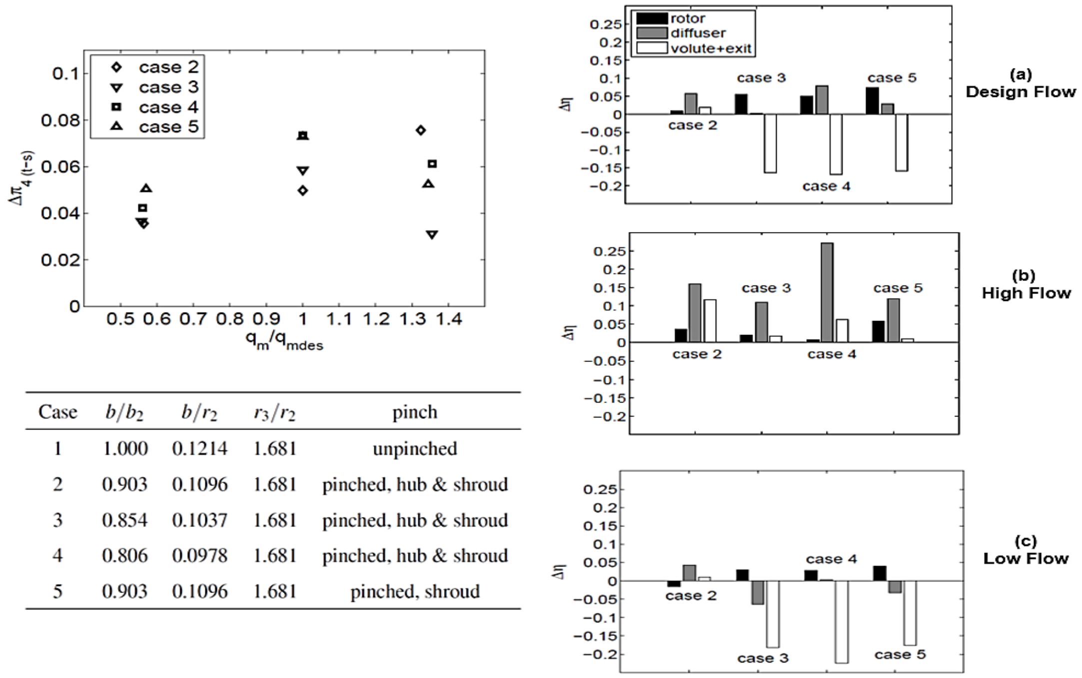

Case	b/b_2	b/r_2	r_3/r_2	pinch
1	1.000	0.1214	1.681	unpinched
2	0.903	0.1096	1.681	pinched, hub & shroud
3	0.854	0.1037	1.681	pinched, hub & shroud
4	0.806	0.0978	1.681	pinched, hub & shroud
5	0.903	0.1096	1.681	pinched, shroud

Figure 3- 14: Effect of Axial Diffuser Width on the Operating Range and Isentropic Efficiency (Adapted from: Turunen-Saaresti et al., 2009)

A similar trend of volute efficiency was found at low flow rates as a result of high radial velocity at diffuser exit. It is clear also that there is a slight increase in the diffuser efficiency at low flow. However, a greater improvement in the diffuser efficiency was observed at high flow rates and with a rise in the rotor and volute efficiencies. As the flow angle becomes more radial at high flow rates, the change in the flow angle distribution might explain this change in the volute efficiency at high flow. Similar results have been obtained by Mohtar et al. (2011). Moreover, the excessive pinching can have an adverse impact on both efficiency and operating range. It is important to understand that the absence of vanes in the flow passages of vaneless diffuser necessities the need for larger radial size to achieve the same pressure ratio as the vaned diffuser. Consequently, the frontal area of vaneless diffuser is usually larger, and it influences the flow uniformity in the diffuser passage resulting in higher pressure losses. The vaneless diffusers (VLD) are typical to provide a wide operating range, but the growing demand for a higher compressor efficiency pushes to use conventional vaned diffusers (CVD).

The vaned diffusers are based on changing the mean flow path radius to reduce the gas velocity. Hence, this configuration is capable of providing a higher pressure rise and efficiency at design flow coefficient but with reduced operating range relative to the previous type as illustrated in figure 3-15. This feature makes the vaned diffusers ideal for higher pressure ratios applications, especially when there is no critical need to adjust the flow rate.

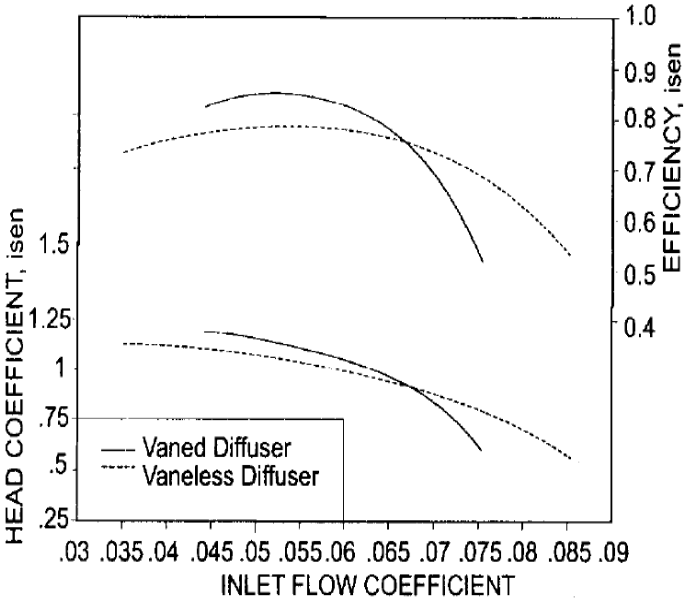

Figure 3- 15: Comparison Between the Head Coefficient and Efficiency of Vaned and Vaneless Diffusers (Flathers, 1997)

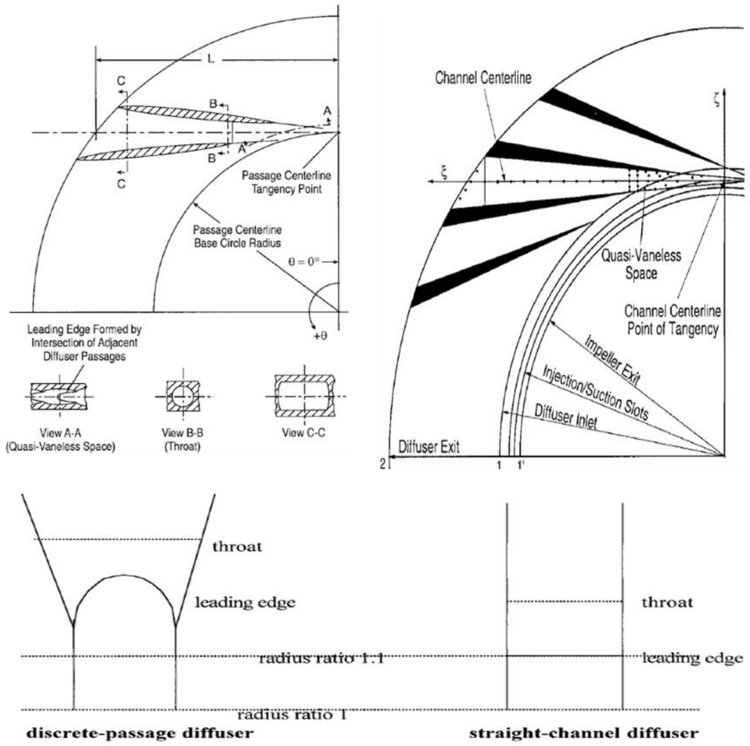

Figure 3- 16: Comparison Between Discrete Passage Diffuser and Straight Channel Diffuser (Adapted from: Deniz et al., 2000 & Filipenco et al., 2000)

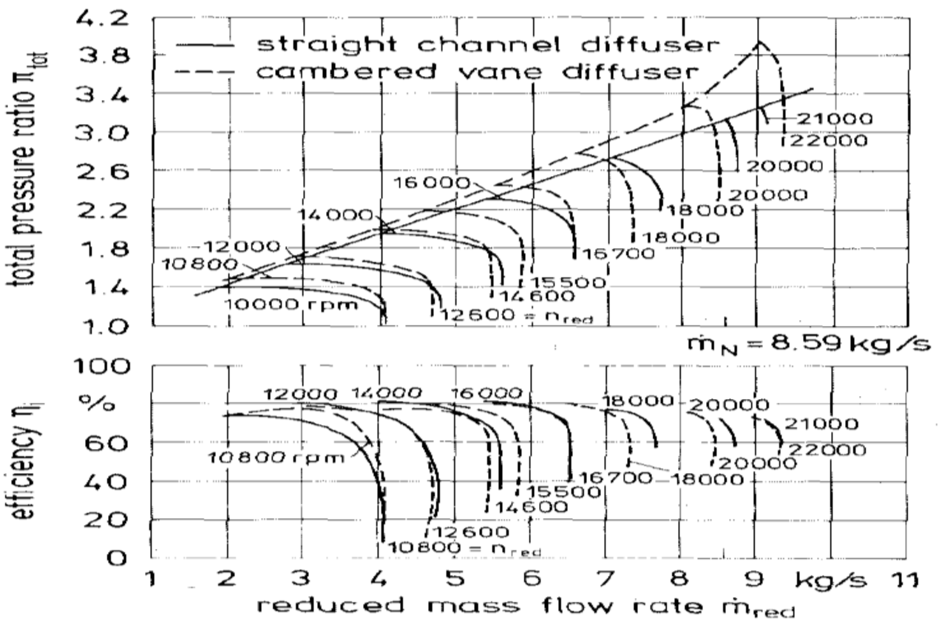

Figure 3- 17: Performance Characteristics of Straight Channel and Cambered Vane Diffuser (Hohlweg et al., 1993)

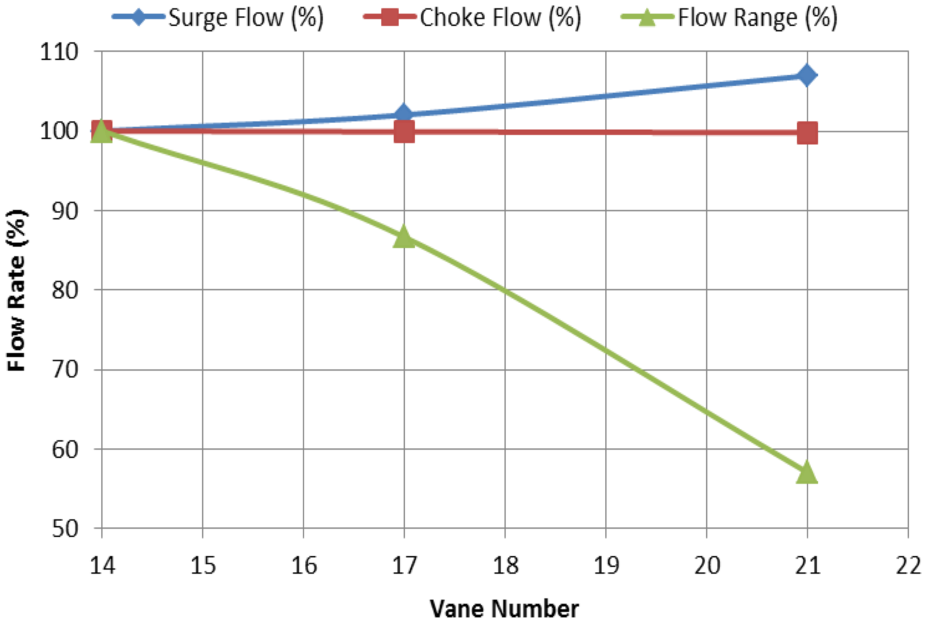

Figure 3- 18: Impact of Vane Number on Operating Range Considering the Diffuser with 14 Vanes As Base Point Based on Published Results by Wu (2010)

Kim et al. (2002) compared between flat plate cambered and airfoil cambered diffusers, and the obtained results revealed that the flat plate cambered diffuser has the highest peak efficiency, but its operating flow range was the narrowest. Comparing with discrete passage diffuser, the straight channel diffuser has a greater overall diffuser pressure recovery by about 10% while the variation in the pressure recovery coefficient with inlet flow angle was found similar for both types (Deniz et al., 2000 and Filipenco et al., 2000). The main geometrical difference between these two kinds is the position of the throat which is at 40% and 15% of non-dimensional distance along the diffuser passage canter-line of discrete passage and straight channel diffusers, respectively as shown in figure 3-16. Haupt et al. (1988) reported a shift in the surge line toward higher mass flow rates for the stage with the straight channel diffuser comparing with the cambered vane type. However, the stage efficiency was greater in the case of cambered vane as illustrated in figure 3-17.

The off-design performance of vaned diffusers is poorer than the vaneless diffuser due to the formation of a geometric throat at the diffuser vane which, in turn, leads to lower choke flow. This can be avoided by reducing the number of diffuser vanes leading to lower solidity percentage. Figure 3-18 plots the obtained results by Wu (2010) which shows a slight effect on the choke flow as the vane number increases. On the other hand, there is a substantial rise in the surge flow with the vane number increase leading to reduce the flow range dramatically. More significant effect on the choke flow was observed by changing the inlet vane angle of the diffuser. The widest mass flow range was achieved at the highest angle value with an increase of 27% in the flow range relative to 7° rise in the vane inlet angle.

Based on the same concept, the low solidity vaned diffusers (LSVD) are characterized by the absence of a geometric throat which is the minimum channel area made by two adjacent diffuser vanes. The low-solidity vaned diffuser is used widely because of its higher efficiency compared with the vaned diffuser and its compatible operating range with the vaneless diffuser. Unlike the vaned diffuser, the choke limit is controlled by the impeller throat area as Mach number approaches unity. This allows to vary the choke flow considerably based on the impeller geometry and according to the rotational speed value. Hohlweg et al. (1993) recorded a reduction by around 2.6% in the efficiency with LSVD at high Mach number and at design flow conditions comparing with the conventional vaned diffuser (CVD). Moreover, the flow range of LSVD was 30% greater than that of the CVD, and its efficiency was 4.9% higher than the efficiency of the vaneless configuration. Similar results have been obtained by Osborne and Sorokes (1988), Sorokes and Welch (1992), Amineni (1996), Koumoutsos et al. (2000), Reddy et al. (2004), Engeda (2001) and Issac et al. (2004).

Figure 3-19 shows the efficiency and operating range of LSVD comparing with the VLD as a function of tip Mach number and blades number. The gain in the efficiency due to the use of LSVD is fluctuated between 2% and 6% comparing with the vaneless diffuser, but with a penalty of flow range reduction which reaches to about 25% in some cases. However, this decrement in operating range can be decreased by reducing the incidence angle and tip Mach number. Cellai et al. (2003) studied the effects of the vane length on the operating range, and the obtained results demonstrated a reduction in the surge flow coefficient when the chord length increases but with lower choke flow. Yoshinaga et al. (1987) found that the optimum vane height to achieve the greatest pressure recovery was little less than a half of the diffuser width. Sorokes and Welch (1992) considered the influences of using an adjustable low solidity vaned diffuser so that the inlet angle of the vanes can be changed with the inlet flow. This helps to enhance the surge margin by adjusting the inlet flow angle. The compressor stability limit is also influenced by the diffuser inlet-to-outlet radius ratio. The results of Ljevar (2007) revealed that the critical flow angle decreases with the reduction in the diffuser radius ratio; thus, the stability range improves. This result totally agrees with the findings of Abdelhamid et al. (1980) and Tsujimoto et al. (1996).

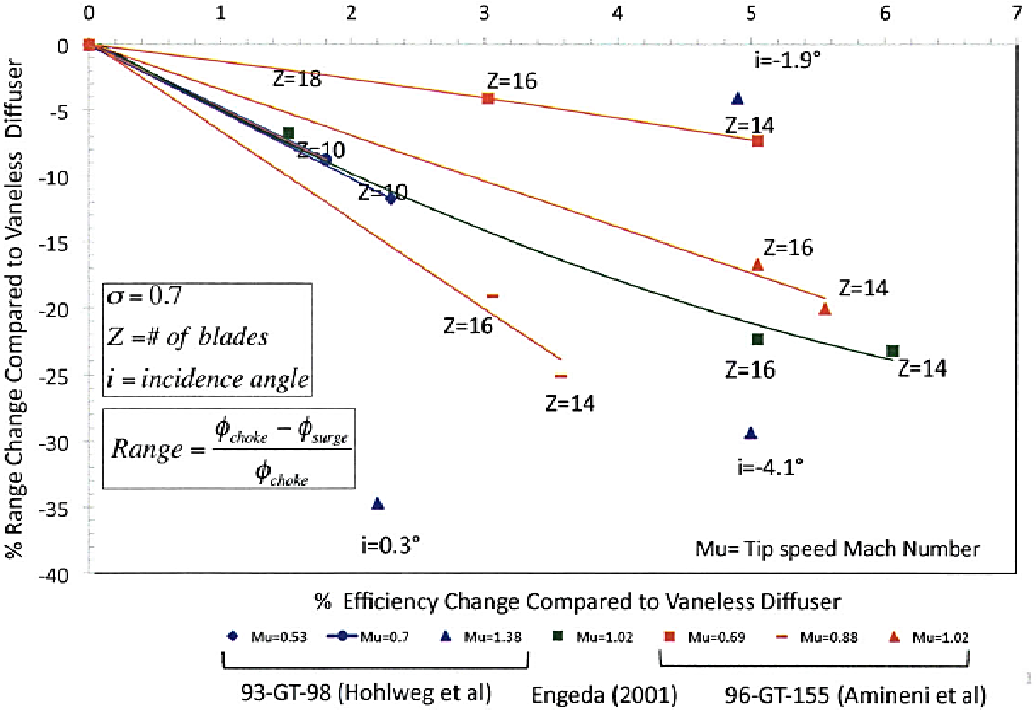

Figure 3- 19: The characteristics of LSVD Relative to Vaneless Diffuser (Aubry, 2012)

A number of conducted investigations have demonstrated several techniques to extend the stable flow range of centrifugal compressors. Jansen (1980) conducted an experimental test to extend the stall margin by treating the impeller wall and vaned diffuser. The treatment of the impeller wall was carried by creating a series of slots adjacent the leading edges of the impeller vanes. This method achieved a remarkable improvement in the operating range both in terms of surge margin and choke flow characteristics. On the other hand, the vaned diffuser treatment was accomplished by creating circular grooves in the wall with slotted diffuser vanes. This technique showed a less significant improvement in the stable flow range comparing with the previous method. However, an appreciable drop in the efficiency was observed in both methods. This conclusion was also emphasized by MacDougal and Elder (1982) and Xu et al. (2011). Moreover, this technique has been applied recently by some turbocharger manufacturers by introducing two grooves in the front of the impeller (Chen and Lei, 2013).

Uchida et al. (2006) investigated the integrated effect of casing treatment with the VIGVs as illustrated in figure 3-20. The drop in surge flow became greater when the VIGVs are associated with the casing treatment reaching to about 59% comparing with only 15% and 30% when the VIGV and the casing treatment, respectively, were used separately. Nelson et al. (2000) used a steady flow and pulsed injection of air into the diffuser channels through slots in the suction vane side to stabilize the axial-centrifugal compressor of a turbo-shaft engine. Stein et al. (2000) found numerically that the air injection eliminated the initiated local separation by flow reversal with an improvement in the impeller stability. Skoch (2003) investigated the effect of using steadily injected air-stream and inserting control tubes into the vaneless region of a vane-island diffuser. This covered the influences on the diffuser flow stability and stage performance as shown in figure 3-21.

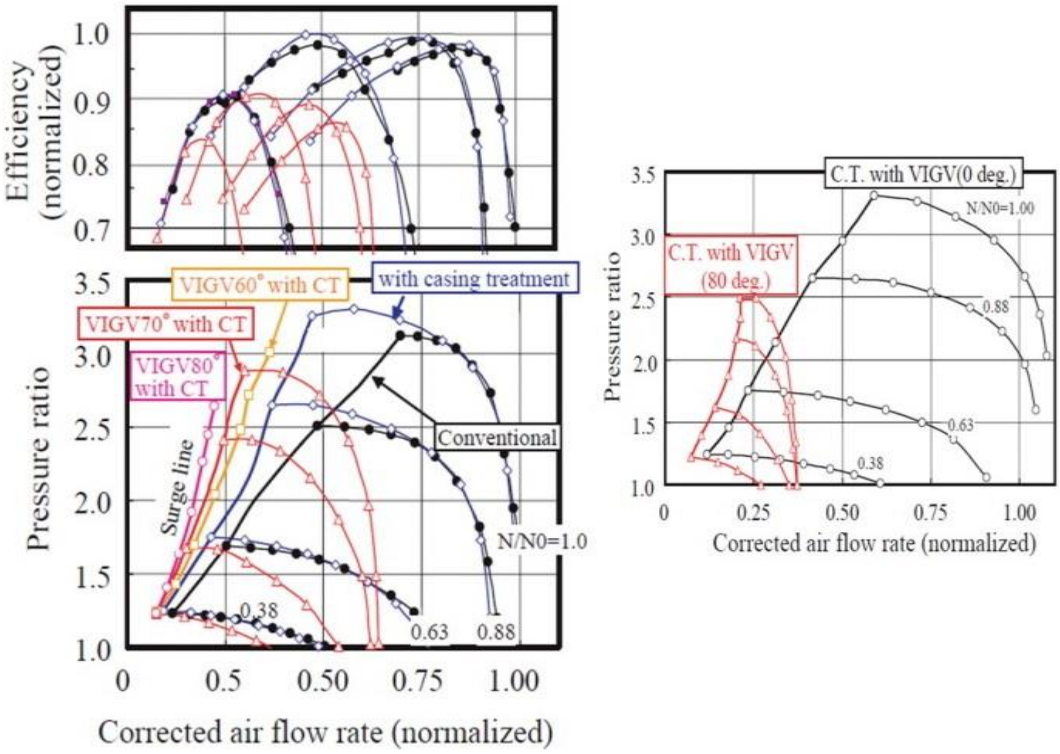

Figure 3- 20: Effect of Casing Treatment and VIGV Setting Angle of 35º Backward Impeller at Left Side and with 20º Backward Impeller at Right Side (Adapted from: Uchida et al., 2006)

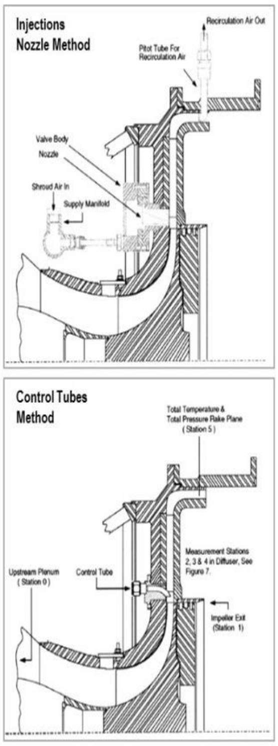

Configuration	A surge margin, percent	B Δ surge margin, percent	C Δ PR at surge, percent
Baseline	11.7		
0.9% forward-tangent	13.4	1.7	−1.0
1.7% reverse-tangent	12.7	1.0	−2.6
4.6% reverse-tangent	9.7	−2.0	−11.0
15% control-tubes	16.1	4.4	−1.4
50% control-tubes	18.2	6.5	−5.5

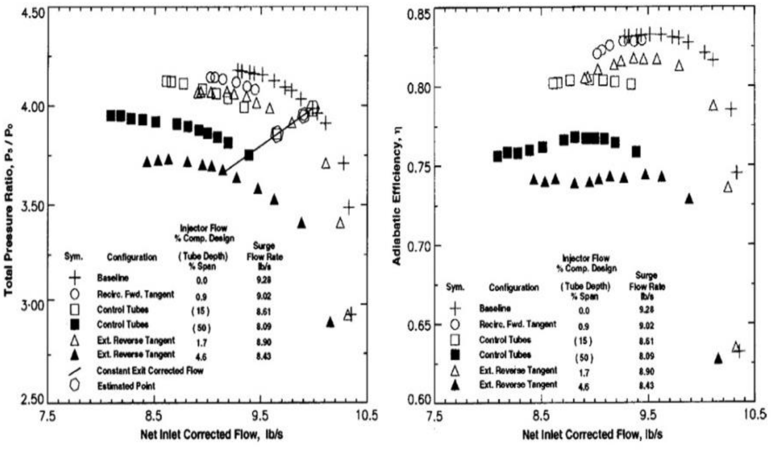

Figure 3- 21: Effect of Injection Nozzle and Control Tubes Techniques on Stage Efficiency and Aerodynamic Stability (Adapted from: Skoch, 2003)

The forward-tangent injection by recirculated air produced a small pressure loss in the diffuser with little improvement in the stable flow range. On the other hand, the reverse-tangent injection generated the highest pressure losses with only a small increase in the surge margin at a low injected flow rate. However, the use of control tubes caused a substantial improvement in stable flow range with a moderate pressure loss in the diffuser as illustrated in figure 3-21.

3.4 Influences of Volute Geometry

The discharge volute is a circular chamber, and it used for the last stage or for a single stage compressor to collect the discharge gas from the external boundary of the diffuser and then conveys it to the discharge nozzle. Besides, the circular chamber is provided with a fin at the opposite side of the chamber from the suction nozzle to prevent the continued gas circulation around the volute. The volute is usually designed using one-dimensional calculations method, and the volute flow is assumed to be frictionless and incompressible. The exit radial and tangential velocities are calculated at the beginning and then the velocity inside the volute cross section is derived assuming constant angular momentum and circumferential static pressure. This can be acceptable at design point operation, but the velocity of volute flow cannot stay constant during the off-design conditions especially if the variation in the inlet mass flow was considered.

Ayder (1993) specified three key geometrical parameters which have a major impact on volute design. These parameters are: circumferential variation and shape of the cross-sectional area, radial position of the cross section and volute inlet and tongue geometry. Ji et al. (2007) considered the connection between the outlet pipe with the volute as another important factor in the design process. Van den Braembussche et al. (1998) stated that the compactness, efficiency and absence of circumferential pressure distortion are the main targets in any volute design. The circumferential pressure distortion occurs at off-design operation, and it is really importance to be predicted since it relates to the unsteady impeller forces, noise and radial forces of the shaft. The obtained results by Hassan [56] revealed that the increase in the volute area ratio leads to raise the diffuser pressure recovery factor, maximum flow rate and pressure rise coefficient of the compressor. The optimum area ratio of volute to achieve the maximum stable operating range was specified to be from 0.6 to 0.7. This can be improved further by increasing the clearance between the diffuser vanes and the volute casing. However, there is still an efficiency loss inside the volute due to the un-fully conversion of the kinetic energy associated with the radial component of the gas discharge velocity from the diffuser.

The effect of radial flow becomes greater when a vaned diffuser is used since the vanes induce more radial flow. This creates a trade-off between increased recovery of the vaned diffuser and reduced recovery of the volute. One of the main issues which should be addressed in the volute design process is the swirling flow and the non-uniformity of the inlet flow which, in turn, leads to unsteady interaction between the rotor and stator flows. Abdelmadjid et al. (2013) concluded that the shape of the volute cross section has more significant impact on the operating range rather than the peak efficiency while the effect of volute inlet location is more substantial on the peak efficiency. The highest efficiency value was observed with the tangential inlet, and the widest operating range was recorded with circular cross section.

CHAPTER 4: BASICS OF OPERATION AND PERFORMANCE ESTIMATION OF CENTRIFUGAL COMPRESSORS

4.1 Compressor Map Prediction Methods

The open literature reveals three different methods to estimate the operating envelope of centrifugal compressor stage as shown in figure 4-1. Although that the predicted results using CFD simulation are sufficiently accurate, it consumes a long time and it might not be possible within the available time frame. Besides, this method requires deep knowledge of the stage geometry which most often not available at the preliminary design stage. The other quick technique is by scaling the performance map of the tested stage to predict the performance of the new stage. However, this method is accurate only when there is no significant difference between the design point of the new stage and the previous tested value especially the work coefficient. The other drawback of this scaling approach is that it does not provide a parametric description at higher or lower speeds than those tested.

4.1.1 Empirical Correlation-Based Method

The common approach for performance maps prediction is by using empirical correlation. Herbert (1980), Cumpsty (1989), Oh et al. (1997), Aungier (2000) and Swain (2005) derived different 1D-empirical correlations to estimate the compressor maps, but all of them fairly require detailed information about the stage geometry. In consequence, this approach becomes less applicable to the initial design phase when defining the geometry is the target. Besides, these models require tweaking of the empirical coefficients, which are usually obtained experimentally, in order generate satisfactory shape of the performance curve. Oh et al. (1997) tested most of the loss models to identify the optimum empirical loss models for centrifugal compressors performance prediction. Besides, a modified parasitic loss model was developed in order to improve the prediction of efficiency curves.

Swain (2005) introduced some improvement in the existing one-dimensional model based on impeller losses. The changes in the losses model were achieved by comparing the losses mechanism of the CFD results with the original impeller loss model. However, this technique can be used only for a single stage compressor, and it requires detailed geometrical features of the impeller to calculate the associated enthalpy losses. Furthermore, the predicted characteristics showed a considerable deviation from the experimental data as shown in figure 4-2(b).

Comparing with scaling method in which the fundamental physical laws are largely ignored (Kurzke and Riegler, 2000), the one-dimensional approach can incorporate a great variety of geometrical features. Casey and Robinson (2013) developed a new set of algebraic equations to predict the compressor maps with less geometrical features. Although that this approach has its advantages over the previous developed equations, it still requires a calibration with the test data with high uncertainty in the prediction of surge line.

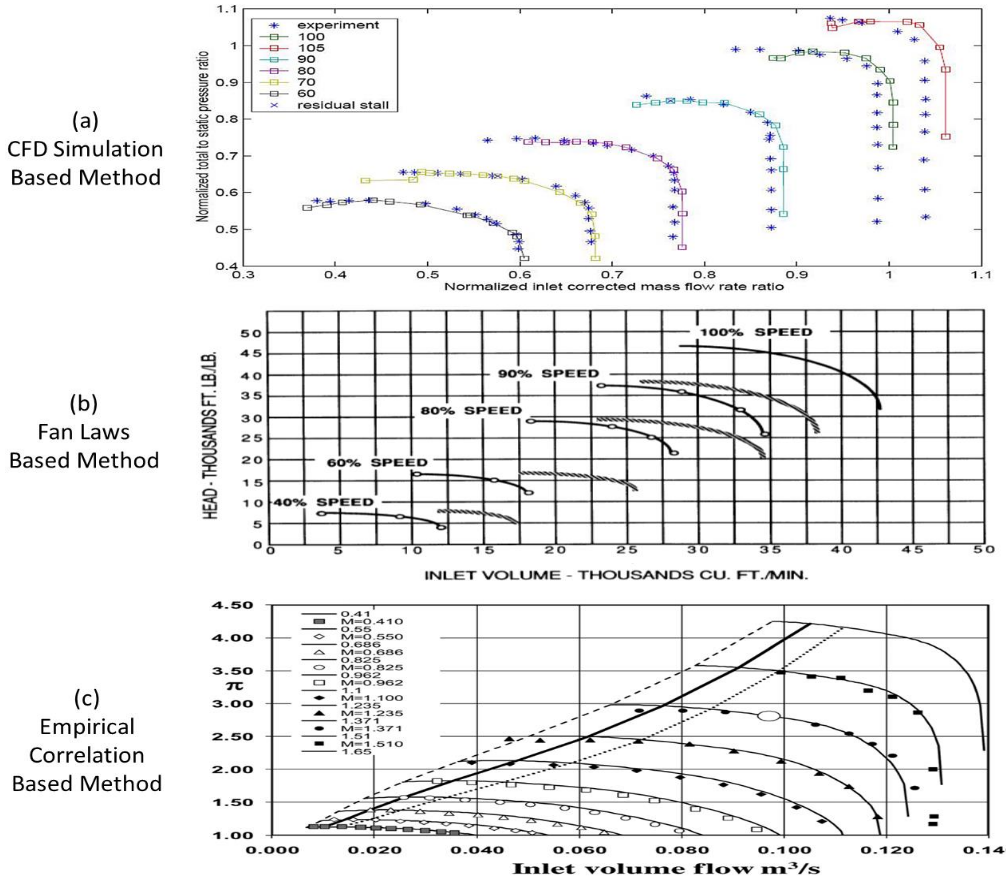

Figure 4- 1: Performance Map Estimation Methods (a). Ding et al. (2006) (b). Chevron Corporation (2001) (c). Casey and Robinson (2013)

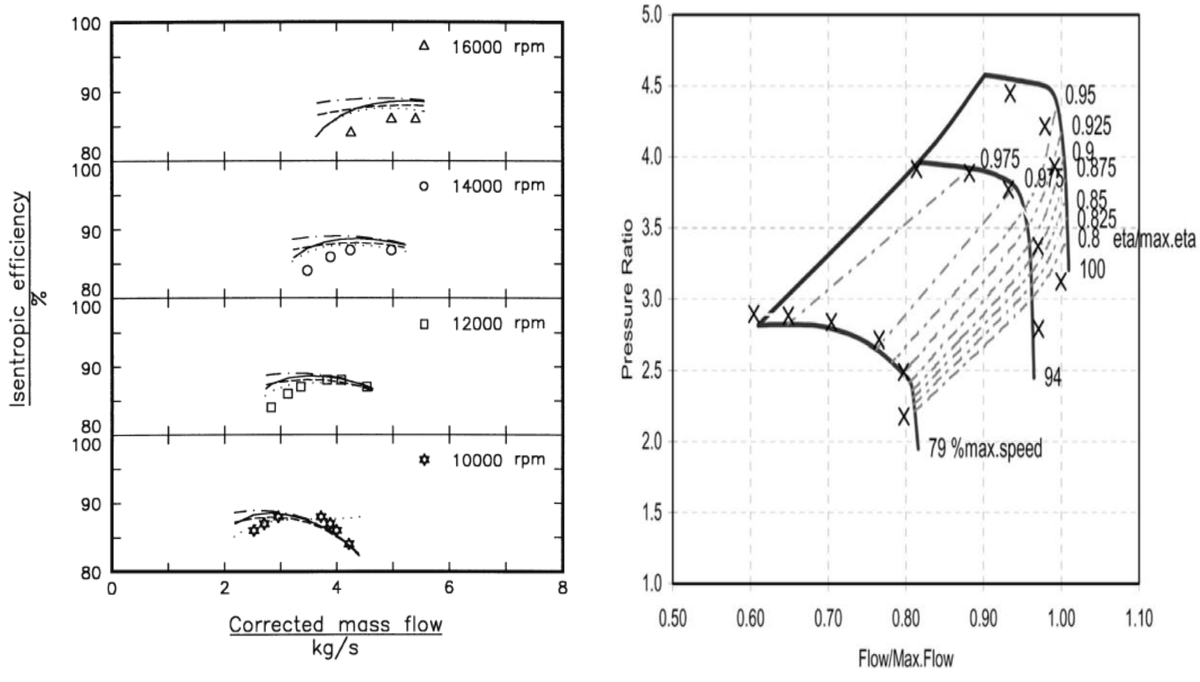

(a) (b)

Figure 4- 2: Comparison between Predicted Compressor Characteristic with Overlaid Experimental Points Using: (a) Oh Model (1997) (b) Swain Model (2005)

4.1.2 Affinity Laws- Based Method

Affinity laws are used to estimate the compressor performance for small changes in speed and flow, but they do not provide very accurate results, so the cautious judgment must be used. These laws are based on the assumption of a non-compressible working fluid. Since the head is related proportionally to the square of tip speed which, in turn, increases with the rotational speed rise, therefore, the head is proportional to the square of the rotational speed. Based on Fan laws, the inlet volume is proportional to the rotational speed. Besides, the polytropic head produced by an impeller is directly proportional to the square of rotational speed. By allowing the flow to increase proportionally to the speed and the head to raise proportionally with the speed squared, the resultant required power will go up with the cubic of speed.

In the open literature, it was found that these laws have been used to predict the performance of centrifugal compressors and surge volumes at off-design speeds. This might result in a substantial percentage of error especially for multistage compressors since these laws do not take into the account the effect of volume ratio. Besides, the Fan laws have been derived assuming a constant flow regime which is not in reality. Wide variation in rotational speed may lead to make some flow laminar, and that will introduce a percentage of errors in the predicted values using Fan laws. Moreover, the internal flow leakage through impeller seals is subjected to change in response to the dramatic variation in the rotational speed which is no considered in this method.

4.1.3 CFD Solver- Based Method

Computational fluid dynamics method is recommended to study the complex flow phenomena within the centrifugal compressors. The CFD uses 3D- partial differential equations as known by Reynolds-Averaged Navier- Stokes (RANS) equations which describe the changes in the momentum, heat and mass transfer. However there is no known analytical solution for these equations until today, but they can be discretised and solved numerically. Despite having several solution methods in CFD codes, the most common way is called finite volume technique in which the geometry of the interested region or components is divided into small control volumes. So, the CFD discretises and solves RANS equations iteratively for every single control volume by applying the conservation of energy, momentum and flow laws. Therefore, an approximated value of each variable is obtained at a specific number of points throughout the domain which gives a full picture of the flow behaviour in the specified region.

The process of performing a CFD simulation can be divided into four main steps which are geometry and mesh creation, physics definition, processing and post- processing. In the first step, the geometry of the interested component is created, and it imported to the software to produce a mesh. To simulate the centrifugal compressor performance, the geometry of a single mechanical stage is created including the impeller, diffuser and return channel. However, before setting the mesh properties, the solid regions of fluid flow are defined and the surface boundaries are named. The mesh file is then loaded into the physics pre- processor to select the required physical models including fluid properties and boundary conditions. In the processing stage, the partial differential equations are integrated over all the control volumes using the basic conservation laws. Some of the terms in these integral equations are approximated to be converted into a system of algebraic equations which can be solved iteratively. These approximations contribute to the deviation between the CFD solution and the real results. The iteration process is essential due to the non-linear nature of the equations, and the results are generated once the solution is converged. The error is reported for every single iteration to indicate the flow properties conservation. However, several factors influence the closeness of the final solution to the exact one such as the size and shape of the control volumes (Zemp, 2007). Finally, the results can be analysed, visualised and plotted in the post-processing step.

Several studies have been conducted to evaluate the centrifugal compressors design, analyse its flow and evaluate its performance using the CFD method. Walitt et al. (1997) performed an unsteady analysis of redesigned centrifugal compressor stage using a CFD optimizer. Niazi et al. (1998) developed a 3D unsteady compressible viscous flow solver using RANS equations to simulate the performance of low-speed centrifugal compressor. It was found that the diffuser stall may be eliminated, and stable operation may be restored by the use of bleed valves located on the diffuser walls. Prasad et al. (2011) demonstrated the procedures of using CFD to simulate the fluid flow in the passage of centrifugal compressor stage with vaneless diffuser including the geometry of impeller blades, diffuser and return channel. Ding et al. (2006) tested the ability of the CFD to predict the compressor operating at highly complex flow regimes and at off-design rotational speeds. Li et al. (2013) implement the CFD (CFX) to simulate the performance of turbocharger centrifugal compressor. Le Sausse et al. (2013) compared the measured radial compressor performance parameters with R134a refrigerant with CFD results at steady conditions. Another flow analysis for the vaneless diffuser of a centrifugal compressor stage was conducted by Kalinkevych and Shcherbakov (2013) by both a commercial CFD package ANSYS CFX and the own-designed computer program.

4.2 Stage Stacking in Centrifugal Compressor

The multistage compressors are used in industry to achieve the desired pressure ratio and efficiency, and to provide a stable operation during the steady and transient processes. However, there are conflict matches in the performance of the individual stages throughout the overall compressor map.

To solve this conflict, the performance map of the multi-stage centrifugal compressors usually represents only a part of the performance characteristics of the individual stage. This part of stable operating envelope is taken so that it does not cause any instability in the operation of the other stages. Besides, each stage has different peak efficiency and associated flow coefficient. In multi-stage compressors, the performance map of each stage is modelled and then matched to obtain the net flow range of the multi-stage group. In axial compressor, two main methods are used to predict the performance of multistage compressors: blade element theory with radial equilibrium and stage stacking. The blade element technique is employed today with modern through-flow solutions for more accurate prediction of the compressor at design point conditions. However, this tends to be more complicated and less efficient when it is used under stall and choke conditions (Howell and Calvert, 1978). The other method is easier for off-design performance prediction since it involves fewer calculations. The mean difficulties in the prediction of performance parameters using such technique had covered by Serovy (1976). The sequential calculation scheme of this method is also shown in figure 4-3.

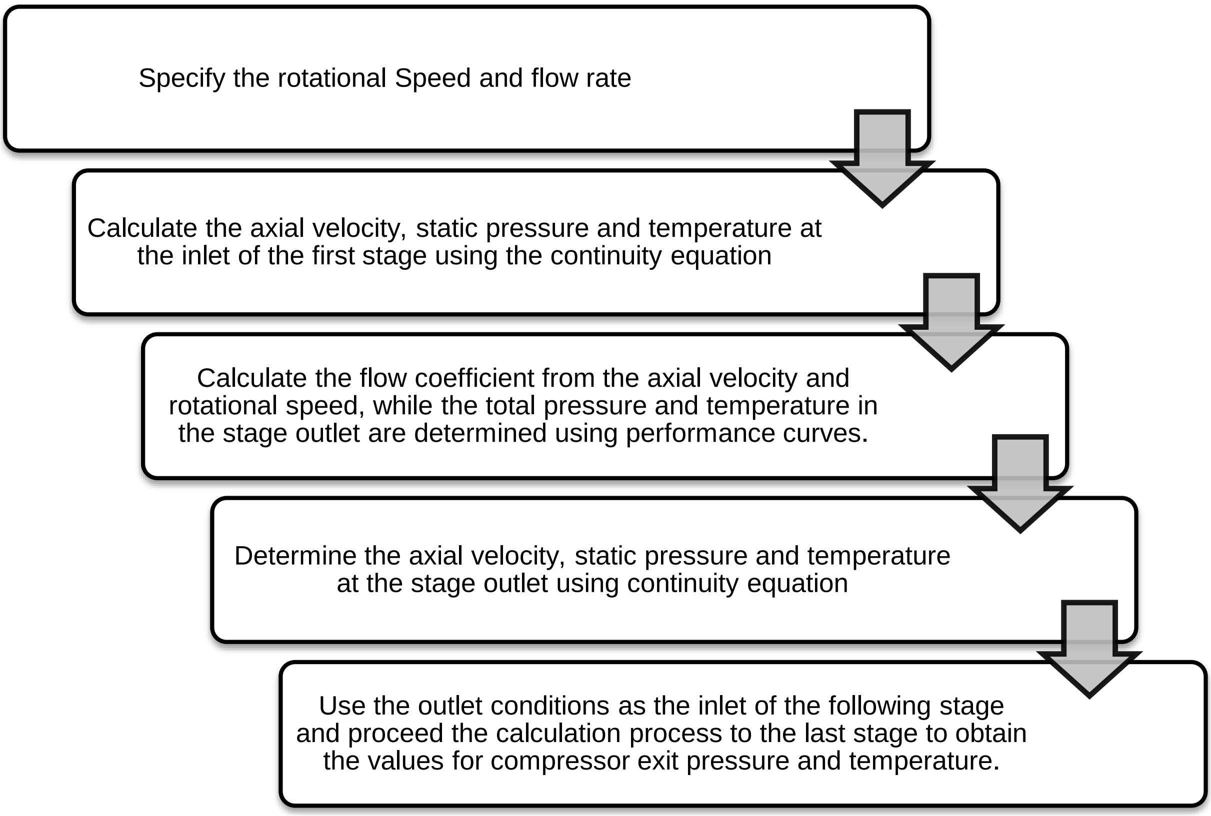

Figure 4- 3: Scheme of Conventional Stage Stacking Method in Axial Compressors

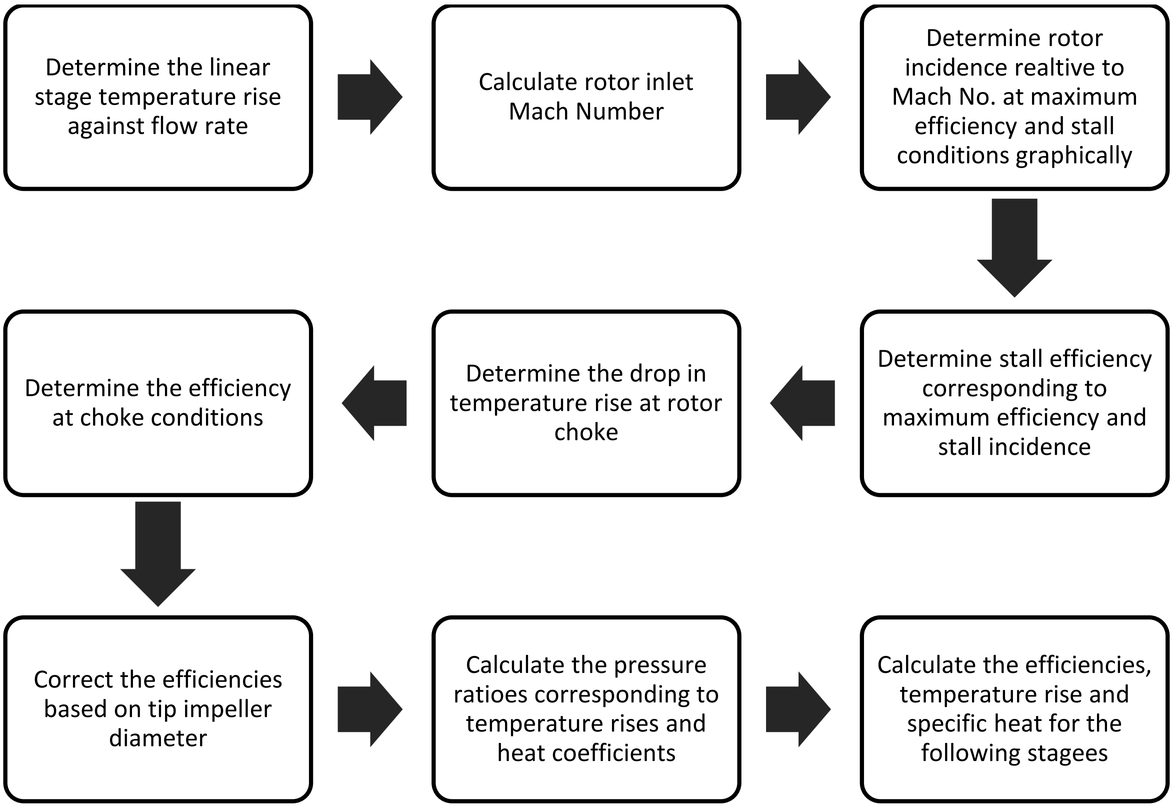

Figure 4- 4: Howell-Calvert Model (1978) for Axial Compressor Performance Prediction

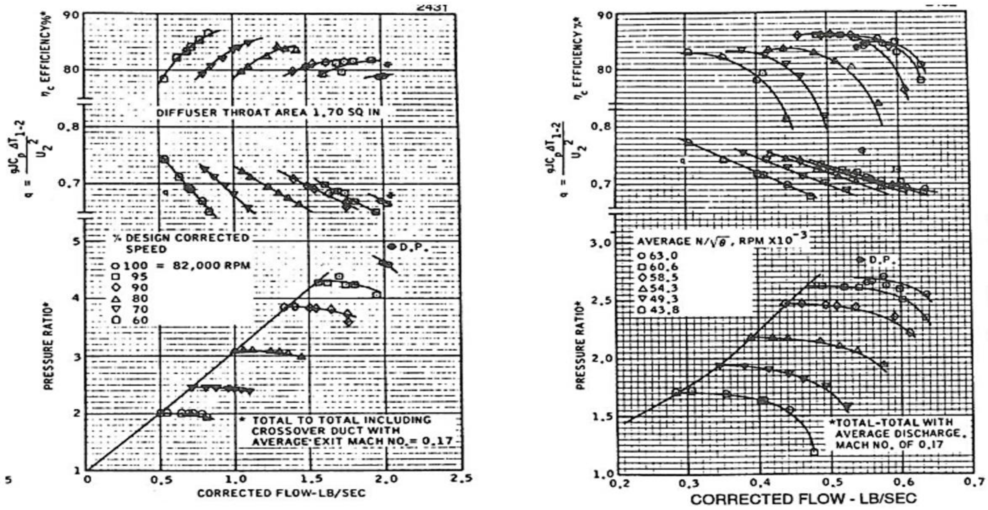

Stage I **Stage II**

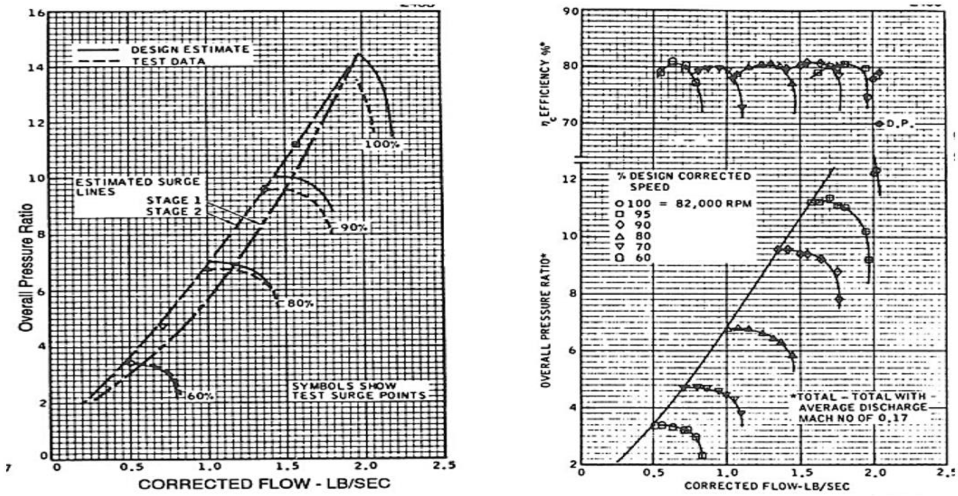

Stages Surge Lines **Multistage Group**

Figure 4- 5: Performance of Single Stages and Multi-stage Group (Rodgers and Langworthy, 1974)

Several models have been developed based on mean-radius stage-by-stage analysis such as Howell and Calvert (1978), Steinke (1982) and recently Jack and Elder (2012). Figure 4-4 illustrates the followed procedures to predict the performance of axial compressor using Howell-Calvert model (1978). The individual stage performance characteristics are estimated based on compressor geometry using different equations in each model, but they are all based on three basic parameters:

- Impeller incidence at maximum efficiency.
- Stall and choke points
- Maximum and stall efficiencies.

Jack-Elder approach (2012) combines the previous two models and it incorporates variable stator stagger setting. However, this model has not been tested to validate the derived correlations as has been done in the previous two. The direction of the flow throughout the axial compressors makes the estimation of the overall compressor performance possible by knowing the performance of every stage since each one contributes to the overall compression process. The main drawback of these models is the inaccurate determination of surge flow since there is no yet developed satisfactory prediction method for this purpose. The simplest used approach is by obtaining the temperature rise, efficiency and specific heats ratio of the last stage, the last two stages and so forward. Therefore, the stage combination that reaches the maximum value, first of all, surges the compressor.

Unfortunately, there is no existing detailed study in the open literature on the procedures of the stage stacking in centrifugal compressors. Rodgers and Langworthy (1974) conducted experimental work to derive the overall two-stage compressor map from the individual stage performance characteristics. By using interstage instrumentation, it was observed that the surge line of the first stage became the stall line in the multistage map, and the overall surge was probably the second stage surge as shown in figure 4-5. Besides, the first stage was operating at left-side of multi-stage efficiency curve during various speed lines while the pressure ratio lines had zero or negative slope. However, due to some mechanical problems, the author was not able to record more test data.

4.3 Capacity Regulation Methods

Using the capacity control techniques allows the compressor to adjust its operating line to satisfy the required new suction conditions. In general, all these methods are based on either modifying compressor characteristic curve or altering the system characteristic curve. Selecting the suitable method is crucial to meet the required flow rate variation range, and to ensure an acceptable change in the performance parameters.

4.3.1 Modifying Compressor Characteristic Curve

4.3.1.1 Variable Speed

The variable speed control method is considered as the most efficient technique at partload operation among the others. However, the speed reduction is mechanically limited since some of the bearings like sliding bearings must rotate at certain minimum speed to avoid the bearing wear. Figure 4-6 demonstrates the effect of using variable speed on the compressor operating line. As the rotational speed decreases, the inlet flow rate declines and, in consequence, the developed head is reduced. Based on Fan Laws, this will allow keeping the new operating point away from the surge line.

4.3.1.2 Suction Throttling

In this method, a throttle valve is installed upstream of the compressor inlet to regulate the flow. This is accomplished by introducing a pressure loss upstream of the compressor which causes an additional resistance to the incoming flow. Figure 4-7 shows the effect of suction throttling. The flow and pressure rise decrease proportionally with the reduction in inlet absolute pressure driven by density reduction. The compressor suction state is referred to the upstream of the valve, and each performance curve represents a constant pressure drop across the throttle valve. As volumetric flow to the compressor increases, the valve will rotate towards the closed position close to maintain a constant suction pressure. This reduces the suction pressure downstream of the valve and subsequently the mass flow, discharge pressure, power requirement and polytropic head.

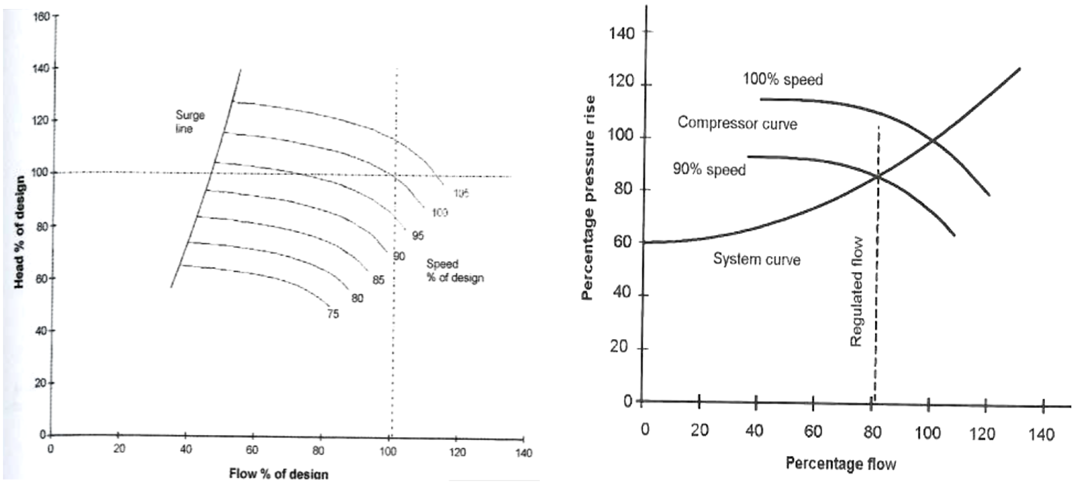

Figure 4- 6: Variable Speed Curves of Centrifugal Compressor (Simmons et al., 2003)

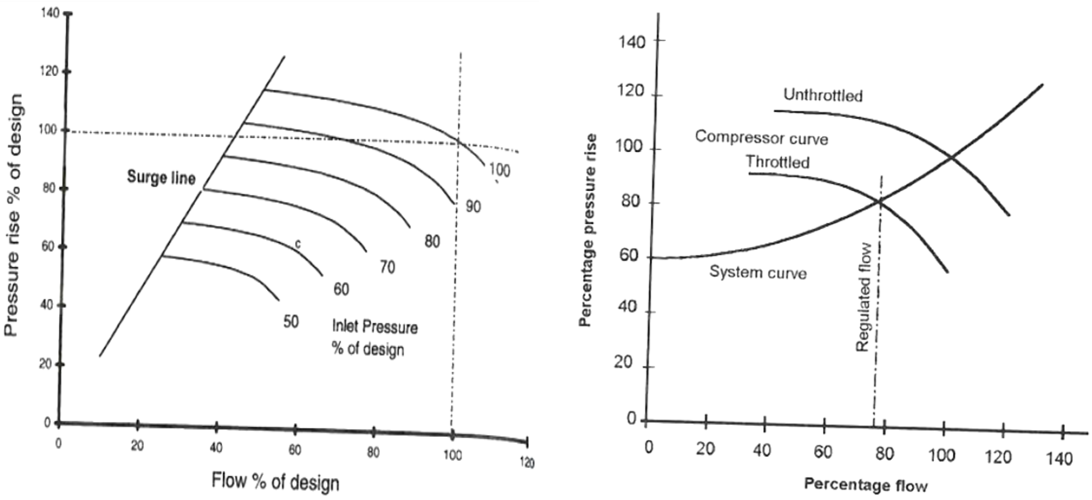

Figure 4- 7: Effect of Suction Throttling (Simmons et al., 2003)

The valve loss is also charged to the compressor efficiency. The partload efficiency is considerably lower than that of variable speed since a part of the pressure is dissipated across the throttle valve. However, the corrected flow rate, polytropic head and efficiency remain almost constant in reality when defined from the downstream of the valve to the compressor discharge. One of the disadvantages of this method is that there is no possibility of overload at constant head; thus, this method is suitable only for a limited number of applications. Based on the initial capital cost, this technique is competitive, but the substantial reduction in the part load efficiency makes it as a second preferred choice.

4.3.1.3 Variable Geometry

4.3.1.3.1 Inlet Guide Vanes

The capacity of centrifugal compressor can be controlled by changing the swirling impeller angle which can be accomplished using the variable inlet guide vanes (VIGVs). The effect of inlet swirl on the process centrifugal compressors performance has been covered in several researches such as Elder (1985), Whitfield (1992), Harada (1996), Coppinger (1999), Xiao et al. (2007) and Higashio (2010). By introducing the

VIGVs, the magnitude and direction of the inlet whirl velocity can be controlled which has a direct effect on the imported work by the impeller on the fluid, so the flow rate and the discharge pressure can be varied. The magnitude of this velocity component ($V_{\theta 1}$) theoretically equals to zero with the absence of VIGVs. Based on Euler equation, the positive prewhirling leads to reduce the Euler head by $U_1 V_{\theta 1}$ while the negative prewhirl results in an increase of the energy transfer by amount of $U_1 V_{\theta 1}$. Figure 4-8 demonstrates the influences of positive and negative swirl angle on the pressure ratio and isentropic efficiency.

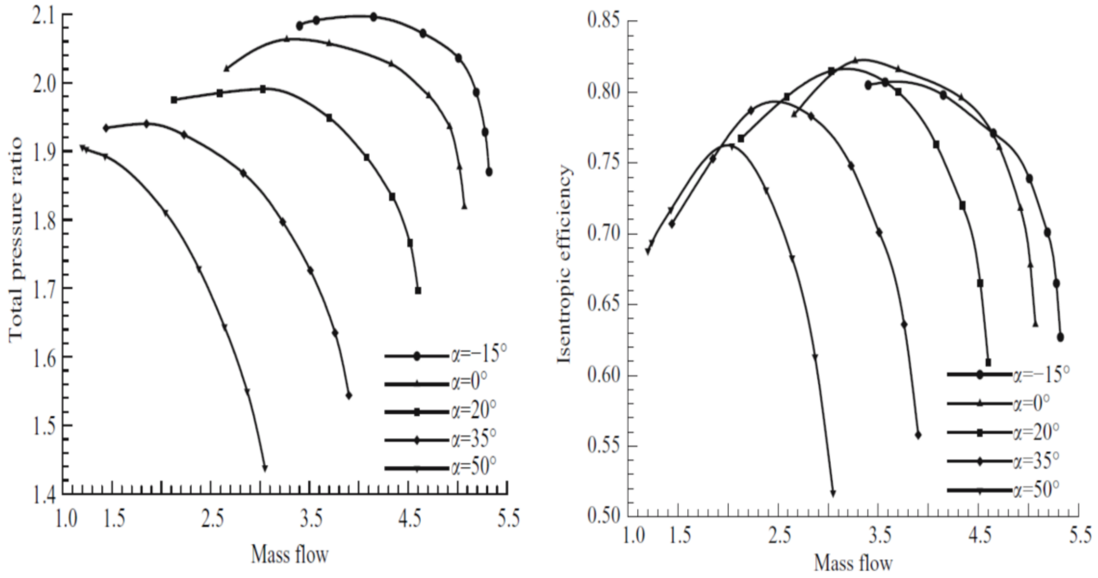

Figure 4- 8: Effect of Swirl Angle on the Performance Curve of Centrifugal Compressor (Xiao et al., 2007)

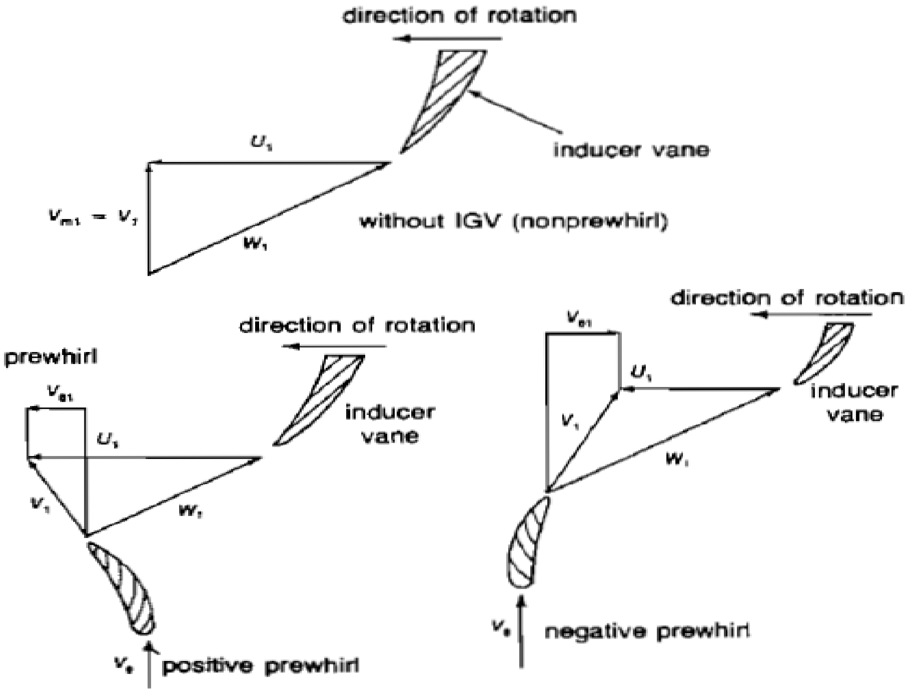

Figure 4- 9: Inlet Velocity Triangle with Pre-whirl (Boyce, 1993)

It can be seen that when the positive inlet guide vanes are used, the performance curves is shifted toward small flow rates leading to reduce the surge flow but with lower maximum isentropic efficiency point relative to zero swirl. The reduction in efficiency is expected due to the higher pressure loss associated with large swirl angles. On the other hand, introducing negative swirl angle raises the choke flow which increases as the swirl angle reduces. Whitfield and Abdullah (1994) concluded that reducing the inlet relative Mach number will allow to operate the compressor at higher choke flow rate. This is mainly due to the associated shock and separation losses with high inlet relative Mach number. By looking to the velocity triangles in figure 4-9, the positive pre-swirl reduces the relative Mach number at the inducer inlet leading to lower developed head but with greater operating margin. The adverse action can be achieved with the negative pre-whirl which makes its used very rarely due to the substantial reduction in the flow range.

The variable inlet guide vanes can be installed on the first impeller of the single stage centrifugal compressors or the first stage of multistage machines driven by a fixed speed electric motor. This is obviously due to the mechanical complexity of such controlling mechanism and the limited available physical space. However, the drop in total pressure yields a greater input power which, in turn, leads to a substantial reduction in the compressor efficiency. Therefore, the capital cost of this method is relatively lower than the variable speed mechanism, but it is less efficient.

Table 4- 1: Estimated Payback Period of Different Capacity Control Methods Based on the Study Conducted by Stebbins (1994)

	Suction Throttling	Inlet Guide Vanes	Variable Speed
Power requirement (kWh/year)	208,880	147,768	107,782
Power cost ($/year) @ $0.08/kWh	16,710	11,821	8,623
Annual saving over Suction throttling	0	4,889	8,087
payback period (year)	-	1.56	1.01

Comparing with the suction throttling, the rotatable inlet guide vanes is very expensive solution for capacity variation, but the greater horsepower savings can cover this additional cost. Table 4-1 compares the payback periods of inlet guide vanes and variable speed control methods with respect to suction throttling technique. Through the consideration of installation and running costs of variable speed and inlet guide vanes, the variable speed method offers a significantly shorter payback period than inlet guide vanes due to the higher efficiency. However, it is important to mention that this period highly depends on the operating circumstances and process conditions.

4.3.1.3.2 Variable Diffuser

Whitfield et al. (1976) studied the application of flexing the vaneless diffuser wall to improve the surge flow only. Abdel-Hamid (1987) considered the use of a variable throttle ring at diffuser exit and this technique was implemented later on for a vaneless diffuser of a turbocharger compressor by Whitfield and Sutton (1989). Although that this method achieved a significant gain in the surge margin, a substantial drop was observed in the overall efficiency at high flow rates. Similarly, Hagelstein et al. (1997) reached a conclusion that the use of a throttle ring at the discharge of vaneless diffuser can lead to improve the circumferential static pressure distribution at impeller discharge.

With regard to the vaned diffuser, Simon et al. (1987) studied the effect of using VIGVs with variable vaned diffusers. The vane stagger was changed by partial compressor disassembly and with conjunction with constant IGV setting. Although it was possible to reduce the surge flow coefficient, the improvement in the efficiency was only locally. Consequently, in order to achieve a full improvement in the operating range and efficiency as well, it is required to select the combination of IGV and diffuser setting freely. Harada (1996) conducted an experimental work to investigate the effect of variable diffuser vanes on the operating range.

The diffuser vane stagger was changed from outside the compressor based on the inside conditions by sensing the differential pressure across the leading edge. This caused an improvement in the operating range but without considering the effect on efficiency. The impact of the axial variation of the diffuser passage area by altering the diffuser walls position was also studied by Comey et al. (1985). Two percent reduction in the stage efficiency was recorded with more than 50% reduction in surge margin. However, closing the diffuser walls alters the exit velocity triangles of the impeller with lower work input comparing with the normal. Sishtla (1996) tested the impact of varying the diffuser throat area without changing the diffuser width and roughly 15% head reduction was reported comparing with 80% flow reduction. So, introducing the variable diffuser vanes alters the performance of centrifugal compressor by shifting the surge margin to lower flow rates. Figure 4-10 illustrates the nondimensional overall performance parameters at fixed and variable inlet and diffuser vanes.

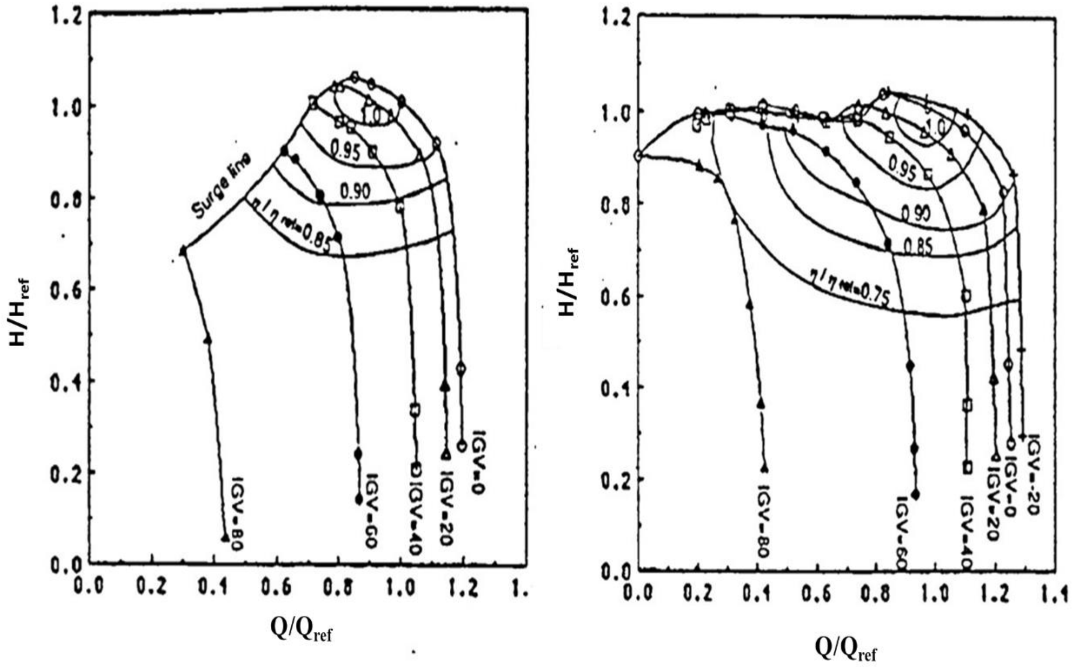

Fixed Vaned Diffuser & VIGV

Variable Vaned Diffuser & VIGV

Figure 4- 10: Effect of Using CVD on the Flow Range (Harada, 1996)

The subscript “ref” denoted the reference measured value at design flow rate when the fixed vanes were used, and inlet vane angle was set to 0 degree. The variable vaned diffuser geometry can be implemented to operate the centrifugal compressor at nearly shut-off flow without any apparent surge. Rotating the vanes towards the closed position decreases the vane angle and reduces the diffuser vane throat which, in turn, leads to reduce the entire diffuser flow area. Although this method has an advantage of stabilizing the diffuser flow, the resulted partload efficiencies are the lowest among all previous methods.

4.3.2 Modifying System Characteristic Curve

One way to control the centrifugal compressor flow is by using cooled bypass technique which is based on modifying the system characteristics curve. In this method, the compressor discharge gas is recycled and returned to the suction side, or it is exhausted directly to the atmosphere in the case of air compressor. The amount of the gas that returns to the inlet side flows through the by-pass line, and it is controlled using a check valve. However, the recycled gas has to be cooled down to match the compressor suction temperature. To reduce the capital investment cost of new cooler, the recycling branch can be taken from the discharge line after the after-cooler if it is available.

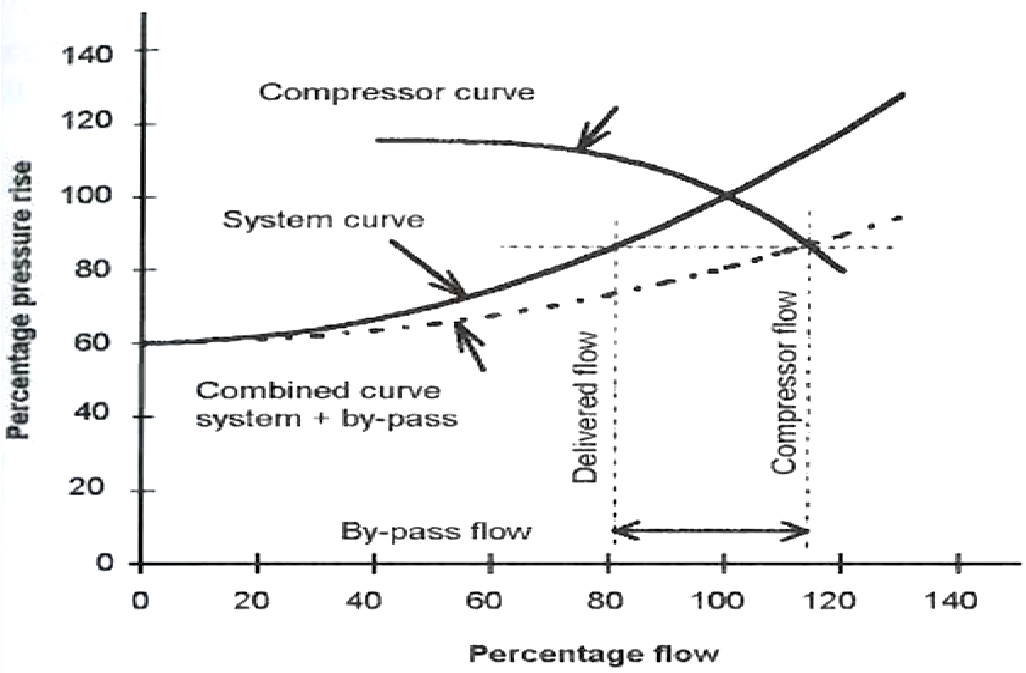

Figure 4- 11: Effect of Using Cooled Bypass (Simmons et al., 2003)

Figure 4-11 shows the change in the system resistance curve as a result of recycle bypass. The new operating point is at the intersection of the system and compressor curves, and then it moves in the direction of higher flow rates so that the power consumption will increase. In general, by-pass recycling is extremely inefficient since the compressor continuously consumes its full load power while a large amount of compressed gas is recycled. So, it should be considered as a last choice and only for small flow reduction especially during start-up or shut-down.

4.4 Deterioration of Compressor Performance

The centrifugal compressor performance is affected by several operating conditions which can lead to degrade the design point performance as illustrated in figure 4-12. The deterioration of centrifugal compressor performance is classified under three basic categories: pressure ratio degradation, efficiency degradation and flow rate degradation. The deterioration in any of these parameters influences the performance map, and it might lead to operate the compressor out of its stable range. There are several causes of centrifugal compressor degradation, and the most common reasons are (Salamat, 2012):

- Fouling
- Labyrinth seal wear
- Erosion
- Corrosion

In process gas applications, the centrifugal compressors are suffering a lot from the fouling as a result of the deposit and a non-uniform accumulation of the debris which flow with the process gas.

The fouling can also occur as a result of polymerization when the gas temperature exceeds the critical point as shown in figure 4-13. The fouling of centrifugal compressors can dramatically reduce the gas throughput of a production plant. Generally, the build-up is usually taking place more on the pressure side than the suction side, and it becomes heavier at the impeller exit where there is a flow separation. Besides, the fouling can lead to increase the surface roughness of flow channels which raises the energy losses due to the gas friction with the flow path surface. Increasing the rotational speed appears as one solution to restore the operating point, but in addition to higher losses, it can cause a high vibration and serious damages for the internal components.

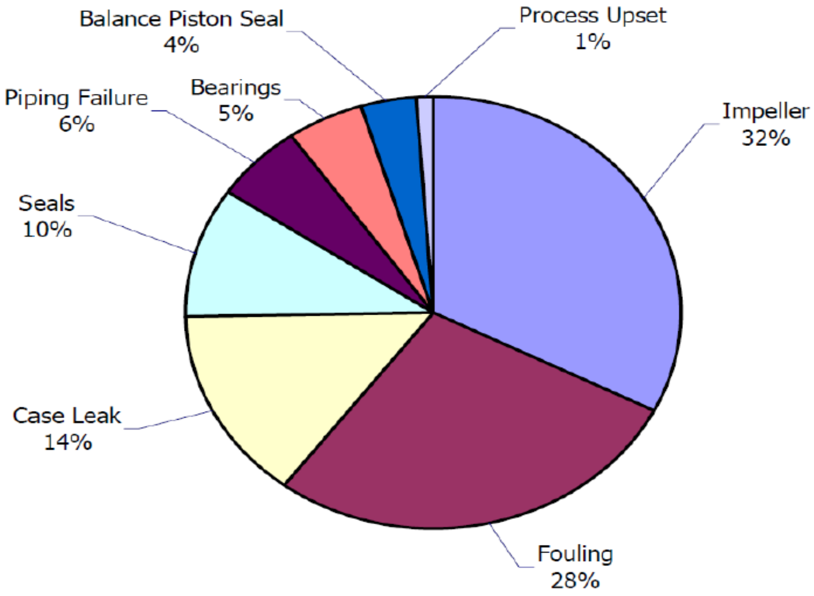

Figure 4- 12: Distribution of Centrifugal Compressor component failures Based on Industry Survey Between 1994 and 1999 (Taylor, 2009)

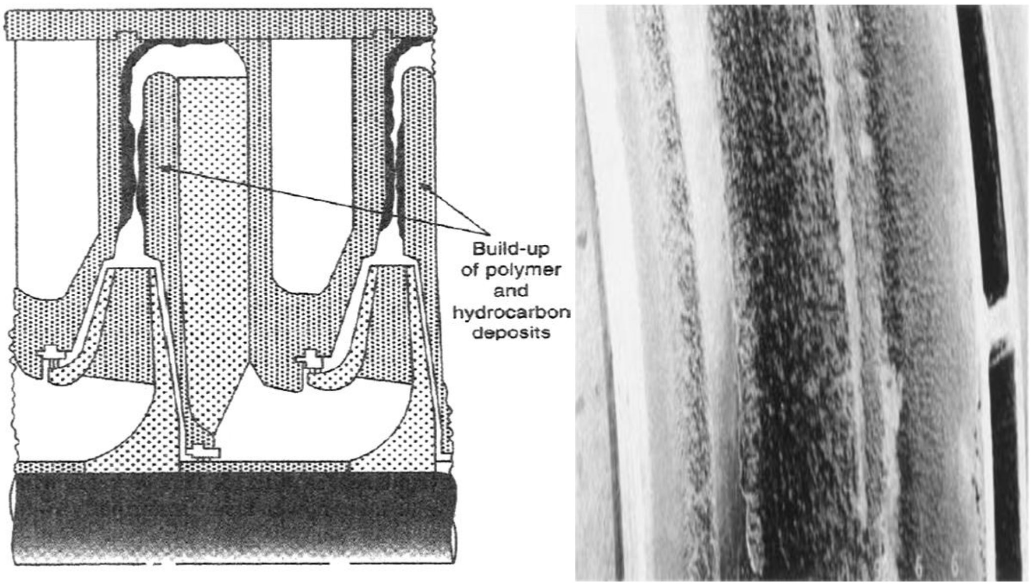

Figure 4- 13: a. Polymerization in a Diffuser Passage of Centrifugal Compressor (Gresh, 2001) b. Impeller Fouling (Zohrabian, 2010)

Moreover, the excessive build up on centrifugal compressor impeller can throw it out of its balance state leading to fatigue loading which reduces the component life and increases the premature shutdowns. Additionally, the compressor erosion raises the tip clearance yielding a higher leakage flow. The excessive leakage flow through the inter-stage seal or the tip clearance causes an increase in viscous losses and reduces the mean stream flow which results in lower capacity and shorter operating range.

4.5 Cleaning of Centrifugal Compressor

The formation of deposits on impeller and diffuser surfaces of the centrifugal compressor eventually leads to flow and efficiency reduction and possibly to a high vibration level when the distribution of these particles is non-uniform. Therefore, it is recommended to prevent the fouling from happening rather than waiting until the foulants started to accumulate. The compressor can be cleaned while it is running to avoid the occurrence of series damages as a result of foulants build up. This helps to reduce the required costly and time-consuming shutdowns for off-line cleaning. The on-line cleaning can be achieved using different techniques, but they can be defined under three working principles. The fouling occurs above particular gas temperature, so reducing this temperature leads to avoid the flow channels fouling. This can be accomplished using purified water based injection. The required quality of the injected water is specified by the manufacturer based on the compressor design and performance.

Another way to prevent the fouling occurrence is by wetting the flow path surface to avoid the particles sticking and accumulation on the surface using atomised solvent injection. Wetting the surface leads to reduce the friction factor of the diffuser and blades surfaces, therefore, reducing the opportunity of foulants accumulation. However, the solvent injection has to be started from the beginning to avoid the flowing of the foulants to the compressor downstream causing blades damage and channel blockage. The location and type of injection nozzles and the selection of solvent are the most two key factors in this method. The solvents can be water-based or petroleum based and both work to dissolve the contaminations. The water-based solvent is effective against salt, but it is relatively poor with oily contaminations. On the other hand, the petroleum-based-solvents are not recommended for salty deposits. Normally, the amount of injected solvent should not exceed 3% of the total flow rate, and the excessive amount of solvent can erode the blade tip leading edge causing problems near the impeller shroud (Boyce, 2003). However, it should be considered that there is a probability of foulants redeposition in the rear compressor stages. To avoid the contamination redeposition, there is a third technique can be used by injecting surfactants which are chemical compounds used to react with the foulants. This method has to be applied on a regular basis and at different load conditions, and it can be used effectively with both organic and non-organic foulants.

Generally, the selection of the appropriate cleaning fluid is highly influenced by the matter of contamination; therefore, the investigation of quantity and type of deposits is recommended. However, it should be noted that the chemical development of the cleaning solutions is still ongoing (Mund and Pilidis, 2006). Moreover, it is a common practice to inject the fouling inhibitors with the cleaning fluids to reduce redepositing. Furthermore, the chemical inhibitors for corrosion and gas hydrate prevention are used in the gas systems to reduce the rate of corrosion and mitigate the hydrate formation (Kidnay et al., 2011). This becomes more critical with high hydrogen sulfide (H_2S) and carbon dioxide (CO_2) levels.

When the compressor is severely fouled, on-line cleaning becomes less effective and the off-line cleaning is recommended, and it can be accomplished as a part of the scheduled maintenance routine. This is most frequently performed using purified water while the buffer and seal gases are kept on when the dry gas seals are used. The failure to immediate removing of the foulants can lead to an excessive vibration level as a result of unbalance state which might cause a catastrophic failure. Although this method is the simplest way and it leads to an effective cleaning, the compressor has to be out of the service leading to reduce the gas throughput and increase the required downtime.

CHAPTER 5: SELECTION, SIZING AND AERODYNAMIC MODELLING OF CENTRIFUGAL COMPRESSOR

This chapter introduces a systematic scheme to evaluate the selection of centrifugal compressor based on the stated process requirements. Besides, the N-method has been used to size the centrifugal compressor with respect to the specified inlet conditions and in order to meet the required duty. The objective of the sizing process is to identify the optimum configuration of the designed compressor to satisfy the working conditions. This has been achieved by evaluating the aerothermodynamic performance of the simulated compressor based on some stated assumptions and by considering the thermodynamic and aerodynamic constraints. In order to validate this algorithm, the obtained parameters are compared with the OEM estimated values. The developed selection and sizing approach generally consists of four basic elements: gas properties estimation, selection evaluation process, aerothermodynamic parameters assessment and compressor sizing. The details of each part will be described in the following sections.

5.1 Evaluation of Centrifugal Compressor Selection

To ensure the appropriate selection of compressor type, the selection of centrifugal compressor is evaluated based on four main factors as illustrated in figure 5-1. These includes: process requirements, initial capital cost, operation cost and logistics consideration.

Figure 5- 1: Scheme of Factors Which Influence Compressor Selection (Sub-Model A)

The followed approach to evaluate the process requirements is based on five criteria: flow capacity, turndown ratio, discharge pressure, specific speed and process gas properties as demonstrated in Appendix (B1). The actual inlet volume has to exceed the minimum value of 500 m^3/h due to smaller required wheels and narrow flow passages; otherwise, the standard diaphragm compressor is preferred especially for discharge pressure higher than 10 bara or for toxic gas. The positive displacement type is typical for high pressure ratio and low inlet volume applications. Besides, the maximum actual inlet volume is considered to be 500,000 m^3/h and for higher than this figure, the axial compressor is suggested. This number has been specified according to Gas Processors Suppliers Association standards (2004).

In terms of capacity turndown ratio, positive displacement compressors are more suitable for capacity turndown ratio below 40%. This obviously due to the high associated surge and power loss with centrifugal compressors as a result of excessive recycle. The discharge pressure is also an important factor which has to be derived based on the required pressure ratio. Based on figure 5-2, the discharge pressure of centrifugal compressor should be between 13.5 bara and 600 bara. Moreover, the centrifugal compressor is considered as a favorable choice when there is only a slight variation in the gas molar mass which not exceed 20% based on the provided running conditions; otherwise, the reciprocating compressor is recommended. The centrifugal compressor head highly depends on the gas molecular weight as the developed kinetic energy by the impeller is a function of gas velocity and molecular weight. On the other hand, the reciprocating compressor has no limit regard to the molecular weight since the very light or heavy gases compressed equally well (Gallick et al., 2006).

Regarding specific speed (N_s), it is obvious from figure 5-3 the radial compressor is commonly used for medium head and flow applications while the positive displacement is recommended for high head and low flow applications. The specific speed is a non-dimensional parameter used to compare the head and flow rate in geometrically similar machines at various speeds. Thus, when the rotor speed below 20, the selection of centrifugal compressor is impractical due to aerodynamic limitations.

$$N_s = \frac{N}{60} . \frac{\sqrt{Q}}{{H_p}^{3/4}} \qquad \textbf{(5-1)}$$

The centrifugal compressor has higher reliability and availability comparing with positive displacement compressors. The reciprocating compressor has many more parts and more rubbing seals which require more frequent replacement leading to lower reliability. As per API617 (2002), the centrifugal compressor has to be designed with a minimum of 5 years of uninterrupted service. However, this can reach to 10 years or longer in clean service, and the maintenance requirements are limited to replacing bearings and seals wearing parts. In reciprocating compressors, the maintenance intervals vary significantly with the applications, so the compressor valve and seal element interval might be as short as few months.

The polytropic efficiency of the centrifugal compressor is relatively higher, and it ranges between 70 percent and 87 percent. This efficiency is substantially affected by the internal leakage and mechanical losses. However, it should be noted that the adiabatic efficiency is typically used for reciprocating compressors rather than the polytropic efficiency. This makes the calculation process of positive displacement compressor simpler. As was explained in chapter 2, this in fact due to substantial effect of pressure ratio variation on the adiabatic process which makes it inappropriate for centrifugal compressor where the inlet flow and rotational speed both vary.

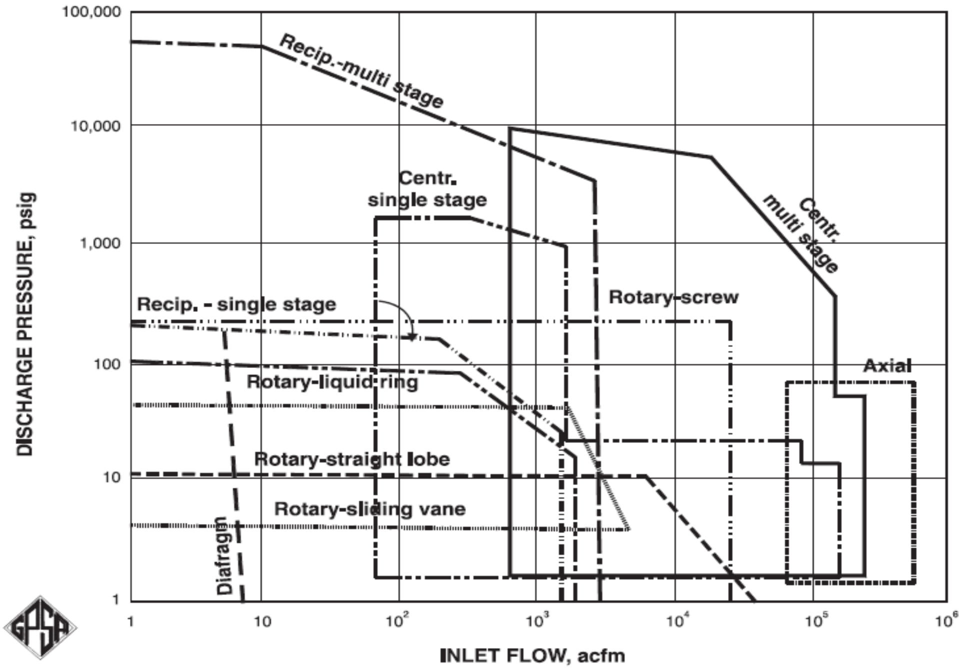

Figure 5- 2: Selection of Compressor Type Based on Discharge Pressure and Flow Capacity (Gas Processors Suppliers Association, 2004)

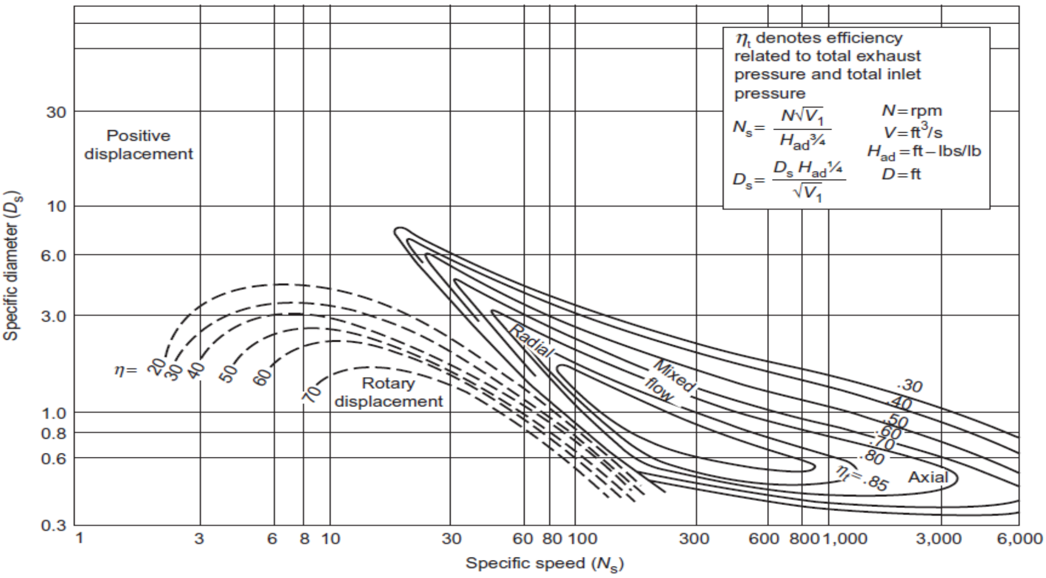

Figure 5- 3: Selection of Compressor Type Based on Specific Speed and Specific Diameter (Boyce, 2012)

Regarding capital and operation costs, the capital cost of the centrifugal compressor is higher than the reciprocating type working at the same conditions since the radial compressor requires parts with complex geometry. On the other hand, the operation cost of centrifugal compressor is relatively lower in terms of downtime, spares and maintenance as it has fewer wearing parts. The lead and installation time are highly influenced by the size and location, number of casing, type of driver and whether this compressor is packaged or not.

5.2 Casing Structure

The casing of centrifugal compressor can be designed in two different types which are the horizontally split casing and vertically split casing. Based on the maintenance, flexibility and reliability perspective, the horizontally split casing is preferred due to the ease of the access to the internal components. This will be considered as the first choice for process applications. However, the use of his type is limited by the maximum allowed working pressure which is imposed to avoid the leak from the joints. This becomes more critical when it is used in sour gas service. Unfortunately, there is no universal exact value of the maximum discharge pressure in the open literature. Lüdtke (2004) and Bidaut (2013) specified 70 bara as maximum discharge pressure of horizontally split casing while it is reduced to 60 bara by Hanlon (2001) and to 50 bara based on Shell regulations (2011). To be on the conservative side, the maximum allowable working pressure (MAWP) for horizontally split will be considered 40 bara in this study.

To comply with the API standards, the partial pressure of the Hydrogen (H_{2pp}) has to be lower than 14.8 bara for horizontally split casing. This can be calculated using equation (5-2). However the beam type of centrifugal compressor becomes a critical option in two areas: high pressure and low molecular weight gas compression.

$$H_{2pp} = x_{H_2}(\%) \times MAWP \tag{5-2}$$

where

x_{H_2}: Highest mole/volume fraction of Hydrogen in the process gas

The use of the integrally geared structure is avoided in high-pressure applications due to the high imposed vibration by the impellers at high rotational speed. Besides, the additional numbers of seals and bearings make it less favorable due to the associated rotordynamic issues. In this study, the use of integrally geared structure is recommended as a single stage only and with a maximum discharge pressure of 25 bara. Appendix (B2) demonstrates the flowchart of the followed procedures to identify the suitable casing structure.

5.3 Process Gas Properties

One of the most common methods of specifying the compressor capacity is by standard volume flow, and it is used extensively in the compressor industry. In this case, the actual flow rate is corrected by the standard inlet conditions including temperature (T_s), pressure (P_s) and compressibility factor (Z_s). The actual flow is used in the compressor performance estimation; thus, the standard volume flow (Q_{std}) is converted to the actual value (Q_{act}) using equation (5-3).

$$Q_{act}(m^3/h) = Q_{std}(m^3/h) \times \left(\frac{Z_s}{Z_{std}}\right) \times \left(\frac{T_s}{T_{std}}\right) \times \left(\frac{P_{std}}{P_s}\right) \tag{5-3}$$

There is one disadvantage of this method which is related to the standard conditions. There are no universal values for the standard conditions in both metric and English systems, especially the standard temperature value. In this research, the standard values which will be used for temperature and pressure are 15℃ and 101.3 kPa while the standard compressibility will be set to 1.

Since the nature of working fluid varies from pure to gas mixture, the developed algorithm has been designed to deal with three different types of gas properties input. For pure gas, the corresponding gas properties are obtained based on the chemical composition at the inlet and exit of each mechanical stage. When the process gas composition is not identified, another option can be used by specifying the average gas properties including the molecular weight (MW), molar specific heat (MC_p) and compressibility factor (Z) as illustrated in Appendix (B3). This is a typical selection when the properties of the compression gas have been specified by the process engineers without identifying the gas composition.

If the process gas is a hydrocarbon mixture, the overall properties can be calculated based on the composition and by knowing the relative mole or volume fraction of each component (x_i). So, the molecular weight (MW_{mix}), molar specific heat ($MC_{p_{mix}}$), critical pressure ($P_{cr_{mix}}$) and temperature ($T_{cr_{mix}}$) of the gas mixture are obtained using equations (5-4) to (5-7).

$$MW_{mix} = \sum_{i=0}^{m} x_i MW_i \tag{5-4}$$

$$MC_{p_{mix}} = \sum_{i=0}^{m} x_i MC_{p_i} \tag{5-5}$$

$$P_{cr_{mix}} = \sum_{i=0}^{m} x_i P_{cr_i} \tag{5-6}$$

$$T_{cr_{mix}} = \sum_{i=0}^{m} x_i T_{cr_i} \tag{5-7}$$

However, it might be found that the mole fraction of every gas component is not known. Therefore, it can be calculated by providing the corresponding flow rate of each compound either in kg/h unit using equation (5-8).

$$x_i(^\circ k.mol/h) = \frac{\dot{m}_i(kg/h)}{MW_i(kg/^\circ k.mole)} \tag{5-8}$$

The reduced temperature (T_r) and reduced pressure (P_r) are obtained at the suction and discharge of centrifugal compressor by dividing the actual pressure and temperature by the their corresponding critical values ($P_c\,, T_c$). These two parameters are used after that to obtain the compressibility factor (Z) either by implementing the equations of state or from the generalized compressibility charts. However, using the compressibility factor charts may introduce a small degree of uncertainty since they are derived based on the Law of Corresponding States. Accordingly, equal values of compressibility factor (Z) are assumed for all gases with the same reduced pressure and temperature. Therefore, the obtained reading from the compressibility charts will be evaluated against the predicted values from three very common equations of state these are: Redlich-Kwong EOS, Soave-Redlich-Kwong EOS and Peng-Robinson EOS. Moreover, the calculated values are compared with the experimental reading in order to select the most accurate method with the minimum deviation from the actual value.

The inlet compressibility factor is also a key parameter to calculate the actual inlet volume flow as shown in equation (5-3). However, the Z factor varies throughout the compression process as the gas pressure and temperature change. Furthermore, using the inlet Z factor to estimate the polytropic head is very conservative, and the deviation from the OEM data is expected to be high. Hence, the compressibility factor in this study is obtained at the suction and discharge of each compression stage, and the average value is then used to calculate the polytropic head of every stage. The gas constant (R) can be derived as a function of gas molecular weight (MW). Thus, the gas density is calculated at the inlet and exit of the compression stage using formula (5-9).

$$\rho = \frac{P}{Z \times \frac{R_0}{MW} \times T} \qquad \textbf{(5-9)}$$

where:$R_0 = \begin{Bmatrix} \text{8.314 in Metric System} \\ \text{1.545 in English System} \end{Bmatrix}$

The density is changing continuously as a result of the variation in the process gas conditions including temperature, pressure and compressibility. The molar specific heat (MC_p) is calculated using equation (5-10) at the corresponding gas temperature and gas mixture.

$$MC_p = (CPVAPA) + (CPVAPB) \times T + (CPVAPC) \times T^2 + (CPVAPD) \times T^3 \qquad \textbf{(5-10)}$$

where

$CPVAPA, CPVAPB, CPVAPC, CPVAPD$: Correlation coefficients

The correlation coefficients ($CPVAPA, CPVAPB, CPVAPC, CPVAPD$) are specified based on the gas composition using the published gas properties in Chemical Engineering Design book (Sinnott, 2005). Therefore, the molar specific heat is calculated for each compound and the overall value of the gas composition is obtained by equation (5-5).

Using the molar specific heat (MC_p), the specific heats ratio (k) is also estimated at both ends of the mechanical stage and, the average value is calculated. This value will be used later to obtain the polytropic exponent (n) value.

$$k = \frac{C_p}{C_p - R} \qquad \textbf{(5-11)}$$

One of the important gas properties is the dynamic viscosity which measures the gas resistance to flow. In order to calculate it, the derived model by Lee, Gonzalen and Eakin (1964) is used. This is considered as the first correlation used to predict the viscosity of hydrocarbon gases. According to this approach, the viscosity is calculated as a function of gas temperature, density and molecular weight.

$$\mu = \left[\frac{0.0001\,T^{\frac{3}{2}}(7.77 + 0.0063\,MW)}{122.4 + 12.9MW + T}\right] \times \exp\left\{\left(2.57 + \frac{1914.5}{T} + 0.0095MW\right) \times \rho^{\left[1.11+0.04\times\left(2.57+\frac{1914.5}{T}+0.0095MW\right)\right]}\right\} \tag{5-12}$$

It was found that this equation generates more accurate results when the temperatures and pressures are ranging from 310°k to 445°k and 1 bara to 552 bara, respectively. Thus, this model has been modified by Ling (2010) to cover wider pressure and temperature ranges.

$$\mu = \left[\frac{0.0001\,T^{1.2288}(9.18999 + 3.0893\,MW)}{208.99 + 18.83933MW + T}\right] \times \exp\left\{\left(3.56014 + \frac{1000.01}{T} + 0.124465MW\right) \times \rho^{\left[2.47862-0.12294\times\left(3.56014+\frac{1000.01}{T}+0.124465MW\right)\right]}\right\} \tag{5-13}$$

Therefore, both these two models will be implemented in this chapter, and the obtained results will be evaluated against the measured value in order to select the suitable correlation.

5.4 Design Constraints

5.4.1 Rotational Speed

Increasing the rotational speed can be achieved either by increasing the impeller tip speed or reducing the mean impeller diameter. Despite the fact that the higher operational speed raises the stage pressure ratio, this can lead to catastrophic failure when it becomes greater than the second critical speed of the shaft. The high vibration level causes serious damages to the internal compressor component. The OEMs in general specified the allowed maximum limit of the rotational speed of single shaft beam and integrally geared compressors by approximately 16,000 rpm and 50,000 rpm, respectively with a gear ratio of 10:1.

5.4.2 Discharge Temperature

It is important to check that the actual discharge compressor is lower than the maximum allowed limit in order to avoid the gas dissociation and decomposition, process fouling, fire hazards, seals and bearings failure. In this study, the upper limit of stage discharge temperature is specified based on Lüdtke's (2004) approach since it considers the effect of gas cracking and hydrocarbon polymerization. In oil and gas industry, the maximum discharge temperature of centrifugal compressor is limited by 170 ℃ when the natural gas is used as a working fluid. This limit is reduced to 150 ℃ if the natural gas is associated with crudes because it is susceptible to cracking at relatively low temperatures. To avoid the aero-channel fouling as a result of hydrocarbon polymerization, it is recommended to keep the gas temperature below 110℃ when there is a presence of polymerizing hydrocarbons within the process gas.

Although that the metallic compressor components can withstand up to 250℃, the non-metallic parts such as elastomeric seals and lube oil usually limit the compressor discharge temperature to approximately 140-150℃. Based on the standards of API617 (2002) and Shell International Petroleum (Shell International Petroleum, 1991), the upper limit of discharge temperature has been specified by 150 ℃, and it will be considered in this study only when the natural gas is subjected to cracking.

5.4.3 Inter-cooling System

When the process requires a higher pressure ratio, the intercoolers are used to reduce the discharge temperature of the compression stage before entering the next stage by exchanging the heat with the relatively cold water. Normally, the inter-stage cooling is used to provide an equal inlet temperature to all compression groups of the intercooled compressors.

Based on API617 (2002) standards, the maximum inlet and outlet temperatures of the cold stream are specified by 30℃ and 50℃, respectively with a temperature rise between 10 and 20 degrees centigrade. In this case, the cost of extra equipment and pressure drop should be considered against the power saving as a result of using the inter-cooling. During the cooling process, the gas temperature should be higher than the saturation temperature and a margin of 5℃ above the saturation point is recommended to consider.

5.4.4 Impeller Geometry

As aforementioned, the stage efficiency varies considerably with the flow coefficient. The high flow coefficient value leads to increase the axial length which, in turn, reduces the maximum number of impellers that can be accommodated in one shaft. Moreover, designing the impeller with shorter outer diameter is not always possible. The volume flow rate decreases towards the rear of centrifugal compressor stages due to the increase of gas density with the pressure rise. So, reducing the diameter of the subsequent impellers cannot achieve the optimum flow coefficient for all stages. Besides, the impact of designing the impeller with smaller diameter on the rotational speed and the head coefficient has to be kept in mind. Generally, it is acceptable to design the compressor rotor with a flow coefficient between 0.01 and 0.15, but that will not ensure the optimum efficiency point.

To avoid the negative effect of small impeller exit width on the compressor head and efficiency and shaft vibration especially when flow congestion or fouling occurs, the exit impeller width has been considered with a minimum value of 3 mm. Practically, it was found that the impellers with exit width above this value are showing a good performance. Besides, the outer diameter of impellers in single shaft centrifugal compressor is specified by OEMs to be lower than 2,000 mm. This designed diameter should be also considered with respect to the maximum rotational speed and in term of manufacturing and transportation costs.

5.4.5 Impeller Tip Speed

The developed approach uses a new methodology to specify the tip speed according to three criteria which are: the type of impeller, molecular weight and tip Mach number. However, the effect of impeller material has not been considered in this study.

Table 5- 1: Impeller Tip Speed with Respect to the Molecular Weight (Mechanical Engineering in Process Equipment, 2009)

MW (g/mol)	Average Tip Speed (m/s)
<35	310
<45	250
<65	200
<120	150

According to the impeller structure, Wharton (2013) and Amano (2008) procedures will be followed. The absence of cover in the open impellers allows them to rotate at higher speed comparing with the closed impellers. The maximum tip speed of shrouded impellers is specified by 350 m/s while it reaches 430 m/s for unshrouded type. Besides, the tip speed is corrected based on the gas molecular weight as shown in table 5-1. Finally, the corresponding tip Mach number (*Mu*) has to be lower than the maximum limit. This study specifies the maximum allowed tip speed of the centrifugal impeller by 90% of the sonic speed in order to reduce the shock losses.

5.4.6 Stage Polytropic Head

The implemented approach for specifying the maximum developed polytropic head per impeller is based on two parameters which are the gas molecular weight and discharge pressure as shown in figure 5-4. So, the maximum allowed polytropic head per impeller is specified at the beginning according to the discharge pressure based on the Simmons's method (2003). Based on this method, the maximum polytropic head is specified to be about 30 kJ/kg for operating pressure lower than 100 bar. At discharge pressures beyond 100 bar, the maximum head is set to be 20 kJ/kg. When the discharge pressure is lower than 100 bar, the obtained value is corrected further by considering the effect of gas molecular weight using Brown method (2005). According to this method, the value 30kJ/kg is used for gas molecular weight between 28 and 30. For molecular weight above this value, 0.3 kJ/kg is subtracted from this head value for every unit increase in molecular weight. On the other hand, 0.6 kJ/kg head is added for every unit decrease in the molecular weight as demonstrated in figure 5-4.

Despite that the high input work and head coefficients reduce the required number of impellers, it is recommended that the work coefficient of the designed stage to be between 0.57 and 0.66 to avoid the high aerodynamic loading effect on the impeller blades. Besides, the head coefficient should be between 0.8 and 1.1 based on the recommended values for the optimum aerodynamic performance (Lüdtke, 2004).

5.4.7 Number of Impellers per Casing

The maximum rotor length and impeller number are mainly limited by the rotor critical speeds. The centrifugal compressors operate between the first and second rotor speeds and increasing the rotor length will lead to reduce these speeds values. This is actually because that the second critical speed decreases faster than the first critical speed.

The number of impellers which can be accommodated by the compressor body varies from one manufacturer to another, but it generally depends on several variables including pressure ratio, flow capacity, tip speed, Mach number, discharge temperature, shaft diameter and span between the bearings (Wharton, 2013). Based on the aerodynamic view, the developed approach uses a conservative technique by specifying the upper limit of impellers per housing with respect to three parameters which are: flow coefficient, Mach number and impeller arrangement. Figure 5-5 illustrates the maximum number of impellers per casing based on the sort of arrangement.

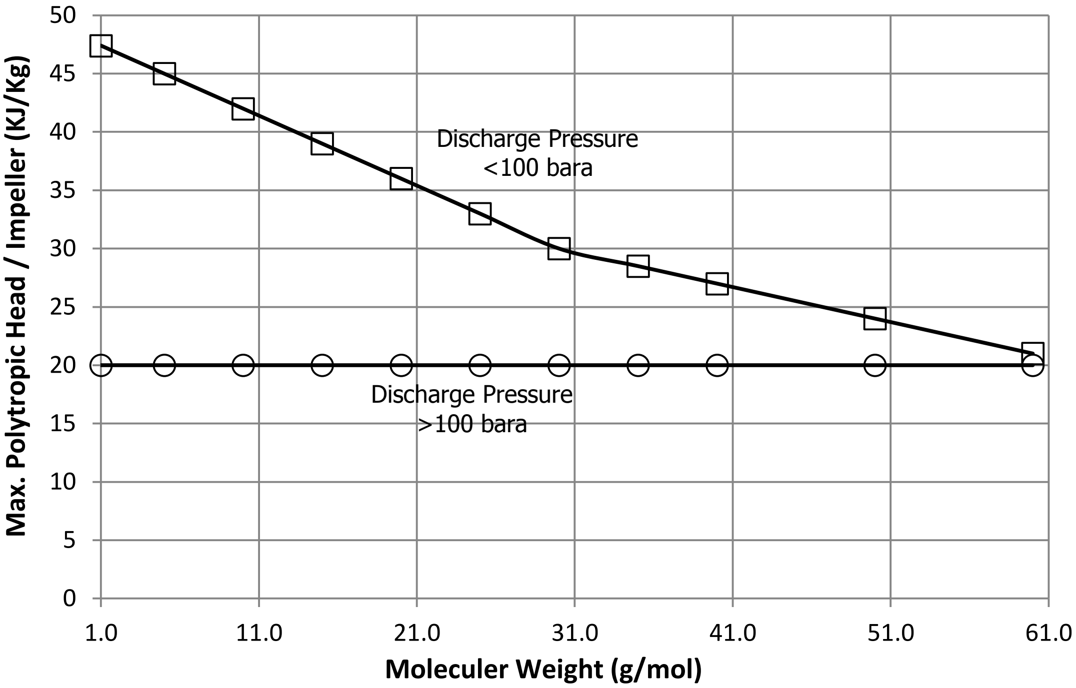

Figure 5- 4: Maximum Polytropic Head per Impeller Based on Molecular Weight and Discharge Pressure

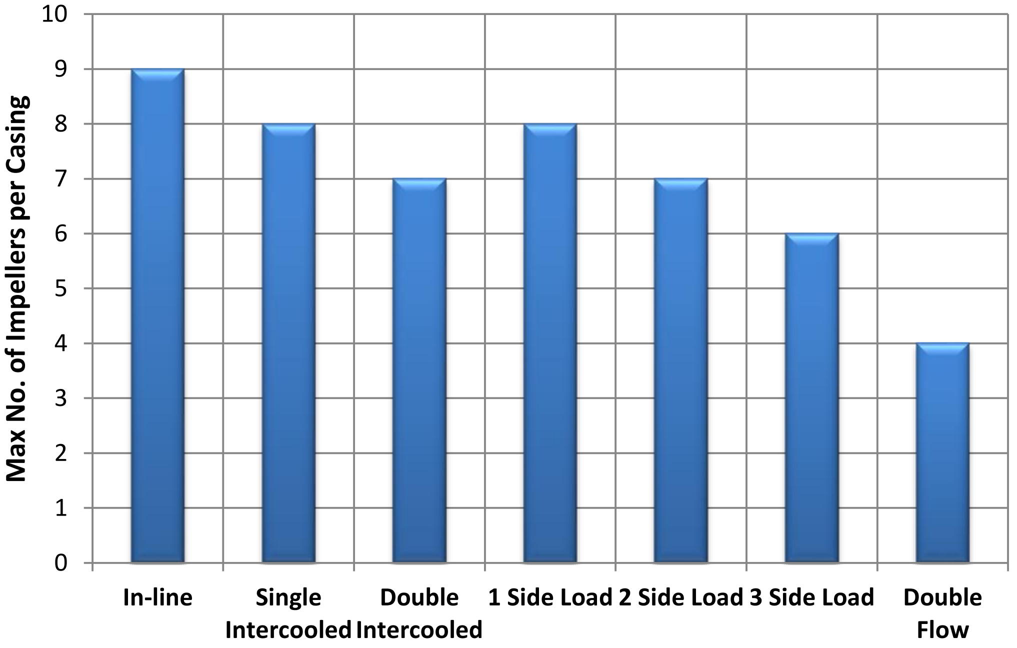

Figure 5- 5: Maximum Number of Impellers per Shaft Based on Impellers Arrangement (Data from Lüdtke, 2004)

The maximum number of impellers for in-line compressors is nine. However, this limit is reduced to eight for single cooled compressor since the required space by the intermediate diaphragm is often equivalent to the impeller axial length. For side load applications, the side diaphragm and the mixing area require a stage space also for each side. A further check is made to estimate the required number of casings with respect to the machine Mach number (*Mu*) and flow coefficient (FC) as shown in figure 5-6. This figure has been constructed based on available data in the literature (MEPE, 2009).

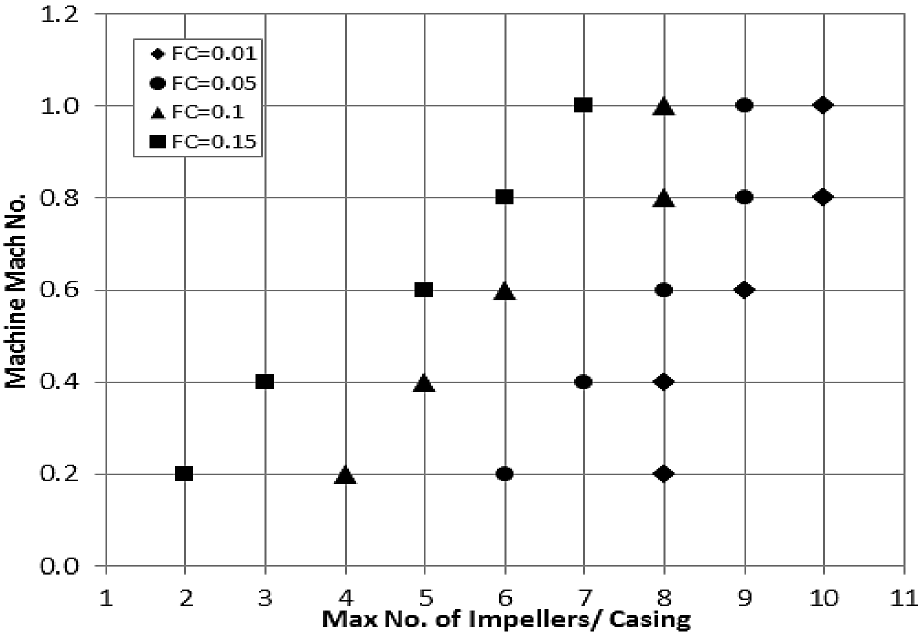

Figure 5- 6: Maximum No. Impellers Based on Tip Speed Mach Number and Flow Coefficient (Data from: MEPE, 2009)

The flow coefficient alters the axial length which, in turn, affects the number of impeller per casing. Besides, the machine Mach Number reflects the impeller diameter so that the high value denotes a smaller impeller diameter and greater casing space for further impellers. By utilizing these two figures, the minimum value is used to obtain the required number of casings.

5.5 Single Stage Centrifugal Compressor

The first step in centrifugal compressor sizing is to estimate the required number of mechanical stages to achieve the specified pressure ratio as demonstrated in Appendix (B4). Using the calculated actual suction volumetric flow rate, the initial polytropic efficiency is obtained from figure 5-7. This curve has been derived based on the standard centrifugal compressor data which are available in the open literature such as Gresh (2001) and Girdhar (2008).

The obtained efficiency value will be iterated in the following stage based on the impeller type and blade profile. Initially, this efficiency is used to calculate the temperature polytropic exponent (n_T) by equation (5-14).

$$n_T = \frac{1}{1 - \frac{ZR}{C_p}\left(\frac{1}{\eta_p} - 1\right) - \frac{k_1}{k_1 - 1}} \tag{5-14}$$

The specific heat ratio of the suction side (k_1) is used and after determining the discharge value, the polytropic exponent will be recalculated again based on the average specific heats ratio.

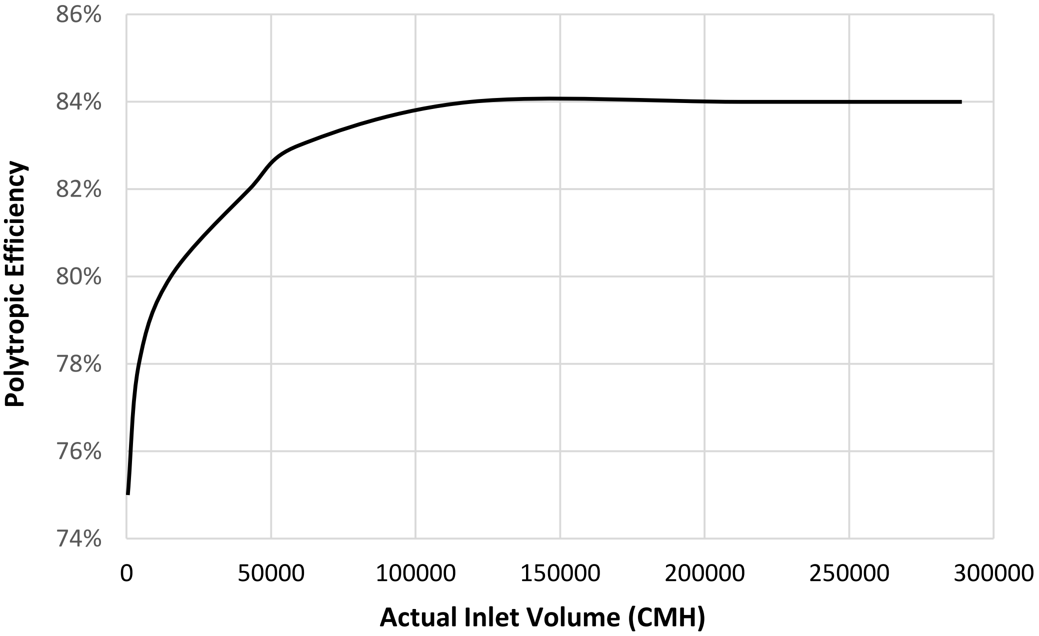

Figure 5- 7: Standard Polytropic Efficiency Based on Inlet Volume Based on Published Data by Gresh (2001) and Girdhar (2008)

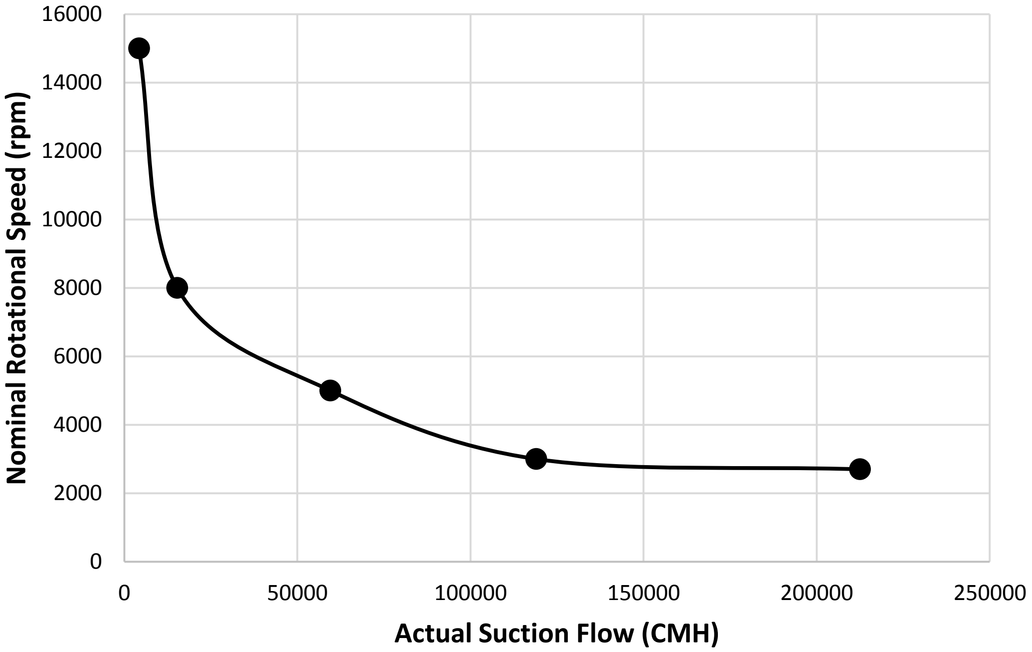

Figure 5- 8: Comparison Between the Standard Nominal Speeds of Different Centrifugal Compressors As A Function of Actual Flow Based on Published Data by Lapina (1982)

The discharge temperature of the compression process is derived in relation to the inlet temperature and the compression ratio. As aforementioned in section 5.4.2, the maximum allowed discharge temperature is specified based on the tendency of the process gas to cracking or polymerization. This value is then used to obtain the maximum pressure ratio per process stage using formula (5-15).

$$PR_{max} = \left(\frac{T_{2,max}}{T_1}\right)^{\frac{n_T - 1}{n_T}} \quad \textbf{(5-15)}$$

For a single stage centrifugal compressor, the maximum pressure ratio has to be greater than the actual required pressure ratio, and the discharge temperature is lower than the maximum value. The discharge pressure and temperature are used to obtain the discharge gas properties including compressibility factor (Z), specific heats ratio (k) and discharge density (ρ).

Initially, the tip relative Mach number is set to 0.9 to eliminate the separation and shock losses. After that, the first iteration tip speed is specified based on the molecular weight and this value will be checked again in the parameters evaluation stage. The selected tip speed has to be lower than 90% of the acoustic velocity (a) to avoid the rotordynamic and aerodynamic instability.

$$U_{1,max} = 0.9\sqrt{k_1 R_1 T_1 Z_1} \quad \textbf{(5-16)}$$

When the rotational speed is specified, the inlet tip diameter (D_1) can be calculated using the obtained tip speed by equation (5-17). However, the rotational speed might not be known at this design stage, so it is initially selected below the allowed limit according to the compressor structure as explained in section 5.4.1. Based on the inlet flow rate, the nominal rotational speed can be specified using the standard available data as illustrated in figure 5-8. Then, the inlet impeller diameter is obtained using formula (5-17), and it is used to calculate the flow coefficient.

$$N\ (rpm) = \frac{60\ U_1}{\pi D_1} \quad \textbf{(5-17)}$$

The flow coefficient has to be within the recommended range. Otherwise, the assumed rotational speed is altered to meet the allowed range.

To determine the required number of impellers, the total polytropic head is divided by the maximum head per impeller ($H_{p,max}$) using equation (5-19). The required head is calculated using the average polytropic volume exponent of the suction and discharge sides by formula (5-18). The maximum head per impeller is estimated from figure 5-4 and by considering the discharge pressure and the molecular weight.

$$n_v = \frac{k}{1 + \left(1 - \frac{1}{\eta_p}\right)\left(\frac{k-1}{k}\right)} \quad \textbf{(5-18)}$$

$$No. Impellers = INT\left[\frac{Z_{avg} R T_1 \left(\frac{n_{v,avg}}{n_{v,avg}-1}\right)\left[PR^{(n_{v,avg}-1)/n_{v,avg}} - 1\right]}{H_{p,max}} + 0.5\right] \quad \textbf{(5-19)}$$

Furthermore, the derived flow coefficient and tip speed Mach number are used to obtain the maximum allowed impeller number per casing according to figure 5-6. Additionally, the upper limit of impeller per housing is identified according to the impeller arrangement as illustrated in figure 5-5 and the minimum value is taken to identify the required number of casings.

To ensure the optimum aerodynamic performance, the head and work coefficients are calculated and the tip speed is checked again to meet the recommended range. The third iteration is performed to correct the polytropic efficiency and tip speed based on the impeller type. The accommodated number of impellers per casing is used to estimate the polytrophic efficiency according to the kind of impeller as shown in figure 5-9(a). The impeller type is selected based on flow coefficient as described previously. However, since this efficiency is at 0.09 flow coefficient, the obtained value is multiplied by the correction factor using figure 5-9(b) with respect to the actual flow coefficient. These two figures are essentially derived from available data in the centrifugal compressor manual reference (Mechanical Engineering in Process Equipment, 2009).

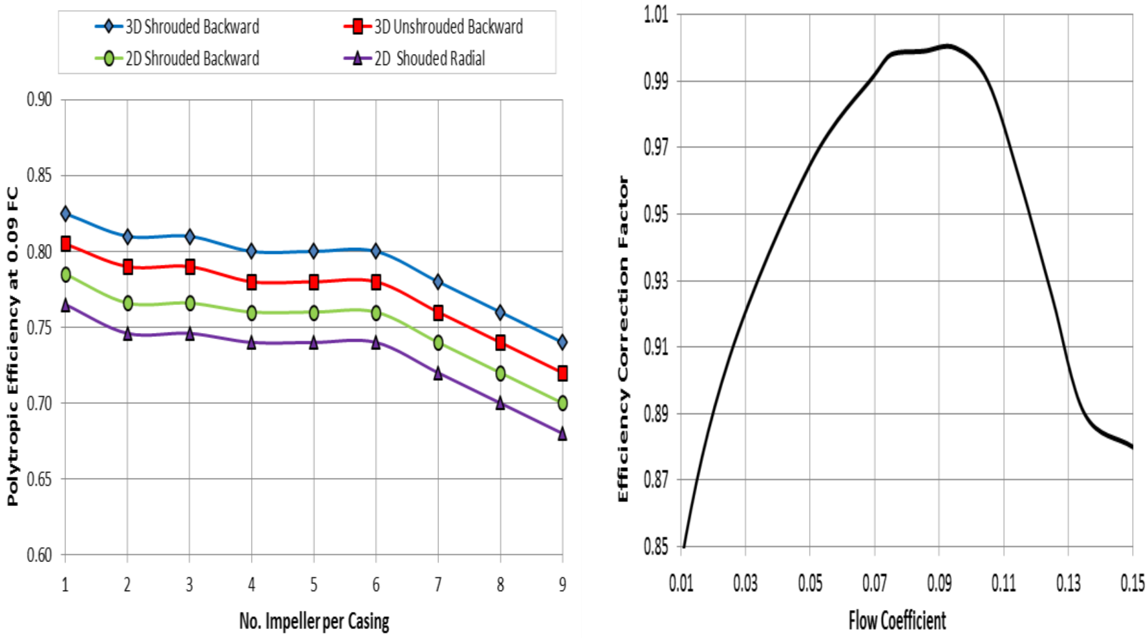

(a) **(b)**

Figure 5- 9: Determination of Polytropic Efficiency According to Impeller Type Based on Published Data by (Mechanical Engineering in Process Equipment, 2009)

The inlet impeller absolute velocity is estimated based on the calculated relative velocity and iterated tip velocity.

$$V_1 = \sqrt{{M_{1,rel}}^2 \, k_1 R_1 T_1 Z_1 - U_1^2} \tag{5-20}$$

To obtain the required inlet flow area (A_1), the continuity equation is implemented as a function of flow rate ($\dot{m}$), gas density (ρ_1) and inlet meridional velocity (V_{1m}).

$$A_{inlet\,A} = \frac{\dot{m}}{V_{1m}\,\rho_1} = \frac{\pi}{4}\left(D_e^2 - D_h^2\right) \tag{5-21}$$

The eye diameter (D_e) is specified according to the impeller type, but it is preferred to be same as the inlet diameter to ensure a smooth flow. The recommended value of the inlet diameter-to-eye diameter (D_1/D_e) is ranging from 0.83 to 0.88 for 3D blades impellers; and between 1.0 and 1.12 for 2D impellers (Lüdtke, 2004).

To obtain the exit impeller diameter (D_2), the optimum diameter ratio is calculated using Wiesner (1967) and Von Backström (2006) models. According to Wiesner model, the slip factor is calculated without knowing the impeller diameter ratio. Then, the SRE equation is implemented to guess the diameter ratio by matching both values.

$$\mu = 1 - \frac{1}{1 + \left[(2 + 3\cos\beta_2)\frac{(1-DR)\,Z_b}{2\pi\,(cos\beta_2)}\right]} = 1 - \frac{\sqrt{\cos\beta_2}}{{Z_b}^{0.7}} \tag{5-22}$$

The blade exit angle (β_2) is assumed based on the selected impeller type. This value is corrected again after that to meet the recommended values of the discharge flow coefficient. By knowing the impeller diameter ratio and inlet diameter (D_1), the exit diameter (D_2) can be calculated. The outlet tip speed (U_2) is estimated using formula (5-17) with respect to the outlet impeller diameter and the rotational speed. However, this diameter is iterated to obtain accepted values of discharge flow coefficient and tip Mach number. By using the outlet impeller diameter, the inlet hub can be calculated as a function of the inlet flow coefficient as shown in figure 5-10. This value is compared with the obtained value from equation (5-21) and both values have to be identical. The matching can be achieved by varying the inlet relative Mach number which in response will alter the inlet absolute velocity and the inlet flow area.

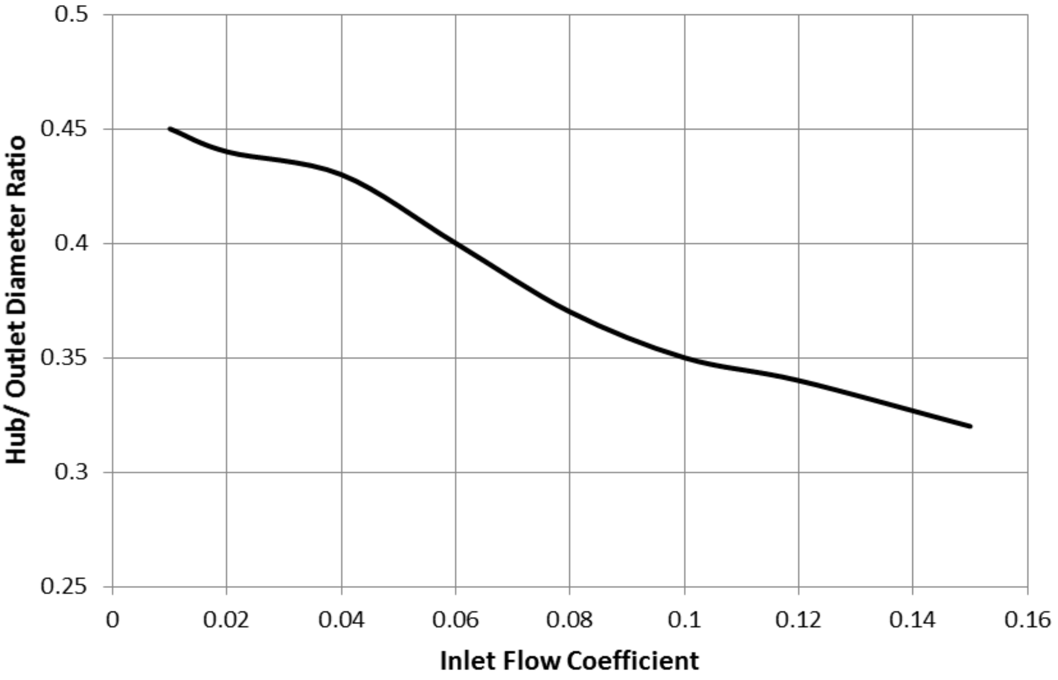

Figure 5- 10: Hub-to-Tip Ratio as a Function of Flow Coefficient Derived from (Ludtke, 2004)

The optimum exit impeller diameter-to-width ratio (b_2/D_2) is derived by the equation (5-23) and the obtained ratio is used to calculate the exit impeller width (b_2).

$$b_2/D_2 = 0.255 \frac{\left(\frac{\varphi_1 Z_2}{4\varphi_2 Z_1}\right)}{\left(\frac{P_2}{P_1}\right)^{(k-1)/k\eta_p}} \quad \textbf{(5-23)}$$

The inlet-to-exit impeller width (b_2/b_1) is assumed and the inlet width (b_1) is iterated based on the inlet Reynolds Number. To account the pressure rise within the impeller, the degree of reaction (γ_d) is calculated as a percentage of impeller static head to the total Euler head.

$$\gamma_d = \frac{W_1^2 - W_2^2}{2(U_2 V_{2\theta} - U_1 V_{1\theta})} \quad \textbf{(5-24)}$$

The discharge static and total pressure and temperature of the impeller are calculated based on the degree of reaction and absolute Mach number.

$$\frac{T_{02}}{T_2} = 1 + \left(\frac{k-1}{2}\right) Mu_2^2 \quad \textbf{(5-25)}$$

$$\frac{P_{02}}{P_2} = \left[1 + \left(\frac{k-1}{2}\right) Mu_2^2\right]^{k/(k-1)} \quad \textbf{(5-26)}$$

After that, the required gas horsepower (GHP) to drive the compressor is calculated using formula (5-27).

$$GHP\ (kW) = \frac{\dot{m} \times H_p \times g}{36 \times 10^5 \eta_p} \quad \textbf{(5-27)}$$

However, a part of the provided energy is used to overcome the mechanical and aerodynamic losses within the compressor stage. Therefore, the accurate estimation of the losses is significant.

The mechanical losses are associated with the bearings and they are counted per casing. Two journal bearings are placed at both ends of the compressor shaft and one thrust bearing at the low-pressure side to support the radial and axial compressor loads, respectively. To calculate the bearings losses (ML_B), a simple formula is well used in the industry as a function of the volume flow rate and the rotational speed.

$$ML_B\ (kW) = R_L(0.001N)^2 = 0.0001 \times \dot{m}^{0.908} \times (0.001N)^2 \quad \textbf{(5-28)}$$

where: R_L is bearing Mechanical losses coefficient (Table 5-2).

The end-shaft seals are commonly used as mechanical seals or oil seal type. Dry seals use high-pressure gas and operate mechanically by opposing the created force by hydrodynamic grooves and static pressure. This results in considerably less power and maintenance requirements leading to better reliability and efficiency. However, using the mechanical seals is not always possible due to its housing design and operational requirements, but it is still considered as a first choice. So, based on the seal type, the appropriate seal losses formula is used.

$$ML_{DS}\ (kW) = 0.001\ R_D N = (9.26 \times 10^{-6} \times \dot{m}^{0.5197}) \times N \tag{5-29}$$

$$ML_{WS}\ (kW) = R_S(0.001N)^2 = 5.764 \times 10^{-5} \times \dot{m}^{0.9077} \times (0.001N)^2 \tag{5-30}$$

where:
ML_{DS}: Dry mechanical seal losses
ML_{WS}: Wet seal losses
R_D: Dry mechanical seals loss coefficient (Table 5-2)
R_S: Wet seals loss coefficient (Table 5-2)

Table 5- 2: Mechanical Losses Coefficients (MEPE, 2009)

Flow (m³/h)	RL	RS	RD
2,500	0.13	0.07	0.54
10,000	0.45	0.24	1.1
50,000	2.9	1.55	3.2
300,000	10	5.4	6.5

The incidence loss is calculated using Conrad et.al (1980) model. This model was found to obtain accurate results for the incidence loss.

$$\Delta h_{inc} = 0.3W_{\theta i}^2 \tag{5-31}$$

$$W_{\theta i} = W_{\theta 2} - W_{\theta 1b} = \frac{V_{m1}}{\tan \beta_1} - \frac{V_{m1}}{\tan \beta_{1b}} \tag{5-32}$$

$$W_{\theta i} = V_{m1}\left[\cot\left(\tan^{-1}\frac{V_{m1}}{W_{\theta 1b}}\right) - \cot\left(\tan^{-1}\frac{V_{m1}}{W_{\theta 1}}\right)\right] \tag{5-33}$$

The Coppage et al. model (1956) is used to calculate the blade loading loss as a result of the boundary layer build up on the impeller flow channel.

$$\Delta h_{bld} = 0.05\left\{\left(1 - \frac{W_2}{W_{1s}}\right) + \frac{K_{BL} \times \Delta h_{Euler}/{U_2}^2}{\left(\frac{W_{1s}}{W_2}\right)\left[\left(\frac{Z}{\pi}\right)\left(1 - \frac{d_{1s}}{d_2}\right) + 2\frac{d_{1s}}{d_2}\right]}\right\}^2 {U_2}^2 \tag{5-34}$$

where: $K_{BL} = \begin{Bmatrix} 0.60 \text{ for convential impellers} \\ 0.75 \text{ with splitter impeller} \end{Bmatrix}$

The clearance (Δh_{cl}) and leakage (Δh_{leak}) losses are obtained using Jansen's (1967) model and Aungier's model (1995), respectively.

$$\Delta h_{cl} = 0.6\frac{\varepsilon_c}{b_2}V_{\theta 2}\left[\left(\frac{4\pi}{b_2 Z}\right) \times \left(\frac{r_{1s}^2 - r_{1h}^2}{(r_2 - r_{1s})(1 + \rho_2/\rho_1)}\right)V_{\theta 2}V_{m1}\right]^{0.5} \tag{5-35}$$

$$\Delta h_{leak} = \frac{0.665856 \times (r_2 V_{\theta 2} - r_1 V_{\theta 1}) \times \varepsilon_c \times U_2}{\left(\frac{r_2 + r_1}{2}\right) \times \left(\frac{b_2 + b_1}{2}\right)} \tag{5-36}$$

The associated losses with the vaneless space and the diffuser part are estimated using the Stanitz (1952) equation (5-37). The diameter ratio of the vaneless space and diffuser are assumed and corrected in order to obtain the required discharge pressure out of the mechanical stage. This Stanitz's model considers the change in the pressure and temperature with the radius in the diffuser, and it has been developed numerically from the differential equations assuming an adiabatic flow and constant geometric depth of the flow passage.

$$\Delta h_{vls} = C_p T_{02}\left[\left(\frac{P_3}{P_{03}}\right)^{(\gamma-1)/\gamma} - \left(\frac{P_3}{P_{02}}\right)^{(\gamma-1)/\gamma}\right] \qquad \textbf{(5-37)}$$

Moreover, the loss associated with the work done due to the backflow recirculation behind the impeller (Δh_{rc}) is expressed by Coppage model (1956). Besides, Shepherd equation (1956) is used to obtain the impeller disk friction enthalpy drop (Δh_{df}).

$$\Delta h_{rc} = 0.02\,\sqrt{tan\;\alpha_2}\,\left[1 - \frac{W_2}{W_{1s}} + \frac{K_{rc}\,\Delta h_{Euler}/{U_2}^2}{\left(\frac{W_{1s}}{W_2}\right)\left[\left(\frac{Z}{\pi}\right)\left(1 - \frac{d_{1s}}{d_2}\right) + 2\,\frac{d_{1s}}{d_2}\right]}\right]^2 U_2 \qquad \textbf{(5-38)}$$

$$\Delta h_{df} = K_{df}\,\frac{(\rho_1 + \rho_2) D_2^2 U_2^3}{2\dot{m} Re^{0.2}} \qquad \textbf{(5-39)}$$

where:

$$K_{rc} = \begin{Bmatrix} 0.60 \text{ for convential impellers} \\ 0.75 \text{ with splitter impeller} \end{Bmatrix} \quad K_{df} = \begin{Bmatrix} \dfrac{2.67}{Re_2^{0.5}} & \text{for } Re_2 < 3 \times 10^5 \\ \dfrac{0.0622}{Re_2^{0.2}} & \text{for } Re_2 \geq 3 \times 10^5 \end{Bmatrix}$$

For simplicity, the aerodynamic losses of each single mechanical stage will be assumed to be identical in every process stage. So, the obtained total aerodynamic losses per process stage will be greater than the actual value due to the inlet volume flow reduction of each subsequent stage. Thus, the total stage aerodynamic losses are corrected by the first stage-to-last stage inlet absolute velocities ratio as these losses are strongly influenced by the gas velocity.

$$\begin{aligned} BHP(kW) = {} & GHP + ML_B + ML_S \\ & + \left[\frac{\dot{m}\left(\Delta h_{vls} + \Delta h_{rc} + \Delta h_d + \Delta h_{df} + \Delta h_{cl} + \Delta h_{bld} + \Delta h_{inc}\right)}{1000} \right. \\ & \left. \times No.Impellers \times \left(\frac{V_{s,1}}{V_{s,n}}\right)^2\right] \end{aligned} \qquad \textbf{(5-40)}$$

5.6 Selection of Capacity Control Method

To maintain a stable operation over wide off-design conditions, the inlet flow has to be varied using one of the regulation methods. There are five different techniques to control the flow capacity of centrifugal compressors. However, there is no standard methodology in the public domain to select the suitable regulation method. So, five basic criteria have been considered to ensure the typical selection which are: casing structure, part-load efficiencies, investment cost, overload operation and suction pressure.

The suction throttling does not allow for overload operation; thus, it has a relatively shorter speed range comparing with the other three methods: variable speed (VS), variable inlet guide vanes (VIGV) and adjustable diffuser vanes (VDV) as shown in Appendix (B5). In addition to the low investment cost, one of the main advantages of suction throttling is its suitability for all the impeller and compressor types. The VS is used when the highest part-load efficiencies has higher priority and although that its investment cost is the greatest, it can be recovered in terms of power savings. The variable rotor and stator methods are limited for the integrally geared centrifugal compressor where the availability of the physical space is not a matter. These two ways are preferred when the low investment cost is the most important criteria in expenses of low part-load efficiencies and high complexity. The VIGVs method is still more efficient than the VDVs, so it might be selected when the efficiency and investment cost are both important.

However, the cooled bypass regulation method is not considered as a choice in this study due to the high dissipated energy leading to the worst part-load efficiencies. Besides, this method requests a cooling of the discharge gas before it is mixed with the suction stream which adds additional costs. Moreover, the suction throttling is based on dissipated the pressure energy of the inlet gas within the control valve, but it is still less than that of bypass technique where the compressor discharge pressure is squandered. In order to limit the dissipated energy of the inlet pressure, the use of suction throttling is also restricted by the compressor suction pressure and a maximum of 10 bara has been specified.

5.7 Multi-Stage Centrifugal Compressor

When the required compression ratio is exceeding the maximum allowed pressure ratio per stage due to the discharge temperature limitation, there will be a need to divide the process into several stages with intercoolers. In order to estimate the required number of process stages and the intercoolers, a sub model (E) has been developed, and it consists of two main blocks as illustrated in Appendix (B6). The first block determines the initial number assuming an identical pressure ratio per stage while the following block deals with each process stage separately.

Without considering the details of every process stage, the required number of intercoolers can be estimated assuming an equal pressure ratio of each compression group. First of all, the stage pressure ratio is calculated assuming one intercooler.

$$r_1 = r_2 = \left(1 + \frac{\Delta P_{cooler}}{100}\right)\left(\frac{P_d}{P_s}\right)^{0.5} \quad \textbf{(5-41)}$$

where:
r_1, r_2: Pressure ratio of first and second process stage, respectively.
ΔP_{cooler}: The percentage of intercooler pressure drop and it is considered 5%.

The obtained pressure ratio has to be lower than the maximum allowed compression ratio per stage to satisfy the first assumption. Otherwise, the second intercooler is added and the process is divided into three compression group.

$$r_1 = r_2 = r_2 = \left(1 + \frac{\Delta P_{cooler}}{100}\right)\left(\frac{P_d}{P_s}\right)^{1/3} \qquad \textbf{(5-42)}$$

The same procedures are carried out until the obtained pressure ratio per stage is lower than the upper limit.

$$r_1 = \cdots = r_n = \left(1 + \frac{\Delta P_{cooler}}{100}\right)\left(\frac{P_d}{P_s}\right)^{1/n} \qquad \textbf{(5-43)}$$

where:
n: The assumed number of compression group

However, this approach gives quick results, but it is not accurate since it does not consider the variation in the gas properties throughout the compression process. Besides, the maximum allowed number of impellers per casing has to be checked. To reduce this uncertainty, a second method is used in this sub-model (E) to deal with each process stage as a separate unit. Based on the obtained suction gas properties using sub-model (C), the stage pressure ratio is selected below or equal to the calculated maximum pressure ratio. Therefore, the sub model (D) is implemented to calculate the rest of parameters including the required number of impellers. The selected pressure ratio is iterated until the necessary impellers number is below the maximum allowed number. Consequently, the obtained discharge pressure ratio is checked against the overall required discharge pressure and if it is below the required pressure, the compression process continues to the second stage. These procedures are repeated until the calculated discharge pressure reaches the required value.

The required amount of cooling water ($\dot{m}_w$) in the inter-cooler is calculated by equating the amount of heat transfer from the process gas to the water using Equation (5-44).

$$\dot{m}_w = \frac{\dot{m}_g \times C_{p,g} \times (T_{inlet,g} - T_{exit,g})}{C_{p,w} \times (T_{exit,w} - T_{inlet,w})} \qquad \textbf{(5-44)}$$

The specific heat of the water ($C_{p,w}$) is estimated based on the average water temperature at the cooler inlet ($T_{inlet,w}$) and exit ($T_{exit,w}$). Furthermore, the allowed temperature rise of the cooling water is specified based on the API617 standards (2002) to be between 10 and 20 degrees.

5.8 Algorithm Validation

The compression duty is specified according to the process requirements. A gas transport compressor is required to work with a standard inlet volume flow of 125068 m^3/h at full load conditions and at inlet temperature and pressure of 121.3°C and 58.81 bara, respectively and with an overall discharge pressure of 302.52 bara. The mole fraction of the gas compositions has been determined by the gas sampling test, and the recorded values are presented in figure 5-11. The working fluid is a sweet gas with zero Hydrogen Sulphide and with no presence of pure Hydrogen. However, these volume fractions are expected to vary slightly from the summer to the winter operation. The predicted molecular weight change was specified by the process engineers to be approximately 7%.

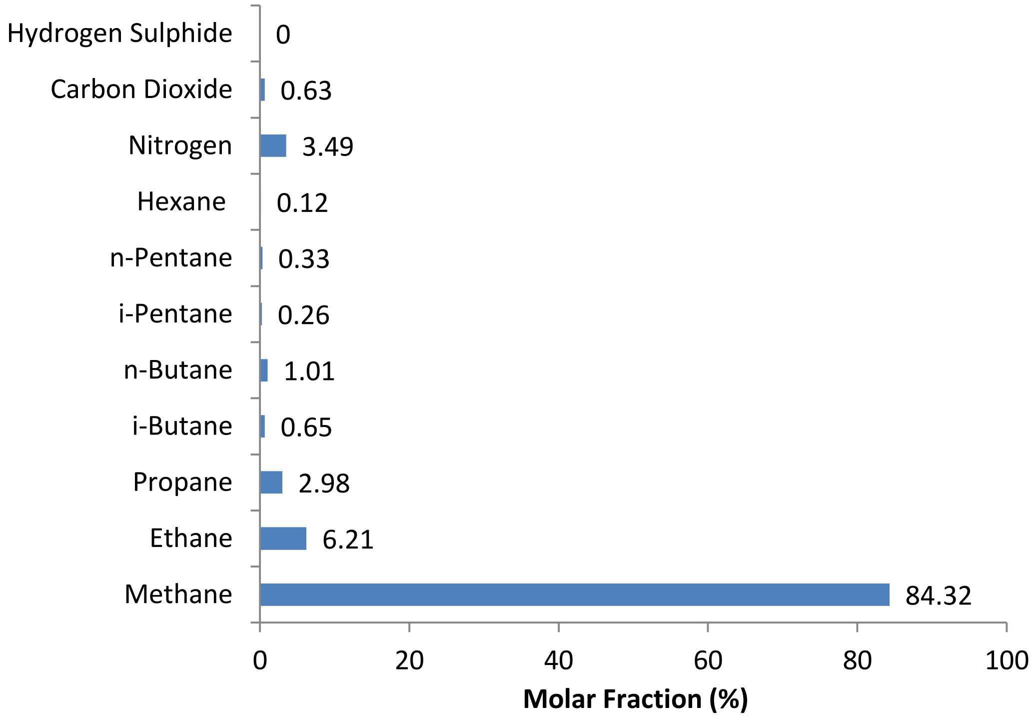

Figure 5- 11: Gas Composition at Compressor Section at Design Point

5.8.1 Evaluation of the Selection Approach

The first step is to evaluate the selection of centrifugal compressor type in such working conditions as shown in figure 5-1. By following sub-models (A), it was found that the use of centrifugal compressor type is recommended, and the single shaft beam has been selected as illustrated in Appendix (C). Besides, the sub-model (B) is implemented to specify the most suitable casing structure. Based on the developed approach, the vertically split case (barrel type) is suggested for this compressor. This was found matching the original casing structure as supplied by the OEM.

5.8.2 Evaluation of Gas Properties Calculation Methods

The provided gas composition is used to evaluate the developed scheme for the gas properties estimation. Table 5-3 compares the obtained gas properties values with the experimental results at the sampling conditions. The calculated molecular weight is perfectly matching the measured value while there is an insignificant difference in the relative density reading. This difference is around 0.45% which is still acceptable. The predicted specific heats ratio (k) was slightly lower than the measured value by approximately 0.082%.

The gas viscosity has been calculated using two models as indicated in table 5-4. The Ling equation obtained roughly the exact viscosity value while the Lee-Gonzalen-Eakin model introduces approximately 13% as a relative error. Hence, Ling model will be used to calculate the gas viscosity in the following procedures. Moreover, the compressibility factor of the gas mixture has been obtained graphically using the generalized compressibility charts and analytically using three common equations of state at two different conditions as demonstrated in table 5-4.

Table 5- 3: Evaluation of Predicted Gas Properties With Reference to the Experimental Values

Gas Properties	Experimental Results	Calculated Values	Deviation (%)
Molecular weight (kg/ºk.mol)	19.500	19.500	0.000
Relative density (15°C; 1atm)	0.673	0.676	0.446
C_p/C_v (275bara; 136°C)	1.219	1.218	-0.082

Table 5- 4: Evaluation of Predicted Compressibility Factor and Gas Viscosity

Conditions	Calculated Value		Experimental Value	Deviation (%)
	Calculation Method	Value		
Gas Viscosity (275 bara, 136ºC)	Lee-Gonzalen-Eakin	0.026	0.023	13.04
	Ling	0.023		0.00
Z (275 bara, 136ºC)	Compressibility Graphs	0.992	0.965	2.798
	Redlich-Kwong	0.9878		2.363
	Soave- Redlich-Kwong	1.0257		6.290
	Peng-Robinson	0.9988		3.503
Z (1atm, 15ºC)	Compressibility Graphs	0.998	0.998	0.000
	Redlich-Kwong	0.9972		-0.079
	Soave- Redlich-Kwong	0.9973		-0.070
	Peng-Robinson	0.9969		-0.110

At line conditions, the closest value to the experimental reading is by using Redlich-Kwong equation while the highest deviation was observed with the Soave- Redlich-Kwong method. At standard conditions (p<200 bar), the compressibility chart value completely matches the experimental value while the obtained value from the Redlich-Kwong equation deviates by roughly 0.79% from the measured value. Generally, the average deviation of both conditions shows that the most accurate results can be obtained by the Redlich-Kwong equation of state while the less precise values are expected with the Soave- Redlich-Kwong equation. Hence, this model will be used in the following procedures to estimate the compressibility factor at the suction and discharge of each process stage. However, this has been decided assumed that the experimental readings are perfectly accurate.

5.8.3 Evaluation of Compressor Sizing and Modeling Methods

The developed approach was used to simulate the design characteristics and the overall performance parameters of the centrifugal compressor, and the obtained values are compared with the OEM's data as shown in the table 5-5.

Table 5- 5: Comparison Between the Predicted Parameters and OEM's Data

	Stage 1			Stage 2			Stage 3		
Parameter	**Calculated**	**OEM**	**Error%**	**Calculated**	**OEM**	**Error%**	**Calculated**	**OEM**	**Error%**
Suction Temp (ºK)	337.950	337.95	**0.00**	332.750	332.75	**0.00**	332.650	332.65	**0.00**
Suction Pressure (bara)	30.470	30.47	**0.00**	57.261	57.261	**0.00**	132.123	132.123	**0.00**
No. Impellers	3.0	3.0	**-**	4.0	4.0	**-**	6.0	6.0	**-**
Suction Z	0.938	0.940	**0.21**	0.880	0.884	**0.41**	0.779	0.778	**0.13**
Head (kJ/kg)	87.89	88.323	**0.49**	110.13	109.861	**0.25**	103.83	102.785	**1.02**
Power (kW)	3719	3725	**0.17**	4773	4763	**0.22**	4964	5005	**0.82**
Discharge Temp (ºK)	391.621	394.45	**0.72**	405.299	410.05	**1.16**	402.642	405.05	**0.59**
Discharge Pressure (bara)	58.81	58.81	**0.00**	133.72	133.72	**0.00**	302.52	302.52	**0.00**
Polytropic Efficiency (%)	80.2	80.2	**0.00**	74.1	74.1	**0.00**	69.7	69.7	**0.00**
Speed (rpm)	11922	11922	**0.00**	11922	11922	**0.00**	11922	11922	**0.00**
Discharge Z	0.939	0.944	**0.50**	0.916	0.923	**0.80**	0.960	0.978	**1.81**

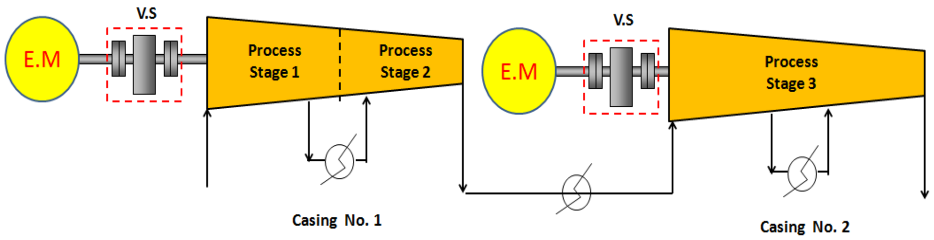

Casing Structure	Vertically Split
Driver	Elec. Motor
Regulation Method	Variable Speed
Required Cooling Water (ton/hr)	350.0

To achieve the required pressure ratio, the centrifugal compressor has been designed with two vertically split casings and with three process stages. The medium pressure compressor is provided with the intercooler before the gas stream enters the second process stage. The discharge gas from the first casing is directed to another intercooler to reduce its temperature; then, it passes through a scrubber to remove any condensed particles. Both intercoolers will require a total amount of 350 ton/hr of cooling water at 25ºC and 45ºC inlet and exit temperatures, respectively. The number of impellers of each stage is specified to be seven and six for the MP and HP compressors, respectively. However, the deviations of all the predicted parameters from the OEM's data are found less than 5% which is acceptable to validate the developed algorithm.

For simplicity, the followed preliminary approach for compressor driver selection is based on volumetric flow rate and operating speeds as indicated in figure 5-12. The right selection will save an enormous amount of money in term of installation cost. In the present case, the electric motor was chosen as demonstrated in table 5-5. However, it should be noted that the initial selection has to be reviewed with respect to process steam supply, capital cost, process control, fuel or energy cost and reliability.

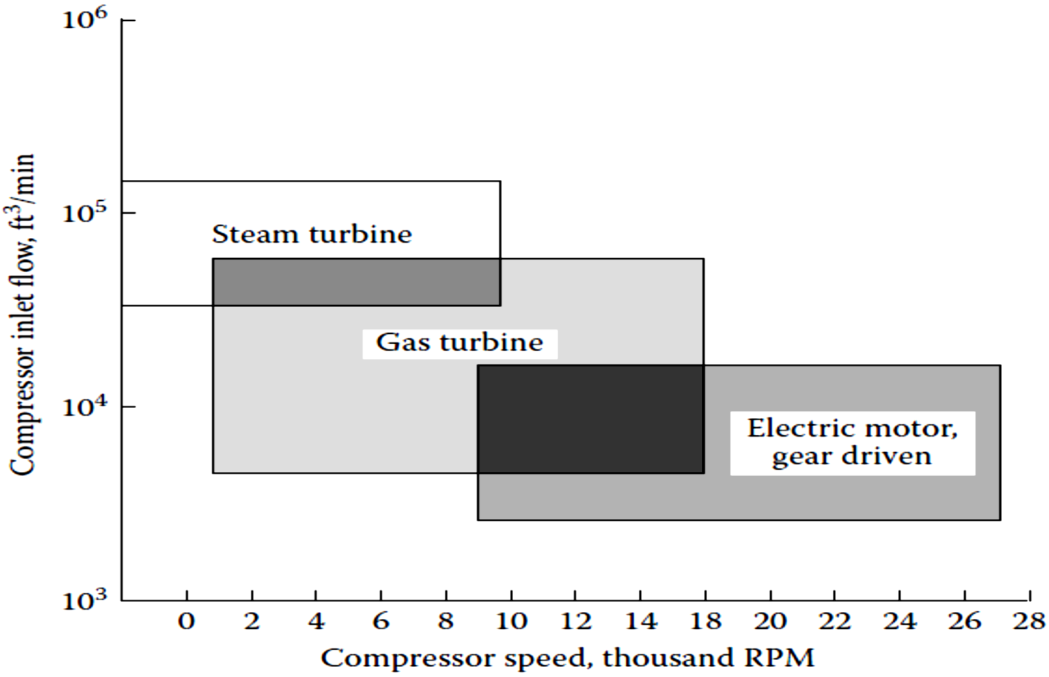

Figure 5- 12: Selection of Compressor's Driver Diagram (Bela, 2003)

5.8.4 Evaluation of Aerothermodynamic Parameters

Looking to the gas density and dynamic viscosity trends in figure 5-13(a), both properties are taking a non-linear upward trend. Although that the gas temperature and pressure are increasing as the gas goes throughout the compression process, the pressure rise is the dominant effect which could overcome the adverse impact of temperature rise yielding a higher density. However, the increase in gas density in the first process gas is less significant comparing with the second stage. This can be explained by looking to the compressibility factor and stage pressure ratio. The high inlet temperature of the first process stage limited the compression ratio which is also restricted by the maximum allowed discharge temperature.

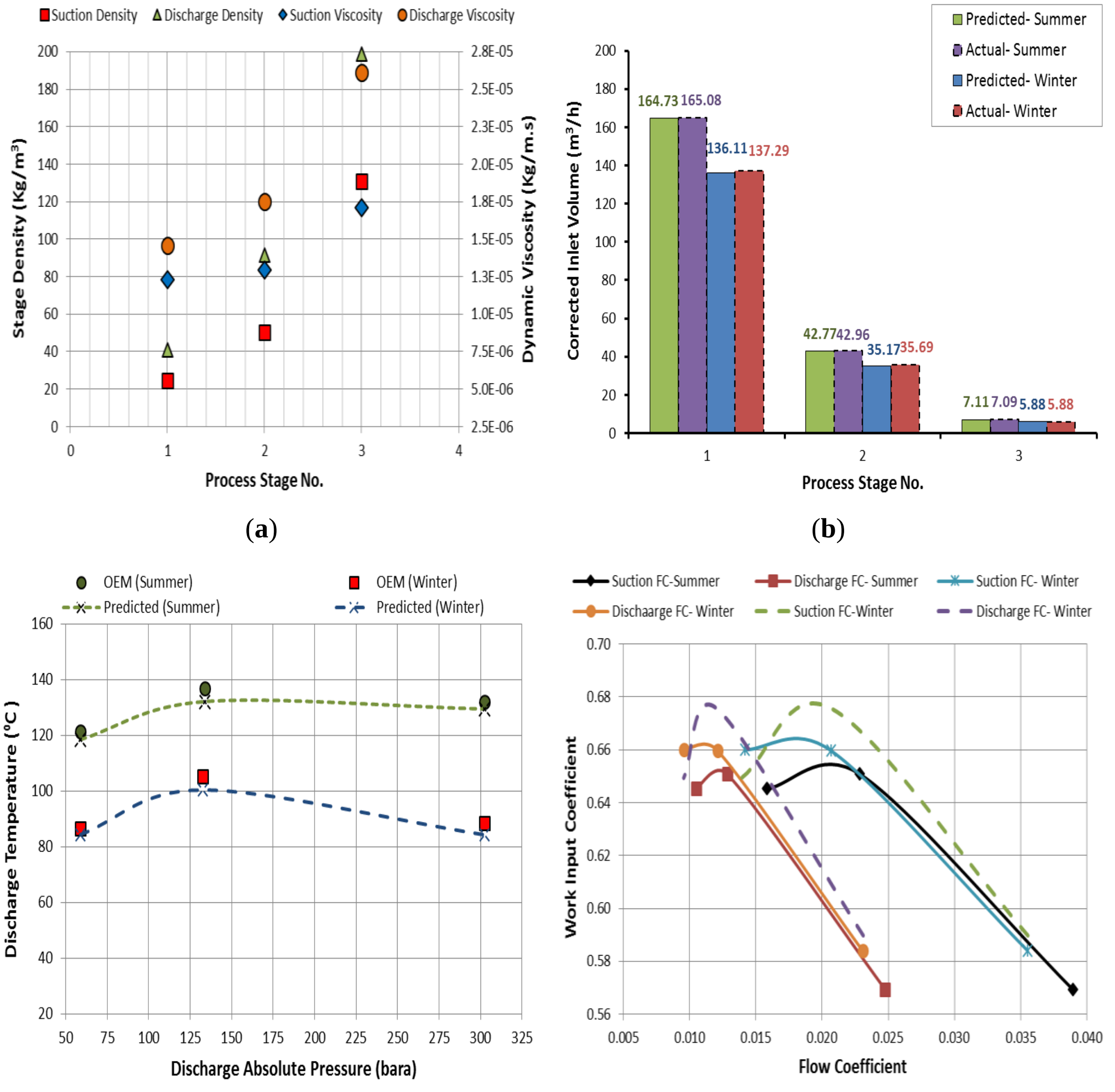

(a) (b)

(c) (d)

Figure 5- 13: Modelling of Performance Parameters and Gas Properties (Summer T1=64.8ºC, WinterT1= 29.7ºC) : (a) Variation of Gas Density and Viscosity (b) Inlet Corrected Volume of Compressor Stages (c) Variation in Discharge Temperature (d) Variation of Work Coefficient

Besides, the increase in the compressibility factor value at the exit of the first process stage with regard to the suction compressibility is roughly 0.136% comparing with about 4% and 23% for the second the last process stages, respectively.

Moving to the dynamic viscosity, the viscosity is increasing with the temperature rise and the largest difference was found in the downstream compressor. At the intercooling process, the gas viscosity decreases while the density goes up as a result of the temperature reduction. The drop in gas density causes the inlet volumetric flow rate to decrease as illustrated in figure 5-13(b). By comparing the predicted inlet volumetric flow rate with the actual value, the largest deviation was observed in the flow of the second stage by about 0.42% which apparently due to the difference in the inlet compressibility factor value. Also, the inlet flow rate is decreasing proportionally with the inlet temperature reduction. At winter operation and specifically at 29.7ºC inlet temperature, the compression process becomes more efficient and the required reduction in volume flow to achieve the designed discharge pressure is relatively lower. Figure 5-13(c) demonstrates the predicted discharge temperature at summer and winter operating time where there is a good matching with the OEM's data. An interesting observation is that there is a slight reduction in the discharge temperature of the last stage comparing with the intermediate stage in both cases. This is expected due to the lower pressure ratio of the HP compressor at constant discharge pressure operation. Besides, it should be noted that the low operation temperature yields to minimize the required cooling water with a reduction rate of 0.85 ton per hour for each degree centigrade.

Furthermore, there is an increase in the input work coefficient with the inlet temperature which indicates a higher specific total work accomplished by the compressor as illustrated in figure 5-13(d). Besides, the peak work coefficient point was observed at the second process stage during summer time. However, the pressure ratio of this stage has to be reduced during cold weather to avoid the high stage loading coefficient. So, the new work coefficient curve is represented by the continuous line while the initial trend is indicated by dotted line. However, the reduction in the second stage pressure ratio by about 1.29% yields a lower work coefficient comparing with the last process stage. By considering a fixed impeller geometry, the tip speed stayed constant at fixed rotational speed operation. So, the change in flow coefficient indicates the variation in the actual flow which can be used as a sign for flow channel blockage, compressor fouling and aerofoil erosion. Figure 5-13(d) shows the variation in the suction and discharge flow coefficients of all process stages. At constant rotational speed, the suction flow coefficient is well below unity, and it is decreasing as the gas pressure increases due to the volume reduction. Besides, as the gas flows through the individual impeller, the tip speed increases with the impeller radius. Furthermore, the variation in the volume flow reduction with the inlet temperature causes the flow coefficient to increase during summer operation.

The velocity has a significant impact on the aerodynamic and mechanical losses as shown in figure 5-14. The derived velocity triangles of each stage are also illustrated in Appendix (C1). The compressor can generate the required pressure ratio at lower rotational speed at low inlet temperature and the resulted mechanical and aerodynamic losses become less as demonstrated in figures 5-14(a) and 5-14(b). However, when the designed rotational speed is fixed as at summer conditions, the observed mechanical and aerodynamic losses at cold environment becomes considerably greater. The adverse effect of rotational speed on the total losses is illustrated in figure 5-14(d) at constant discharge pressure and inlet temperature. Figures 5-14(a) and 5-14(c) demonstrate that the greatest power drop is dissipated as blade loading loss due to the high blade loading in first and last process stages. This suggests a high diffusion of the internal working fluid to the rotating impeller which consequently generates great momentum loss and un-uniform loading distribution over the compressor blades.

In order to minimize this power loss, the ratio of exit-to-inlet relative velocities at the shroud has to be increased either by increasing the flow rate or raising the rotational speed. Furthermore, the vaneless space loss is high for the first stage of MP compressor and the HP compressor as well due to the high velocity ratio. An interesting observation is that the blade loading and disc friction losses of the second stage become greater during winter operating time which indicates a greater diffusion in the impeller channels due to the high flow incidence. Considering the mechanical losses, both casings are designed with dry gas seals to minimize the power losses and maintenance requirements. The calculated power saving by using the mechanical seal is about 8.5 kW and 5.8 kW during the summer and winter operations, respectively. However, it is recommended to conduct a detailed optimization to balance the capital cost with the power saving and maintenance cost.

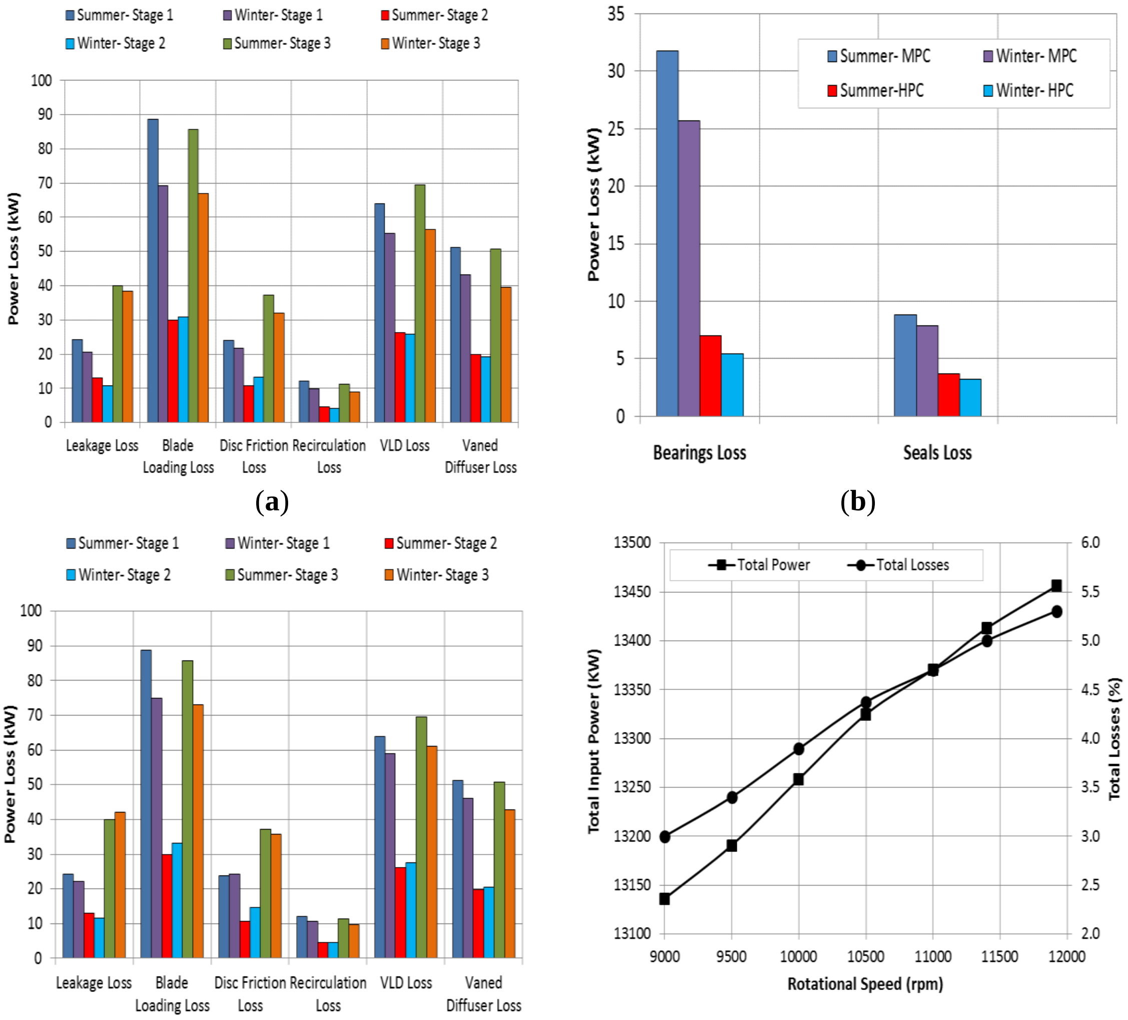

(a) (b)

(c) (d)

Figure 5- 14: Predicted Aerodynamic and Mechanical Losses: (a). Aerodynamic Losses at Variable Rotational Speed (b). Bearings and Seals Losses at Variable Rotational Speed (c). Aerodynamic Losses at Constant Rotational Speed (11,922 rpm) (d). Input Power and Total Losses at Constant Discharge Pressure (T1= 64.8°C)

Moreover, it was observed that the bearings and seals losses of the MP compressor are significantly greater in both operating conditions. This is mainly due to the high volumetric flow rate of the MP compressor which directly affects the loss factor.

5.9 Closing Remarks

To ensure the highest technical value, the selection of centrifugal compressor was evaluated using a simple approach which incorporates four key elements: process requirements evaluation, initial capital cost consideration, operation cost review and logistics consideration. Although that each of the manufacturers is using a different approach for compressor selection, the introduced method can be used as a basic line for the public domain to evaluate different gas compression duties. Moreover, the typical casing structure was designated concerning the maximum allowable working pressure (MAWP) and partial pressure of the Hydrogen. Despite that the horizontally split casing is preferred in terms of maintenance, flexibility and reliability; the maximum allowable working pressure (MAWP) for the horizontally split was considered to be 40 bara to avoid any consequential leak from the joints. As the variation of hydrocarbon properties has a substantial influence on the stage performance, this chapter introduced GasProp tool to estimate the gas properties at different operating conditions and for different types of working fluids including the pure gas and gas mixture. This model was tested and the predicted values showed a fair and satisfactory agreement with the experimental data.

The compressor selection and sizing process were also incorporated with a sequential approach to derive the optimum geometrical features and aerodynamic parameters for various process requirements. It is mostly depending on evaluating the aerothermodynamic parameters against several design constraints to ensure the highest possible efficiency. The developed approach uses a new methodology to specify the tip speed according to three criteria which are: the type of impeller, molecular weight and tip Mach number. Moreover, the maximum developed polytropic head per impeller is specified based on two parameters which are the molecular weight and discharge pressure. Since there are different methods in the open literature to estimate the maximum number of impellers per casing, the developed approach implements a conservative technique by defining the upper limit of impellers per housing with regard to three parameters which are: flow coefficient, Mach number and impeller arrangement. Furthermore, the selection of flow capacity control method was based on five basic criteria which are: casing structure, part-load efficiencies, investment cost, overload operation and suction pressure.

To assess the validity of the overall approach; it was used to design a compressor for gas transport duty, and the obtained compressor characteristics were compared with the actual manufacturer data. The conducted comparison revealed a good matching of the performance parameters of all the process stages with the actual values. Finally, a parametric study was performed on the estimated aerothermodynamic parameters to investigate the effect of the variation in the running time (summer, winter) on the overall compressor performance. However, it is important to mention here that this approach can be used to identify the optimum centrifugal compressor configuration based on a single operating point evaluation while the prediction of the overall compressor map will be discussed in the following chapter.

CHAPTER 6: PREDICTION OF CENTRIFUGAL COMPRESSOR PERFORAMNCE MAP AT DESIGN CONDITIONS

The wide stable operating range and the high efficiency have been the most two features that drive the selection of centrifugal compressor for any particular applications. However, the variation in the suction parameters and operating circumstances makes the testing of the acceptability of any compressor unit to deal with these variables crucial during the preliminary design stage. The performance of the new compressor has to be reliable in order to develop the required polytropic head at the expected efficiency within the stable region. Therefore, this chapter aims to introduce a new integrated method for reliable performance prediction of multi-stage industrial centrifugal compressor based on stage stacking technique. First of all, Lüdtke (2004) and Casey-Robinson (2013) methods are adapted to be valid for industrial centrifugal compressors, and the predicted characteristics are evaluated against measured data. Based on the conducted evaluation, a new model will be derived to incorporate the merits of both approaches with more accurate prediction. To emphasize the validity of the new method; it has been evaluated for high and low flow coefficients applications, and the obtained parameters have been compared with the existing models results and the measured data.

6.1 Introduction

Public literature reveals three different approaches to predict the performance of centrifugal compressor stage. Several studies have been conducted to estimate the compressor map numerically using CFD simulation such as Niazi et al. (1998), Prasad et al. (2011), Le Sausse et al. (2013) and Kalinkevych and Shcherbakov (2013). This approach has proven to provide relatively accurate results, but it consumes a long time which might not be possible within the available time frame. Besides, this method requires deep knowledge of the stage geometry which is usually not available at this design stage. Additionally, this becomes more difficult while dealing with multistage centrifugal compressors. The other quick technique is based on Affinity laws. However, this method is accurate only when there is no substantial difference between the design point of the new stage and the previous experienced one especially the flow and work coefficient. The other drawback of this approach is that it does not provide a parametric description at higher or lower speeds than those tested since it assumes a constant flow regime. The third used technique for performance maps prediction is based on empirical correlations. Herbert (1980), Oh et al. (1997), Aungier (2000) and Swain (2005) derived different 1D-empirical correlations to estimate the compressor operating envelope, but all of them are based on the detailed geometrical features of the designed impeller.

Similar to Swain (1990), (2005) and Casey (1994) studies, Rodgers and Langworthy (1974) did not give any equation for these curves. Lüdtke (2004) developed an approach to derive the design stage efficiency by correcting the experimental value based on the new compressor design. However, this method has not been tested, and it was used for a single speed and flow values. Casey and Robinson (2013) introduced a new set of algebraic equations to predict the compressor map with less geometrical features. Despite that this approach has advantages over the previous developed numerical equations; there is still a need to calibrate the empirical coefficients with the test data. Besides, a high uncertainty was observed in the predicted surge line. Furthermore, this model was used for a single stage turbocharger compressor, and it requires a prior knowledge of the design and peak efficiencies and associated flow coefficients at normal and low Mach number conditions.

6.2 Overview of Developed Stage Stacking–Based- Method

In industry, the stage stacking is commonly applied by measuring the flow and the head coefficients of the first mechanical stage at a wide range of Mach numbers. This will allow to estimate the stage efficiency and work coefficient at various speeds and volume rates. These curves are then dimensionalized with speed and impeller diameter to obtain the required power and discharge pressure, temperature and volume flow. After that, the equations of state are used to obtain the gas properties at the discharge of this stage. The discharge parameters are considered as the inlet for the following stage so that this process continues until reaching to the final compressor discharge and the flange to flange performance curves are derived.

In this study, the initial rotational speed value at specified volume flow rate is set lower than the upper allowed limit based on the inlet volume, and it is iterated to correct the inlet diameter. Figure 6-1 demonstrates the developed approach to derive the overall compressor performance map based on stage-stacking principle.

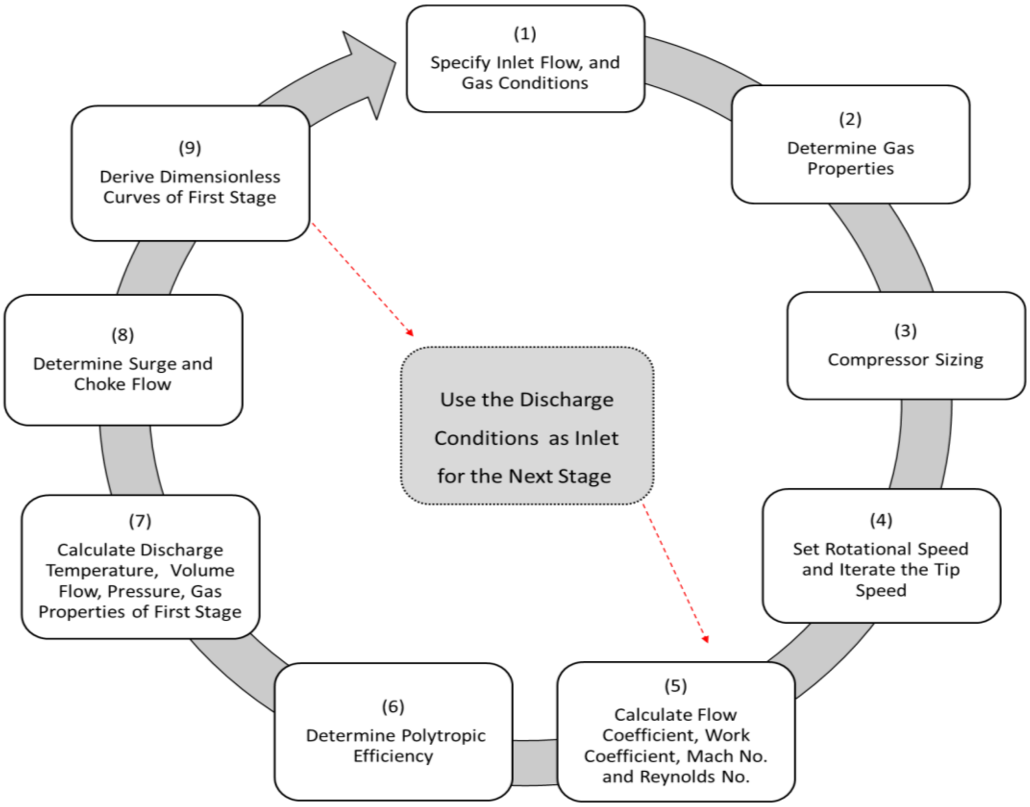

Figure 6- 1: Developed Approach for Centrifugal Compressor Performance Prediction

Generally, it can be divided into nine basic steps as following:

1. The inlet flow rate and the composition of the process gas are defined based on specified design point conditions.
2. The relative inlet conditions and gas composition are then used to determine the physical gas properties at the suction side of the compression stage including gas molecular weight, compressibility factor (Z), specific heats ratio (k), density (ρ) and viscosity.
3. Based on the required pressure ratio, the obtained suction conditions are used to specify the required number of mechanical and process stages.

4. The initial rotational speed (N) is assumed based on the inlet volume flow and then iterated to meet the maximum allowed tip speed (*U*).
5. A further check is performed by comparing the relative flow coefficient (φ), work coefficient (ψ_w), Mach number (*Mu*) and Reynolds number (*Re*) with the maximum allowed aerodynamic limits.
6. Based on the determined polytropic head and work coefficient, the polytropic efficiency of the compression stage is calculated.
7. Accordingly, the discharge parameters of the first mechanical stage are defined based on derived performance parameters.
8. In order to determine the stable operating range, the surge and choke flows are calculated with relative to the calculated Mach number and flow coefficient.
9. The procedures (1-8) are repeated using different flow rates and rotational speeds to derive the performance curves of the first mechanical stage which are then dimensionalized with speed and impeller diameter. The discharge parameters are considered as the inlet conditions for the following stage so that this process continues until reaching to the last stage and the flange to flange performance curves are determined.

The rotational speed is affected proportionally with the tip speed and inversely with impeller diameter. To calculate the inlet diameter, the correlation (6-1) has been derived from flow coefficient formula and rotational speed and tip Mach number equations. This will ensure the allowable corresponding flow coefficient and tip Mach number values simultaneously.

$$D_1 = \frac{Mu_{max}\sqrt{k_1 R_1 T_1 Z_1}}{\pi N} \geq \left[\frac{4\dot{V}}{\varphi_{max}\pi A\sqrt{k_1 R_1 T_1 Z_1}}\right]^{0.5} \qquad \textbf{(6-1)}$$

Accordingly, this formula is used to derive a new correlation for relative Mach number (Mu_{rel}).

$$Mu_{rel} = \left[\frac{U_1^2 + \left(\frac{4\dot{V}}{\pi D^2}\right)^2}{k_s R_s T_s Z_s}\right]^{0.5} \qquad \textbf{(6-2)}$$

6.3 Pressure Ratio Estimation Approach

One of the main issues in the performance estimation process is the determination of the pressure ratio of each single mechanical stage. Some studies assume a homogenous distribution of pressure rise across the compressor stages. This approach introduces a high degree of uncertainty since in reality the front stages can develop a higher compression rate relative to rear ones. Howell and Calvert (1978) developed a correlation for this purpose by calculating the temperature rise as a function of flow rate, but it is only valid for axial compressors. So, the current study will use a different way based on the maximum impeller polytropic head and Mach number. Initially, the equation (6-3) is implemented to identify the pressure ratio based on the maximum allowed polytropic head. The pressure ratio is then calculated with respect to the suction conditions, and it is used to obtain the stage discharge gas properties and tip Mach number.

$$\frac{p_2}{p_1} = \left[\frac{H_{p,max}}{Z_1 \times R_1 \times T_1 \times \left(\frac{n_v}{n_v - 1}\right)} + 1\right]^{\frac{n_v}{n_v - 1}} \qquad \textbf{(6-3)}$$

After that, the correlation (6-4) is implemented to correct the pressure ratio according to the obtained work coefficient, polytropic efficiency and exit tip Mach number.

$$\frac{p_2}{p_1} = [\psi_w \ (k-1)Mu_2^2 + 1]^{\frac{k\eta_p}{k-1}} \qquad \textbf{(6-4)}$$

The new pressure ratio value is expected to be lower than the first iteration value at high flow coefficients, and greater at low flow coefficients due to the contribution of work coefficient on impeller head. Besides, the obtained polytropic head value with regard to the calculated pressure ratio from equation (6-4) is substituted in formula (6-3), so the derived pressure ratios from both equations have to be matched. The work coefficient is calculated using Casey-Robinson in terms of flow coefficient and tip speed Mach number.

$$\psi_w = \left(1 + \frac{k_{df}}{\varphi}\right)\left[\frac{V_{\theta 2}}{U_2} - \frac{V_{m2}}{U_2}\tan(\beta_2) + \varphi k_s\right] \qquad \textbf{(6-5)}$$

The disc friction (k_{df}) is assumed to be 0.003 initially and then the disc friction loss is calculated which, in turn, used to specify the actual value. The correlation coefficient (k_s) is obtained by substituting the work coefficient at design point in equation (6-5) and the variation in its value with the rotational speed is obtained by correlation (6-6).

$$\frac{k_{si}}{k_{sd}} = \frac{\left[1 + (k_d - 1)\gamma_d \psi_{w_d} Mu_d^2\right]^{\frac{1}{n_d - 1}}}{\left[1 + (k_i - 1)\gamma_d \psi_{w_d} Mu_i^2\right]^{\frac{1}{n_d - 1}}} \qquad \textbf{(6-6)}$$

The slip factor is assumed to stay constant in this study for a specific mechanical stage, and the impeller efficiency was considered identical to stage efficiency.

6.4 Casey-Robinson Model –Based- Method

The Casey-Robinson model has an advantage of its dependency on the flow coefficient, tip Mach number and work coefficient only to derive the rest of aerothermodynamic parameters. Despite having less geometrical parameters, the used non-dimensional coefficients define the characteristics of the stage geometry such as diffuser-impeller matching, flow channel width and aerodynamic losses. However, the dependency on the peak efficiency and associated flow coefficient at both normal operation and low Mach number makes the use of this model more difficult when these parameters are unknown which is the most often case at this design stage.

6.4.1 Developed Approach Based on Casey-Robinson Model

In the original method, the Mach number is varied to generate the corresponding pressure ratio, flow rate and polytropic efficiency. This way of determination is changed in this study as demonstrated in figure 6-2 so that the expected speed variation is specified according to the process requirements to meet the off-design working conditions and to avoid the inefficient and unstable compressor operation. Thus, the inlet volume of the first mechanical stage is varied at each speed line and the relevant tip speed Mach number and flow coefficient are calculated for every speed-volume point. The speed range is used to estimate the highest and minimum tip Mach numbers.

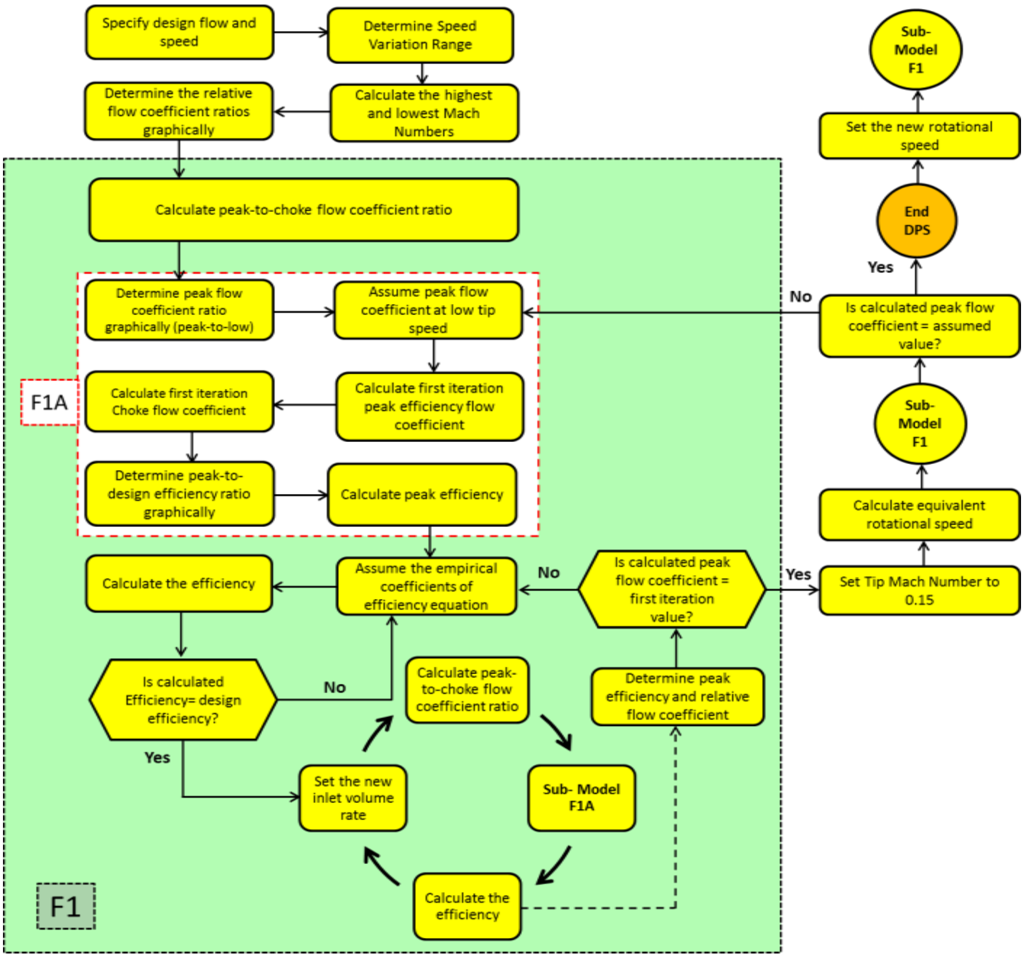

Figure 6- 2: Developed Algorithm Based on Casey-Robinson Method

Figure 6-3 shows the variation in the ratio of flow coefficient at peak efficiency to that at choke conditions (φ_p/φ_c) over a range of tip speed Mach numbers. This has been adapted from Casey-Robinson model (2013) to be valid for industrial centrifugal compressors after hundreds of trials. However, this figure is used only for the first iteration process as initial values to estimate the flow coefficient ratio to the high and low tip Mach numbers. These two flow coefficients are substituted in equation (6-7) to calculate the initial ratio of the flow coefficient at peak efficiency to the flow coefficient at choke point (φ_p/φ_c). It is obvious that this flow coefficient ratio is influenced in general by the tip Mach number, so it has to be constant for a fixed rotational speed operation. The values of the empirical coefficients (A, B, C) vary with the tip speed Mach number, and the recommended ranges were obtained based on the conducted iteration process for several industrial compressor models.

$$\frac{\varphi_p}{\varphi_c} = \left[1 - \frac{1}{1+e^{-(Mu-B)(A\times Mu+C)}}\right]\left(\frac{\varphi_p}{\varphi_c}\right)_{Lo} + \frac{1}{1+e^{-(Mu-B)(A\times Mu+C)}}\left(\frac{\varphi_p}{\varphi_c}\right)_{Hi} \qquad \textbf{(6-7)}$$

where:
A: Formula coefficient (0 - 1) based on inlet tip Mach number
B: Formula coefficient (0.8- 0.9) based on inlet tip Mach number
C: Formula coefficient (4 – 5) based on inlet tip Mach number

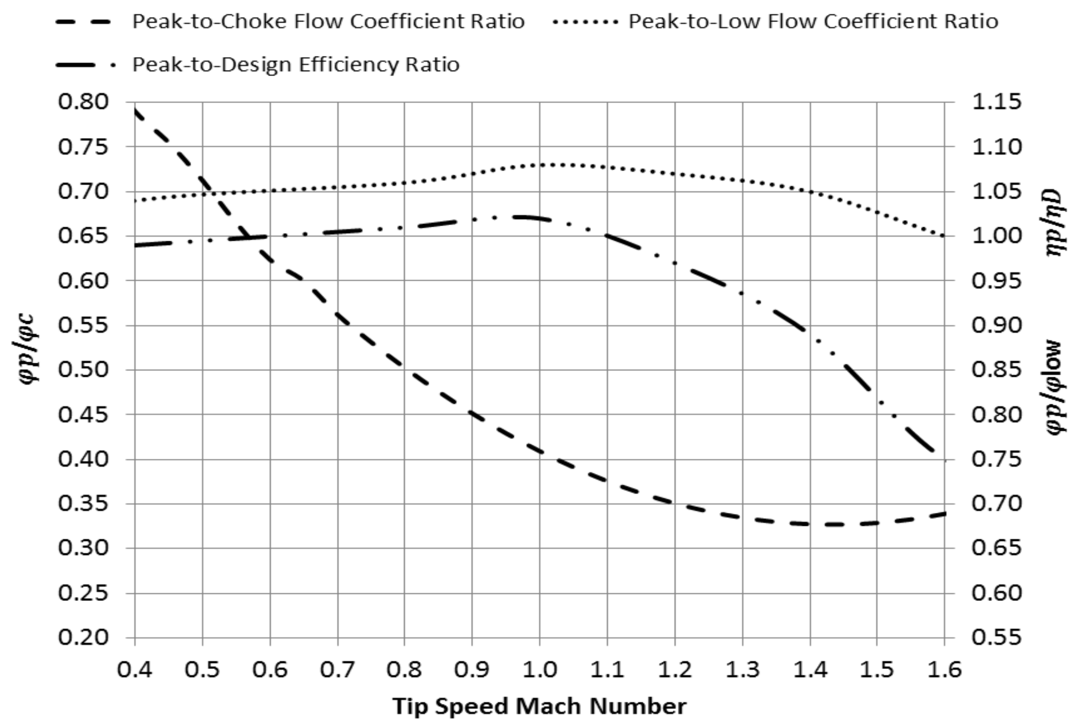

Figure 6- 3: Flow Coefficient and Efficiency Ratios as A function of Tip Mach Number

Figure 6-3 is also used to estimate the ratio of flow coefficient at peak efficiency to that at low speed (φ_p/φ_{Low}) for first iteration process according to the calculated Mach number. The low speed flow coefficient value (φ_{Low}) has to be lower than the design value (φ_D); thus, it is assumed at the beginning and it is used to calculate the peak efficiency (φ_p) and choke flow coefficient (φ_c). Besides, the peak efficiency value is obtained from the same figure by specifying the stage Mach number and design efficiency.

The off-design stage efficiency is calculated using equations (6-8) and (6-9). These two equations are taking elliptic curve equation form, and the appropriate formula is specified according to the inlet volume flow ($\dot{V}$). The volume flow at peak efficiency ($\dot{V}_{\eta_p}$) is defined by varying the flow rate at constant speed until the highest efficiency is identified.

When $\dot{V} \leq \dot{V}_{\eta_p}$:

$$\eta = \eta_p \left[1 - \left(1 - \frac{\varphi}{\varphi_p}\right)^D\right]^{1/D} \tag{6-8}$$

When $\dot{V} > \dot{V}_{\eta_p}$:

$$\eta = \eta_p \left\{(1 - G) + G\left[1 - \left(\frac{\frac{\varphi}{\varphi_c} - \frac{\varphi_p}{\varphi_c}}{1 - \frac{\varphi_p}{\varphi_c}}\right)^H\right]^{1/H}\right\} \tag{6-9}$$

The empirical coefficients (D, G, H) in these two correlations are specified by iteration to match the constant speed line trend. However, there is no available exact range of these coefficients that can be used for this sort of application. Hence, the recommended values of each of these variables have been derived by conducting an extensive number of trials at various Mach number and flow coefficients. The D coefficient has greater value at low-speed operation reaching to 3.3 while it drops to 2.7 at high Mach number conditions. Similarly, the H value is taking the same trend, and it varies from 1.42 at high speed to 2.02 at low-speed conditions. On the other hand, the coefficient G has greater value at high Mach number operation, reaching to 0.49, while it decreases to 0.14 when the stage operates at low rotational speed.

Initially, the mechanical stage is assumed to have an identical efficiency as the overall compressor design point value. So the coefficients of the efficiency correlation are adjusted to achieve the same efficiency. At design speed, the design point flow is usually near but less than the peak efficiency flow. However, the rest of coefficients are modified to obtain the normal running speed line. The flow coefficient at peak efficiency has to be identical to the calculated value which, in turn, used to select the efficiency equation. By setting the efficiency correlation coefficients, these equations are used to derive the efficiency at low Mach number operation (approximately below 0.2) at which the gas is approaching the behaviour of incompressible fluid and the impact of the Mach number on the flow shift becomes insignificant. The inlet volume flow is changed to derive the constant speed line. Hence, the flow coefficient at peak efficiency (φ_p) can be deducted and used to replace the assumed value. However, there might be a need to modify the empirical coefficients (D, G, H) at this stage to match the design efficiency.

This model predicts the choke point by calculating the choke flow coefficient using equation (6-9). So, the impeller is choked when the following condition is satisfied.

$$\left(1-\frac{\varphi_p}{\varphi_c}\right) \leq \left(\frac{\varphi}{\varphi_c}-\frac{\varphi_p}{\varphi_c}\right) \qquad \textbf{(6-10)}$$

On the other hand, these equations of efficiency do not cover the flow separation or instability at low flow region which can be considered as one of this model weaknesses. However, the correlation (6-7) can be rewritten to predict the surge flow coefficient based on the derived choke flow coefficient.

$$\frac{\varphi_s}{\varphi_c} = \left[1-\frac{1}{1+e^{-C_s(Mu-B_s)}}\right]\left(\frac{\varphi_s}{\varphi_c}\right)_{Lo} + \frac{1}{1+e^{-C_s(Mu-B_s)}}\left(\frac{\varphi_s}{\varphi_c}\right)_{Hi} \qquad \textbf{(6-11)}$$

Initially, this formula was set to match the actual surge flow of specified industrial centrifugal compressor in order to obtain the values of the presented empirical coefficients (B_s,C_s). Accordingly, the values of B_s and C_s were found to be 0.814 and 4.75, respectively.

6.4.2 Validation of Adapted Casey-Robinson Model

The developed methodology was tested to derive the performance map of a gas export centrifugal compressor driven by 14.5 MW electric motor. The design point operation requires 21 bara at the compressor discharge with a standard inlet volume flow of 6 MMSCM/D and suction pressure and temperature of 8 bara and 324.35ºK, respectively. The process gas is a hydrocarbon mixture with zero Hydrogen Sulphide and a molecular weight value of about 19.10 g/mol at design conditions. The specified gas compositions are used to estimate the gas properties at stage suction corresponding to inlet pressure and temperature values. According to the obtained flow coefficient and gas properties, this casing was designed to accommodate five mechanical stages with 17 blades each. The geometrical specifications of every stage are shown in table 6-1.

Table 6- 1: Geometrical Parameters of the Used Impellers

Parameter	1st Impeller	2nd Impeller	3rd Impeller	4th Impeller	5th Impeller
Blade exit angle	50	49	48	48	48
Impeller inlet Width, b_1 (mm)	100	92	85	77	69
Inlet hub/outlet Tip ratio	0.342	0.353	0.367	0.380	0.392
exit impeller diameter (mm)	655	655	655	650	645
b_2/D_2	0.0810	0.0743	0.0688	0.0627	0.0569
Exit blade width, b_2 (mm)	53.0	48.0	45.0	41.0	37.0
D_1/D_2	0.409	0.409	0.409	0.412	0.416

A further step is taken to estimate the performance of each mechanical stage reaching to flange to flange performance. The inlet conditions are used as suction parameters for the first stage. The exit tip diameter of the impeller was set to match the exact used impeller diameter which will ensure the use of exact flow and head coefficients.

The work coefficient is calculated by equation (6-5) and then substituted in equation (6-4) to derive the stage pressure ratio. The polytropic efficiency is obtained using Casey-Robinson model after setting the empirical coefficients and low-speed flow coefficient (φ_{Low}). The rotational speed range was specified according to the process requirements to be from 105% to 60% of the full capability. Figure 6-4(a) illustrates the variation of work coefficient with the flow coefficient and Mach number at fixed polytropic exponent (n), degree of reaction (γ_d) and slip factor (μ). The case 1 in this figure represents the design point speed at which the compressor is running at 98.34% of the full speed operation. It is clear that the surge point of the low Mach numbers shifts towards lower flow region. Furthermore, the work coefficient is increasing inversely with the flow coefficient and proportionally with the Mach number.

The work coefficient reflects the enthalpy rise within the stage, and it can be used to derive the slope of pressure rise at different characteristics. However, the stage impeller has been designed to satisfy the aerodynamic constraints related to work coefficient. Figure 6-4(b) shows the obtained pressure ratios of the first mechanical stage at various speeds where the large red dot represents the design point conditions. It was found that the design point is not located at the greatest pressure ratio in order to ensure the highest efficiency point. However, operating the compressor at highest efficiency point might lead to reduce the surge margin. Hence, the design flow usually tends to approach the maximum efficiency point from the high flow region as demonstrated in polytropic efficiency curve in figure 6-4(c). However, it is important to mention that the exact figures cannot be ensured until meeting the actual discharge conditions at the overall compressor discharge. So, these figures need to be iterated further by reaching the last mechanical stage. Furthermore, the engineering judgment is required here to check that the speed lines are reflecting the normal compressor performance trend.

Looking to polytropic efficiency curve (Fig. 6-4c), it is obvious that the choke is taking place at relatively greater efficiency when the compressor is operated at low rotational speeds due to the reduction in the incidence losses.

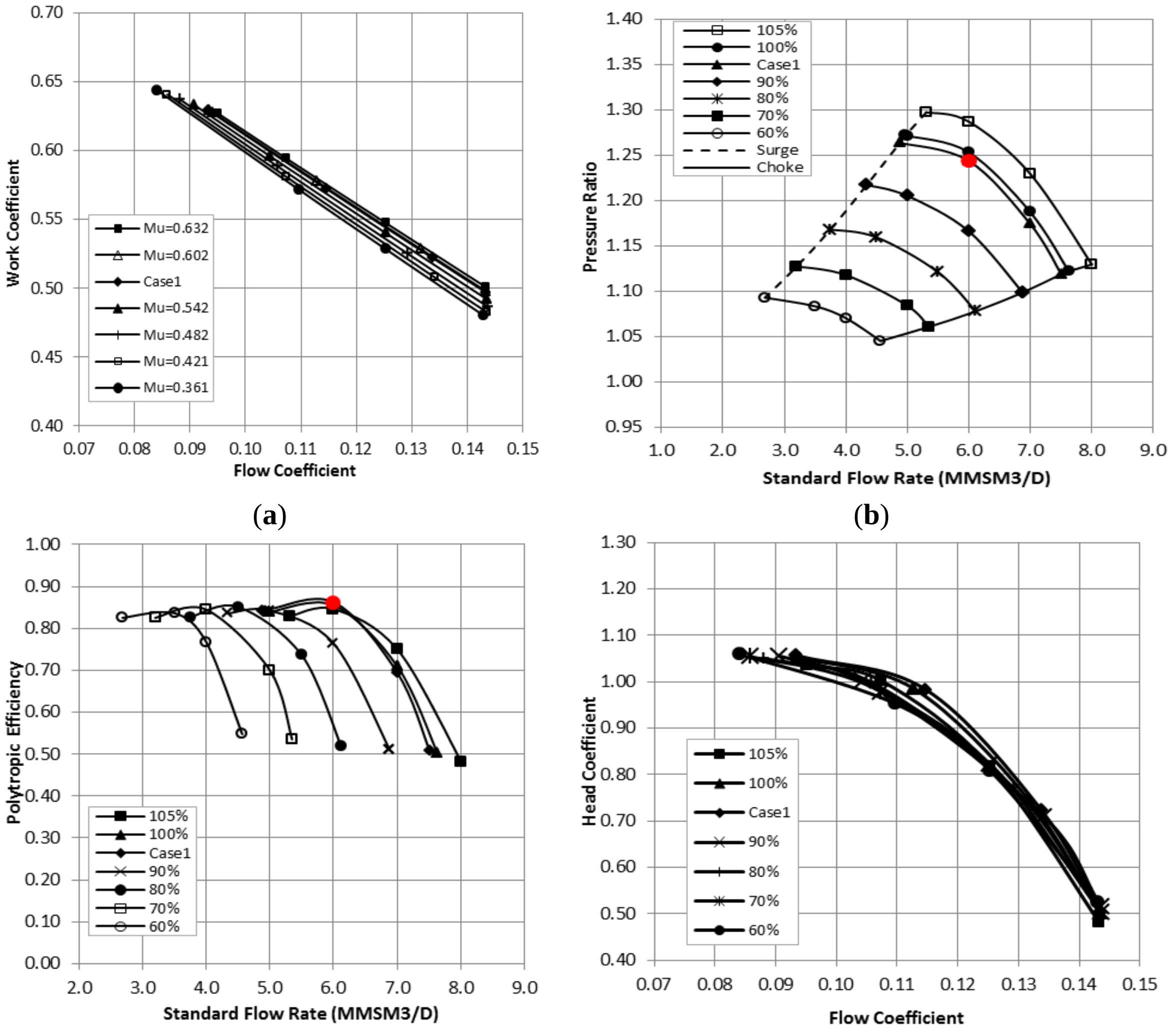

(a) (b)

(c) (d)

Figure 6- 4: Predicted Performance Parameters of First Mechanical Stage: (a). Work Coefficient Variation (b). Pressure Ratio Curve (c). Efficiency Curve (d). Head Coefficient Variation

Besides, the peak efficiency point is shifted to low flow region as the speed decreases. The drop in flow rate reduces the required power to achieve the corresponding polytropic head. The stage pressure ratio goes up inversely with the mass flow rate prior the surge point leading to a higher head but with lower efficiency. However, the reduction in suction flow places a greater thermal load on the impeller blades while the rise in Mach number yields a higher aerodynamic load in addition to the thermal stress. This can be observed by plotting the variation of head coefficient as shown in figure 6-4(d). The greater head coefficient at low flow region is behind the high temperature ratio. By comparing the impact of Mach number on the polytropic head at high and low flow coefficient regions; the increase in the head coefficient at higher rotational speed becomes more substantial at low flow region. The greater variation in the head coefficient slope at low flow coefficient makes the impact of Mach number on the thermal and aerodynamic load more significant. Furthermore, the high head and flow coefficients confirm the sort of impeller blades configuration with shrouded 3D structure and backward leaning vanes.

As long as the discharge pressure is lower than the required overall value, the compression process continues to the next stage and the discharge conditions of the previous stage are used as suction parameters for the following one. By reaching the required pressure ratio, the flange-to-flange performance curve can be derived and consequently the calculated overall efficiency is compared with the measured value. In this case, the required discharge pressure can be accomplished by installing five mechanical stages and the obtained performance curve of each one is showing in figure 6-5.

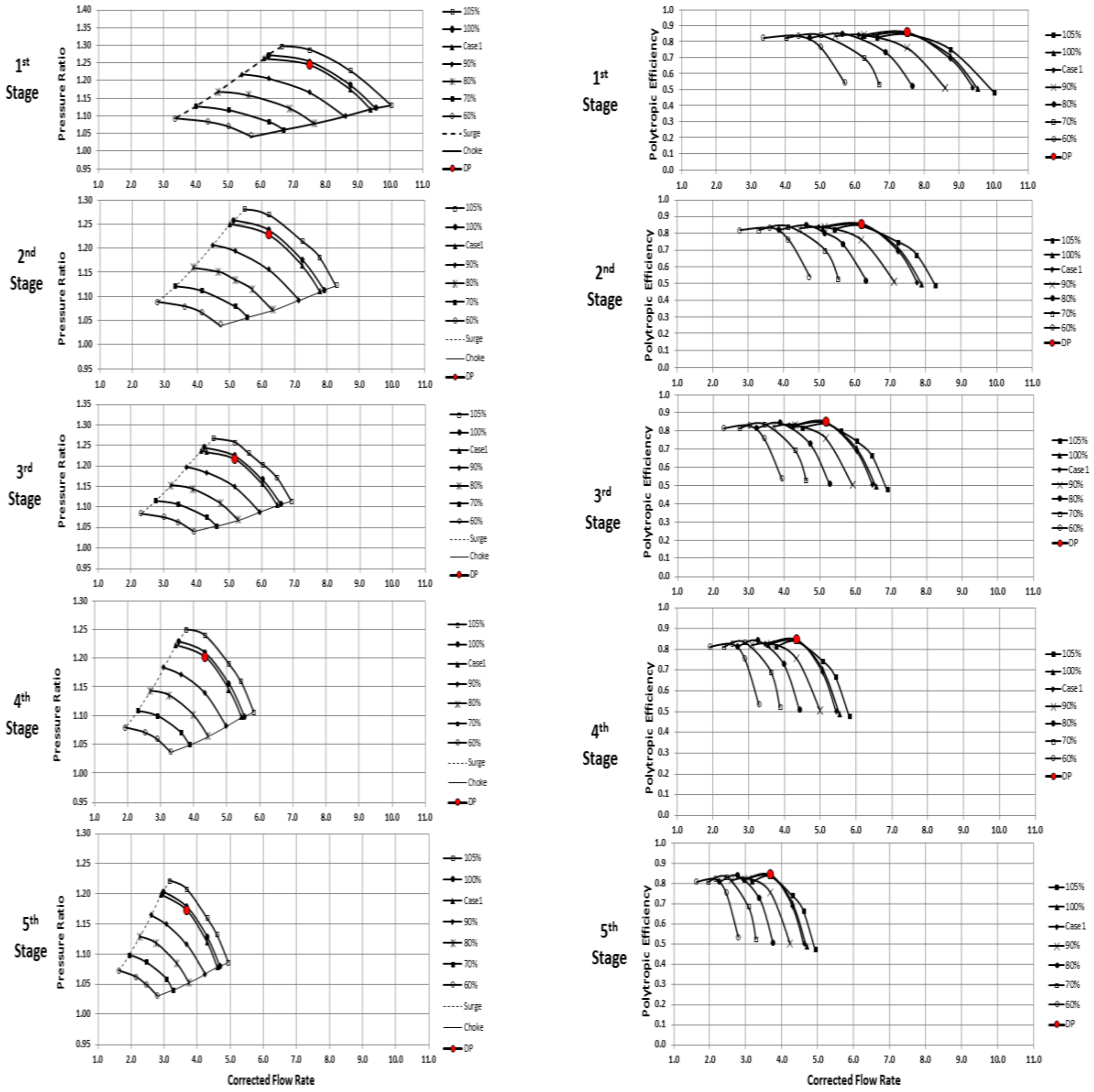

(a) **(b)**

Figure 6- 5: Predicted Pressure Ratio and Efficiency Curves of the Five Mechanical Stages

In order to make these figures valid for wide range of working pressures and temperatures, the flow rate is corrected corresponding to a reference temperature and pressure of 15ºC and 1atm, respectively. The vertical axis in figure 6-5(a) denotes the stage pressure ratio while the horizontal axis represents the corrected flow rate. It is clear that the span between the choke and surge limits decreases as speed is reduced. The derived dimensional performance map of every stage are also illustrated in Appendix (D). Comparing with the first stage, the constant speed lines shifted toward lower flow rate. However, the rear stages are operating with relatively lower pressure ratio due to the greater inlet gas temperature which makes the compression process more difficult.

The rated stable range is expressed as a percentage, and it can be simply estimated using equation (6-12) where the rated point is determined as the intersection of the 100% speed line and the highest flow during operation.

$$Stability\ Range = \frac{Q_r - Q_s}{Q_r} \tag{6-12}$$

where
Q_r: Capacity at rated point
Q_s: Capacity at surge point along 100% speed line

The predicted stability range of the first stage was found roughly 33.67%, and it increased to approximately 35.42% for the fifth stage with an averaged rise rate of about 1.27% for each single stage. Moreover, it was observed that the first mechanical stages tend to surge relatively earlier and at lower flow rates.

Figures 6-6(a) and 6-6(b) compare the estimated overall pressure ratios and polytropic heads with the measured values at different flow rates and various speed lines. The measured values were found roughly suited on the derived constant speed lines especially at lower than full speed operation. However, the greater uncertainty in the obtained pressure ratios and polytropic heads was observed at high Mach number conditions. The predicted choke flow is quite matching the actual values at all speed lines. However, the choke pressure ratio was found greater than the measured value, and the deviation between the measured and predicted values becomes more significant at high speed values. The largest difference was detected when the compressor overloaded by 5% above the full speed with approximately 2.94% higher than the measured pressure ratio. By referring to the pressure ratio equation (Eqn. 6-4), it is obvious that this model does not account for the individual component losses and the change in the pressure losses at choke conditions as a result of aero-channels blockage due to the flow shocks and separation. These losses become greater as the rotational speed increases and at higher than the nominal design Mach number. Generally, these losses are proportional to the absolute velocity which is taking upward trend as the speed and flow rate increase. At surge point, the predicted surge flow approximately matches the measured value at high speed operation. On the other hand, it was found that the compressor is surging at greater flow coefficient than the predicted value at lower speeds, and this deviation increases as the Mach number is reduced. The prediction of back-flow initiation requires considering the performance and the related aerodynamic losses of each single component which have not been covered in this method. However, the measured polytropic head and pressured ratio still fall in the predicted speed lines even at low speed operation excluding the surge point of high Mach number lines. The calculated surge pressure ratio of overloaded compressor case is below the actual value by roughly 1.9%.

Another effect of the high choke pressure ratio at high speed operation can be observed from the shaft power curve in figure 6-6(c). It is clear that the measured power points fall on the constant speed lines until approaching the choke flow. The estimated shaft power near the choke flow was found considerably greater than the actual data, and the difference between the predicted and measured power goes up as the Mach number increases. The greatest uncertainty was found at choke flow of the overloaded speed by about 8.34%. The predicted overall efficiencies are plotted in figure 6-6(d) with the measured data at various volume flows and rotational speeds.

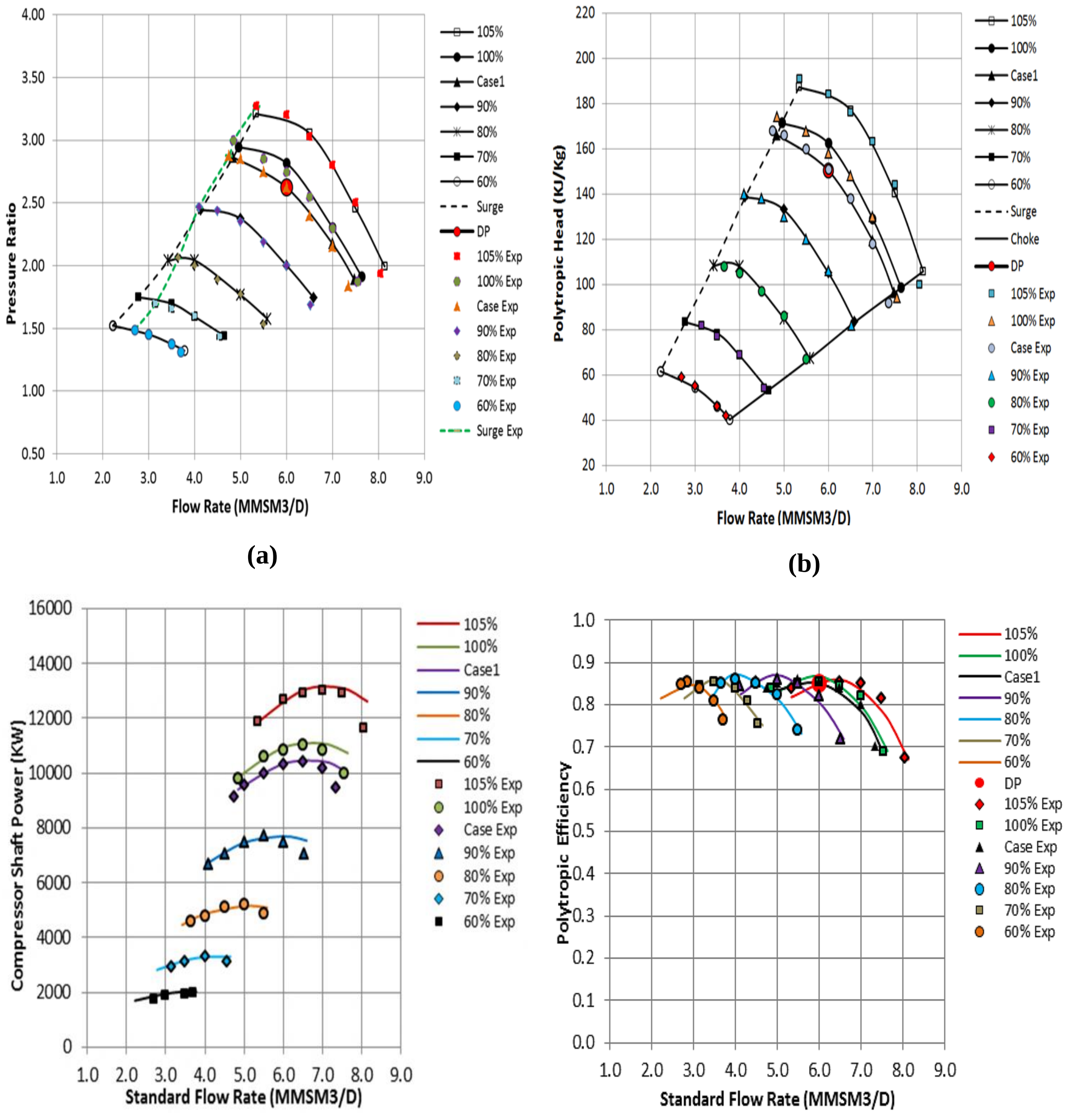

(a) **(b)**

(c) **(d)**

Figure 6- 6: Evaluation of Developed Performance Map Using the Adapted Casey-Robinson Model Against Measured Data

Generally, the accuracy of the derived efficiency tends to decrease at overload operation. The largest percentage of error was observed at 7.5 MMSM3/D when the compressor is operating at highest rotational speed with approximately 3.64%. Besides, the predicted surge efficiency was found lower than the measured value at all speed lines which, in turn, pushed the polytropic head at surge flow to be greater than the actual value.

6.5 Lüdtke Model –Based- Method

This method requires more details about the stage geometry in order to obtain the polytropic efficiency. This dependency on geometrical features can be considered as one of the disadvantages of this technique. The fundamental concept behind this method is shown in figure 6-7.

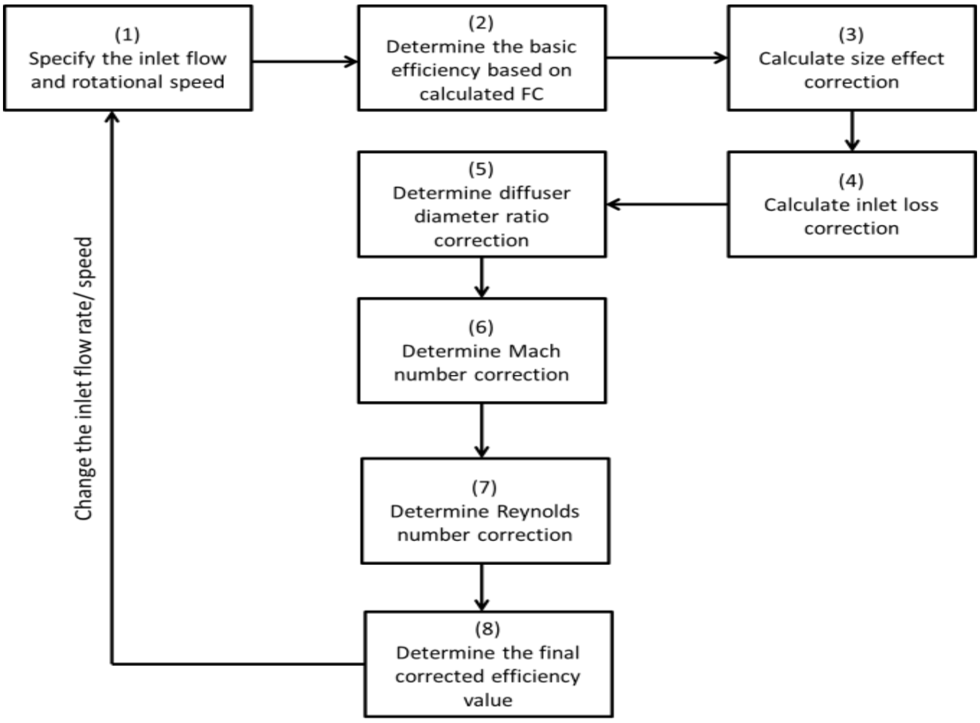

Figure 6- 7: Developed Approach Based on Lüdtke Model

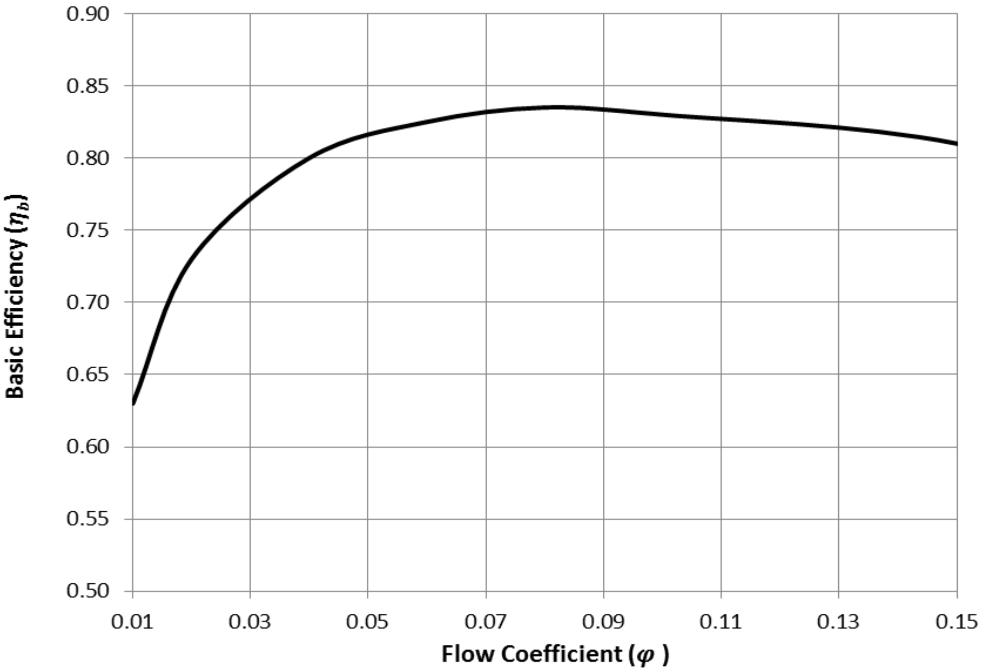

Figure 6- 8: Basic Efficiency Curve Based on Lüdtke Model

At the beginning, the basic efficiency is estimated according to the recorded values at various flow coefficients as illustrated in figure 6-8. These values have been derived experimentally by Lüdtke (2004) for fixed stage geometry. The design characteristics of the tested compressor are:

- Exit impeller diameter =400mm
- Diffuser diameter ratio = 1.65

- Mach number = 0.77
- Flow coefficient = 0.093

So, the obtained efficiency has to be corrected in order to consider the effect of changing the geometrical and aerodynamic characteristics of the new compressor design. First of all, the inlet flow rate and the specified rotational speed at design point conditions are used to calculate the flow coefficient and Mach number of the first mechanical stage. This will allow deriving the initial basic efficiency value (η_b) corresponding to the flow coefficient. The efficiency of the new design compressor (η_{New}) is calculated using this formula:

$$\eta_{New} = \eta_b + \Delta\eta_{SC} + \Delta\eta_{DD} + \Delta\eta_{ic} + \Delta\eta_{Mu} + \Delta\eta_{Re} \qquad \textbf{(6-13)}$$

These procedures are repeated at different flow rates and rotational speeds in order to derive the overall stage performance curve. The obtained efficiencies are then substituted in pressure ratio equation (Eqn. 6- 4) to calculate the stage pressure ratio and polytropic head.

6.5.1 Developed Approach Based on Lüdtke Model

Based on this method, the new compressor model is derived from the original design by scaling the initial component size including the main dimensions, surface roughness, blade thicknesses and labyrinth clearances. However, the scaling can be performed to a certain extent to avoid any contravene with safety issues and aerodynamic aspects. In addition to the manufacturing tolerances, the impact of imperfect scaling is considered under the size effect correction. Experimentally, the incremental change in the efficiency value is 2% for impeller diameter of 800 mm and -5% to -2% for 100 mm diameter at high and low flow coefficients, respectively (Lüdtke, 2004). So, the change in the efficiency has been assumed to be homogeneous with zero change at the original diameter value as shown in figure 6-9(a). Besides, the size correction value ($\Delta\eta_{\mathrm{sc}}$) at smaller than the original impeller diameter is specified according to the difference between the new and initial flow coefficient values. When the impeller diameter is exceeding 400mm, the impact of flow coefficient is neglected due to the insignificant variation comparing with the small diameter impeller designs. Figure 6-9(a) illustrates the derived distribution of the efficiency size correction ($\Delta\eta_{\mathrm{sc}}$) as a function of the exit impeller diameter (D_2) and flow coefficient (FC). When the design flow coefficient of the new compressor matches the tested compressor value but with smaller impeller diameter than the original design, the change in the efficiency is interpolated between the two curves.

After size effect correction, the change in the inlet nozzle loss as a result of suction-nozzle sizing has to be taken into the consideration. This induced pressure loss is caused by the change in the flow direction and turbulent wall friction. Since the alteration in the total pressure loss is synonymous with the efficiency variation, the initial efficiency value has to be corrected. The isentropic head increase (y_r) can be calculated using the following equation.

$$y_r = \left[\frac{\left(\frac{PR_{fd}}{1-\xi\frac{k_v}{2}M_s{}^2}\right)^{\frac{k_v-1}{k_v}} - 1}{PR_{fd}{}^{\frac{k_v-1}{k_v}} - 1}\right] - 1 \qquad \textbf{(6-14)}$$

The loss coefficient (ξ) is derived according to the suction Reynolds number from figure 6-9(b) based on the recorded measured data (Lüdtke, 2004).

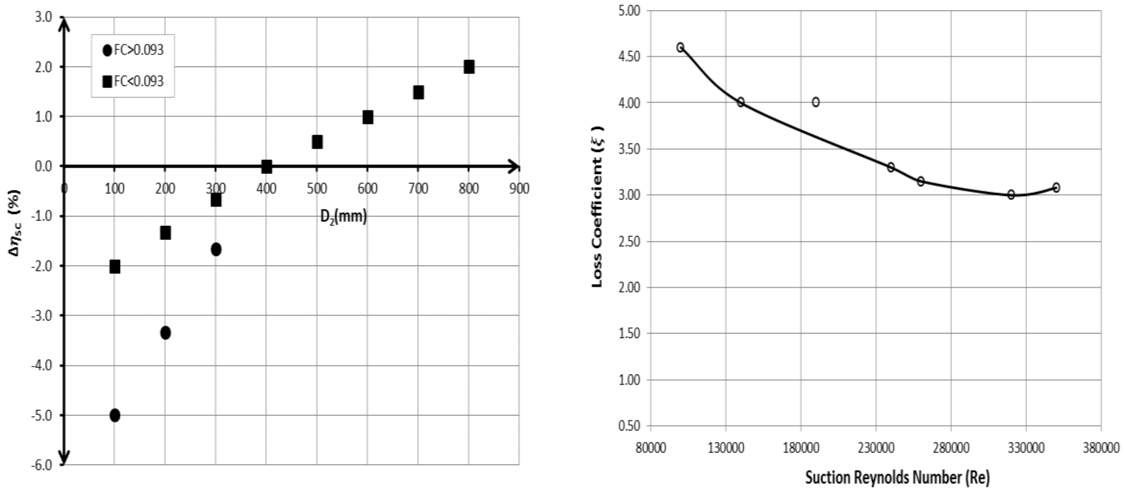

(a) Size Effect Correction **(b) Inlet Loss Coefficient**

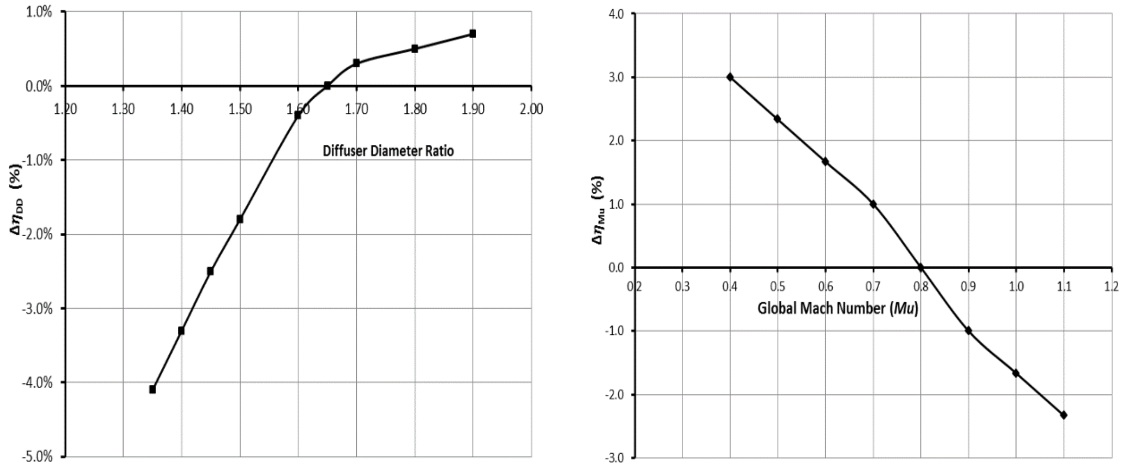

(c) Diffuser Diameter Ratio Correction **(d) Mach Number Correction**

Figure 6- 9: Correction Factors According to Experimental Measurements of Lüdtke (2004) and Linder (1983)

All the experimental readings situated on the best curve fit except one point located well over the obtained curve. The fitted curve indicates a non-linear inverse relationship between the suction Reynolds number and loss coefficient and this point will be considered as a reading error. Hence, the inlet loss correction ($\Delta\eta_{ic}$) is calculated using formula (6-15), and it is accounted only for the mechanical stage downstream of the inlet nozzle.

$$\Delta\eta_{ic} = \frac{y_r}{1 + y_r}\eta_b \qquad \textbf{(6-15)}$$

The original method also considers the effect of changing the blade exit diameter assuming a fixed hub and cover disc geometry. This obviously will alter the discharge velocity from the impeller and the wall friction in the downstream diffuser leading to different polytropic head and efficiency values. However, this is not applicable for the present study since the entire impeller geometry is changed including the hub and tip.

Another geometrical factor which has a substantial influence on the total stage efficiency is the diffuser diameter ratio. The longer flow path downstream of the impeller allows achieving a greater extracted pressure from the discharge impeller gas yielding a greater efficiency. On the other hand, the excessive diffuser diameter ratio can have a negative impact on the stage efficiency by allowing more significant pressure drop to take a place throughout the flow channel. Figure 6-9(c) is used to estimate the efficiency change ($\Delta\eta_{DD}$) due to the change in diffuser ratio according to the conducted experimental tests by Lüdtke (2004) and Linder (1983). Furthermore, there is no exact method to correct the obtained efficiency of the new compressor design based on the global Mach number. However, the accumulated test data show a reduction by about 1% in the stage efficiency when Mach number reaches 0.9 while the change was found roughly -3% for 1.2 Mach number. Based on these results and by considering the original Mach number value, the Mach number correction curve ($\Delta\eta_{Mu}$) is derived as demonstrated in figure 6-9(d).

For Reynolds Number correction, a formula published by Strub et al. (1987) is used to determine the influence of Reynolds number on the total efficiency ($\Delta\eta_{Re}$). This correlation was developed based on the recorded measured data and by considering the difference between the reference efficiency at test conditions and the actual value at specified conditions.

$$\Delta\eta_{Re} = 1 - \left(1 - \eta_{p-ref}\right)\left(\frac{0.3 + 0.7\frac{\lambda_{act}}{\lambda_{cr-act}}}{0.3 + 0.7\frac{\lambda_{ref}}{\lambda_{cr-ref}}}\right) - \lambda_{p-ref} \qquad \textbf{(6-16)}$$

The friction factor (λ) is calculated at reference and actual conditions using Colebrook-White formula (Eqn. 6-17).

$$\lambda = \left[1.74 - 2log\left(\left(2\frac{Ra}{b_2}\right) + \frac{18.7}{Re\sqrt{\lambda}}\right)\right]^{-2} \qquad \textbf{(6-17)}$$

At reference conditions, the Reynolds number is calculated at atmospheric conditions. The arithmetic average roughness of the impeller surface (Ra_{ref}) is estimated by about 5µm at reference conditions from the centerline. So, the critical friction factor (λ_{cr}) is obtained at infinite Reynolds number.

6.5.2 Validation of Lüdtke Model –Based- Approach

Following the developed stage stacking approach, the estimated efficiencies using variable speed control are plotted in figure 6-10(a) against measured data. It is clear that this method does not measure the aerodynamic instability at high and low flow regions. Besides, the efficiency decreases continuously with the flow coefficient rise and with almost a constant slope throughout the operating flow range. However, it is obviously by looking to this model that there is a change in the flow turbulence level at very high flow points where the flow shocking and separation are taking place.

Focusing on the stable flow region, the predicted variation in the efficiency with the inlet volume is relatively less intense. However, it is an interesting to observe that this method was able to predict the design efficiency with an acceptable level of accuracy reaching to roughly -0.96% as a relative error. This proves the capability of this method to estimate the total efficiency at design point conditions. Besides, the large deviation between the calculated off-design efficiency and the measured values invalidate the suitability of this model for the off-design conditions. This is because this method predicts the total efficiency without considering the design point conditions assuming an identical flow behavior at all flow regions.

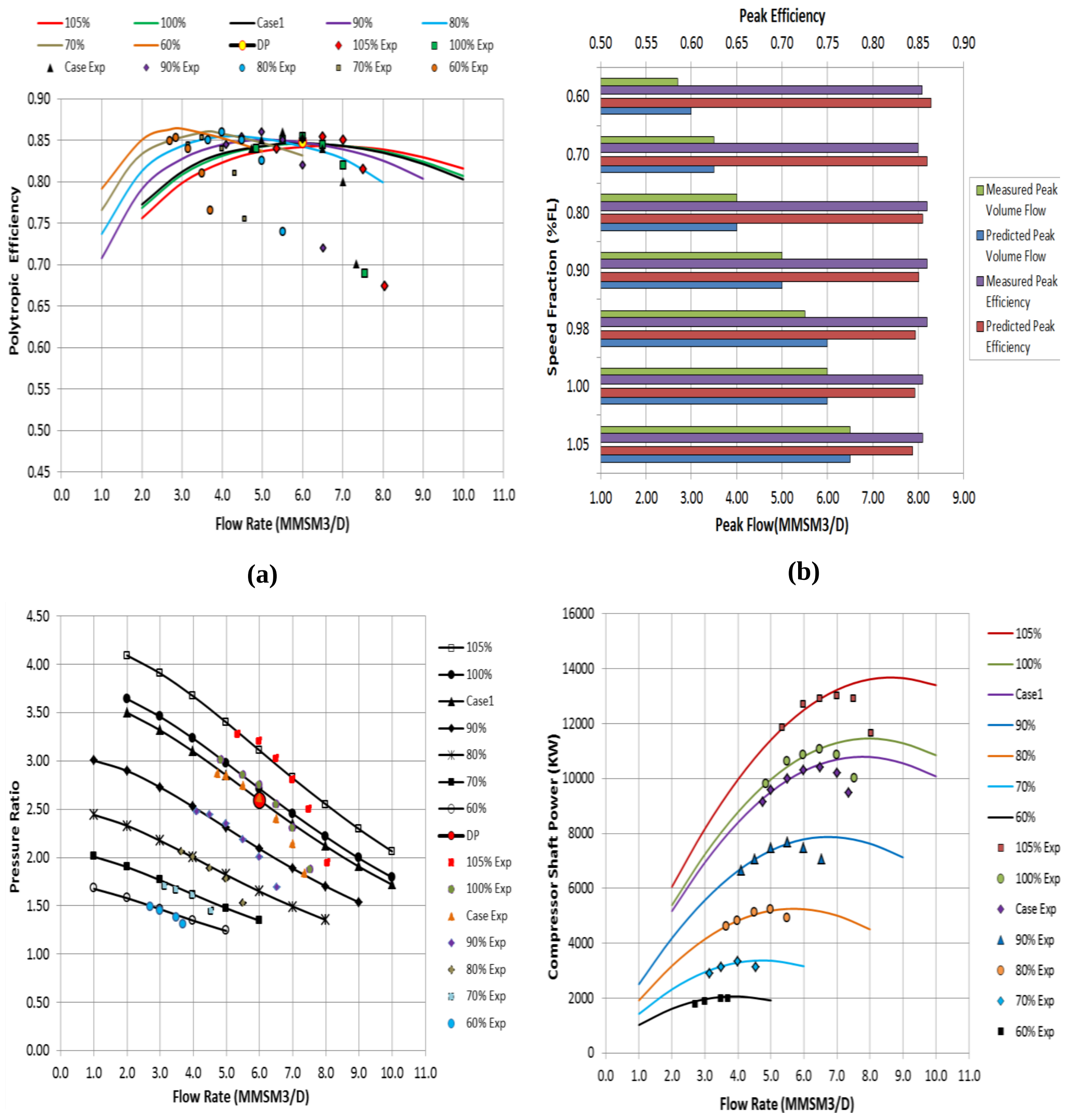

(a) (b)

(c) (d)

Figure 6- 10: Comparison Between the Predicted Parameters Using Lüdtke Model and the Measured Data: (a) Efficiency (b) Peak Flow and Efficiency (c) Pressure Ratio (d) Power

Another point which can be noticed from this figure is that the difference between the predicted and measured efficiencies becomes smaller at low flow coefficients and at various Mach number values. The higher degree of accuracy can be observed in the prediction of peak efficiency as illustrated in figure 6-10(b).The largest percentage of error in the peak efficiency value was found at the design point operation with a relative deviation of only1.53%. Moreover, the results of predicted peak flow coefficients show an acceptable estimation comparing with the actual values.

The pressure ratio curve in figure 6-10(c) tends to have almost a constant slope throughout the flow range. It should be noted that this figure has been constructed assuming variable polytropic exponent and degree of reaction. Most of the measured pressure ratio points fall on the predicted constant speed lines at low flow rate region. This ultimately agrees with the efficiency trend in figure 6-10(a). However, the failure to determine the efficiency at high flow region especially while the flow approaches the choke point leading to greater pressure ratios than the measured values. As a result of high predicted discharge pressure, the estimated overall discharge temperature was found well above the measured value at choke flow. Figure 6-10(d) compares the predicted shaft power with the measured data at various speeds and flow rates. The required shaft power near the choke point is still higher than the measured value. This denotes that the increase in the predicted polytropic head over the measured value is greater than the power rise. Additionally, the difference between the measured and calculated choke pressure ratios and shaft power become greater as the Mach number goes up due to the increase in pressure losses which have not been accounted in this model.

6.6 Evaluation Summary

The original Casey-Robinson model has been applied for turbocharger compressor hence a new set of empirical coefficients and flow coefficients and efficiencies ratios have been derived after hundreds of trials to be suitable for industrial compressors. Although that this method does not require a deep geometrical knowledge, the dependency on the peak efficiency and associated flow coefficient at both normal operation and low Mach number makes this model more difficult to use when these parameters are unknown. Moreover, the adapted method results show an acceptable level of accuracy comparing with the measured values. However, the derived surge flow coefficient value at low speed conditions was found well below the measured flow which should be aware of in the future. This is mainly due to the difficulty in predicting the back-flow initiation without considering the individual component losses. Besides, the conducted comparison between the measured and estimated performance parameters revealed a substantial difference between the predicted pressure, temperature, power and efficiency and the measured values near the choke and surge points and this deviation increases at high speed operation.

On the other hand, Lüdtke method requires more geometrical details in order to correct the basic efficiency value for the new design. In addition to the global flow coefficient, Mach number and work coefficient, this approach considers the Reynolds Number as the fourth parameter to correct the basic efficiency value. Furthermore, this study introduces a new mechanism that can be used for size and Mach number corrections. The accuracy of the predicted efficiencies using Lüdtke method was found substantially lower than the obtained results by Casey-Robinson model, especially at very high flow region. The difference between the measured and calculated efficiency values increases with the flow rate rise. Moreover, this method fails to predict the stable flow region limits. However, the predicted design and peak efficiencies and corresponding flow coefficient were very close to the measured values, but with less degree of accuracy comparing with Casey-Robinson approach results.

6.7 New Integrated Method

The derived method consists of three main steps as shown in figure 6-11:

1. Design efficiency calculation using the adapted Lüdtke method at fixed speed value and variable suction flow. The predicted curve is then used to define the peak efficiency and the associated flow coefficient.
2. The calculated efficiencies and flow coefficients are used to obtain the off-design efficiency value at various speed lines for the first mechanical stage by implementing the adapted Casey-Robinson model.

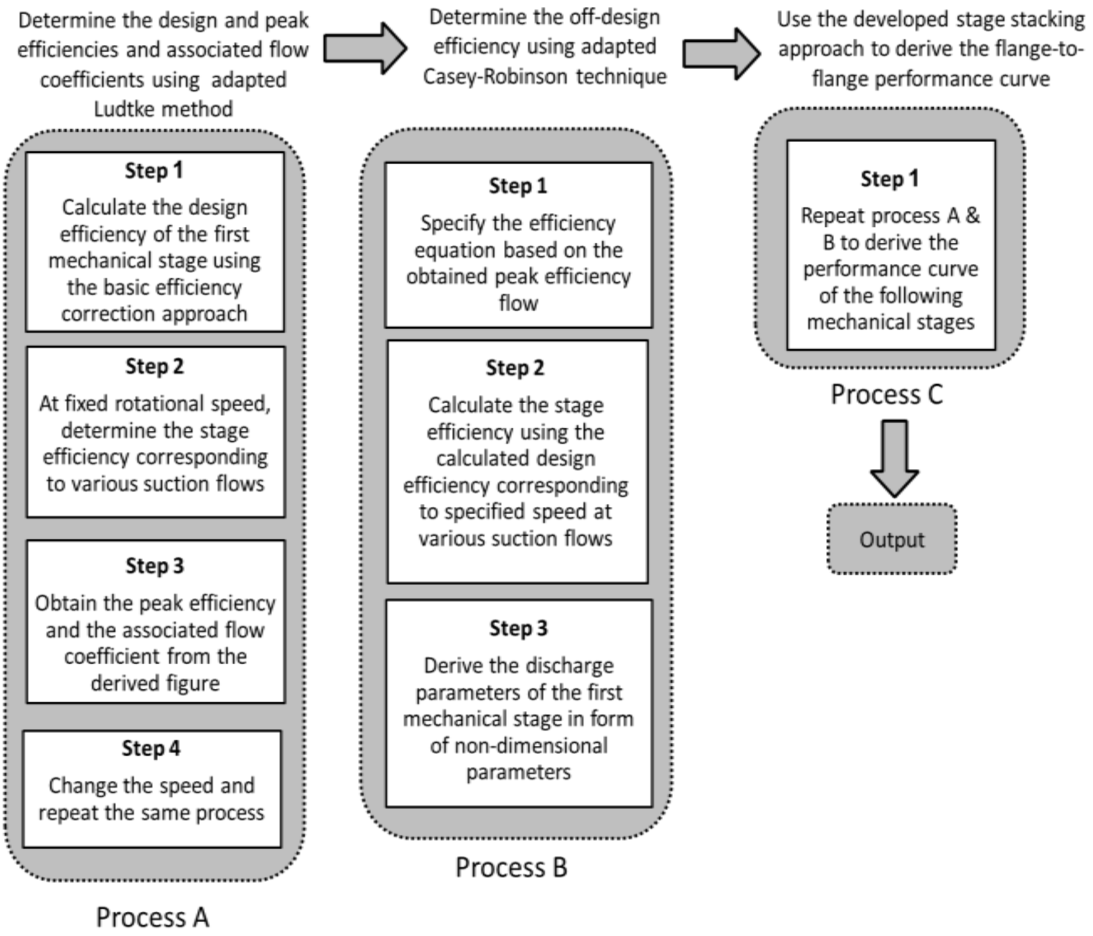

Figure 6- 11: Developed Integrated Model Approach

3. The proposed stage stacking approach is used to derive the characteristics of the following stage reaching to flange-to-flange performance curve.

One of the main disadvantages of the Casey-Robinson model is the dependency on the design and peak efficiencies and associated flow coefficients for every speed line in order to derive the off-design efficiency value. This necessitates the need for iteration process since these variables are most often unknown at this design process. However, this becomes more difficult for multi-stage centrifugal compressor in which the design efficiency of each mechanical stage has to be identified. In the original method, the efficiency curve at constant speed line is derived and then corrected based on the peak efficiency and flow coefficient.

To calculate the design efficiency for every single mechanical stage, the Lüdtke model is used by correcting the efficiency value of the initial design based on the new design features. This, in fact, requires the prior knowledge of some geometrical characteristics of the impeller and diffuser including impeller diameter and diffuser diameter ratio. Furthermore, the adapted Lüdtke approach will be used to predict the efficiencies and flow coefficients at design and peak points. However, the basic efficiency curve in this method has to be corrected as well to be valid for high and low flow coefficients applications as illustrated in figure 6-12. The horizontal axis represents the shift in the flow coefficient at design peak efficiency from the initial measured value. This is based on assumption that the design point of the new compressor design is closer to the peak efficiency value. At constant rotational speed, the basic efficiency is derived at various flow rates; thus, the peak efficiency and associated flow coefficient value are obtained. This process is performed for every mechanical stage and at each speed line.

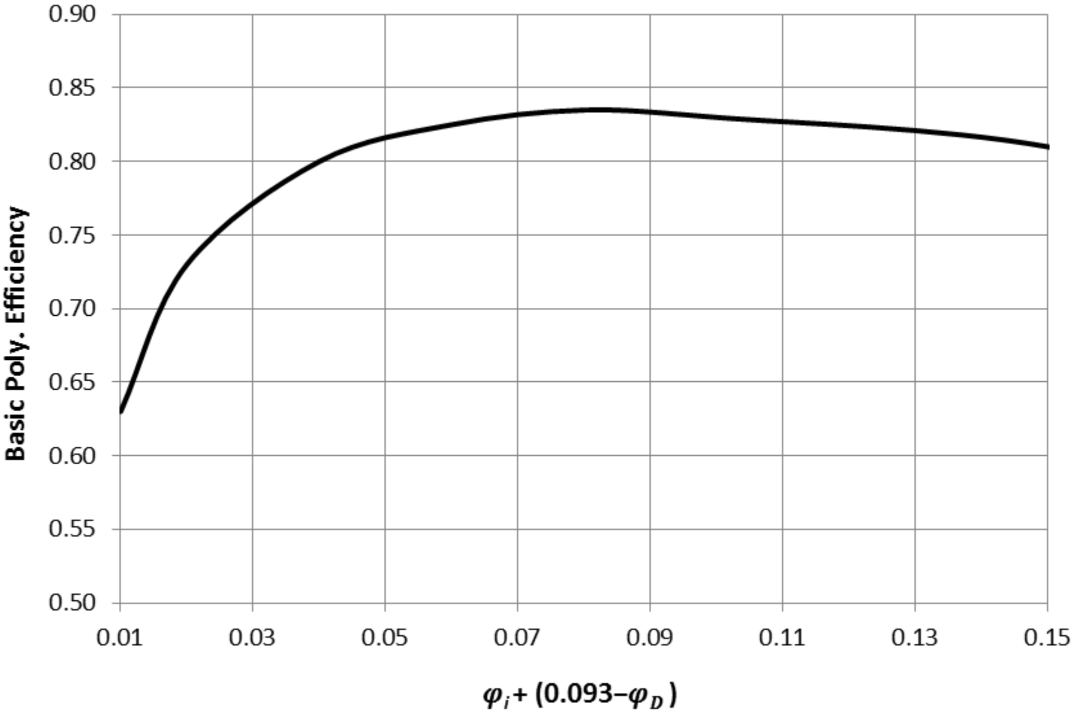

Figure 6- 12: Adapted Basic Efficiency Curve

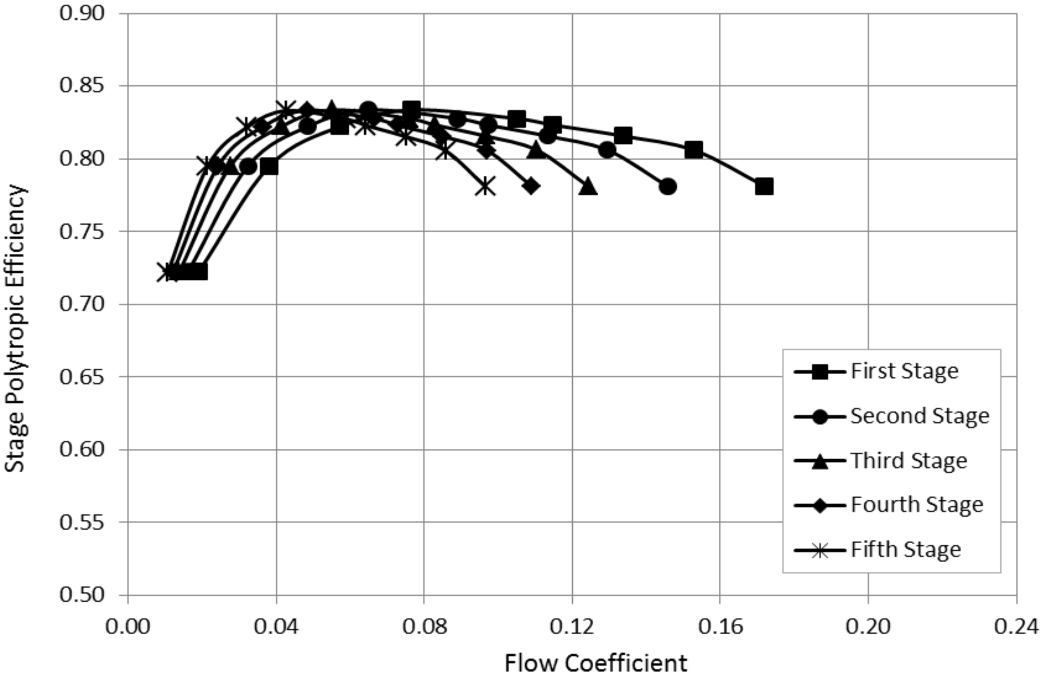

Figure 6- 13: Determination of Peak Efficiency and Associated Flow Coefficient At Design Speed of 14.5 MW Centrifugal Compressor Using Adapted Lüdtke Model

There is another advantage from the determination of design and peak efficiencies and flow coefficients using adapted Lüdtke model. Casey-Robinson model requires a prior knowledge of the peak flow coefficient at low Mach number condition in order to estimate the peak flow coefficient during normal operation. This might not be available at early design stage. Hence, several iterations should be performed to identify the actual flow coefficient at low-Mach number conditions. However, this is not necessary for the new developed model where the peak flow coefficient can be obtained easily by deriving the corrected efficiency curve at various flow coefficients as illustrated in figure 6-13.

By considering the work coefficient model, it was found that the assumption of constant polytropic exponent, slip factor and degree of reaction have an adverse impact on the pressure ratio curve. The main concern about this approximation appears at high flow and high speed conditions. At higher than nominal design Mach number, the pressure ratio characteristic of the stage becomes steeper at choke flow, which is different from the behaviour of low speed operation. This happens due to the greater drop in the work coefficient at choke flow of high speed impellers comparing with low Mach number impeller. Aerodynamically, the quick reduction in the impeller efficiency as the choke point is approached raises the polytropic exponent and degree of reaction sharply yielding, in turn, to a rapid fall in the density ratio.

The original method does not take into the account the impact of speed on the polytropic exponent and degree of reaction which explains the obtained linear relationship between the work coefficient and flow coefficient. The bearing of this approximation might be insignificant while dealing with a single stage centrifugal compressor but, it becomes substantial for the multi-stage compressors. To consider the impact of the polytropic exponent, degree of reaction and slip factor on the work coefficient; the Casey-Robinson work coefficient equation can be rewritten in a new form (6-18), and the obtained results for the first mechanical stage of 14.5 MW centrifugal compressor are plotted in figure 6-14.

$$\frac{k_{si}}{k_{sd}} = \frac{\left[1 + (k_d - 1)\gamma_d \psi_{w_d} Mu_d^2\right]^{\frac{1}{n_d - 1}}}{\left[1 + (k_i - 1)\gamma_i \psi_{w_d} Mu_i^2\right]^{\frac{1}{n_i - 1}}} \tag{6-18}$$

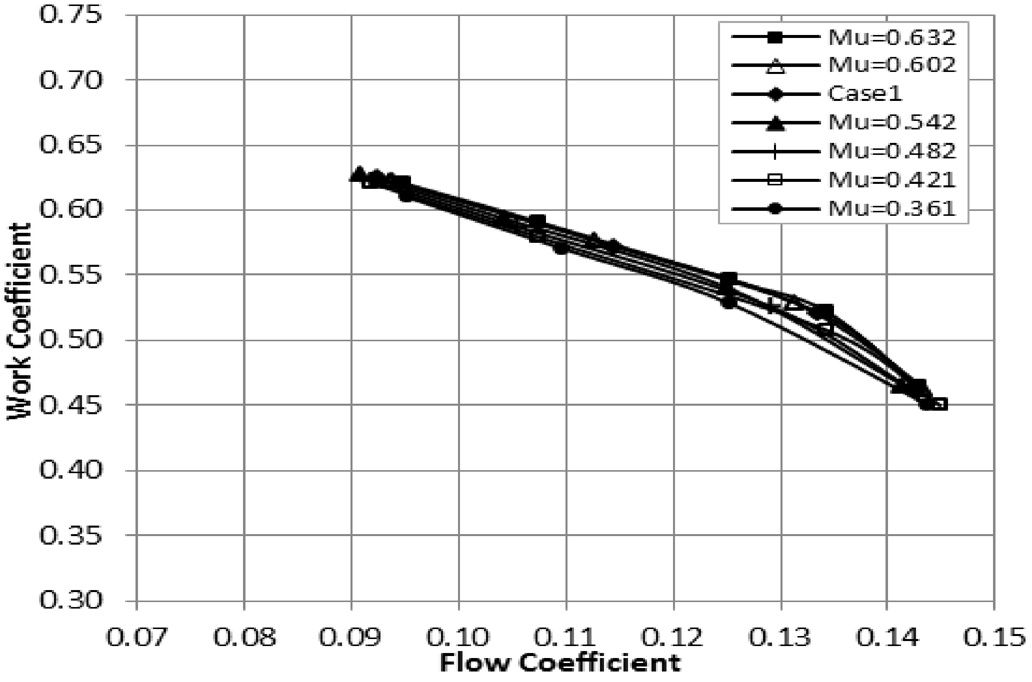

Figure 6- 14: Work Coefficient of First Mechanical Stage of 14.5 MW Centrifugal Compressor at Variable polytropic Exponent, Slip Factor and Degree of Reaction at Choke Condition

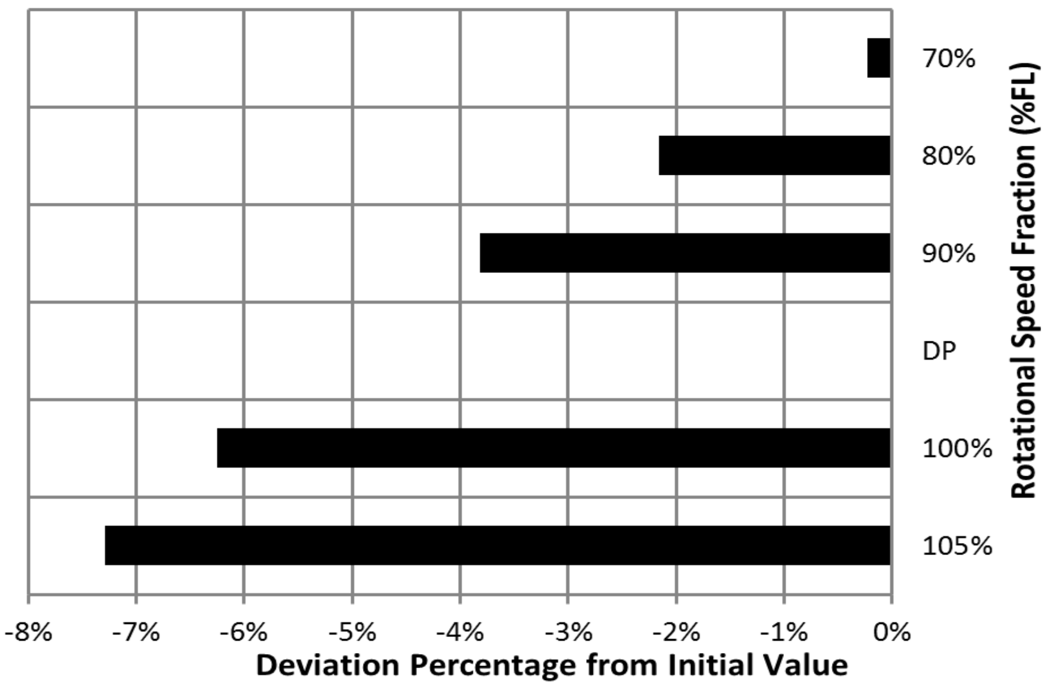

Figure 6- 15: Detected Change in the First Mechanical Stage Work Coefficient of 14.5 MW Centrifugal Compressor at Variable polytropic Exponent, Slip Factor and Degree of Reaction at Choke Condition

The variation of work coefficient is no longer linear with the flow coefficient, and the constant speed lines shifted downward slightly. Moreover, the introduced change in the calculated work coefficient value is shown in figure 6-15. However, it is important to mention here that a small difference in the work coefficient can have a considerable impact on the pressure ratio, especially when the pressure ratio of the entire compressor is considered. At choke flow and 105% of full speed, the work coefficient decreases by approximately 7.29% when the impact of polytropic exponent and degree of reaction has been taken into the account. This negative deviation is increasing continuously as the speed goes further. On the other hand, the deviation of the work coefficient becomes positive at very low speed, and it is growing with the Mach number reduction.

The efficiency equation at lower than the peak efficiency flow point does not consider the change in the efficiency variation slope near the surge flow. The efficiency curve takes different slope at higher and lower than full speed operating point. Accordingly, a new term has been added to efficiency equation to account for the deviation between the operating and the design Mach numbers.

$$\eta = \eta_p \left[1 - \left(1 - \frac{\varphi}{\varphi_p}\right)^D\right]^{1/D} + \varphi_i(Mu_D - Mu_i) \qquad \textbf{(6-19)}$$

Figure 6-16 illustrates the difference between the new derived efficiency and the Casey-Robinson model value at various flow coefficients and Mach numbers. This curve is plotted assuming a design Mach number of about 0.59 at which both efficiencies are identical. At higher than design speed, the new efficiency value tends to be lower, and the deviation increases as the speed and flow coefficient go up.

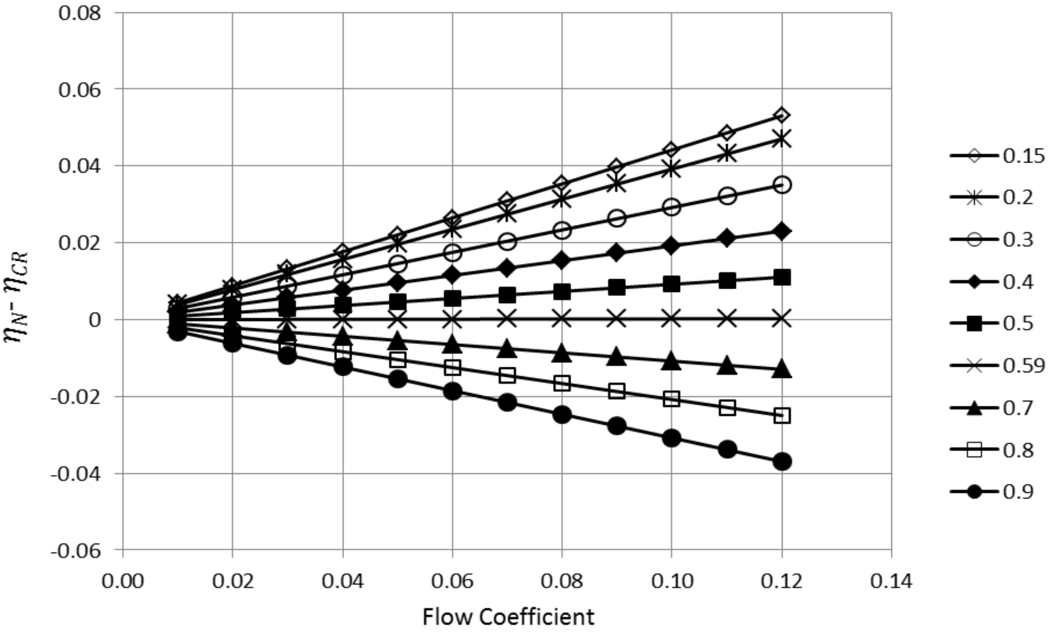

Figure 6- 16: Change in the Predicted Efficiency at Lower then Peak Flow at Various Mach Numbers

The high Mach number operation leads to greater incidence losses at very low flow coefficients. This in turns reduces the compressor efficiency with higher slope than the low rotational speed conditions. This change in efficiency trend with speed characteristics is also reflected by varying the coefficient D with Mach number from about 3.3 at low Mach number to around 2.7 at high speed conditions.

To improve the prediction capability of the surge flow coefficient especially at low running speed, the original equation has been modified to consider the flow shift from the design point and the deviation from high Mach number value. This will contribute to consider the impact of operating at higher or lower speed than the design point.

$$\emptyset_{s_i} = \left[1 - \frac{1}{1 + e^{-C_s(Mu_i - B_s)}}\right] \left\{ \left(\frac{\emptyset_s}{\emptyset_c}\right)_{Lo} \emptyset_{c_i} + \frac{\left(\emptyset_{p_D} - \emptyset_{p_i}\right)(Mu_{max} - Mu_i)}{\left(\frac{\emptyset_{c_D}}{\emptyset_{c_i}}\right)^2 - \left(\frac{\emptyset_{p_i}}{\emptyset_{p_D}}\right)^2} \right\} + \frac{\emptyset_{c_i}}{1 + e^{-C_s(Mu_i - B_s)}} \left(\frac{\emptyset_s}{\emptyset_c}\right)_{Hi} \qquad \textbf{(6-20)}$$

6.7.1 Validation of Developed Model for High-Flow Coefficient Applications

The 14.5 MW centrifugal compressor in section 6.5 is used here to evaluate the prediction capability of the developed model comparing with the existing methods. This compressor is designed with five shrouded impellers and vaned diffusers. By implementing the new model, the obtained results in figures 6-17(a) and 6-17(b) shows a noticeable improvement in the pressure ratio and polytropic head values especially at surge and choke flow conditions. The slope change in the new model pressure ratio varies at both curve ends, and it becomes closer to the actual behavior. The greater drop in the work coefficient at choke flow leads to a quick reduction in the pressure ratio.

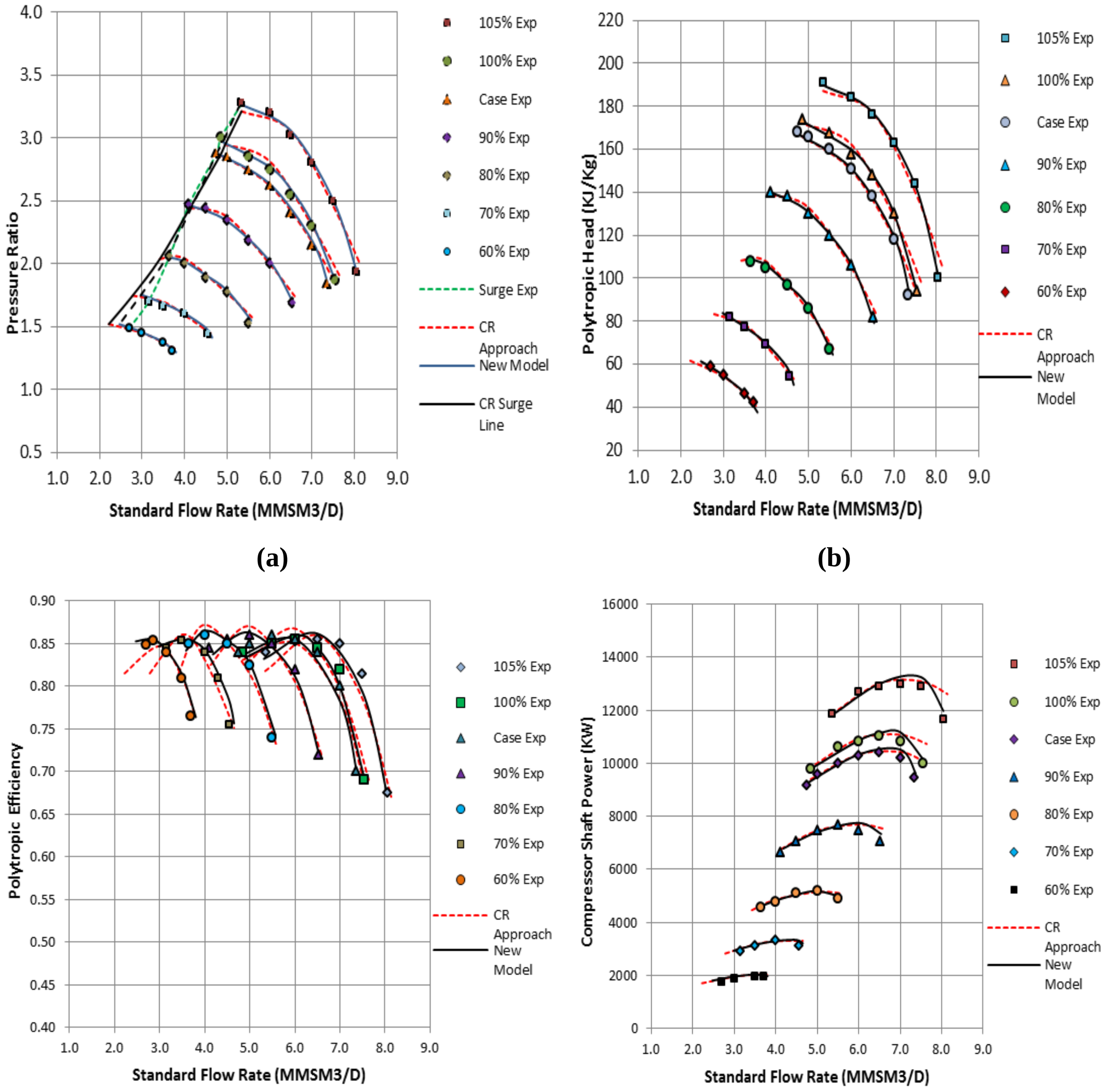

(a) (b)

(c) (d)

Figure 6- 17: Evaluation of Developed Performance Map Using the Developed Method Against Measured Date and Adapted Casey-Robinson Model Results

It was observed that the relative pressure ratio error from the measured value at the highest Mach number and design speed was reduced by about 2.29% and 2.27%, respectively. Besides, the prediction of surge flow becomes closer to the measured value, especially at low flow coefficients. For Example, at 60% of the full load speed, the relative error of the surge flow was dropped by almost 9.22% comparing with an improvement of roughly 6.35% when the compressor operates at 70% of full speed capability. Looking to figure 6-17(a), the variation in the pressure ratio trend becomes steeper when the compressor is approaching the choke flow. This was achieved by considering the change in the polytropic exponent, degree of reaction and slip factor. Another remarkable enhancement in the predicted off-design efficiency values can be observed in figure 6-17(c).

Generally, most of the measured points are well situated on the derived speed lines. The slope of efficiency variation curve near surge flow becomes closer to the actual trend. Furthermore, the improvement in the surge efficiency prediction capability can be observed clearly in this figure reaching to about 1.7% relative error reduction at highest speed. This generates more accurate surge pressure ratio and polytropic head results which, in turn, makes the predicted shaft power more precise. The improved pressure ratio variation slope near the choke point leads to a substantial improvement in the associated power value as shown in figure 6-17(d).

6.7.2 Validation of New Model for Low-Flow Coefficient Applications

To emphasise the validity of the derived model for low flow coefficient compressors, this method is used to predict the performance curve of a 17.2 MW centrifugal compressor. This compressor is driven by electric motor and it is required for depletion plant to produce a discharge pressure of 112.4 bara at an inlet pressure and temperature of 38 bara and 59.8ºC, respectively and standard inlet flow of 265812m^3/h. The gas composition at guaranteed point is illustrated in figure 6-18. The inlet pressure varies from 38 bara to 60 bara while the discharge compressor is almost constant. Moreover, the speed range has been specified from 5,940 rpm to 10,395 rpm and with a maximum tip speed of 275m/s at full speed operation.

In order to satisfy the aerodynamic and thermodynamic constraints, the compressor has been designed with five mechanical stage and one process stage. The derived geometrical features of the compressor stages are demonstrated in table 6-2. It is shown that the flow coefficients of the designed impellers are relatively low. The value between 0.02 and 0.08 indicates a shrouded, 2D impeller structure. This is used for low flow high head applications and with lighter molecular weight gases which can be confirmed by looking into the gas composition in figure 6-18. The developed stage stacking approach is used to derive the performance curve of the individual mechanical stages, and the overall discharge parameters at design point are compared with the measured values as shown in table 6-3. For such application, the wide operating range has a higher priority than the high efficiency in order to maintain a stable operation over various suction pressure values. Accordingly the compressor stages are designed with backwards leaning impeller vanes and vaneless diffusers. This can be checked from the polytropic efficiency value in table 6-3.

Table 6- 2: Derived Geometrical Features of the Tested Stages

Parameter	Stage 1	Stage 2	Stage 3	Stage 4	Stage 5
Stage pressure ratio	1.276	1.257	1.240	1.226	1.213
D_1 (mm)	190	190	190	190	190
D_2 (mm)	530	530	530	530	530
Inlet hub/tip (mm/mm)	0.374	0.334	0.296	0.262	0.232
Flow coefficient	0.039	0.032	0.027	0.023	0.020
No blades per impeller	17	17	17	17	17
b_2/b_1	0.530	0.530	0.530	0.530	0.530
Impeller tip diameter (mm)	190	190	190	190	190
Exit tip speed (m/s)	267	267	267	267	267
D_2/D_3	0.870	0.870	0.870	0.870	0.870
D_4/D_3	1.400	1.400	1.400	1.400	1.400

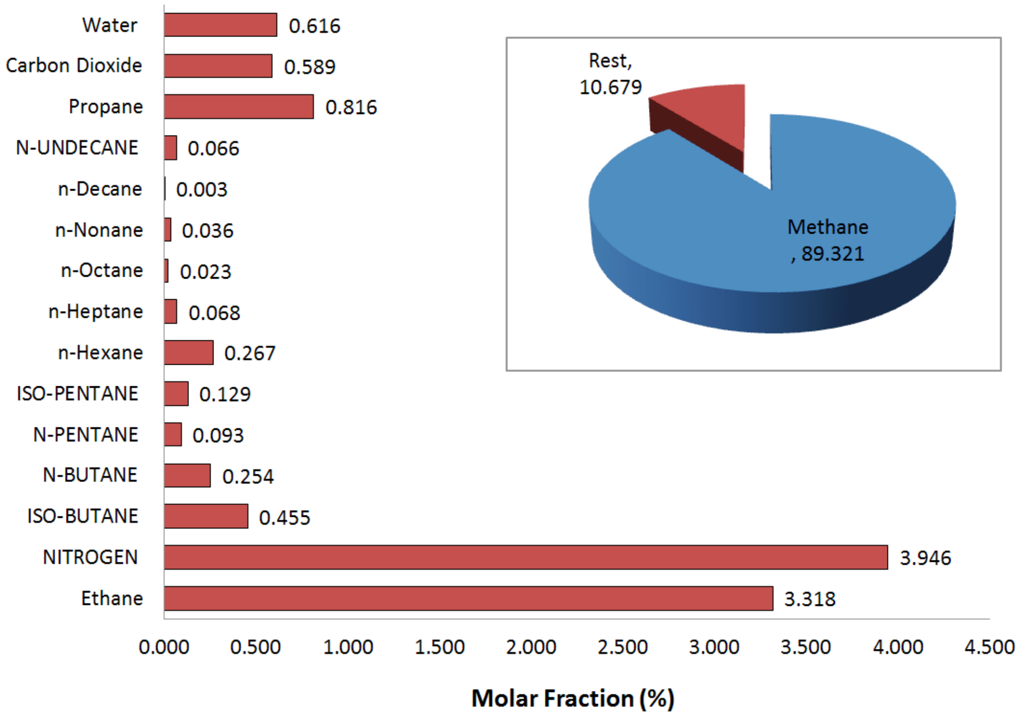

Figure 6- 18: Gas Composition at Compressor Suction and At Design Point in Molar Fraction

Table 6- 3: Comparison between the Predicted and Measured Overall Performance Parameters at Design Point Conditions

Parameter	Calculated	Measured	Error (%)
No. Impellers	5	5	-
Head (kJ/kg)	181.00	182.37	-0.75
Power (MW)	13.65	13.40	1.91
Discharge temperature (°K)	433.85	440.00	-1.32
Discharge pressure (bara)	112.4	112.4	0
Polytropic efficiency	0.796	0.80	0.5

The obtained performance characteristics of each mechanical stage are shown in Appendix (E). The pressure ratio trend illustrates an increase in the stable operating range comparing with the previous compressor model. This is essential to meet the expected variation in suction pressure. Moreover, the work-to-flow coefficients curve (Appendix E1) demonstrates relatively lower operating flow coefficients. The high isentropic exponent gas leads fairly to a lower operating efficiency. The discharges parameters of the last stage have to meet the required overall characteristics at design conditions. However, it is important to use the engineering judgment to evaluate and compare the performance of the compressor stages to ensure more precise results. The derived flange –to- flange compressor performance curve is illustrated in figures 6-19 to 6-21 in terms of pressure ratio, efficiency and shaft power. Most of the measured pressure ratio points fall on the constant speed lines throughout the flow range as demonstrated in figure 6-19. Furthermore, the predicted surge and choke flows are close enough to the experimental values. Small deviation is observed at the surge flow of low running speeds, but it was less significant than the previous case. The estimated choke pressure ratio was slightly higher than the measured values, and this difference grows with the speed. This is obviously owing to the increase in the aerodynamic losses near the choke point. Moreover, the majority of the measured efficiency points are well matching the predicted values as shown in figure 6-20.

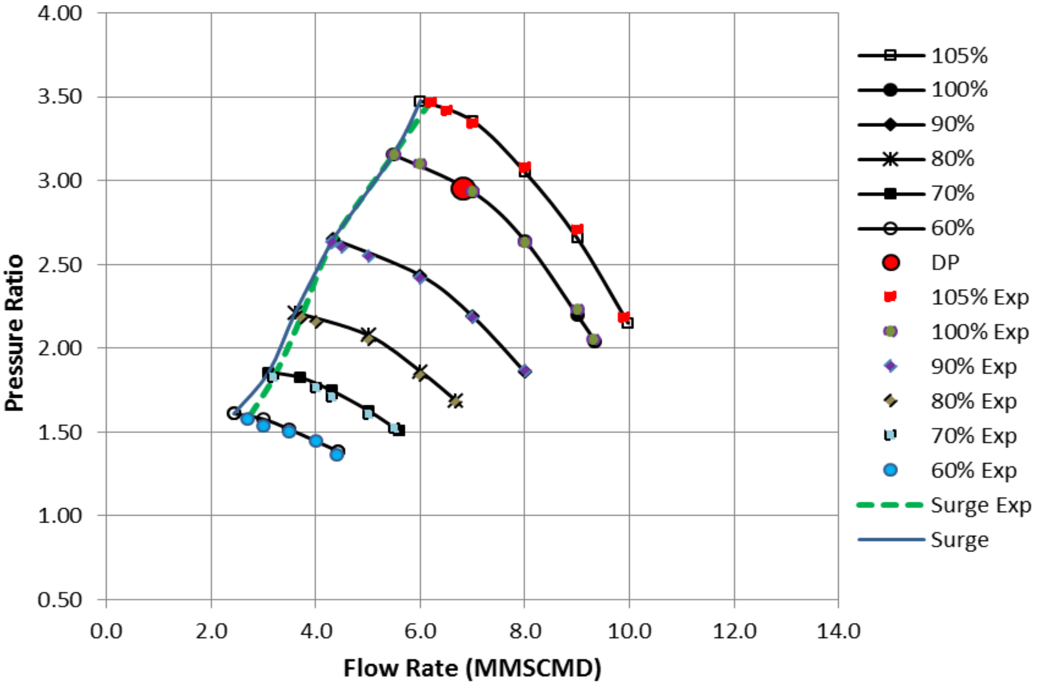

Figure 6- 19: Flange-to-Flange Pressure ratio As a Function of Standard Flow

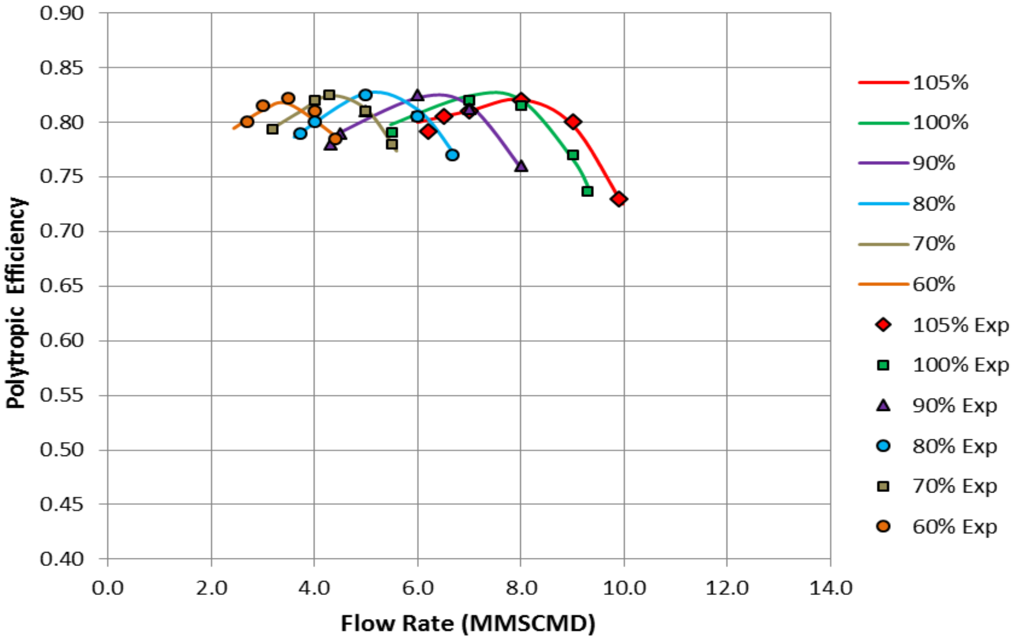

Figure 6- 20: Overall Efficiency Curve As a Function of Standard Suction Flow

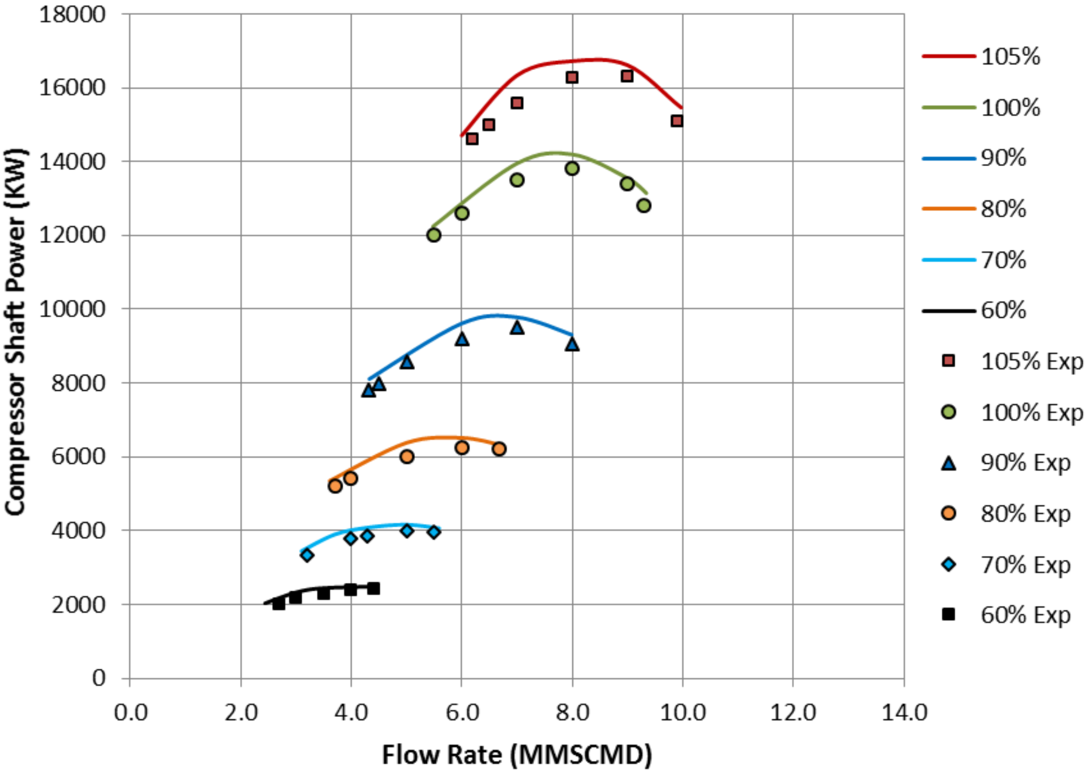

Figure 6- 21: Overall Shaft Power As A Function of Standard Flow

The highest percentage of error was detected near the surge flow and at all speed lines. The estimated efficiency at surge point was slightly higher than the actual value but with less than 1.4% difference. However, the predicted peak efficiency and associated flow coefficient using adapted Lüdtke method match the actual values at all speed lines. Additionally, the power curve in figure 6-21 agrees with the previous findings, and the largest deviation between the measured and predicted values was observed near the peak flow coefficient especially at high Mach number. This emphasises the validity of the efficiency prediction model for both high and low flow coefficients applications.

6.8 Chapter Summary

This chapter proposed a new performance prediction method for multistage industrial centrifugal compressors. The original Casey-Robinson model has been applied for turbocharger compressor hence, a new set of empirical coefficients and flow coefficients and efficiencies ratios have been derived after hundreds of trials to be suitable for industrial compressors. Although that this method does not require a deep geometrical knowledge, the dependency on the peak efficiency and associated flow coefficient at both normal operation and low Mach number makes this model more difficult to use when these parameters are unknown. Moreover, the adapted method results showed an acceptable level of accuracy comparing with the measured values. However, the derived surge flow coefficient value at low speed conditions was found well below the actual flow which should be aware of in the future. This is mostly due to the difficulty in predicting the back-flow initiation without considering the individual component losses. Besides, the conducted comparison between the measured and estimated performance parameters revealed a considerable difference between the predicted pressure, temperature, power and efficiency and the measured values near the choke and surge points and this deviation increases at high speed operation.

On the other hand, Lüdtke method requires more geometrical details to correct the basic efficiency value for the new design. In addition to the global flow coefficient, Mach number and work coefficient; this approach considers the Reynolds Number as the fourth parameter to correct the basic efficiency value. The accuracy of the predicted efficiencies using Lüdtke method was found substantially lower than the obtained results by Casey-Robinson model, especially at very high flow region. Moreover, this method fails to predict the stable flow region limits. However, the predicted design and peak efficiencies and corresponding flow coefficient were very close to the measured values but with less degree of accuracy comparing with Casey-Robinson approach results.

Based on the conducted evaluation, a new method was introduced to consider the advantages of Casey-Robinson and Lüdtke models. The Lüdtke method was improved and implemented to derive the peak and design efficiencies and the relative flow coefficients. The obtained values are then used to estimate the off-design efficiencies at various flows and speeds by the adapted Casey and Robinson method. The derived model has been evaluated at both low and high flow coefficient applications, and the obtained results show a significant improvement in the estimated efficiency and pressure ratio comparing with the existing methods with less dependency on the geometrical features. However, the accuracy of the estimated performance map was found greater in the case of low flow coefficient compressor. Besides, the derived empirical correlations were proven to predict the stability limits for every speed line with a greater degree of accuracy. Moreover, one of the main advantages of the new method is that it does not require a prior knowledge of the design and peak efficiencies and associated flow coefficients at normal and low operating Mach number conditions.

The key aspects of the new method can be summarized as following:

- Unlike the existing methods, this technique can be used to derive the performance curve of every single mechanical stage reaching to the overall flange-to-flange performance map with less empirical coefficients.
- It does not require a prior knowledge of the design and peak efficiencies and the associated flow coefficients at normal and low Mach number operation of each speed line and every mechanical stage.
- This method shows a higher degree of accuracy in the prediction of performance parameters especially at choke and surge conditions comparing with the most recent theories.
- The derived surge flow model has proven to provide more precise estimation for surge flow at various speeds especially at high Mach numbers operation.

However, this approach is suitable for the continuity of this research as further validations are still required for the developed approach to evaluate the prediction capability of this model and to identify its potential and limitations. Furthermore, the accuracy of the estimated parameters near the choke and surge points can be improved by considering the variation in the component losses at different operating flow rates and rotational speeds.

CHAPTER 7: CENTRIFUGAL COMPRESSOR PERFORMANCE AT OFF-DESIGN CONDITIONS

The prediction of centrifugal compressor efficiency and operating range is essential to maintain the gas production sustainability and machine availability and to reduce the operation cost. Several external process parameters affect the centrifugal compressor in the working environment. These factors can introduce a substantial impact on the compressor characteristics which, in turn, influence the compressor efficiency and aerodynamic stability. Testing the new machine performance at the field conditions will help to evaluate the design specifications prior to the installation process. However, the actual suction parameters might be different from those tested by the manufacturers, so the test results have to be correlated with the actual conditions. Moreover, predicting abnormal compressor performance and aerodynamic issues of the running machines at an early stage can help to avoid failures or premature shutdowns.

7.1 Introduction

Schultz (1962) developed a polytropic model to predict compressor performance based on ideal and real gas correlations. Mallen and Saville (1977) found that the assumed polytropic path function in this method was only accurate at lower pressure levels, so they proposed an alternate path function and accompanying analysis. On the other hand, the conducted comparison by Huntington (1985) revealed a larger percentage of error in the obtained results by Mallen and Saville method (1977). One of the main disadvantages of these two approaches is that some of the stated assumptions are only applicable for ideal gas conditions. Furthermore, these two models are based on the fact that the stage efficiency is a function of the process gas properties only without considering the impact of Mach number and flow coefficient.

Another alternative approach to derive the compressor performance at off-design conditions is by using the existing correction factors. This method is used extensively in the open literature due to its simplicity such as Lapina (1982), Kong et al. (2002), and Santinelli (2006). However, this technique does not consider the change in the gas properties which can introduce a higher degree of uncertainty while dealing with hydrocarbons. To address this issue, this method has been modified in ASME PTC-10 (1997) to correct the test results with a consideration of the gas properties variation. This report introduced only the instructions to carry out the mentioned correction without developing a sequential approach to implement it. Moreover, the proposed guidelines require a large set of data and meter readings which are practically not available without conducting a machine test. Sandberg and Colby (2013) reported some issues with the accuracy of the predicted parameters using this approach in high pressure applications and especially with high carbon dioxide percentages, including the stage efficiency and polytropic head. Ma et al. (2013) proposed another methodology which depends on the transformation of the real operating parameters to specific reference conditions. This method was developed basically assuming that the polytropic efficiency is independent of the thermodynamic parameters and with a constant density ratio. However, it is important to mention here that both methods address only a single flow and rotational speed values and without considering the entire compressor map.

Thus, this chapter will propose a new iterative systematic method to derive the equivalent centrifugal compressor performance at various suction conditions and gas compositions. One of the unique features of the developed approach is its capability to derive the overall compressor performance map at different operating conditions from the reference point.

Furthermore, the variation in the stage efficiency and gas properties are considered including the density ratio and with less dependency on the test data. Unlike the existing models, the efficiency is obtained as a function of gas composition, suction conditions, Mach number and flow coefficient leading to more precise prediction of performance parameters.

7.2 Developed Method Approach

The proposed method in this chapter is based on the fact that the compressor performance parameters can be estimated based on the suction parameters, process gas properties, flow coefficient, Mach number and work coefficient. The influences of these variables on the stage performance characteristics vary significantly based on the compressor design and gas compositions. Accordingly, the developed approach can be divided into three main steps as illustrated in figure 7-1:

1. Define the compressor performance characteristics at design conditions in terms of discharge pressure and temperature corresponding to various flow coefficients and Mach numbers.
2. Use the new suction conditions to derive the equivalent inlet gas properties which are then used to correct the design flow rates based on the new operating conditions. The efficiency and the discharge conditions are estimated initially based on the first polytropic exponent (n_T, n_V) and compressibility functions (X and Y) values.
3. Recalculate the polytropic exponents and the compressibility functions based on the obtained efficiency using the Lüdtke equations of polytropic temperature and volume exponents. Thus, the new values are then used again to derive the corresponding efficiency and discharge conditions by Schultz model.

At constant speed operation, the global flow coefficient (φ) can be defined a function of suction volumetric flow rate, exit impeller diameter and tip speed.

$$\varphi = \frac{4\dot{m}}{\pi {D_2}^2 u \rho} \tag{7-1}$$

To derive the mass flow rate at the new operating point, the flow coefficient is assumed to stay constant at that particular speed. Additionally, the tip speed and impeller diameter are fixed at the specified rotational speed and impeller geometry. The performance parameters at design conditions are considered as a reference point in this method to obtain the equivalent characteristics at new suction conditions. The gas constant (R) can be written in term of molecular weight. Thus, the Equation (7-1) leads to the following final correlation (7-2):

$$\dot{m}_{OD} = \dot{m}_{Ref} \left(\frac{p_{OD}}{p_{Ref}}\right) \left(\frac{Z_{Ref}}{Z_{OD}}\right) \left(\frac{T_{1Ref}}{T_{1OD}}\right) \left(\frac{MW_{OD}}{MW_{Ref}}\right) \tag{7-2}$$

The compressibility factor (Z) is calculated as a function of the gas composition and at particular gas pressure and temperature using equations of state.

$$\mathrm{Z} = f\ (p_r\ , \mathrm{T_r}) = f\ \left(\frac{p}{p_{cr}}\ , \frac{\mathrm{T}}{T_{cr}}\right) \tag{7-3}$$

The derived equation (7-2) can be used to correct the design flow rate at a new operating point in terms of suction gas parameters and the design flow rate.

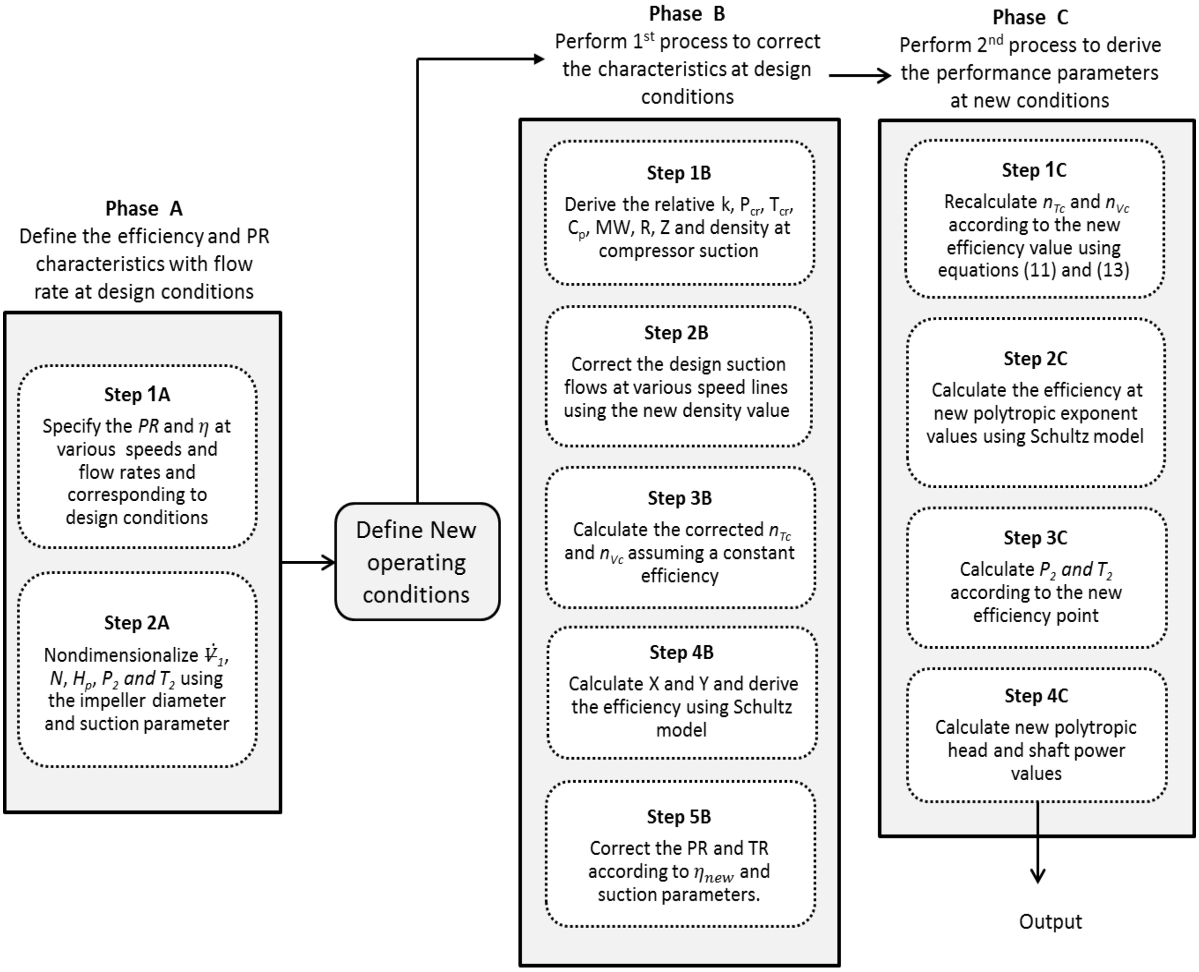

Figure 7- 1: Scheme of Developed Method

The gas properties can be considered at the suction side or as an average value. However, the same approach should be followed for both reference and off-design conditions. In order to estimate the pressure ratio at the new operating point, equation (7-4) can be used. According to Casey-Robinson work coefficient model (2013), the work coefficient ($\psi_{w_{OD}}$) is only a function of impeller geometry and flow coefficient (φ_{OD}). Therefore, at fixed flow coefficient and rotating speed, the impeller work coefficient has to be constant.

$$\frac{PR_{Ref}}{PR_{OD}} = \frac{\left[\psi_{w_{Ref}}\left(k_{Ref}-1\right)Mu_{Ref}^2+1\right]^{\frac{k_{Ref}\eta_{Ref}}{k_{1Ref}-1}}}{\left[\psi_{w_{OD}}\left(k_{OD}-1\right)Mu_{OD}^2+1\right]^{\frac{k_{OD}\eta_{OD}}{k_{OD}-1}}} \qquad \textbf{(7-4)}$$

When there is a change in the suction flow rate, the work coefficient is no longer constant. Accordingly, the new work coefficient ($\psi_{w_{OD}}$) is obtained by applying equation (7-5) where the correlation coefficients (A_b, B_b) are specified by matching the work coefficient value at design point operation.

$$\psi_{w_{OD}} = \psi_{w_{Ref}} \times \left[\frac{\left(1+\frac{0.002}{\varphi_{Ref}}\right)\left(A_b+B_b\varphi_{Ref}\right)}{\left(1+\frac{0.002}{\varphi_{OD}}\right)\left(A_b+B_b\varphi_{OD}\right)}\right] \qquad \textbf{(7-5)}$$

Furthermore, the speed of sound is the only factor influencing the Mach number when such impeller is rotating at the same speed. Hence, the equation of pressure ratio can be expressed in terms of design pressure ratio, gas properties and polytropic efficiency.

$$PR_{OD} = PR_{Ref} \left\{ \frac{\left[\frac{(k_{OD}-1)\times {U_{OD}}^2}{R_{OD}\, Z_{OD}\, T_{1OD} k_{OD}} + 1\right]^{\frac{k_{OD}\eta_{OD}}{k_{OD}-1}}}{\left[\frac{(k_{Ref}-1)\times {U_{Ref}}^2}{R_{Ref}\, Z_{Ref}\, T_{1Ref} k_{Ref}} + 1\right]^{\frac{k_{Ref}\eta_{Ref}}{k_{Ref}-1}}} \right\} \tag{7-6}$$

The polytropic efficiency will be calculated by Schultz polytropic exponent equation:

$$n_v = \frac{(1+X)}{Y\left[\frac{1}{k}\left(\frac{1}{\eta} + X\right) - \left(\frac{1}{\eta} - 1\right)\right]} \tag{7-7}$$

The compressibility functions (X, Y) can be estimated graphically in terms of reduced pressure (P_r) and temperature (T_r). However, rounding the corresponding X and Y variables can introduce a small deviation from the actual value which has a significant impact on the obtained efficiency value as demonstrated in figure 7-2.

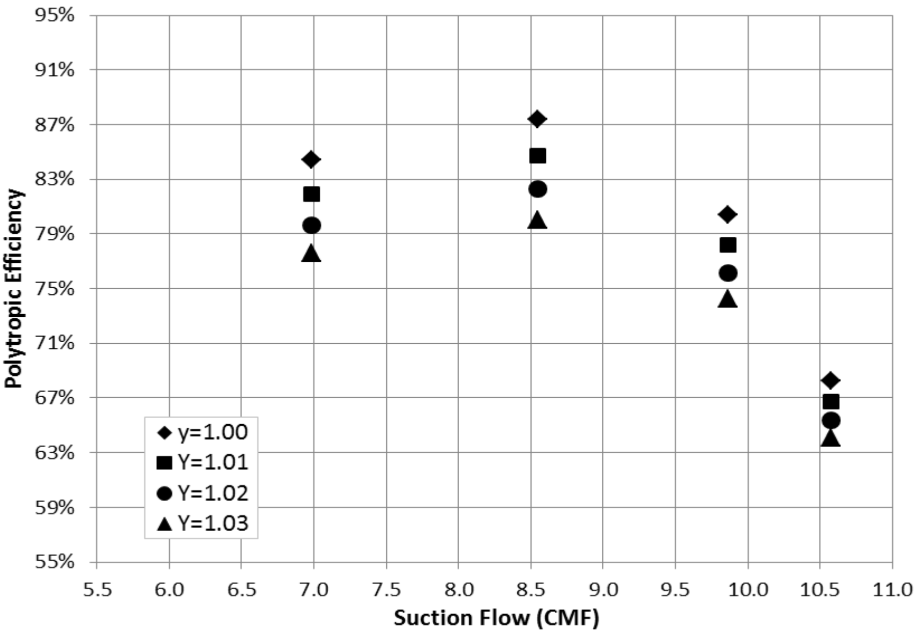

Figure 7- 2: Effect of Compressibility Function (Y) on Polytropic Efficiency

To avoid that, the values of X and Y are calculated by applying equations (7-8) and (7-9).

$$X = \frac{T}{Z}\left(\frac{\partial Z}{\partial T}\right)_P = \frac{T}{V}\left(\frac{\partial V}{\partial T}\right)_P - 1 \tag{7-8}$$

$$Y = 1 - \frac{P}{Z}\left(\frac{\partial Z}{\partial P}\right)_T = -\frac{P}{V}\left(\frac{\partial V}{\partial P}\right)_T \tag{7-9}$$

Despite that these two correlations are derived by approximating some terms, the developed method is dealing with the ratio of the X and Y at reference and off-design conditions. Thus, the effect of this approximation can be ignored. By rearranging equation (7-7), the polytropic efficiency can be calculated using the following formula:

$$\eta = \frac{n_v\, Y(1-k)}{(1+X)k - n_v Y(X+k)} \tag{7-10}$$

This equation derives the efficiency as a function of gas properties only. Hence, a further correction will be performed to consider the effect of flow coefficient and Mach number.

Accordingly, the temperature polytropic exponent (n_T) is derived assuming a constant efficiency by equation (7-11). This correlation is derived from the basic temperature polytropic exponent equation (7-12).

$$n_{T,OD} = n_{T,DP}\left[\frac{1-\frac{Z_{DP}R_{DP}}{C_{p,DP}}\left(\frac{1}{\eta_p}-1\right)-\frac{k_{DP}}{k_{DP}-1}}{1-\frac{Z_{OD}R_{OD}}{C_{p,OD}}\left(\frac{1}{\eta_p}-1\right)-\frac{k_{OD}}{k_{OD}-1}}\right] \tag{7-11}$$

$$n_T = \frac{1}{1-\frac{ZR}{C_p}\left(\frac{1}{\eta_p}-1\right)-\frac{k}{k-1}} \tag{7-12}$$

Thus, the volume polytropic exponent (n_v) is calculated from formula (7-13) in terms of temperature exponent (n_T) and gas properties.

$$n_{v,OD} = \frac{k_{OD}}{1+\left[\frac{C_{p,OD}\,(k_{OD}-1)}{Z_{OD}R_{OD}}\times\left(\frac{1}{n_{T,OD}}+\frac{k_{OD}-1}{k_{OD}}-1\right)\right]} \tag{7-13}$$

The polytropic exponent is substituted in equation (7-10) to obtain the first efficiency value at new operating conditions. Accordingly, this is used to derive the resultant pressure ratio by applying equation (7-6). Hence, the initial overall discharge pressure and temperature can be calculated.

The calculated efficiency and discharge parameters are acceptable for the first approximation but, to achieve more accurate results; a second process is performed using the obtained parameters from the first trial. The estimated polytropic efficiency is substituted in equation (7-11) to get the temperature polytropic exponent and the polytropic volume exponent from equation (7-13). Hereafter, a new polytropic efficiency value is derived using equation (7-10) and the corresponding discharge pressure and temperature are recalculated. The discharge parameters are expected to be closer to the actual values as the constant efficiency assumption is no longer valid. The polytropic head (H_p) is obtained using equation (7-15). This correlation has been derived from the basic polytropic head equation (7-14).

$$H_p = Z\times\frac{8.314}{MW}T_1\left(\frac{n_v}{n_v-1}\right)\left[PR^{(n-1)/n}-1\right] \tag{7-14}$$

$$H_{p,OD} = H_{p,Ref}\left[\frac{Z_{OD}\times MW_{Ref}\times T_{1OD}\times n_{v,OD}\left(n_{v,Ref}-1\right)\times\left(PR_{OD}^{\frac{n_{v,OD}-1}{n_{v,OD}}}-1\right)}{Z_{Ref}\times MW_{OD}\times T_{1Ref}\times n_{v,Ref}\left(n_{v,OD}-1\right)\times\left(PR_{Ref}^{\frac{n_{v,Ref}-1}{n_{v,Ref}}}-1\right)}\right] \tag{7-15}$$

When there is a change in the flow coefficient from the design values, a further step is taken to correct the obtained efficiency based on the new work coefficient value.

$$\eta_{OD} = \eta_{Ref}\left(\frac{\psi_{w_{Ref}}}{\psi_{w_{OD}}} \times \frac{H_{p,OD}}{H_{p,Ref}} \times \frac{U_{Ref}^2}{U_{OD}^2}\right) \qquad \textbf{(7-16)}$$

The total shaft power is calculated assuming a constant rate of the aerodynamic and mechanical losses at the specified rotating speed and flow coefficient.

$$BHP_{OD} = BHP_{Ref}\left[\frac{\dot{m}_{OD} \times H_{p,OD} \times \eta_{Ref}}{\dot{m}_{Ref} \times H_{p,Ref} \times \eta_{OD}}\right] \qquad \textbf{(7-17)}$$

7.3 Developed Method Validation

In order to qualify the developed approach, it is implemented to predict the equivalent performance of the investigated gas lift centrifugal compressor in section 6.7.1 driven by 14.5 MW electric motor. The design point operation requires 21 bara at the compressor discharge with an inlet volume flow of 6 MMSCMD and suction pressure of 8 bara. The gas is a hydrocarbon mixture, and the design point performance was derived at 51 °C inlet temperature. However, the compressor is expected to run at various inlet temperatures ranging from 20 to 55 °C. The developed methodology was followed to derive the equivalent compressor performance at an inlet temperature of 34 °C and suction pressure of 8.10 bara. The estimated discharge pressures are plotted against the measured data as shown in figure 7-3(a).The obtained curve shows a good matching with actual values, especially at low flow rates. There is a slight increase in the measured discharge pressure at the surge point comparing with the predicted values. This deviation is growing at high speed operation. The largest percentage of error was observed near the surge pressure of 105% speed line with approximately 2.21%, which is still acceptable. The rise in the measured discharge pressure at high speed is possibly caused by the reduction in the associated pressure losses at low inlet temperature. Besides, the predicted surge and choke flows were found very close to the measured data at all speed lines. The lower suction temperature and the higher inlet pressure push the pressure ratio to shift towards higher value than the design pressure driven by density reduction.

The power curve in figure 7-3(b) demonstrates that most of the measured points fall on the constant speed lines. However, the higher measured pressure ratio near the surge point of high Mach number operation yields a slight increase in the measured power. As the speed goes down, the deviation between the measured and estimated power decreases gradually. Figure 7-4 compares between the predicted and measured efficiencies at various suction flows and rotational speeds. The measured efficiencies are obtained at the measured pressure ratios and shaft power which illustrated in figure 7-3. Despite the increase in the measured pressure ratio and shaft power near the surge point, the corresponding efficiency matches the predicted value with an insignificant difference. The greatest percentage of error was found near the choke point of the 105% speed line by about 1.49%. This value is greatly under the 5.0% allowed deviation.

To demonstrate the validity of the derived method when there is a change in the gas properties, it has been implemented to estimate the performance of a three-process stages centrifugal compressor driven by a 3.7 MW gas turbine. The first two stages consist of six impellers arranged in series with the aftercoolers and scrubbers while the third casing accommodates eight impellers.

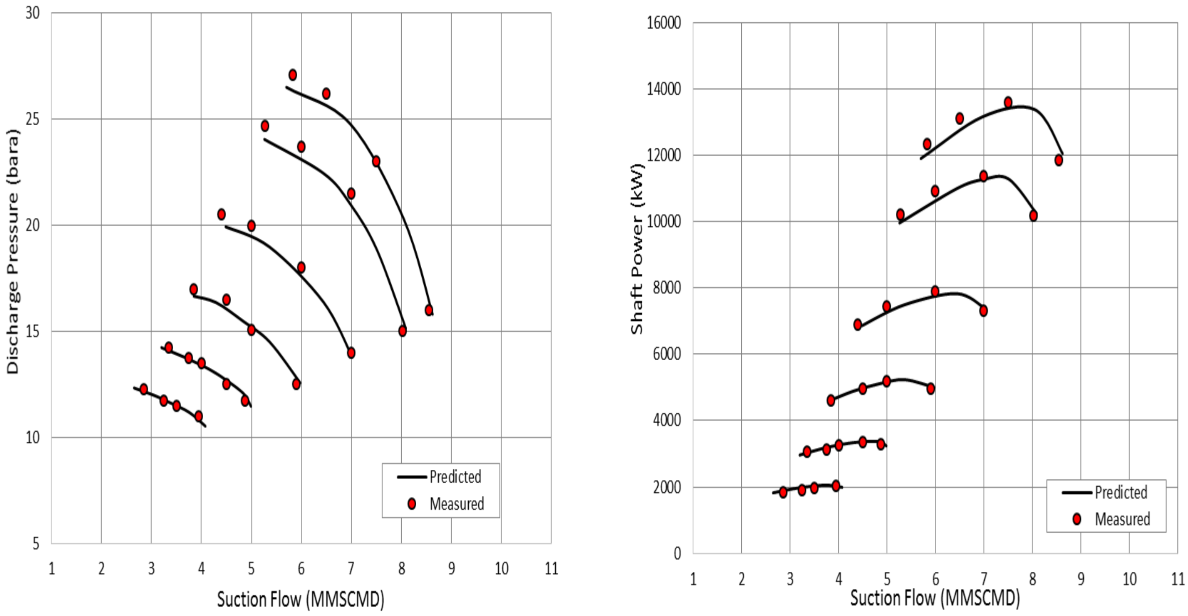

(a) **(b)**

Figure 7- 3: Comparison Between the Predicted and Measured Discharge Pressure and Power

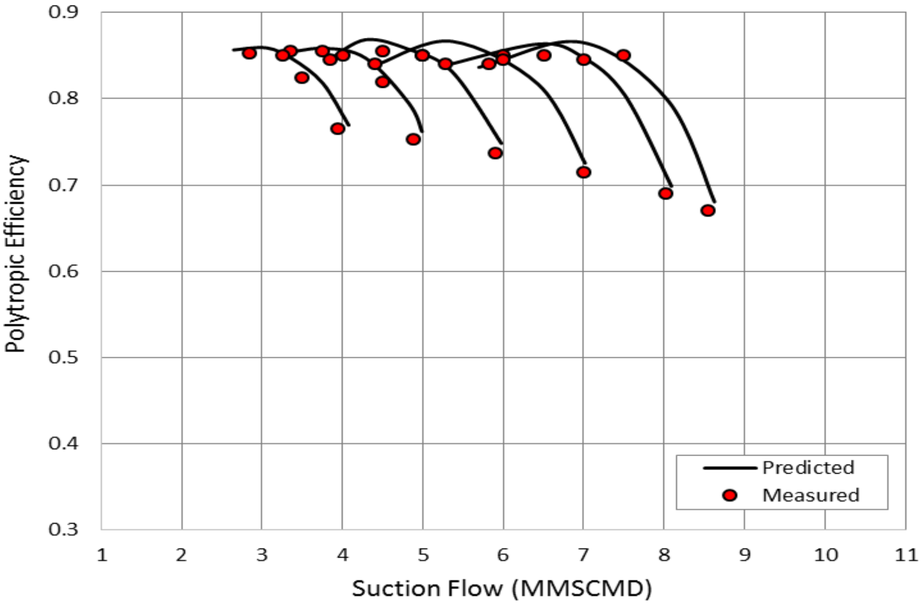

Figure 7- 4: Comparison Between the Predicted and Measured Polytropic Efficiencies

The compressor has been in service for about 32 years, so the gas composition has varied from the original values. Figure 7-5 shows the recorded change in the measured properties of the gas sample comparing with the initial design values. Since these properties have been measured in the laboratory, it is necessary to check the uncertainty of the measurement methods to improve the quality of the measurements. Unfortunately, the exact uncertainty of each measurement method is not specified. However, the uncertainty of the gas density measurement is estimated to be about ±0.3251%, which will be considered for the rest of the properties. The gas sample test demonstrates a significant reduction in the gas molecular weight and a slight increase in the *Z*-factor and *k*-value. This obviously affects the performance characteristics, as illustrated in figures 7-7 and 7-8. The measured discharge pressure of the first process stage was found to be lower than the relative actual design value at the same rotational speed as illustrated in figure 7-8. Hence, the derived approach is used to obtain the equivalent performance of the first process stage with respect to the new gas properties. The corresponding rotational speed to the measured suction and discharge parameters is determined and compared with the actual value. It is clear from figure 7-9 that the operating point suits between the constant speed lines of 15,700 rpm and 15,000 rpm and at approximately 15,251 rpm.

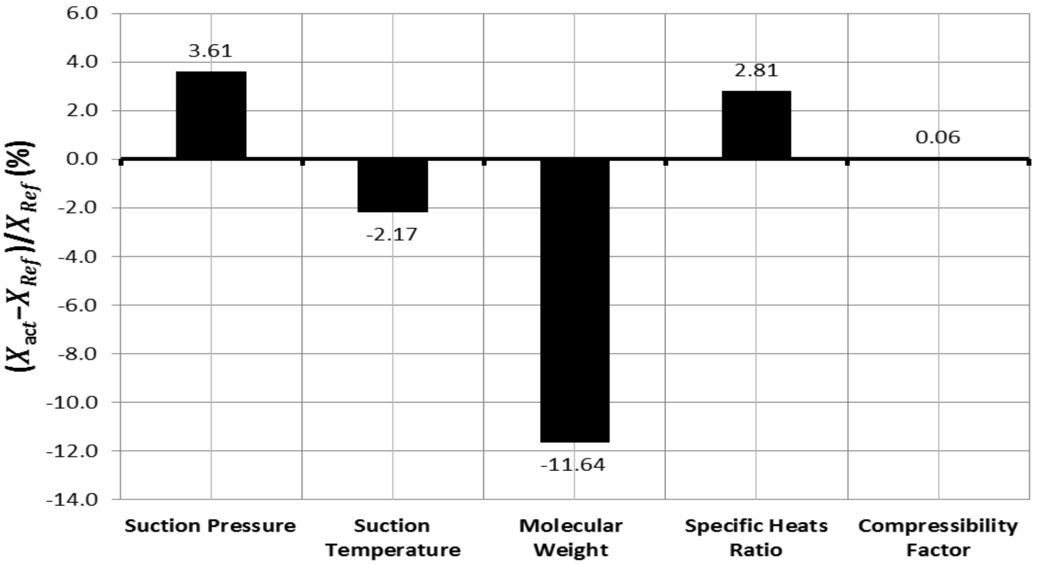

Figure 7- 5: Measured Change in Suction Parameters Relative to Initial Design Values

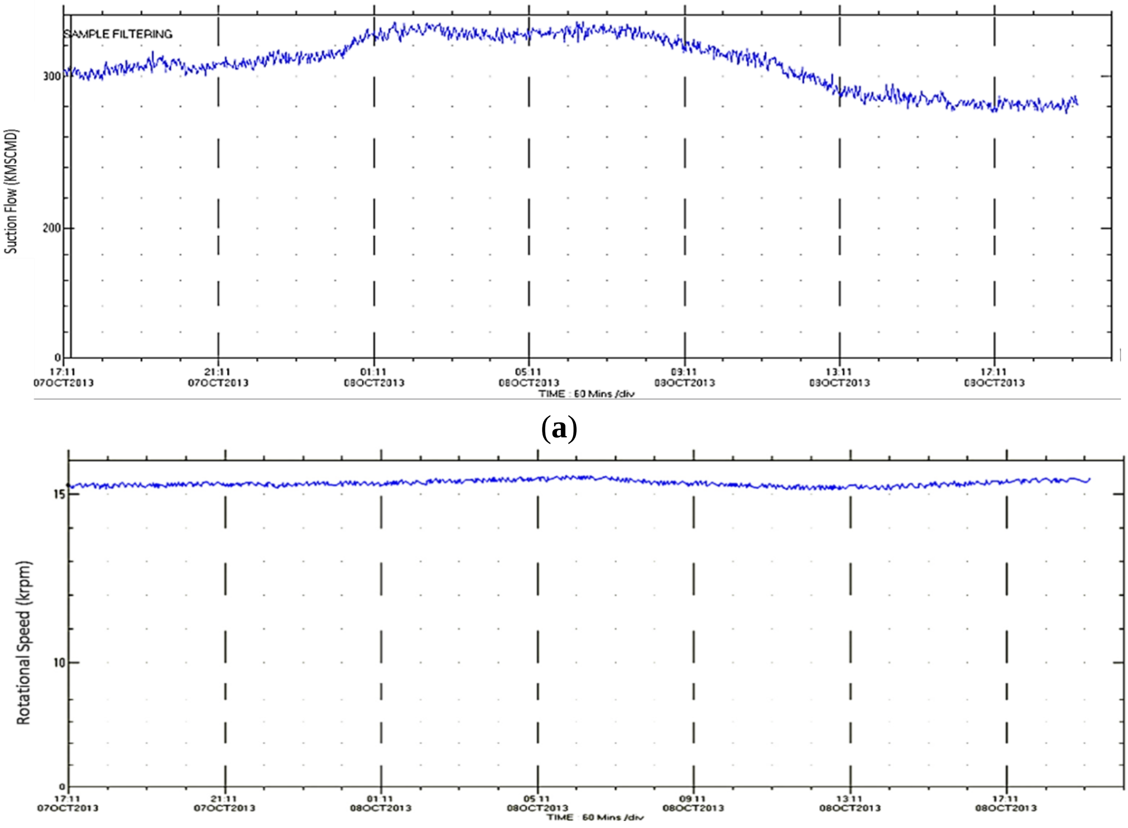

(**a**)

(**b**)

Figure 7- 6: Measured Performance Parameters of the First Process Stage: (a) Suction Flow; (b) Rotational Speed

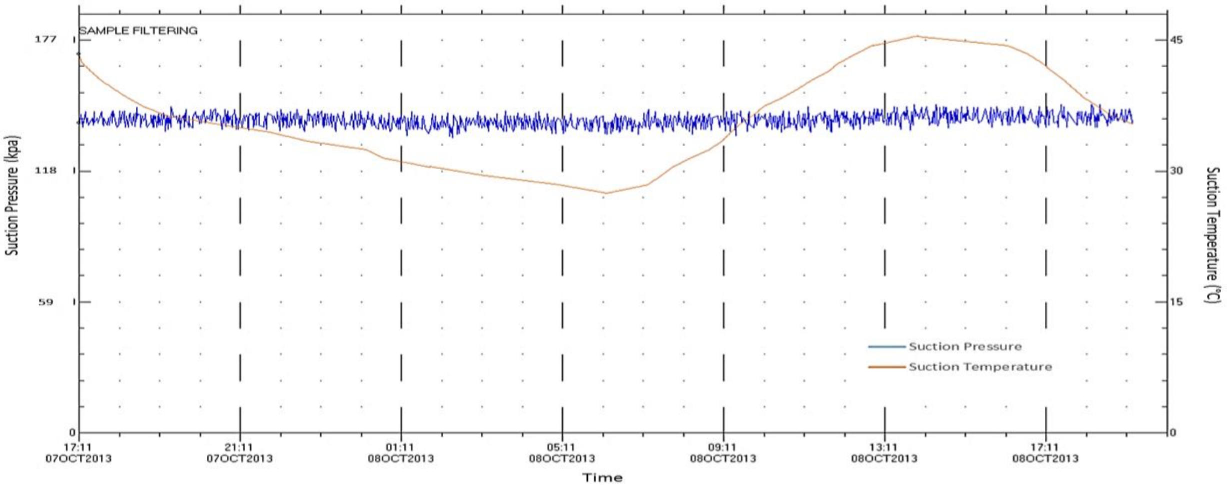

Figure 7- 7: Measured Suction Pressure and Temperature of the First Process Stage

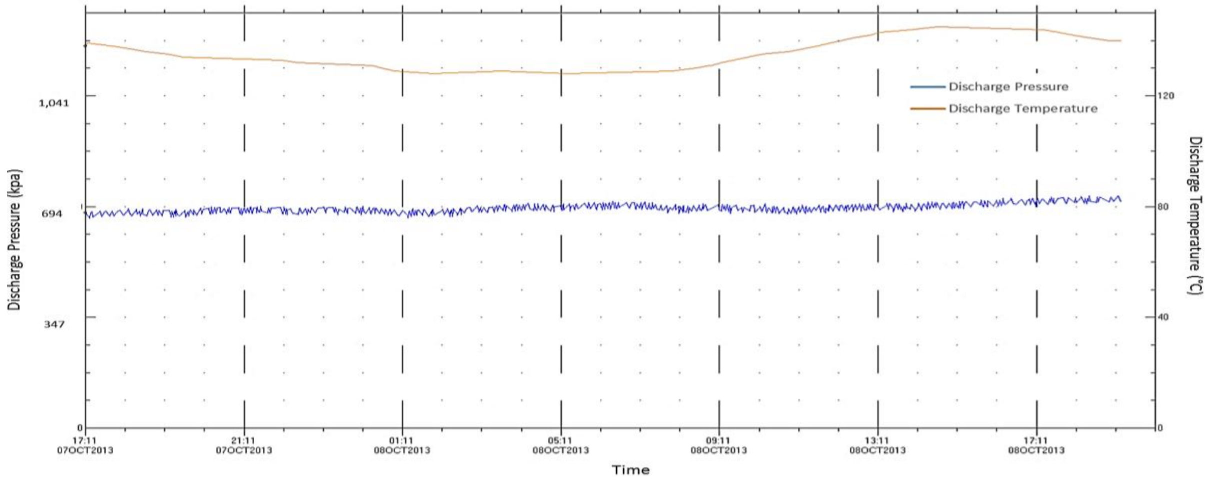

Figure 7- 8: Measured Discharge Pressure and Temperature of the First Process Stage

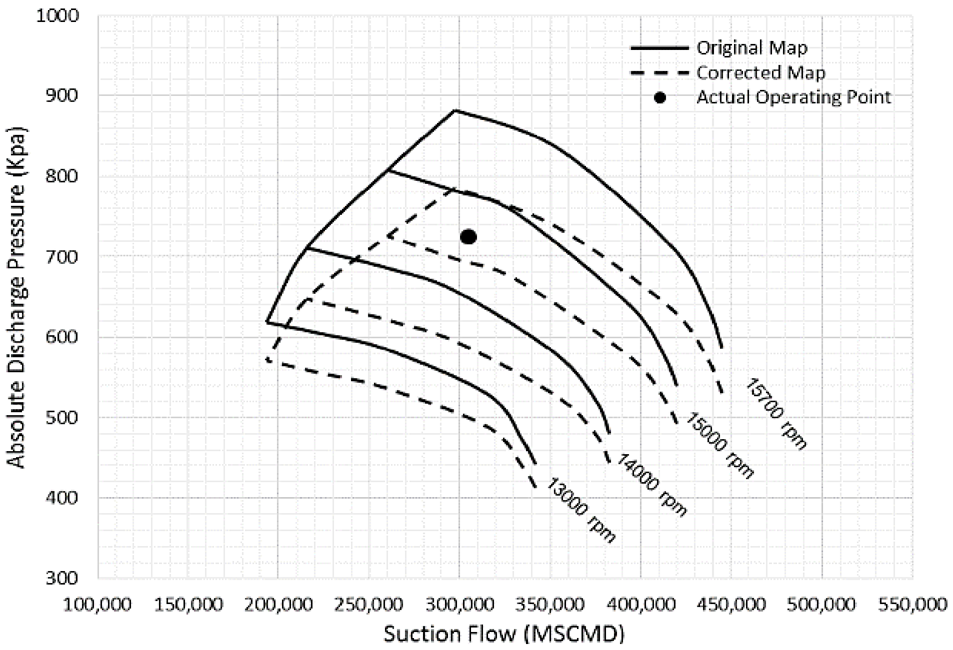

Figure 7- 9: Validation of Developed Method to Predict the New Rotational Speed of First Stage

This speed is close enough to the actual rotational speed in figure 7-6(b), with a relative error of about 0.085% only. Moreover, it was observed that the pressure ratio trend moves down to lower pressure ratio regions, driven by the substantial reduction in the molecular weight, which was the dominant effect in this case. This finding confirms the fact that the variation in the gas properties was the key factor behind the low discharge pressure.

7.4 Demonstration of New Method Validation for Design Evaluation

The centrifugal compressor head highly depends on five critical inlet variables: inlet pressure (P_1), inlet temperature (T_1), gas molecular weight (MW), compressibility factor (Z), and specific heats ratio (k). These factors affect the required kinetic energy to compress the flowing gas, which is then converted to pressure in the diffuser. Furthermore, these characteristics influence the necessary number of stages to achieve the desired head, as will be investigated here. This can be performed in the preliminary design stage to avoid the high aerodynamic and thermal loads on the compressor blades. Despite the fact that the change in gas compositions causes a variation in the real gas properties simultaneously, the impact of every single property on the stage performance will be considered separately, assuming that the rest of the features remain constant. This will help to assess the effect of each variable. Besides, at constant molecular weight value, the change in specific heats ratio and gas compressibility can be owing to the change in the gas temperature and pressure. This offers a great advantage in evaluating a new compressor design corresponding to the expected variation in the gas compositions.

7.4.1 Significance of Suction Temperature

Figure 7-10 shows a rise in the compressor pressure ratio as the gas temperature drops. The incremental increase in the discharge pressure at constant suction pressure varies based on the rotational speed and the suction flow. However, the influence of suction temperature becomes more significant as the compressor flow starts approaching the stonewall point. When there is a variation in the process temperature, more noticeable fluctuation in the discharge pressure can be observed at high flow rate operation. A steeper reduction in the pressure ratio was found at high suction temperature as the flow approaches the choke point. Additionally, the discharge pressure difference is greater at high rotational speed. Accordingly, it is recommended at such temperature variation conditions to avoid running the compressor at very high flow rates and rotational speeds.

At constant rotational speed and suction flow, the surge margin is reduced further and further in response to the suction temperature drop. This causes the pressure ratio of low inlet temperature curves to decline at greater suction flow yielding a smaller deviation in pressure ratio values at low capacity rates. When a constant discharge pressure is targeted, the compressor speed has to be reduced as the suction temperature decreases. Two basic gas properties contribute to the discharge pressure rise, which are the compressibility factor (Z) and specific heats ratio (k). The variation in these two parameters are, relatively, very small for air process so that it can be ignored, but it is not the case for other gases in which their variation impact can be proven to be significant. The molar heat capacity is taking a non-linear proportional relationship with the inlet temperature rise which results in a lower specific heats ratio. On the other hand, the high suction temperature leads to greater compressibility gas causing the gas density to decrease.

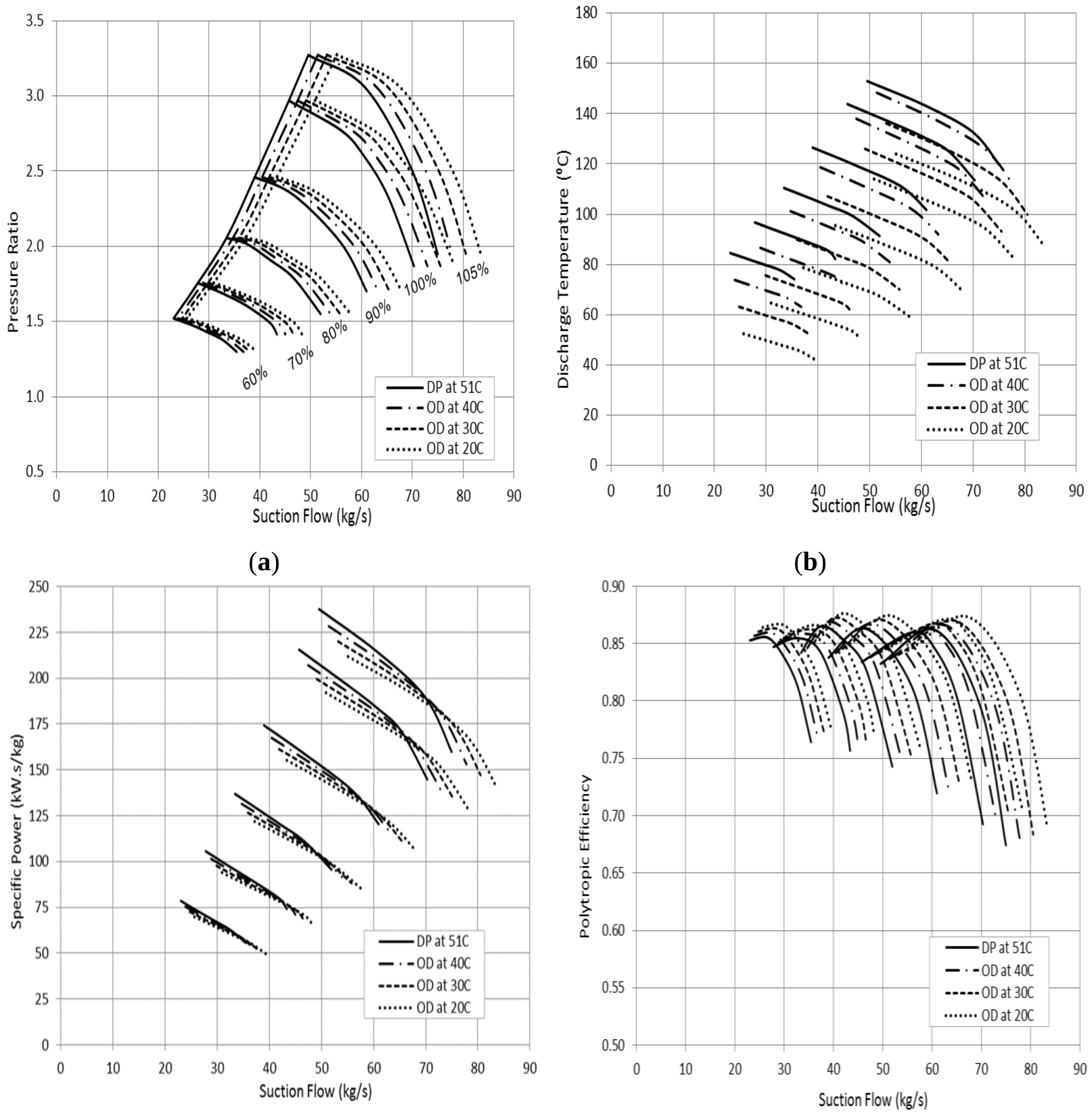

(**a**) (**b**)

(**c**) (**d**)

Figure 7- 10: Effect of Suction Temperature on the Compressor Performance: (a) Pressure Ratio (b) Discharge Temperature (c) Specific Power (d) Polytropic Efficiency

One direct symptom of increasing the suction gas temperature can be observed from the discharge temperature measurement as shown in figure 7-10(b). Generally, the high discharge temperature is more associated with the increase in the developed head so that it could be a sign for flow surging. The specific power trend demonstrates an increase in the required shaft power at high suction temperature driven by the head rising and the efficiency drop as shown in figure 7-10(c). In terms of density, the high operating temperature reduces the gas density, leading to lower Reynolds number and higher frictional and heat losses. The power consumption at low inlet temperature was found to be greater at very high flow coefficients and only for narrow flow range due to the increase in the choke flow. Moreover, the power saving at low inlet temperature becomes greater as the suction flow decreases. This finding agrees with the efficiency trend in figure 7-10(d).

7.4.2 Effect of Suction Pressure

The investigated depletion compressor in section 6.7.2 is designed to generate a discharge pressure of 112.4 bara at inlet pressure and temperature of 38 bara and 59.8 °C and standard inlet flow of 265,812 m^3/h. The inlet pressure varies from 38 to 60 bara while the discharge compressor is almost constant. However, the suction pressure is expected to vary from around 30 to 60 bara due to the fluctuation in the exit pressure from the wells or separators, or it might be as a result of filter blockage.

Figure 7-11(a) shows the variation in the overall pressure ratio at different suction pressure and constant pressure ratio. Unlike the suction temperature, the low inlet pressure causes the operating envelope to shift towards lower flow rates. Additionally, it is evident that the surge margin is decreasing proportionally with the suction pressure reduction. Furthermore, the stable operating margin is shorted by reducing the suction pressure.

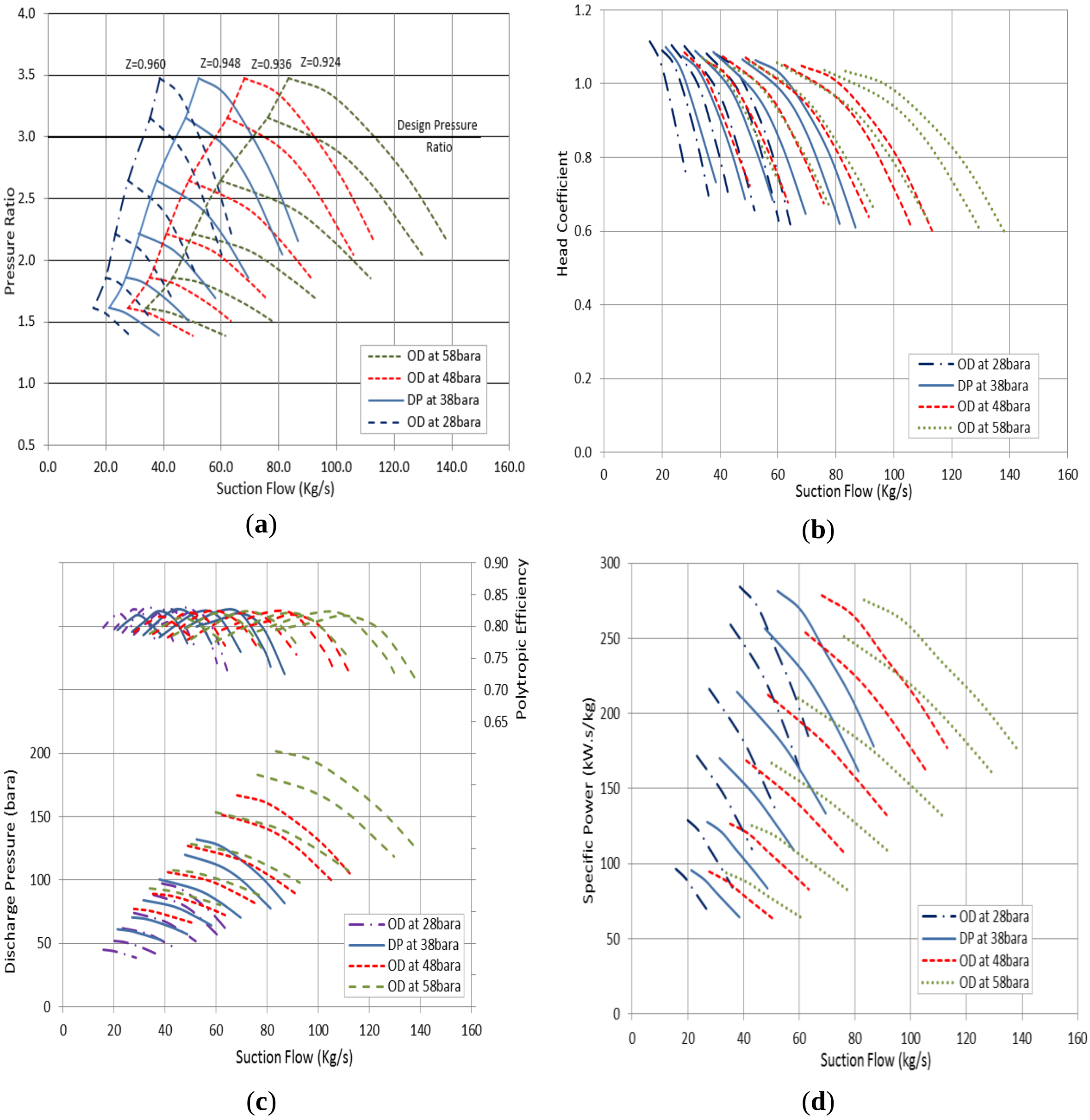

(a)

(b)

(c)

(d)

Figure 7- 11: Effect of Suction Pressure on Compressor Performance Parameters: (a) Pressure Ratio; (b) Head Coefficient; (c) Polytropic Efficiency (d) Specific Power

It is also interesting to observe that when there is a small change in the suction pressure ranging from +17% to −17%, the suction flow can be maintained to achieve the desired pressure ratio by controlling the rotational speed. When the deviation in the inlet pressure goes beyond this range, the pressure ratio cannot be sustained without changing the flow rate. However, this suction pressure variation range might vary according to the stage design, desired flow rate and design pressure ratio. In terms of compressibility factor, the compressibility factor (Z) is increasing as the inlet pressure decreases due to the reduction in the reduced pressure while the reduced temperature is constant. This totally agrees with the compressibility factor charts. The head curve in figure 7-11(b) is following the pressure ratio trend and shifting towards lower flow as the inlet pressure reduces. However, the higher pressure losses associated with low gas density leads to a slight increase in the required polytropic head in order to achieve almost the same pressure ratio. The specific power curve demonstrates a small increase in the power consumption at low suction pressure. The impact of the suction pressure variation in the polytropic efficiency is illustrated in figure 7-11(c).

It was found that operating the compressor at constant pressure ratio yields a lower overall efficiency as the suction pressure goes down. This can be deduced by observing the change in the peak efficiency value in consequence of inlet flow shift. Lowering the suction pressure leads to reduce Reynolds number due to the density decrease. This number profoundly influences the induced boundary layer and frictional losses of the flowing gas along its path. The low gas Reynolds number causes higher frictional losses and heat losses through the casing which, in consequence, yield a lower overall efficiency. This conclusion apparently agrees with the specific power curve in figure 7-11(d) which demonstrates a greater power consumption at low inlet pressure operation. The compressor is typically designed with an optimum flow coefficient to ensure the high efficiency. However, when there is a small fall in the flow rate as a result of inlet pressure drop, this can be balanced by reducing the rotational speed. Looking to the discharge pressure variation, it is clear that the capacity control is necessary to keep a stable compressor running while the suction pressure is changing. As the suction pressure rises, the discharge pressure increases proportionally but, to keep the running point away from the surge, the inlet flow should be raised. At constant speed line, a fixed discharge pressure can be achieved by altering the inlet pressure. However, to shift the compressor curve to new suction pressure curve, it would be necessary to throttle the suction by a certain amount of pressure which is dissipated in the throttling valve as wasted energy.

To obtain the compressor performance at constant discharge pressure, three main steps were followed:

1. The compressor map was derived at the beginning, assuming a constant suction pressure. Then, the obtained pressure ratio is used to calculate the corresponding suction pressure, assuming a constant discharge pressure.
2. The suction gas properties have to be corrected based on the new inlet pressure value. In the next step, the gas properties at compressor suction are recalculated for every suction pressure value including compressibility factor (Z_1), compressibility functions (X_1, Y_1), and density (ρ_1).
3. For more accurate results, the new pressure ratio values in the first process are used again to recalculate the suction pressure, which then used to estimate the suction gas properties.

The discharge pressure was considered fixed at the design point value, and the corresponding suction pressures are plotted in figure 7-12 at various suction temperatures. This sort of presentation is advantageous to obtain the equivalent rotational speed and flow rate to achieve the same discharge pressure at different suction pressure and temperature values. To develop the same discharge pressure, the required rotational speed has to be reduced as the inlet pressure increases. At constant speed operation, this can be accomplished by raising the suction flow in order to keep the running point in the stable region. Figure 7-13 illustrates a rise in the compression pressure ratio to accommodate the reduction in suction pressure. At constant suction flow, the compressor is pushed to work with a greater pressure ratio when the inlet temperature goes down due to the reduction in suction pressure.

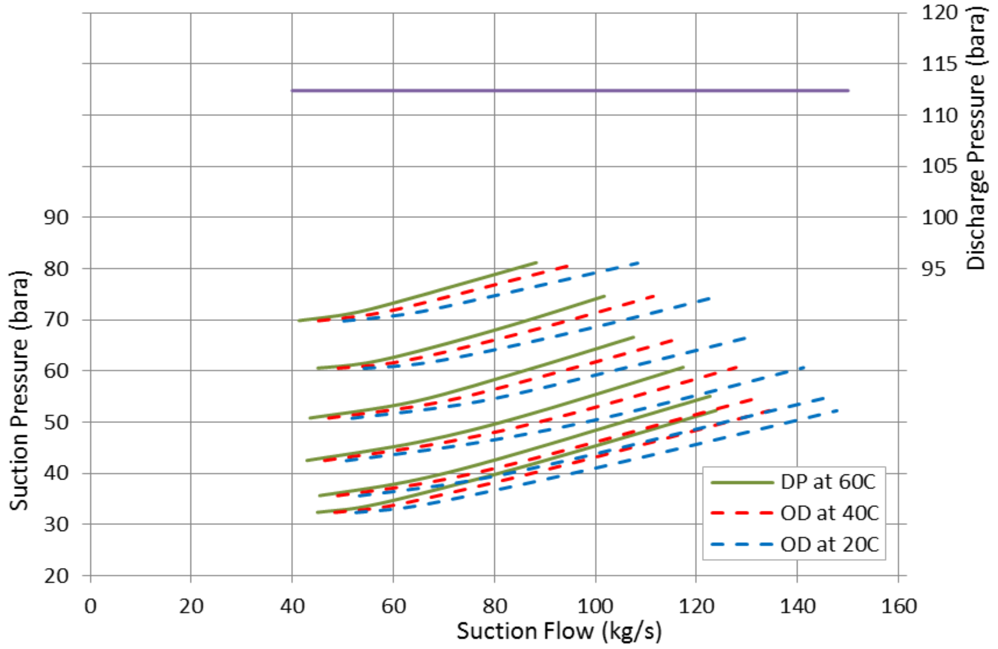

Figure 7- 12: Prediction of Suction Flow and Rotational Speed at Various Suction Pressures to Maintain a Constant Discharge Pressure

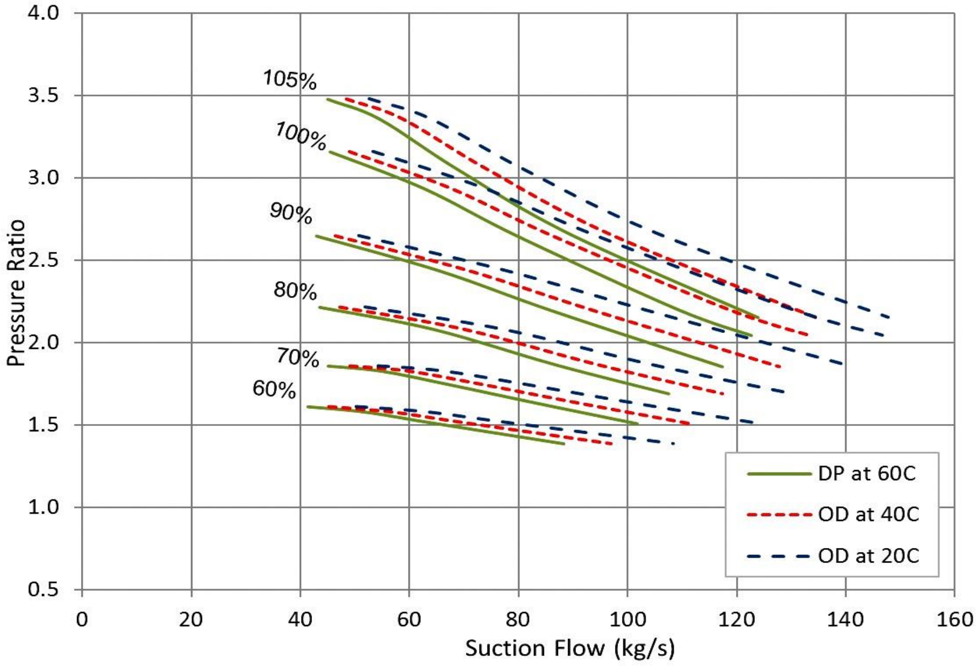

Figure 7- 13: Effect of Suction Pressure and Temperature on Compressor Pressure Ratio at Constant Discharge Pressure

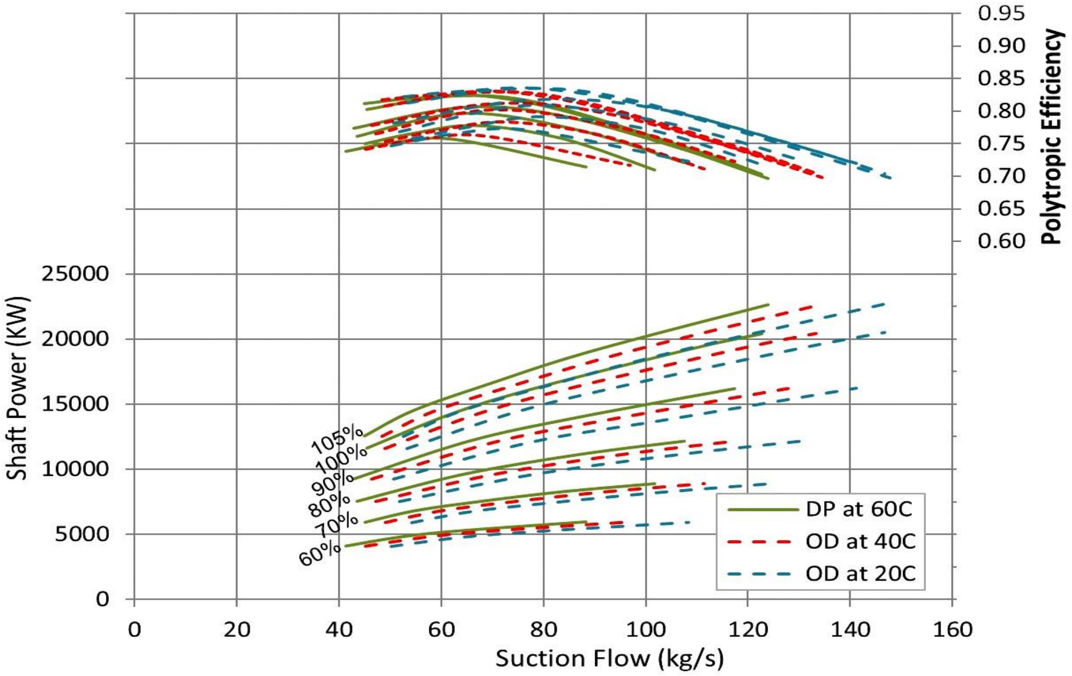

Figure 7- 14: Effect of Suction Pressure and Temperature on Efficiency and Shaft Power

According to the polytropic head, the effect of inlet temperature on the constant speed and discharge pressure curve becomes more significant at low flow rates. On the high flow region, the low inlet temperature can introduce a greater increase in the pressure ratio which offsets its direct effect on the polytropic head. The adverse impact of the inlet temperature and pressure ratio on the compressor head results in, relatively, very close head values at this flow region. However, as the operating point moves to the low flow coefficients region, the rise in the pressure ratio as a result of inlet temperature reduction starts to decline which makes its impact on the polytropic head insignificant comparing with the low inlet temperature effect. Consequently, the developed head of high inlet temperature becomes greater at low flow rates.

Despite that the compressor is working with lower head at high suction pressures, the power curve in figure 7-14 demonstrates an increase in the required power value at high suction pressure region. This is due to the fact that the pressure losses are increasing as the deviation of the pressure ratio from the design value increases. When the suction pressure rises beyond 38 bara, the required discharge pressure can be accomplished with smaller pressure ratio than the design point value which, in turn, leads to dissipate a greater part of the supplied energy.

7.4.3 Impact of Gas Molecular Weight

The variation in the molecular weight for air-water vapor mixtures is usually small, so it can be ignored. However, the gas compressors are designed to be capable of dealing with wide ranges of molecular weight, which makes the effect of this variable quite significant. The gas density is significantly affected by the molar mass of its compositions. So, the presence of light compositions reduces the gas relative density, which yields lower flow rates. Consequently, the developed pressure ratio of the investigated compressor in section 7.4.1 decreases as gas molecular weight reduces, if the rest of the gas properties are kept constant as illustrated in figure 7-15(a). However, the pressure ratio rise starts to decline gradually as the flow goes down since the heavy gases tend to surge earlier and at higher flow rates.

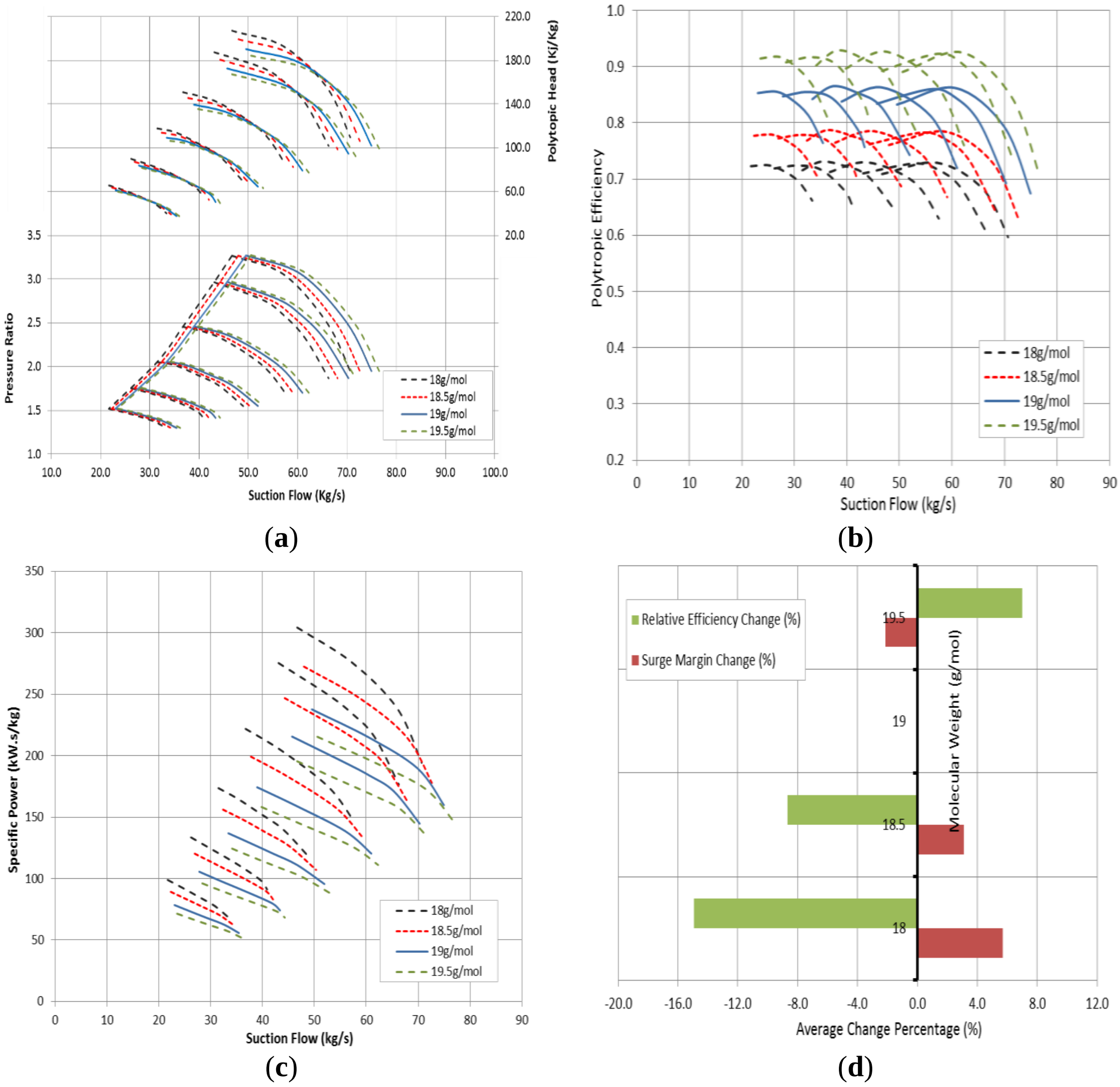

(a) (b)

(c) (d)

Figure 7- 15: Effect of Gas Molecular Weight on (a) Compressor Head and Pressure Ratio (b) Compressor Efficiency (c) Specific Power (d) Efficiency and Surge Margin at a Fixed Flow Rate

The polytropic head is increasing proportionally with the gas molar mass driven by the rise in the pressure ratio as shown in figure 7-15(a). As the operating point moves towards the surge line, the increase in the pressure ratio at high molecular weight starts to decrease, causing the head value to drop. By looking to the centrifugal compressor head equation, it is evident that the polytropic head is also influenced by the gas constant, which decreases as the molecular weight increases. So, the reduction in the gas constant was the dominant factor offsetting the effect of a high pressure ratio. The other reason behind this sort of head behavior is because the head is increasing exponentially with the pressure ratio raised to the power of $(n-1)/n$. This makes the impact of pressure ratio variation negligible when compared with the gas constant impact.

Figure 7-15 (a) demonstrates a reduction in the surge margin as the gas molecular weight increases, leading to a shorter stability range. The required polytropic head of low molecular weight tends to grow as the flow rate reduces. This indicates higher frictional losses, associated with low gas density and viscosity. Furthermore, the surge intensity is increasing proportionally with the gas density, which can happen as a result of a rise in pressure and molecular weight or as a consequence of the temperature reduction. The compressor efficiency is also affected by the gas constant. The high molecular weight value leads to a decrease in the gas constant (R) yielding a lower volume polytropic exponent, which is inversely related to the stage efficiency. As the gas density decreases, the compression ratio through the impeller is reduced, which will result in a higher discharge volume flow acting on the same vane area. This, in turn, leads to a lower tangential velocity and correspondingly lower generated head. In addition to Mach number, the gas density influences the gas Reynolds number, which decreases proportionally with the molecular weight, leading to higher frictional losses and lower efficiency as shown in figure 7-15(b). There is an increase in the power consumption when handling the low density gases despite the reduction in the discharge pressure. One interesting observation that stands out from figure 7-15(c) is the dramatic variation in the specific power due to the gas molecular weight at the low flow region. This impact becomes more substantial at high rotational speeds. The significance of this finding appears when dealing with a centrifugal compressor with a wide operating molecular weight range.

Figure 7-15(d) illustrates the average change in the stage efficiency and surge margin as a result of molecular weight variation with respect to the design values at a fixed flow rate. It is clear that there is an opposite effect on the efficiency and surge margin. Operating the compressor with heavy gases leads to an increase in the stage efficiency and pressure ratio but simultaneously reduces the surge margin value. More substantial impact can be observed on the efficiency value. Figure 7-16 demonstrates the impact of the molecular weight on the compressor structure. The effect of gas molar mass on the compressor head causes the required number of mechanical stages to vary. The low molecular weight gas raises the required head to achieve the desired discharge pressure, leading to greater pressure coefficient on the impeller blades. Therefore, the required number of impellers has to be reviewed at an early stage to consider the expected variation in gas relative density.

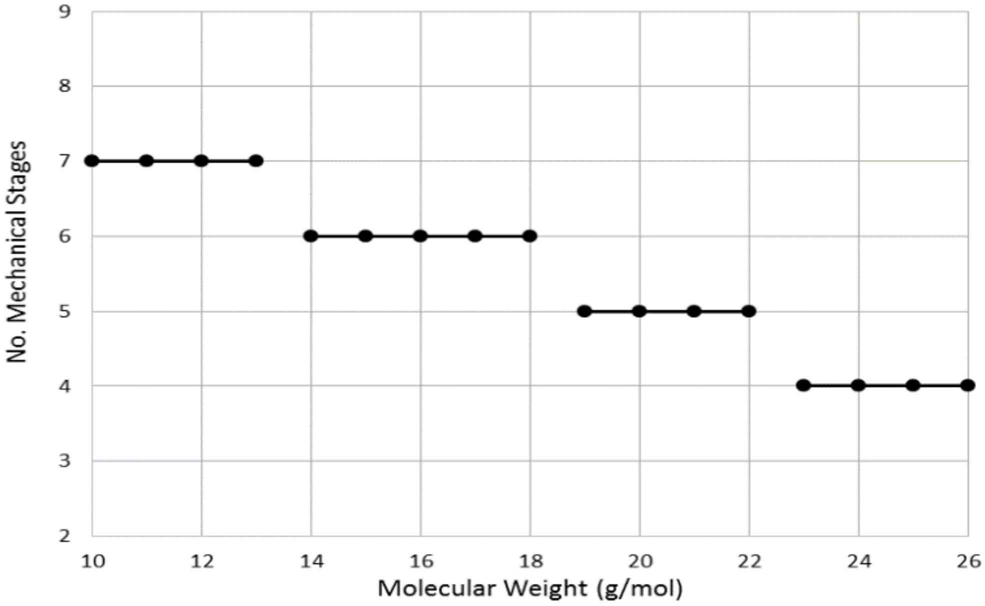

Figure 7- 16: Effect of Gas Molecular Weight on Compressor Structure

7.4.4 Effect of Gas Compressibility (Z)

The compressibility factor is obtained according to the gas compositions and gas temperature and pressure values. At a fixed inlet pressure and temperature, the increase in the critical properties causes the reduced pressure and temperature to decrease, yielding a lower compressibility factor. Figure 7-17(a) illustrates the effect of the compressibility factor on the compressor pressure ratio and polytropic head when the rest of the gas properties are fixed. Since the pressure ratio is a function of tip speed Mach number, the low compressibility causes the gas to flow at a higher Mach number, yielding a greater pressure ratio. This is indeed due to the greater inlet expansion from flange to impeller eye and increased pressure recovery in the diffuser at a high Mach number. However, the reduction in compressibility factor leads to lower peak efficiency, as shown in figure 7-17(b). This offsets the effect of the Mach number on the pressure ratio rise, with a more pronounced impact near surge point. The greater decrease in the part-load efficiency causes the pressure ratio trend to be flatter near the surge flow. Furthermore, a slight reduction in the operating range was observed at a low compressibility factor. The high pressure ratio at high flow region raises the required polytropic head. This increase in the head is obviously influenced by the pressure ratio rise. However, the high surge flow of low compressibility gases pushes the polytropic head to drop earlier.

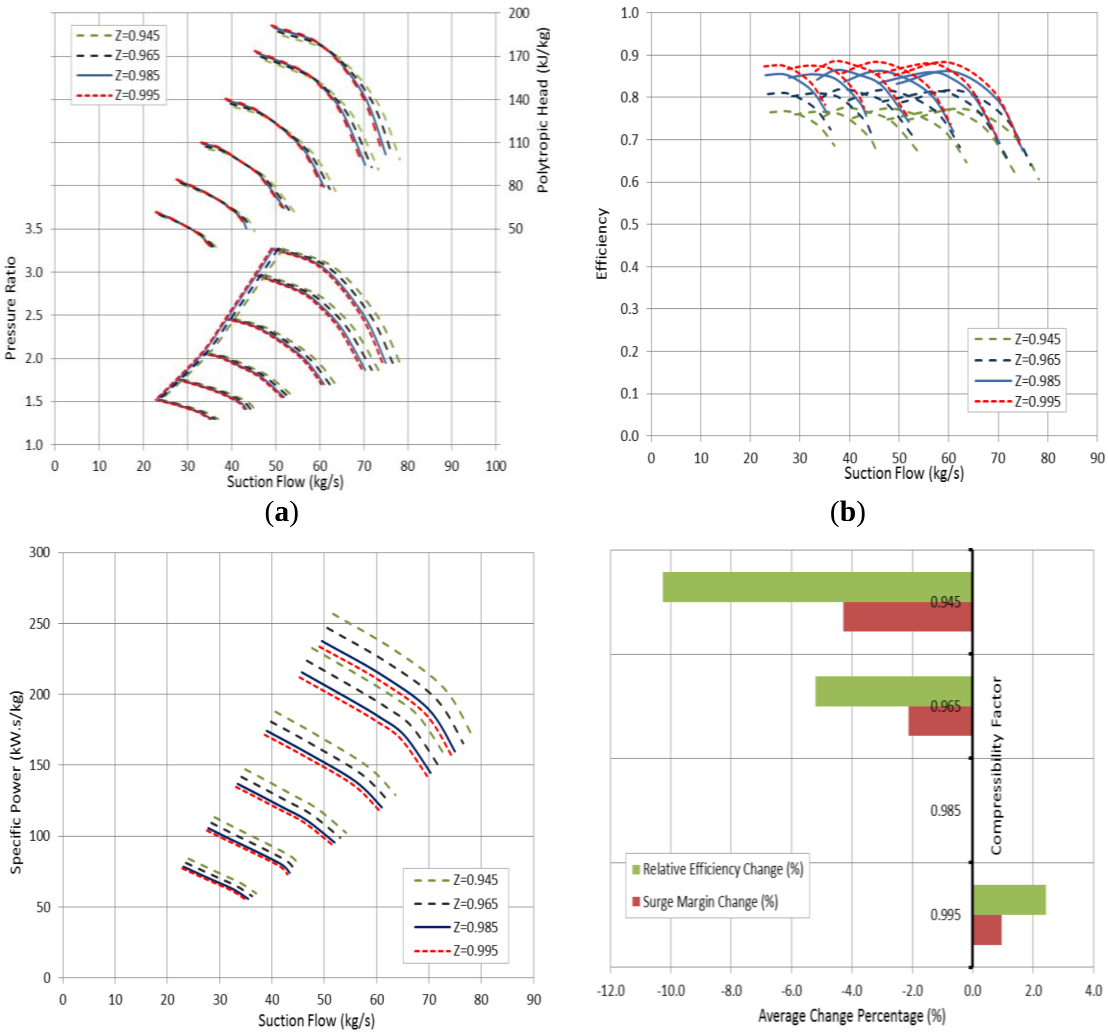

(a) (b)

(c) (d)

Figure 7- 17: Effect of Gas Compressibility on (a) Compressor Head (b) Compressor Efficiency (c) Specific Power (d) Surge Margin and Efficiency Change at Fixed Flow Rate

Figure 7-17(c) illustrates an increase in the specific power at a low gas compressibility factor. Unlike the gas molecular weight, the change in the specific power is almost constant at all speed lines and throughout the flow range. In terms of efficiency and surge margin, Figure 7-17(d) demonstrates a similar trend for both stage efficiency and surge margin. The high *Z* value shifts the pressure ratio curve to lower values, leading to a lower pressure ratio value and simultaneously to higher surge margin and greater efficiency value.

7.4.5 Effect of Specific Heats Ratio (k)

A slight decrease in the pressure ratio was observed at a high specific heats ratio when the molecular weight is constant. On the other hand, the polytropic head has an upward trend with the *k* value rise, as demonstrated in figure 7-18(a). The head is increasing proportionally with the volume polytropic exponent, which in turn increases as the specific heats ratio goes up. However, the influence of the pressure ratio on the head value is less significant when it is compared with the volume polytropic exponent effect.

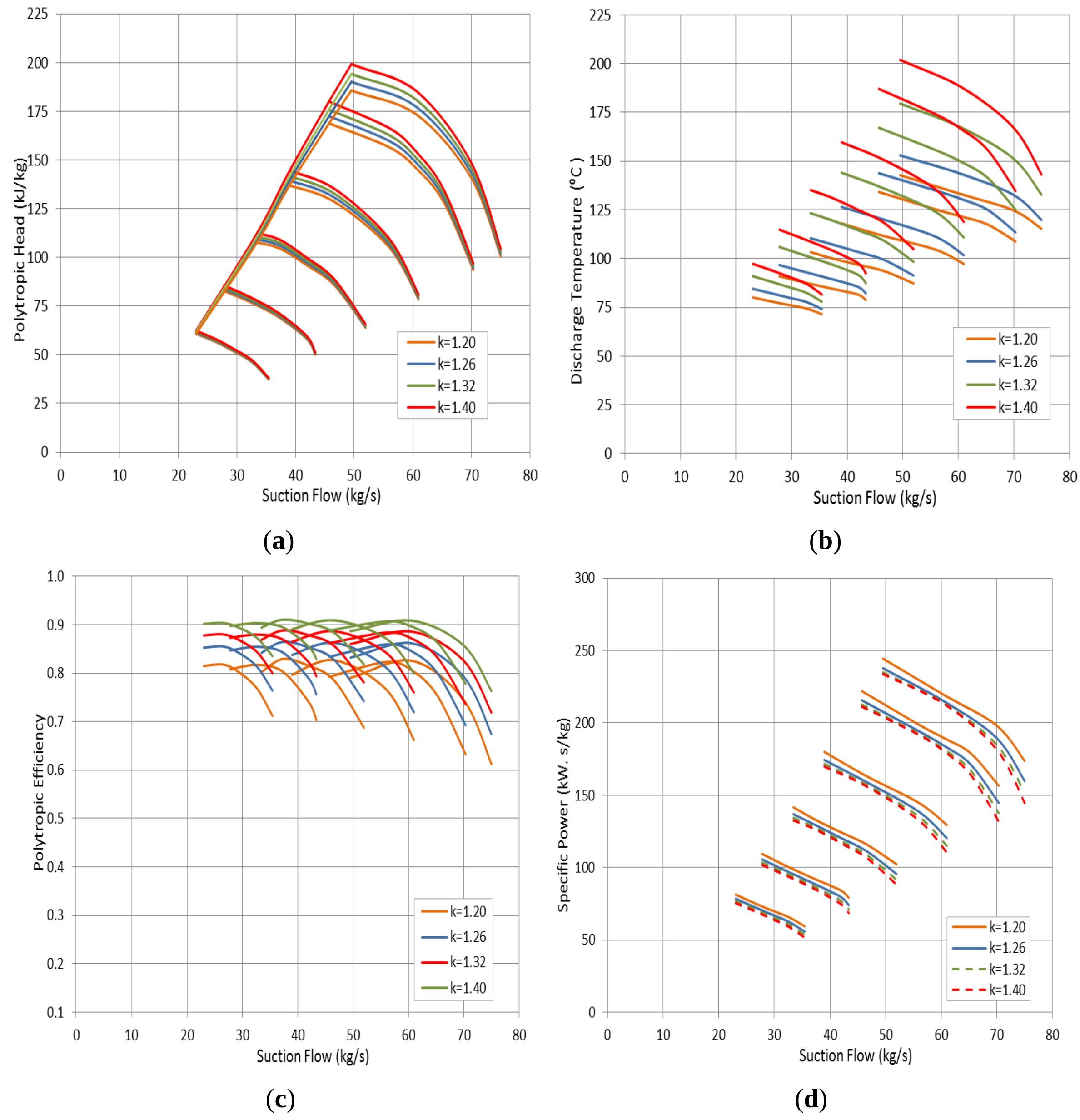

(a) (b) (c) (d)

Figure 7- 18: Effect of Gas Specific Heats Ratio on (a) Compressor Head (b) Discharge Temperature (c) Compressor Efficiency (d) Specific Power

Additionally, it was found that the impact of gas heats ratio on the compressor head becomes more pronounced at high rotational speed. Furthermore, the operating range is decreasing as the specific heats ratio of the handled gas reduces. There is another effect of the high specific heats ratio gases, illustrated in figure 7-18(b). The high specific heats ratio (k) causes the temperature polytropic exponent to rise, yielding a higher discharge temperature at the same pressure ratio. This can elucidate the slight reduction in the discharge pressure value at a high specific heats ratio. Similar to gas compressibility effect, the efficiency curve in figure 7-18(c) shows a reduction at low specific heats ratio (k) driven by the rise in the Mach number. This indicates higher frictional losses and lower pressure recovery, which dissipated a part of the shaft power.

In order to confirm that, the specific power curve is derived as illustrated in figure 7-18(d). This demonstrates an increase in the specific power value at low specific heats ratio gases, which in turn denotes a higher power consumption when the low k-value gases are used. Figure 7-19 shows a gradual reduction in the work coefficient as the specific heats ratio (k) increases.

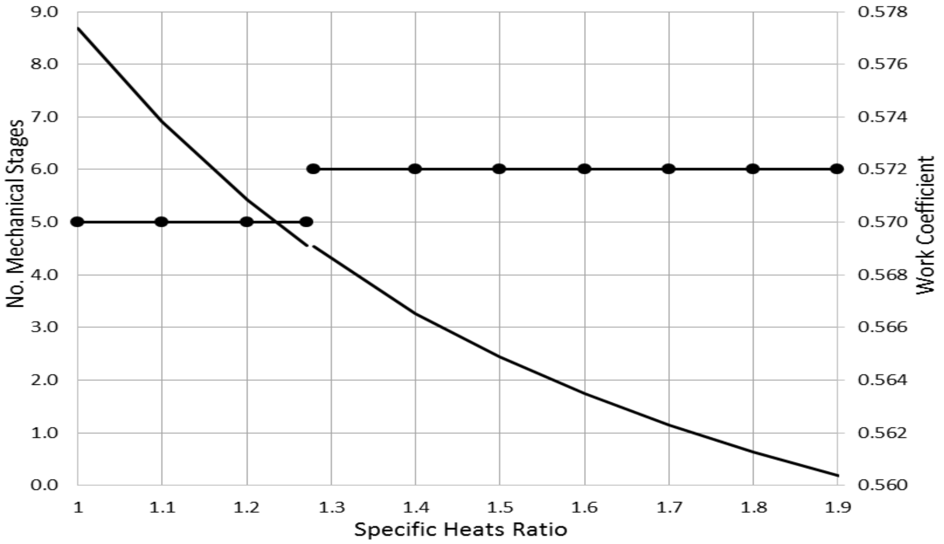

Figure 7- 19: Effect of Gas Specific Heats Ratio on Compressor Structure and Work Coefficient

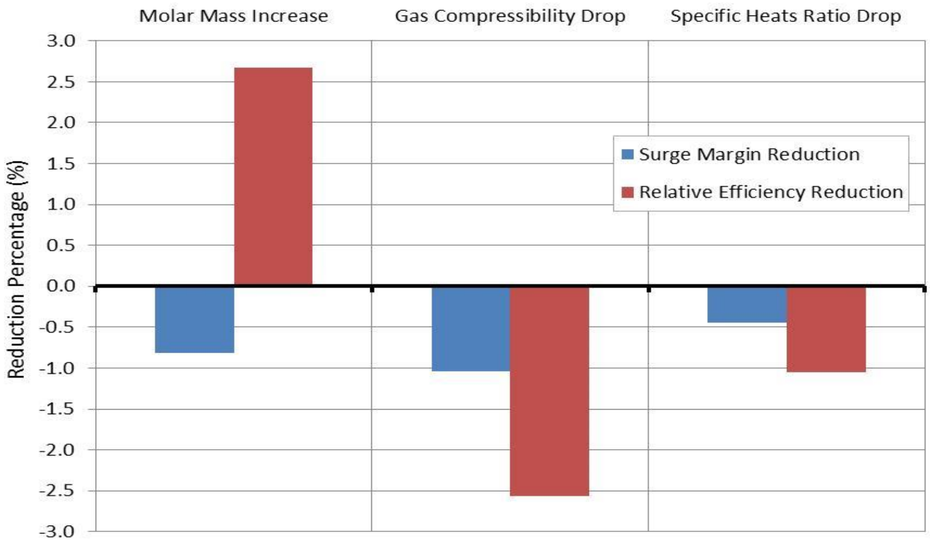

Figure 7- 20: Comparison Between Gas Properties Effect on Efficiency and Surge Margin

The limitation in the pressure rise at a high specific heats ratio pushes the compressor designers to accommodate more mechanical stages while handling the high *k*-value gases. Figure 7-20 illustrates the estimated reduction in surge margin and efficiency at a low specific heats ratio. A more significant drop was detected in the efficiency value. Compared with the molecular weight and gas compressibility effect, the impact of *k*-value drop on efficiency and surge margin is less substantial. The largest reduction in surge margin was observed with a gas compressibility drop while the highest difference in stage efficiency was caused by a molecular weight increase.

7.5 Compressor Operation Diagnosis Using Developed Model (Case Study)

A high vibration level was detected with the 3.7 MW centrifugal compressor in section 7.3, reaching the alarm level and causing the machine to shut down. The vibration trend at the afterward bearings of the first stage demonstrates higher levels of amplitude reaching 79 μm. However, that vibration value was still below the trip level, as illustrated in figure 7-21(a). Furthermore, the vibration trend in figure 7-21(b) indicates a high vibration level at the forward bearing reaching to the alarm level while the vibration at the afterward bearings remained steady at 35 μm. Before analyzing the recorded data, it is necessary to check the conditions of all instrumentations around the compressor to ensure they gave the actual readings.

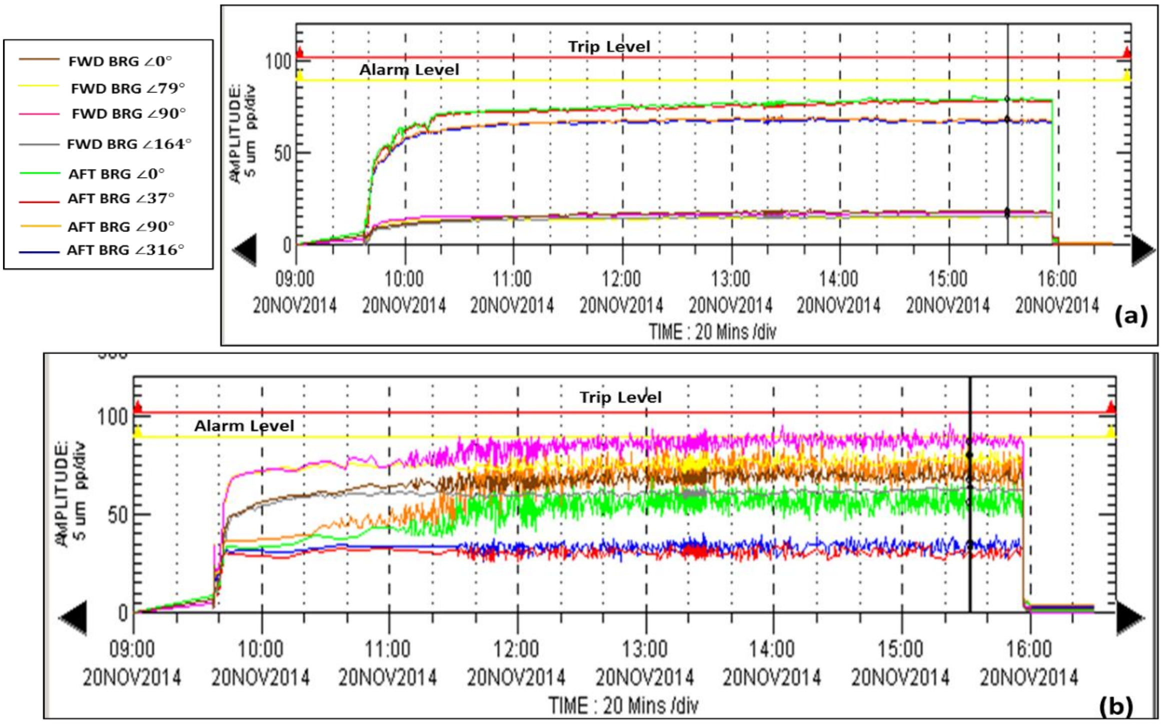

Figure 7- 21: Recorded Vibration Trends at 15516 rpm for Forward and Afterward Bearings of (a) First Process Stage (b) Intermediate Process Stage

By reviewing the operational data in figures 7-22 to 7-24, the first stage is working with a relatively higher pressure ratio reaching 3.15, against only 2.88 at equivalent corrected inlet gas properties. Continuing operating this machine at the same conditions will lead to greater fluctuation in the discharge pressure as was observed in the region (A), yielding a higher vibration level.

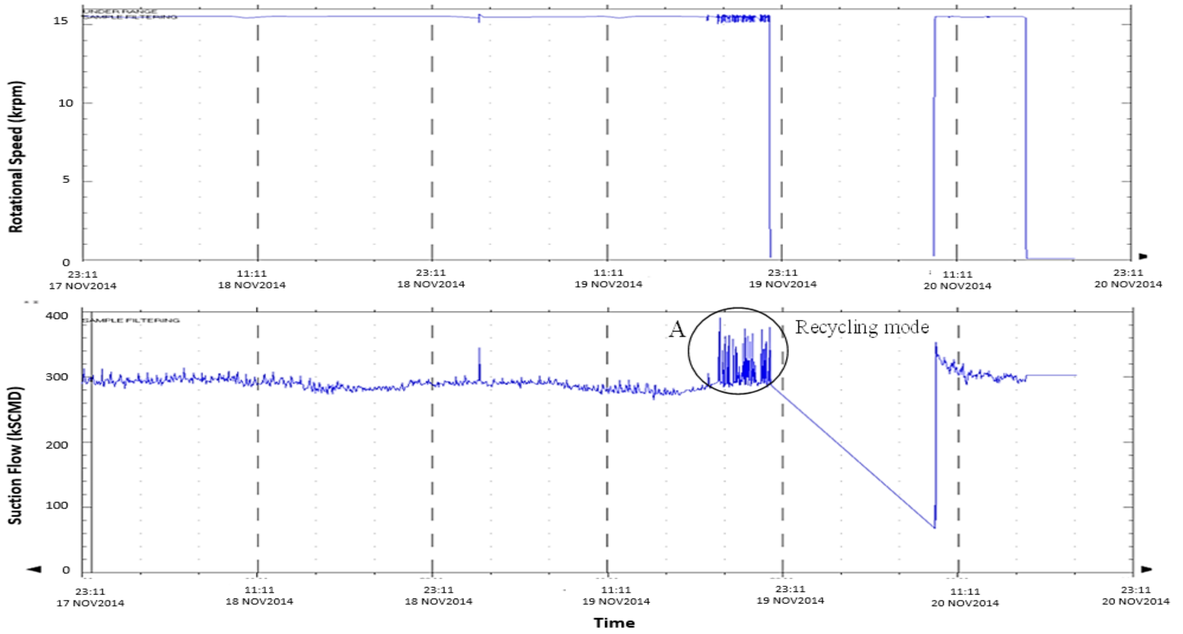

Figure 7- 22: Recorded Rotational Speed and Suction Flow in the Gas Plant

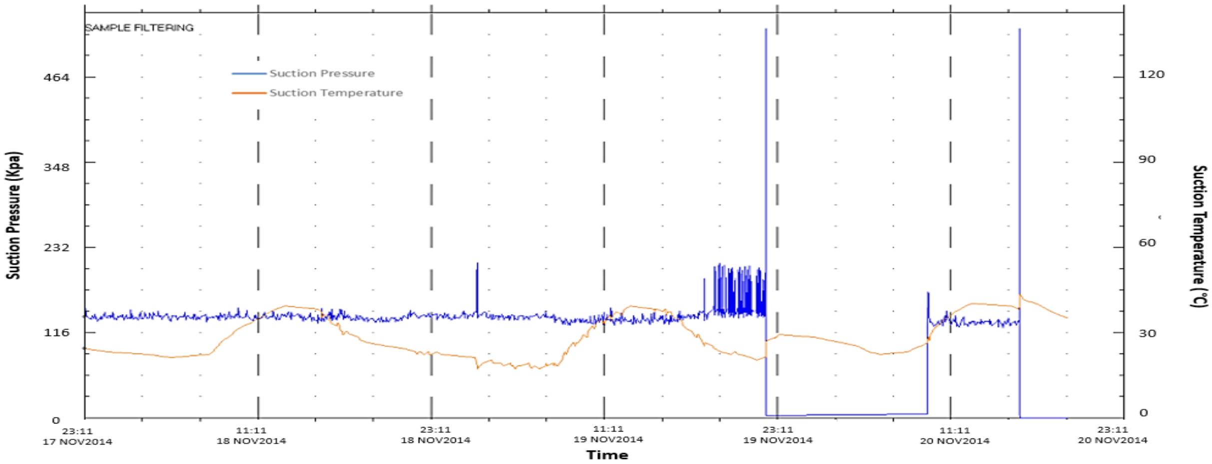

Figure 7- 23: Recorded Suction Pressure and Temperature

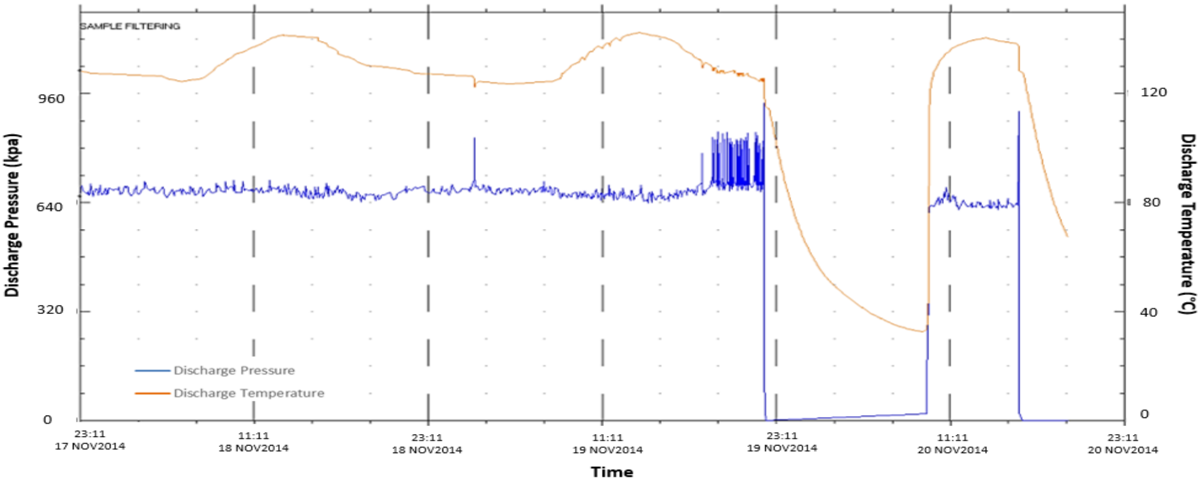

Figure 7- 24: Recorded Discharge Pressure and Temperature

In this region, the high increase in the discharge pressure drives the machine into the recycle mode in order to pull the operating pressure ratio away from the surge control line. This can be observed evidently from the suction flow trend in figure 7-22. Furthermore, it was also found that the surge margin of the overall compression system dropped from 25% to 10%. However, the compressor is rotating with one percent higher rotational speed than the design value. From the performance curve, the compressor operates at a low suction flow and high rotational speed to satisfy the required rise in the polytropic head due to high pressure ratio. When the speed reached a very high value only one percent lower than the maximum speed point, the increase in the polytropic head is compensated by suction flow reduction. The recorded suction temperature before the machine trip was lower than the design temperature by about 10°C. Besides, the suction pressure trend in figure 7-23 demonstrates a slight fluctuation in the absolute suction pressure ranging between 2.28 and 2.40 bara. This value is still close to the design operating value of 2.41 bara. The low suction temperature raises the suction flow density, leading to a higher pressure ratio. On the other hand, the low inlet pressure reduces the gas density, pushing it to a lower pressure ratio. However, the impact of low suction temperature was more significant than the low inlet pressure, yielding a slight rise in the pressure ratio but still lower than the detected value.

Considering the gas properties, the design compressor map has been corrected based on the recorded gas properties one year before the trip date, as indicated in figure 7-5. The operating envelope (figure 7-25a) shifts down towards a lower pressure ratio. This makes the deviation between the predicted pressure ratio and the actual value greater. Point (A) in this figure indicates the normal operating pressure ratio at the same detected speed and suction flow just before the machine failure while point (B) denotes the actual measured pressure ratio value in the field. The pressure rise from point A to B causes the surge margin to drop substantially from 12.04% to 2.45%. Any further increase in the pressure ratio will cause the compressor to run in the recycling mode, which is what happened in the previous shutdown, as indicated in the region (A) in figure 7-22. The change in the overall pressure ratio of the entire compression system is illustrated in figure 7-25(b). The predicted surge margin of the new point is approximately 11.77% and 1.75% based on the design surge line and the corrected one, respectively.

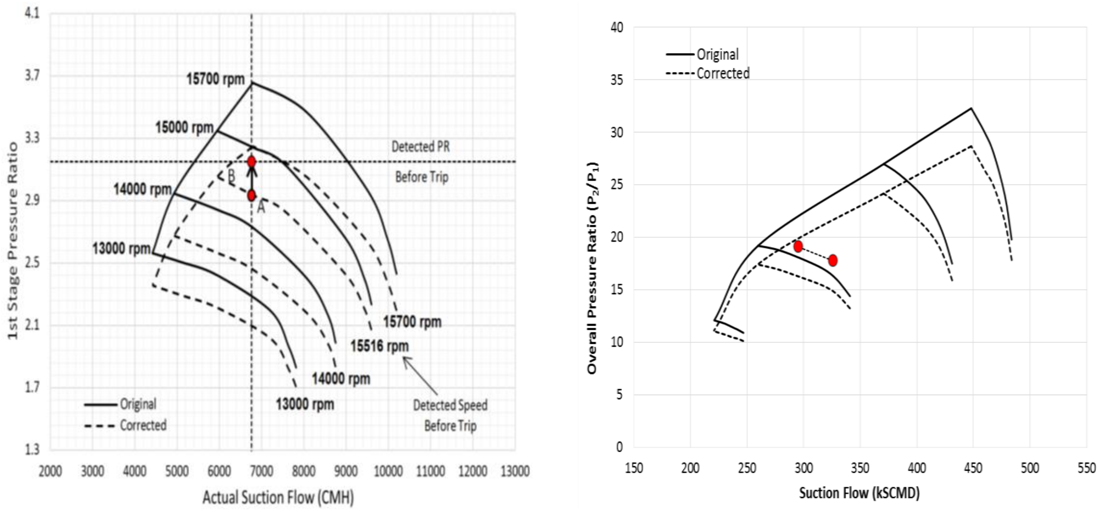

(**a**) (**b**)

Figure 7- 25: Prediction of Actual and Normal Operating Points at Reference Conditions of (a) First Process Stage (b) Overall Compression System

However, the measured surge margin in the field just before the trip was around 10%, which lies between these two values. Considering the high generated level of vibration, it implies that the operating point is very close to the unstable region and supports the estimated surge margin value in this study. Furthermore, the predicted surge margin reveals the fact that the machine was running into stall condition for longer than 3 hours, which affects the compressor stability and the internal component lives.

For more precise results, the surge margin reduction is compared with the measured value. The estimated drop was about 11.7% and 21.7% with respect to the design and corrected maps, respectively compared with the measured value of around 15%. The actual value falls within the predicted range, which indicates a change in the compressor performance curve due to either a sudden change in the gas properties or a flow blockage in the downstream system. Based on the unanticipated gas properties' change assumption, Figure 7-26 illustrates the effect of the molecular weight variation on the discharge pressure at the detected speed line.

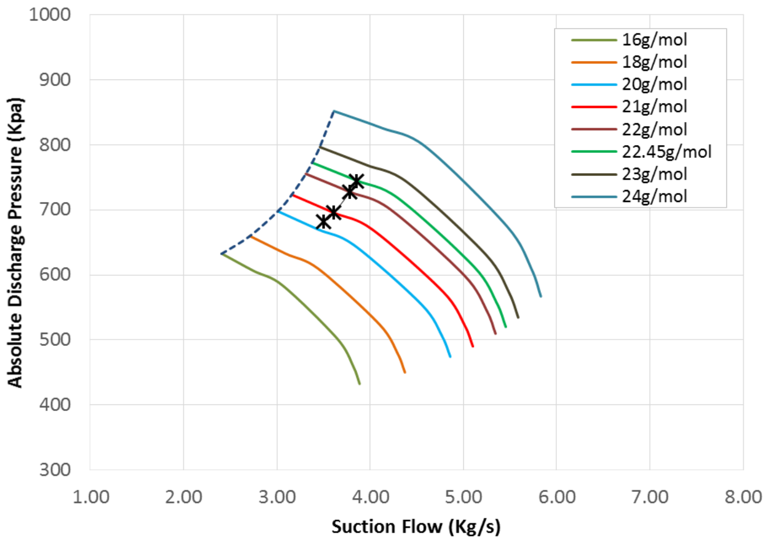

Figure 7- 26: Prediction of Gas Molecular Weight to Match the Discharge Pressure at Measured Speed

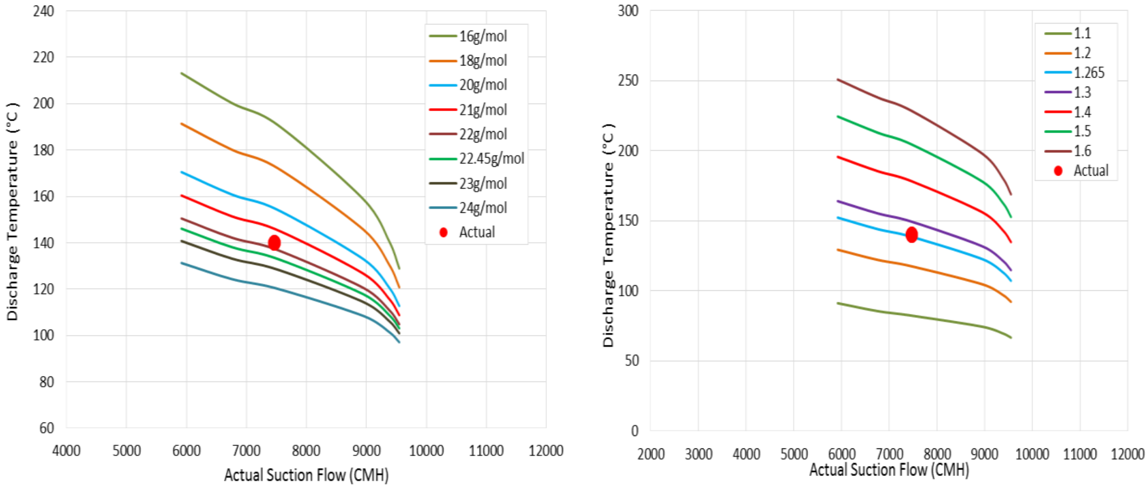

(a) (b)

Figure 7- 27: Comparison between Estimated and Measured Discharge Temperature at (a) Variable Molecular Weight (b) 22.45 g/mol

It is shown that an increase in the molar mass of around 1.57 g/mol over the design value can generate the same recorded discharge pressure before the machine shutdown. In order to assess this hypothesis, the predicted discharge temperature at 22.45 g/mol is compared to the measured value, as shown in figure 7-27(a). It was found that the estimated discharge temperature corresponding to this specific gravity value was lower than the actual temperature by approximately 7 °C. This difference is smaller than ±5% which is still acceptable, and it might be caused by the estimation error or the increase in the specific heats ratio as illustrated in figure 7-27(b).

The conducted analysis revealed that a specific heats ratio of about 1.265 can generate roughly the same detected discharge temperature, with a rise of about 1.56% over the initial *k*-value. Although this specific heats ratio is relatively high, it is still within the expected range for this molecular weight. To validate the predicted change in the suction gas properties, the change in the surge margin has to be considered. Figure 7-28 compares the operating envelopes of the first process stage at reference and predicted gas properties, where the reference map represents the performance at the measured conditions in figure 7-5. Figure 7-29 demonstrates an estimated surge margin of approximately 9.29% at the obtained gas properties. It is interesting to observe that the estimated value is very close to the measured one with less than 1% difference. This supports the first hypothesis regarding the unanticipated change in the properties of the process gas.

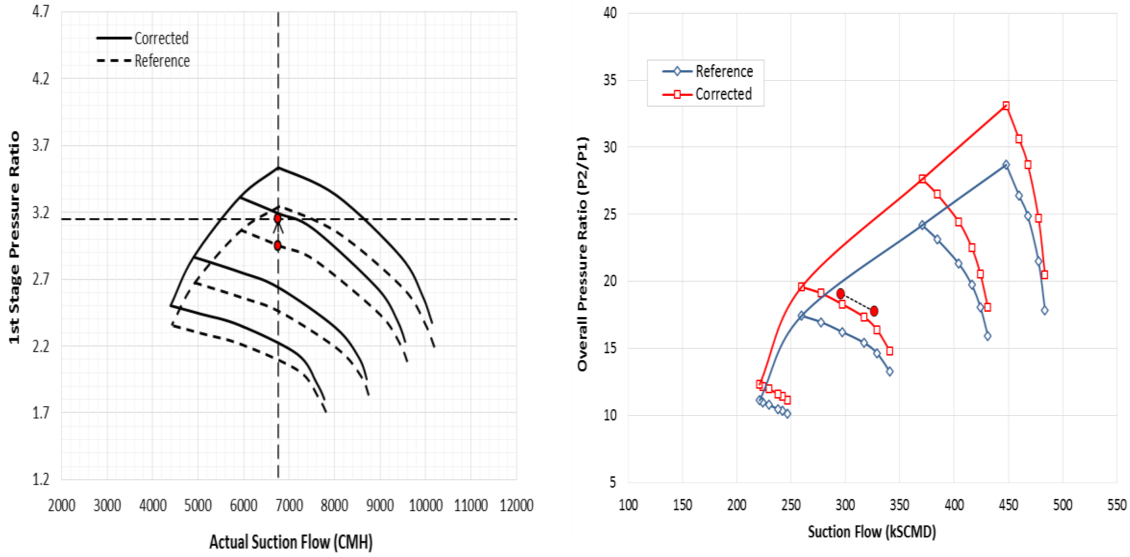

(a) (b)

Figure 7- 28: Prediction of Performance Map Based on Estimated Gas Properties (22.45 g/mol and k = 1.265) of (a) First Stage Performance (b) Overall Compression System

The high pressure at the first stage discharge can also be caused by the internal blockage in the gas path of the downstream equipment of the first stage including the aftercooler, scrubber, check valve and intermediate process stage. One way to assess the possibility of a flow blockage inside the aftercooler, scrubber, and check valve is by monitoring the pressure drop and temperature difference between the IPC inlet and LPC exit gas. By reviewing the operational data, the recorded pressure difference between the discharge of the first stage and the suction of the second stage is around 41 kpa, which is very close to the normal value. So, there is no indication for fouling across the second stage scrubber and the check valve.

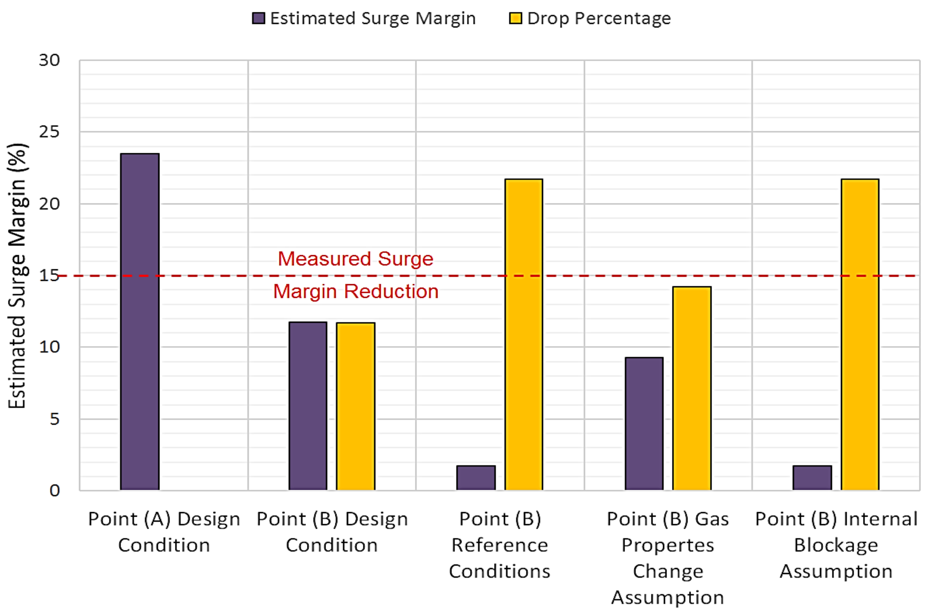

Figure 7- 29: Estimated Drop in Surge Margin at Different Assumptions

Considering the temperature change, the inlet temperature of the intermediate stage agrees with the measured value at normal operation conditions. Besides, the pressure rise across the intermediate pressure compressor is relatively normal, so there is no sign of blockage inside the second stage. Furthermore, the pressure and temperature difference between the first stage exit and the second stage inlet does not give any sign of a fouled first stage aftercooler. Moreover, the predicted surge margin reduction assuming a downstream blockage is substantially greater than the observed drop as illustrated in figure 7-29.

In brief, it was concluded that the unstable operation of the compression system was due to a sudden change in the gas properties. The predicted discharge parameters and the reduction in the surge margin matched the measured values. The compression system was operating very close to the surge line with a surge margin of only 9.2%, which is enough to run the compressor into the recycling mode. However, the first process stage was running in the stall condition for the last three hours with only 1.75% surge margin, yielding unstable flow behavior and a high level of vibration. This conclusion has been verified by conducting an internal inspection of the inlet guide vanes (IGVs) and the first impeller blades, which do not show any sign of deposit accumulation or corroded surface. Therefore, this operating case elucidates the importance of testing a gas sample frequently and correcting the performance map to avoid any catastrophic damages to the compressor internals. Moreover, since the correct measurement is critical for the map correction accuracy, the uncertainty of the measurement method has to be checked in order to improve the accuracy of the measurement. Besides, the gas sample should be taken from both the suction and the discharge stream of the compression system for more precise measurement.

7.6 Chapter Summary

Comparing with the air compressor, the variation of the gas properties has a significant impact on the compressor performance, especially when the hydrocarbons are used as working fluid. Therefore, a new iterative method was derived to obtain the equivalent compressor performance at various inlet parameters and gas compositions. This approach has been validated using two cases study to predict the compressor characteristics at different suction parameters and gas compositions, and the obtained results were compared against the measured data. The conducted comparison shows an acceptable level of accuracy in the obtained results with a maximum uncertainty near the surge point at the overload speed by about 2.21%.

Furthermore, this chapter demonstrated the impact of high suction temperature and low suction pressure on the compressor efficiency and surge margin. Moreover, a parametric study has been conducted to investigate the effect of gas properties on the stage efficiency, surge margin, and compressor structure. The outcomes of this study supported the need for considering the gas properties variation when the off-design performance is derived. The influence of gas molecular weight on the specific power was found to be more substantial at high flow coefficients and Mach numbers. Besides, the greatest impact on the stage efficiency was predicted by the gas molecular weight variation, while the gas compressibility reduction was found to cause the more significant surge margin drop. Additionally, this study emphasized the validity of the new model for the compressor design evaluation based on the expected fluctuation in suction parameters and physical gas properties. Moreover, a case study was presented to demonstrate the overall impact of gas properties’ variation on the operating point and aerodynamic stability.

CHAPTER 8: DETERMINATION OF LOW HEAD CAUSES IN CENTRIFUGAL COMPRESSORS OPERATION

This chapter describes an investigation into the major factors that cause a reduction in the pressure ratio of the centrifugal compressors in oil and gas industry. The low head can be a symptom of several reasons as shown in figure 8-1, so it is important to study the bearing of every factor on the compressor performance characteristics. Five causes of pressure ratio deterioration have been investigated in the previous chapter, including low suction pressure, high inlet temperature, low gas molecular weight, low compressibility factor and low specific heats ratio. However, there are other causes for head deterioration as will be discussed in this chapter. To achieve this objective, the developed method in chapter 7 has been modified to account the effect of work and flow coefficients. This approach is qualified by three operating cases, and the obtained results are evaluated against the internal inspection findings.

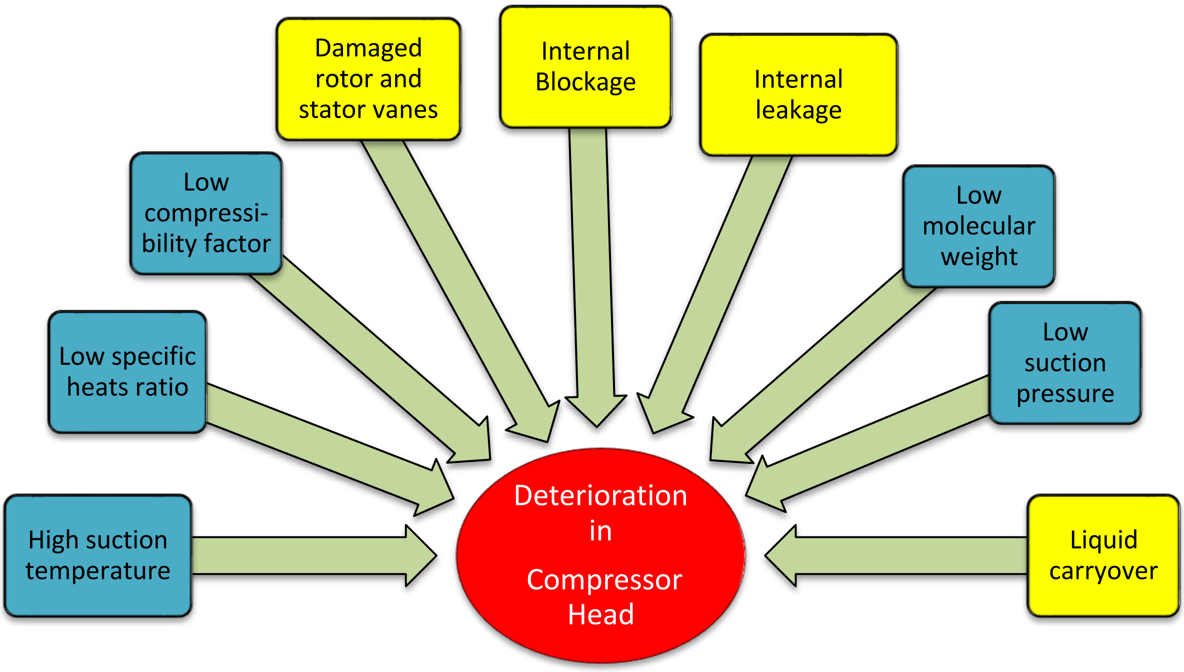

Figure 8- 1: Possible Causes of Low Pressure Ratio

8.1 Impact of Internal Blockage on Compressor Head

One of the main causes of unstable and inefficient operation of centrifugal compressors is the fouling which occurs as a result of deposits and contaminations build-up in the flow channels of the compression system. This leads to narrow the flow passages and to increase the surface roughness which, in turn, yields a higher pressure drop along the gas path.

There are two main categories of contaminations which deteriorate the compressor performance. The first group is the non-reactive contaminations which flow with the process gas through the compression system without experiencing any change in their physical state including dust, scale and catalyst fines. This kind of contaminations is expected to settle down in quiet flow regions inside the compressor such as the erode labyrinth and the leading edge of the first impeller blade. The adverse effect of this sort of deposits can vary greatly depending on the rate and composition of the deposits. The slow buildup on the stage internals alters the state of balance leading to a high vibration level and deterioration of the compressor performance. However, the fast buildup can cause immediate shutdown due to the high induced vibration and possibly internal component damage.

Unlike the non-reactive deposits where appropriate filtration system is enough to reduce the risk of accumulation, the other type is relatively more difficult to deal with due to the change in the physical state of these contaminations as they pass through the compression circuit. So, they enter the suction line of the compressor as gas or liquid, but they become as adhesive or abrasive polymers while flowing through the compression stage and discharge system depending on the working conditions and hydrocarbon compositions of the process gas. This polymer material can agglomerate in the labyrinth, drain lines and intercoolers creating more severe pressure drop. Besides, the chemical reaction between the reactive contaminations and the flow path surface degrade the internal component life. Hence, it is important to consider the overall compression system component and to understand the chemistry of the generated fouling material. In general, the physical and chemical reactions of these contaminations are highly governed by the surface finish, deposit material, gas composition as well as the gas temperature and pressure.

8.2 Description of Fouling Modelling Approach

The followed methodology consists of four main steps as illustrated figure 8-2. This approach is based on the fact that the flow channels blockage alters the aerothermodynamic performance of centrifugal compressors through three mechanisms:

- Effective area reduction.
- Frictional losses increase.
- Flow and pressure profile distortion.

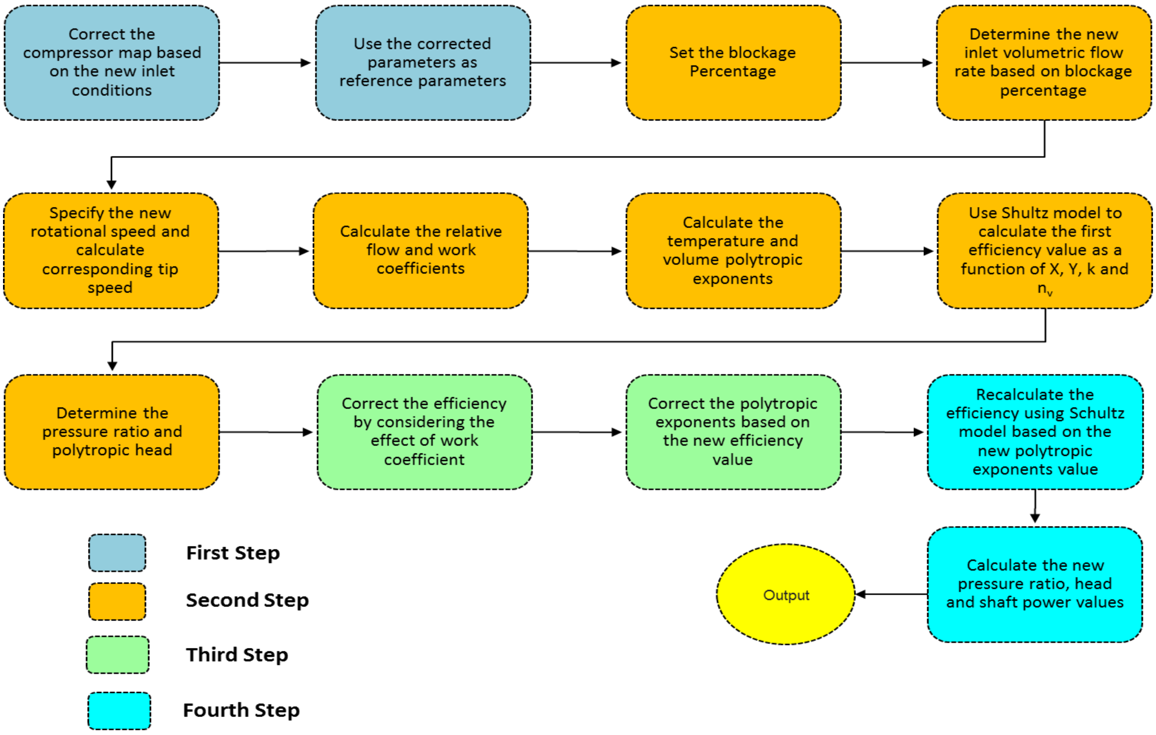

Figure 8- 2: Developed Methodology for Internal Blockage Effect Modelling

Firstly, the original compressor map at design conditions is corrected based on the new suction parameters including inlet temperature and pressure and gas properties. The derived performance parameters are then set as reference conditions for the blockage effect study. The new inlet volumetric flow rate is calculated based on the blockage percentage (BP %) in the case of upstream or internal fouling. Accordingly, the tip speed is calculated based on the new rotational speed value and assuming a fixed impeller diameter. Furthermore, the corresponding flow coefficient is obtained using the calculated flow rate.

$$\mathrm{\varphi} = \frac{4\dot{\mathrm{V}} \times \mathrm{BP\%}}{\mathrm{\pi D_2{}^2 U_2}} \tag{8-1}$$

The work coefficient (ψ_w) is then derived using equation (8-2) based on the new flow coefficient value. The correlation coefficient (k_s) is defined by matching the work coefficient value at clean operation with the design point. The basic correlation has been derived from Casey-Robinson model which has been adapted assuming fixed impeller geometry.

$$\psi_{w_{\mathrm{OD}}} = \psi_{w_{\mathrm{Ref}}} \times \left[\frac{\left(1 + \frac{0.002}{\varphi_{\mathrm{Ref}}}\right)\left(1 - \frac{\mathrm{c_{s,Ref}}}{\mathrm{U_{2,Ref}}} + \varphi_{\mathrm{Ref}}\mathrm{k_s}\right)}{\left(1 + \frac{0.002}{\varphi_{\mathrm{OD}}}\right)\left(1 - \frac{\mathrm{c_{s,OD}}}{\mathrm{U_{2,OD}}} + \varphi_{\mathrm{OD}}\mathrm{k_s}\right)}\right] \tag{8-2}$$

To calculate the temperature polytropic exponent ($\mathrm{n_T}$), equation (8-3) is used assuming that the off-design efficiency is identical to the design point. The approximated value will be corrected later for more accurate estimation.

$$\mathrm{n_{T,OD}} = \mathrm{n_{T,Ref}}\left[\frac{1 - \frac{\mathrm{Z_{Ref}R_{Ref}}}{\mathrm{C_{p,Ref}}}\left(\frac{1}{\eta_\mathrm{p}} - 1\right) - \frac{\mathrm{k_{Ref}}}{\mathrm{k_{Ref}-1}}}{1 - \frac{\mathrm{Z_{OD}R_{OD}}}{\mathrm{C_{p,OD}}}\left(\frac{1}{\eta_\mathrm{p}} - 1\right) - \frac{\mathrm{k_{OD}}}{\mathrm{k_{OD}-1}}}\right] \tag{8-3}$$

Then, the obtained temperature polytropic exponent ($\mathrm{n_T}$) is substituted in equation (8-4) to get the volume polytropic exponent ($\mathrm{n_v}$).

$$\mathrm{n_v} = \frac{\mathrm{k}}{1 + \left[\left(\frac{\mathrm{C_pMW(k-1)}}{8.314\mathrm{Z}}\right)\left(\frac{1}{\mathrm{n_T}} + \frac{\mathrm{k-1}}{\mathrm{k}} - 1\right)\right]} \tag{8-4}$$

The efficiency is calculated with respect to the obtained gas properties by correlation (8-5).

$$\eta_{\mathrm{OD}} = \eta_{\mathrm{Ref}} \times \left[\frac{\mathrm{n_{v,OD}\,Y_{OD}(1 - k_{OD})}}{\mathrm{n_{v,Ref}\,Y_{Ref}(1 - k_{Ref})}}\right] \times \left[\frac{\mathrm{(1 + X_{Ref})k_{Ref} - n_{v,Ref}Y_{Ref}(X_{Ref} + k_{Ref})}}{\mathrm{(1 + X_{OD})k_{OD} - n_{v,OD}Y_{OD}(X_{OD} + k_{OD})}}\right] \tag{8-5}$$

This equation calculates the efficiency as a function of reference efficiency, compressibility functions and polytropic and isentropic exponents. However, this model does not consider the effect of the variation in the flow coefficient, so it has to be corrected. Accordingly, the calculated efficiency is substituted in formula (8-6) to derive the pressure ratio.

$$\frac{PR_{Ref}}{PR_{OD}} = \frac{\left[\frac{MW_{OD}\psi_{w_{Ref}}(k_{OD}-1)\times \mathrm{U}_{OD}{}^2}{8.314\, Z_{OD}\, T_{1OD}k_{OD}} + 1\right]^{\frac{k_{Ref}\eta_{Ref}}{k_{1Ref}-1}}}{\left[\frac{MW_{Ref}\psi_{w_{OD}}(k_{Ref}-1)\times U_{Ref}{}^2}{8.314\, Z_{Ref}\, T_{1Ref}k_{Ref}} + 1\right]^{\frac{k_{OD}\eta_{OD}}{k_{OD}-1}}} \tag{8-6}$$

To account for the effect of the change in the flow coefficient, the calculated pressure ratio from equation (8-6) is substituted in correlation (8-7) to correct the efficiency with respect to the new work coefficient.

$$\eta_{\mathrm{OD}} = \eta_{\mathrm{Ref}} \frac{Z_{\mathrm{OD}} \psi_{w_{\mathrm{Ref}}} \mathrm{MW}_{\mathrm{DP}} T_{1\mathrm{OD}} U_{\mathrm{Ref}}^{2} n_{\mathrm{v,OD}} \left(n_{\mathrm{v,DP}} - 1\right) \left(\mathrm{PR}_{\mathrm{OD}}^{\frac{n_{\mathrm{v,OD}} - 1}{n_{\mathrm{v,OD}}}} - 1 \right)}{Z_{\mathrm{DP}} \psi_{w_{\mathrm{OD}}} \mathrm{MW}_{\mathrm{OD}} T_{1\mathrm{DP}} U_{\mathrm{OD}}^{2} n_{\mathrm{v,DP}} \left(n_{\mathrm{v,OD}} - 1\right) \left(\mathrm{PR}_{\mathrm{DP}}^{\frac{n_{\mathrm{v,DP}} - 1}{n_{\mathrm{v,DP}}}} - 1 \right)} \qquad \textbf{(8-7)}$$

In the third calculation process, the corresponding polytropic exponents and compressibility functions to the derived efficiency in the second process are recalculated. The obtained polytropic exponents (n_v, n_T) and compressibility functions (X, Y) are substituted in equation (8-5) to calculate the final efficiency value. Accordingly, the pressure ratio and polytropic head are derived using the new efficiency value. Based on the mass flow rate and polytropic head, the required shaft power is calculated by formula (8-8).

$$\mathrm{BHP}_{\mathrm{OD}} = \mathrm{BHP}_{\mathrm{Ref}} \left(\frac{\dot{V}_{\mathrm{OD}}}{\dot{V}_{\mathrm{Ref}}} \right) \left(\frac{\eta_{\mathrm{Ref}}}{\eta_{\mathrm{OD}}} \right) \left(\frac{p_{\mathrm{OD}}}{p_{\mathrm{Ref}}} \right) \left(\frac{Z_{\mathrm{Ref}}}{Z_{\mathrm{OD}}} \right) \left(\frac{T_{1\mathrm{Ref}}}{T_{1\mathrm{OD}}} \right) \left(\frac{\mathrm{MW}_{\mathrm{OD}}}{\mathrm{MW}_{\mathrm{Ref}}} \right) \left(\frac{H_{\mathrm{p,OD}}}{H_{\mathrm{p,Ref}}} \right) \qquad \textbf{(8-8)}$$

In order to model the impact of downstream equipment blockage, the discharge volume flow at the reference conditions is calculated assuming clean flow path. This value is then multiplied by the blockage percentage to identify the expected discharge volumetric flow rate at specified fouling degree. Moreover, the gas density at the compressor exit is calculated and used to obtain the expected discharge pressure. By knowing the suction and discharge pressure, the pressure ratio; polytropic head and shaft power can be calculated.

8.3 Multiphase Flow Impact on Compressor Performance

The multiphase behaviour of water and hydrocarbon mixture has been one of the main concerns of engineers due to its significant impact on the compressor performance. Several studies have been conducted to investigate the wet gas effect on the compressor performance such as Al-Yahyai et al.(2014), Svensson (2014), Bertoneri et al. (2012), Fabbrizzi et al.(2009), Hundseid et al. (2008), Shibata et al. (2008), Abdelwahab (2006), Brenne et al. (2005), Hartel and Pfeiffer (2003) and Zheng et al. (2002). In the present study, the impact on the liquid carryover on the thermodynamic parameters of the centrifugal compressor will be considered.

There two basic parameters have to be defined to describe the process gas quality which are gas volume fraction (GVF) and liquid volume fraction (LVF). Bertoneri et al. (2012) found that the compressor efficiency drops as the mass fraction of liquid increases driven by the internal losses rising as shown in Appendix (F). Besides, at constant gas volume fraction (GVF), more significant impact on the efficiency was observed at low suction pressure due to the increase in the density difference between the gas and the condensate as the inlet pressure is reduced. Furthermore, Fabbrizzi (2009) concluded that the compression characteristics of the compressor are reduced as the GVF decreases which is exactly the opposite of what Brenne et al. (2005) and Hundseid et al. (2008) found in their studies. This effect on pressure ratio will be investigated further in this study. Regarding the temperature ratio, a slight reduction was observed by Brenne et al. (2005) due to the increase in the internal energy of liquid phase and liquid evaporation as it flows through the compressor.

Another fundamental reason to study the two-phase flow behaviour is the possibility of hydrate formation which causes a flow channels blockage leading to unstable compressor operation. The hydrogen bonds in water are considerably stronger when they are compared with the hydrocarbon molecules bonds which lead consequently to low hydrocarbon solubility in water. There is very limited number of resources that can be found about the gas hydrate phenomenon since it is still not fully understood. However, the hydrate formation in both process facilities and pipelines has been one of the main concerns in gas industry as it can lead to machine shutdowns and it can also cause catastrophic damage to the internal components. Additionally, the occurrence of this phenomenon is not easily detectable in compressor systems because it does not leave any trace.

Hydrates are formed when the light hydrocarbons of the process gas mixture react with the free water at high pressure and low temperature to create a solid matrix. These hydrocarbon molecules place themselves in the empty lattice spaces in the water structure to form solid crystalline compounds which have the appearance of snow but with lower density than ice and at a higher temperature than water freezing point. From this definition, there are four key optimum conditions for hydrate formation which are:

- The presence of free water.
- Lower operating temperature than the HFT
- High operating pressure.
- The initiated turbulent flow by high gas velocity and pressure pulsations.

Therefore, it is essential to prevent these circumstances from happening in order to avoid the hydrate formation. Besides, the presence of acid gases such as CO_2 and H_2S can promote the form of hydrate due to their high solubility in water. In addition to free water, there are three main parameters are important to evaluate the possibility of hydration occurrence which are gas mixture, gas temperature and gas pressure. One way to do that is by estimating the hydrate temperature corresponding to the gas mixture and pressure. There are several empirical correlations can be found in the open literature to calculate the hydrate formation temperature (HFT) based on specific gravity and gas pressure such as Berge (1986), Motiee (1991) and Sloan (1998) correlations. One of the most common correlations in the industry is Motiee's model (1991) which estimates the HFT as a function of specific gravity and gas pressure (psi).

$$HFT(°F) = -238.24469 + 78.99667 \times \log(P) - 5.352544 \times [\log(P)]^2 + 349.473877 \times SG + 150.854675 \times SG^2 - 27.604065 \times \log(P) \times SG \qquad \textbf{(8-9)}$$

Baillie and Wichert (1987) chart is the preferred method for sour gas systems when the gas mixtures contain Carbon Dioxide and Hydrogen Sulfide with a concentration less than 50%. This chart is shown in Appendix (G), and it is limited for the gases with a specific gravity between 0.6 and 1.0 with a Propane concentration lower than 10%. The effect of propane comes in the form of a temperature correction, which is a function of the pressure and the H_2S concentration.

Towler and Mokhatab (2005) proposed another correlation for natural gases with more accurate estimation:

$$HFT\ (°F) = -13.47\ln(P) + 34.27\ln(SG) - 1.675 \times\times [\ln(P) \times \ln(SG)] - 20.35 \qquad \textbf{(8-10)}$$

Bahadori and Vuthaluru (2009) introduced a new equation for HFT calculation with a higher degree of complexity and accuracy as well. The coefficients in this model are varied based on the gas pressure (kpa).

$$\begin{aligned}\ln(HFT) = {} & (A_1 + B_1MW + C_1MW^2 + D_1MW^3) \\ & + \left(\frac{1}{P}\right)(A_2 + B_2MW + C_2MW^2 + D_2MW^3) \\ & + \left(\frac{1}{P}\right)^2 (A_3 + B_3MW + C_3MW^2 + D_3MW^3) \\ & + \left(\frac{1}{P}\right)^3 (A_4 + B_4MW + C_4MW^2 + D_4MW^3)\end{aligned} \quad \textbf{(8-11)}$$

8.4 Stage Internals and Suction Strainer Blockage: Case Study (1)

The investigated compressor is three process stages centrifugal compressor used for gas transport driven by 3.7 MW gas turbine as illustrated in figure 8-3. The first two stages consist of six impellers arranged in series with the aftercoolers and scrubbers while the third casing accommodates eight impellers.

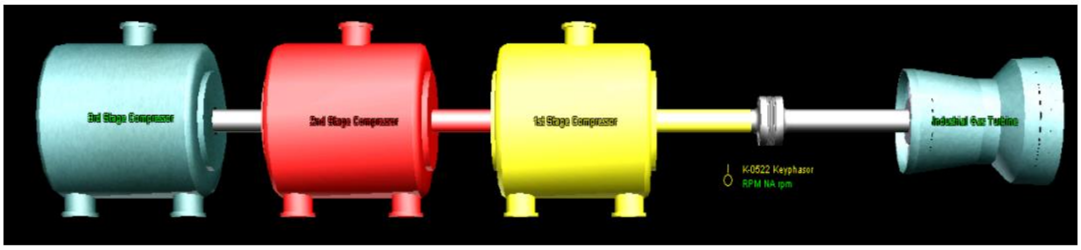

8 Impellers	6 Impellers	6 Impellers	No. Stages
178	305	305	1st Impeller Diameter (mm)
22,300	15,700	15,700	Max Rotational Speed (rpm)
190	190	190	Max Discharge Temp (°C)

Figure 8- 3: Specifications of Modelled Centrifugal Compressor

However, after start-up, the first and second stages experienced unacceptable vibration levels. Besides, the overall vibration levels of the first stage approached the danger level as shown in figure 8-4. The shaft centre line plot in figure 8-5 demonstrates an excessive rotor travel against the bearing clearance causing the shaft to come very close to the bearing surface. Besides, the X probe of the first stage indicates a distorted amplitude pattern which is probably generated by excessive bearing clearance or seal rub. Figure 8-6 shows an increase in the suction flow during the unit start-up where the dotted line indicates the shutdown time. It is clear that the stage tripped immediately after the flow reaches the rated point (325 kSCMD). Furthermore, the rotational speed trend shows that the compressor reached the trip vibration level before even reaching the normal rotating speed of about 15,264 rpm. The maximum rotational speed at full load operation is 15,700 rpm, so the machine is running at almost 92.3% of full speed. The resulted vibration level with the speed increase can be identified from shaft centre line trend and orbit plot (figure 8-5). Comparing with the normal operating pressure and temperature, the recorded pressure and temperature values prior the shutdown indicate a steady trend with a small and acceptable difference.

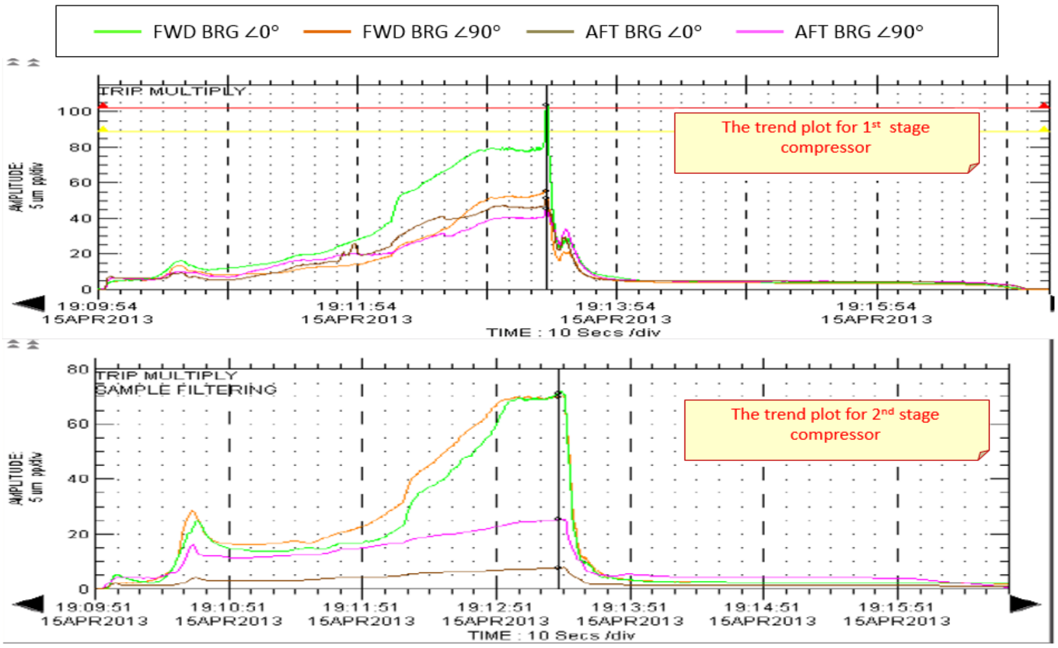

Figure 8- 4: Amplitude Readings of FWD and AFT Bearings of First and Second Stages at 14,788 rpm Rotational Speed

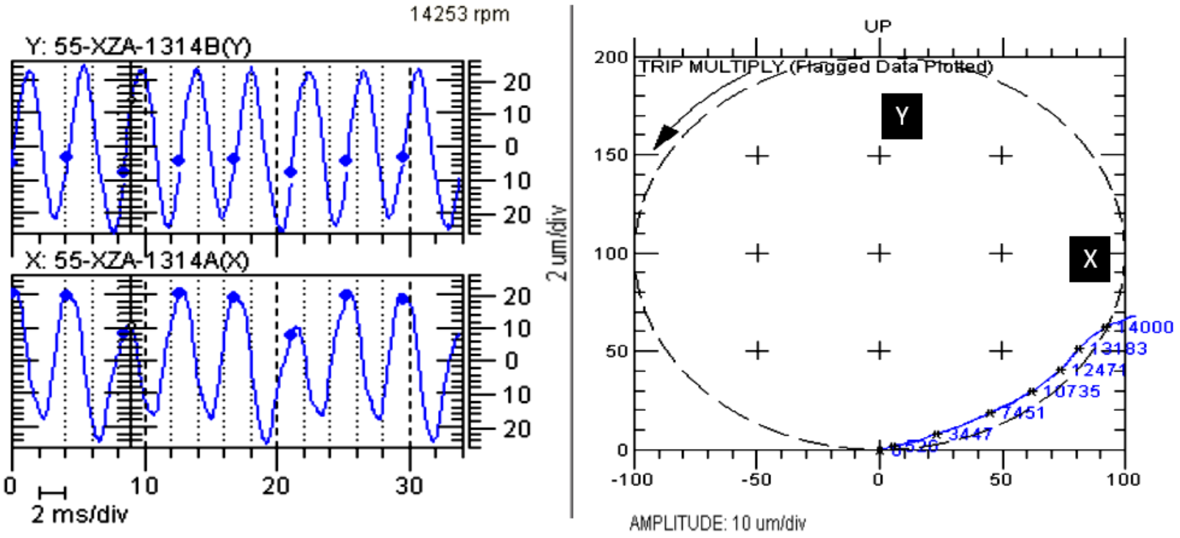

Figure 8- 5: Orbit Timebase and Shaft Centre Line Plots

The recorded averaged difference between the measured suction pressure and temperature and the design values were found about 7 kpa and 5°C, respectively. The suction pressure trend in figure 8-7 exposes a continuous and steady decline in the inlet pressure throughout the operating time. This can be owed to a deposits build up on the suction strainer of the first stage causing a higher pressure drop downstream of the strainer. In order to assess this hypothesis, the suction flow trend illustrates a slight reduction just before the trip which practically indicates a partial blockage at the suction strainer. Figure 8-8 demonstrates that the measured discharge pressure and temperature were well below the normal values. At full operating flow, the absolute discharge pressure is lower than the normal reading by about 249.8 kpa. It is obvious that the partial blockage at the suction strainer was not the only responsible factor behind this substantial reduction in the discharge pressure.

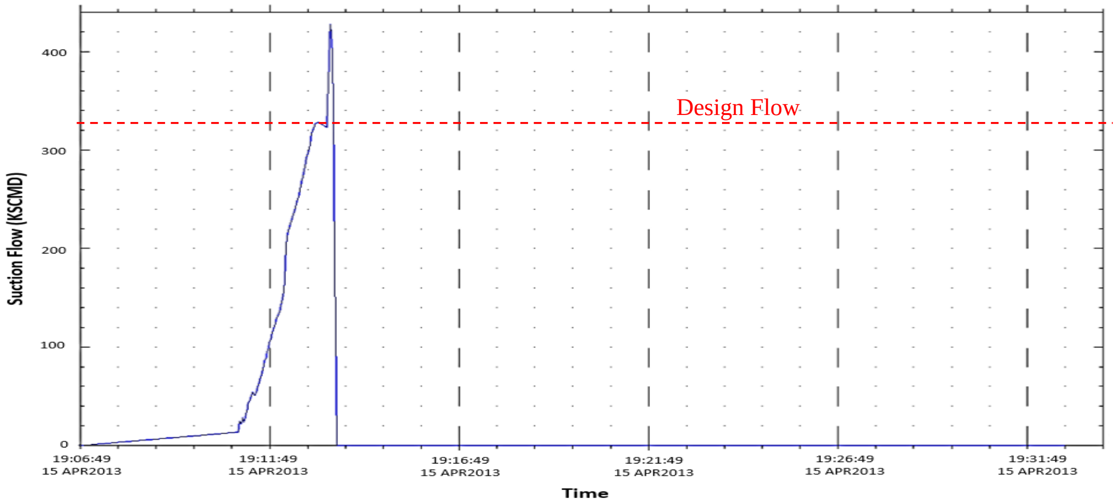

Figure 8- 6: Recorded Suction Flow of First Stage

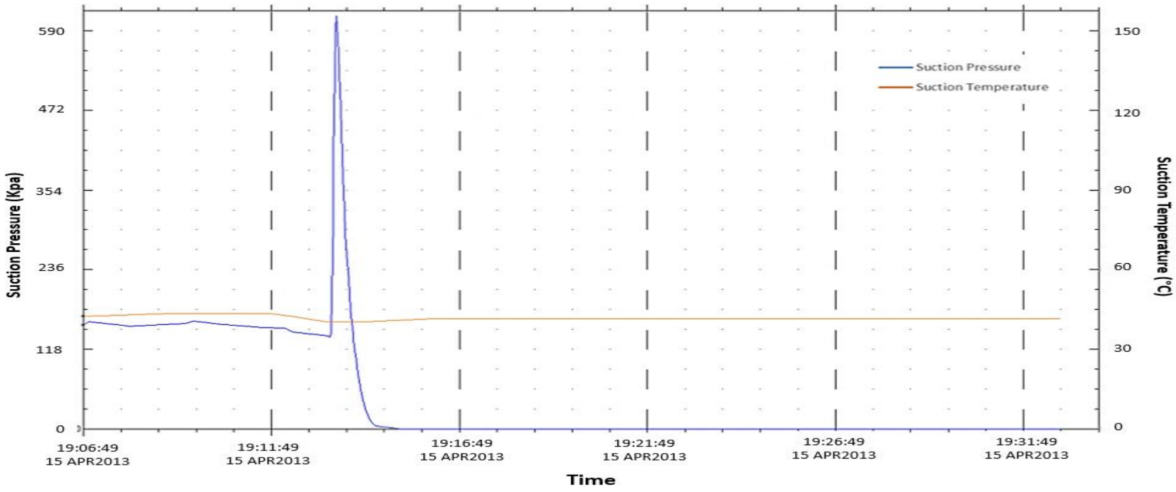

Figure 8- 7: Recorded Suction Pressure and Temperature of First Stage

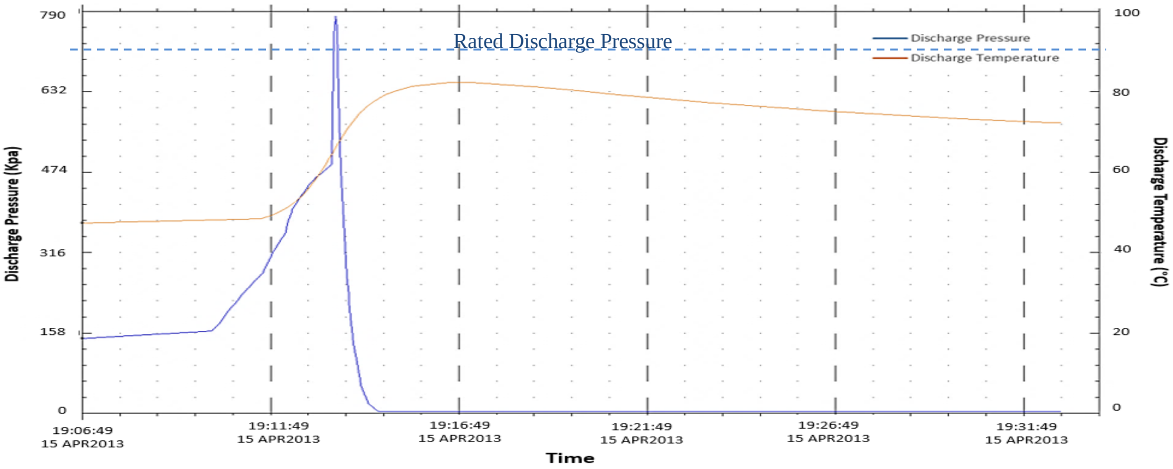

Figure 8- 8: Recorded Discharge Pressure and Temperature of First Stage

To investigate the causes of the low discharge pressure, it is necessary to consider the change in the suction parameters and gas properties. The design compressor map is corrected based on the measured operating suction pressure and temperature as shown in table 8-1.

Table 8- 1: Inlet Conditions Change From the Design Values

Suction Parameter	Design Value	Reference Value	Change Direction
Pressure (kpa)	*2.413*	*2.50*	*Increase*
Temperature (°C)	*49.0*	*42.0*	*Decrease*
Molecular Weight (g/mol)	*23.636*	*20.885*	*Decrease*
Ratio of Specific Heats	*1.2115*	*1.2455*	*Increase*
Compressibility Factor	*0.99603*	*0.99667*	*Increase*

However, the measured gas properties three months before the failure indicate a significant reduction in the gas specific gravity by about 11.7% and with a drop by around 0.709% and 4.950% in the critical pressure and temperature, respectively. The low density gas tends to have a lower discharge pressure due to its inverse relationship with the gas constant and specific heats ratio. This can be detected easily from figure 8-9(a) where the corrected performance curve moves down to lower pressure ratio values. The impact of the inlet parameters change on the overall pressure ratio is plotted in figure 8-9(b). The operating envelope shifts towards lower pressure ratio with a considerable reduction in the surge flow. However, the change in the inlet pressure and temperature and the recorded gas properties was a contribution factor, in this case study, since the measured discharge pressure is still well below the predicted value.

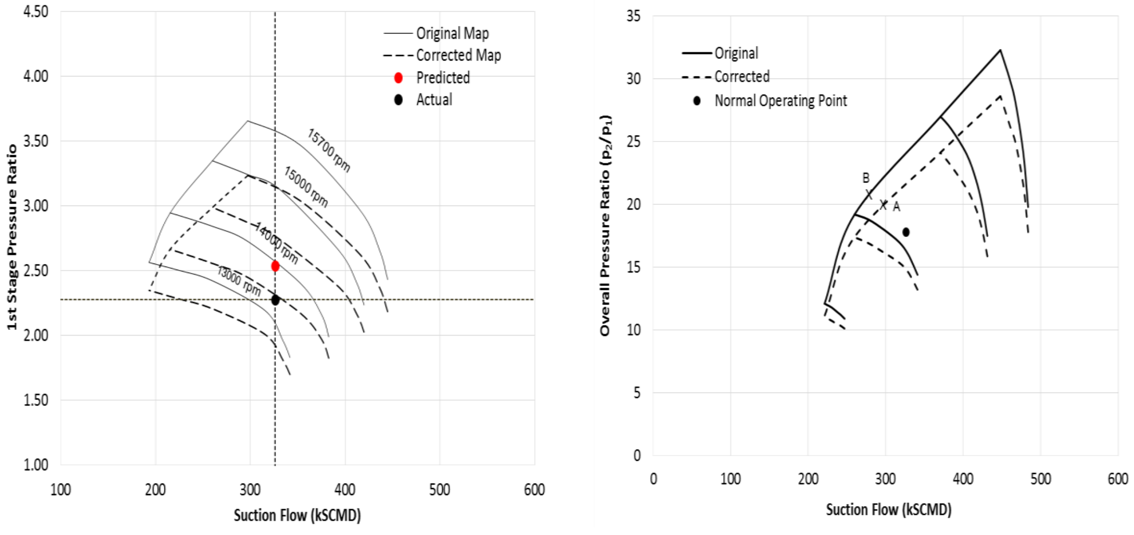

(a) **(b)**

Figure 8- 9: Correction of Design Pressure Ratio Curve According to the Reference Suction Conditions of (a) First Process Stage (b) Overall Compressor Map

This requires further investigation to identify the main causes of the unstable compressor operation. Considering the substantial drop in the pressure ratio, the effect of three different factors will be analysed including:

- Unanticipated change in the gas properties.
- Flow blockage at stage internals and suction strainer.
- Damaged stator or rotor blades.

The flow of light molecular weight hydrocarbons reduces the gas density which leads to lower discharge pressure. Therefore, the variation in the gas molar mass can obviously create a fluctuation in the pressure value. Figure 8-10(a) illustrates the change in the operating discharge pressure due to the variation in the gas molecular weight at the measured rotational speed. It was found that the actual discharge pressure is predictable at estimated molar mass of 12.7 g/mol which is lower than the recorded value (20.885 g/mol) by about 39%. This difference is fairly high and it is out of the expected range. Another way to evaluate the contribution of molecular weight change is by comparing the estimated and actual discharge temperatures. Despite the reduction in the pressure ratio, figure 8-10(b) demonstrates a significant deviation between the two temperature values driven by the substantial efficiency drop at low specific gravity.

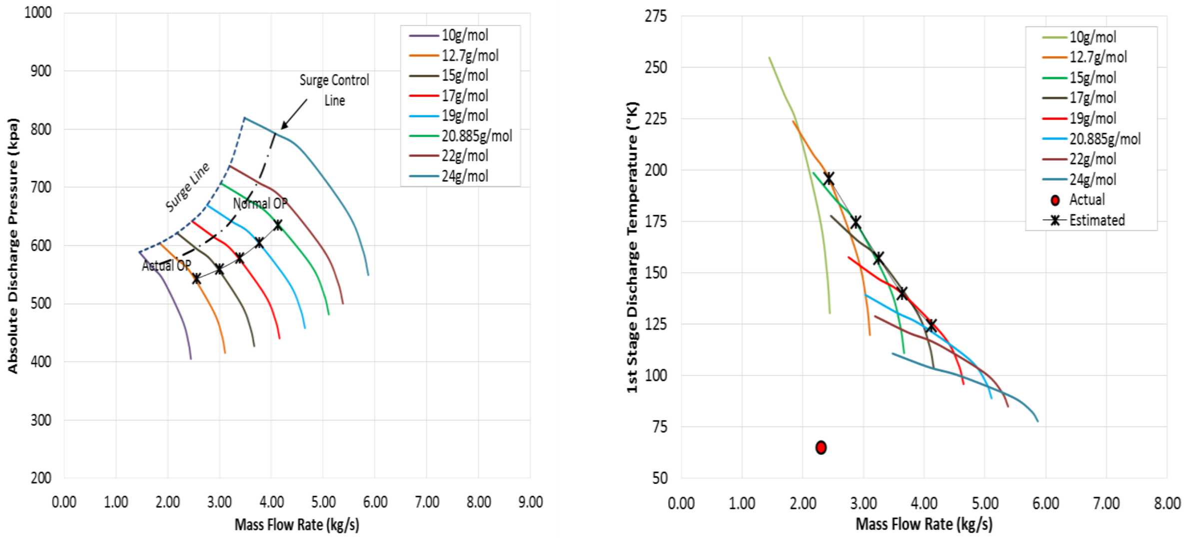

(a) **(b)**

Figure 8- 10: Comparison Between Predicted and Actual Discharge Temperature Based on Molecular Weight Change

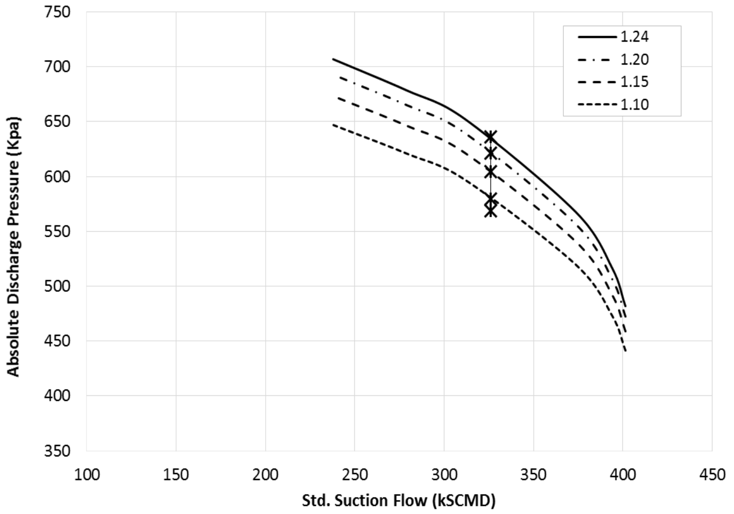

Figure 8- 11: Effect of Ratio of Specific Heats on the Pressure Ratio of First Process Stage

The predicted temperature at the measured discharge pressure was found approximately 196°C while the actual value was around 65°C. This substantial difference leads to exclude this assumption. However, it should be noted that non-calibrated flow instrumentation can cause the measured flow to be higher than actual flow. Therefore, it is important to check the conditions of all instrumentations around the compressor before analysing the recorded data. Despite the fact that the change in specific heats ratio and molecular weight happen simultaneously, the impact of k value on the compressor discharge pressure is shown in figure 8-11 assuming a constant molecular weight. The low k-value reduces the stage pressure ratio leading to lower discharge pressure. However, the measured discharge pressure was found out of the possible range which, in fact, supports the previous findings.

The next assumption which will be considered is a possibility of the blockage in the internals of the first stage. The fouling can occur in the first stage flow internals or the downstream system of the first stage such as aftercooler and the scrubber. The fouled aftercooler will create a higher flow resistance to the discharge flow from the first process stage due to the back pressure. This will create a build-up pressure region at the first stage discharge leading to higher exit pressure which is not the case in this compressor.

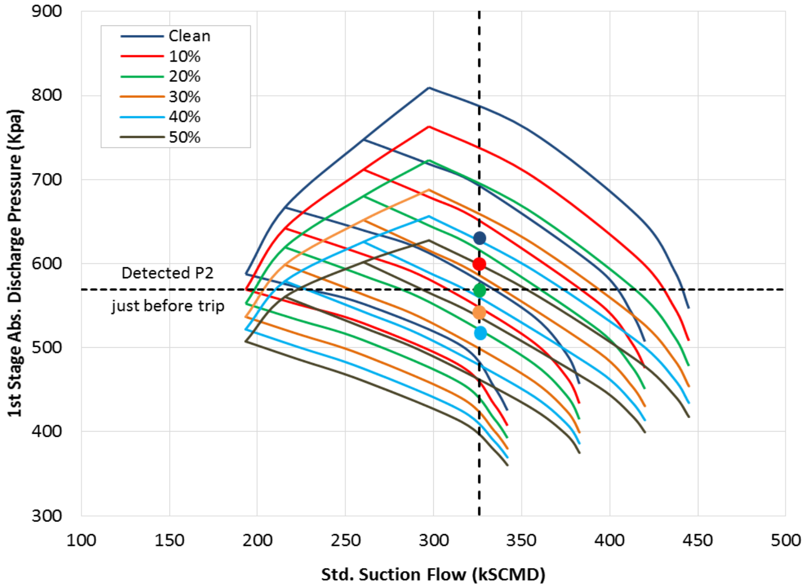

Figure 8- 12: Effect of First Stage Blockage on the Discharge Pressure At Variable Speed and Reference Conditions

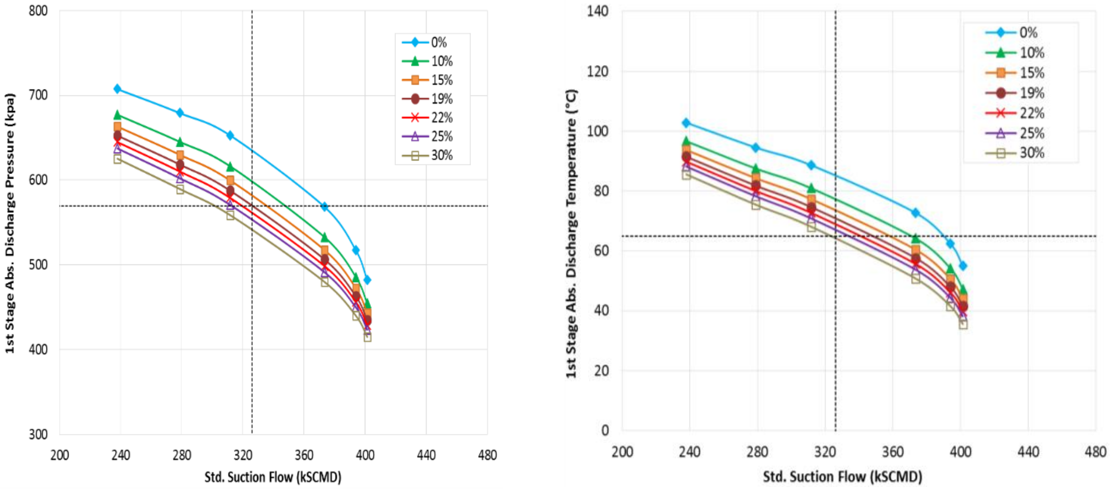

(a) (b)

Figure 8- 13: Effect of First Stage Blockage on the Discharge Pressure and Temperature at 14,500 rpm Rotational Speed and Reference Conditions

The impact of the flow blockage in the first stage internals on the stage discharge pressure is illustrated in figure 8-12. An interesting observation is that the identical discharge pressure is predicted at the same suction flow at the blockage percentage between 15% and 20% from the total flow channel. The iteration process is performed to match the deducted discharge pressure, and the predicted fouling percentage was found roughly 19% as shown in figure 8-13(a). Practically, it was found that the first impeller is highly subjected to fouling comparing with the downstream impellers since it received the carried deposits immediately after flowing through the IGVs.

To evaluate the contribution of internal fouling on the low discharge pressure, the estimated discharge temperature is plotted for different blockage percentages as shown in figure 8-13(b). Unlike the gas density effect, the stage discharge temperature was found lower at higher fouling degrees. Furthermore, the estimated discharge temperature at a blockage percentage of 19% was found closer to the measured value with only 6ºC differences. This can be due to two reasons: inaccurate estimation of the temperature polytropic exponent or as a result of specific heats ratio (k) change. The performed iteration process to match the actual discharge temperature using the specific heats ratio variation principle revealed that the actual discharge temperature is predictable with k-value of about 1.22 as shown in figure 8-14.

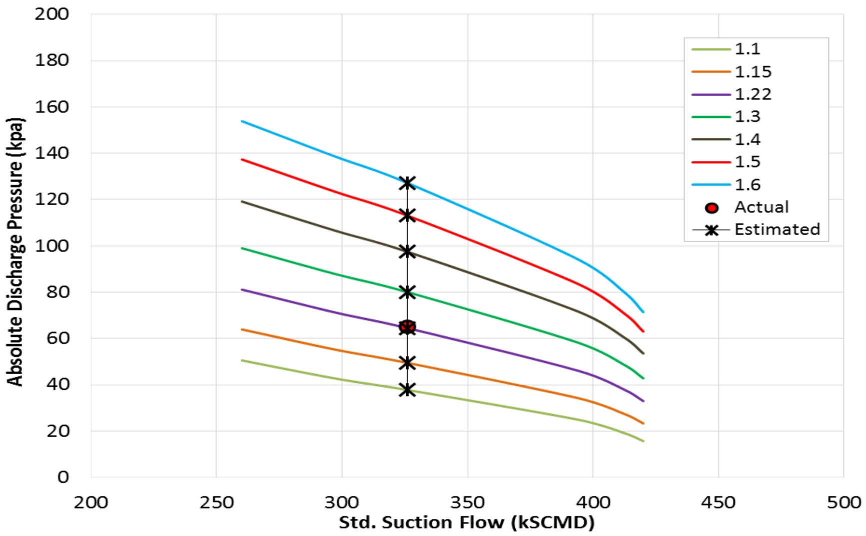

Figure 8- 14: Prediction of Detected Discharge Temperature of First Process Stage Based on Specific Heats Ratio Variation at 19% Blockage Percentage

This value is lower than the reference value, but it is closer to the design value with a relative difference of approximately 0.70%. It is obvious that the blockage in the first stage internals reduces the inlet pressure of the second stage. Besides, the actual inlet flow from the intercooler becomes smaller as the blockage percentage goes up. Therefore, the second stage is working with higher pressure ratio as the flow blockage grows.

From figure 8-8, there is a continuation of the discharge temperature rise after the compressor trip for about 2 minutes before it started to fall gradually. This behaviour of discharge temperature can be caused by the reduction in the gas volume which leads to lower Reynolds number and higher frictional losses. The discharge temperature is normally balanced between the temperature rise due to the friction and the temperature drop due to the gas expansion. So, the high fluid friction is an evidence for internal flow blockage which can be caused by either deposits or hydrates. To validate the developed methodology in Appendix (H), the hydrate formation assumption will be assessed.

The hydrate formation leads to raise the discharge temperature with a reduction in discharge pressure and flow rate as aforementioned in section 8.2. To evaluate the possibility of hydrate formation, the suction temperature and the HFT have to be checked. However, figure 8-7 does not indicate any sign for suction temperature drop at this time which does not support the hydrate assumption. Besides, the reduction in flow rate and discharge pressure in the current case is driven by the machine shutting down. Furthermore, the HFT is calculated corresponding to the suction pressure using three different models, and the results are compared with the HYSYS results. Figure 8-15 compares the estimated HFT using different approaches corresponding to suction pressure and at various molecular weight. HYSYS code is based on Baillie-Wichert method while Bahadori-Vuthaluru model is not used due to the limitation in gas pressure range. It is clear that the suction pressure is not high enough to form the hydrates at the detected temperature. Besides, the measured discharge temperature is significantly greater than the HFT according to all three approaches.

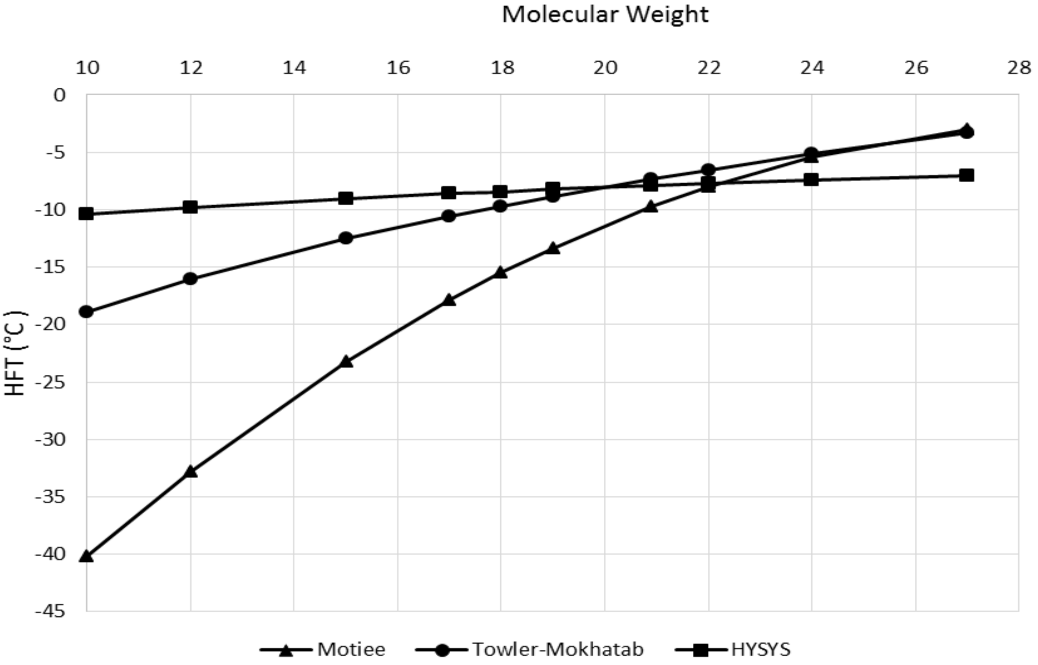

Figure 8- 15: Determination of HFT Using Different Approaches

In addition to the resulted damages to the compressor internals, the fouling causes a significant increase in the power losses and the associated operating cost. The low efficiency value raises the demanded power of the fouled unit as demonstrated in figure 8-16. However, this incremental increase in the input power is dissipated in the form of pressure losses since the overall developed pressure ratio is lower than the normal. From the economic perspective, this is revealed in very quickly growth in the operating cost as shown in figure 8-17. The presence of deposits in the first stage internals can cause an increase in the operating cost by about $95,300 and $133,300 at 30% and 40% blockage percentage, respectively. Thus, the earlier detection of fouling and the quick corrective action can save a lot of money. Besides, as the fouled area increases, the consequential rise in the power cost goes up which can be avoided by fixing a regular compressor cleaning. Furthermore, the high degree of fouling reduces the lifetime of the internal components which should be taken into the consideration. However, one of the disadvantages of the developed method is that it cannot be used to predict the exact location of flow blockage within the first stage internals.

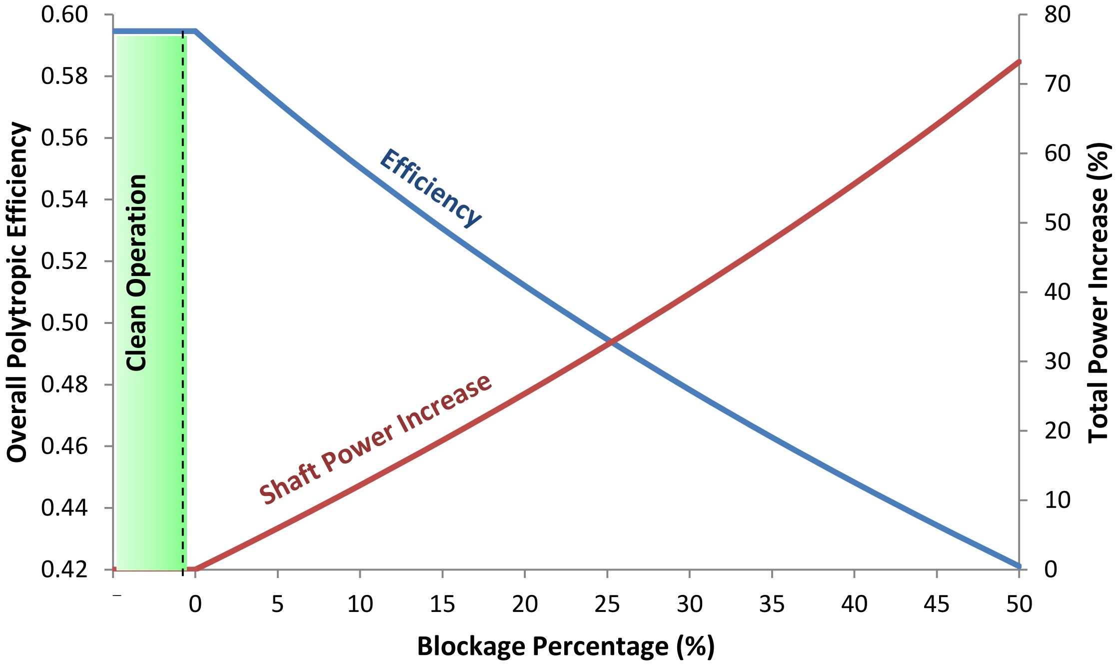

Figure 8- 16: Effect of First Stage Blockage on Overall Efficiency and Shaft Power at Normal Operating Point

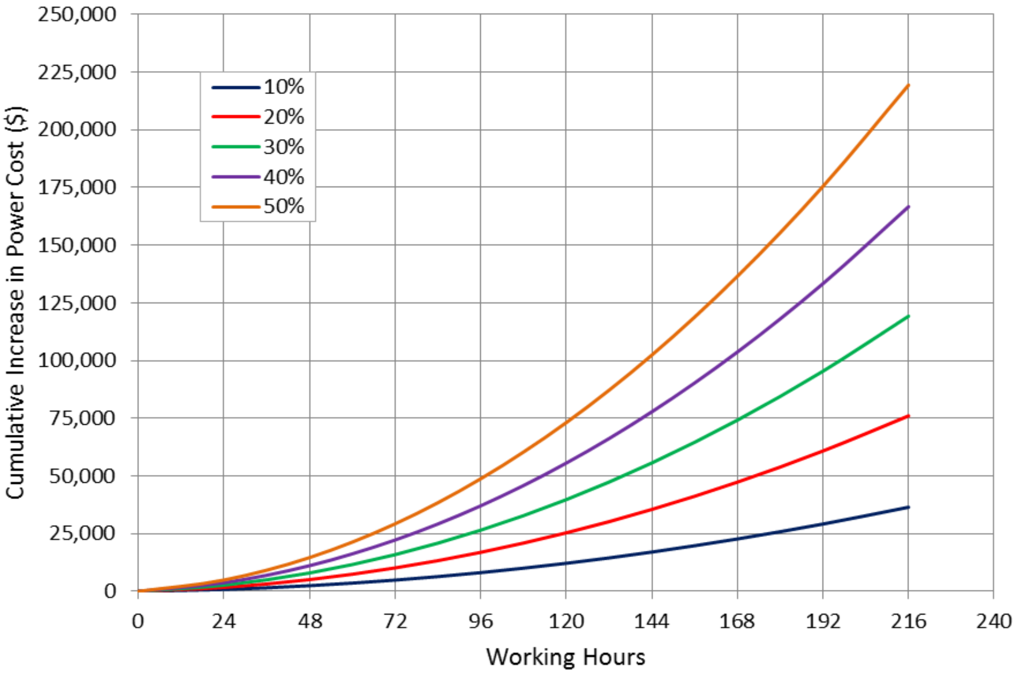

Figure 8- 17: Growth of Cumulative Power Cost Due to Internal Blockage of First Process Stage at Inlet Power Cost of 0.06$/KWh(e)

The internal inspection during the first stage overhaul revealed heavy deposits in the first impeller as illustrated in figure 8-18(a). The observed solid contaminations are of different sizes with no corrosion or erosion damage on the flow passages surface which can affect the mechanical integrity of the blades. This can be also identified by checking the impeller desk which does not show any initiated crack on its surface. A fast accumulation rate of these contaminations on the impeller flow passages raises the vibration to a trip level which causes an immediate shutdown of the machine after a couple of hours after starting up. This can be confirmed by the recorded amplitude curve of the first stage afterward bearings and the excessive axial shaft displacement in figure 8-5.

(a) **(b)** **(c)**

Figure 8- 18: Heavy Deposits in First Impeller, IGV and Suction Strainer of First Process Stage

Some non-sticky deposits were also found in the inlet guide vanes with no evidence for damage or corrosion as shown in figure 8-18(b). Moreover, a partial blockage was observed in the suction strainer caused by heavy deposits as demonstrated in figure 8-18(c). This explains the rise in the suction flow during the investigated period. However, the observed approximated blockage percentage was found slightly greater than the predicted value by the developed model. Moreover, there is no sign for the gas polymerization at the detected operating conditions. For further check, the polymerization formation temperature should be calculated and compared with operating temperature which has to be lower to eliminate this assumption. However, this becomes difficult without specifying the deposits and surface materials, so it requires more investigation.

8.5 Fouled Aftercooler Effect on Compressor Performance

One way to indicate the fouled aftercooler is by monitoring the pressure drop and temperature difference between the intermediate process stage inlet and first process stage exit gas. The high inlet temperature to the second stage is a symptom of fouled upstream cooler which leads to increase the required polytropic head to achieve the same pressure ratio. Thus, the low polytropic efficiency causes the demanded power to increase. Besides, the fouled coolers in variable speed drivers can cause a rise in the driver speed. However, it is recommended to consider the effect of the variation in the front stage suction temperature on the cooler discharge temperature. Besides, the pressure drop of the fouled cooler is higher than the normal due to the greater frictional and heat losses. Figure 8-19(a) demonstrates the increase in the discharge pressure of the first stage pushed by the greater flow resistance at discharge side as a result of effective flow area reduction. Comparing with the internal fouling, the fouled cooler has more significant effect on the stage discharge pressure. This can be observed clearly from figure 8-19(b) in which the operating point reached the surge point at 15% blockage percentage only. Figure 8-19(c) illustrates a higher slope of the front stage discharge pressure against the efficiency reduction. This indicates a greater impact of the fouled cooler on the discharge temperature comparing with its effect on power.

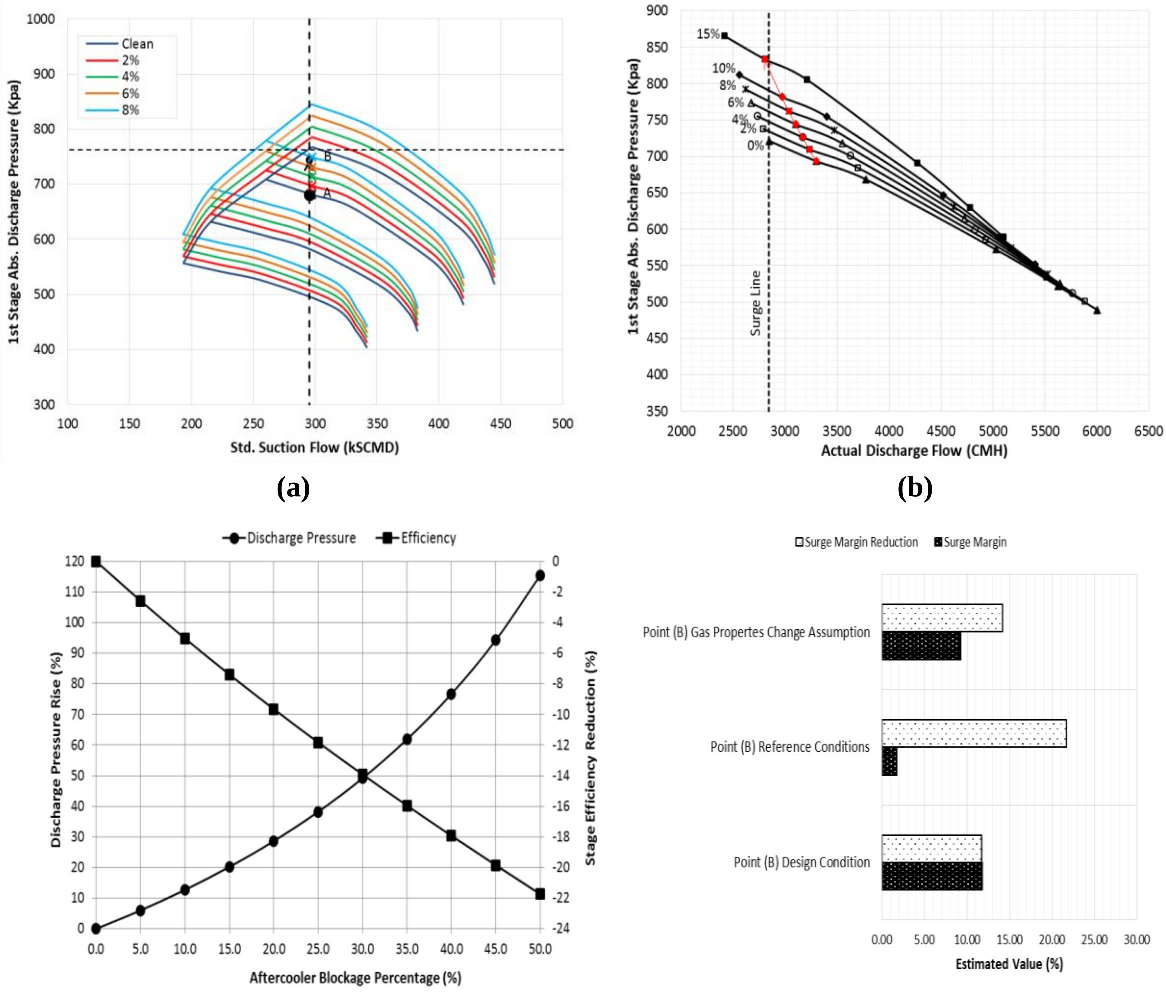

(a) (b)

(c) (d)

Figure 8- 19: Effect of Aftercooler Fouling on First Stage Performance: (a) Discharge Pressure at Various Speeds (b) Operating Point and Constant Speed Line (c) Discharge Pressure Rise and Efficiency Reduction (d) Surge Margin of First Process Stage

Figure 8-19(d) compares the predicted surge margin reduction when the discharge pressure increases from point A to point B using gas properties change and fouled aftercooler assumptions. A larger surge margin reduction was detected when the first stage was operating with a fouled aftercooler comparing with the measured drop as a result of sudden gas molecular weight rise.

8.6 Overload Operating Condition Case Study (3)

The first process stage of the previous compressor train tripped at high vibration level. The suction pressure is lower than the normal by about 15.3 kpa(a) as demonstrated in figure 8-20. Besides, the recorded averaged inlet temperature is lower than the reference point by approximately 14ºC.

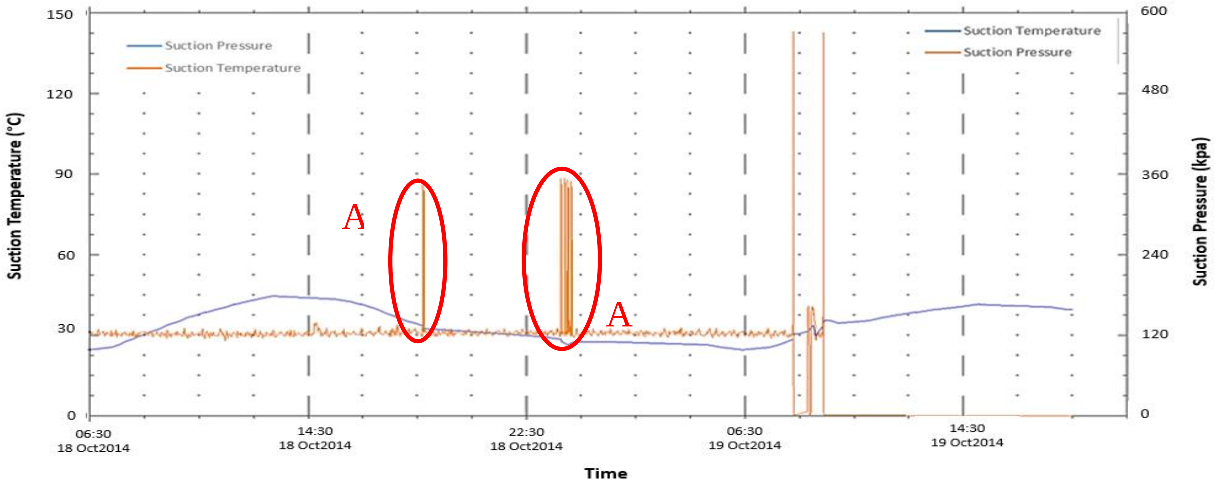

Figure 8- 20: Measured Suction Pressure and Temperature

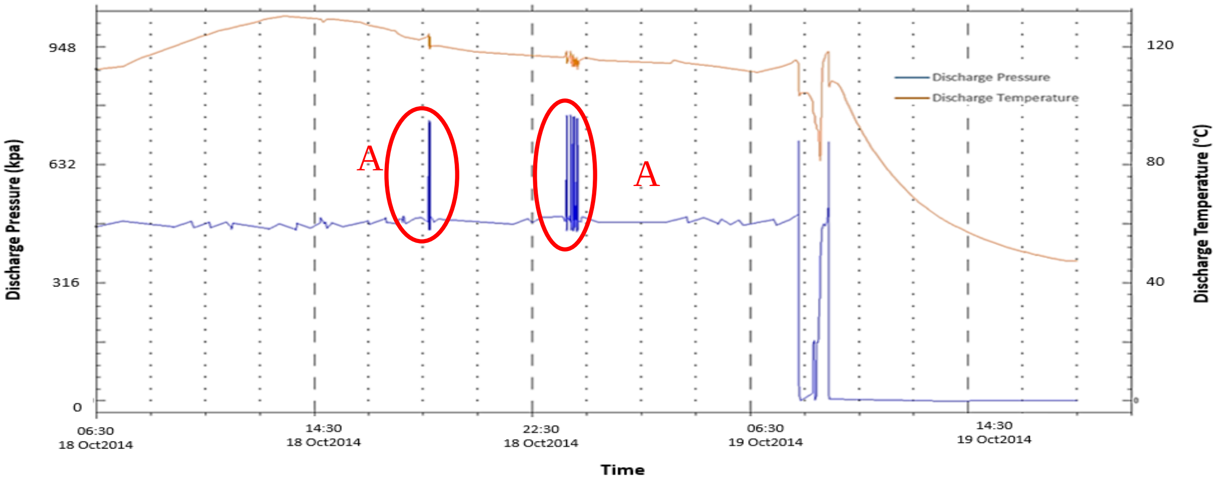

Figure 8- 21: Measured Discharge Pressure and Temperature

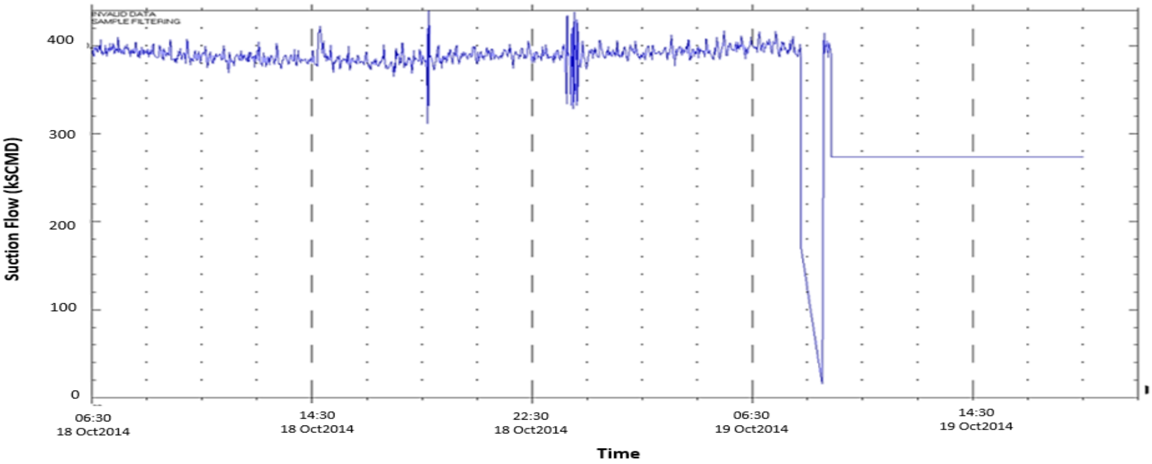

Figure 8- 22: Recorded Suction Flow

On the other hand, the generated discharge pressure in figure 8-21 was considerably lower than the normal at such inlet conditions by about 151 kpa(a). Unlike the first case study, the discharge temperature was found extremely higher than the expected value at the recorded discharge pressure. Besides, the rotational speed was also greater than normal reaching to around 15,500 rpm which is roughly 98.7% of maximum speed value. This indicates an increase in the required polytropic head. Furthermore, the suction flow is significantly exceeding the normal flow by about 24.1% as demonstrated in figure 8-22. At constant speed, the high flow pushes the operating point towards the choke end leading to lower pressure ratio value. However, it is important to investigate the reasons which pull the compressor into high flow region.

By reviewing the operational data prior the failure, the gas density was low at the LPC suction. Besides, the unit was running at significantly lower suction temperature and pressure for around 48 hours, but the impact of the decreased pressure was more significant. Furthermore, it is evident that the compressor is working at overload condition throughout the specified operating period.

There is no clear reason beyond the high increase in the suction flow, but it can generally happen due to several causes which have to be investigated including:

- Process changes
- Parallel compressor trains
- Excess driver power due to alternate operating conditions
- Performance degradation
- Unanticipated gas characteristics change

The process conditions are subjected to change during the operating life of the compressor. The increase in the incoming flow to the compressor pushes the operating point towards the overload condition yielding a lower discharge pressure as shown in figure 8-23(a).

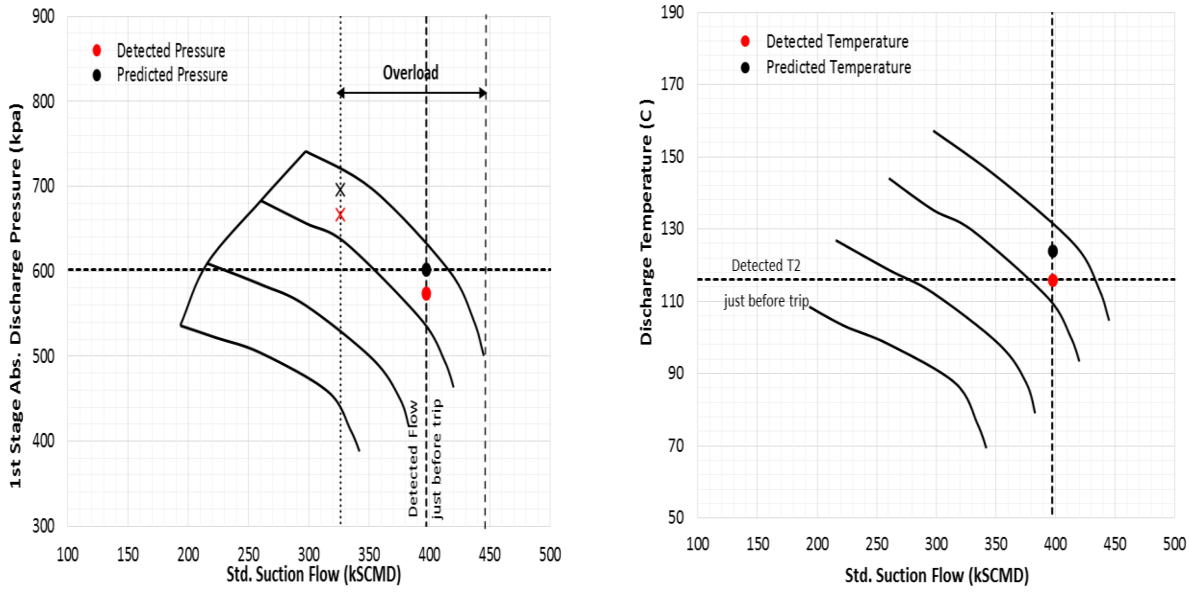

(a) **(b)**

Figure 8- 23: Comparison Between the Predicted and Measured Discharge Pressure and Temperature at Reference Conditions

The dot points indicate the predicted and measured pressure values at the detected flow while the cross marks denote the pressure at the same rotational speed but at the normal flow. The measured discharge pressure value at the field was found slightly lower than the predicted value by approximately 28 kpa(a). The speed controller raises the rotational speed to high value reaching to about 99% of maximum speed. This will allow the impeller to impose a higher work into the flowing gas to sustain the pressure ratio. The estimated discharge temperature was found slightly greater than the actual value by about 8 degrees centigrade as demonstrated in figure 8-23(b). There is no doubt that the high predicted discharge pressure contributes to this elevated temperature value, but it is also influenced by the inlet specific heats ratio which could be changed during this running time.

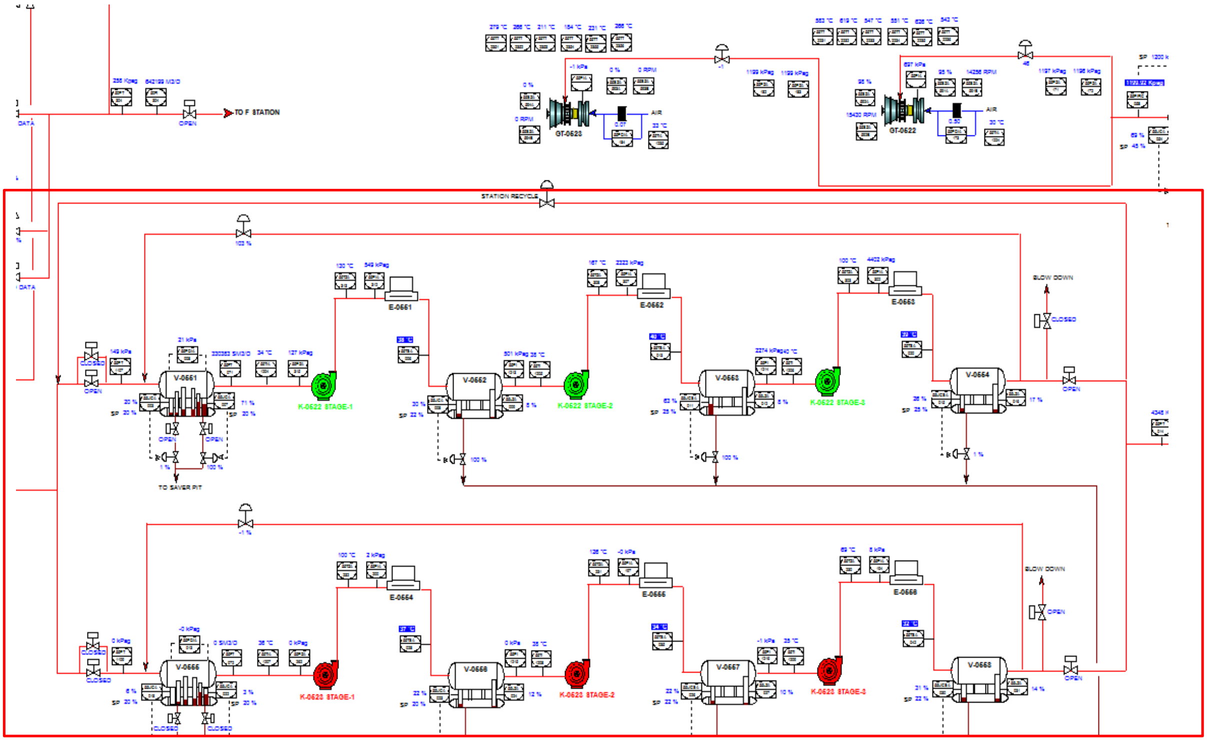

Figure 8- 24: Process Diagram of the Compressor Investigated

Although that this compressor is working in parallel with another multi-stage centrifugal compressor as illustrated in figure 8-24, the first compressor is in service and it is operating normally; thus, it is not expected to cause any increase in the suction flow of the studied compressor. However, it is possible to operate the compressor in overload conditions for extended periods of time when one of the conducted lines is off to maintain the production requirements, but this will deteriorate the compressor performance. Besides, it is normal practice to rate the gas turbine based on the highest expected inlet temperature. The estimated increase in the power can reach to about 10.56 % when the inlet temperature drops from 49ºC to 30ºC. However, by reviewing the historical data including the case in section 6.6, the flow at very close inlet temperature to the current reading was found substantially lower than the detected value. Another possible cause of overload operation is the deterioration of the front stage performance which, in turn, leads to a higher discharge volumetric flow rate.

If the performance degradation is substantial, the subsequent stages will receive significantly higher flow than the expected, so that they will operate at or near the choke condition. However, since the existing case is focusing on the first process stage, this reason can be ignored. Furthermore, the compressor inlet volume is also influenced by the gas characteristics at the station. The decrease in the gas molar mass causes the gas density to reduce which leads to increase the volumetric flow rate. The effect of the gas specific gravity on the operating point is illustrated in figure 8-25(a) which shows a shift towards the high flow region. The conducted iteration process revealed a total change by 3.5 g/mol in the gas molecular weight at the measured suction flow value. To validate this hypothesis, the discharge temperature is predicted at the obtained molar mass value, and it is compared with the actual value as shown in figure 8-25(b).

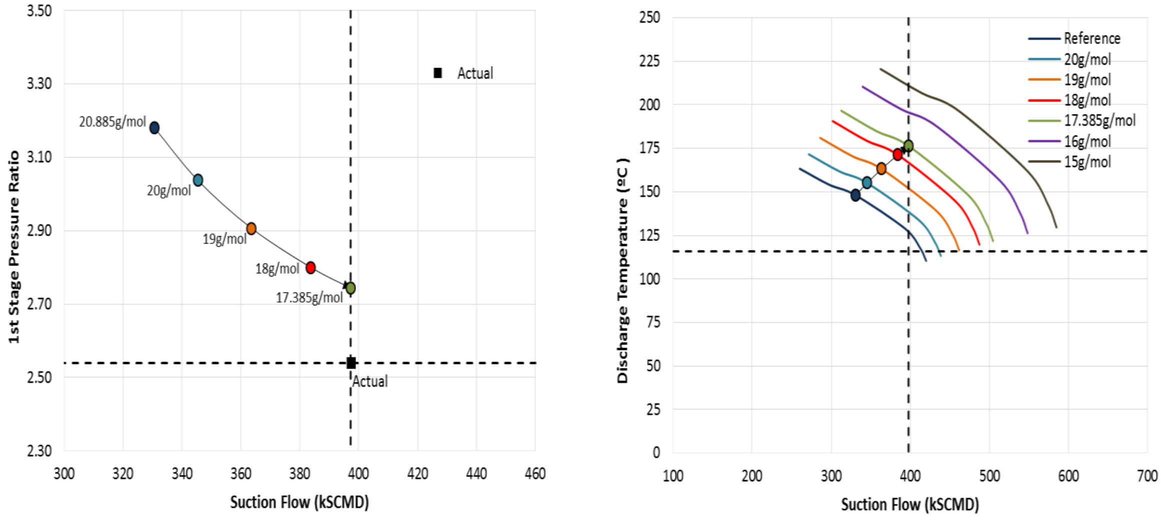

(a) **(b)**

Figure 8- 25: Impact of Gas Molar Mass at Detected Rotational Speed on (a) Stage Pressure Ratio (b) Discharge Temperature

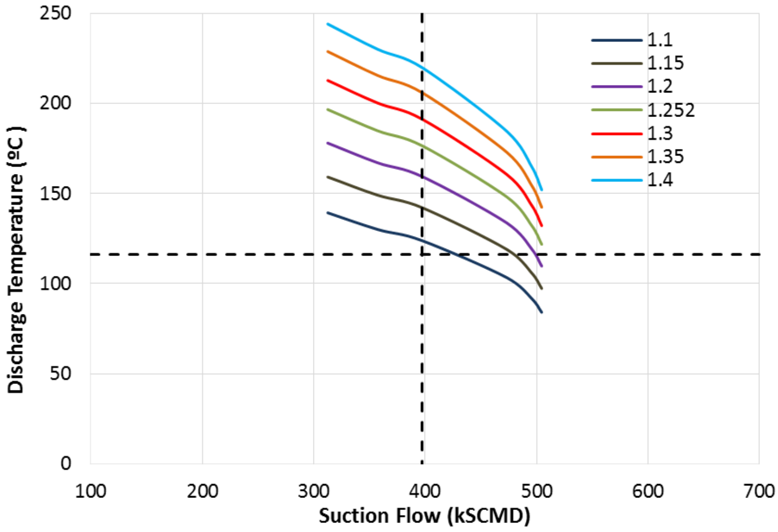

Figure 8- 26: Impact of Gas Molar Mass on Discharge Temperature at 17.385 g/mol

The discharge temperature at low molecular weight value is affected by two variables: the higher discharge pressure which raises the equivalent discharge temperature, and the flow rate increase which on the other hand leads to reduce the discharge temperature. The predicted discharge temperature was found higher than the actual value by approximately 35.5ºC. This difference between the predicted and measured discharge temperature can be caused by three possible reasons: change in specific heats ratio, low measured discharge pressure and the contribution of low k-value and high discharge pressure. Based on the first assumption, an iteration process is performed to predict the actual discharge temperature value based on specific heats ratio variation. The measured temperature value at the first stage discharge is unpredictable even at very low k-values as shown in figure 8-26 which in this case supports the hypothesis of low generated discharge pressure.

The deterioration in the compressor discharge pressure indicates a flow blockage in the first process stage. Unfortunately, there is no available data for compressor power, but the power trend is expected to be unstable due to the increased flow rate, lower measured pressure ratios than the actual and the internal recirculation in the first process stage. To examine the possibility of flow blockage at suction side, it is necessary to consider the suction flow trend. Figure 8-22 demonstrates a noticeable fluctuation in the suction flow reading with a gradual drop in the flow value from the starting point. This supports the previous hypothesis, and it might be an indication of the partly blocked suction strainer. Based on the internal blockage assumption, there are two scenarios will be evaluated:

Case 1: Overload due to process conditions variation.

Case 2: Overload operation to accommodate an unanticipated gas properties change.

According to the first scenario, figure 8-27(a) illustrates the change in the discharge pressure and operating envelope at reference conditions using different blockage percentages. The measured discharge pressure value is predicted at a blockage percentage of around 6.2%, and the corresponding discharge temperature was found two degrees less than the actual value (figure 8-27b). Therefore, both predicted discharge pressure and temperature are very close to the actual values which, in fact, supports the hypothesis of internal deposits and process conditions upsets.

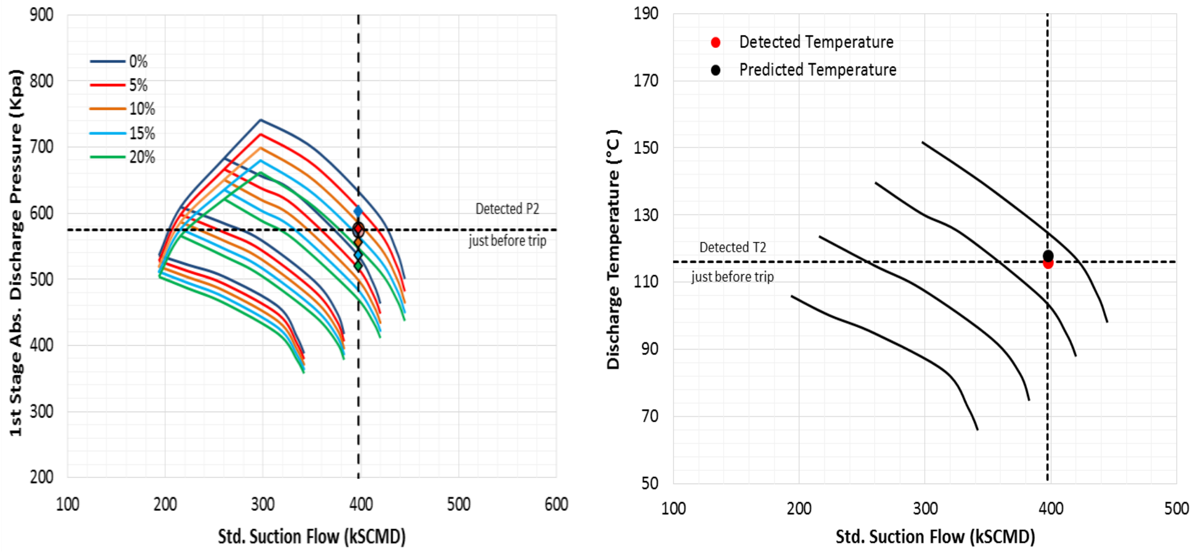

(a) (b)

Figure 8- 27: Prediction of Measured Discharge Pressure at Reference Conditions using Internal Blockage Assumption at (a) Variable BP (b) 6% BP

Considering the second case with gas characteristics change, figure 8-28 shows a higher fouling degree than the previous case with an estimated blockage percentage of 11%. Furthermore, the discharge temperature is significantly greater than the actual by about 44 degrees as illustrated in figure 8-29(a). However, this can also be due to specific heats ratio change; thus, the variation in discharge temperature with k value is plotted in figure 8-29(b). The obtained results demonstrate that the actual discharge temperature can be met by setting the specific heats ratio to about 1.1 which is not valid for such operating conditions.

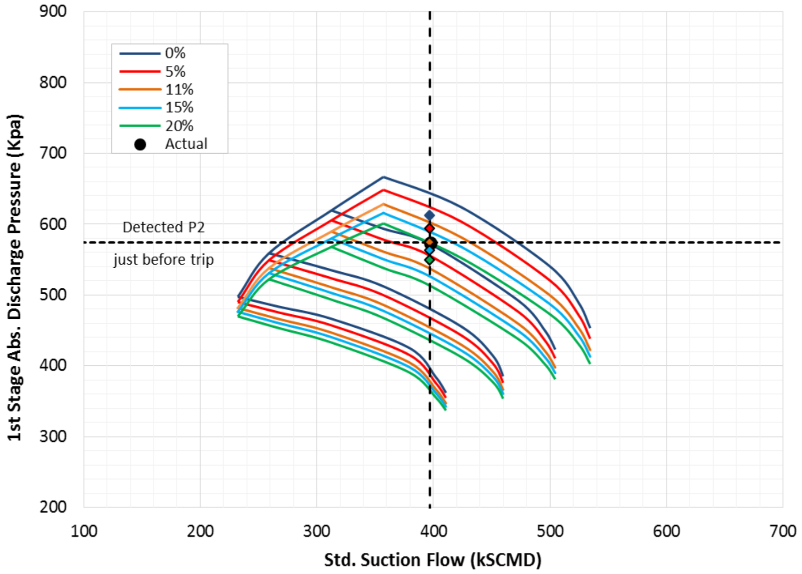

Figure 8- 28: Prediction of Measured Discharge Pressure at 17.385 g/mol using Internal Blockage Assumption

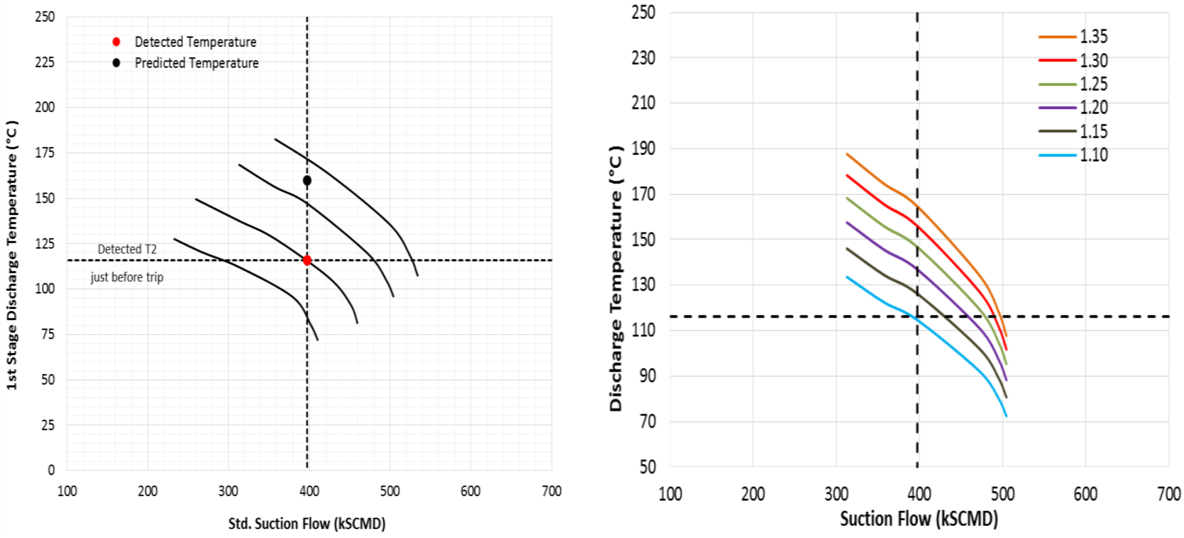

(a) **(b)**

Figure 8- 29: Prediction of Discharge Temperature at 17.385 g/mol and 11% Blockage Percentage at: (a) k=1.252 (b) Variable k-Value

Thus, the results of second scenario optimisation do not agree with the provided operation data, and it is most likely that the compressor was running in high flow region due to the changes in the process conditions. At high incidence angle, the flow separation reduces the effective flow area and generates higher pressure losses which might be the cause of the drop in the pressure ratio value. Furthermore, the high inlet flow velocity creates excessive forces on the IGVs and first impeller surfaces which might lead to vane fracture. The loss of material created an unbalanced state on the rotor leading to high radial vibration. Therefore, the compressor has to be taken offline for repair. This could also explain the increase in the radial vibration level of first and second process stages. To check for any damages in the IGV, the stage overhauling has to be conducted.

Looking again at the discharge pressure trend in figure 8-21, there is a sharp increase in the discharge pressure value for a very short time as indicated by (A). This indicates a high density value of the handled fluid which is usually attributed to the low gas volume fraction. The discharge temperature trend shows a slight decrease at this point. Furthermore, figure 8-22 illustrates a significant fluctuation in standard flow rate driven by the gas mass flow rate alteration. This variation can imply a variation in the fluid quality, so it started to drop when the liquid is contained within the flowing gas then it increased once the phase transition began. The small amount of heat was probably used to heat up the liquid and for phase transfer from liquid to gas. Besides, the short period in which the fluctuation in the pressure and temperature occurred can denote the presence of small droplets of liquid that require limited evaporation phase transition through the compressor. This is likely accompanied by a reduction the compressor efficiency which should be observed in term of high shaft power and lower pressure ratio. However, since the power trend is not available, the pressure ratio is used to assess the possibility of wet gas at this running time. From the suction and discharge pressure trends, the pressure ratio dropped from around 2.54 to 1.889 which supports the findings of Michelangelo's study (2009) and disagrees with the conclusion of Brenne et al. (2005) and Hundseid et al. (2008). It is obvious that the pressure ratio increases as the GVF decreases due to the density rise of the processed fluid. However, the influence of wet gas on the pressure ratio is also affected by another parameter which is the difference between the two phases densities.

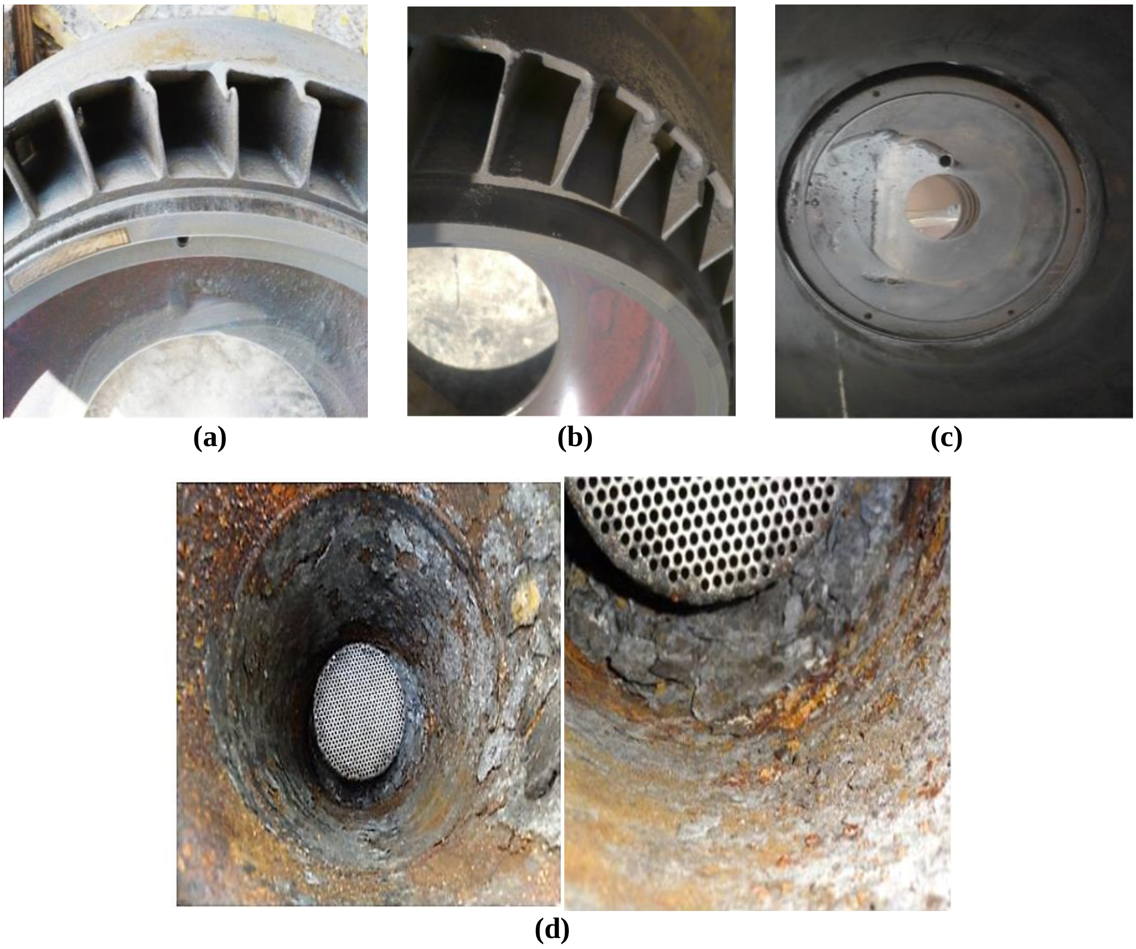

(a) **(b)** **(c)**

(d)

Figure 8- 30: Internal Inspection Findings of First Stage Overhauling: (a) Observed Deposits on First Impeller (b) Thin Deposits Layer on IGVs During (c) Liquid Carryover in the First Stage Casing (d) Heavy Deposits in the Suction Line

The significant difference between the two phases in this study leads consequently to lower total density and discharge pressure. The works of Brenne et al. (2005) and Hundseid et al. (2008) are based on the experimental study where the density difference between the dry and wet conditions was slight while it was significant in Michelangelo's study (2009).

The first process stage overhauling confirms the prediction of liquid carryover with the contaminated gas. Some non-sticky deposits were found in the first impeller as illustrated in figure 8-30(a). The visual inspection revealed a thin layer of deposits on the IGVs with a corroded surface which most probably occurs due to condensation of water. Moreover, a small amount of liquid was observed in the compressor casing as shown in figure 8-30(c). An initial inspection of the suction pipeline demonstrates corroded surface with heavy deposits accumulation especially near the suction strainer as illustrated in figure 8-30(d). This creates a greater resistance to the incoming flow which explains the substantial increase in the suction flow at this period of operation.

Moreover, the non-homogeneous distribution of the fouling materials causes instability in the suction flow as was found in figure 8-22 by a continuous fluctuation near the failure time. However, it was observed that the inspected suction pipeline is suffering from corrosion and erosion damages. The flow of water with the process gas is, of course, a contribution factor to initiate the corrosion phenomenon on this pipeline surface. One interesting point which stands out from the internal inspection findings is the fact that the developed model is not valid to assess the effect of reactive deposits. Hence, the predicted blockage percentage of about 6% represents only the observed thin layer of solid particles on the first impeller and IGVs surfaces. Furthermore, this method can be used only to evaluate the possibility of flow blockage at suction and discharge sides and stage internals only. This elucidates the unpredicted deposits accumulation on the suction pipeline.

8.7 Prevention and Mitigation Methods

The centrifugal compressors in process gas applications are highly subjected to the risk of flow channels fouling which might significantly limit the compression system performance. This can be also associated with internals failure leading to greater shutdown time and high maintenance cost. Since the filtration system is not sufficient to prevent the flow of deposits into the compressor suction, the heavy fouling requires a plant stoppage for compressor cleaning purposes. This normally performed on a yearly basis, but it is not enough to avoid the unexpected machine shutdown. As was found, such fouling of the compressor reduces the operating efficiency; therefore, the fouling control and prevention are very critical processes. Furthermore, monitoring the performance and operation conditions of the centrifugal compressor is important to prevent the catastrophic failure of the stage internals.

It has been shown that measuring the suction and discharge pressures is not enough to indicate the internal flow blockage. The compressor polytropic efficiency fundamentally depends upon the gas composition and suction and discharge temperatures and pressures. Therefore, the change in any of these parameters will directly affect the efficiency value. Accordingly, they have to be monitored simultaneously for more precise prediction of the deposits flow using temperature, pressure and flow sensors. There are distinct available instruments for this purpose; however, it is important to check that the measuring instrumentations have been calibrated correctly, and they are capable of working efficiently in harsh operating environments. Practically, the orifice plates and venturi meters were found very prone to the collection of deposits which will participate in a drop in the pressure/velocity reading. The conducted evaluation in this chapter has well defined the trend of flow, pressure and temperature in both normal and degraded operating modes. The main challenge here is to analyze the process gas composition in real time which in most cases requires laboratory gas sample test. Using the gas chromatography (MGC) reduces the consuming time, but it still needs complicated instrument field calibration. Therefore, this study compared the influences of the non-reactive deposits with the effect of the unanticipated gas composition change. This will help to differentiate the influences of each of these factors.

8.8 Closing Remarks

This chapter proposed an approach to model the impact of non-reactive deposits flow on the centrifugal compressor aerothermodynamics performance. The derived method has been validated by two operating cases, and the obtained discharge parameters were found close to the measured values with less than 1.82% relative deviation. Moreover, the effect of upstream equipment fouling, stage internal fouling and fouled aftercooler on the performance characteristics has been modelled and compared. The significant of these findings appears in the diagnostic process of the unstable centrifugal compressor performance in order to avoid the consequential internals failures. One of the disadvantages of using this method is that it cannot be used to locate the blockage position within the stage internals. In brief, the main findings can be summarized as following:

- A new n approach was proposed to model the impact of non-reactive deposits flow on the centrifugal compressor aerothermodynamics performance. This model can be used to simulate the flow blockage effect at the suction side, compressor internals and downstream equipment.
- A methodology has been established to evaluate the possibility of deposits accumulation in the gas path of the compression system based on the operational data of the discharge parameters.
- Unlike the molecular weight reduction, the internal blockage caused the discharge pressure and temperature of the process stage to decrease which can be used as an indication to distinguish its impact from the effect of the sudden drop in the gas molar mass. Therefore, the pressure ratio parameter is not enough to assess the possibility of flow blockage and unanticipated gas properties change.
- It was observed that the fouled cooler has more significant impact on the stage discharge pressure comparing with suction and internal blockage. However, the effect of contaminated aftercooler on the on the surge point and discharge pressure and temperature of the upstream stage was found greater than its impact on the shaft power. Therefore, a larger surge margin reduction was observed when the first stage was operating with a fouled aftercooler comparing with the measured reduction as a result of unanticipated gas properties change.
- A larger pressure ratio drop was measured in the case of liquid carryover which indicates a more significant impact of the two phases densities difference comparing with the GVF effect.

CHAPTER 9: EFFICIENCY DETERIORATION IN PROCESS CENTRIFUGAL COMPRESSOR OPERATION

There are several factors influence the stage efficiency in the operating environment leading to a deterioration in the compressor performance in addition to its impact on the mechanical integrity of the internal components. These variables can be classified into three main groups which are: suction parameters variation, flow profile distortion and compressor component damage. The determination of the root-cause will help for a proper maintenance plan and to reduce the machine downtime. Hence, this chapter addresses two key causes of inefficient compressor operation in process gas applications which are suction parameters variation and flow channel fouling. The investigated case is a three-stage gas transport centrifugal compressor driven by 2.9 MW two-shaft gas turbine. The outcomes from the conducted optimisation are compared with the measured discharge parameters and the findings from the internal inspection observation to emphasize the results from the derived approach.

9.1 Introduction

The efficient performance and availability of centrifugal compressors are two critical factors to maintain the gas throughput of a production plant and to achieve the highest techno-economic value. Performance deterioration in centrifugal compressors will result in low developed head, so high power consumption and low discharge pressure are the basic symptoms of inefficient operation. The API617 standards (2002) require the vendor to guarantee the absorbed power within a ±4% tolerance only without ensuring the compressor efficiency. Furthermore, the supplied performance data and the conducted factory tests by the original equipment manufacturer (OEM) are for a specific set of inlet gas compositions and environmental conditions. Therefore, the compressor efficiency is highly subject to change due to variation in the suction and process conditions in the field. Besides, the high fluctuation in the performance parameters of the compression system can cause an increase in the axial displacement of the rotor leading to a greater level of vibration.

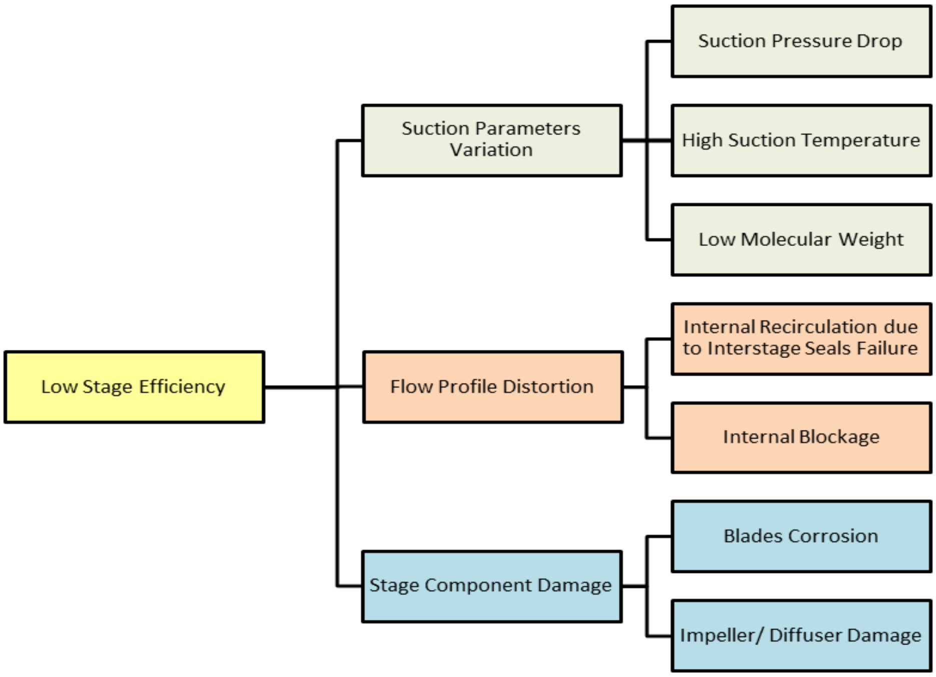

Figure 9- 1: Causes of Efficiency Deterioration

In some cases, this is also associated with aerodynamic instability when the operating point shifts towards surge line. This, in turn, can lead to fatigue failure, which is considered one of the most difficult diagnosis problems for the centrifugal compressor. However, the stable performance does not necessary mean an efficient operation. Several causes affect the compressor efficiency by introducing a change in the gas properties or altering the flow pattern. Theodore Gresh (2001) specified seven causes for low compressor efficiency which can be classified into three main categories as shown in figure 9-1. These three groups include suction parameters variation, flow profile distortion and compressor component damage.

9.2 Case Study Background

A centrifugal compressor is used for gas transport applications driven by a 2.9 MW two-shaft gas turbine as illustrated in figure 9-2. This compressor receives the gas from the low pressure compressor after flowing through the scrubber and aftercooler. Furthermore, the high pressure compressor (HPC) is connected to a gear box in order to raise the rotational speed by a ratio of 1: 3. The investigated compressor model consists of two process stages with 4 impellers each and with a total pressure ratio of about 4.775 at design point operation. This compressor was in service for around 30 years, and the physical properties of the process gas and the suction conditions at design point are shown in table 9-1.

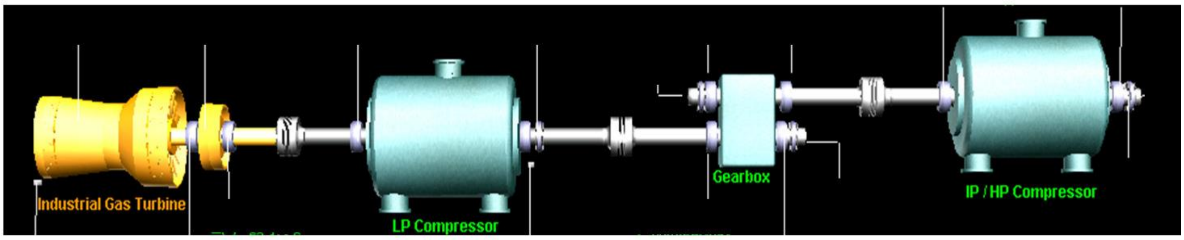

Figure 9- 2: Schematic Diagram of the Compressor Investigated

Table 9- 1: Gas Physical Properties and Suction Parameters at Design Point

Parameter	Section 2	Section 3
Inlet pressure (**bara**)	10.963	25.063
Inlet temperature (°**C**)	31.00	31.00
Inlet flow ($\mathbf{m^3/h}$)	1553.00	649.00
Molecular weight (**g/mol**)	22.27	22.28
Inlet isentropic exponent (k)	1.244	1.255
Compressibility factor (**Z**)	0.968	0.934
Discharge pressure (**bara**)	25.546	52.334
Discharge temperature (°**C**)	103.9	103.2
Operating speed (**rpm**)	17069	17069

The compressor was shut down for maintenance which takes almost 13 days to be completed. After startup, the third stage was operating stably as shown in figure 9- 3 but with a pronounced reduction in the polytropic efficiency. This caused the equivalent pressure ratio to the operating speed to be lower than the normal value. There are no recorded details for the conducted corrective actions which were taken during this shutdown. Figures 9-4 to 9-6 illustrate the actual performance parameters of this stage including efficiency, shaft power and polytropic head. The efficiency trend demonstrates that the polytropic efficiency before the shutdown was approximately 62.2% while it dropped to around 47% after the startup. The recorded increase in the shaft power after the machine startup was about 11.5% as shown in figure 9- 5.

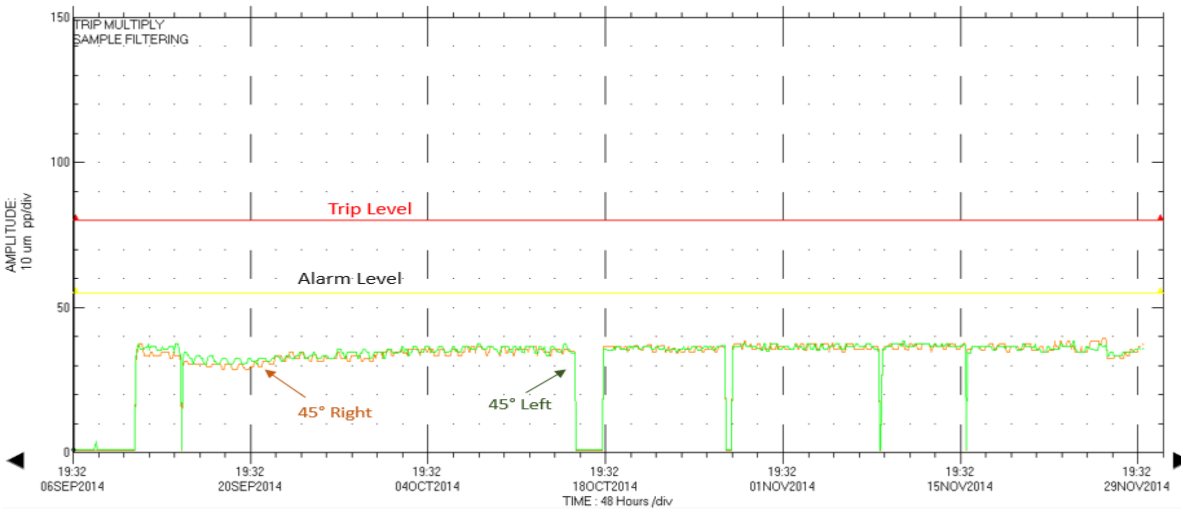

Figure 9- 3: Vibration Trends of the Third Stage Forward Bearings

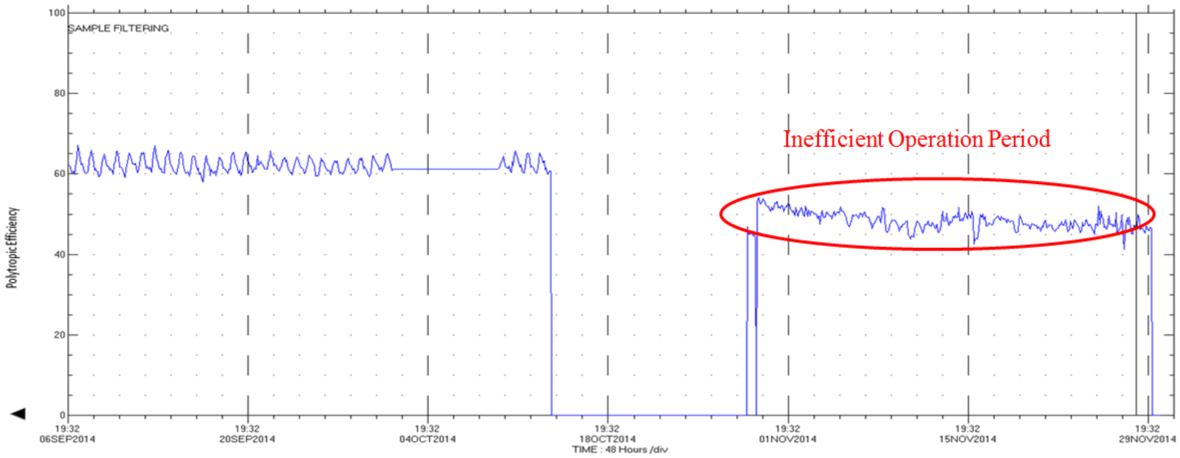

Figure 9- 4: Recorded Polytropic Efficiency of the Third Stage

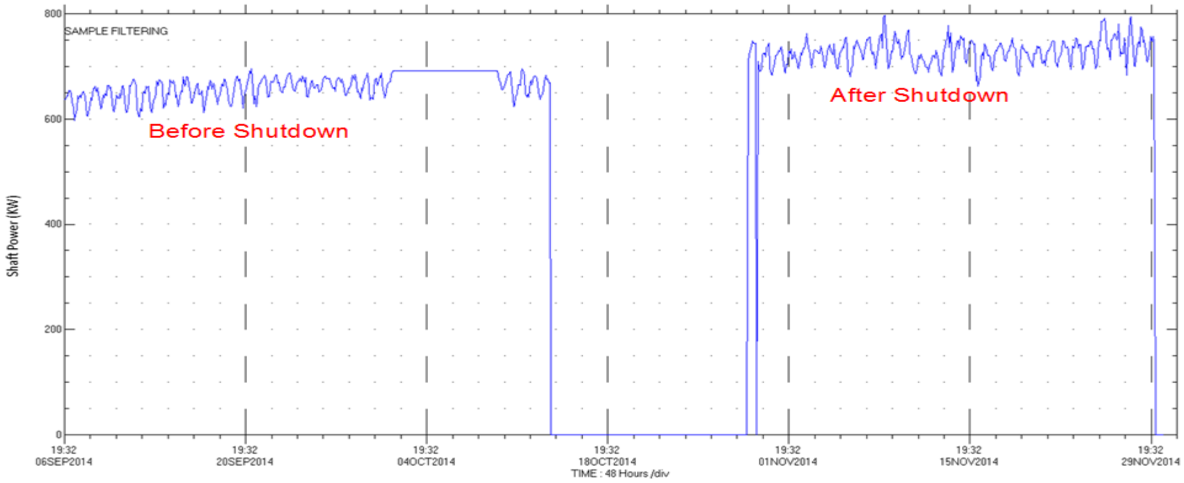

Figure 9- 5: Measured Shaft Power of the Third Stage

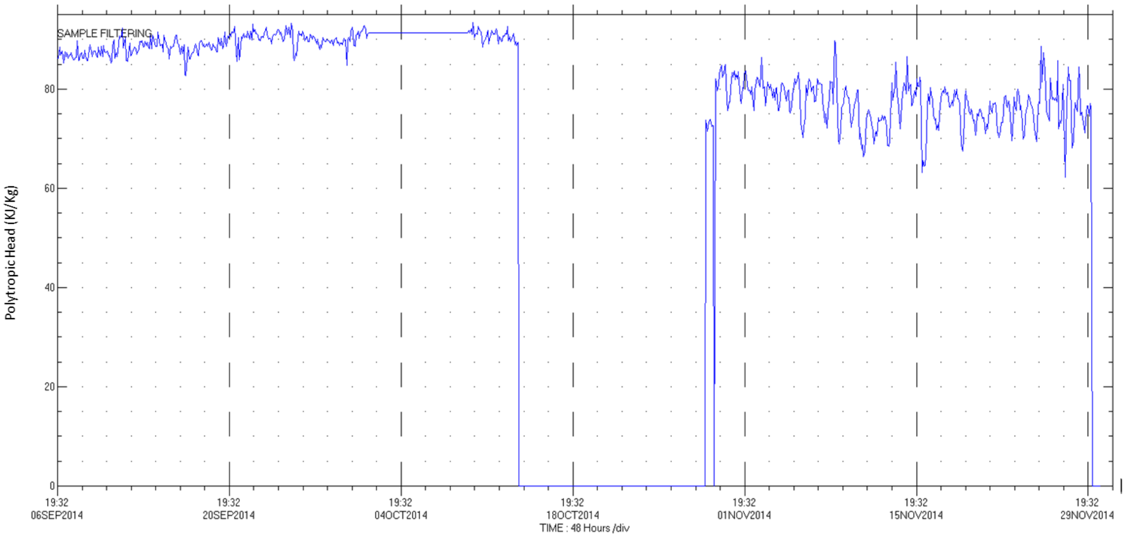

Figure 9- 6: Recorded Polytropic Head of the Third Stage

However, the developed polytropic head was significantly below the optimum value despite the increase in the shaft power as illustrated in figure 9- 6. The detected rotational speed was about 17,000 rpm which is very close to the rated speed with a slight difference by about 0.4%. Consequently, the low operating speed was not the main cause of efficiency reduction.

9.3 Operational Data Analysis

Since the compressor was in service for a long time, it is necessary to consider the variation in the suction conditions and process gas composition. The most recent gas sample test was taken one year before the investigated time. Figure 9-7 illustrates the measured change in the gas properties and inlet conditions from the initial design point values both before and after the shutdown. A slight increase was observed in the molecular weight.

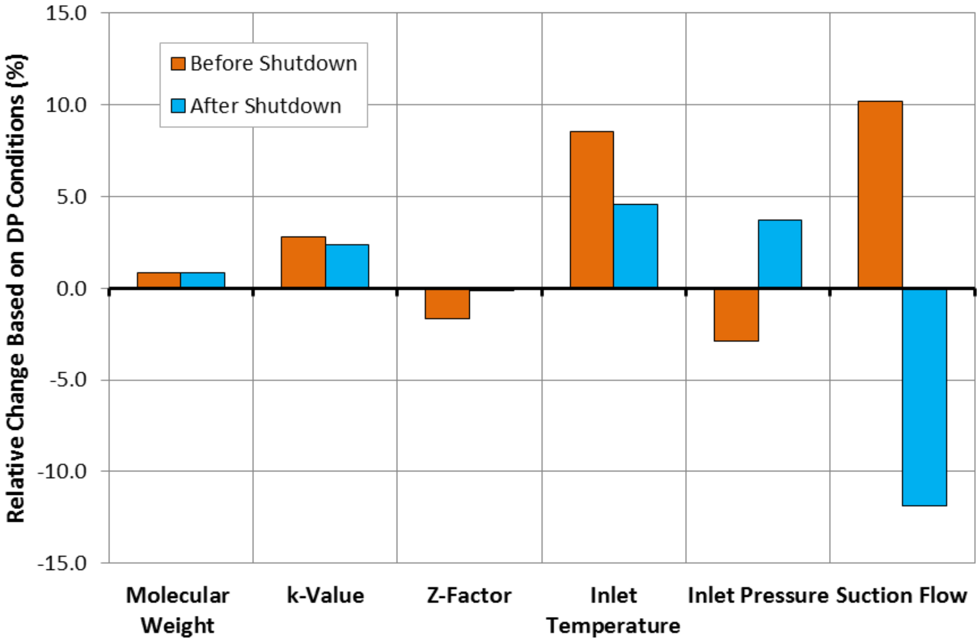

Figure 9- 7: Measured Change in the Suction Parameters with Reference to Design Point

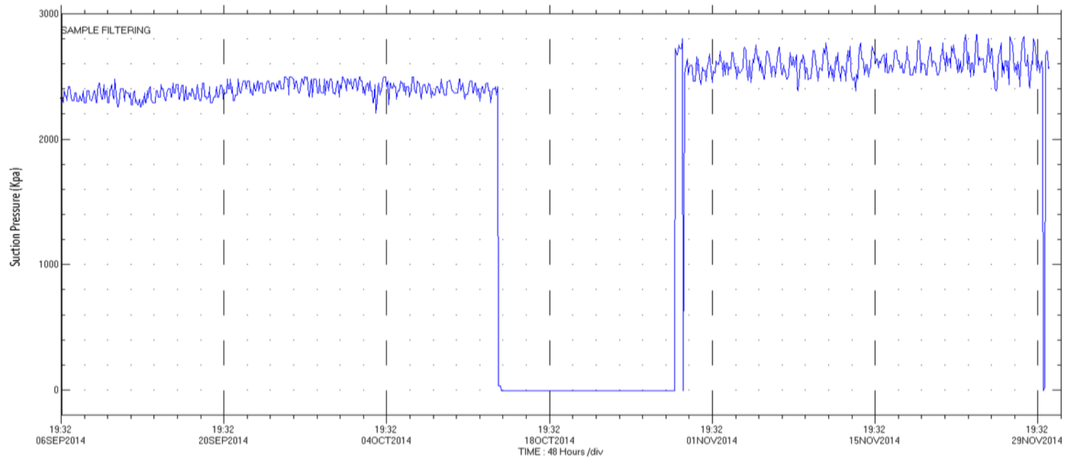

Figure 9- 8: Measured Suction Pressures of the Third Stage

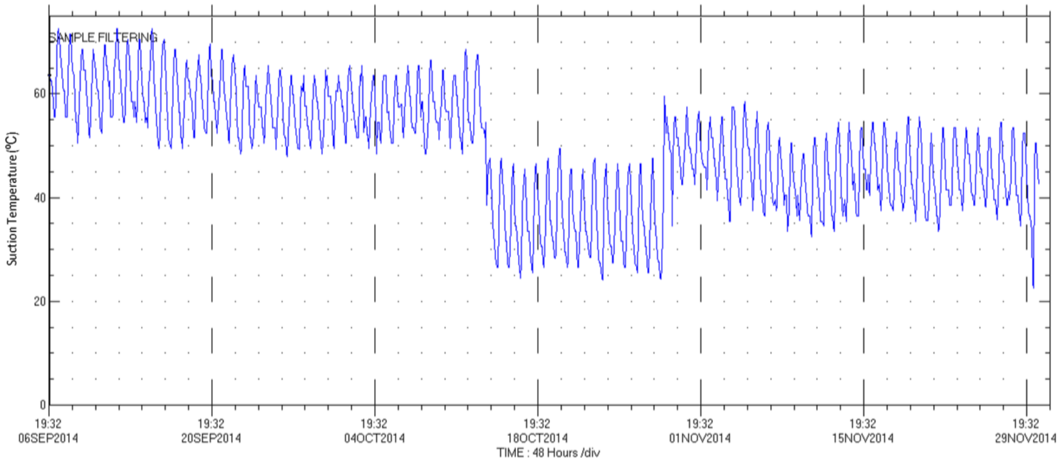

Figure 9- 9: Measured Suction Temperatures of the Third Stage

The effect of gas composition becomes more pronounced in the k- value and Z-factor due to the associated impact of gas temperature. A significant increase in the inlet temperature was found of about 26 degrees centigrade. This was perhaps because the temperature at design point was measured in winter conditions during the machine installation time while the actual operating point was affected by high summer ambient temperature.

To investigate the cause behind this change, it is necessary to check the suction and discharge parameters of the upstream stage as illustrated in figure 9-10(a-b). There is a decrease in the suction temperature of the second compression stage after the shutdown as shown in figure 9-10(a) at 01 Nov 2014. This, in turn, caused the process stage to generate a higher discharge pressure which obviously led to almost a constant discharge temperature (fig. 9-10(b)). However, the detected fluctuation in the suction temperature reading of the third stage is very similar to the second stage trend as demonstrated in figure 9-9. This agrees with the hypothesis that the alternation in the suction temperature is due to the unstable performance of the intercooling system. This instability is obviously caused by the variation of the ambient temperature which affects the discharge temperature from the intercooler. After the shutdown, the suction pressure increased dramatically exceeding the design value by approximately 3.7% as illustrated in figure 9-8 due to the variation in the suction pressure of the low pressure compressor. Considering the suction flow, the machine was operating at greater flow rate before the shutdown time which causes the generated discharge pressure to decrease.

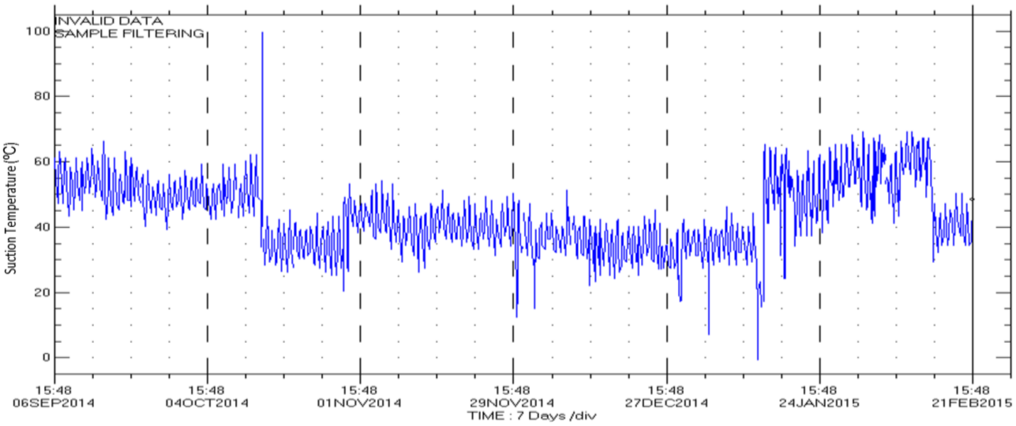

(a) Suction Temperature

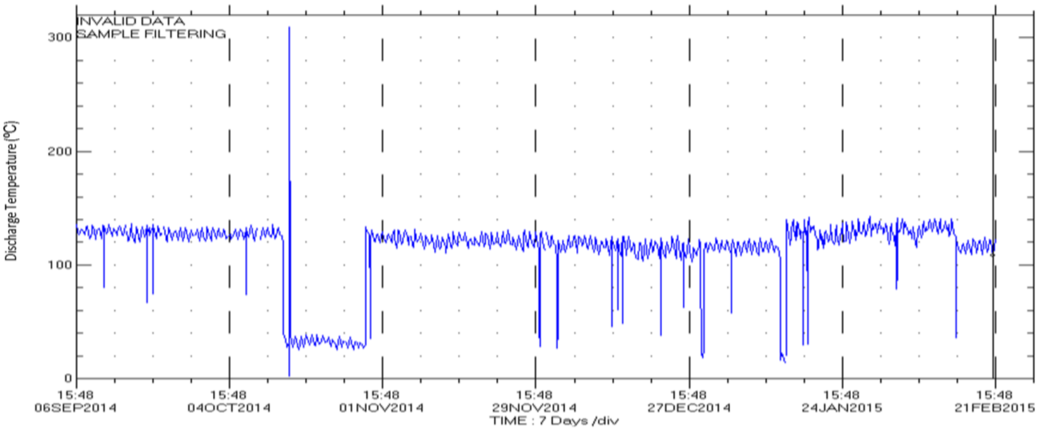

(b) Discharge Temperature

Figure 9- 10: Measured Suction and Discharge Temperatures of the Second Stage

On the other hand, a reduction by around 11.9% was observed in the operating flow after the shutdown. This leads to raise the stage pressure ratio and reduces the surge margin. This fluctuation in the suction flow was driven by the upsets in the process conditions of the upstream equipment.

9.4 Performance Evaluation

Figure 9-11 compares the actual operating pressure ratio with the design value. The change in the gas composition and suction parameters causes the performance curve to shift down, leading to lower pressure ratios. However, the measured pressure ratio after the shutdown is well below the initial design value by around 16% at the measured rotational speed and flow rate. The equivalent speed to the detected pressure ratio is approximately 85% of full speed operation. Comparing with the initial design value, a slight reduction was observed in the suction flow after the shutdown while it was greater before the shutdown by about 10.1 %. Moreover, the deterioration in the developed head covers also the operation prior the shutdown which is below the expected pressure ratio. The measured pressure ratio before the shutdown falls on the constant speed line of 96% of full speed value. An interesting observation is that a noticeable shift in the stage performance curve was found under the existing operating conditions before the machine shutdown. This is due to the significant increase in the suction temperature compared with the other operating scenarios. The degraded pressure ratio of this stage is caused by the reduction in the operating efficiency.

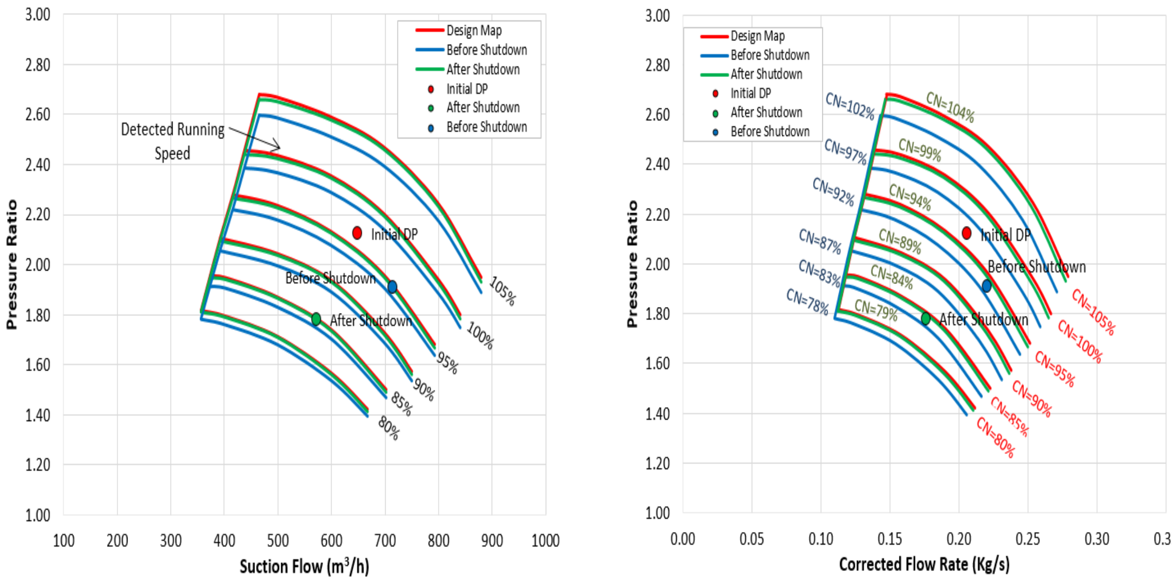

(a) **(b)**

Figure 9- 11: Comparison Between the Measured and Design Pressure Ratios in Terms of Actual and Corrected Flow Rates

Figure 9-11(b) illustrates the obtained compressor map in terms of corrected rotational speed and flow rate. The corrected speed is derived by maintaining a fixed tip Mach number and with consideration of the gases properties variation. This will help to estimate the equivalent speed at various off-design conditions including suction parameters and gas properties.

$$N_c = \frac{N_{act}}{a_{act}/a_{ref}} \tag{9-1}$$

This equation is applied to the same physical machine where the impeller diameter is constant. To consider the impact of the gas properties, the correlation (9-1) becomes:

$$\mathrm{N_c} = \mathrm{N_{act}}\sqrt{\frac{\mathrm{k_{Ref}}}{\mathrm{k_{act}}}}\sqrt{\frac{\mathrm{Z_{Ref}}}{\mathrm{Z_{act}}}}\sqrt{\frac{\mathrm{R_{Ref}}}{\mathrm{R_{act}}}}\sqrt{\frac{\mathrm{T_{Ref}}}{\mathrm{T_{act}}}} \tag{9-2}$$

Berdanier et al. (2015) added the effect of humidity factor to the correction equation which can be ignored for this particular application due to insignificant effect. Similarly, the corrected mass flow rate is derived based on Buckingham Pi Theorem.

$$\dot{\mathrm{m}}_\mathrm{c} = \dot{\mathrm{m}}_\mathrm{act}\left(\frac{\rho_\mathrm{Ref}a_\mathrm{Ref}}{\rho_\mathrm{act}a_\mathrm{act}}\right) \tag{9-3}$$

When there is no change in the diameter, equation (9-4) is used for corrected flow rate.

$$\dot{\mathrm{m}}_\mathrm{c} = \dot{\mathrm{m}}_\mathrm{act}\frac{\mathrm{p_{Ref}}}{\mathrm{p_{act}}}\sqrt{\frac{\mathrm{k_{Ref}}}{\mathrm{k_{act}}}}\sqrt{\frac{\mathrm{Z_{act}}}{\mathrm{Z_{Ref}}}}\sqrt{\frac{\mathrm{R_{act}}}{\mathrm{R_{Ref}}}}\sqrt{\frac{\mathrm{T_{act}}}{\mathrm{T_{Ref}}}} \tag{9-4}$$

where:

$\mathrm{k_{Ref}}$: Reference specific heats ratio $= 1.4$

$\mathrm{Z_{Ref}}$: Reference compressibility factor $= 1.0$

$\mathrm{R_{Ref}}$: Reference gas constant $= 287.058\mathrm{J/(kg.K)}$

T_{Ref}: Reference suction temperature = 288.15 °K
p_{Ref}: Reference suction pressure = 101.325 kPa

The corrected speed shows a reduction by around 3% at the actual suction conditions driven by high inlet temperature. This percentage decreased after the shutdown to only about 1% due to lower suction temperature.

The estimated polytropic efficiency is plotted against the measured and design values as illustrated figure 9-12. The influence of the suction conditions variation on the efficiency curve was less substantial. However, there is a dramatic reduction in the machine efficiency at the measured rotational speed by approximately 8.77% and 45.3% before and after the shutdown, respectively. Moreover, the actual efficiency after the shutdown period was well below the stable operating envelope.

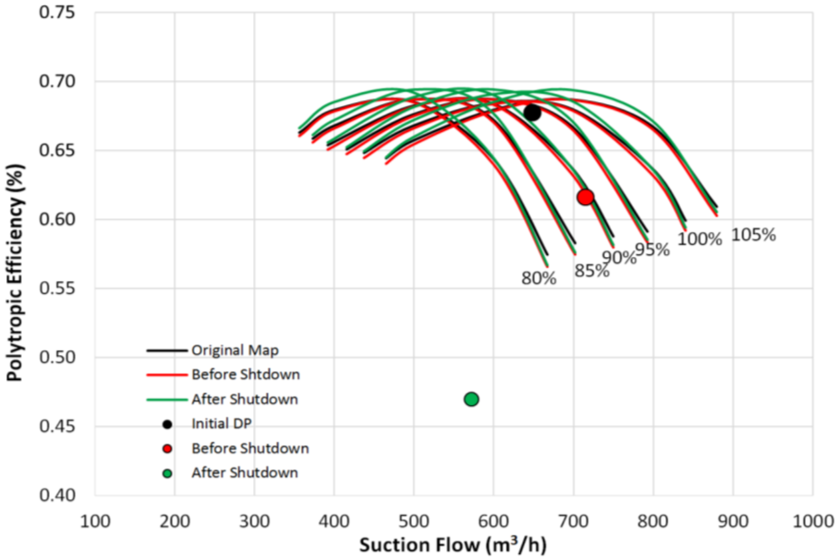

Figure 9- 12: Comparison Between the Measured and Predicted Efficiency of Third Stage

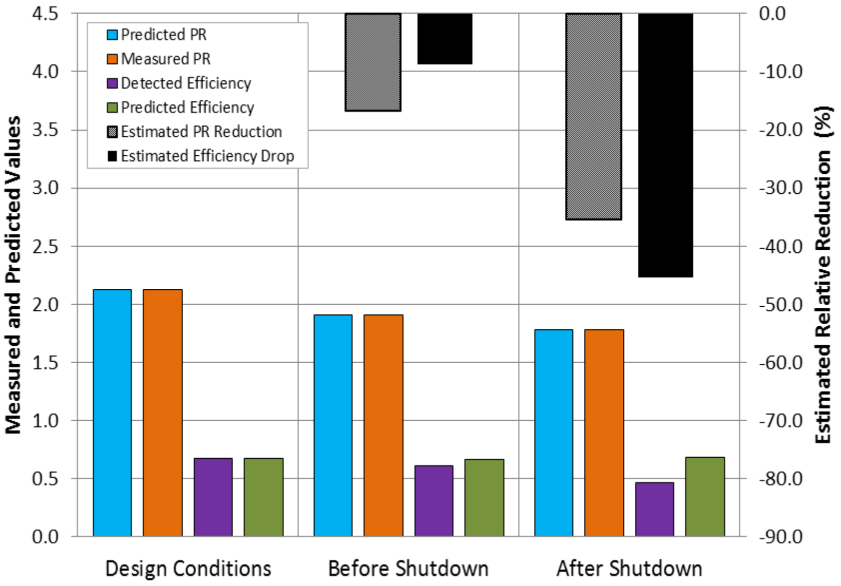

Figure 9- 13: Estimated Change in the Efficiency and Pressure Ratio Values at Measured Rotational Speed

Figure 9-13 illustrates the estimated reduction in the stage pressure ratio and polytropic efficiency corresponding to the measured rotational speed. The deterioration in the stage performance becomes more significant after the shutdown. Furthermore, the drop in the efficiency after the shutdown is higher than that before the shutdown by more than four times, as demonstrated by the efficiency curve in figure 9-12.

Figure 9-14 shows a noticeable rise in the shaft power due to the deterioration in the stage efficiency. The measured operating power after the machine shutdown was found to be out of the predicted range. This range is obtained by considering the equivalent power to the predicted and measured pressure ratios. The operating shaft power was slightly higher than the relative maximum speed line at the same suction flow by around 5.83%. Moreover, the increase in the recorded shaft power over the estimated value was lower before the shutdown due to the higher stage efficiency. This supports the assumption that the stage was running inefficiently even prior the shutdown. There are several possible causes for deterioration in stage efficiency which will be further investigated.

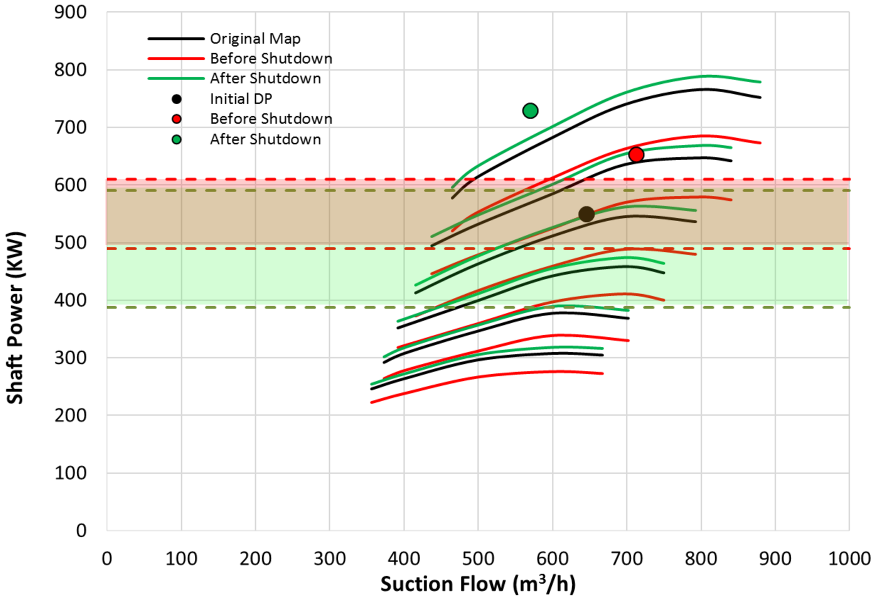

Figure 9- 14: Comparison Between the Measured and Predicted Shaft Power of Third Stage

In order to evaluate the discharge temperature prediction model, the estimated discharge temperature at design conditions is compared with the measured value as demonstrated in figure 9-15. The model shows a good match with the measured temperature with less than 1% relative error which is acceptable. Besides, the shift in the constant speed lines for the three operation cases is highly affected by the suction temperature. Moreover, it is interesting to observe that the predicted discharge temperature at actual conditions corresponding to the detected speed is slightly higher than the measured value both before and after machine shutdown by approximately 6 degrees Centigrade. Considering the obtained uncertainty at design conditions, the predicted temperatures are lower than the actual values by only around 5ºC. However, the equivalent temperatures at the measured pressure ratios are significantly lower than the actual values by about 6.3% and 23.8% before and after shutdown, respectively. This implies an increase in the generated pressure losses leading to lower discharge pressure especially after the shutdown period, which can be due to the flow profile distortion and gas composition change.

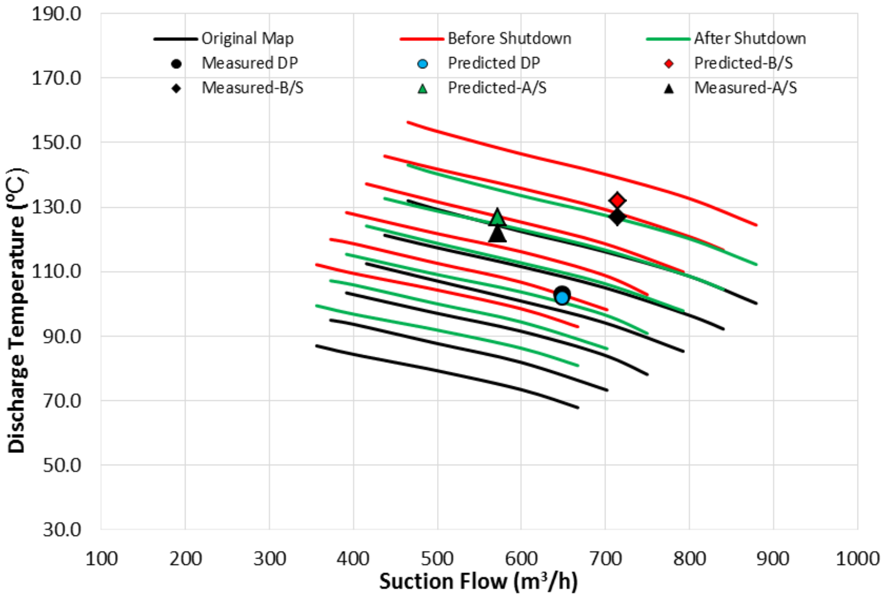

Figure 9- 15: Comparison Between the Measured and Predicted Discharge Temperature of the Third Stage

Figures 9-16 and 9-17 test the possibility of gas molecular weight variation by matching the stage discharge temperature and pressure at the measured speed. As the gas density decreases, the compression ratio through the impeller is reduced which will result in a higher discharge volume flow acting on the same vane area. This, as a result, produces a lower tangential velocity and correspondingly lower generated head. In addition to Mach number, the gas density influences the gas Reynolds number which decreases proportionally with the molecular weight, leading to higher frictional losses and lower efficiency. An interesting observation is that the measured discharge temperature before the shutdown is predictable at 23.8 g/mol gas molecular weight which is higher than the reference value by around 5.9%.

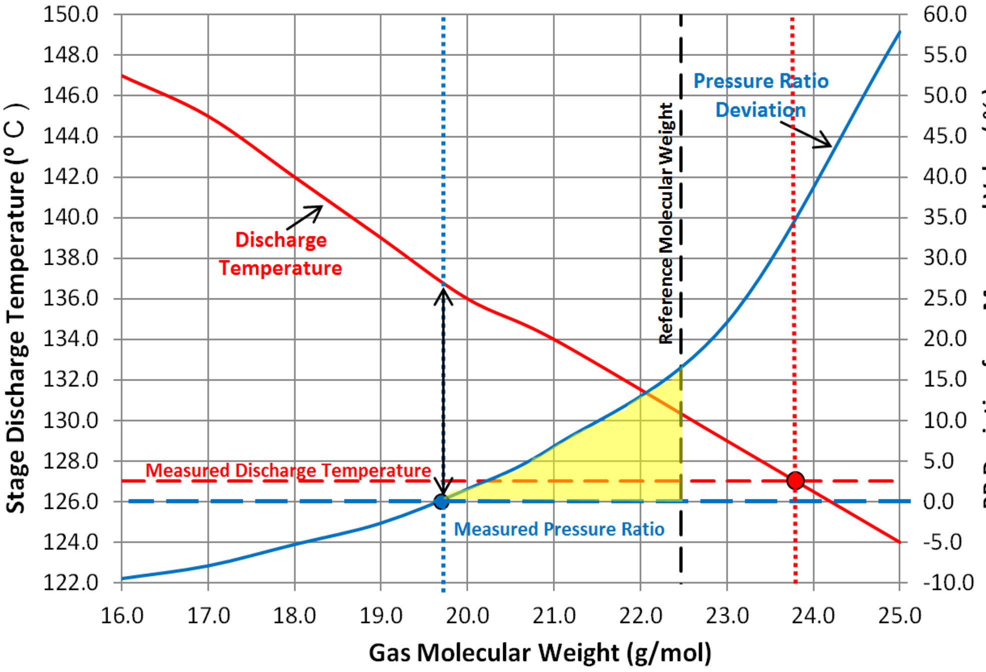

Figure 9- 16: Prediction of Measured Discharge Temperature Based on Molecular Weight Variation and Stage Pressure Ratio Before Machine Shutdown At Detected Rotational Speed

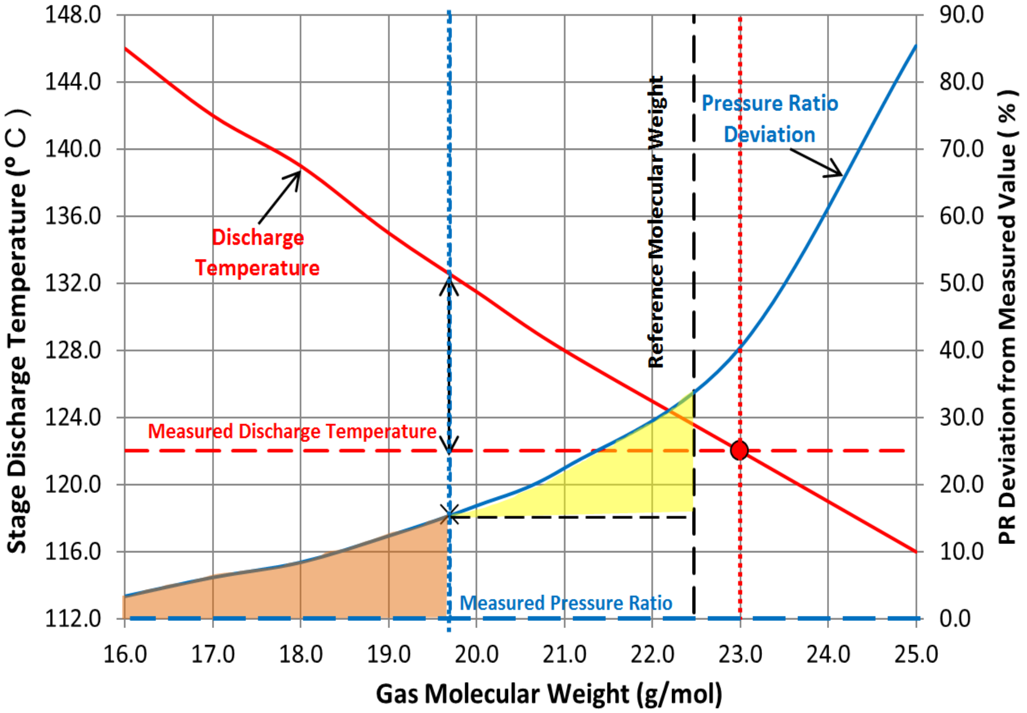

Figure 9- 17: Prediction of Measured Discharge Temperature Based on Molecular Weight Variation and Stage Pressure Ratio After Machine Shutdown At Detected Rotational Speed

However, the estimated pressure ratio at this gas density was found higher than the measured value by roughly 35%. Moreover, the actual pressure ratio is obtained at a gas molecular weight of 19.7 g/mol with a discharge temperature deviation by approximately 2.3%. This can be due to one of the following reasons:

- An instrumentation error in the measured discharge temperature.
- A slight reduction in the actual specific heats ratio.
- Uncertainty in the implemented discharge temperature prediction approach

Considering the machine operation after shutdown, figure 9-17 demonstrates that the measured pressure ratio is unpredictable throughout the tested molecular weight range. On the other hand, the estimated discharge temperature is matching the measured value at the gas molar mass of about 23.0 g/mol. This is indeed very close to the predicted gas density before the shutdown case in figure 9-16. However, the significant deviation between the estimated and actual pressure ratio at this molecular weight value does not support this assumption. The pressure ratio deviation at 19.7 g/mol ($\Delta PR = 0$ before shutdown) is approximately 15.5% with only 11 degrees difference in the discharge temperature reading.

In order to evaluate the validity of the gas composition variation assumption, the required power is predicted at various gas molecular weights and at the measured rotational speed as illustrated in figure 9-18. The predicted power matches the measured value before the shutdown at a molecular weight of 19.7 g/mol as shown in figure 9-18(a). An interesting observation from figure 9-18(b) is that the predicted demanded power at 19.7 g/mol ($\Delta PR=0$ before shutdown) is close to the measured value with only 0.69% as an approximate deviation. This difference is reduced after the shutdown time reaching to about 0.52% with a slight increase in the measured power.

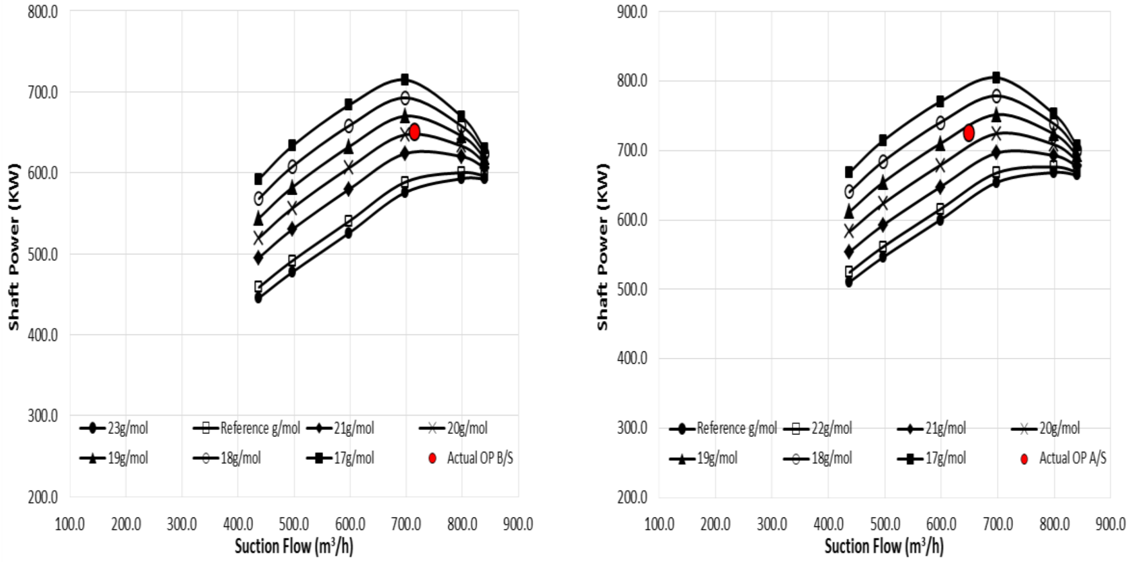

(a) (b)

Figure 9- 18: Evaluation of Estimated Gas Molecular Weight Based on Actual Shaft Power at Detected Rotational Speed: (a) Before Shutdown (b) After the Shutdown

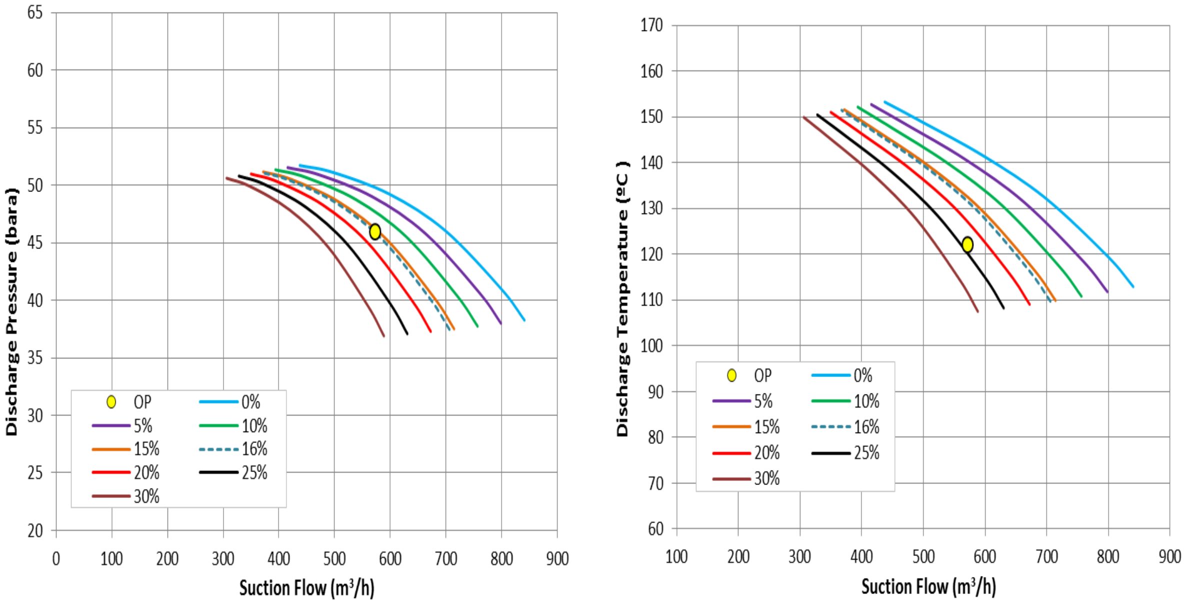

(a) (b)

Figure 9- 19: Effect of Internal Blockage on the Third Stage Discharge Pressure and Temperature After Shutdown at 19.7 g/mol and Detected Rotational Speed

The findings of both figures actually support the previous assumption of gas composition change. However, the predicted deviation in the pressure ratio after the shutdown is most probably caused by higher internal pressure losses due to the flow profile distortion. This region is represented by the orange area in figure 9-17. Therefore, the change in the suction parameters contributes to the efficiency degradation. However, this was not the only reason behind this performance deterioration.

To investigate the internal blockage assumption, the stage performance curve is derived at 19.7 g/mol molar density and corresponding to various blockage percentages as illustrated in figure

9-19. The surge margin increases as the blockage percentage increases, so the operating point is still in the stable flow range which elucidates the stable operation of the studied compressor. At the measured rotational speed, figure 9-19(a) shows the change in the position of the constant speed line at different level of fouling. The conducted analysis reveals that the measured discharge pressure suits on the speed line of 16% blockage percentage. In order to assess this hypothesis, the predicted discharge temperature is compared against the measured value. Figure 9-19(b) demonstrates a higher discharge temperature at this blockage percentage by around 2.28% over the actual measured temperature. The effect of flow blockage on the polytropic efficiency is illustrated in figure 9-20 which shows a gradual reduction in the stage efficiency as the blockage percentage increases driven by low pressure ratio. A reduction by approximately 5% was found at 16% blockage percentage comparing with the clean operation.

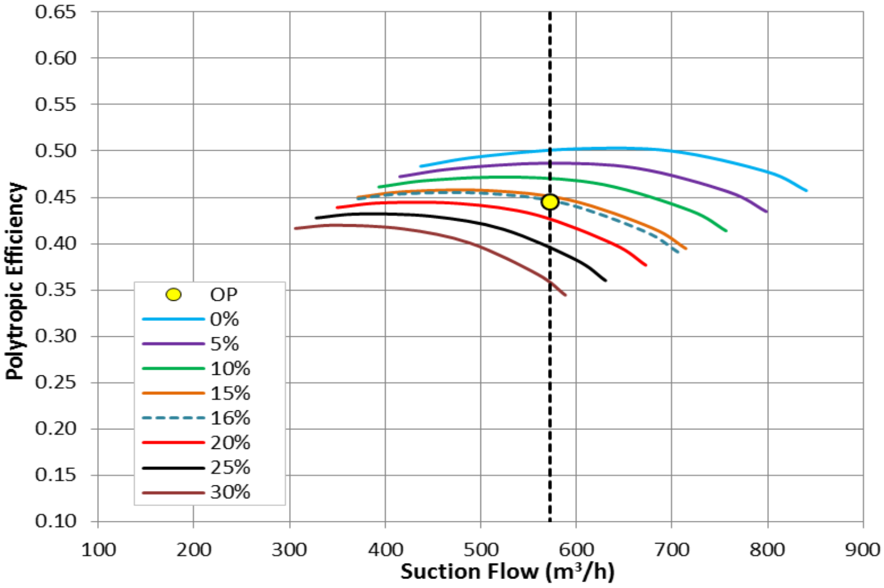

Figure 9- 20: Determination of Stage Polytropic Efficiency After Shutdown at Detected Rotational Speed and Corresponding to 19.7 g/mol and 16% BP

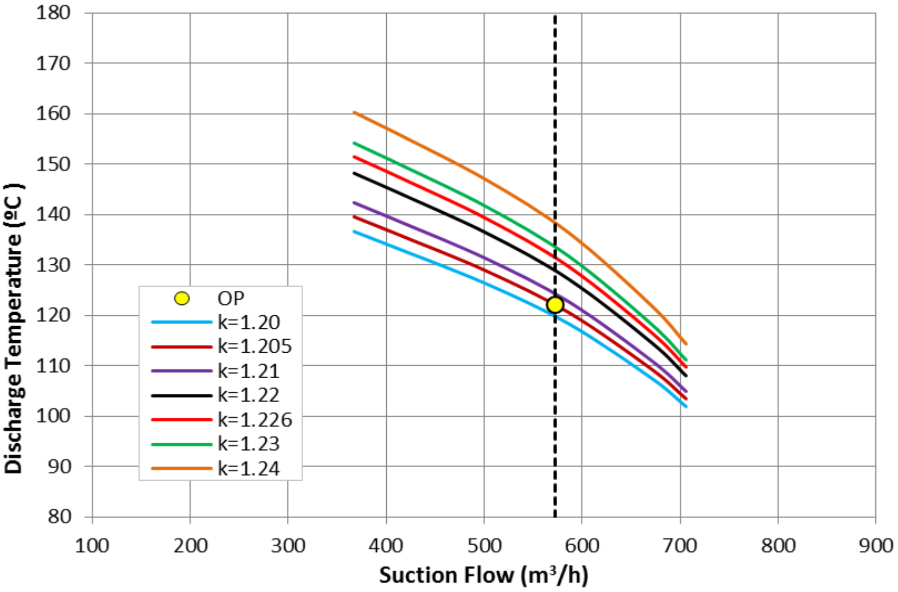

Figure 9- 21: Comparison Between the Predicted and Measured Discharge Temperature of the Third Stage After Shutdown at Detected Speed and Corresponding to 19.7 g/mol and 16% BP

An interesting observation which stands out from this figure is that the predicted efficiency at this operating condition is lower than the recorded value by about 2.5%. To assess the possibility of sudden change in the specific heats ratio, the predicted discharge temperature at the detected speed is plotted against the measured value at various specific heats ratios as shown in figure 9-21. As the heats ratio decreases, the discharge temperature is reduced and it is getting closer to the actual value. The estimated temperature matches the measured value at a specific heats ratio of around 1.205 with a relative change by about 1.71% only.

In order to evaluate this assumption, the obtained polytropic efficiency and shaft power at this specific heats ratio are plotted against the measured values as shown in figures 9-22 and 9-23. Four cases have been considered and compared which are:

- **Case 1**: clean operation (0%BP) at reference measured gas properties one year before the investigated period (22.4 g/mol & k=1.226).
- **Case 2**: clean operation (0%BP) at obtained gas compositions (19.7 g/mol & k=1.226).
- **Case 3**: operation at obtained gas compositions (19.7 g/mol & k=1.226) and 16% blockage percentage.
- **Case 4**: operation at obtained gas compositions (19.7 g/mol & k=1.205) and 16% blockage percentage.

The efficiency at reference condition is significantly greater than the rest of the cases driven by high gas molecular weight value. A reduction by around 18% was predicted in Case 2 due to the unanticipated change in the gas composition. The estimated molecular weight was predicted to be about 12% as an outcome from the previous analysis. A further drop in the efficiency was observed in Case 3 due to the internal flow channel blockage by roughly 5%. This blockage percentage was determined by matching the predicted stage discharge pressure with the measured value as illustrated in figure 9-19. However, the corresponding stage efficiency, in this case, was found below the actual value by approximately 2.5% as shown in figure 9-22.

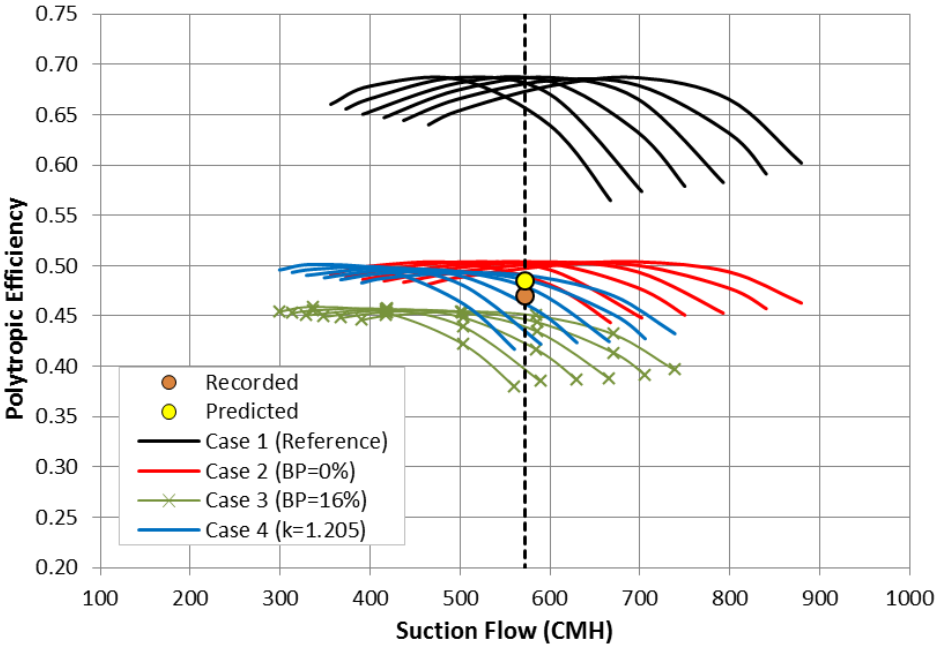

Figure 9- 22: Comparison Between the Predicted Polytropic Efficiencies at Various Operating Scenarios

Considering Case 4, the obtained efficiency at the operating flow rate is the closest to the recorded value among the other cases as denoted by a large yellow dot in figure 9-22.This represents different gas composition with a lower specific heats ratio than the previous case.

However, it is important to check the corresponding shaft power in these four cases in order to assess this hypothesis. Figure 9-23 demonstrates an increase in the required shaft power in Case 2 and Case 3 driven by low gas molecular weight and high blockage percentage, respectively. Moreover, the largest deviation between the estimated and measured power was observed in Case 1 as shown in figure 9-24.

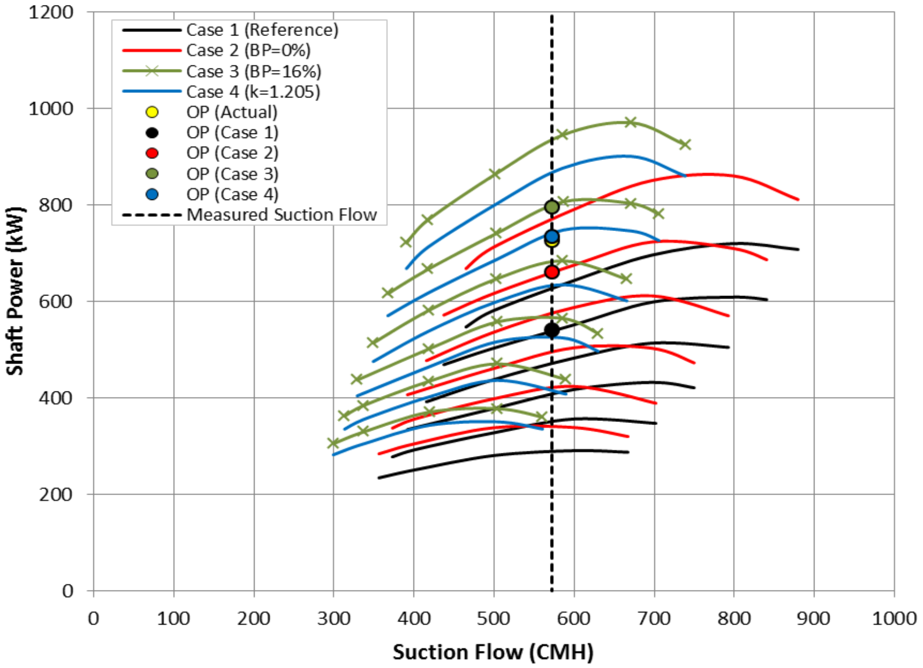

Figure 9- 23: Comparison Between the Predicted Shaft Power at Various Operating Scenarios

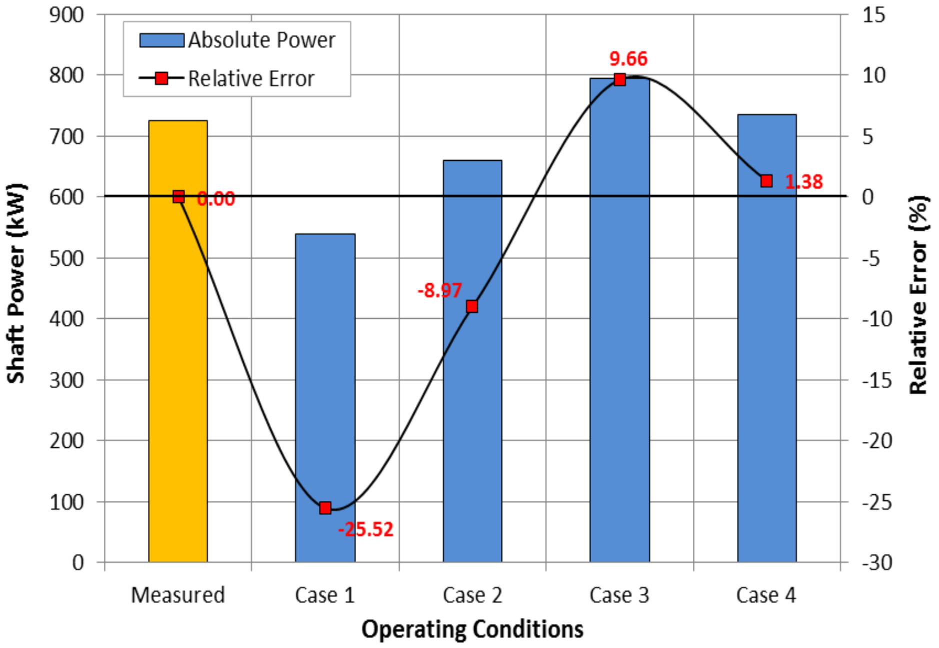

Figure 9- 24: Comparison Between the Predicted Shaft Power at Various Operating Scenarios

On the other hand, the closest estimated power to the actual value was obtained in Case 4 with a relative error of about 1.38%. This supports the previous assumption of combined effect of the internal blockage and gas composition change.

A further verification is presented in figure 9-25 which compares the predicted discharge pressure at Case 2 and Case 4 with the measured pressure after shutdown. An approximated reduction by about 6.9% was found in the discharge pressure when the blockage percentage reached 16%. The estimated discharge pressure in operating Case 4 at the measured rotational speed was found near the actual value with only 1.08% relative error.

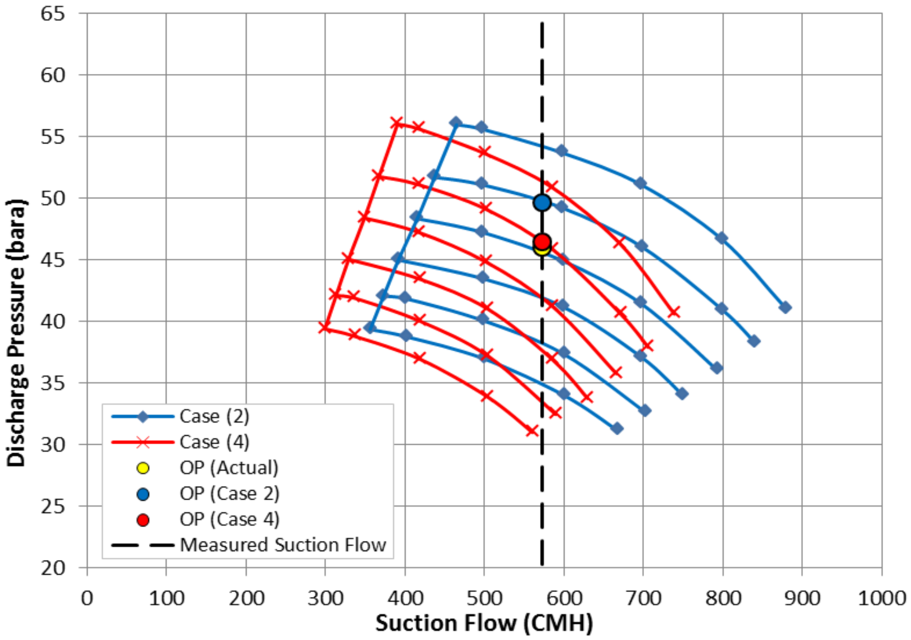

Figure 9- 25: Evaluation of Predicted Third Stage Map at Estimated Flow Conditions and Suction Gas Properties After the Machine Shutdown

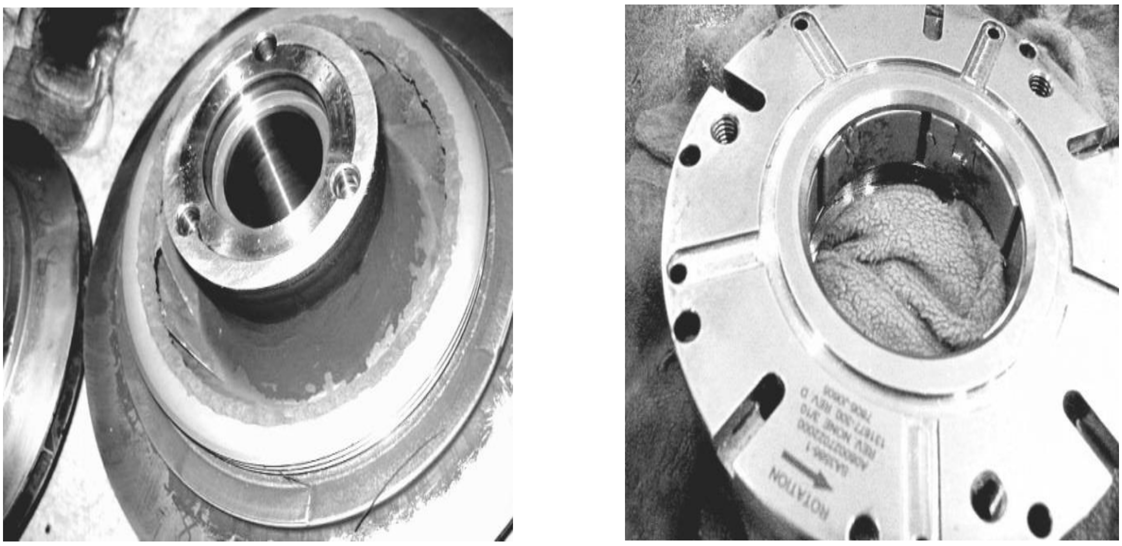

(a) (b)

Figure 9- 26: Internal Inspection Findings: (a) Thin Layer of Deposits on the First Impeller (b) Bearings in Good Conditions

Additionally, the operating point is still within the stable operating range. The predicted discharge pressure before the machine shutdown is slightly higher than the actual value by around 2.12%. This causes the obtained discharge temperature to be higher than the measured value by only 4°C. Therefore, this analysis demonstrated two causes for the loss in efficiency after the shutdown which are: gas composition change and internal flow blockage by about 16% as blockage flow area of the third process stage. This was evaluated by comparing the predicted discharge performance parameters with the actual values.

By overhauling the investigated stage, the internal inspection revealed a thin layer of deposits on the first impeller as shown in figure 9-26(a). The level of fouling roughly agrees with the predicted blockage percentage. However, the bearings were in good condition as shown in figure 9-26(b) which is expected since the compressor was still running in stable mode.

9.5 Chapter Summary

This chapter assessed two causes of inefficient centrifugal compressor operation which are process conditions variation and flow channel fouling. The investigated case is a three-stage gas transport centrifugal compressor driven by 2.9 MW two-shaft gas turbine. The compressor was running in the stable region but with a significant reduction in the efficiency. The preliminary aerothermodynamic evaluation revealed an unanticipated change in the gas composition causing the stage to operate at lower polytropic efficiency before and after conducted maintenance tasks. The drop in the efficiency was found significantly greater after the shutdown. By matching the predicted discharge parameters with the measured values, it was proven that this further deterioration in the stage performance is owing to the internal flow blockage by around 16% from the total flow area. This factor combined with the low gas molar density in the stage efficiency reduction leading to higher shaft power and lower discharge pressure. By overhauling the investigated stage, the internal inspection revealed a thin layer of deposits on the first impeller while the bearings were in a good condition.

CHAPTER 10: EVALUATION OF THE INFLUENCE OF DESIGN CHARACTERISTICS ON EFFICIENCY AND OPERATING RANGE OF CENTRIFUGAL COMPRESSORS

10.1 Introduction

This chapter discusses the effect of the design characteristics of centrifugal compressor aerodynamic components on stage efficiency and stable operating range. To improve the imposed work by the impeller, two basic geometrical parameters have been considered: shrouded percentage and blade exit angle. More efforts have been made to enhance the pressure recovery in the diffuser and these in general focused on five major design parameters which are: diffuser width, radius ratio, chord length, vane number and inlet vane angle. Based on the impeller design and its matching with the diffuser component, these variables can greatly influence the location of stability limit of the centrifugal compressor. Thus, an empirical approach has been developed to evaluate the effect of diffuser characteristics on the static pressure recovery, energy parameters, stage efficiency, flow range and power loss cost.

10.2 Determination of Optimum Shrouded Percentage

The modelling of impeller shroud effect on stage aerothermodynamic performance was performed based on the following stated assumptions:

- The rotational speed and flow rate are assumed to stay constant as the design value.
- The flow is assumed to be fully axial at the inlet.
- The initial velocity of tip clearance flow is assumed to be like the mean stream velocity. Then, this is iterated to obtain more precise value.
- This method does not account for the effect of impeller configuration on the unsteady interaction between the rotor and stator.
- The initial impeller configuration is set to be at fully shrouded or unshrouded percentage so that the performance parameters at design conditions can be matched.
- The corresponding physical gas properties have been assumed to be fixed at inlet conditions. These then iterated based on the new discharge parameters based on average value approach.
- The disc friction, slip factor and slip velocity are assumed to be constant.
- The impeller flow channel height is fixed as initial designed geometry while the variation in the tip clearance was achieved by modifying the blade height.

The developed method to obtain the effect of partially shrouded impeller configuration on the stage performance is shown in figure 10-1. This approach consists in general of five steps as following:

1. The tip leakage flow and the corresponding pressure drop are estimated at the beginning assuming a constant mean stream tip velocity. Thus, the discharge pressure and temperature can be estimated.
2. The gas properties are corrected according to the predicted discharge conditions which then used to calculate the new tip velocity at impeller exit.

3. The new tip velocity is substituted to derive the new leakage flow, pressure loss and enthalpy drop across the tip clearance. Therefore, the initial efficiency can be obtained using the basic power equation (Eqn. 10-8).
4. The polytropic head is used to get the efficiency based on work coefficient equation (Eqn.10-9).
5. The pressure rise and work coefficients are calculated and then substituted in Senoo and Ishida model (Eqn.10-10) to perform the third calculation process.

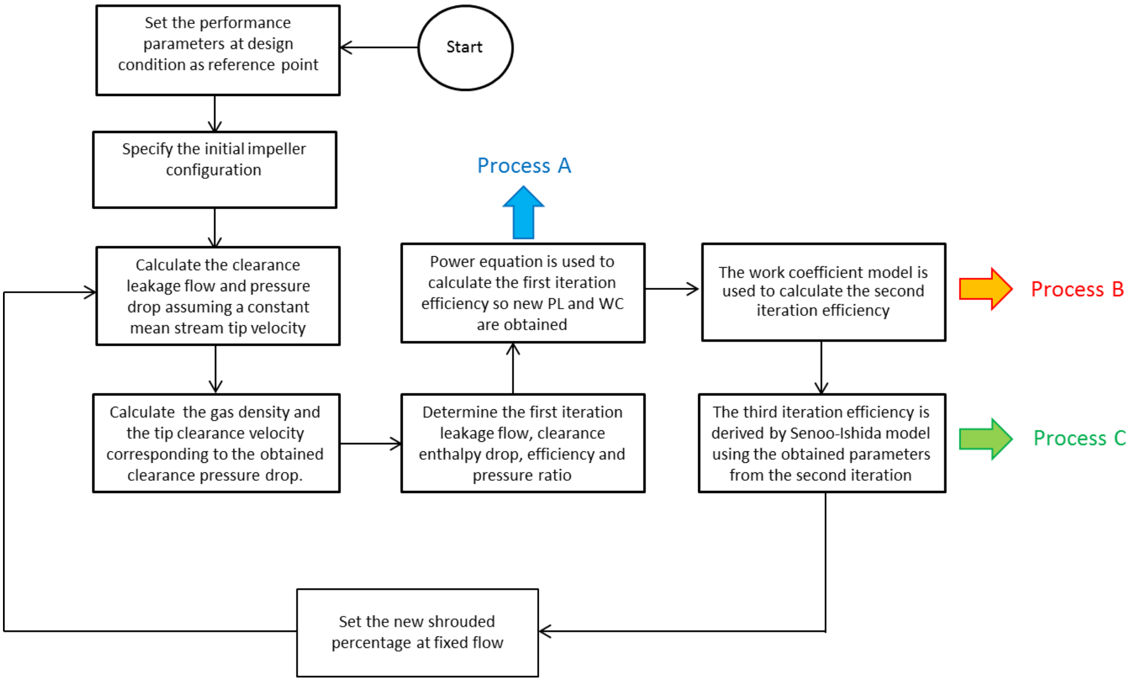

Figure 10- 1: Scheme of the Developed Approach

These procedures are repeated at different shrouded percentage. Besides, the constant speed line is derived by varying the flow coefficient at fixed impeller configuration using the method developed in chapter 6. Initially, the clearance leakage flow and pressure drop are calculated using equations (10-1) and (10-2) assuming a constant exit tip speed of the mean stream.

$$\dot{m}_{cl} = \rho_2 \times Z \times \varepsilon_c \times L_\theta \times U_2 \tag{10-1}$$

$$\Delta p_{cl} = \frac{\dot{m} \times (r_2 V_{\theta 2} - r_1 V_{\theta 1})}{Z \times \left(\frac{r_2+r_1}{2}\right) \times \left(\frac{b_2+b_1}{2}\right) \times L_\theta} \tag{10-2}$$

The blade mean streamline meridional length (L_θ) is redefined to consider the effect of shrouded percentage (SP) by applying formula (10-3).

$$L_\theta = A_c \frac{2\pi(r_2 - r_1)}{4} \times \left(1 + \frac{SP\%}{100}\right) \tag{10-3}$$

The empirical coefficient (A_c) is ranging between 0.7 and 0.45 and it can be defined by matching the stage efficiency at initial impeller configuration with the estimated efficiency at design conditions.

By specifying the inlet and discharge pressures at the design point, the new discharge pressure of the specified configuration can be calculated from the derived pressure drop. Thus, a new exit density value (ρ_2) is obtained using the basic gas thermodynamic equation (10-4).

$$\rho_2 = \frac{p_2}{Z_2 R T_2} \tag{10-4}$$

Based on the obtained discharge density (ρ_2), the leakage flow across the tip clearance is recalculated by formula (10-1) to consider the predicted exit parameters. Furthermore, the corresponding tip clearance velocity (U_{cl}) is estimated using equation (10-5).

$$U_{cl} = 0.816\sqrt{(2\Delta p_{cl}/\ \rho_2)} \tag{10-5}$$

Accordingly, the tip clearance enthalpy drop (Δh_{cl}) can be calculated by Aungier model (1995) in order to obtain the induced power loss as a function of the mass flow rate ($\dot{m}$). The throttling coefficient (C_T) was estimated to be 0.816 by assuming an abrupt contraction followed by an abrupt expansion as the flow passes through the gap.

$$\Delta h_{leak} = \frac{C_T \times \dot{m}_{cl} \sqrt{(2\Delta p_{\mathrm{cl}}/\ \rho_2)} \times U_2}{2\dot{m}} \tag{10-6}$$

where:
C_T: Throttling coefficient
$\dot{m}_{cl}$: Leakage flow through tip clearance
ψ_w: Work coefficient

Besides, the pressure difference across the leakage area is calculated using formula (10-7) according to the principle of the change in fluid angular momentum.

$$\Delta p_{cl} = \frac{\dot{m} \times (r_2 V_{\theta 2} - r_1 V_{\theta 1})}{Z\ \times \left(\frac{r_2+r_1}{2}\right) \times \left(\frac{b_2+b_1}{2}\right) \times L_\theta} \tag{10-7}$$

This model was derived assuming a constant slip factor across the tip clearance. The velocity profile and pressure distribution through the clearance gap were assumed to be uniform; thus, greater uncertainty is expected at very high flow and Mach number conditions.

The power equation (Eqn. 10-8) is used to obtain the initial efficiency.

$$\eta_p = \dot{m}\frac{Z_{avg} R T_1 \left(\frac{n_v}{n_v - 1}\right)\left[\left(\frac{p_2}{p_1}\right)^{\frac{(n_v-1)}{n_v}} - 1\right]}{Power} \tag{10-8}$$

Moreover, the polytropic head (h_p) is calculated using equation (10-9) as a function of efficiency, work coefficient and tip velocity.

$$h_p = Z_{avg} R T_1 \left(\frac{n_v}{n_v - 1}\right)\left[\left(\frac{p_2}{p_1}\right)^{\frac{(n_v-1)}{n_v}} - 1\right] = \psi_w \eta_p {U_2}^2 \tag{10-9}$$

Initially, the work coefficient (ψ_w) is derived using Casey-Robinson model (2013) in terms of flow coefficient and Mach number.

$$\psi_w = \left(1 + \frac{k_{df}}{\varphi}\right)\left[\frac{v_{\theta 2}}{u_2} - \frac{v_{m2}}{u_2} tan(\beta_2) + \varphi k_s\right] \tag{10-10}$$

Therefore, the efficiency is recalculated from basic work coefficient equation (10-9) to consider the effect of the head coefficient, Mach number and work coefficient. Then, the discharge parameters are calculated based on the new efficiency value which, in turn, used to correct the pressure loss coefficient (ψ_l). Accordingly, the new work and pressure loss coefficients' values are substituted in Senoo and Ishida model (1986) to derive the new efficiency value as represented by "Process (C)" in figure 10-1.

$$\frac{\eta_0 - \eta}{\zeta} = \frac{\psi_l + (1 - \eta_0)(\psi_{w0} - \psi_w)}{\zeta \, \psi_w} \tag{10-11}$$

where:
η_0: Efficiency at zero tip clearance
ψ_l: Pressure loss coefficient due to tip clearance
ψ_w: Work coefficient
ζ: Tip Clearance Ratio (ε_c/b$_2$)

The Senoo-Ishida model was developed assuming the pressure loss due to tip clearance to consist of the induced loss by the leakage flow through the clearance and the pressure loss for supporting fluid against the pressure gradient in the blade channels and the space between the impeller and shroud. This model has been tested, and the predicted efficiency reduction showed fair agreement with the experimental data of high speed and low speed compressors. However, this expression does not account for the variation in the slip factor and incidence losses; thus, it is limited to design conditions while the prediction was found less accurate at off-design conditions.

The predicted tip clearance velocity can be used to calculate the equivalent Mach number (Mu). This value is then substituted to obtain the surge flow coefficient (φ_s) using equation (10-12).

$$\varphi_{s_i} = \left[1 - \frac{1}{1 + e^{-4.75(Mu_i - 0.814)}}\right]\left\{\left(\frac{\varphi_s}{\varphi_c}\right)_{Lo} \varphi_{c_i} + \frac{\left(\varphi_{p_d} - \varphi_{p_i}\right)(Mu_{max} - Mu_i)}{\left(\frac{\varphi_{cd}}{\varphi_{c_i}}\right)^2 - \left(\frac{\varphi_{p_i}}{\varphi_{p_d}}\right)^2}\right\} + \frac{\varphi_{c_i}}{1 + e^{-4.75(Mu_i - 0.814)}}\left(\frac{\varphi_s}{\varphi_c}\right)_{Hi} \tag{10-12}$$

The surge margin can be defined as a function of design (φ_d) and surge flow (φ_s) coefficients:

$$SM(\%) = \frac{\varphi_d - \varphi_s}{\varphi_d} \times 100\ (\%) \tag{10-13}$$

10.3 New Method Evaluation

The approach described in the previous section will be used to model the effect of shrouded percentage on efficiency and operating range. This method has been applied for three different centrifugal stage designs in order to emphasize its validity under various operating conditions as shown in table 10-1. Figure 10-2 demonstrates the variation in the derived polytropic efficiency of the first stage design (I) with shrouded percentage and at different phases. The calculated leakage flow and pressure drop across the tip clearance are used to estimate the discharge conditions and enthalpy drop by Aungier model (Eqn. 10-6). Thus, the initial efficiency is obtained using power equation (Eqn.10-8) as indicated by "Stage A" in figures 10-1 and 10-2.

Table 10- 1: Geometrical Features of Investigated Centrifugal Compressor Stage Design

Parameter	Case (I) High Speed High Flow	Case (II)* High Speed Low Flow	Case (III)** Low Speed Low Flow
d_{1t} (mm)	*250.0*	*28.5*	*300.0*
$d_{1h}(mm)$	*134.0*	*14.0*	*160.0*
d_2 (mm)	*655.0*	*48.0*	*500.0*
$b_2(mm)$	*53.0*	*1.80*	*32.5*
N_d (rpm)	*7346*	*48000*	*2000*
π_d (p_2/p_1)	*1.244*	*2.87*	*1.173*
Z_b	*17*	*16*	*16*

**Jin Tang et al. (2008)   ** Sitaram and Swamy (2012)*

A further step is taken to correct this curve by considering the effect of work coefficient using formula (10-9) as represented by Stage (B) in figure 10-2. For more accurate estimation, a third process is performed using Senoo and Ishida model (Eqn. 10-10) by substituting the new work and pressure loss coefficients. This is denoted by "Stage C" in figures 10-1 and 10-2. The sensitivity of the shrouded percentage variation on the stage efficiency becomes greater than the previous curve. It was observed that the efficiency is reduced by about 5.12% when the shrouded impeller configuration is replaced by fully unshrouded one. This difference is expected to vary with the stage design, rotational speed and inlet flow rate.

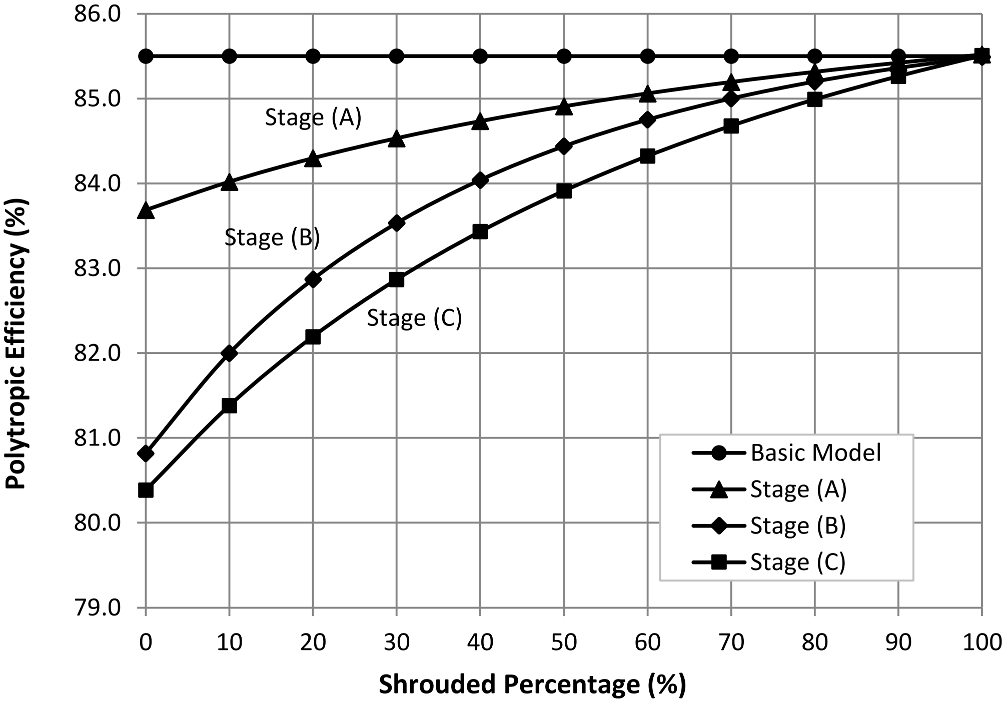

Figure 10- 2: Comparison Between the Estimated Efficiency At Different Process

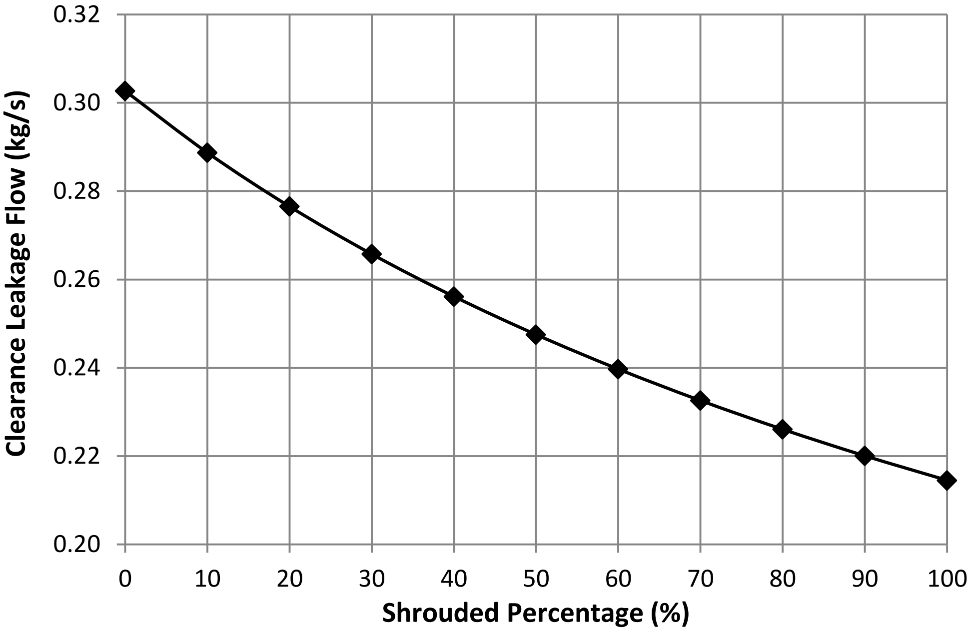

Figure 10- 3: Determination of Clearance Leakage Flow at Various Shrouded Percentage

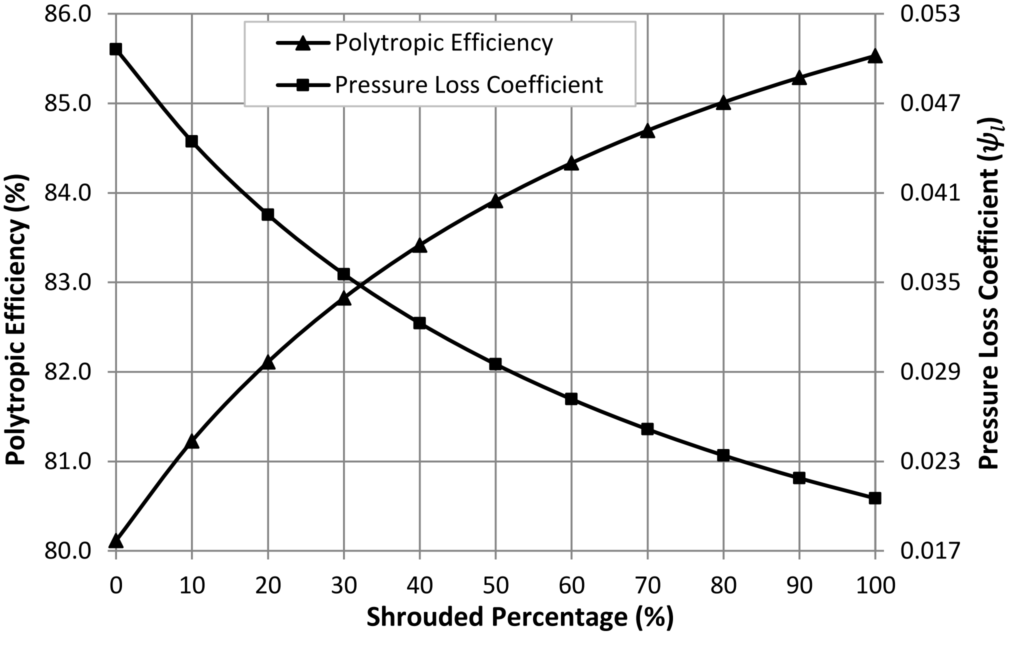

Figure 10- 4: Determination of Clearance Leakage Flow and Pressure Drop at Various Shrouded Percentage

The shroud on centrifugal compressor impeller has a significant effect on the internal flow of the impeller. Based on the efficiency view, the reduction in the polytropic efficiency at low shrouded percentage is governed by two main factors which are the leakage flow and pressure loss rise. The open unshrouded impellers are suffering from a higher tip leakage flow as shown in figure 10-3 which demonstrates an increase in the leakage flow rate as the shrouded percentage reduces. This is also incorporated with a higher pressure loss as illustrated in figure 10-4 in terms of pressure loss coefficient. So, there is a need for optimisation between the shrouded area and the stage efficiency to balance between the efficiency improvement and high capital cost. However, it should be noted that both leakage flow and pressure loss coefficient are expected to grow up at high rotational speed and flow rate. Moreover, designing the impeller with a smaller tip clearance will obviously decrease the efficiency reduction at low shrouded percentage.

When considering resonance frequency, the absence of cover allows the unshrouded impellers to operate at higher rotational speed because of the greater resonance frequency. If very high tip speeds are required, the shrouds should be eliminated to reduce the resulted centrifugal stresses by the additional mass. This becomes more significant with multistage compressors where the large changes in operating clearance can cause greater thrust loads. Since the failure in the centrifugal impeller might lead to extensive damages, it is necessary to select the proper design parameters in order to avoid the critical resonances. Moreover, the generated pressure ratio by the impeller is proportional to the square of tip speed. Consequently, the higher rotational speed of the unshrouded impellers makes them capable of producing a higher pressure ratio relative to the shrouded impellers. So, the selection of impeller configuration is highly affected by the desired rotational speed. Thus, the unshrouded impeller might become the only available option to consider for very high rotational speed applications.

To test the validity of the developed approach for high speed and low flow rate compressors, this method is used to obtain the efficiency of the studied compression stage by Tang et al. (2008) as denoted by Case (II) in table 10-1. Figure 10-5 compares the derived isentropic efficiency curve against the obtained results from the CFD simulation. The obtained efficiency at fully shrouded configuration matches the CFD value with a relative deviation of only around 0.236% because the initial stage design is with shrouded centrifugal impeller.

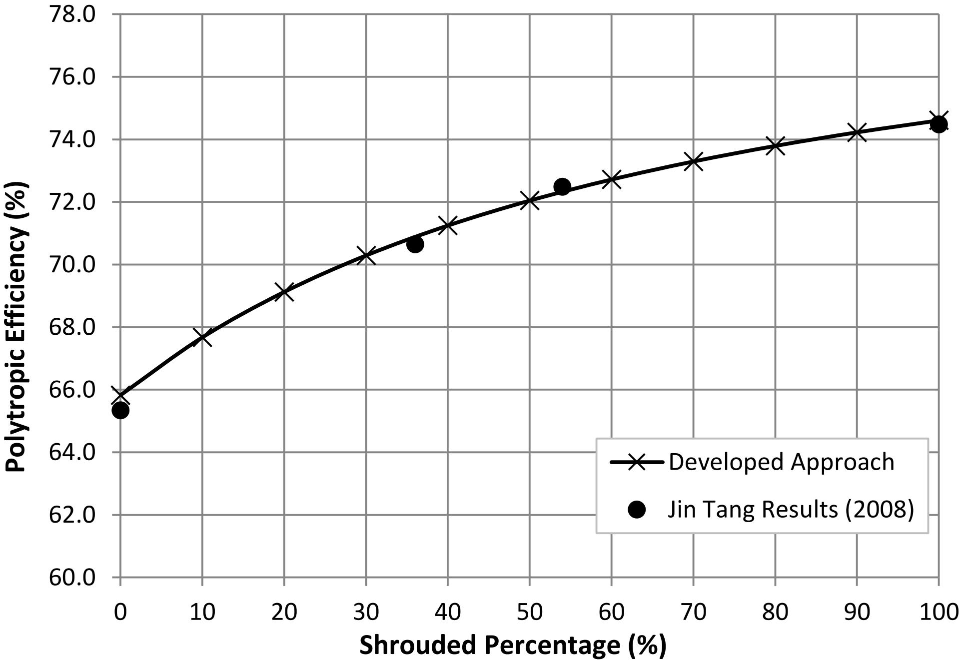

Figure 10- 5: Comparison Between the Obtained Efficiencies and CFD Results for Case (II)

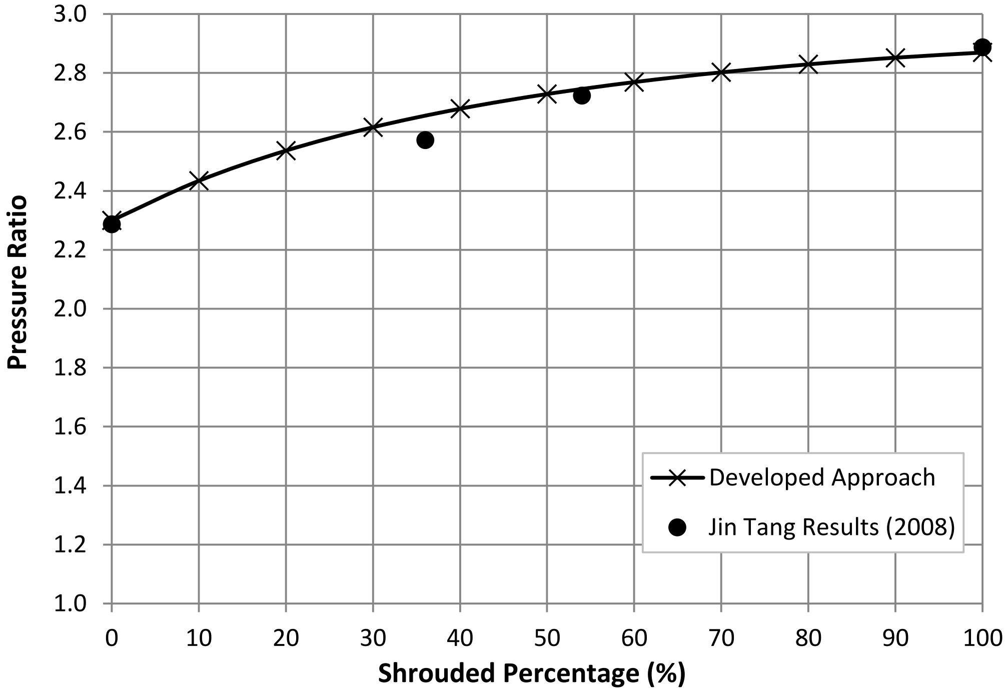

Figure 10- 6: Comparison Between the Obtained Pressure Ratios and CFD Results for Case (II)

The calculated parameters tend generally to be lower than the CFD results which is expected as the developed approach does not account all associated pressure losses to the flow recirculation. Therefore, this method can be used to derive the shape of the performance curve with an acceptable uncertainty in the predicted parameters. However, it is interesting to observe that all the points roughly situated on the line derived from the developed model. The maximum deviation between the two approaches' results was found in the fully unshrouded configuration by about 0.74% as a relative difference. Figure 10-6 compares the calculated pressure ratio with the CFD simulation results. The maximum uncertainty can be observed at the shrouded percentage of 36% by approximately 3% relative error. This in fact still falls under the allowed maximum uncertainty of ±4.0%.

A further validation has been conducted to emphasize the suitability of the new model for low-speed and low-flow-rates operating conditions. The geometrical features of the tested stage are shown in table (10-1) as represented by Case (III). Figure 10-7 shows the derived head coefficient at tip clearance ratio of 5.1% against the measured data obtained by Sitaram and Swamy (2012) for both unshrouded and partially shrouded impeller configurations. The initial design is with unshrouded impeller as denoted by a continuous line in figure 10-7. The measured data fall roughly on the estimated head coefficient line, and the greatest difference can be observed near the surge and choke flow rates. However, the recorded improvement in the head coefficient due to the use of partially shrouded impeller was found quite greater than the predicted values throughout the flow range. This is might be because the developed approach does not account for all associated pressure losses to the flow recirculation and unsteadiness. The largest deviation between the estimated and measured head coefficient is about 2.03% and 1.74% near the choke flow of fully unshrouded and partially shrouded designs, respectively.

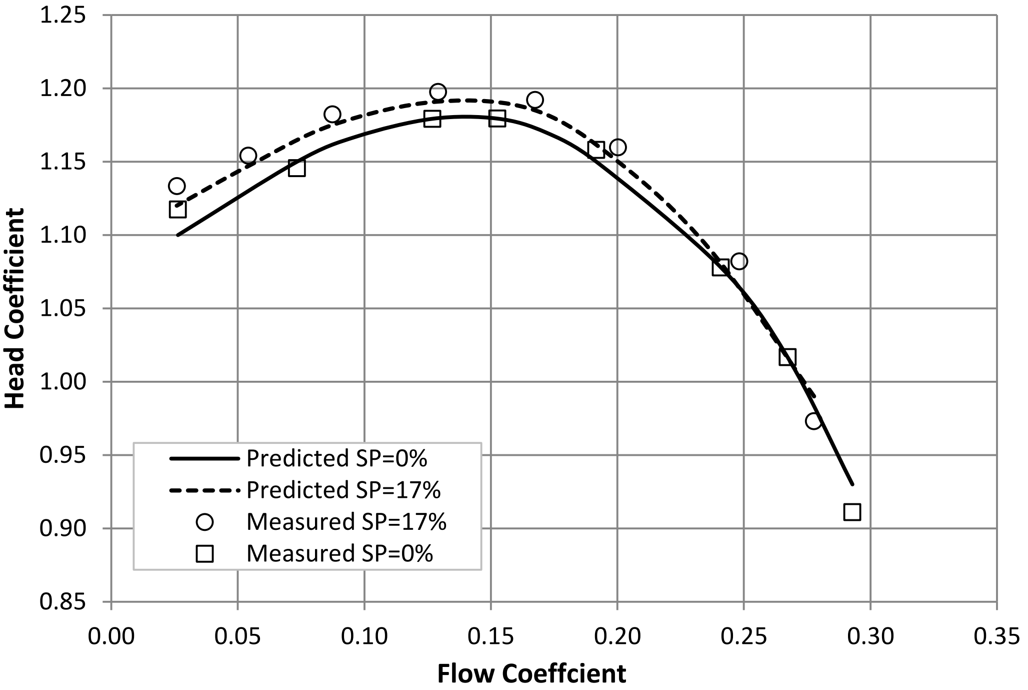

Figure 10- 7: Comparison Between the Recorded Measured data by Sitaram and Swamy (2012) and the Obtained Head Coefficient using Developed Approach for Case (III)

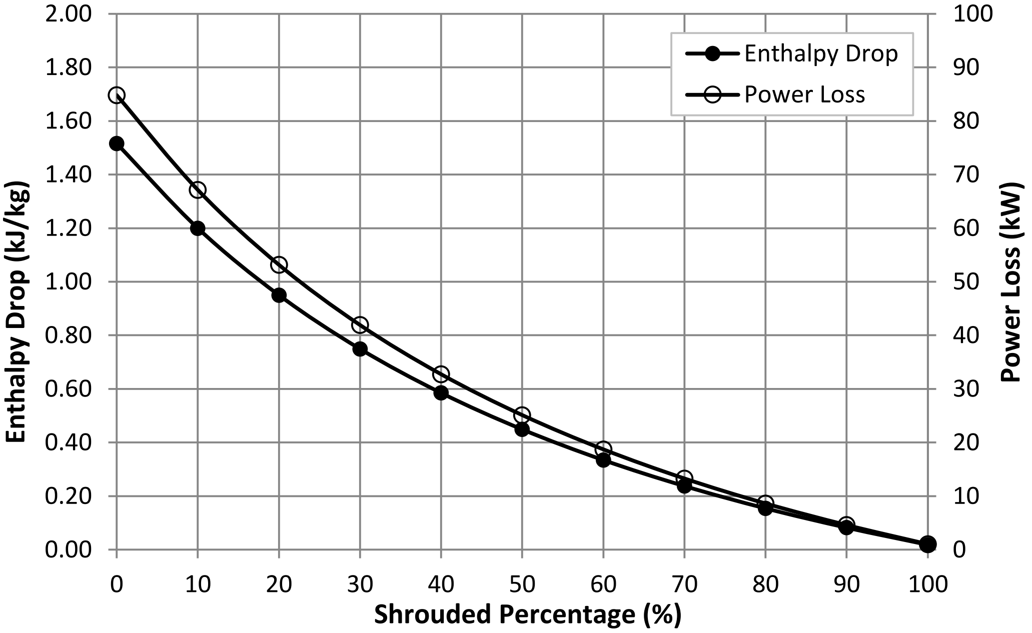

Figure 10- 8: Determination of Enthalpy Drop and Power Loss as A Result of Clearance Leakage Flow Clearance at Various Shrouded Percentage

Despite the fact that the manufacturing cost of shrouded impeller is higher, it is important to compare that with the cost saving in terms of performance improvement. The high loss coefficient at low shrouded percentages reduces the amount of transferred energy from the impeller blade to the fluid. This can be expressed in terms of enthalpy drop as shown in figure 10-8. Based on the design flow rate, the power drop can be obtained as plotted in the same figure.

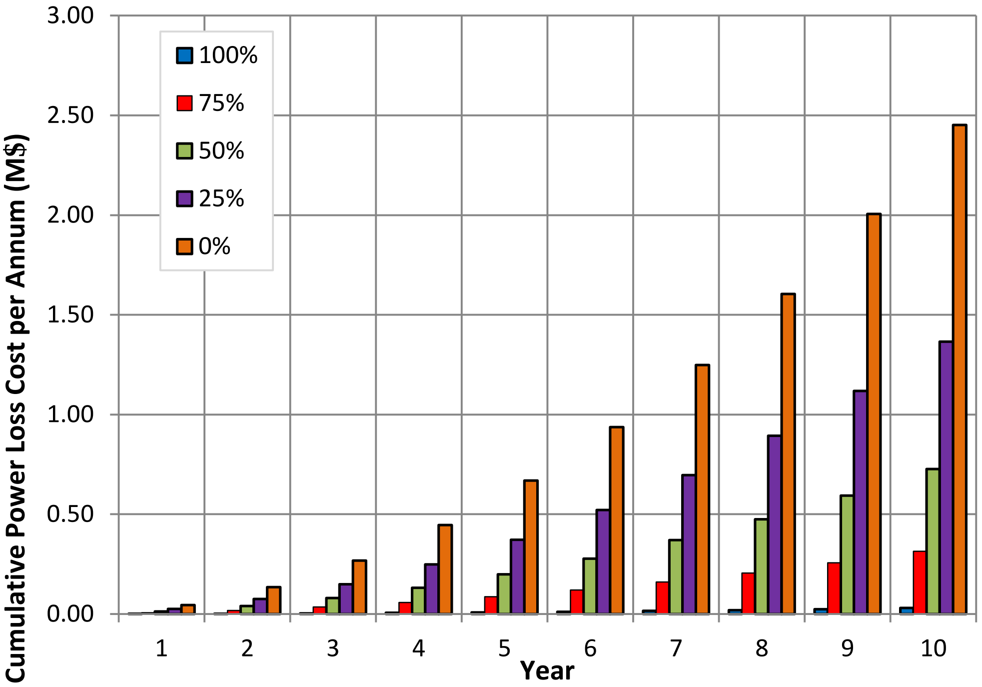

Figure 10- 9: Effect of Shrouded Percentage on the Cumulative Power Loss at Electricity Price of 0.06$/kWh(e)

The reduction in the stage efficiency at low shrouded percentage raises the demanded power to achieve the required pressure ratio due to the high pressure losses. This power loss, in fact, increases at high flow rate operation. Economically, the power drop can be expressed in terms of the cumulative power loss cost as illustrated in figure 10-9 assuming an electricity price of 0.06$/kWh. The estimated power loss cost with unshrouded impeller is around 2.657 M$ at the end of year ten. This figure decreases gradually as the shrouded percentage increases. An interesting point which stands out from this figure is that investing in a partially shrouded impeller configuration with 50% shrouded percentage is expected to save approximately 1.93M$ comparing with the fully unshrouded impeller. This represents about 72.6% of the predicted power loss cost at the shrouded percentage of 0%.

One of the key parameters which has to be investigated while dealing with the impeller configuration is the stable flow range. The prediction of the shrouded percentage effect on operating range is based on the estimated change in the Mach number and work coefficient. Figure 10-10 demonstrates an increase in the surge flow coefficient as the shrouded percentage increases, reaching the peak value at fully shrouded design. This obviously indicates a reduction in the operating range at high shrouded percentages driven by high Mach number. It is clear that the shrouded impellers have narrower operating range. Figure 10-11 shows the trade-off between the efficiency and choke-to-surge flow coefficients ratio at various shrouded percentages. The obtained results demonstrated that the shrouded impellers have higher efficiency but relatively shorter flow range. The green area in this figure indicates the region of shrouded percentage at which the operating range has higher priority than efficiency. When the higher efficiency is targeted, the shrouded percentages of the pink area should be selected. The significant of the shrouded percentage effect on the choke-to-surge flow coefficients can be detected as a function of surge margin as illustrated in figure 10-10.

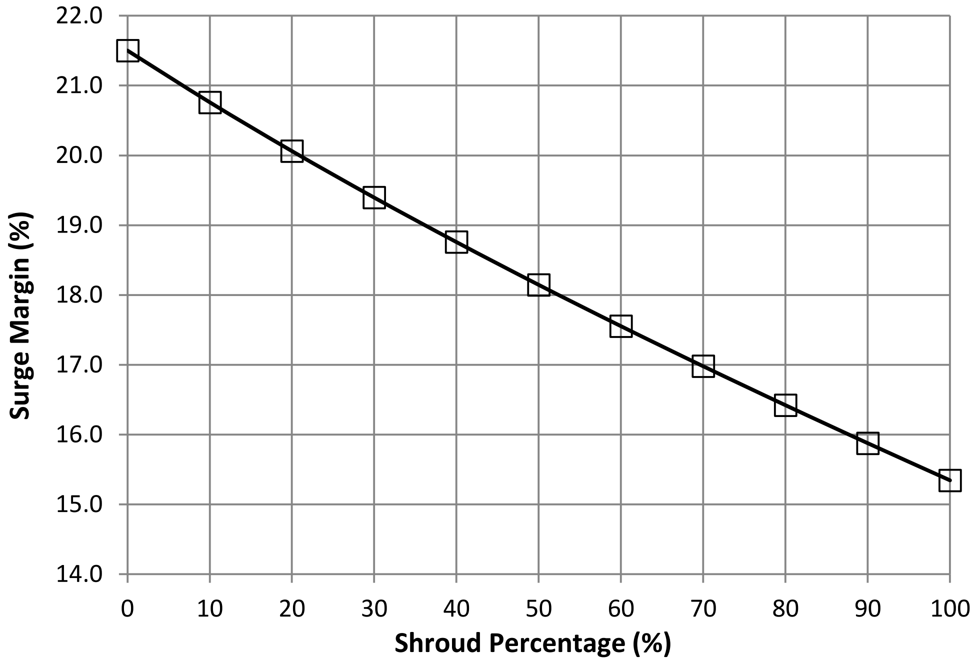

Figure 10- 10: Effect of Shrouded Percentage on Surge Margin

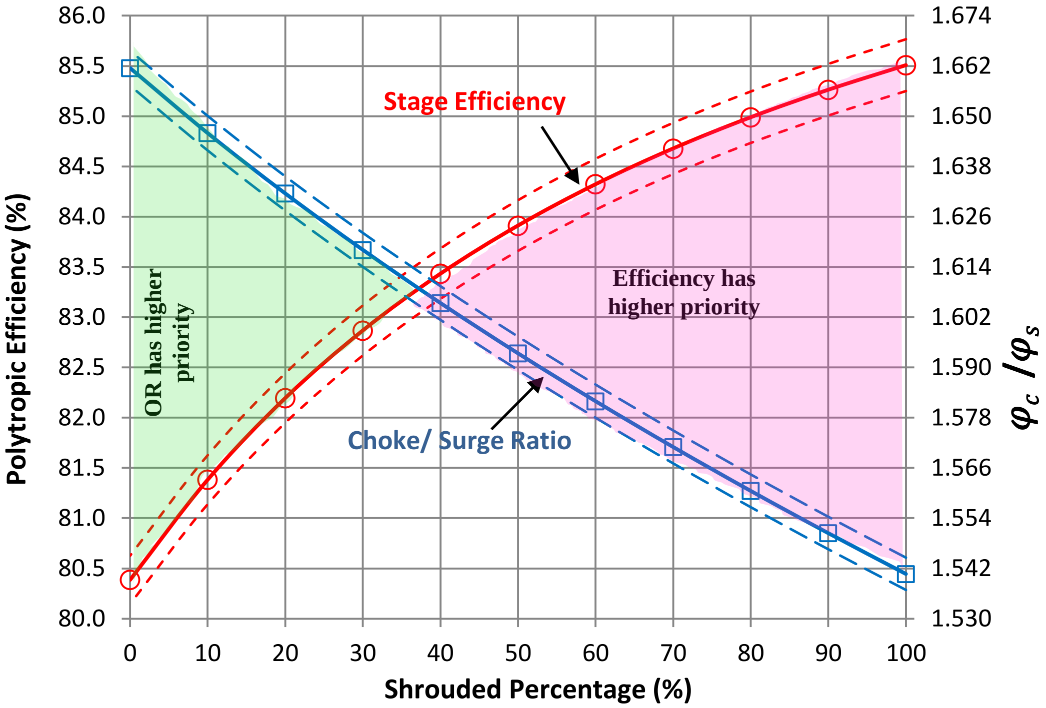

Figure 10- 11: Effect of Shrouded Percentage on the Stage Efficiency and Choke-to-Surge Flow Coefficients Ratio

The dotted lines denote the acceptable uncertainty in the predicted efficiency and choke-to-surge flow coefficients ratio. The shrouded percentage at the intersection point between the two curves varies accordingly. This figure becomes more useful to select the optimum shrouded percentage in order to fit with the required duty. However, it is important to mention here that the optimum shrouded percentage highly varies based on the sort of application and the expected range of the operating conditions variation.

10.4 Effect of Impeller Blade Exit Angle

The impeller blade angle is another design factor that influences the centrifugal compressor performance. Based on blade exit angle, the impeller geometry can be classified into three categories which are: forward-leaning blades ($\beta_2 > 90°$), radial blades ($\beta_2 = 90°$) and back-leaning blades ($\beta_2 < 90°$). The effect of blade exit angle on the stage pressure ratio is obtained by considering its influences on the work coefficient using equation (10-14).

$$\psi_w = \left(1+\frac{k_{df}}{\varphi_i}\right)\left(1-\frac{c_s}{U_2}+k_{\psi_w}\right) \qquad \textbf{(10-14)}$$

The slip velocity ratio is calculated by formula (10-15) as following:

$$\frac{c_s}{U_2} = 1-\frac{V_{\theta 2}}{U_2}+\varphi_2 tan\beta_2 \qquad \textbf{(10-15)}$$

Furthermore, the exit flow coefficient can be expressed in terms of global flow coefficient, density ratio and global tip Mach number. Thus, the Mach number is defined based on suction conditions and exit tip velocity.

$$\varphi_2 = \varphi_i \frac{1}{\pi}\frac{D_2}{b_2}[1+(k_i-1)\gamma_d k_i Mu_i^2]^{\frac{1}{n_d-1}} \qquad \textbf{(10-16)}$$

By obtaining the equivalent work coefficient to the specified blade exit angle, the pressure ratio can be calculated, respectively using equation (10-17).

$$\frac{P_2}{P_1} = [\psi_w\,(k_i-1)Mu_2^2+1]^{\frac{k_i\eta_p}{k_i-1}} \qquad \textbf{(10-17)}$$

This pressure ratio value is then substituted in equation (10-8) to derive the stage efficiency. Moreover, the effect on the operating range is evaluated by calculating the surge flow coefficient using correlations (10-12) and (10-13).

Figure 10- 12: Effect of Blade Exit Angle on Exit Mach Number

Using the shown stage geometry (I) in table 10-1, the developed approach is used to investigate the influences of exit baled angle on the stage head, efficiency and operating range. Figure 10-12 demonstrates a continuous increase in the tip Mach number at impeller exit as the blade exit angle increases. The lowest exit tip Mach number value can be observed with backward curved blades. This basically indicates more efficient conversion of the imposed kinetic energy by the rotating impeller at low blade angles. However, the forward-leaning blades provide a positive sloping head curve and the maximum head output as shown in figure 10-13 in terms of pressure ratio and head coefficient since the tangential component of relative velocity (V_{θ}) is increasing with growing flow. In the straight radial blades impeller ($\beta_2 = 90$), the tangential velocity does not change with the flow leading theoretically to a constant head curve.

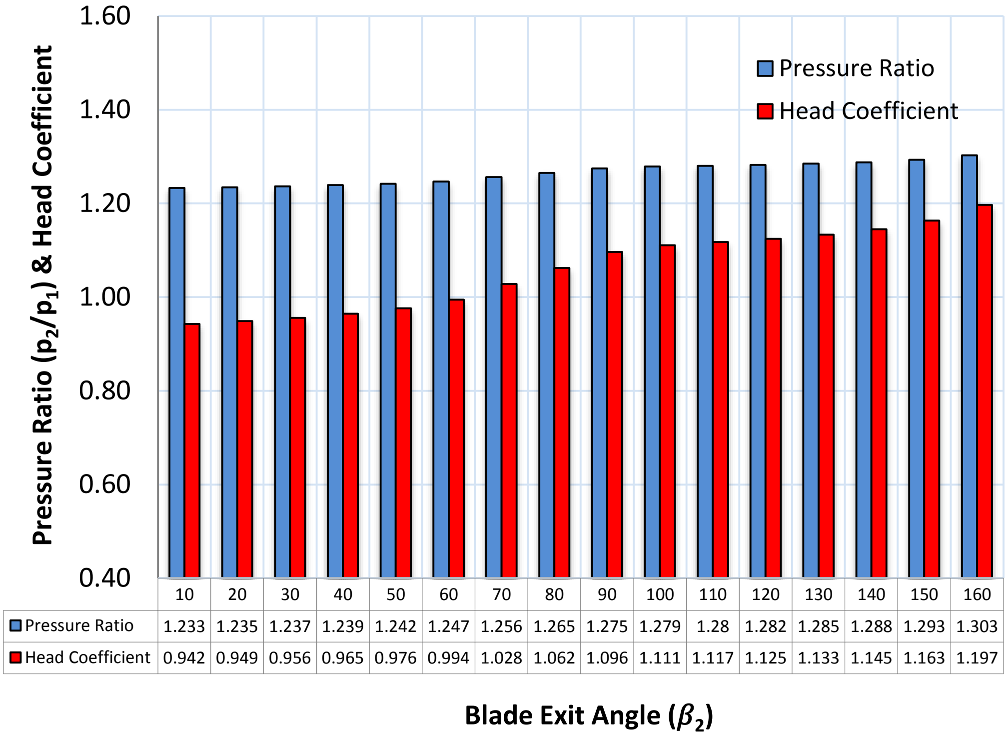

	10	20	30	40	50	60	70	80	90	100	110	120	130	140	150	160
🟦 Pressure Ratio	1.233	1.235	1.237	1.239	1.242	1.247	1.256	1.265	1.275	1.279	1.28	1.282	1.285	1.288	1.293	1.303
🟥 Head Coefficient	0.942	0.949	0.956	0.965	0.976	0.994	1.028	1.062	1.096	1.111	1.117	1.125	1.133	1.145	1.163	1.197

Figure 10- 13: Effect of Blade Exit Angle on Stage Pressure Ratio and Head Coefficient

Despite the low head coefficient of backward curved vanes, figure 10-14 demonstrates one of the main advantages of using this sort of vane configuration. It is clear that the choke-to-surge flow coefficient ratio decreases with the blade exit angle increase yielding a narrower operating range at high angle values. The low tip Mach number associated with backward leaning blades leads to make the stable flow range wider than the radial and forward leaning blades. Focusing on the backward curved vanes, figure 10-15 shows the predicted stage efficiency and surge margin at various blade angles. The efficiency is taking an opposite trend to the head coefficient which increases proportionally with the angle while the efficiency decreases. This, in fact, supports the previous finding of the higher diffuser inlet Mach number at high blade angles. To confirm that, it is important to consider the overall impact on stage efficiency. The estimated efficiencies at various angles demonstrate a non-linear drop in the efficiency value as the blade angle increases. However, the efficiency change is taking higher slope than the surge margin.

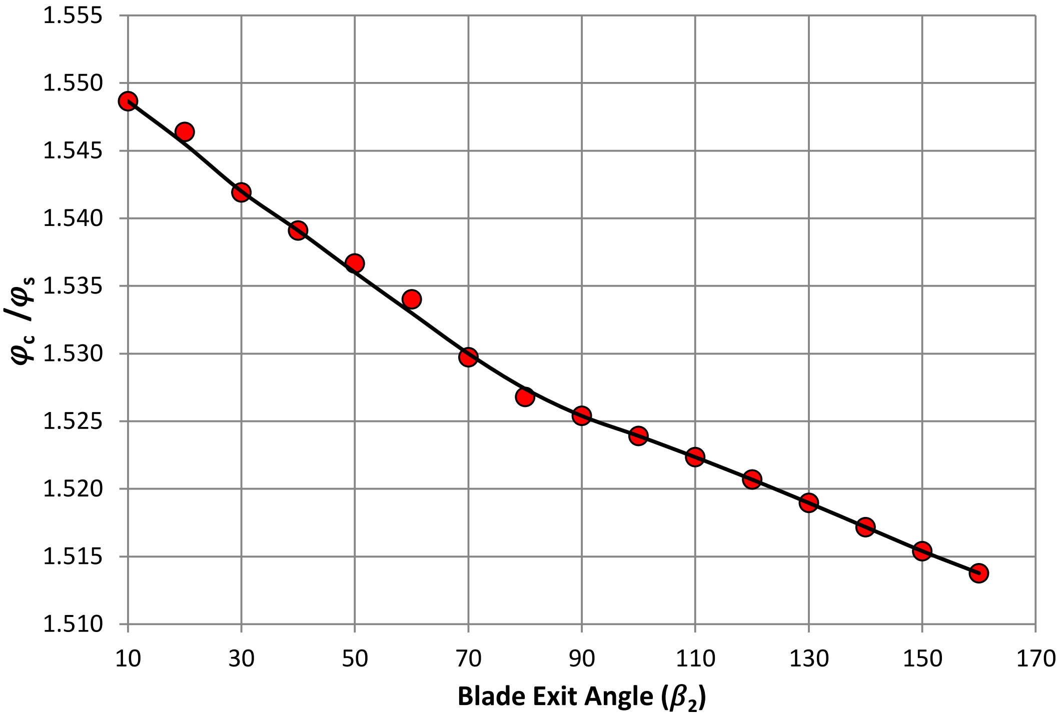

Figure 10- 14: Effect of Blade Exit Angle on Choke-to-Surge Flow Coefficients Ratio

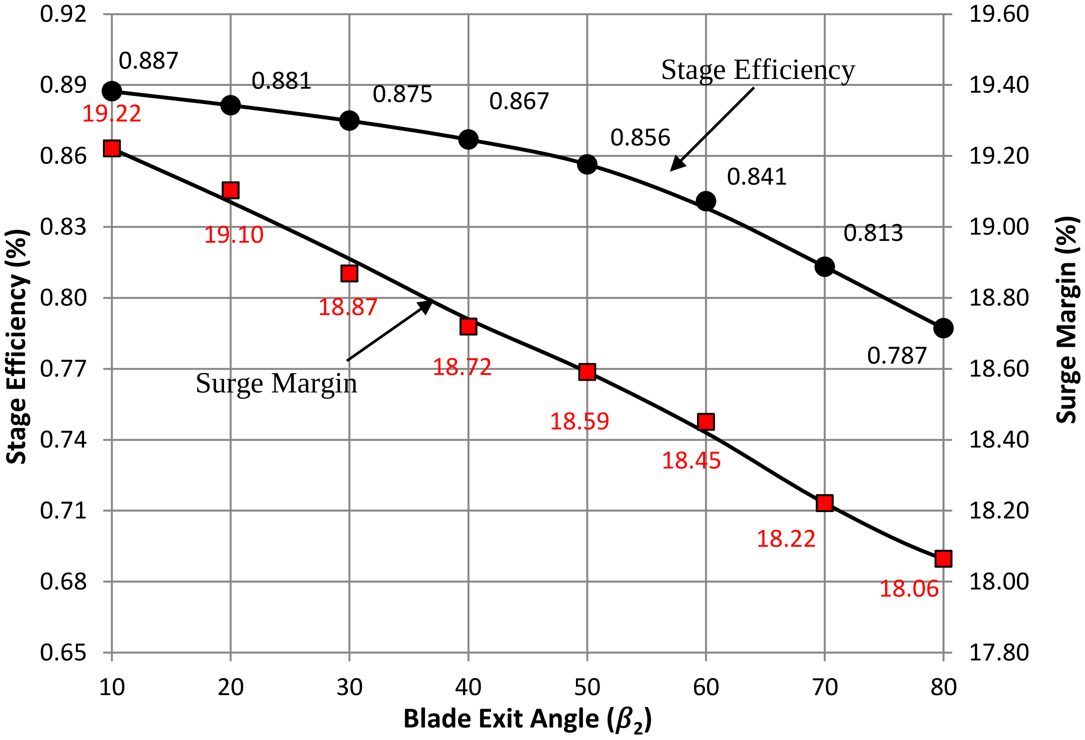

Figure 10- 15: Effect of Blade Exit Angle of Backward Curved Vanes on Stage Efficiency and Surge Margin

By comparing the three different blades shapes, figure 10-16 illustrates that the highest overall stage efficiency can be achieved by using backward-leaning impellers while the minimum value is expected with forward-leaning blades.

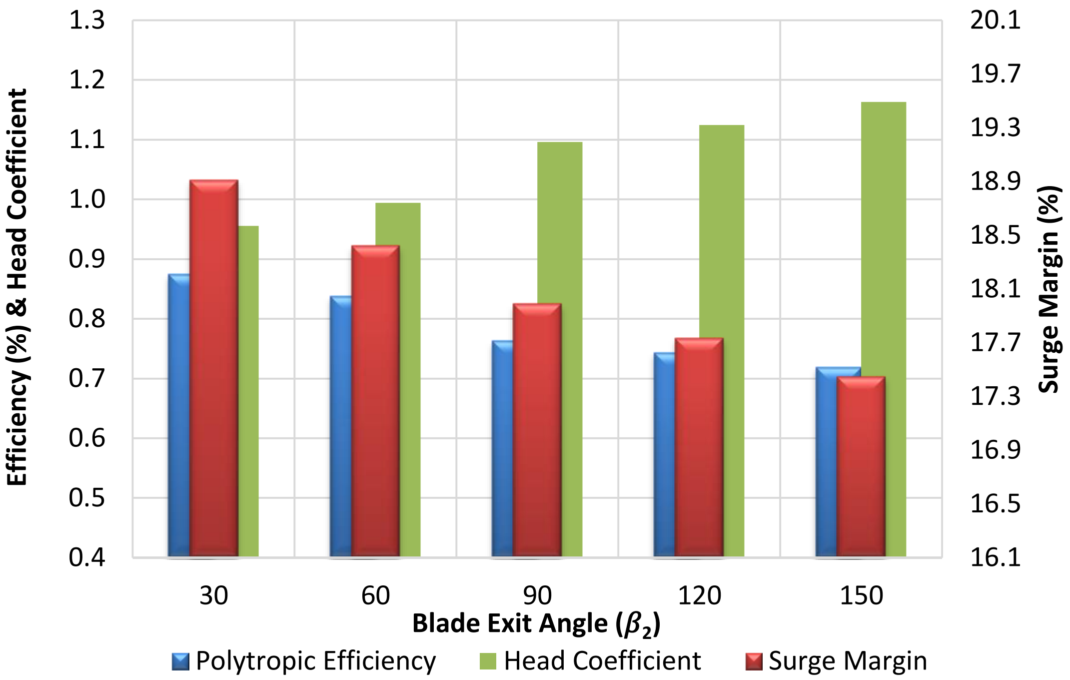

Figure 10- 16: Effect of Blade Exit Angle on Polytropic Efficiency and Surge Margin

Table 10- 2: Comparison Between Impeller Vanes

Vanes Type	Flow Rate and Size	Pressure Ratio	Surge Margin	Output
Forward curved vanes	small volume and size	high	surge margin is the narrowest	high speed, high noise, high diffuser inlet Mach number, low efficiency
Radial vanes	medium volume and size	medium to high		good efficiency
Backward curved vanes	large volume and size	low to high	surge margin is the widest	high efficiency, low noise, low diffuser inlet Mach number

Moreover, as the backward lean increases, the achieved efficiency increases, but this also leads to lower head as shown in figure 10-16. However, the observed effect of the exit vane angle on the performance parameters agrees with the expected trend by Boyce (2003) and Hanlon (2001). So, the blade angle should be selected to achieve the best fit with the desired head and efficiency requirements in any particular application. In terms of operating range, the widest surge margin was found at lower exit blades angle. This indicates another advantage from using the backward curved vanes in addition to high stage efficiency. Therefore, it is strongly recommended to consider the expected variation in the operating conditions while selecting the blade curve. Table 10-2 summarized the advantages and disadvantages of each type of impeller vanes with respect to flow rate, size, pressure ratio, surge margin and efficiency.

10.5 Influences of Diffuser Characteristics

The literature review exposed five main design parameters which have a significant impact on the overall performance of the diffuser which are diffuser width, radius ratio, chord length, vane number and inlet vane angle. Kalinkevych et al. (2011) proposed a method to calculate the flow parameters and energy characteristics of vaneless diffuser based on the boundary-layer theory. The flow was assumed to be in steady state, and circumferentially uniform and inlet velocities were assumed to be invariable by the width of the diffuser. Galerkin et al. (2015) derived a new model to account the loss coefficient of the vaneless diffuser. The fundamental principle of this model is based on the fact that the loss coefficient (ξ) is a function of friction coefficient (λ_{fr}), diameter ratio (D_4/D_3), flow angle (α_3) and inlet diffuser width (b_3).

$$\xi = \lambda_{fr}\left[\frac{\left(1-\frac{1}{D_4/D_3}\right)}{4\frac{b_3}{D_3}sin\alpha_3}\right] \tag{10-18}$$

$$\lambda_{fr} = \frac{0.316X_2}{{Re_3}^{0.25}} + \left(\frac{45^{\circ}-\alpha_3}{35^{\circ}}\right)^{X_1}\left[0.012+0.314\left(\frac{b_3}{D_3}-0.014\right)-\frac{0.316X_2}{{Re_3}^{0.25}}\right] \tag{10-19}$$

where:
X_1, X_2: Empirical coefficients

The obtained quantitative results agreed fairly with the CFD results except in the zones of flow separation of wide diffusers which can be considered as one of this model limitations.

The diffuser width is defined based on the exit impeller geometry and the type of the diffuser inlet configuration (pinched, un-pinched). The estimation of the impeller exit width (b_2) is critical for performance estimation and basic dimension setup due to its significant impact on flow coefficient and stage pressure ratio. Xu and Ryoichi (2012) derived a simple correlation for this purpose from Rodgers diffusion factor equation (Rodgers, 1978).

$$b_2 = \frac{10(D_2-D_1)}{1+(W_2/W_1)}\left[D_f - 1 + \frac{W_2}{W_1} - \frac{\pi D_2 U_2 \psi_w}{2Z_b \mathrm{L}_{\theta} W_1}\right] - \frac{(D_{s1}-D_{h1})}{2} \tag{10-20}$$

The diffusion factor (D_f) is estimated using Jansen model (1967) which estimates the diffusion as a function of flow deceleration and turning.

$$D_f = 1 - \frac{W_2}{W_{1s}} + \frac{0.75\,\Delta h_{Euler}/{U_2}^2}{\left(\frac{W_{1s}}{W_2}\right)\left[\left(\frac{Z_b}{\pi}\right)\left(1-\frac{D_{1s}}{D_2}\right)+2\frac{D_{1s}}{D_2}\right]} \tag{10-21}$$

Based on the diffusion factor; Rodgers, (1978) derived a formula to correlate the initiation of the stall with the limitation in the impeller diffusion capability.

$$\frac{\varphi_c}{\varphi_{stall}} \approx \frac{1}{\left(1.05-D_f\right)\left[1+\psi_w Mu^2\left(\frac{k-1}{2}\right)\right]^{1/(k-1)}} \tag{10-22}$$

Kim et al. (2002) presented design procedures of the conventional vaned and low solidity vane diffusers system aiming to achieve a wider flow range for centrifugal compressor stage.

According to Kalinkevych and Skoryk model (2013), the flow rate in vaned diffuser is calculated based on the fundamental continuity equation.

$$\dot{m} = \eta.\varepsilon(\eta).a_{cr}.\rho^*.2\pi.r.b.\left[1 - \frac{(\delta_v + \sum\delta^*)\,Z_v}{2\pi r sin\alpha}\right].\sin\alpha \qquad \textbf{(10-23)}$$

where:
η: Velocity coefficient (v_m/a_{cr})
$\varepsilon(\eta)$: Gas dynamic function of density
a_{cr}: Critical sonic speed
ρ^*: Stagnation density

The gas dynamic functions of density ($\varepsilon(\eta)$) and pressure ($\pi(\eta)$) can be determined in terms of gas properties as following:

$$\varepsilon(\eta) = \frac{\rho}{\rho^*} = \left(1 - \frac{k-1}{k+1}\eta^2\right)^{1/(k-1)} \qquad \textbf{(10-24)}$$

$$\pi(\eta) = \frac{p}{p^*} = \left(1 - \frac{k-1}{k+1}\eta^2\right)^{k/(k-1)} \qquad \textbf{(10-25)}$$

The vaned diffuser throat blockage factor (τ) measures the ratio between ineffective flow area $\left(1 - \frac{A_E}{A}\right)$ to the total area (A). This is estimated by formula (10-26) as a function of vane thickness (δ_v) and number of vanes (Z_v) based on Kalinkevych et al. model (2011).

$$\tau = 1 - \left[\frac{2\pi r_3 sin(\alpha_3) - (\delta_v + \sum\delta^*)\,Z_v}{2\pi r_3 sin(\alpha_3)}\right] \qquad \textbf{(10-26)}$$

where:
$\sum\delta^*$: Total displacement thickness of boundary layers

This model is valid only for the subsonic flow along the entire diffuser. Thus, by substituting equation (10-24), the equation (10-23) can be written in a new form:

$$\dot{m} = 2v_m\,\rho\pi rb.\left[1 - \frac{(\delta_v + \sum\delta^*)\,Z_v}{2\pi r sin\alpha}\right]\sin\alpha \qquad \textbf{(10-27)}$$

For the purpose of simplicity, the effect of boundary layer will be ignored in this study. Assuming a linear pressure distribution along the vane pitch, the average flow velocity (η) can be calculated in terms of velocities on the vane suction (η_{ss}) and pressure surfaces (η_{ps}).

$$2\pi(\eta) = 2\pi(\eta_{ss}) + \pi(\eta_{ps}) \qquad \textbf{(10-28)}$$

The presence of the flow separation zone at the pressure side of vaned diffuser vane causes the effective area of the flow channel to decrease leading to higher flow velocity and friction losses. Therefore, the prediction of preseparation condition of the boundary layer and using flow separation control will help to improve the stage characteristics. The velocity distribution at pressure surface can be predicted using equation (10-29).

$$\eta_{ps} = \eta_1\left[1 + \frac{(\bar{l} - \bar{l}_1).(2 + H_s).(-f_s)}{\bar{\delta}_1^{\,**}}\right]^{-1(2+H_s)} \qquad \textbf{(10-29)}$$

where:

$\overline{\delta}^{**}$: Relative momentum thickness $=\delta_1{}^{**}/L_v$
L_v: Vane centerline length.
l: Vane centerline length coordinate.
H_s,f_s: Boundary layer shape parameters.

The recommended value of boundary layer shape parameter (f_s) is -0.02 while the value of coefficient (H_s) varies between 2.4 and 3.0.

The impeller exit blockage factor (τ_{IEB}) is calculated using the derived equation by Okhuahesogie et al. (2012).

$$\tau_{IEB} = 1 - \left[\frac{2\pi r_2 sin(\alpha_2) h_{b2} - 0.5(\delta_{h2} + \delta_{s2})\, h_{b2}\, Z_v}{2\pi r_2 sin(\alpha_2)}\right] \tag{10-30}$$

where:
δ_{h2}: Blade thickness at impeller exit hub.
δ_{s2}: Blade thickness at impeller exit shroud.
h_{b2}: Blade height at impeller exit

Since the vaneless space is designed to reduce the high velocity of the discharge flow from the impeller, the leading edge radius of the diffuser (r_3) can be estimated by applying equation (10-31) based on the flow Mach number (M_2) and exit flow angle (α_3) (Kim et al., 2002).

$$\frac{r_3}{r_2} = \frac{1 + \alpha_3}{360} + \frac{M_2^2}{15} \tag{10-31}$$

The vane passage length (L_v) is calculated according to the divergence angle (θ_d), number of vanes (Z_v), inlet and exit radius and vane angle. The equivalent divergent angle is used to account the flow diffusion losses and it is modelled by the two-dimensional diffuser analogy.

$$L_v = \pi \frac{r_4 sin\beta_4 - r_3 sin\beta_3}{Z_v \tan\theta_d} \tag{10-32}$$

For low solidity vane diffusers with straight vanes, the vane length (L_v) is calculated by equation (10-33). This model has been proposed by Engeda (1996).

$$L_v = 2r_3 sin\left(\frac{180}{Z_v}\right)\cos\left(\beta_3 + \left(90 - \cos^{-1}\left[sin\left(\frac{180}{Z_v}\right)\right]\right)\right) \tag{10-33}$$

The blade exit angle (β_4) is specified to satisfy the maximum allowed solidity without forming a throat using the derived equation by Engeda (10-34). This value is then substituted in equation (10-35) to define the optimum exit diffuser radius.

$$\beta_4 = \tan^{-1}\left[\tan\beta_3 + \frac{2\sin(180/Z_v)}{\cos\beta_3} - \frac{\delta_3}{2r_3\sin\beta_3}\right] \tag{10-34}$$

$$r_4 = r_3 \frac{\cos\beta_3}{\cos\beta_4} \tag{10-35}$$

The Engeda model (1996) was developed assuming a maximum solidity, which means the highest possible solidity without forming a geometric throat. The maximum allowed solidity at no throat conditions is calculated using equation (10-36).

$$\sigma = \frac{\left(l + \frac{\delta_3}{2\tan\beta_3}\right)}{2r_3 sin\left(\frac{180}{Z_v}\right)} \qquad \textbf{(10-36)}$$

Generally, there are two basic parameters are used to measure the diffuser performance: blade loading parameter (BL) and static pressure recovery coefficient (PRC).

$$BL = \frac{2\pi\ (r_3 v_{\theta 3} - r_4 v_{\theta 4})}{Z_v L_v (v_{m3} - v_{m4})} \qquad \textbf{(10-37)}$$

$$\mathrm{PRC} = \frac{p_4 - p_3}{p_{t3} - p_3} \qquad \textbf{(10-38)}$$

10.5.1 Developed Approach Description

There are several available models in the open literature that define the design procedures for vaneless and vaned diffusers, but they generally depend on the detailed geometrical features of the diffuser system and require a calibration with experimental data. The established model aims to derive the characteristics and energy coefficients of the diffuser system assuming different configurations as demonstrated in figure 10-17. This can be then used to evaluate the appropriate diffuser type for such duty by analyzing its impact on stage efficiency and flow range. The fundamental principle of the developed method is based on the determination of the potential effect of diffuser geometrical features and inlet conditions on diffuser system characteristics. This is defined by five key parameters which are: diffuser inlet Mach number (Mu_3), inlet vane (β_3) and flow angles (α_3), number of vanes (Z_v) and radius ratio (r_4/r_3).

The inlet width of vaneless diffuser (b_3) is estimated according to the specified inlet configuration and based on the calculated exit impeller width (b_2) from equation (10-39). The diffusion factor of the impeller is given by Jansen model (1967).

$$\begin{aligned} b_3 = PP\% \times \Bigg[& \frac{10(D_2 - D_1)}{1 + (w_2/w_1)} \Bigg\{ \Bigg[1 - \frac{W_2}{W_{1s}} + \frac{0.75\ \Delta h_{Euler}/{U_2}^2}{\left(\frac{W_{1s}}{W_2}\right)\left[\left(\frac{Z_b}{\pi}\right)\left(1 - \frac{D_{1s}}{D_2}\right) + 2\frac{D_{1s}}{D_2}\right]} \Bigg] \\ & - 1 + \frac{w_2}{w_1} - \frac{\pi D_2 U_2 \psi_w}{2Z_b \mathrm{L}_\theta w_1} \Bigg\} - \frac{(D_{s1} - D_{h1})}{2} \Bigg] \end{aligned} \qquad \textbf{(10-39)}$$

The diffuser diameter ratio (D_4/D_3) is set at the beginning based on the recommended range (1.25-1.6) in the open literature such as Ljevar et al. (2005) and Rajput (2010). This value is iterated later to satisfy the demanded stage pressure ratio at the design point. The exit flow velocity is calculated as a function of the diameter ratio, and it is substituted to obtain the exit absolute Mach number and flow coefficient. The gas properties are assumed to be constant at the beginning as the inlet values. This allows to derive the first pressure ratio and the stage discharge parameters.

In the second calculation process, the obtained discharge pressure is compared with the required at design conditions and the diameter ratio is reviewed accordingly. Moreover, the physical gas properties are recalculated using the new discharge pressure and temperature values. For the CVD, the blockage factor at inlet throat is obtained by equation (10-26). Furthermore, the velocity distribution is estimated according to Kalinkevych and Skoryk model (2013).The number of vanes is set based on the standard values. The selection of the optimum diffuser vane number is complicated due its aerodynamic interaction with the impeller and volute. However, it is necessary to check that the diffuser vane number is less than the number of impeller blades in order to avoid the early stalling due to the created diffuser passage blockage by the initiated wakes at the impeller exit blades.

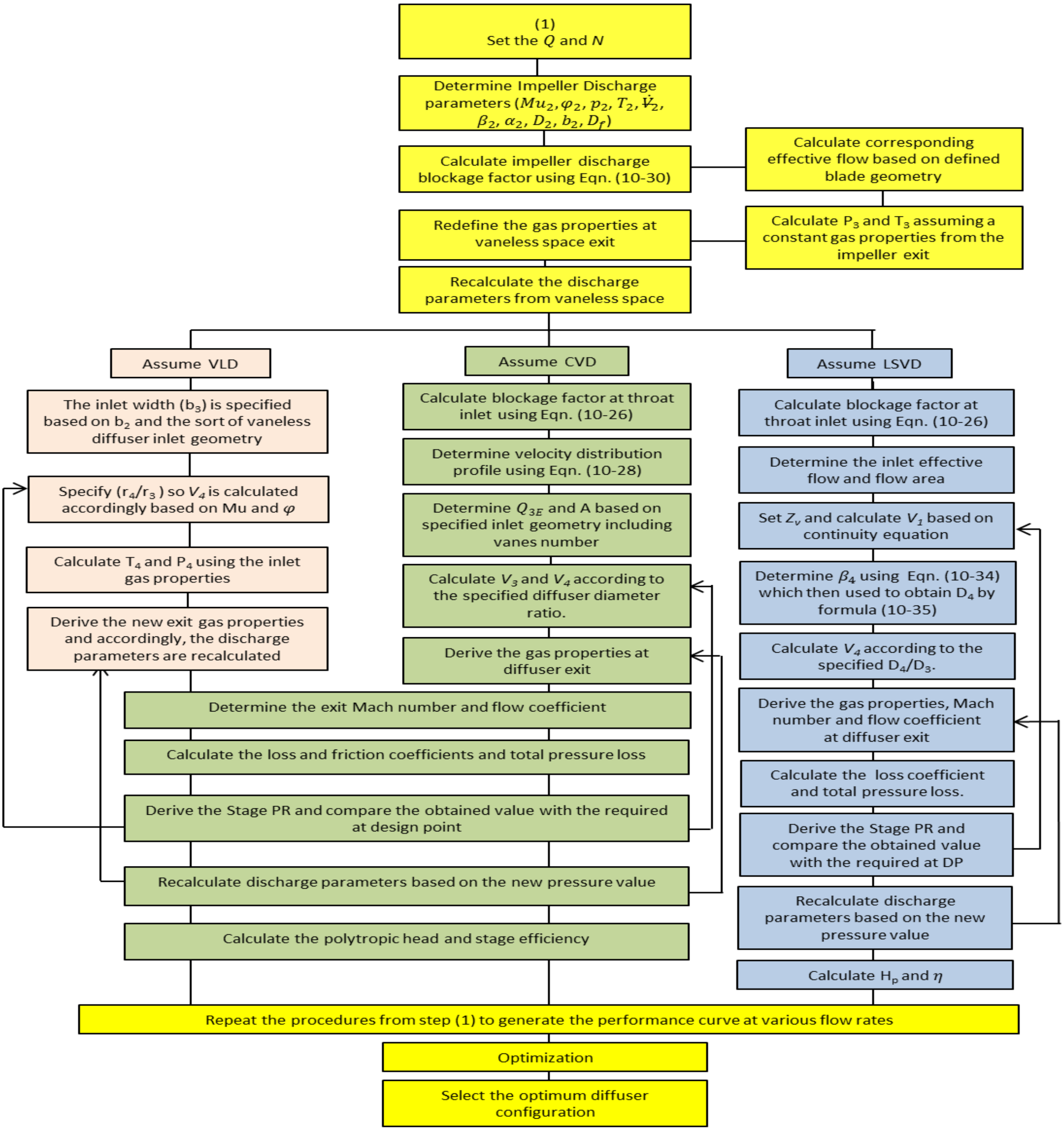

Figure 10- 17: Developed Method to Evaluate the Diffusion System Performance

Moreover, the surge flow tends to increase as the number of vanes increases due to the unsteady distribution of the flow near vanes which creates a kind of obstruction to the incoming flow to the diffuser. For low solidity vane diffuser, the exit vane angle is calculated assuming straight vanes with the maximum allowed solidity at no throat conditions. After that, it is substituted in equation (10-35) to obtain the exit diffuser diameter (D_4). The same procedures are then applied to derive the performance parameters of the centrifugal compressor stage. Therefore, the obtained performance curves of each diffuser configuration at various flow coefficients are analyzed to select the optimum design with respect to stage efficiency and operating range.

10.5.2 Results and Discussion

The vaneless region in this study is referred to the space between the impeller exit and the diffuser throat which is critical to guide the impeller flow to the diffuser and to ensure an effective diffusion process. This gap serves to reduce the diffuser inlet Mach number and to settle the flow before reaching the leading edge of diffuser vane. However, this space is not a basic part since there are some compressors are designed without this gap. For better performance, it is important to consider the right size since the large space leads to increase the overall radial size and the boundary layer growth which, in turn, causes a flow blockage in the diffuser, while the excessive short space causes a high level of noise, vibration and stresses. Figure 10-18 shows the variation of the overall stage pressure ratio and efficiency at different diameter ratios.

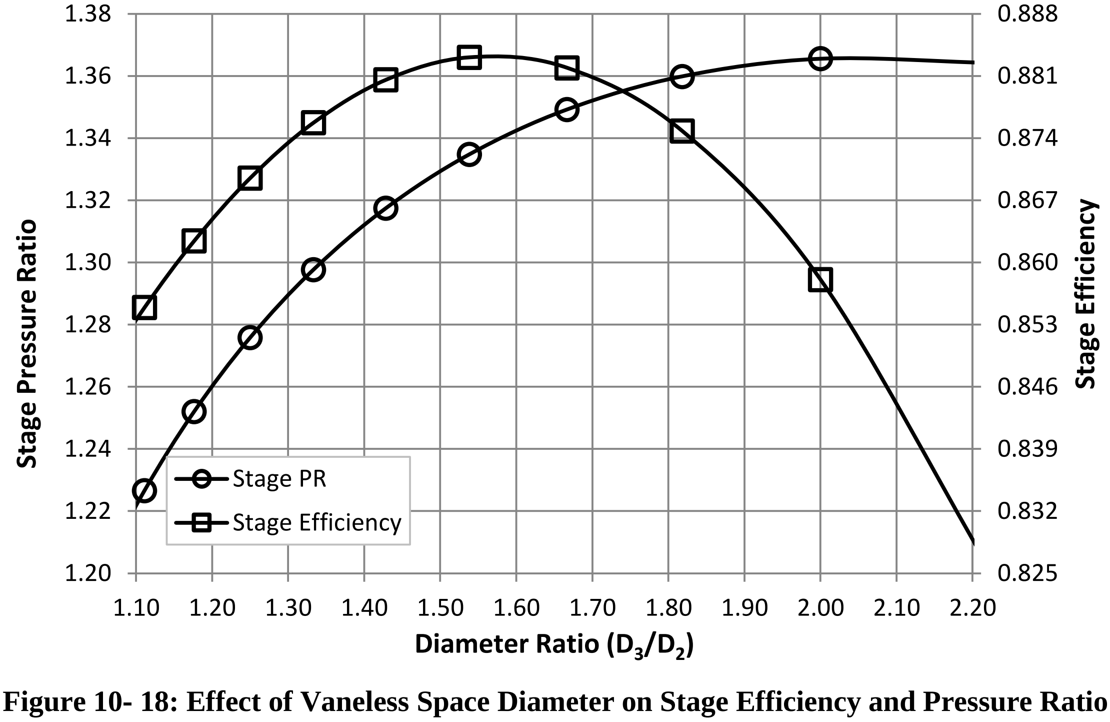

Figure 10- 18: Effect of Vaneless Space Diameter on Stage Efficiency and Pressure Ratio

The larger diameter size of the vaneless space enhances the static pressure recovery of the discharge gas from the impeller leading to a greater pressure ratio. This is owing to the higher diffusion factor which increases proportionally with the diameter ratio. However, the normalized efficiency trend demonstrates a reduction in the overall efficiency value at large diameter size despite the continuous rise in the stage pressure ratio. This sort of behavior can be elucidated by looking at the pressure loss coefficient curve in figure 10-19 which clearly shows that the pressure losses are increasing proportionally with the diameter ratio. Furthermore, the pressure loss trend is taking a greater slope as the diameter ratio increases. This, in fact, yields a higher pressure loss coefficient rise comparing with the static pressure recovery growth leading consequently to lower overall stage efficiency.

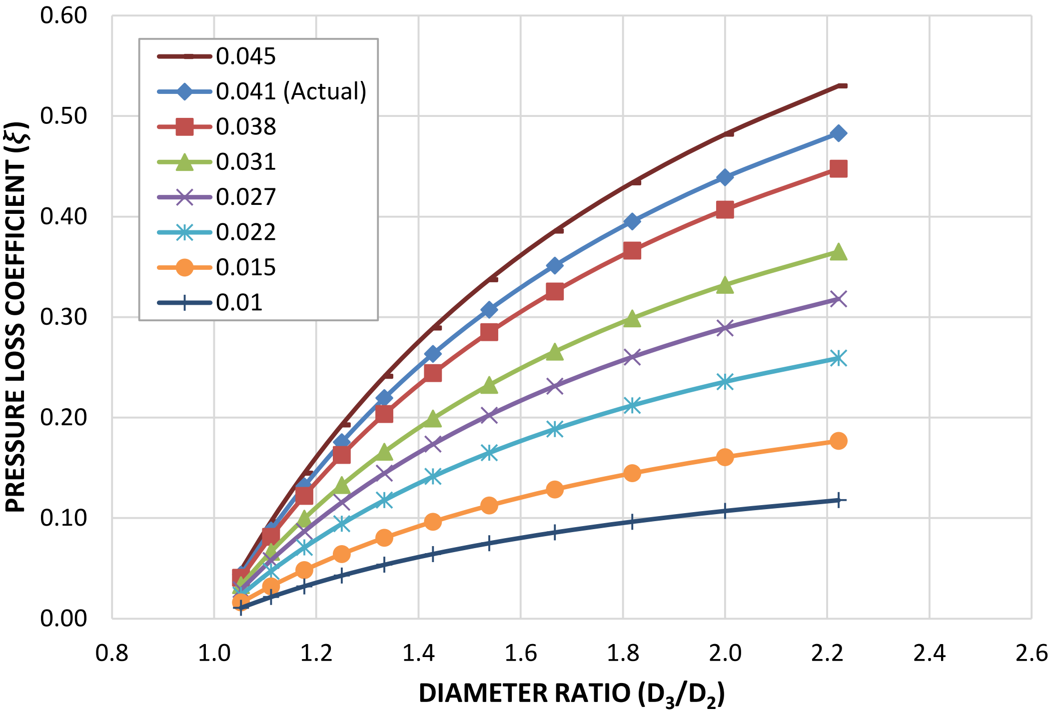

Figure 10- 19: Determination of Vaneless Space Loss at Various Diameter Ratio and Friction Factors

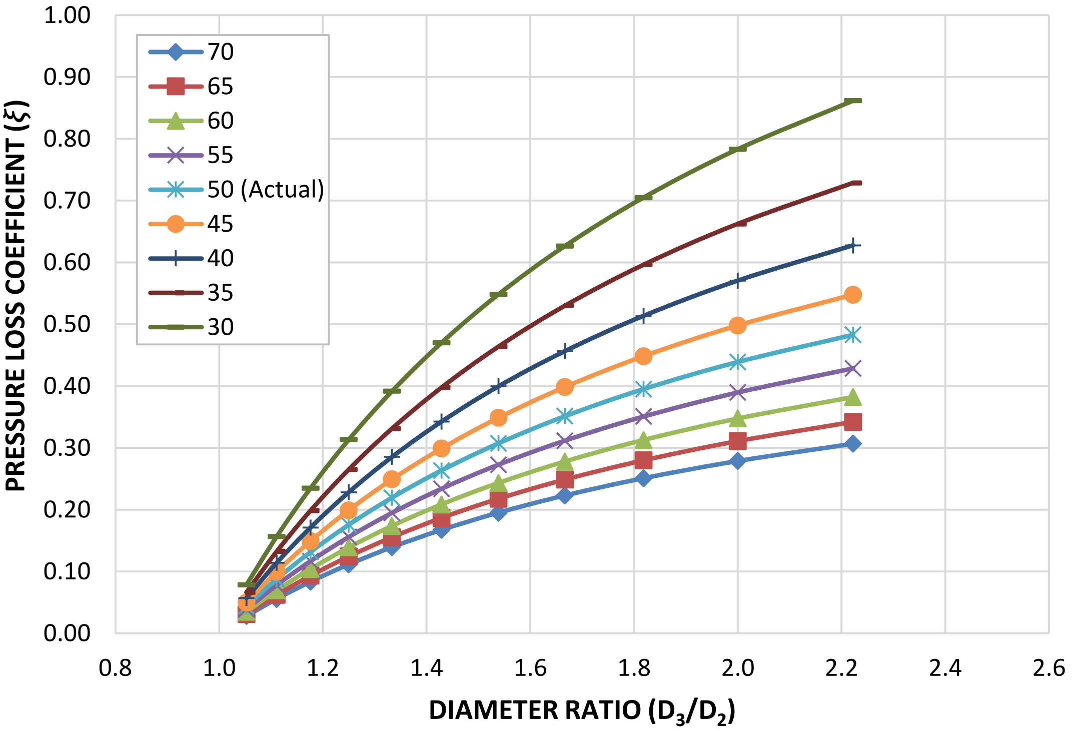

Figure 10- 20: Determination of Vaneless Space Loss at Various Diameter Ratio and Blade Exit Angles

Two of the main parameters which have influence on the diffuser pressure losses are the friction factor (λ_{fr}) and blade exit angle (β_2). Figure 10-19 shows the effect of friction factor on the pressure loss coefficient at various diameter ratio and fixed blade exit angle. When there is a need for large gap size, the high associated pressure losses can be reduced by decreasing the friction factor which can be controlled by considering the surface roughness of the vaneless space. Figure 10-20 demonstrates that the blade exit angle has more significant effect on the pressure loss coefficient due to its impact on the flow unsteadiness at impeller discharge. At high blade exit angle, the flow enters the vaneless diffuser at larger flow angle (α_2), so that the associated pressure losses in the downstream vaneless space are reduced substantially especially at large diameter ratios. Therefore, the optimum blade angle has to be selected to consider the best fit with the diffuser size.

For further investigation on the effect of diffuser configuration on stage efficiency and operating range, six different diffuser schemes have been studied as shown in figure 10-21. The first four diffusers have conventional vaned diffuser configuration but with a different number of vanes.

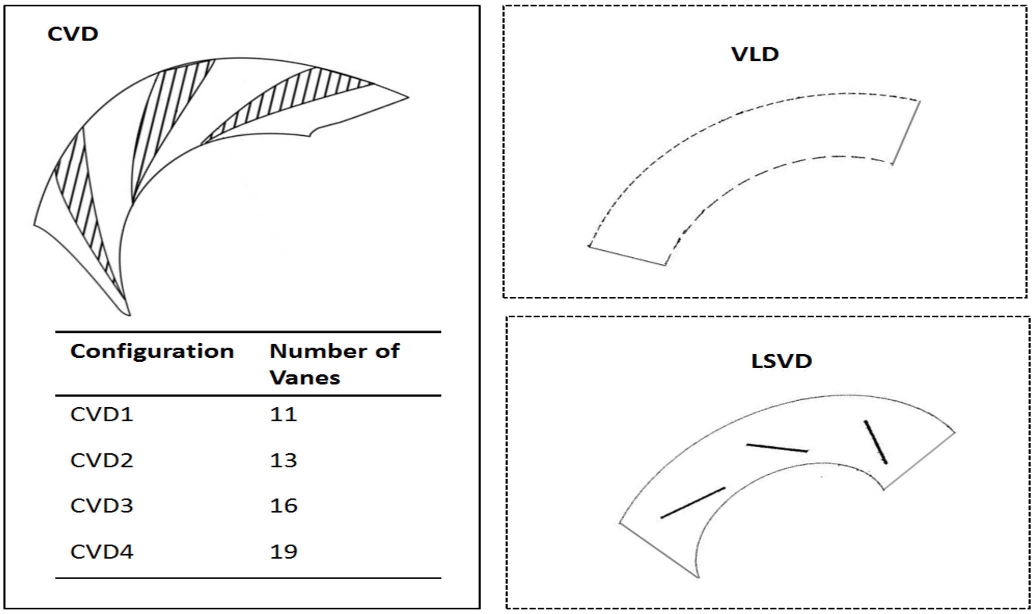

Configuration	Number of Vanes
CVD1	11
CVD2	13
CVD3	16
CVD4	19

Figure 10- 21: The Configurations of the Studied Diffusers

Table 10- 3: Characteristics of the Studied Diffuser by Kalinkevych and Skoryk (2013)

Design Parameter	Value
Inlet Diffuser Pressure (kpa)	118
Inlet Diffuser Temperature (ºk)	319
Mass Flow Rate (kg/s)	1.775
Number of Vanes	17
Inlet Diffuser Radius (mm)	262
Outlet Diffuser Radius (mm)	309
Width of Diffuser (mm)	15.5

In order to obtain the velocity at the inlet and exit of each diffuser, the velocity distribution at suction and pressure sides of every diffuser vane along the flow channel is predicted using Kalinkevych and Skoryk model (2013). These will be then used to calculate the average velocity at each diffuser inlet and exit. However, this model contains some empirical coefficients which have to be set before using this method. There are no given specific values for the boundary layer shape factors (f_s, H_s), therefore, the iteration process is first of all performed to match the predicted velocity profile of the studied diffuser configuration (table 10-3) with the estimated values. After several trials, figure 10-22 illustrates the closest predicted velocity distribution to the actual profile at f_s and H_s of -0.02 and 2.8, respectively which will be considered for the rest of diffusers.

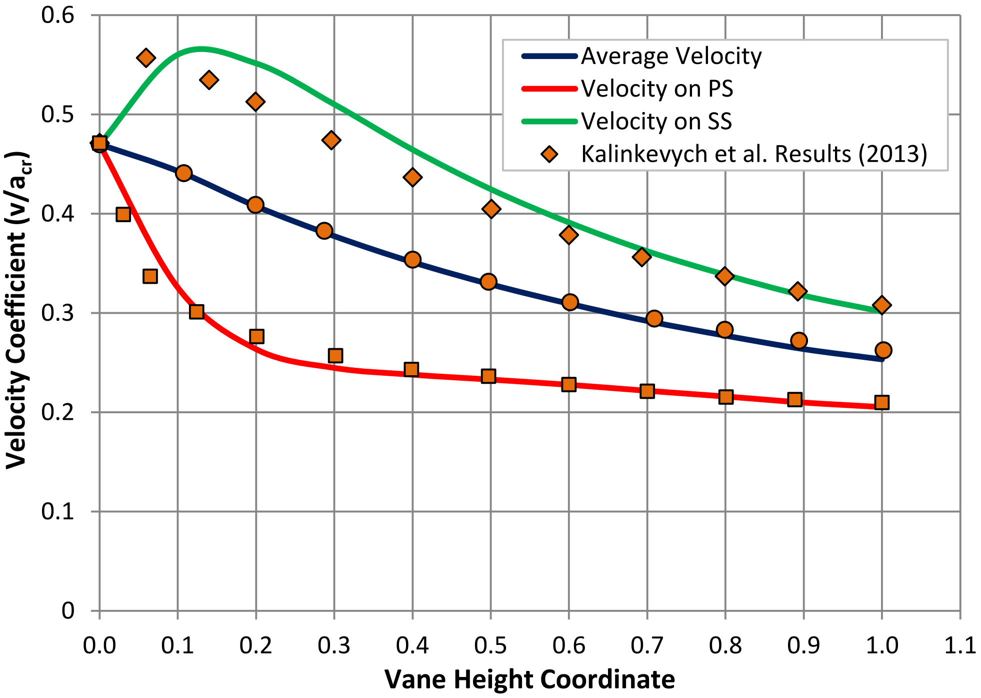

Figure 10- 22: Prediction of Boundary Layer Shape Factors of Kalinkevych-Skoryk Model (2013)

Figure 10-23 shows the estimated velocity distribution along the channel vaned diffuser and for four various configurations. It is clear that the velocity at suction and velocity sides of the diffuser vane surface is decreasing as the vane number increases. However, it is interesting to observe that the difference between the velocities profiles becomes more significant at the suction surface of the diffuser vane. This demonstrates the impact of diffuser geometry on the aerodynamic interaction with the impeller discharge. The smaller available flow area of CVD4 reduces the gas velocity at vanes suction. Moreover, the low velocity at vanes pressure side demonstrates a greater static pressure recovery as the vane number increases. The highest average velocity was obtained at CVD1 while the minimum was found at CVD4. The CVD1 has the highest absolute Mach number at the diffuser exit comparing with the rest of diffusers. As aforementioned, this indicates a lower diffusion factor and less static pressure recovery.

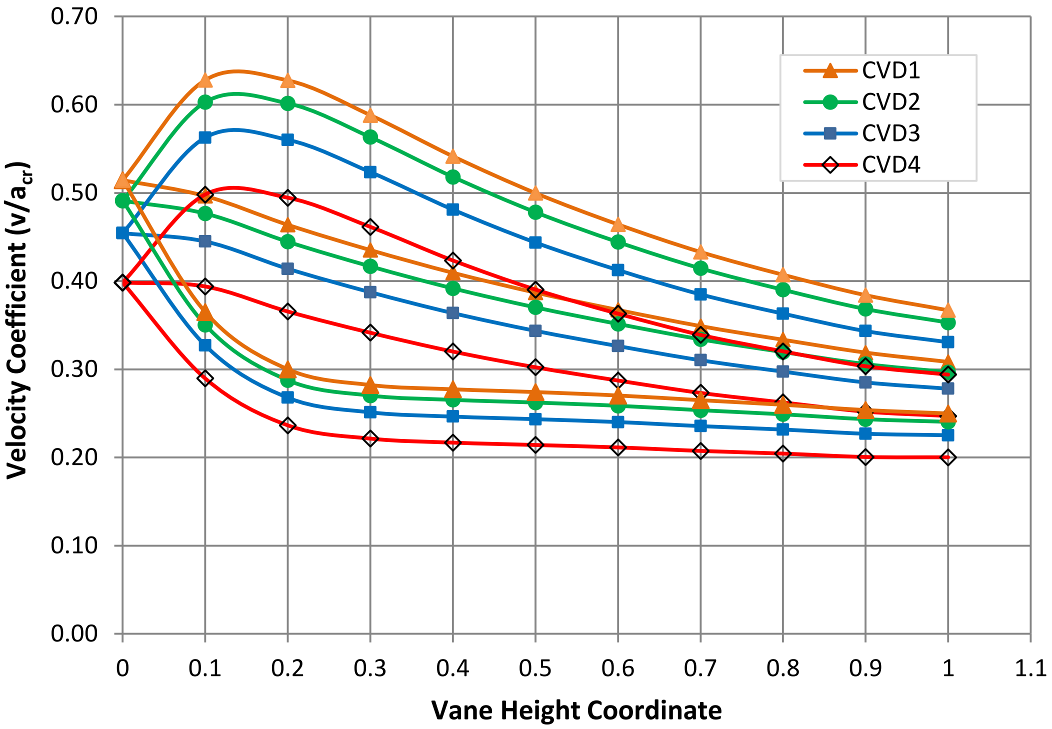

Figure 10- 23: Predicted Velocity Distribution at Suction and Pressure Diffuser Along the Flow Path of Studied Conventional Diffusers Configurations

In terms of stage pressure ratio, the predicted overall pressure ratio at various vaned diffuser configurations are plotted in figure 10-24(a) at different flow coefficients.

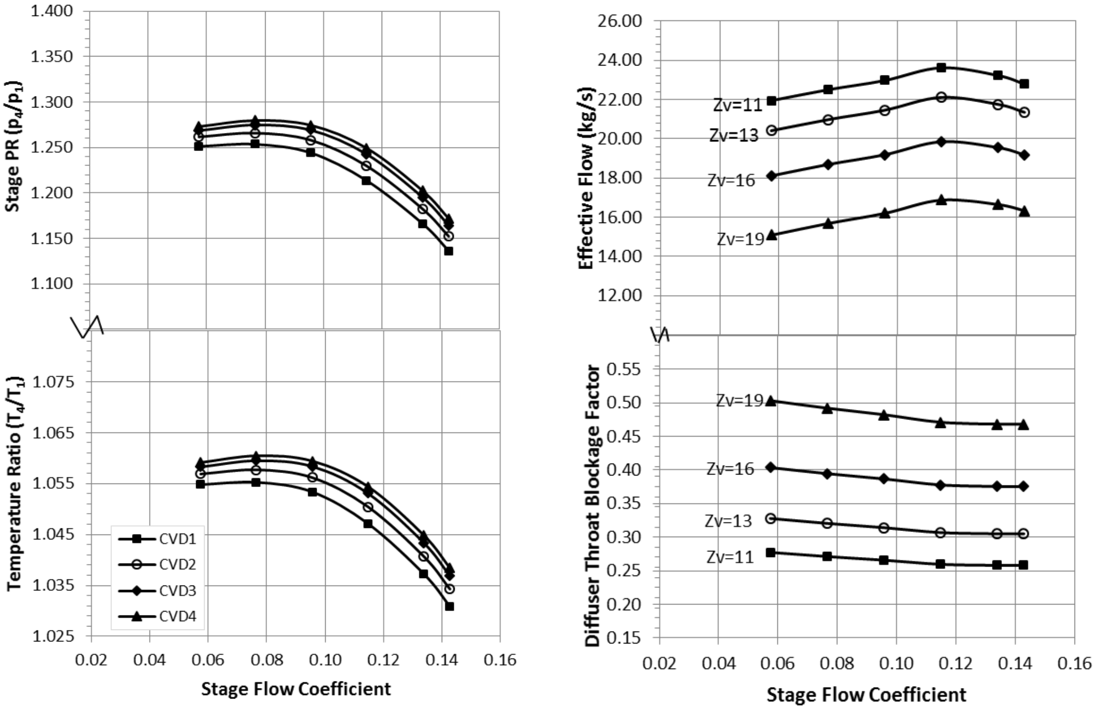

(a) (b)

Figure 10- 24: Predicted Stage Characteristics at Various Vaned Diffuser Configurations: (a) Normalized Stage Pressure and Temperature Ratios (b) Blockage Factor and Effective Flow at Diffuser Throat

The vanes are designed to increase and control the diffusion rate and then reduce the losses. The high number of vanes in CVD4 allows for greater static pressure recovery throughout the diffuser channel which leads to a greater overall pressure ratio. However, the effect of vane number on pressure ratio becomes less substantial as the number of vanes increases. This is because the number of diffuser vanes started to exceed the impeller blades number leading to greater flow distortion and throat diffuser blockage as shown in figure 10-24(b).

The diffuser blockage factor is increasing proportionally with the vane number, and it reached the highest value at CVD4. This blockage effect is created due to the local boundary layer and the formation of throat area. The blockage factor was also found greater at low flow coefficients due to the higher flow distortion at diffuser inlet. For a given inlet temperature and pressure to the leading edge of diffuser vanes, the effective mass flow is specified based on the throat area of the diffuser passage. Therefore, the high blockage factor at high vane number limits the available effective flow area. This obviously leads to reduce the effective flow through the diffuser channel gradually as shown in figure 10-24(b).

The effect of diffuser vane number is also illustrated in figures 10-25 and 10-26 in terms of stage efficiency and operating range. The high static pressure recovery at larger vane number leads to raise the stage efficiency due to lower frictional losses as shown in figure 10-25.

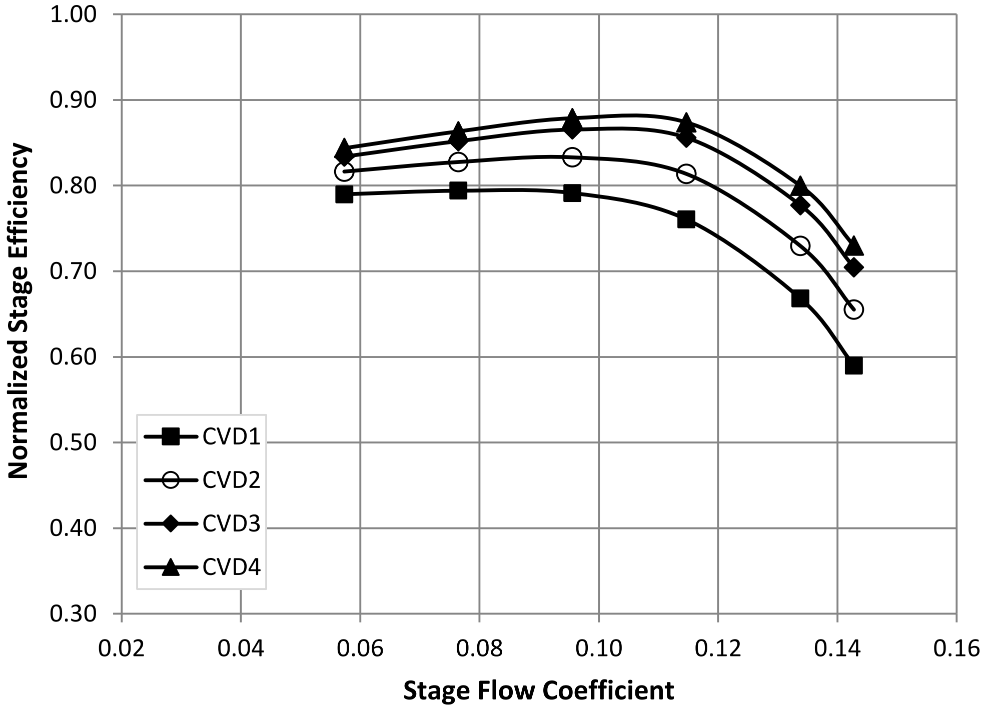

Figure 10- 25: Predicted Stage Efficiency with Various Vaned Diffuser Configurations

However, this impact on stage efficiency becomes less significant at high vane number due to the substantial increase in the pressure losses. At surge condition and as the number of diffuser vanes increases, the pressure recovery coefficient of the vaneless space is reduced with more distorted velocity distribution. Figure 10-26(a) compares the obtained surge margin and overload percentage at various diffuser configurations.

It is clear that there is a slight increase in the choke flow as the vane number increases. On the other hand, the effect on surge flow was found more significant leading to reduce the flow range dramatically at high vane number. The surge generally occurs when the incoming flow gets obstructed by the friction near the vanes. As the number of vanes increases, it becomes difficult to divide the working gas equally between the diffuser passages. So, when the inlet flow drops at a constant speed, the amount of flowing gas through each passage decreases.

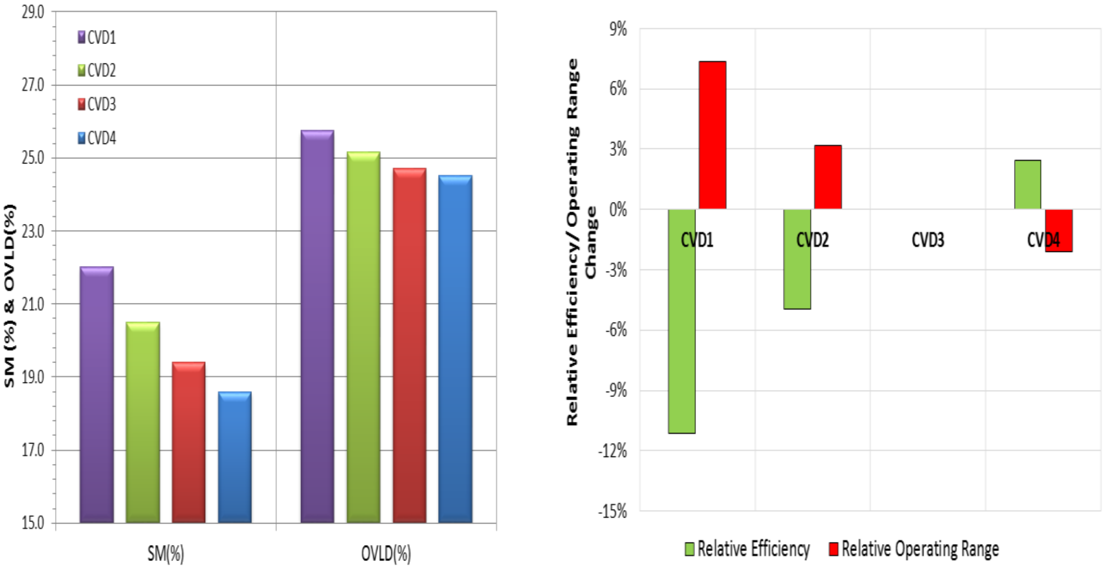

(a) **(b)**

Figure 10- 26: Predicted Operating Range at Various Vaned Diffuser Configurations

Consequently, the inlet relative velocity and flow angle are reduced causing an excessive positive incidence at the leading edge of the diffuser vane. This, in turn, leads to increase the length of the flow path spiral; thus, the flow momentum at the diffuser walls is dissipated excessively by friction and stall. Figure 10-26(b) shows the relative change in the efficiency and operating range with respect to the reference design (CVD3). More pronounced effect was observed in the estimated polytropic efficiency based on the overall stage total-to-total conditions. By upgrading the diffuser design to CVD4, the stage efficiency was improved by roughly 2.4% over the initial design. However, this was achieved in expenses of about 2.1% reduction in the stable flow range. A greater rise in the operating range can be achieved by reducing the diffuser vane number to 13 by around 3.1% against 4.9% drop in stage efficiency.

Figure 10-27 demonstrates the obtained blockage factor of the vaneless diffuser (VLD) at impeller discharge which denotes the distortion rate of impeller exit flow profile. The high incidence angle at low flow coefficients causes the blockage factor to increase due to the growth of boundary layer separation. This agrees with the obtained trend of the vaned diffuser throat blockage factor in figure 10-24(b). However, the inlet effective flow is higher in the VLD due to the reduction in the created blocked area by boundary layer growth and throat area formation. The blockage factor is approximately 9% at design flow. This, in fact, can be used as an indication of late stall comparing with the vaned diffuser.

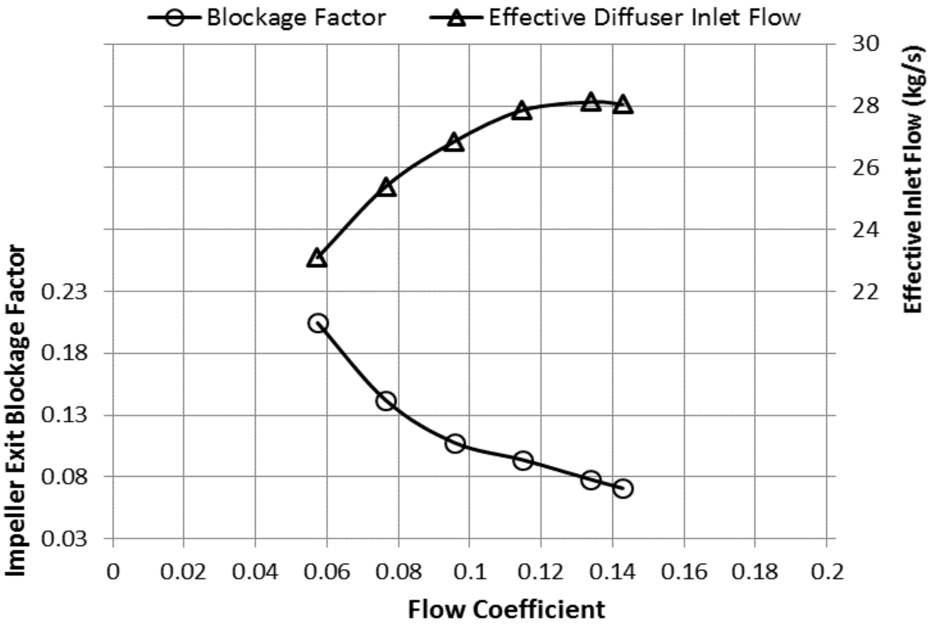

Figure 10- 27: Predicted Impeller Exit Blockage Factor and Inlet Effective Flow of Vaneless Diffuser (VLD)

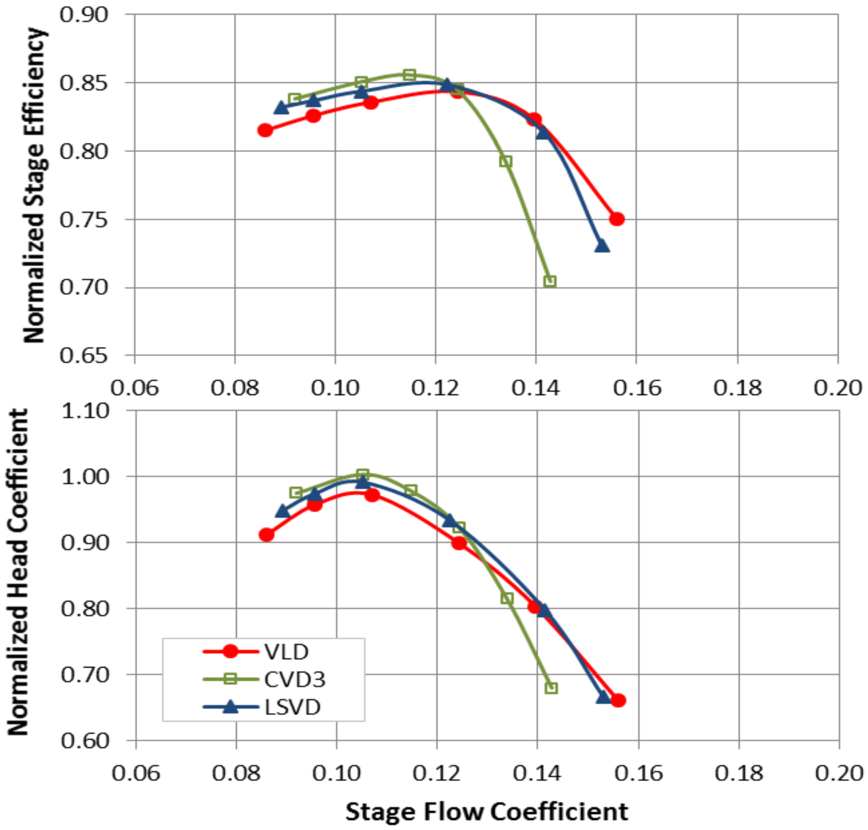

Figure 10- 28: Comparison Between Normalized Stage Efficiency and Head Coefficient of Various Diffuser Types At Design Speed

Figure 10-28 compares the normalized head coefficient and stage efficiency of various diffuser configurations at design rotational speed. The head coefficient of the LSVD stage is very close to the CVD stage, and both are higher than the obtained head by

VLD stage. The peak efficiency of the CVD3 is the greatest among the studied configurations. The absence of vanes in the vaneless diffuser leads to increase the moved particle distance through a vaneless diffuser yielding a higher wall friction and greater kinetic energy loss. However, the minimum mass flow of the CVD3 stage is approximately 6.9 % greater than the VLD. Moreover, the LSVD has quite well efficiency over a wide flow range comparing with the VLD slightly lower than the CVD3. Besides, the behaviour of the LSVD performance curve at overload flow range is similar to the VLD, and it was not affected substantially by the higher negative incidence angles as the conventional vaned diffuser. The peak efficiency of the LSVD was attained at higher flow rate than with the CVD3.

Furthermore, it was observed that the vaneless diffuser stage has a flatter speed line near the peak efficiency point, and the peak efficiency occurred at higher flow coefficient than the CVD3 and LSVD. From head coefficient curve in figure 10-28, the CVD3 has the highest head coefficient comparing with the LSVD and VLD but with earlier stall. One noticeable aspect of the LSVD performance is its reduced head coefficient rise to the surge. At low flow rates, the efficiency of the VLD decreases dramatically because of flow separation and rotating stall inception. Figure 10-29 illustrates the predicted surge margin and overload range for the three different diffuser configurations. This has been predicted using correction factors method based on the measured performance characteristics by Hohlweg et al. (1993).

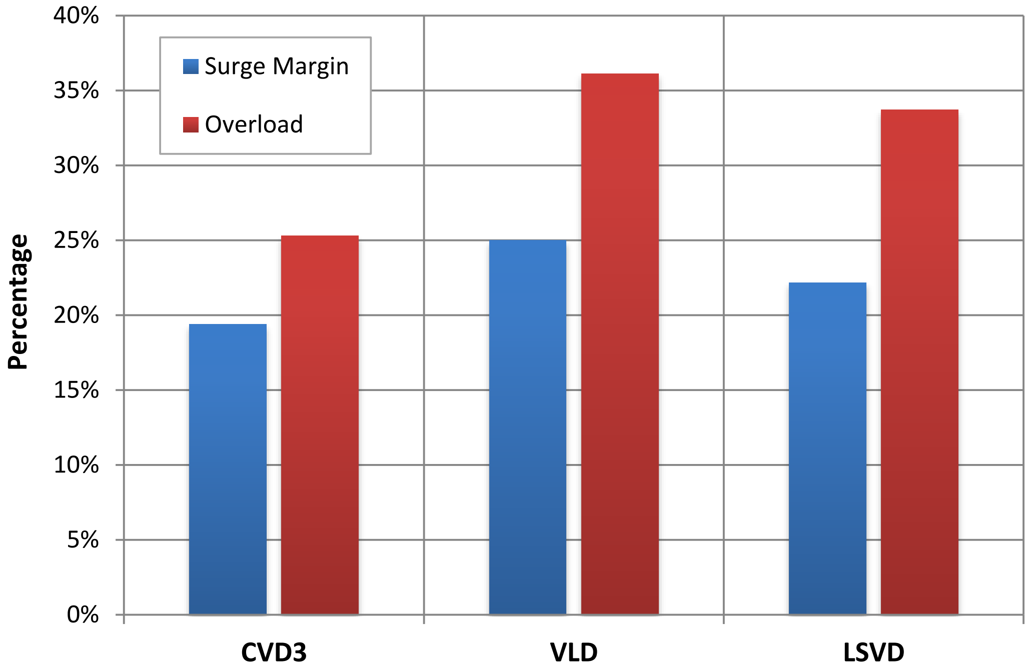

Figure 10- 29: Comparison Between Operating Range of Various Diffuser Types

The vaned diffuser tends to stall at higher flow coefficient and with limited overload flow range. Thus, the conventional vaned diffuser (CVD) has the shortest flow range comparing with the other configurations. The high positive incidence at the leading edge of the CVD3 vane at low flow rates brings the stage to a stall condition. The recorded drop in the surge margin of CVD3 was about 5.63% with relative to the VLD. This difference is reduced in the case of the LSVD to approximately 2.83%.

Economically, the diffuser performance can be plotted in terms of the cumulative cost of power loss in the diffuser as shown in figure 10-30. Despite the fact that the manufacturing cost of the vaneless diffuser is the lowest, the cumulative cost of power loss is the highest among the other configuration.

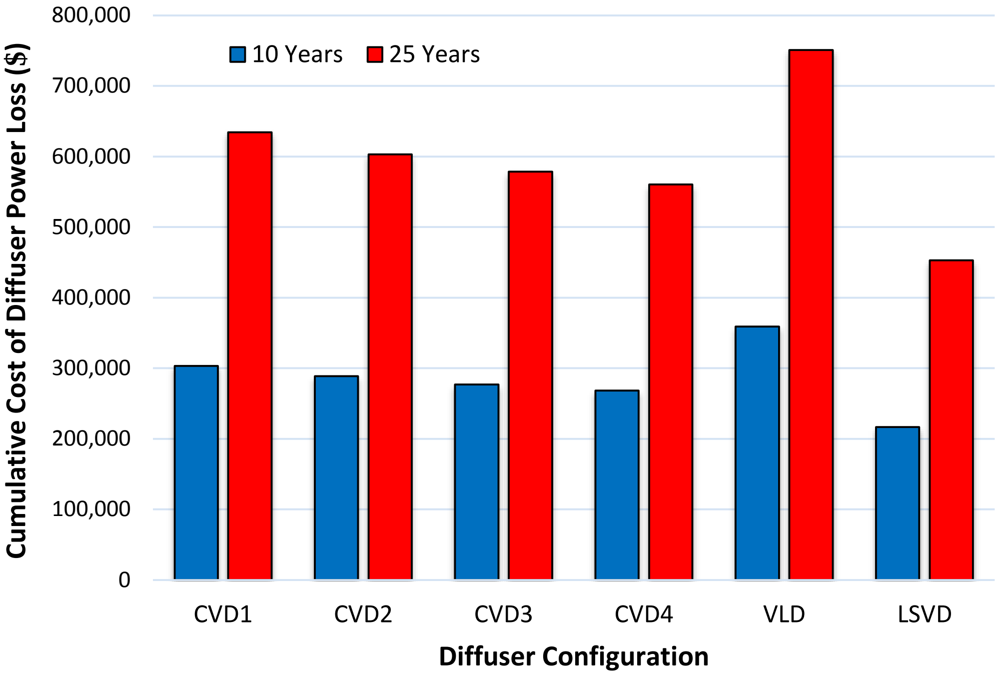

Figure 10- 30: Cost Estimation of Diffuser Power Loss for Different Configuration at Power Cost of $0.06/kWh(e)

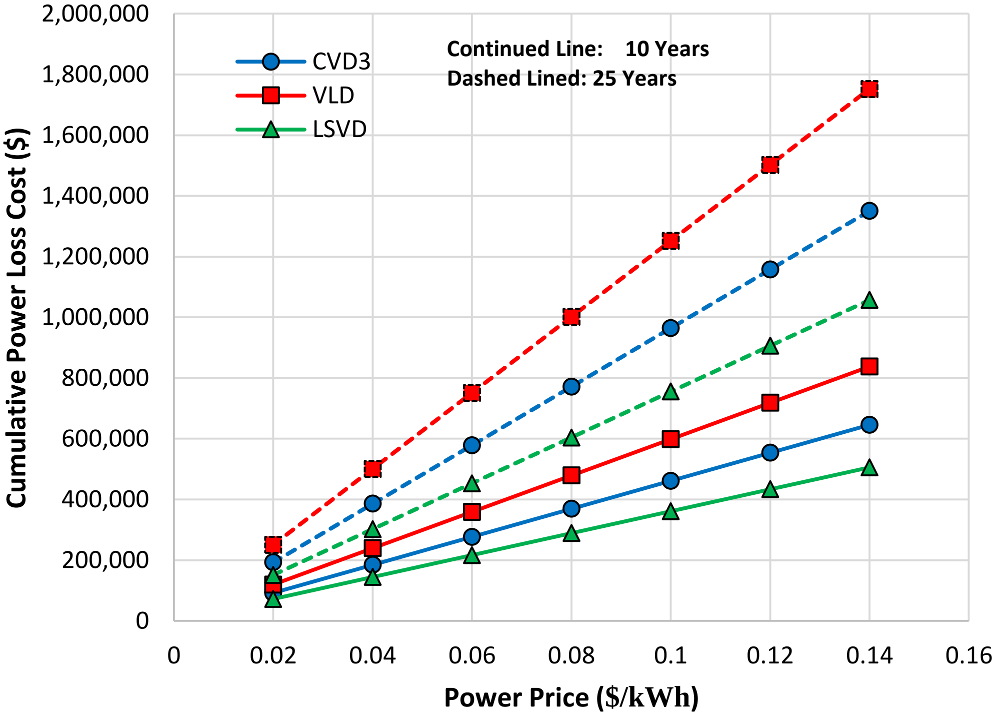

Figure 10- 31: Cost Estimation of Diffuser Power Loss for Different Configuration at Various Power Price Rate

This is clearly influenced by the project lifetime. Therefore, the total power loss cost has to be evaluated and balanced with the total manufacturing cost. However, the shown figure is for one compression stage, so this power loss cost will be obviously much greater while dealing with the multi-stage compressor Moreover, the lowest power loss cost was found with low solidity vaned diffuser as a result of high overall operating efficiency. An interesting point is that the difference between the power loss cost of the tested conventional diffusers (CVD1, CVD2, CVD3, CVD4) are close to each other due to the effect of flow blockage at high vane number. The power rate cost is another factor which has a direct impact on the economic value of the studied diffuser configurations. Figure 10-31 illustrates the predicted cost of diffuser loss at various power prices. More substantial effect can be observed at high power price. Therefore, this graph can be used as a general guideline to select the suitable diffuser configuration according to the existing power cost rate and based on the specified project lifetime. For multi-stages compressors, the estimated value can be roughly multiplied by the number of stages to estimate the overall value.

10.6 Efficiency Enhancement Options for Installed Machines

The previous sections focus on the chances of improving the stage efficiency and operating range for new compressor designs. However, the following options can be considered to improve the performance of installed machines from design perspective:

- Most of the operating compressors in the Middle East region are installed before 1990, and they have been provided with oil seal system. Therefore, the dry gas seals can be used to replace the old seal system for greatly reducing the leakages resulting in higher efficiency and higher reliability as investigated in chapter 5. Figure 10-32 shows the predicted seal losses for the investigated compressor in section 6.4 and 6.5 using the introduced approach in chapter 5.

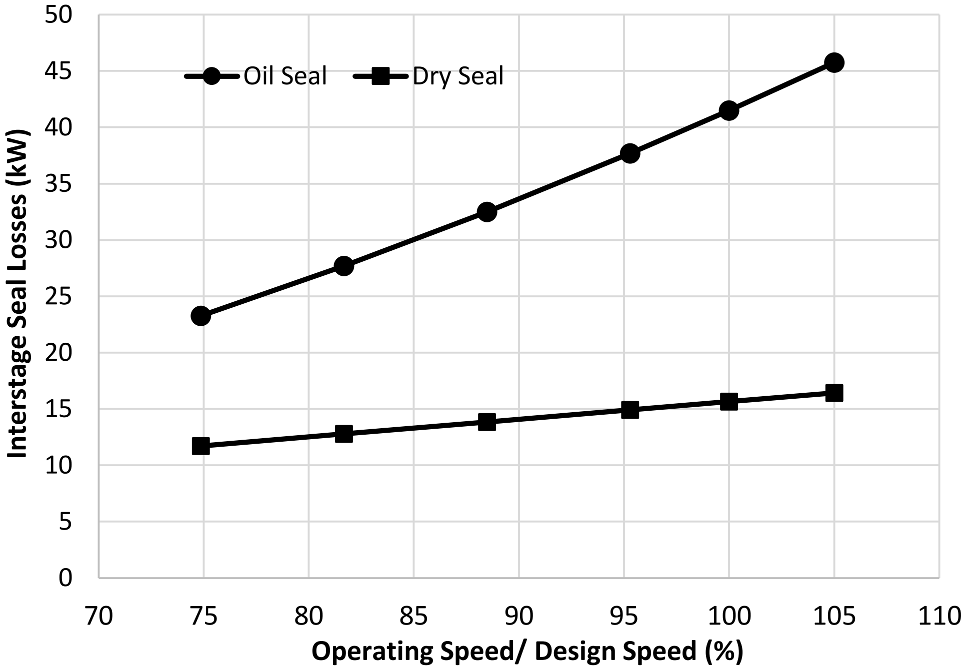

Figure 10- 32: Comparison Between the Oil and Dry Seals Losses at Different Speeds

It is clear that the power saving due to the use of dry gas seals increases proportionally with the operating speed. The losses of dry seals are also less sensitive to the change in the shaft speed which can be considered as a second advantage.

- The change of stage internals can be considered as an option for a substantial increase in efficiency, wider operating range, improved machine life, lower investment as compared to installing a new machine. This includes the rotor, diaphragms and labyrinth seals. Therefore, the developed approaches to define the optimum rotor and stator configurations can be also applied for aged centrifugal compressor units.
- The mechanical losses can be reduced by changing the gear couplings to dry flexible couplings (multi-membrane or diaphragm type). This will contribute to reduce the axial thrust loads yielding less thrust bearing losses and with lower lube oil requirement.
- The use of abradable labyrinth seals in place of conventional labyrinth seal for interstage sealing can help to reduce the internal recirculation losses by minimizing the clearance which, in turn, leads to higher efficiency.

10.7 Closing Remarks

This chapter described an investigation into the effect of the design characteristics of centrifugal compressor aerodynamic components on stage efficiency and stable operating range. Focusing on the centrifugal impeller, two basic geometrical parameters have been considered: shrouded percentage and blade exit angle. An empirical approach was proposed to model the impact of shrouded percentage on the stage efficiency and stable operating range of centrifugal compressors. This method has been validated using three different impeller designs at various operating conditions including high and low flow rates and rotational speeds. The conducted comparison with the CFD results and measured data revealed a fair and satisfactory agreement with the parameters obtained by the proposed model. The estimated performance parameters were found generally lower than the CFD results and experimental readings, which is expected because the developed approach does not account for all associated pressure losses to the flow recirculation and unsteadiness. Therefore, this can be used to derive the shape of the performance curve with an acceptable uncertainty in the predicted parameters. One of the unique advantages of the developed method over the CFD approach is the fact that it does not require deep knowledge of the stage geometrical features; accordingly, it can be used in the early preliminary design process. Moreover, this chapter included further analysis to demonstrate the effect of shrouded percentage on the stage performance parameters.

By comparing the three different blades shapes, the highest overall stage efficiency was achieved by using backward-leaning impellers while the minimum value was found with forward-leaning blades. As the blade angle decreases, the achieved efficiency increases, but in penalty, this leads to lower head. Thus, the blade angle should be selected to achieve the best fit with the desired head and efficiency requirements in any particular application. In terms of operating range, the widest surge margin was found at lower exit blades angle. Therefore, it is strongly recommended to consider the expected variation in the operating conditions while selecting the blade geometry.

Considering the design characteristics of the diffuser, a simplified approach was introduced to evaluate the diffuser characteristics of centrifugal compressor stage. It was found that the high associated pressure losses with the large vaneless space size can be reduced by decreasing the friction factor which can be controlled by considering the surface roughness of the vaneless space. However, more significant effect on the diffuser pressure loss coefficient was recorded by controlling the impeller blade exit angle due to its influences on the flow unsteadiness at impeller discharge. Additionally, the performed comparison exposed that low solidity vaned diffuser has quite well efficiency over a wide flow range comparing with the vaneless diffuser but slightly lower than the conventional vaned diffuser. Besides, the vaned diffuser tended to stall at higher flow coefficient and with limited overload flow range. Hence, it has the shortest flow range comparing with the other configurations. The estimated drop in the surge margin of the conventional vaned diffuser was about 5.63% and 2.83% with relative to the vaneless diffuser and low solidity vaned diffusers, respectively. From an economic perspective, the cumulative cost of power loss of vaneless diffuser was the highest among the other configuration. However, this has to be balanced with the total capital cost and the project lifetime in order to make the optimum decision.

Generally, it was found that there is no absolute answer to the question of optimum rotor and stator configuration. The preliminary aerothermodynamic evaluation revealed that the selection of the optimum impeller structure is governed by several factors: stage efficiency, pressure losses coefficient, manufacturing cost, required power cost, resonance frequency and stable operating range. Hence, an optimization is required to compromise between these parameters to guarantee better performance. Furthermore, it was argued throughout this study that the decision-making process of the typical stage geometrical features has to be based upon the long-term economic performance optimization. Thus, for higher long-term economic performance, it is not enough to select the characteristics of the impeller and diffuser geometry based on the low manufacturing cost or efficiency improvement criterion only.

CHAPTER 11: AEROTHERMODYNAMIC EVALUATION OF THE TURBOEXPANDER PERFORMANCE

11.1 Introduction

The conversion of natural gas into liquid has an advantage of reducing the natural gas volume making it more economical for store and transport. This process is called liquefaction and is achieved through the refrigeration. However, the separation of these hydrocarbons requires an understanding of their physical and chemical properties. As aforementioned in chapter 1, the relative weight is a critical factor in analysing the performance of hydrocarbon processing systems. It has an effect on the condensation temperature so that the heaviest weight hydrocarbons condense at a higher temperature. In theory, the temperature at which the hydrocarbon starts to condensate is called "dew point" and managing this point is necessary for the extraction of hydrocarbons to prevent hydrate formation. Besides, this point is also changed in relation to the gas pressure as illustrated in figure 11-1.

Prior the expansion process, the inlet gas is cooled using the heat exchanger and demethanizer side exchanger as shown in figure 11-2. The gas enters the separator where the condensed liquid is separated from the vapour as indicated by point (2) in figure 11-1. At the separator downstream, the resulting vapour has a different pressure-temperature diagram than the process diagram as represented by the dashed curve. This gas flows to the turboexpander suction from dew point line, and its temperature and pressure are reduced reaching to station 3. When there is a failure in the turboexpander, the gas flows through a bypass line towards Joule-Thomson valve. In this valve, a cooling effect occurs as a result of the gas expansion without extracting any work as indicated in the temperature-pressure diagram by a dashed line from point 2 to point 4.

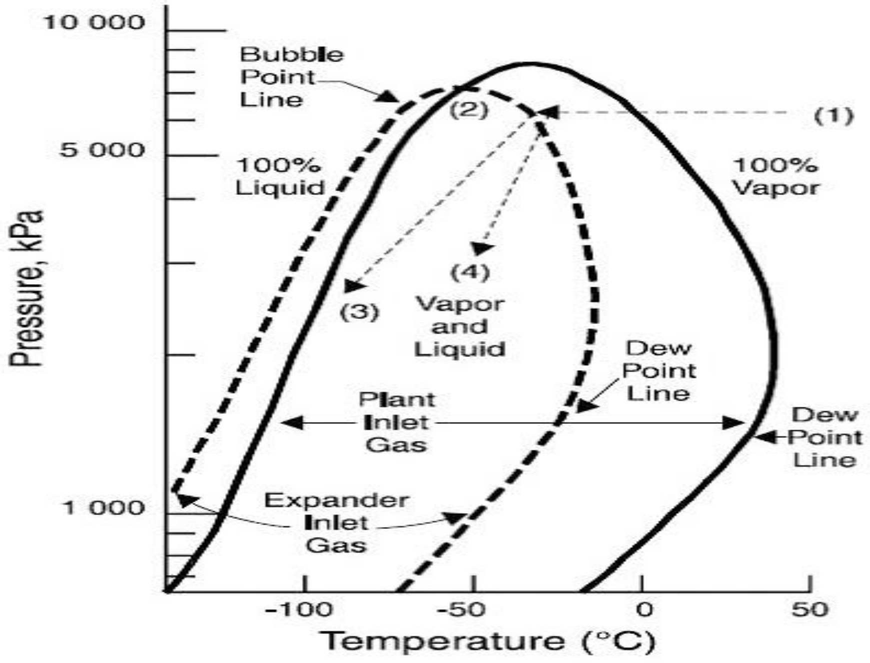

Figure 11- 1: Pressure-Temperature Diagram of Expander Gas (Gas Processors Suppliers Association, 2004)

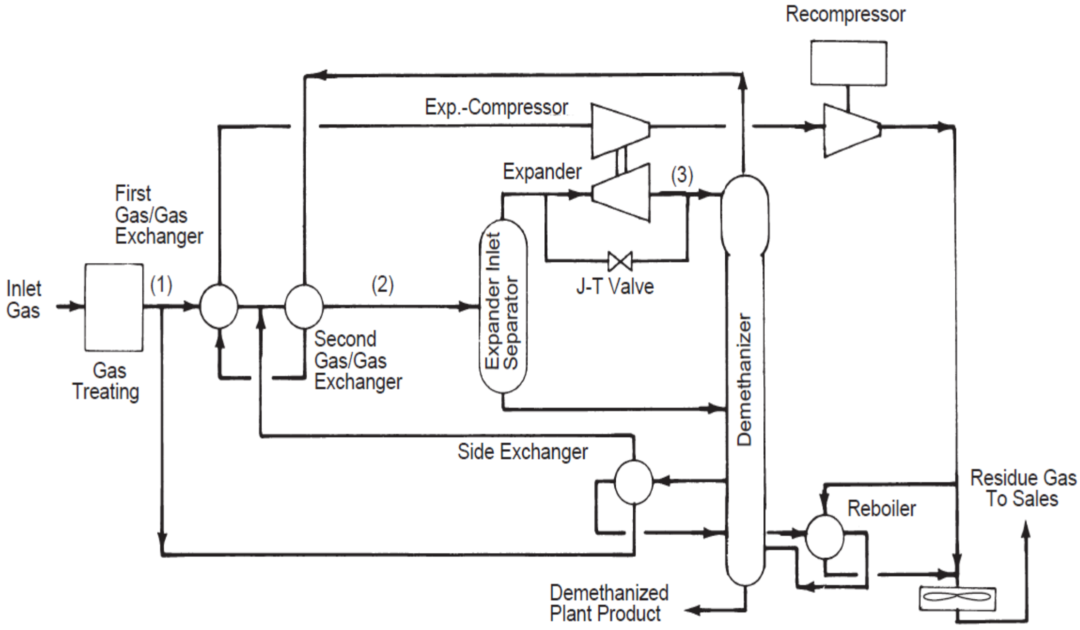

Figure 11- 2: Overall System of Hydrocarbon Process Plant (Gas Processors Suppliers Association, 2004)

This expansion process in Joule-Thomson valve is known by constant enthalpy expansion, and the discharge temperature and pressure would be higher than that accomplished in the turboexpander. However, the high exit temperature from Joule-Thomson valve leads to reduce the effectiveness of hydrocarbon recovery. Besides, the use of turboexpander will allow achieving a higher expansion ratio. The discharge gas from the turboexpander flows to the demethanizer tower where the condensates are removed. The residue gas from the demethanizer is used to cool down the inlet gas to the turboexpander inlet separator through a gas heat exchanger. Hereafter, it is compressed using the turboexpander compressor where its pressure increases. Before boosting this gas to the export gas header, it flows through the mercury removal unit and filter to ensure a clean gas.

11.2 Types of Turboexpanders

The main types of turboexpanders are listed in table 11-1. In the aspect of inlet flow, it is clear that the radial-inflow turbine has the highest flow capacity comparing with the others. This is also coupled with the greatest rotational speed, which obviously puts more strict requirements on the designed bearing and shaft seals as well as the rotating parts strength. This elucidates the high manufacturing cost of such machines. For the system operation, the present of liquid, especially at the end of the expansion process, can cause severe damage to the radial-inflow turbine which is not the case for scroll and screw expanders. However, one of the main disadvantages of the positive displacement machine is the complexity of the lubrication system as it requires an oil separator.

Based on thermodynamic aspects, the turboexpander can be classified into impulse and reaction turbines. In the impulse turbine, the total pressure drop is taking place in the nozzle, and the kinetic energy is captured by the turbine blades as illustrated in figure 11-3(a). This has an advantage of a minimum blade tip leakage and shaft thrust.

Table 11- 1: Comparison of Various Turboexpander Types (Based on: Bao and Zhao, 2013)

Type	Capacity (kW)	Speed (rpm)	Cost	Advantages	Disadvantages
Radial- inflow turbine	50-500	8,000-80,000	High	Light weight, high efficiency, handle high capacity	High cost, low off-design efficiency, cannot bear two phases
Scroll expander	1-10	<6,000	Low	Light weight, high efficiency, simple manufacture, tolerable two-phase, low speed	Low capacity, lubrication and modification requirement
Screw expander	15-200	<6,000	Medium	Light weight, high efficiency in off-design conditions, simple manufacture, tolerable two-phase, low speed	Lubrication requirement, difficult to made and seal
Reciprocating piston expander	20-100	-	Medium	High pressure ratio, adapted to variable working conditions, tolerable two-phase	Many moving parts, heavy weight, have valves and torque impulse
Rotary vane expander	1-10	<,6000	Low	Tolerable two-phase, torque stable, simple structure, low cost and noise	Low capacity and lubrication requirement

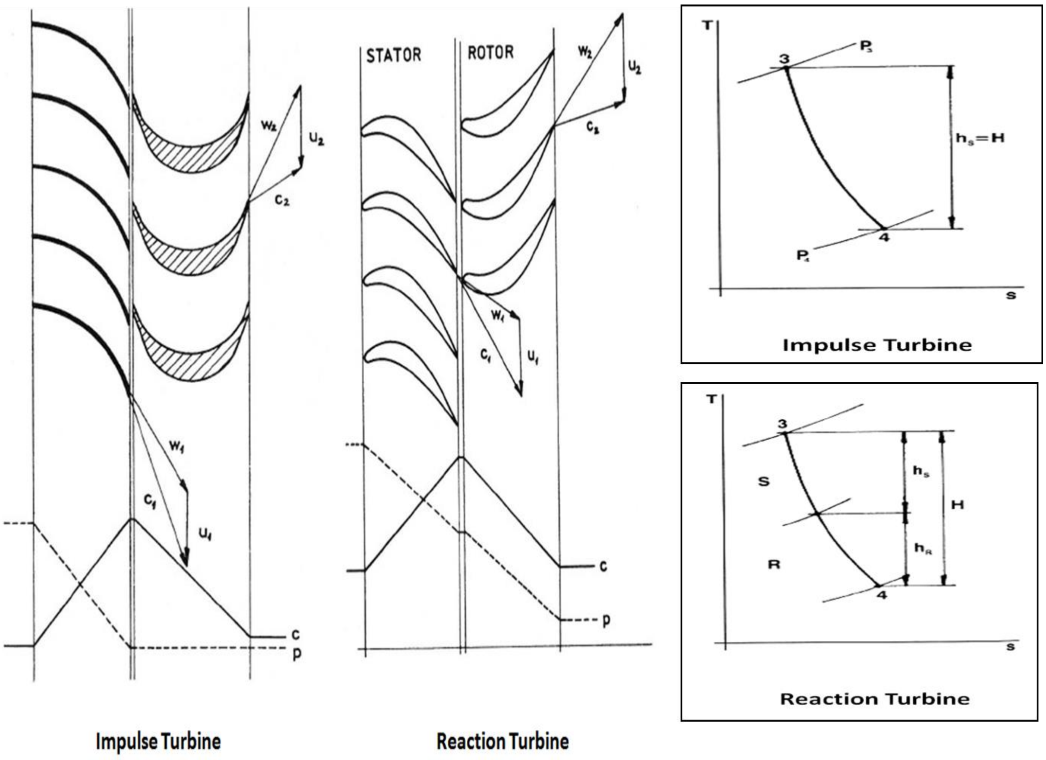

Figure 11- 3: Velocity-Pressure Diagram of Impulse and Reaction Turbines (Adapted from: Giampaolo, 2014)

Due to the high relative velocity of the gas stream at the rotor inlet, the impulse turbine is typical for specific speed range applications where the flow coefficient is low. At low tangential velocity, the impulse turbines can operate efficiently than the reaction machines. The exit gas leaves the rotor without significant residual absolute velocity since roughly 8% of its energy is lost by making U-turn between the rotor blades.

To solve the high blade velocity issue of the impulse turbine, the reaction turbines are used for high and medium flow coefficient. In this kind of turbines, a half of the enthalpy change occurs in the rotor and the other half is taking place in the stator as shown in figure 11-3. The reaction turbines are generally more efficient than the impulse machines, especially for high volume applications. Besides, this type is the most common used for expanding hydrocarbons since the high molecular weight flow results in a lower enthalpy drop and that allows using only a single stage. However, the pressure reduction across the rotor area causes a larger thrust load on the shaft, and it leads to flow leakage over the tip of the blade.

According to the principal direction of the flow, the turbines can be categorized into axial and radial flow turbines. The radial turbine can be arranged in two types as well: inward and outward radial flow turbines. The gas in radial inward flow turbine (IFR) enters the inlet nozzle radially and leaves the rotor axially while the opposite happens in the outward flow turbines. Unlike the outward radial flow turbines, the guide vanes in radially inward flow turbine surround the wheel. This type of turbines is preferred since the centrifugal force on the inward flow reduces the relative velocity yielding lower diffuser losses. Thus, the radial turbine can accommodate a higher expansion ratio in lower number of stages. Moreover, it has a relatively wide range of power, flow rates and rotational speeds.

For gas liquefaction, the radial inflow reaction turbine is used widely due to its higher efficiency and flow rate flexibility. Besides, the shorter discharge diameter leads to reduce the diameter of the rotor seal generating lower seal leakage and shaft thrust load. In contrast, the airflow in the axial turbine is parallel to the shaft, and the working fluid leaves the rotor axially. The axial turbines usually have higher efficiency and shorter operating range, and they are typical for very high flow rates and low expansion ratios as shown in figure 11-4.

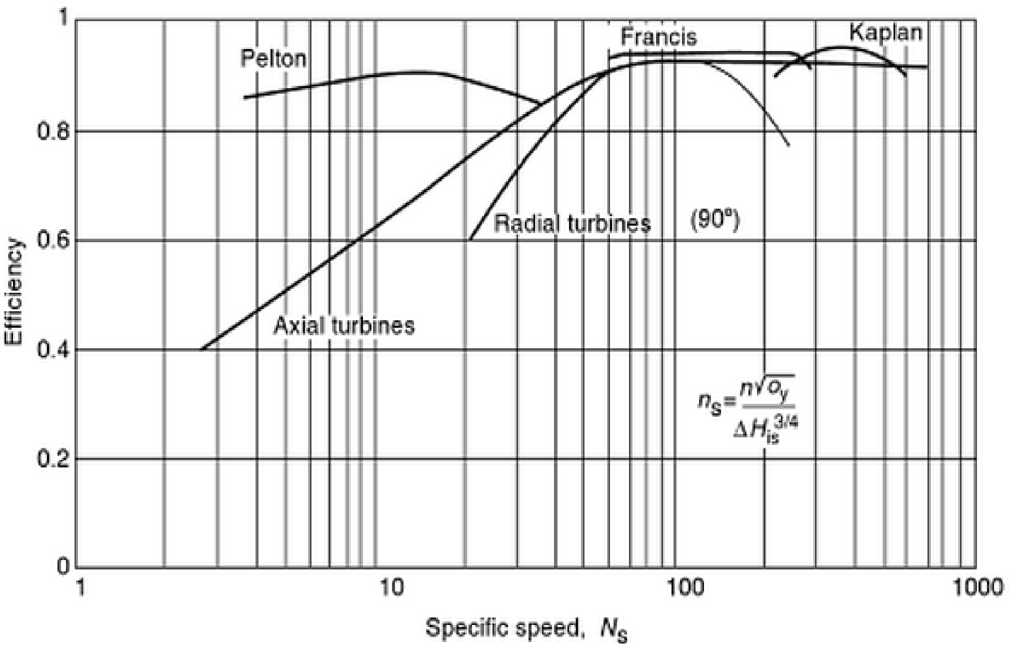

Figure 11- 4: Variation of Adiabatic Efficiency with Specific Speed for Radial and Axial Turbines (Kerry, 2007)

One of the main drawbacks of the radial turbines, in general, is the gas temperature limitation since the cooling technology is not employed in this type of turbines. This is due to the fact that the blade shape is thinner and not rounded at the leading edge and the space between the blades is limited. However, this blade passage allows for higher convergence level to extract a greater amount of work while the gas flows through the straight convergent passage and then curve-linear passage.

11.3 Fundamentals of Turboexpander Design

This section discusses the basics of turboexpander aerodynamic design. The final design is usually a combination of several engineering disciplines: fluid dynamics, stress analysis, mechanical vibration, controls, mechanical design and fabrication. However, the selection of turboexpander is strongly influenced by the process conditions which are: flow rate, gas compositions, inlet pressure and temperature and outlet pressure.

11.3.1 Inlet Nozzle Design Parameters

The inlet turboexpander gas comes with high pressure and temperature and flows through the nozzle blades with inlet absolute and relative velocity of C_1 and W_1, respectively. The convergent passages of the nozzle accelerate the high pressure gas and a part of the pressure energy is converted to kinetic energy. Figure 11-5(a) shows the velocity triangle of the flow at the rotor inlet where its relative velocity raised to W_2. The absolute velocity at the nozzle exit has a radial direction and it equals to the radial component of its relative velocity. In corresponding to the velocity increase; the static pressure of the working gas decreases from P_1 to P_2 as demonstrated in *h*-*s* diagram in figure 11-5(b-c). The static gas temperature declines as a result of static pressure fall. The static pressure is decreasing gradually while the gas flows outward the nozzle vanes with a larger reduction across the convergent passage. Moreover, there is a small amount of total pressure decrease in the nozzle due to the friction loss as indicated by P_{01} to P_{02} with acceptably small wake regions, while there is no change in the stagnation temperature. During this process, a part of the gas energy is extracted in the nozzle in the form of static enthalpy drop (Δh_N).

$$\Delta h_N = h_1 - h_2 = \frac{1}{2}\left(W_2^2 - W_1^2\right) \qquad \textbf{(11-1)}$$

So, the nozzle efficiency is calculated as a ratio of the ideal enthalpy drop to the actual enthalpy drop.

$$Nozzle\ Efficiency = \frac{W_2^2}{W_{2'}^2} = \frac{h_{01} - h_2}{h_{01} - h_{2'}} \qquad \textbf{(11-2)}$$

11.3.2 Turboexpander Wheel Design

The gas enters the rotor passages radially and it is converged to extract the remaining part of the energy as can be clearly seen in the enthalpy-entropy diagram. Based on the velocity triangle in figure 11-5(a), the absolute velocity at the impeller exit has increased to C_3 with a lower relative velocity (W_3). Considering *h*-*s* diagram (figure 11-5c), the static pressure and temperature continue to drop while the gas stream flows through the impeller reaching to P_3 and T_3, respectively. Besides, the stagnation temperature and pressure decrease as a result of work extraction in the rotor. Operating the impeller at high static pressure ratio enhances the work extraction capability, hence the static pressure of the impeller exit gas is relatively low.

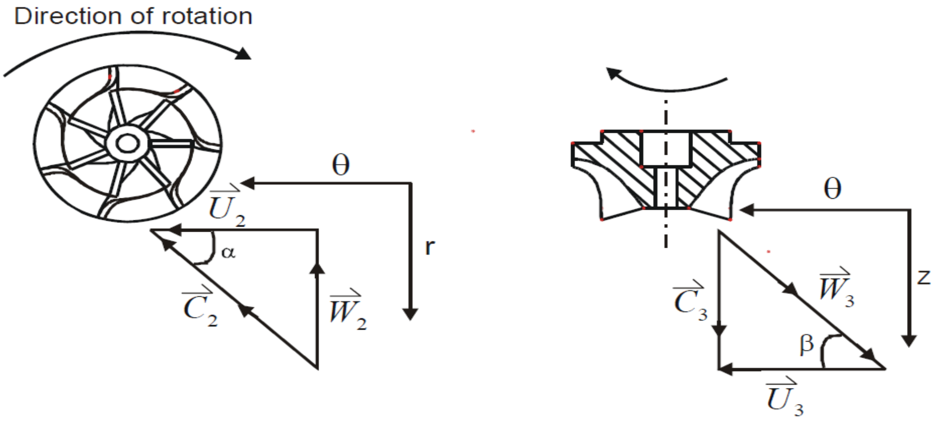

(a) Inlet and Exit Velocity Triangles of Expander Wheel (Ghosh, 2008)

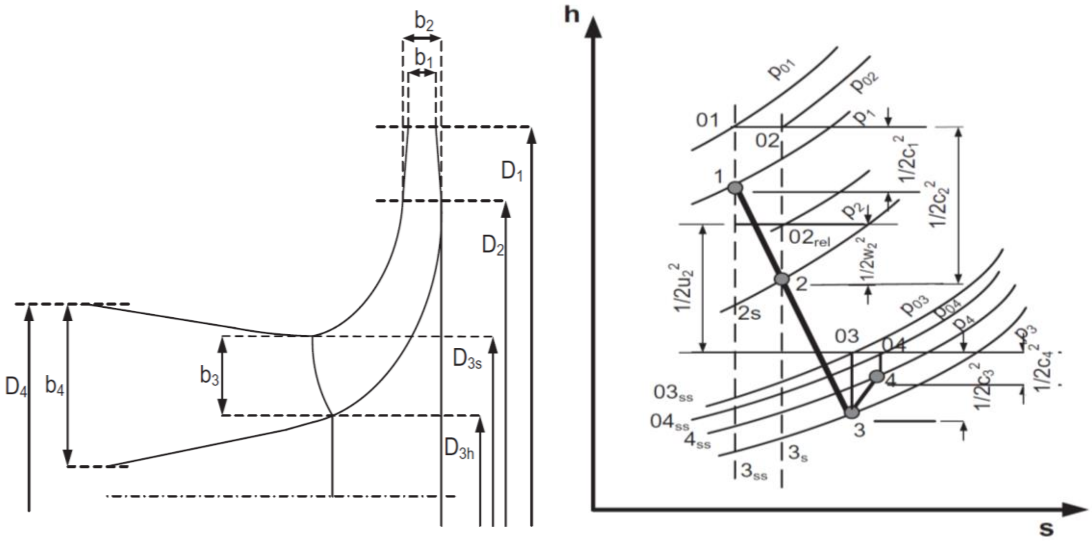

(b) Expander Basic Components (Fiaschi et al. 2012)   (c) *h-s* Diagram (Fiaschi et al. 2012)

Figure 11- 5: Schematic of Radial Inflow Turbine with Enthalpy-Entropy Diagram and Wheel Velocity Triangles

Hereafter, the gas leaves the impeller axially and flows towards the diffuser exit where the gas absolute velocity is reduced. This causes a slight increase in the static pressure and temperature to match the required discharge pressure for the system. Additionally, there is a slight rise in the gas enthalpy, reaching to h_4 as demonstrated in figure 11-5(c). This is also associated with a small reduction in the total pressure due to friction loss. So, the turboexpander efficiency can be defined as the ratio of the work output (W_e) to the input heat (Q_e), and it is crucial to ensure the greatest extracted work from the high pressure gas.

Ideally, the provided work to the compressor can be calculated using formula (11-3) and by neglecting the heat exchanger pressure drop.

$$W_c = \eta_c W_e = \eta_c \eta_e Q_e \qquad \textbf{(11-3)}$$

The turboexpander performance is usually plotted as a function of its isentropic efficiency and velocity ratio (U_1/C_0) where U_1 is the tip speed at the outlet diameter and C_0 is the isentropic spouting velocity as illustrated in figure 11-6(a). So, the tip speed is estimated at the beginning from equation (11-4) as a function of the rotational speed (N) and the impeller diameter (D).

$$U = \frac{\pi N\ (rpm) D}{60} \quad \textbf{(11-4)}$$

The velocity ratio (U_2/C_0) is used also to obtain the degree of reaction of the turboexpander stage as demonstrated in figure 11-6(b).

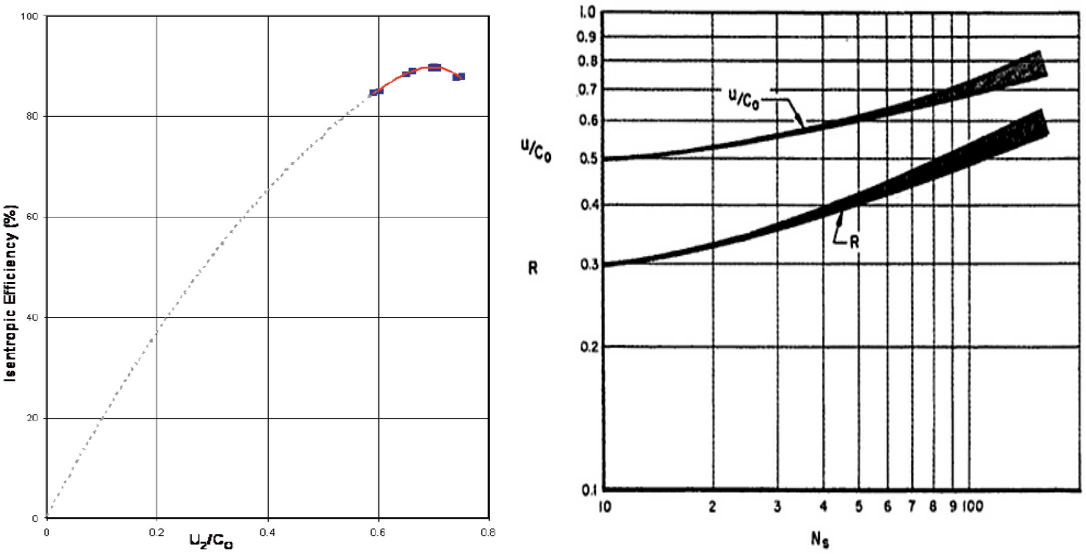

(a) Velocity Ratio (Jumonville, 2004)

(b) Ns-(u/Co) Diagram (Bloch and Soares, 2001)

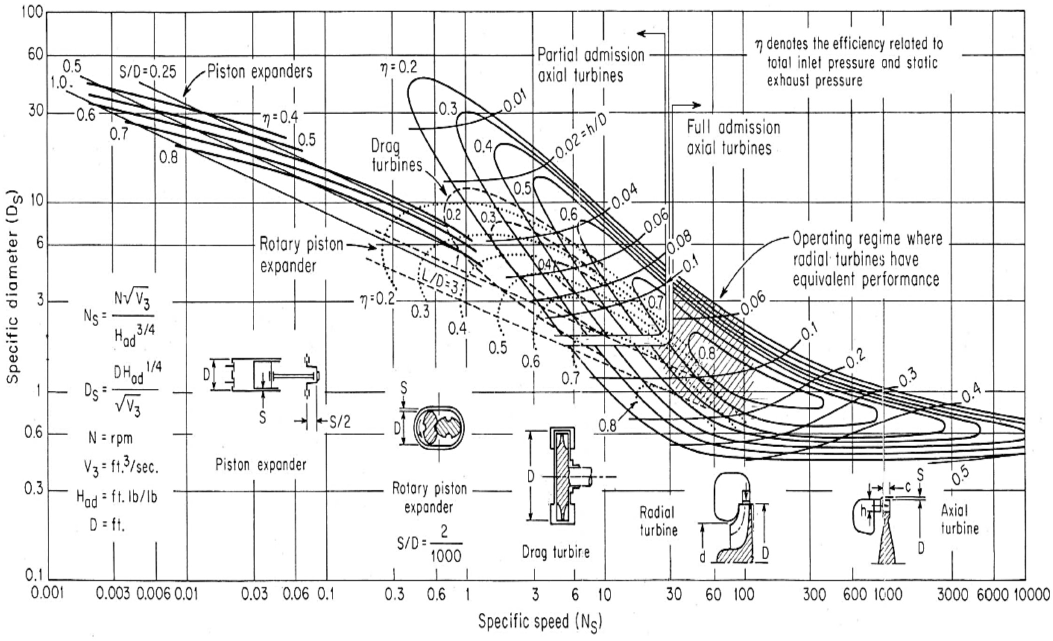

(c) N_s-D_s Diagram at β_2=90° and Re>10^6 (Barber-Nichols Inc., 2015)

Figure 11- 6: Determination of Specific Speed Based on Velocity Ratio (U/Co) and Normalized Isentropic Efficiency

The spouting velocity is the fluid speed at which the entire isentropic enthalpy drop is converted into speed. It increases proportionally with the square root of the isentropic enthalpy drop throughout the stage, and it can be defined by knowing the required enthalpy drop (Δh_{is}).

$$C_o = \sqrt{2(h_{t1} - h_{4s})} \tag{11-5}$$

The specific speed is another important dimensionless parameter frequently used in the industry to define the turboexpander performance. Graphically, this value can be specified from figure 11-6(b) corresponding to the velocity ratio; thus, the rotational is calculated using equation (11-6). By identifying the optimum velocity ratio from figure 11-6(a), the optimum impeller diameter is estimated using formula (11-8).

$$N_s = \frac{N}{60} \cdot \frac{\sqrt{Q_3}}{\Delta h_{t1-4s}{}^{3/4}} \tag{11-6}$$

$$D_s = \frac{D_2 \Delta h_{t1-4s}{}^{1/4}}{\sqrt{Q_3}} \tag{11-7}$$

$$D_3 = \frac{20\sqrt{5\Delta h_{is}}}{\omega} \left(\frac{U_2}{C_o}\right)_{optimum} \tag{11-8}$$

The specific speed (N_s) is related to the maximum enthalpy drop that one stage can handle as shown in table 11-2. The exact value is greatly influenced by the type of applications and the required output in order to meet the design constraints.

Table 11- 2: Typical Values for Design Conditions of Turboexpander Based on: (Fiaschi et al., 2012) (Byrne and Mariotti, 2010)

No.	Variable	Typical Value
1	Work coefficient (ψ)	1.5-2.4
2	Flow coefficient (φ)	0.17-0.35
3	Degree of reaction (R)	0.13-0.28
4	Nozzle diameter ratio (D_1/D_2)	1.4
5	Rotor diameter ratio (D_3/D_2)	0.55-0.66
6	Diffuser diameter ratio (D_4/D_3)	1.4-1.6
7	Nozzle height ratio (b_1/b_2)	0.8-1
8	Maximum enthalpy drop per stage (kJ/kg)	150 ($0.025< \varphi <0.18$) 120 ($0.18\leq \varphi <0.28$)

The specific speed and the specific diameter can be used to define dynamic similarity. The physical meaning of these two variables is that the combination of operating parameters at fixed values of specific speed (N_s) and specific diameter (D_s) permits similar flow conditions to exist in geometrically similar turbomachines (Subrata, 2008).

Despite that the expansion ratio and the extracted energy are highly influenced by the velocity ratio, the turboexpander wheel must operate at lower than the maximum practical limit. This is set according to the allowable stresses of impeller materials and manufacturing technique. To overcome this issue, multi-stage turboexpander can be used, but it will lead to a higher cost and more complicated system.

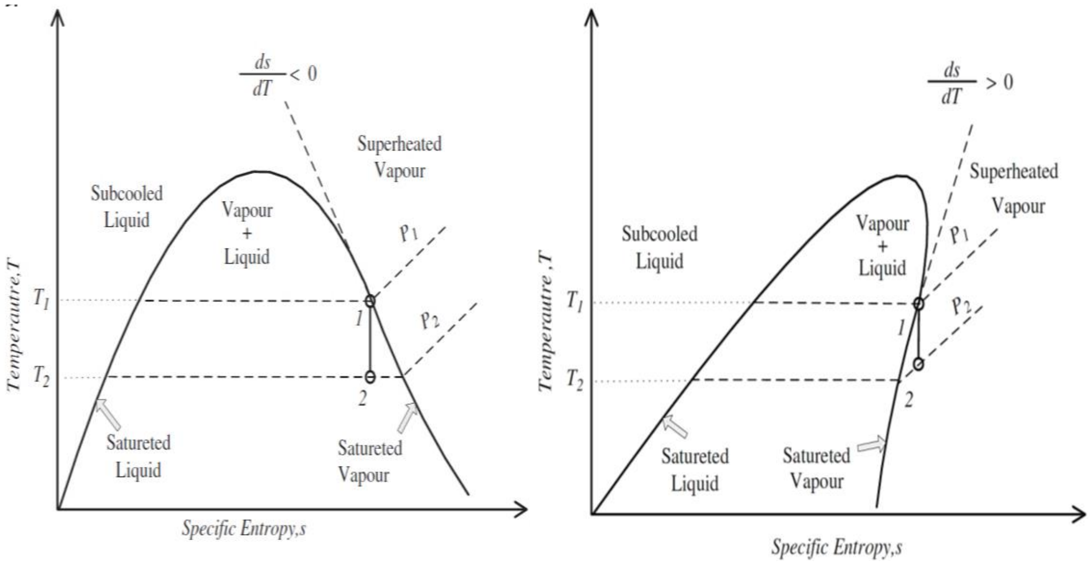

(a) Wet Fluid **(b) Dry Fluid**

Figure 11- 7: Expansion Process of Wet and Dry Fluids in *T-S* Diagram (Bao and Zhao, 2013)

The use of two-phase flow can limit the necessary degree of superheat to avoid the exhausting wet stream as shown in figure 11-7. The presence of liquid inside the turboexpander can reduce the isentropic efficiency and damage the blades. This possibly leads to unstable turboexpander operation which affects negatively on the bearings (Badr et al., 1985). The minimum dryness fraction at the turboexpander discharge flow should be kept typically above 85%, and this might necessitate the need for superheating the wet fluid at the inlet of the turboexpander (Desai and Bandyopadhyay, 2009).

11.4 Developed 1D-Design Approach

The actual work and efficiency are key parameters in the turboexpander design and performance. The standard method to obtain the turboexpander efficiency is based on the determination of specific speed, velocity ratio and specific diameter. Hence, these three parameters are defined graphically in order to achieve the highest possible efficiency at specified inlet Reynolds number, Mach number and gas composition. The geometrical specifications are set based on the obtained discharge parameters with respect to the targeted expansion ratio. These then evaluated and iterated by changing the efficiency or the expansion rate. The parameters required for Turboexpander sizing are:

- Gas composition
- Flow rate
- Inlet pressure
- Inlet temperature

11.4.1 Method Description

The followed methodology is illustrated in figure 11-8.The turboexpander efficiency is identified at the beginning to achieve the optimum value. Besides, the corresponding specific speed (N_s) and velocity ratio (u_2/C_o) are obtained from figures 11-6(b) and 11-11. In general, the maximum efficiency of radial turbine is at specific speeds between

45 and 90 and specific diameters of about 2 to 1.2. However, the limitation in the specific speed range comparing with figure 11-6(c) is caused basically by the assumption that the inlet blade angle is 90°.

The turboexpander discharge pressure is normally specified based on the efficiency of the booster compressor through a complex iterative analysis. However, this value will be assumed in this study to simplify the sizing method. The properties at the turboexpander inlet are referring to the stagnation condition while the properties at the exit state are estimated in static condition. The physical properties have been obtained using the developed gas properties estimation tool (GasProp), and the thermodynamic properties are calculated by IPSEpro software. The gas density at rotor exit is derived based on the obtained discharge pressure, temperature and gas properties. This is then used to find the discharge rotor flow (Q_3).

$$Q_3 = \dot{m}_3 \frac{Z_3 R_3 T_3}{p_3} \tag{11-9}$$

The total enthalpy drop is predicted at specified efficiency using IPSEpro software. Hereafter, it is substituted in specific speed equation (11-6) to estimate the rotational speed. This value will be then iterated to consider the enthalpy drop of the single stage. The wheel inlet diameter is initially defined using formula (11-8) with respect to the specified velocity ratio. Besides, the rotor diameter ratio is obtained from figure 11-9 at specified efficiency point, and this has to meet the recommended values in table 11-3. Furthermore, the tip velocity (U_2) is computed at rotor inlet and exit from the angular velocity and the inlet and exit impeller diameter, respectively using formula (11-10). This will be used as first iteration process.

$$U = \omega \frac{D}{2} = \pi D \frac{rpm}{60} \tag{11-10}$$

Accordingly, the spouting velocity (C_o) is obtained from the defined velocity ratio and it has to match the obtained value from equation (11-5). The radius ratio of the rotor is then found by the following correlation.

$$\frac{r_3}{r_2} = \frac{U_3}{a_{01}} \frac{a_{01}}{u_3} \tag{11-11}$$

The exit rotor diameter is recalculated to consider the new velocity ratio and tip speed by implementing equation (11-12).

$$D_3 = 2\sqrt{\frac{Q_3}{2\pi U_2}\left(\frac{U_2}{C_o}\right)\left(\frac{1+\mu^2}{1-\mu^2}\right)} \tag{11-12}$$

Therefore, the inlet rotor diameter is specified by identifying the diameter ratio from equation (11-11) and based on the calculated exit diameter from formula (11-12). In order to estimate the required number of stages, the obtained total enthalpy drop is divided by the maximum allowed enthalpy drop according to the flow coefficient criterion in table 11-2. Therefore, the tip velocity has to be recalculated using equation (11-10) if the number of stages is greater than 1. Besides, the rotor diameter ratio and exit diameter are determined with respect to the new tip velocity value by implementing equations (11-11) and (11-12).

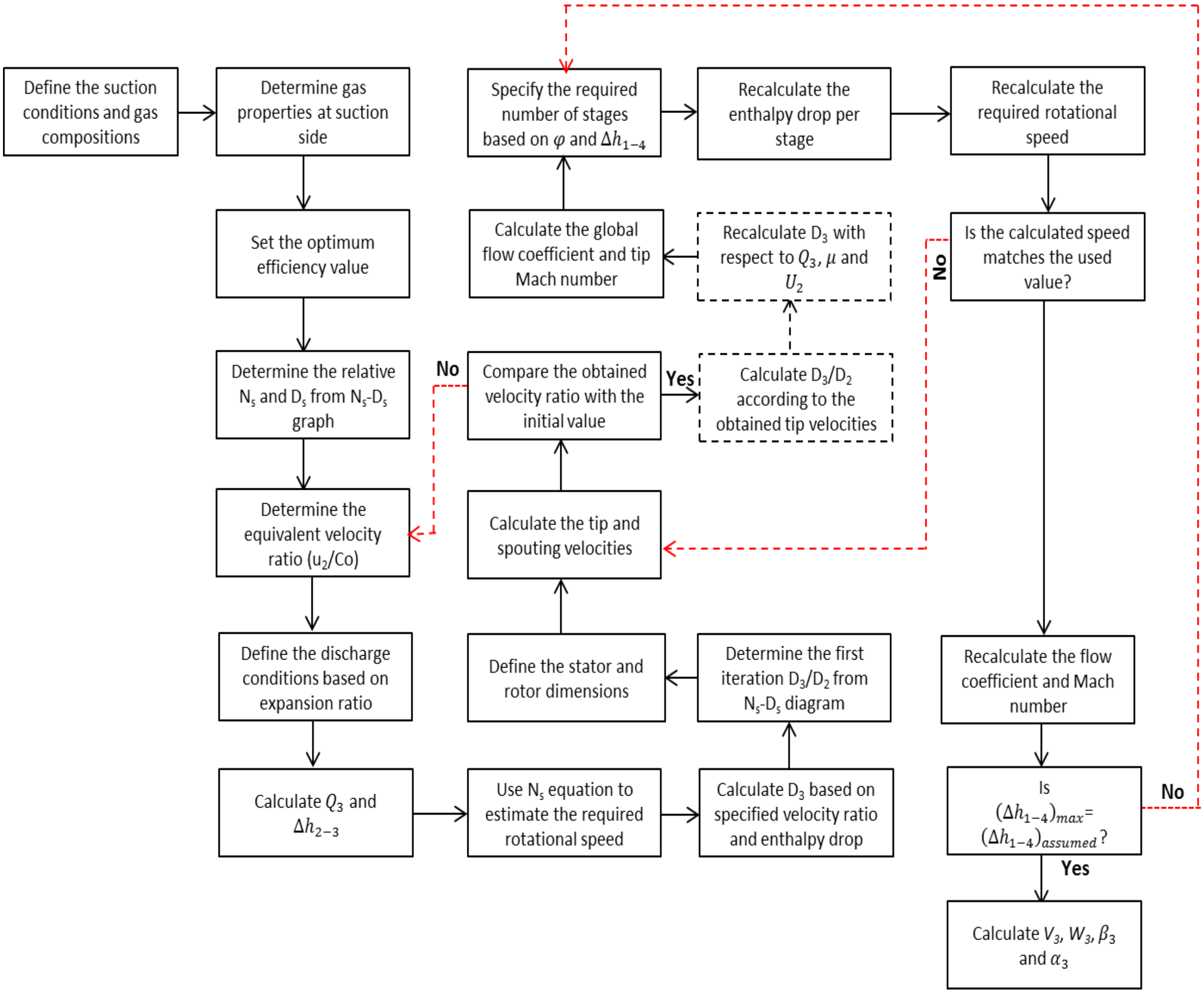

Figure 11- 8: Scheme of Developed Methodology for Expander Design

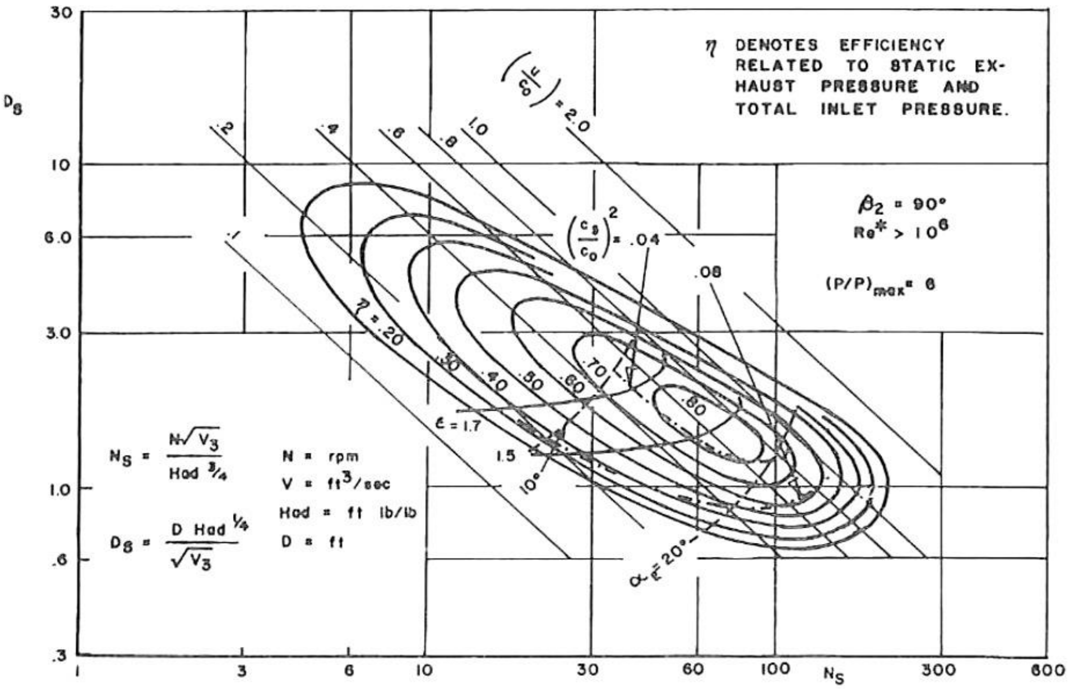

Figure 11- 9: D_s-N_s Diagram of Radial Turbine (Balje, 1962) Where ($\varepsilon = D3/D2$)

The flow coefficient and Mach number are corrected, and the maximum enthalpy drop has to match the used value. Finally, the power ratio (S_w) is calculated by applying the below formula (Eqn. 11-13).

$$\left(\frac{p_{01}}{p_4}\right) = \frac{1}{1-\left(\frac{S_w}{\eta_{ts}}\right)} \qquad \textbf{(11-13)}$$

The exit flow area from the rotor is estimated using equation (11-14).

$$A_3 = \frac{\pi}{4}\left(D_{3t}^2 - D_{3h}^2\right) - \frac{Z_b t_b (D_{3t} - D_{3h})}{2 sin\beta_3} \qquad \textbf{(11-14)}$$

$$Q_3 = A_3 C_3 \qquad \textbf{(11-15)}$$

where:
C_3: Exit absolute velocity
t_b: Blade thickness

The absolute exit angle is found by matching the discharge flow from equation (11-15) with the actual value. Thus, the exit relative velocity (W_3) and flow angle (α_3) are obtained from velocity triangles.

11.4.2 Off-Design Performance Prediction

In most of the applications, the inlet conditions including suction flow, temperature, pressure and molecular weight are varying. This fluctuation in the suction parameters alters the turboexpander performance. Hence, it is necessary to investigate the impact on performance parameters over the expected variation range. This will also help to assess the selection of the optimum design conditions for turboexpander operation.

A simple approach is followed here to evaluate the effect of inlet conditions and gas compositions change in the turboexpander efficiency. By specifying the predicted change in the working conditions, the design efficiency is corrected using corrections factor according to equation (11-16).

$$\eta_i = B_Q \times B_p \times B_T \times B_{MW} \times \eta_D \qquad \textbf{(11-16)}$$

where:
B_Q: Suction flow correction factor
B_p: Inlet pressure correction factor
B_T: Inlet temperature correction factor
B_{MW}: Molecular weight correction factor

The correction factors are obtained to account for the deviation of flow, pressure, temperature and molecular weight with reference to the design values. Typically, these coefficients are derived graphically using figure 11-10 assuming a constant speed operation. Based on this figure, the isentropic efficiency is more sensitive to the inlet pressure reduction than the increase over the design value. On the other hand, the efficiency is reduced symmetrically with the increase and decrease in the inlet gas temperature change.

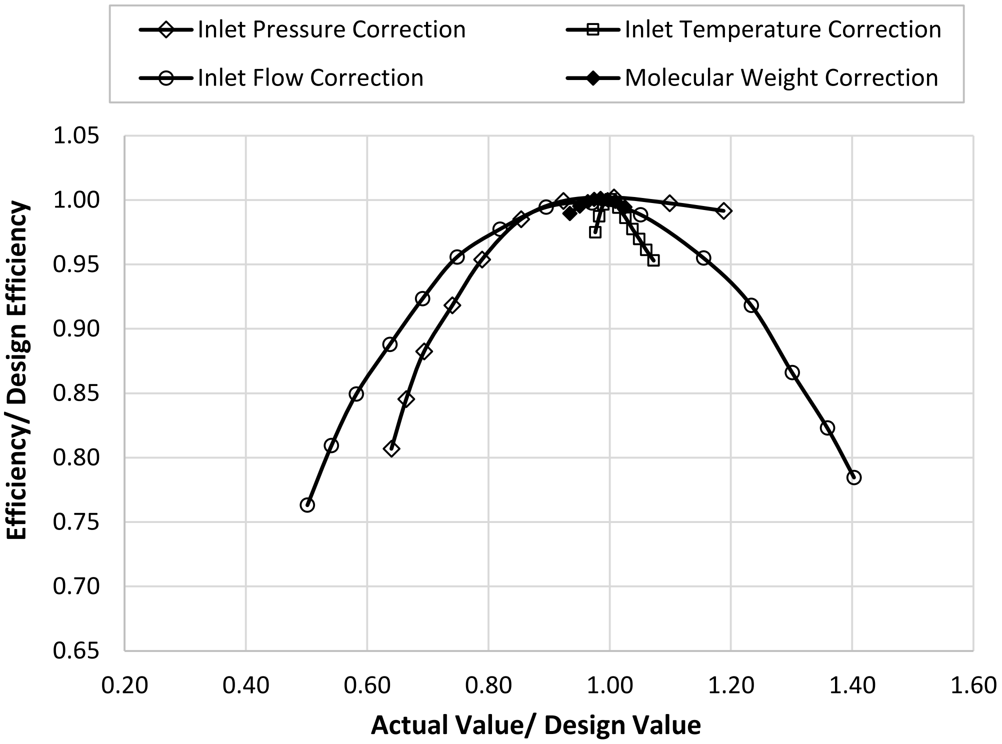

Figure 11- 10: Correction Factors of Design Efficiency at Constant Speed Based on Presented Figures in (Bloch and Soares, 2001)

Less significant effect can be observed with the variation in the molecular weight. The variable speed turboexpanders are more sensitive to operating conditions fluctuation in normal. Despite the fact that the correction factor trend is almost the same as the constant speed operation, more substantial drop is expected in the efficiency of variable speed turboexpander when the inlet pressure drops below the design value. However, the sensitivity of variable speed machines to temperature variation is less significant than constant speed machines.

11.4.3 Case Study

The method proposed in the previous section is used to obtain the geometrical specifications of a turboexpander for liquefaction process. The initial inlet conditions are shown in table 11-3. For the preliminary estimation of the expected expander efficiency, the effect of Reynolds number will be ignored initially ($Re \geq 10^6$). The inlet conditions have been specified according to the studied design by Fiaschi et al. (2012). From table 11-1, the radial inflow turbine will be used to fit with the required power output and specified speed range. For higher efficiency, the optimum specific speed range from figure 11-9 is $20 < N_s < 140$. However, four different design options will be considered and assessed to obtain the optimum efficiency value based on the aerothermodynamic parameters evaluation. Table 11-4 compares the basic non-dimensional parameters of the studied designs. The isentropic efficiency has been obtained graphically according to figure 11-9 while the velocity ratio (u_2/C_o) represents the final iterated value after considering the geometrical specifications of the designed stage. The generated power in table 11-4 has been estimated using IPSEpro simulator corresponding to the specified isentropic efficiency. The rotational speed is derived from the specific speed correlation as was described earlier.

Table 11- 3: Inlet Conditions of Designed Turboexpander

Parameter	Units	Value
Fluid Name	-	Hydrocarbons1
Application	-	Liquefaction (Methane/Ethane)
Inlet Pressure (p_1)	bar	10.0
Inlet Temperature (T_1)	°C	147
Inlet Flow Rate ($\dot{V}$)	m^3/h	806.4
Outlet Pressure (P_4)	bar	0.90

Table 11- 4: Characteristics of the Evaluated Design Options

Parameter	Design (A)	Design (B)	Design (C)	Design (D)
N_s	57.0	52.0	45.0	31.0
η_{t-s}	0.85	0.80	0.75	0.7
u_2/C_o	0.584	0.521	0.455	0.341
Speed (rpm)	62,441	53,520	43,505	28,021
Power (kW)	344.0	324.0	303.0	283.0

Table 11- 5: Physical and Thermodynamic Gas Properties at Suction and Discharge of Studied Turboexpander Configurations

Parameter	Design (A)	Design (B)	Design (C)	Design (D)
k_1	1.224	1.224	1.224	1.224
Z_1	0.994	0.994	0.994	0.994
R_1	0.483	0.483	0.483	0.483
Molecular Weight (g/mol)	18.3	18.3	18.3	18.3
ρ_1 (kg/m^3)	4.956	4.956	4.956	4.956
T_4 (°C)	3.7	12.9	22.3	31.3
Z_4	0.997	0.998	0.998	0.998
k_4	1.298	1.292	1.286	1.280
h_1(kJ/kg)	332.6320	332.6320	332.6320	332.6320
s_1(kJ/kg.°k)	10.7904	10.7904	10.7904	10.7904
v_1(m^3/kg)	0.2017	0.2017	0.2017	0.2017
h_{4a}(kJ/kg)	7.6461	26.5410	46.380	65.2740
v_{4a}(m^3/kg)	1.4833	1.5359	1.574	1.6255
Δh_{1-4} (kJ/kg)	324.9859	306.0910	286.2520	267.3580
ρ_4 (kg/m^3)	0.672	0.649	0.633	0.612

Table 11- 6: Geometrical Features of the Generated Turboexpander Designs

Parameter	Design (A)	Design (B)	Design (C)	Design (D)
Stages No.	3.0	3.0	3.0	3.0
Q_4 **(CMH)**	6428	6658	6826	7050
D_1**(mm)**	116.4	117.5	122.0	137.3
U_3 **(m/s)**	176.67	156.42	130.9	87.15
D_3 **(mm)**	54.0	56.0	57.0	59.0
D_4**(mm)**	76.0	78.0	80.00	83.00
D_2**(mm)**	83.2	84.0	87.2	98.1
U_2 **(m/s)**	271.88	235.27	198.56	143.92
D_1**(mm)**	120.0	120.0	121.0	137.0
β_3 **(°)**	61.1	63.3	65.9	58.6
Blades No.	12.0	12.0	12.0	12.0
α_3 **(°)**	23.5	21.9	19.5	24.7

Table 11-5 demonstrates the obtained physical and thermodynamic properties at both sides of the turboexpander. The suction conditions are fixed for all design configurations while the discharge parameters vary with respect to the performance characteristics. Despite the fact that all the design cases are at constant expansion ratio, the gas properties at exit side are affected by the change in the discharge temperature. The defined geometrical specifications of each design are listed in table 11-6. However, it should be noted that the obtained relative and absolute velocities and angles are at design flow value.

Figure 11-11 illustrates the trends of specific speed and velocity ratio with the isentropic efficiency. A greater efficiency was observed at high specific speed and velocity ratio. This, in fact, agrees with the generalized N_s-D_s graph in figure 11-9. Another form of representation is shown in figure 11-12 in terms of rotational speed. Although that all the designed expanders are working at almost a constant expansion ratio, the high demanded power at high efficiency value forces the turboexpander wheel to rotate at higher speed. Thus, the Design (A) has the greatest speed value while the lowest speed was obtained with Design (D) at 70% isentropic efficiency. However, the high rotational speed is not always possible due to its direct effect on the aerodynamic performance. It was also observed that there is a significant drop in the rotational speed when the efficiency is reduced from 75% to 70% by around 35.5%. The influence of speed rise is demonstrated in figure 11-13 as a function of enthalpy drop. The high rotational speed at Design (A) allows for greater enthalpy drop with approximately 2.3% over the Design (B). An interesting observation was that the enthalpy drop is taking roughly a linear trend with the isentropic efficiency. However, the amount of incremental reduction in the enthalpy per efficiency rise is decreasing gradually reaching to a certain point where no further decline would be expected.

The enthalpy drop is also used to obtain the expected generated power by multiplying the predicted enthalpy drop by the amount of flow rate as shown in figure 11-14. One observation from this figure is the significant change in the specific speed value at low isentropic efficiency (Design C and D). Additionally, more pronounced increase in the generated power was recorded when the specific speed is raised from 45 to 52.

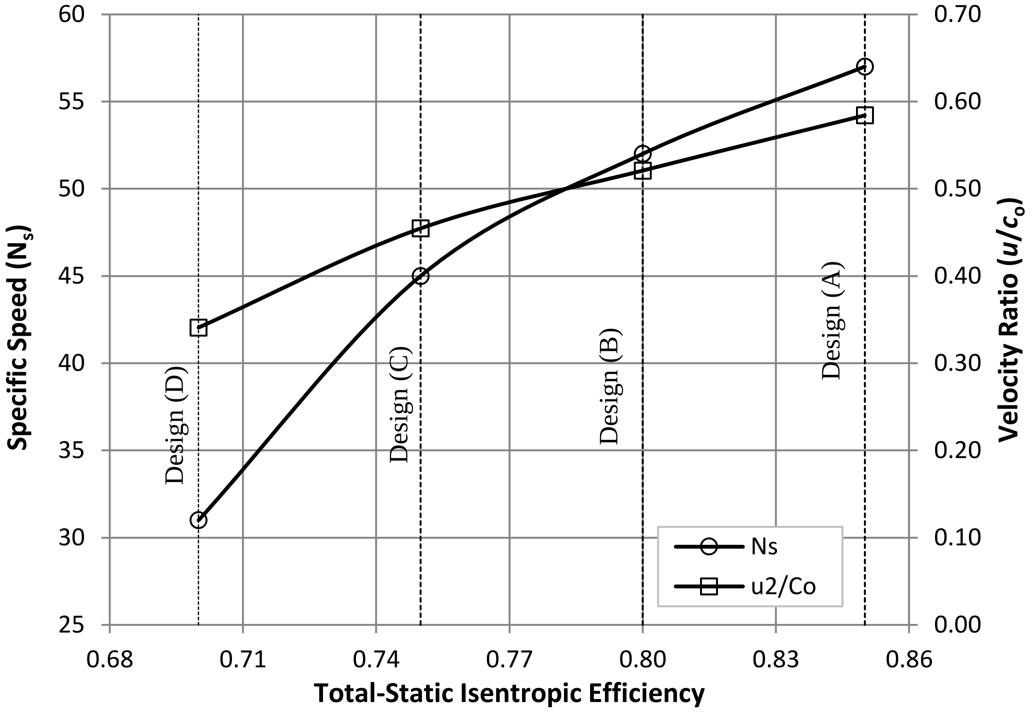

Figure 11- 11: Effect of Specific Speed and Velocity Ratio on Isentropic Efficiency

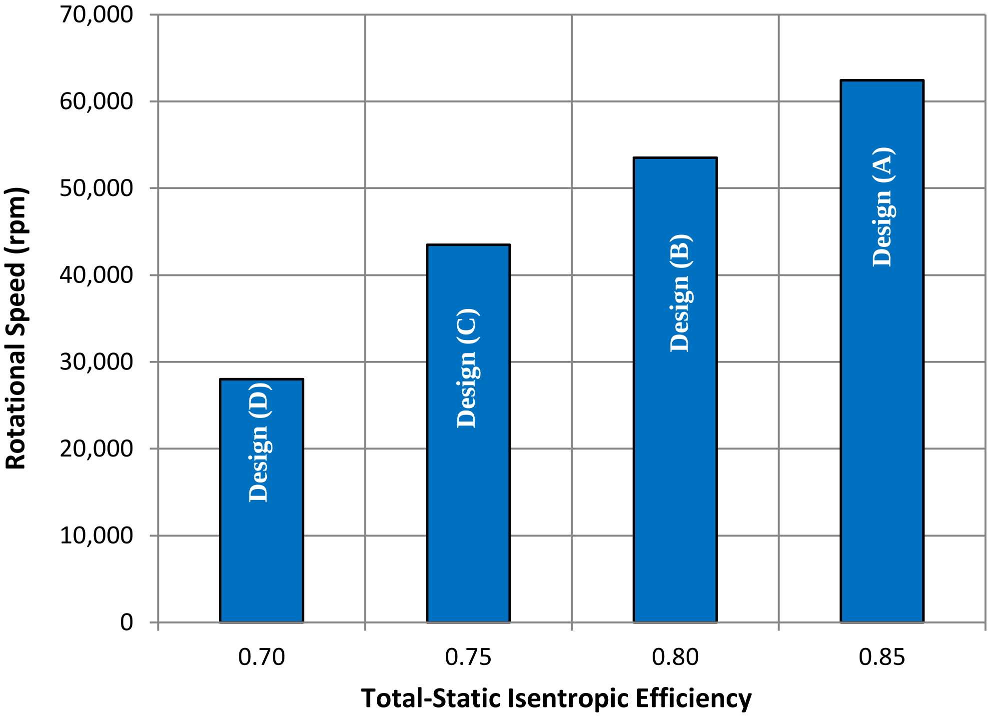

Figure 11- 12: Comparison Between the Predicted Rotational Speed at Different Designs

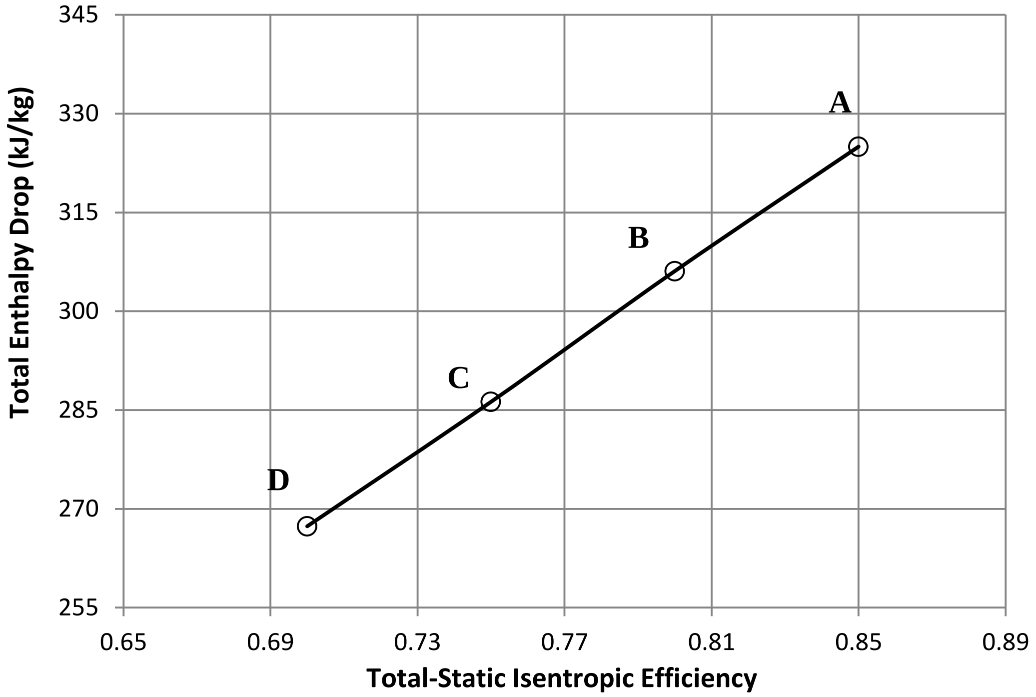

Figure 11- 13: Predicted Change in the Total Enthalpy Drop at Various Designs

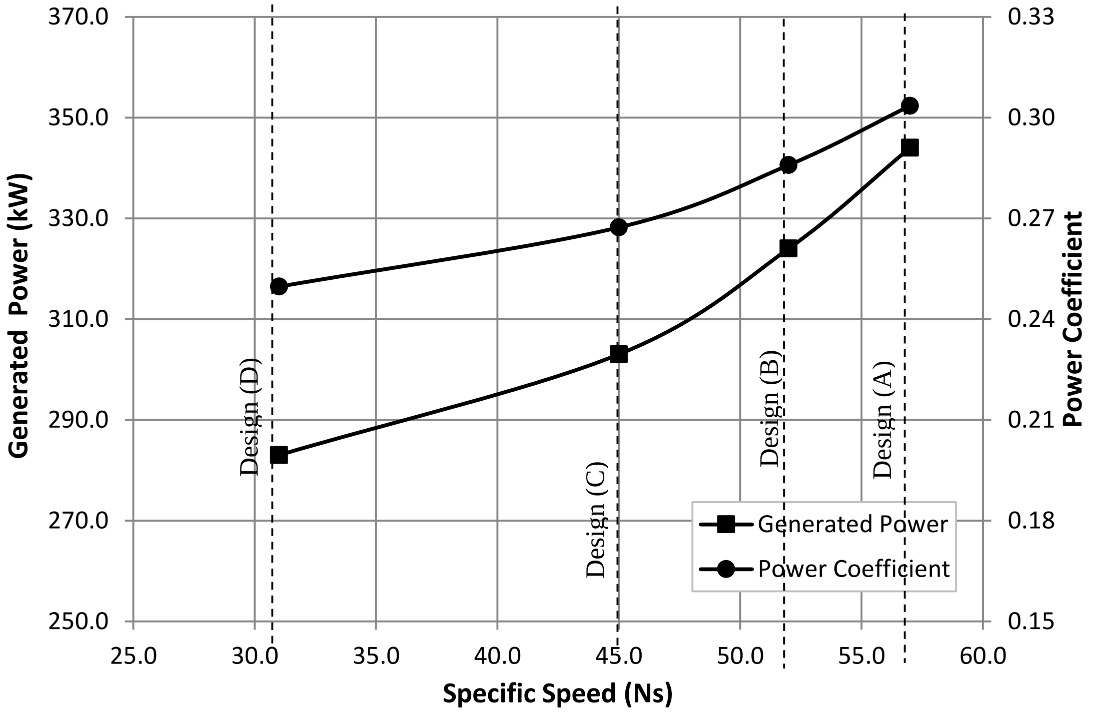

Figure 11- 14: Determination of Generated Power and Power Coefficient

Figure 11-15 illustrates the influences of specific speed on the discharge temperature and enthalpy. The high efficiency at high specific speed leads to reduce the predicted discharge temperature at constant exit pressure. This is associated with the gas enthalpy which decreases proportionally with the gas temperature. However, this reduction in gas temperature has to be within the allowed limit to avoid the droplets formation.

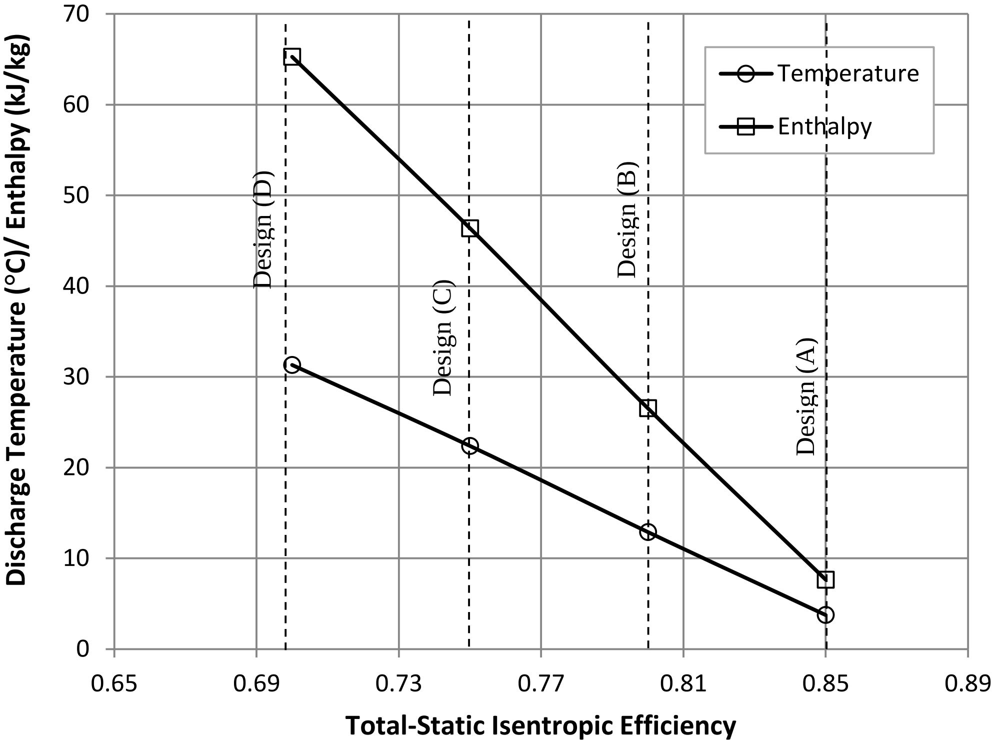

Figure 11- 15: Estimated Discharge Temperature and Enthalpy at Different Designs

The hydrate formation conditions have to be analysed to determine whether inhibition or dehydration procedures are required. A sufficient margin should be allowed from the HFT, which normally ranges between 2.5°C and 5 °C.

In order to evaluate the proposed designs, the predicted aerodynamic performance parameters are compared against the recommended values in table 11-1. The estimated work coefficients of all designs are lower than the maximum allowed limit except Design (A) where the work coefficient was found greater than the upper limit by around 6.1% as shown in figure 11-16. This indeed is due to the significant enthalpy drop through the stages of the proposed Design (A) which can cause high load and stress on the wheel blades. Moreover, the high rotational speed at the isentropic efficiency of 85% raises the tip Mach number above the unity. This has to be avoided to eliminate the possibility of flow separation. However, the tip Mach number of the rest of designs is lower than the allowed limit. A further effect of high operating speed can be illustrated in terms of flow coefficient. It was found that the high tip velocity at Design (A) causes the flow coefficient to be lower than the minimum recommended limit at design flow. Besides, the flow coefficient of Design (B) is close to the lower limit, but it is still acceptable. Therefore, the designs B, C and D are aerodynamically acceptable. However, the Design (B) is more recommended for higher power output.

However, a further procedure is followed to define the optimum design aiming to achieve the highest possible efficiency and with the satisfaction of the aerodynamic constraints. Figure 11-17 shows the predicted work coefficient at different isentropic efficiencies. Each of the presented points denotes a different turboexpander design. Thus, this curve can be used to specify the maximum allowed efficiency to satisfy the aerodynamic constraints.

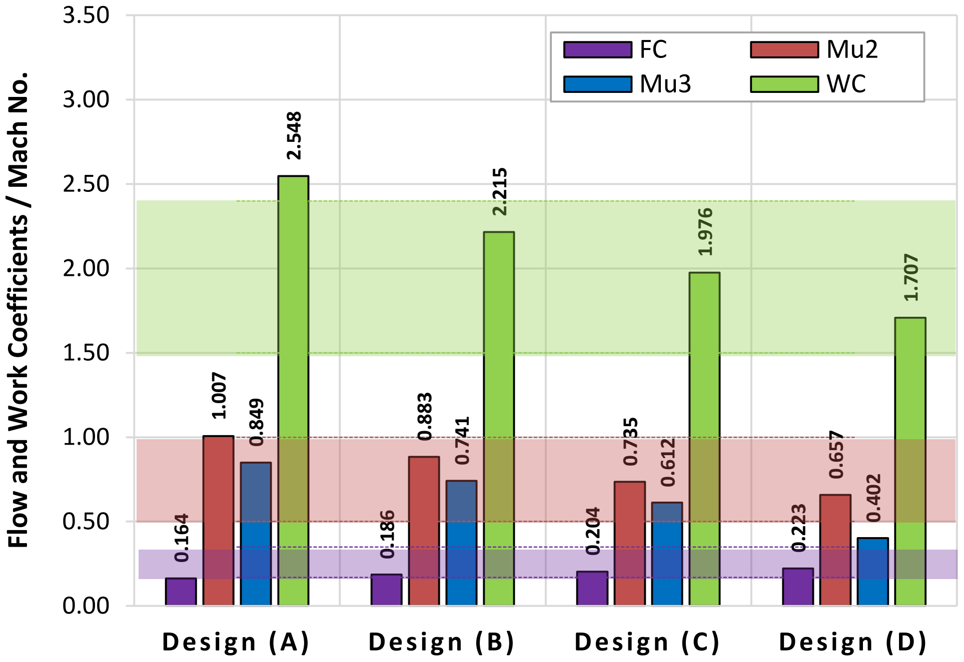

Figure 11- 16: Evaluation of Generated Designs Aerodynamic Parameters Against Recommended Ranges

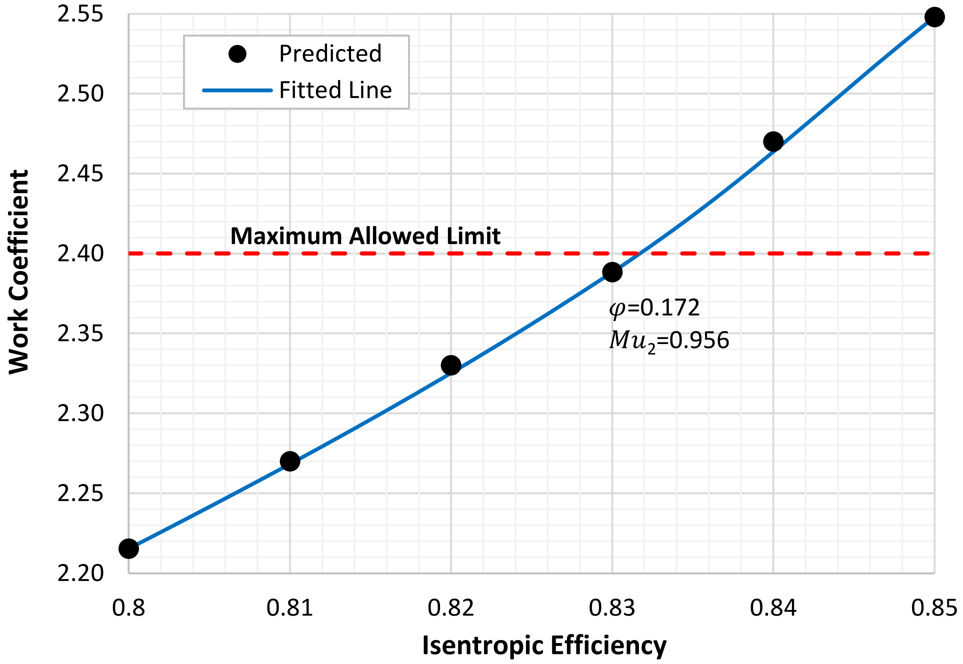

Figure 11- 17: Determination of the Optimum Efficiency Value to Satisfy the Maximum Allowed Work Coefficient

It is clear that the turboexpander design at 83% isentropic efficiency is the highest possible efficiency value lower than the upper work coefficient limit. By assessing the other aerodynamic parameters at this point, the flow coefficient and tip Mach number are slightly higher and lower than the recommended limits, respectively. Therefore, this design will be selected for the following processes.

Evaluating the off-design performance is highly recommended for higher operation reliability of both power recovery sets and processing plants. The performance of the selected expander design is estimated at various suction flow rates as shown in figure 11-18. The used technique is based on the assumption that the highest efficiency value is at design conditions. It is clear that the flow curve is nearly symmetrical, so either lower or higher flow than the design point can cause a reduction in the turboexpander efficiency. This in turns leads to reduce the expansion ratio and the generated power as illustrated in figures 11-18. Hence, the turboexpander design flow should be obtained to consider the expected variation in flow capacity. If there is a substantial fluctuation in the suction flow, then it might be economically feasible to select two turboexpanders units to avoid the significant drop in the efficiency.

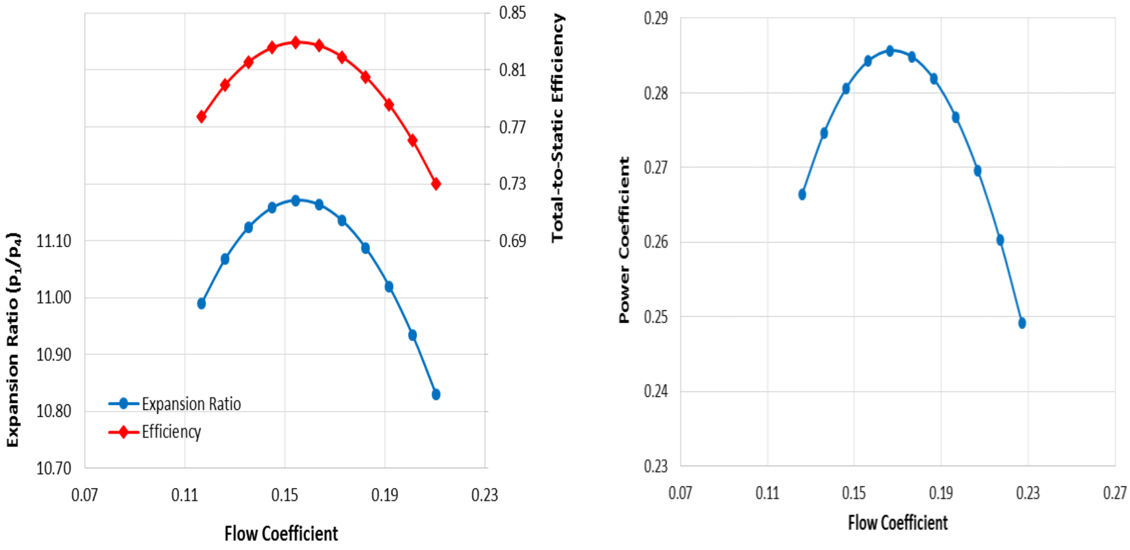

(a) **(b)**

Figure 11- 18: Predicted Running Line of Selected Design at Design Speed: (a). Expansion Ratio and Isentropic Efficiency (b). Power Coefficient

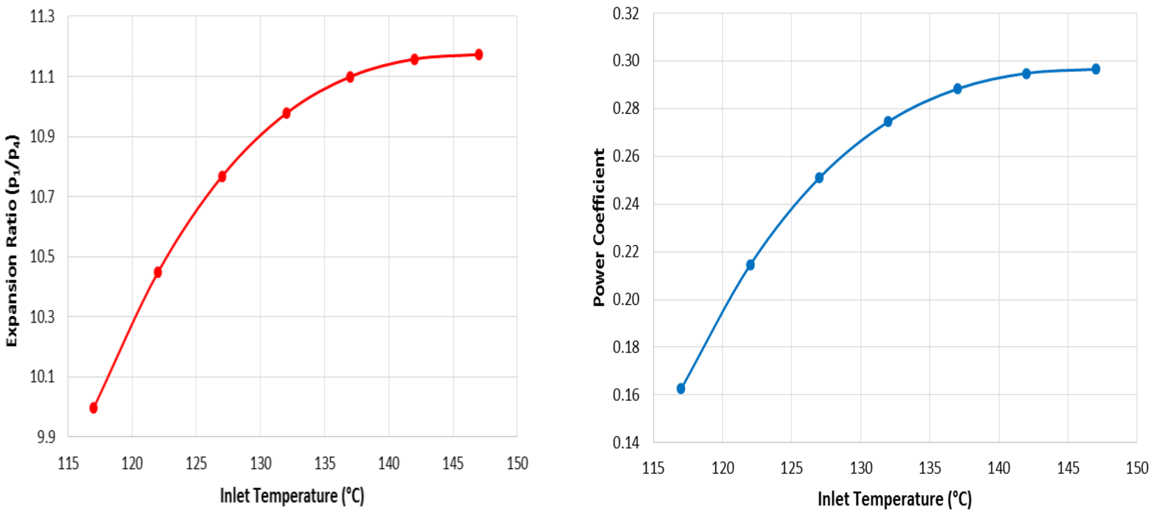

(a) **(b)**

Figure 11- 19: Effect of Inlet Gas Temperature on: (a). Expansion Ratio (b). Power Coefficient

One of the key parameters which has to be assessed here is the inlet gas temperature. Figure 11-19(a) shows an increase in the expansion ratio as the inlet temperature goes up, and it is also associated with an improvement in the power coefficient as demonstrated in figure 11-19(b). This elucidates the need for gas pre-heating prior the turboexpander entrance. Another reason for gas pre-heating is to avoid reaching to the minimum allowed limit for droplets and hydrate formation. Therefore, the pre-heating of the turboexpander inlet gas is controlled by considering the discharge temperature and the lower allowed limit.

11.5 Chapter Summary

This chapter introduced a simplified design method for turboexpander based on Ns-Ds principle and with respect to the stated aerothermodynamic constraints. The gas physical properties were obtained using the developed GasProp tool while the thermodynamic properties have been estimated by IPSEpro software. To evaluate this approach, a case study was included to define the optimum design characteristics for hydrocarbon liquefaction process. Five different turboexpander designs have been evaluated aerodynamically to attain the highest possible performance. The required number of stages was specified as a function of enthalpy drop, flow coefficient and Mach number. It was concluded that designing a turboexpander stage with the maximum isentropic efficiency is not always possible due to the limitations of the aerodynamic parameters of each single component.

The off-design performance was predicted using the correction factors method by considering the effect of gas compositions, gas pressure and temperature and flow rate. The flow curve was found almost symmetrical, so either lower or higher flow than the design point can cause a reduction in the turboexpander efficiency. This is associated with a decrease in the expansion ratio and power output. Hence, if there is a substantial fluctuation in the suction flow, it is strongly recommended to consider two turboexpanders units as an alternative to avoid the significant drop in the efficiency. This option should also be optimized from an economic perspective to make the optimal decision. Moreover, an increase in the expansion ratio was found at high inlet temperature with an improvement in the power coefficient. This emphasized the need for gas pre-heating at the upstream of turboexpander. However, the turboexpander inlet gas pre-heating is controlled by considering the discharge temperature and the lower allowed limit.

CHAPTER 12: CONCLUSION AND RECOMMENDATIONS

12.1 Conclusion

In oil and gas industry, there are numerous external process parameters affect the performance of centrifugal compressor and turboexpander in the operating environment. The prediction of the performance at different working conditions and operating modes will contribute to evaluate the causes of abnormal machine behaviour. Hence, this study was conducted to model and assess the causes of inefficient and unstable operation of centrifugal compressors and turboexpanders in order to provide a solution for performance restoration and enhancement. To accomplish that, this study considered the opportunities for efficiency and operating range enhancement options of both installed and new units. The first part of this thesis discussed the performance of centrifugal compressor units which covered the majority of this study works while the last part dealt with the turboexpander design and performance analysis.

12.1.1 Centrifugal Compressor Part

This study introduced a novel integrated approach to assess the performance and design of multi-stage centrifugal compressors. This model includes five basic elements: evaluation of compressor selection process, compressor sizing and casing structure, performance prediction at design and off-design conditions, modelling of efficiency and head deterioration causes; and stage design evaluation. The developed method was found to be valid for performance assessment and design evaluation of new and aged centrifugal compressor units. Moreover, this tool will help the users to determine the root-cause of inefficient and unstable operation for installed units by evaluating the available operation data.

For performance prediction at design conditions, a new method has been developed to predict the performance curve of multi-stage centrifugal compressor at design conditions based on stage stacking technique. This has been established to combine the advantages of Lüdtke and Casey-Robinson methods yielding more precise performance map prediction comparing with existing models for both high and low flow coefficients applications. In order to estimate the required number of mechanical and process stages, the developed approach is incorporated with a unique methodology for compressor selection and sizing. Besides, the derived empirical correlations were proven to predict the stability limits for every speed line with a greater degree of accuracy and the biggest percentage of error was found near the surge flow with less than 1.7% relative error.

The obtained performance map at design conditions was then used to predict the equivalent performance at various suction conditions and different gas compositions. To accomplish this objective, a new iterative method has been developed with less dependency on the geometrical features. One of this technique advantages is that it considers the variation in the stage efficiency and gas properties throughout the compression process leading to more accurate prediction over the correction method. This method has been tested to predict the performance of two multistage centrifugal compressors, and the estimated characteristics showed good agreement with the measured data. The maximum uncertainty was observed near the surge point at the overload speed by about 2.21%. However, it was found that the developed approach can be implemented for design evaluation and operation diagnosis as well.

To evaluate the impact of internal blockage on the performance parameters, this study introduced an approach to model the effect of non-reactive deposits which has been supported by four operation cases and the obtained results were compared with the internal inspection findings from the stage overhauling process. This involved a discussion of the internal blockage impact on the stage performance technically and economically. Since the main challenge here is to analyse the process gas composition in real time, the influences of the non-reactive deposits have been compared with the effect of the unanticipated gas composition change. One of the key findings was that the pressure ratio parameter is not enough to assess the possibility of flow blockage and unanticipated gas properties change. Moreover, it was observed that the stage discharge pressure is more sensitive to the fouled cooler comparing with suction and internal blockage. However, the effect of contaminated aftercooler on the surge point and discharge pressure and temperature of the upstream stage was found greater than its impact on the shaft power. Thus, a substantial surge margin reduction was detected when the first stage was operating with a fouled aftercooler comparing with the measured reduction as a result of sudden gas properties change. Furthermore, a larger pressure ratio drop was measured in the case of liquid carryover which indicates more significant impact of the two phases densities difference comparing with the gas volume fraction (GVF) effect. The possibility of hydrate formation has been assessed using hydrate formation temperature (HFT) criteria.

Additionally, this research reviewed the options of efficiency and operating range improvement by evaluating the influences of design characteristics of centrifugal compressor stage on the operating efficiency and stable flow range. This also covered the unsteady interaction between the aerodynamic component and the trade-off between the stage efficiency and stable operating range. Besides, an empirical-based-model has been established to select the optimum impeller and diffuser configurations in order to make a compromise decision based on technical and economic perspective. This method has been examined at high and very low flow coefficients and Mach numbers operating conditions, and the obtained parameters are compared with the CFD simulation results and the recorded measured data. It is argued throughout this study that the decision-making process of the typical stage geometrical features has to be based upon the long-term economic performance optimization. Thus, for higher long-term economic performance, it was found that is not sufficient to select the characteristics of diffuser geometry based on the low manufacturing cost or efficiency improvement criterion only.

12.1.2 Turboexpander Part

Focusing on turboexpander, a simple and low cost tool has been developed to evaluate the optimum turboexpander characteristics by analysing the generated design alternatives. This method was based on N_s-D_s method and it used the aerothermodynamic constraints as an evaluation criterion. The gas physical properties were obtained using the developed GasProp tool while the thermodynamic properties have been estimated by IPSEpro software. To evaluate this approach, it was used in designing a turboexpander for hydrocarbon liquefaction process. Five different turboexpander designs have been evaluated aerodynamically to attain the highest possible performance. The required number of stages was specified as a function of enthalpy drop, flow coefficient and Mach number. It was concluded that designing a turboexpander stage with the maximum isentropic efficiency is not always possible due to the limitations of the aerodynamic parameters. Thus, it is necessary to optimize the stage geometrical features prior the construction process to balance between the high capital cost and the high energetic efficiency.

As the turboexpander is expected to work under severe gas conditions, the off-design performance was predicted using the correction factors method by considering the effect of gas compositions, gas pressure and temperature and flow rate. The flow curve was found almost symmetrical around the design point, and it is associated with a reduction in the expansion ratio and power output. Hence, if there is a substantial fluctuation in the suction flow, it is strongly recommended to consider two turboexpanders units as an alternative to avoid the significant drop in the efficiency. This option should be optimized from an economic perspective to make the optimum decision. Moreover, an increase in the expansion ratio was found at high inlet temperature with an improvement in the power coefficient. This emphasized the need for gas pre-heating prior the turboexpander entrance. However, the turboexpander inlet gas pre-heating is controlled by considering the discharge temperature and the lower allowed limit.

12.2 Contribution to Knowledge

The present study introduced a comprehensive approach to assess the causes of efficiency deterioration and aerodynamic instability of centrifugal compressors and turboexpanders. This was achieved based on aerothermodynamics flow analysis for radial turbomachinery, operational data evaluation and the available models and experimental data in the cited open literature. The developed approach has been qualified with different operational cases and the conducted comparison with the existing models results, measured data and internal inspection findings emphasized the validity of this approach for operation diagnosis and design evaluation of new and installed units. Over the available models of radial compressors in the literature, the new approach was derived to compromise between the high efficiency requirements and wide stable flow range of multi-stage process centrifugal compressor and with hydrocarbon process gas. One of the main features of this integrated approach is the incorporation of five different elements as following:

- ✓ A technique to evaluate the selection of compressor structure and capacity control method.
- ✓ A tool to estimate the gas properties of different hydrocarbon mixtures.
- ✓ A reliable method to predict the compressor map at design conditions.
- ✓ A new method for more accurate estimation of centrifugal compressor performance at different off-design conditions and various operating modes.
- ✓ A systematic methodology to identify the causes of inefficient and unstable centrifugal compressor performance.
- ✓ A simplified technique to define the optimum configuration of impeller and diffuser.

The novel aspects of this study have been published in several research papers as shown in Appendix (A), and they can be summarized in the following points:

- Develop a novel integrated model to predict the performance map of multi-stage centrifugal compressor at design conditions based on stage –stacking principle.

This model has been validated at both low and high flow coefficient applications, and the obtained results show a significant improvement in the estimated efficiency and pressure ratio comparing with the existing methods with less dependency on the geometrical features.

- Introduce a new iterative method to derive the equivalent compressor performance at various suction conditions and different gas compositions. This has been proven to be valid for design evaluation and operation diagnosis of new and aged centrifugal compressor units.
- Investigate the impact of non-reactive deposits on the performance parameters of centrifugal compressor. The proposed method has been verified by four operation cases, and the estimated results were compared with the internal inspection findings from the stage overhauling process.
- Derive a systematic methodology to assess the causes of inefficient and unstable centrifugal compressor operation including the impact of gas compositions, internal blockage, hydrate formation, multi-phase flow and fouled aftercooler. Moreover, the influences of the internal flow blockage have been also compared with the effect of the unanticipated gas composition change.
- Propose a simplified method to select the typical shrouded percentage as a function of static pressure recovery, energy parameters, stage efficiency, operating range and power loss cost. This model has been evaluated against the CFD simulation results and the recorded measured data.
- Conduct a techno-economic assessment for the influences of diffuser configuration on centrifugal compressor performance. This will contribute to define the optimum diffuser characteristics according to the required duty.

12.3 Recommendations for Future Work

1- The conducted study on the sources of enthalpy losses in the centrifugal compressor stage demonstrates a significant effect of the vaneless space design on the aerodynamic losses. Therefore, a detailed study is recommended for the flow analysis and the design characteristics of vaneless space with the aim of minimizing this component loss. This also requires more attention to the unsteady interaction with the upstream rotor and downstream diffuser. Furthermore, it is also suggested to consider the effect of return channel geometry on the aerodynamic interaction with the diffuser.

2- Chapter 5 discussed the impact of oil and dry seals on the aerodynamic losses and stage efficiency. However, further investigation is required to consider the techno-economic value from replacing the old oil seal by the dry gas seals. Moreover, a detailed study has to be placed on the losses mechanism through interstage sealing system.

3- The introduced approach for capacity control method selection is based on casing structure, part-load efficiencies, investment cost, overload operation and suction pressure. However, more focus should be placed to define the effect of the operating efficiency, flow range and rotational speed limitations. Additionally, the compressor driver selection has to be reviewed to consider other factors such as process steam supply, capital cost, process control, fuel or energy cost and reliability.

4- Further detailed validation studies are required for the developed approach for performance prediction at both design and off-design conditions to evaluate the prediction capability of this model and to identify its potential and limitations.

5- Despite the fact that the developed model for design performance prediction can be used for high and low flow coefficients applications, the accuracy of the estimated parameters can be improved further by considering the variation in the detailed aerodynamic losses with rotational speed and flow rates. This study focuses only on the major sources of enthalpy losses in the compression stage, and it does not account all the individual component losses and the change in the pressure losses at choke conditions as a result of the aero-channels blockage.
6- The derived method in chapter 7 for off-design performance prediction of centrifugal compressor can be improved by considering the effect of operating conditions fluctuation on the aerodynamic losses of the stage component and the unsteady interaction between the impeller and diffuser. The developed model in this study assumes that the aerodynamic losses are constant as design operation which can be considered as a valid assumption when there is no substantial fluctuation in the suction conditions and gas composition.
7- Further investigation is required on the influences of multi-phase flow on the aerothermodynamic performance of centrifugal compressor and the ways to detect its bearing on the temperature and pressure trends.
8- This study concentrates on the effect of non-reactive deposits on the aerothermodynamic performance. However, it did not cover the influences of reactive deposits. The chemical mechanism to generate polymerization is not well understood. While flowing through the compression stage, the polymer material can agglomerate in the labyrinth, drain lines and intercoolers creating more severe pressure drop. Besides, the chemical reaction between the reactive contaminations and the flow path surface has an adverse effect on the internal components life. Hence, it is important to consider the overall compression system component and to understand the chemistry of the generated fouling material which requires further investigation.
9- The evaluation of compressor cleaning methods has not been covered in this study. Therefore, a multi-decision optimization is recommended to consider the most effective cleaning method based on technical, economic and environmental values. The on-line cleaning should be considered as an option which is accomplished by injecting the suitable liquid in the gas flow path either in suction piping or the intermediate compressor stages. The liquid is atomized with special spray nozzles that are directed against the gas flow for uniform distribution of liquid sprayed.
10- The modelling of shrouded effect on stage aerothermodynamic performance was performed in chapter 10 assuming constant disc friction, slip factor and slip velocity. Practically, these parameters are affected by the shrouded percentage so they are expected to vary. Therefore, this model is recommended to be further improved to consider the impact of the variation of these parameters.
11- The proposed method to select the optimum diffuser configuration in chapter 9 did not consider the effect of boundary layer growth on the diffuser throat blockage. Thus, this model can be improved further to account this effect using one of the boundary-layer theories.
12- The developed approach for turboexpander design is based on Ns-Ds method. However, there are different methods which can be used for this purpose. Therefore, it is recommended to compare the outcomes of different method in order to select the optimum geometrical parameters. This has to involve the technical and economic assessment. More focus has to be also placed on the off-design performance prediction.

REFERENCES

- Abdelhamid, A. N. (1980), Analysis of Rotating Stall in Vaneless Diffusers of Centrifugal Compressors, In ASME 1980 International Gas Turbine Conference and Products Show, ASME.
- Abdel-Hamid, A. N. (1987), A New Technique for Stabilizing the Flow and Improving the Performance of Vaneless Radial Diffusers, Journal of Turbomachinery, 109(1), 36-40.
- Abdelmadjid, C., Mohamed, S. A., & Boussad, B. (2013), CFD Analysis of the Volute Geometry Effect on the Turbulent Air Flow through the Turbocharger Compressor, Energy Procedia, 36, 746-755.
- Abdelwahab, A. (2006), An Investigation of the Use Of Wet Compression In Industrial Centrifugal Compressors, In ASME Turbo Expo 2006: Power for Land, Sea, and Air pp. 741-750, American Society of Mechanical Engineers.
- Adewumi, M. (2011), Soave-Redlich-Kwong EOS (1972), Pennsylvania State University, Available at: https://www.e-education.psu.edu/png520/m10_p5.html (Accessed on: 11/04/2014)
- Al Yahyai, M., & Mba, D. (2014), Rotor Dynamic Response of A Centrifugal compressor Due to Liquid Carry Over: A case study. Engineering Failure Analysis, 45, 436-448.
- Aligoodarz, M. R., Tehrani, M. R. S., Karrabi, H., & Roshani, M. R. (2012), Numerical Analysis of Deposits and Corrosion Influence on a Centrifugal Compressor Performance, In ASME 2012 International Mechanical Engineering Congress and Exposition American Society of Mechanical Engineers, pp. 925-929.
- Amano, R. S. & Sunden, B. (2008), Thermal Engineering in Power Systems, Southampton WIT press, UK
- American Petroleum Institute (2002), API Standard 617; Axial and Centrifugal Compressors and Expander-compressors for Petroleum, Chemical and Gas Industry Services, Seventh Edition, Northwest Washington.
- Amineni, N. K. (1996), Design and Development of Advanced Vaned Diffusers for Centrifugal Compressors, Doctoral dissertation, Michigan State University, East Lansing, MI.
- ASME PTC-10 (1997), Performance Test Code on Compressors and Exhausters, ASME, New York.
- Aubry, Anne-Raphaelle (2012), Return Channel Loss Reduction in Multi-stage Centrifugal Compressors, Massachusetts Institute of Technology, Master Thesis, Cornell University.
- Aungier, R. H. (1995), Mean Streamline Aerodynamic Performance Analysis of Centrifugal Compressors, Journal of Turbomachinery, 117(3), pp. 360-366.
- Aungier, R. H. (2000), Centrifugal Compressors: A Strategy for Aerodynamic Design and Analysis, ASME.
- Ayder, E. (1993), Experimental and Numerical Analysis of the Flow in Centrifugal Compressor and Pump Volutes, Doctoral dissertation, Von Karman Institute for Fluid Dynamics, Rhode Saint Genese, Belgium.
- AZTech Training & Consultancy (2010), Reciprocating Compressors: Training Manual, Dubai, UAE
- Badr, O., Probert, S. D., & O'callaghan, P. W. (1985), Selecting A Working Fluid for a Rankine-Cycle Engine, Applied Energy, 21(1), 1-42.
- Bahadori, A., & Vuthaluru, H. B. (2009), A novel Correlation for Estimation of Hydrate Forming Condition of Natural Gases, Journal of Natural Gas Chemistry, 18(4), 453-457.
- Baillie, C. & Wichert, E. (1987), Chart Gives Hydrate Formation Temperature for Natural Gas, Oil and Gas Journals, 85(4):37–39.

- Balje, O. E. (1962), A Study on Design Criteria and Matching of Turbomachines: Part A—Similarity Relations and Design Criteria of Turbines, Journal of Engineering for Gas Turbines and Power, 84(1), 83-102.
- Bao, J., & Zhao, L. (2013), A Review of Working Fluid and Expander Selections for Organic Rankine Cycle, Renewable and Sustainable Energy Reviews, 24, 325-342.
- Barber-Nichols Inc. (2015), Turbines, Available at: http://www.barber-nichols.com/products/turbines (Accessed on : 27/11/15)
- Bela, L. G. (2003), Instrument Engineers Handbook: Process Measurement and Analysis, Volume 2, Fourth edition, CRC Press, US
- Berdanier, R. A., Smith, N. R., Fabian, J. C., & Key, N. L. (2015), Humidity Effects on Experimental Compressor Performance—Corrected Conditions for Real Gases, Journal of Turbomachinery, 137(3), 031011.
- Berge, B. K. (1986), Hydrate Prediction on A Microcomputer, paper SPE 15306, symposium on petroleum industry applications of microcomputers.
- Bertoneri, M., Duni, S., Ransom, D., Podestà, L., Camatti, M., Bigi, M., & Wilcox, M. (2012), Measured Performance of Two-Stage Centrifugal Compressor Under Wet Gas Conditions, In ASME Turbo Expo 2012: Turbine Technical Conference and Exposition, ASME, GT2012-69819.
- Bidaut, Y. (2013), The Influence of Thermal Loading on the Leak Tightness Behaviour of Horizontally Split Centrifugal Compressors, Proceedings of the Second Middle East Turbomachinery Symposium, Doha, Qatar.
- Blahovec, J. F., Matthews, T., & Eads, K. S. (1998). Guidelines for Specifying and Evaluating New and Rerated Multistage Centrifugal Compressors, In Proceedings of the Twenty-Seventh Turbomachinery Symposium, pp. 215-231.
- Bloch, H. P. (2006), A Practical Guide to Compressor Technology, Second edition, John Wiley and Sons Inc., New York.
- Bloch, H. P., & Soares, C. (2001), Turboexpanders and Process Applications, Gulf Professional Publishing, 1st edition, Butterworth-Heinemann.
- Boyce, M. P. (1993), Principles of Operation and Performance Estimation of Centrifugal Compressors, In Proceedings of the 22nd Turbomachinery Symposium, pp. 161-178.
- Boyce, M. P. (2003), Centrifugal Compressors: a Basic Guide, PennWell Books.
- Boyce, M. P. (2012), Gas Turbine Engineering Handbook, 4th Edition, Elsevier, USA.
- BP (2011), BP Energy Outlook. London: BP, (Cited in: Duissenov, 2013).
- BP (2012), Oil Reserves, Retrieved 2013, from British Petroleum: http://www.bp.com/sectiongenericarticle800.do?categoryId=9037157&contentId=7068604 (Cited in: Duissenov, 2013).
- BP (2012). Natural Gas Reserves, Retrieved 2013, from British Petroleum: http://www.bp.com/sectiongenericarticle800.do?categoryId=9037178&contentId=7068624 (Cited in: Duissenov, 2013).
- BP (2013), World Energy Outlook, London: BP (Cited in: Duissenov, 2013).
- Brenne, L., Bjørge, T., Gilarranz, J. L., Koch, J., & Miller, H. (2005), Performance Evaluation of a Centrifugal Compressor Operating under Wet-Gas Conditions, In Proceedings of the 34th Turbomachinery Symposium, pp.111-120.
- Brown, R. N. (2005), Compressors: Selection and Sizing, Third Edition, Elsevier Inc, USA.
- Byrne, K. & Mariotti, G. (2010), Turboexpander-Compressor Technology for Ethylene Plants, GE Oil and Gas, USA
- Carroll, J. (2014), Natural Gas Hydrates, 3rd Edition, Gulf Professional Publishing
- Casey, M. & Robinson, C. (2013), A Method to Estimate the Performance Map of a Centrifugal Compressor Stage, Journal of Turbomachinery, ASME, 135(2), 021034.

- Casey, M. V. (1994), Computational Methods for Preliminary Design and Geometry Definition in Turbomachinery, In AGARD, Turbomachinery Design Using CFD 22 p (SEE N95-14127 03-34) (Vol. 1).
- Cellai, A., De Lucia, M., Ferrara, G., Ferrari, L., Mengoni, C. P., & Baldassarre, L. (2003), Application of Low Solidity Vaned Diffusers to Prevent Rotating Stall in Centrifugal Compressors: Experimental Investigation, In ASME Turbo Expo 2003, pp. 703-710, American Society of Mechanical Engineers.
- Cellai, A., Ferrara, G., Ferrari, L., Mengoni, C. P., & Baldassarre, L. (2003), Experimental Investigation and Characterization of the Rotating Stall in a High Pressure Centrifugal Compressor: Part III—Influence of Diffuser Geometry on Stall Inception and Performance (2nd Impeller Tested), In ASME Turbo Expo 2003, pp. 711-719, American Society of Mechanical Engineers.
- Chen, H., & Lei, V. M. (2013), Casing Treatment and Inlet Swirl of Centrifugal Compressors, Casing Treatment and Inlet Swirl of Centrifugal Compressors, Journal of Turbomachinery, 135(4),
- Chevron Corporation (2001), Compressor Manual, Centrifugal Compressors.
- Comey, D., Miccio, J., Plamreuter, E. and Waterman, W. (1985), Variable Cyclic Technology Propulsion System Program, Volume I, Variable Geometry Diffuser, Part II- Industry Version, AFWAL-TR-84-2090, Vol. I, Pt. II Wright- Patterson Airforce Base, OH.
- Conrad, O., Raif, K., & Wessels, M. (1980), The Calculation of Performance Maps for Centrifugal Compressors with Vane-Island Diffusers, In ASME Twenty-fifth Annual International Gas Turbine Conference and Twenty-second Annual Engineering Conference on Performance Prediction of Centrifugal Pumps and Compressors, c, pp.135-147.
- Coppage, J. E., Dallenbach, F., Eichenberger, H. P., Hlavaka, G. E., Knoernschild, E. M. and Van Lee, N. (1956), Study of Supersonic Radial Compressors for Refrigeration and Pressurization Systems, AiResearch Mfg. Co. WADC Report 55–257.
- Coppinger, M. (1999), Aerodynamic Performance of an Industrial Centrifugal Compressor Variable Inlet Guide Vane System, Doctoral dissertation, Loughborough University, UK.
- Cumpsty, N. A. (1989), Compressor Aerodynamics, Longman Group, Pearson Education Ltd, Harlow, Essex, UK.
- Daily, J. W., & Nece, R. E. (1960), Chamber Dimension Effects on Induced Flow and Frictional Resistance of Enclosed Rotating Disks, Journal of Fluids Engineering, 82(1), 217-230, ASME.
- De Jager, B. (1995), Rotating Stall and Surge Control: A survey. In Proc. 34th IEEE Conf. on Decision and Control, V.2, 1857–1862, New Orleans, LA, USA.
- Deniz, S., Greitzer, E. M., & Cumpsty, N. A. (2000), Effects of Inlet Flow Field Conditions on the Performance of Centrifugal Compressor Diffusers: Part 2—Straight-Channel Diffuser, In ASME 1998 International Gas Turbine and Aeroengine Congress and Exhibition, Journal of Turbomachinery, ASME, 122(1),pp. 11-21
- Desai, N. B., and Bandyopadhyay, S. (2009), Process Integration of Organic Rankine Cycle, Energy, 34(10), 1674-1686.
- Ding, M., Groth, C., Kacker, S., & Roberts, D. (2006), CFD Analysis of Off-design Centrifugal Compressor Operation and Performance, Conference Paper, Available at: http://resource.ansys.com/staticassets/ANSYS/staticassets/resourcelibrary/confpaper/2006-Int-ANSYS-Conf-252.pdf (Accessed on 02/06/2014)
- Dixon, S. L. (1998), Fluid Mechanics and Thermodynamics of Turbomachinery, Elsevier Butterworth-Heinemann, Inc.
- Duissenov, D. (2013), Production and Processing of Sour Crude and Natural Gas-Challenges Due to Increasing Stringent Regulations, Norwegian University of Science and Technology

- Elder, R. L. & Gill, M. E. (1985), A Discussion Of The Factors Affecting Surge In Centrifugal Compressors, Journal of Engineering for Gas Turbines and Power,107 (2), pp. 499-506, ASME, 84-GT- 194.
- Emmons, H. W., Pearson, C. E., & Grant, H. P. (1955), Compressor Surge and Stall Propagation, ASME, 77 (4), PP. 455-467
- Energy Information Administration, International Energy Statistics, Available at: https://www.eia.gov/cfapps/ipdbproject/iedindex3.cfm?tid=3&pid=26&aid=1&cid=MU,&syid=1980&eyid=2014&unit=BCF (Accessed on: 23/12/2015)
- Engeda, A. (1996), Design Procedures for Low Solidity Vaned Diffusers, Internal Report, Turbomachinery Lab, Michigan State University (Cited in Kim et al., 2002).
- Engeda, A. (2001), The Design and Performance Results of Simple Flat Plate Low Solidity Vaned Diffusers, Proceedings of the Institution of Mechanical Engineers, Part A: Journal of Power and Energy, 215(1), 109-118.
- Engeda, A. (2003), Experimental and Numerical Investigation of the Performance of a 240 kW Centrifugal Compressor with Different Diffusers, Experimental Thermal and Fluid Science, Experimental Thermal and Fluid Science, 28(1), 55-72.
- Fabbrizzi, M., Cerretelli, C., Del Medico, F., & D’Orazio, M. (2009), An Experimental Investigation of A Single Stage Wet Gas Centrifugal Compressor, In ASME Turbo Expo 2009: Power for Land, Sea, and Air, pp. 443-453
- Ferrara, G., Ferrari, L., Mengoni, C. P., De Lucia, M., & Baldassarre, L. (2002), Experimental Investigation and Characterization of the Rotating Stall in a High Pressure Centrifugal Compressor: Part I—Influence of Diffuser Geometry on Stall Inception, In ASME Turbo Expo 2002: Power for Land, Sea, and Air (pp. 613-620).
- Fiaschi, D., Manfrida, G., & Maraschiello, F. (2012), Thermo-Fluid Dynamics Preliminary Design of Turbo-Expanders for ORC Cycles, Applied Energy, 97, 601-608.
- Filho, O. D., Ramalho, E. & Donda, P. A. L. (2012), Hydrate Occurrence in Centrifugal Compressor Systems, 41st Turbomachinery Symposium, Texas, USA
- Filipenco, V. G., Deniz, S., Johnston, J. M., Greitzer, E. M., & Cumpsty, N. A. (2000), Effects of Inlet Flow Field Conditions on the Performance of Centrifugal Compressor Diffusers: Part 1—Discrete-Passage Diffuser, Journal of Turbomachinery, ASME, 122(1),pp. 1-10
- Flathers, M. B. (1997), Design and Retrofit of A Low Solidity Diffuser for A Pipeline Centrifugal Gas Compressor Application, Proceedings of the 26th Turbomachinery Symposium, Houston, Texas.
- Fukushima, Y., Shibata, T., Yagi, M., Murai, Y., & Miura, H. (2009), Solutions for Reduced Life Cycle Costs of Centrifugal Compressors in Oil and Gas Industry, Hitachi Review, 58(1), 7.
- Galerkin, Y., Soldatova, K., & Solovieva, O. (2015), Numerical Study of Centrifugal Compressor Stage Vaneless Diffusers, In IOP Conference Series: Materials Science and Engineering (Vol. 90, No. 1, p. 012048). IOP Publishing.
- Gallick, P., Phillippi, G., & Williams, B. F. (2006), What’s Correct for My Application-A Centrifugal or Reciprocating Compressor?, In Proceedings of the Thirty-Fifth Turbomachinery Symposium, Turbomachinery Laboratory, Texas A&M University, College Station, Texas.
- Gao, L. M., Guang, X., & WANG, S. J. (2002), Influence of Tip Clearance on the Flow Field and Aerodynamic Performance of the Centrifugal Impeller, Chinese Journal of aeronautics, 15(3), 139-144.
- Gas Processors Suppliers Association (2004), Engineering Data Book, 12th edition, in Cooperation with the Gas Processors Association, Section 13: Compressors and Expanders, Tulsa, Oklahoma.
- Ghosh, P. (2002), Analytical and Experimental Studies on Cryogenic Turboexpander, Doctoral dissertation, IIT Kharagpur.

- Ghosh, S. K. (2008), Experimental and Computational Studies on Cryogenic Turboexpander, PhD Thesis, Mechanical Engineering Department, National Institute of Technology, India
- Giampaolo, T. (2014), Gas Turbine Handbook Principles and Practices, 3rd Edition, Digital Designs.
- Girdhar, P. (2008), Performance Evaluation of Compressors and Pumps, Published by Lulu.com
- Golden, S., Fulton, S. A., & Hanson, D. W. (2002), Understanding Centrifugal Compressor Performance in a Connected Process System, Process Consulting Services Inc., Texas, USA.
- Goodwin, A. R., & Sengers, J. (2010), Applied Thermodynamics of Fluids, Royal Society of Chemistry, 1st Edition.
- Gorla, R. S., & Khan, A. A. (2003), Turbomachinery: Design and Theory, 1th edition, Marcel Dekker, Inc, New York, USA.
- Greitzer, E. M. (1981), The Stability of Pumping Systems—the 1980 Freeman Scholar Lecture, Journal of Fluids Engineering, 103(2), 193-242.
- Gresh, T. (2001), Compressor Performance: Aerodynamics for the User, 2nd edition, pp.22-80, Butterworth-Heinemann, Woburn.
- Hagelstein, D., Van den Braembussche, R., Keiper, R., & Rautenberg, M. (1997), Experimental Investigation of the Circumferential Static Pressure Distortion in Centrifugal Compressor Stages, In ASME 1997 International Gas Turbine and Aeroengine Congress and Exhibition, ASME Paper No. 97-GT-50.
- Hanlon, P. C. (2001), Compressor Handbook, McGraw-Hill, New York.
- Hansen, C. (2008), Dynamic Simulation of Compressor Control Systems, Final Thesis for the degree of M.Sc. in Oil & Gas Technology, Aalborg University Esbjerg
- Harada, H. (1985), Performance Characteristics of Shrouded and Unshrouded Impellers of A Centrifugal Compressor, Journal of engineering for gas turbines and power, 107(2), 528-533.
- Harada, H. (1996), Study of Surge-Free Centrifugal Compressor With Automatically Variable Inlet and Diffuser Vanes, In ASME 1996 International Gas Turbine and Aeroengine Congress and Exhibition, No.96-GT-153.
- Hartel, C., & Pfeiffer, P. (2003), Model Analysis of High-Fogging Effects on the work of Compression, In ASME Turbo Expo 2003, pp. 689-698, ASME, Gt-2003-38117.8.
- Haupt, U., Seidel, U., Abdel-Hamid, A. N., & Rautenberg, M. (1988), Unsteady Flow in a Centrifugal Compressor with Different Types of Vaned Diffusers, Journal of turbomachinery, 110(3), pp. 293-302.
- Helvoirt, J. (2007), Centrifugal Compressor Surge Modeling and Identification for Control, Eindhoven University of Technology.
- Herbert, M. V. (1980), A Method of Performance Prediction for Centrifugal Compressors, HM Stationery Office, Aeronautical and Research Council, London, UK
- Higashio, A., Yamashita, H., & Ota, M. (2010), Dynamic Stress Measurement of Centrifugal Compressor Impeller and Study for Strength Criteria Based on Correlation by Unsteady CFD, In Proceedings of the Thirty-ninth Turbomachinery Symposium.
- Hohlweg, W. C., Direnzi, G. L., & Aungier, R. H. (1993), Comparison of Conventional and Low Solidity Vaned Diffusers. In ASME 1993 International Gas Turbine and Aeroengine Congress and Exposition, ASME, In 93-GT-98.
- Holloway, M. D., Nwaoha, C., & Onyewuenyi, O. A. (2012), Process Plant Equipment: Operation, Control, and Reliability, John Wiley & Sons, Inc., Hoboken, Canada
- Howell, A. R., & Calvert, W. J. (1978), A New Stage Stacking Technique for Axial-Flow Compressor Performance Prediction, Journal of Engineering for Gas Turbines and Power, 100(4), 698-703.

- Hundseid, O., Bakken, L. E., Grüner, T. G., Brenne, L., & Bjørge, T. (2008), Wet Gas Performance of a Single Stage Centrifugal Compressor, In ASME Turbo Expo 2008: Power for Land, Sea, and Air, pp. 661-670. ASME, GT-2008-51156.
- Huntington, R. A. (1985), Evaluation of Polytropic Calculation Methods for Turbomachinery Performance, Journal of Engineering for gas Turbines and Power, 107(4), 872-876.
- International Organization for Standardization (1992), Turbocompressors – Performance Test code.
- Issac, J. M., Sitaram, N., & Govardhan, M. (2004), Effect of Diffuser Vane Height and Position on the Performance of a Centrifugal Compressor, Proceedings of the Institution of Mechanical Engineers, Part A: Journal of Power and Energy, 218(8), pp.647-654.
- Jaatinen, A., Grönman, A., Turunen-Saaresti, T., & Röyttä, P. (2011), Effect of Vaneless Diffuser Width on the Overall Performance of a Centrifugal Compressor, Proceedings of the Institution of Mechanical Engineers, Part A: Journal of Power and Energy, 225(5), 665-673.
- Jaatinen-Värri, A., Röyttä, P., Turunen-Saaresti, T., & Grönman, A. (2013). Experimental Study of Centrifugal Compressor Vaneless Diffuser Width, Journal of Mechanical Science and Technology, 27(4), 1011-1020.
- Jack, T. K., & Elder, R. L. (2012), A Modified Stage-Stacking Method for Multi-Stage Axial Flow Compressor Calculations, International Journal of Scientific and Engineering Research, vol.3, pp.538-544
- Jansen, W. (1964), Rotating Stall in Radial Vaneless Diffuser, Journal of Fluids Engineering, ASME, 86 (4), pp.750-498.
- Jansen, W. (1967), A Method for Calculating the Flow in a Centrifugal Impeller When Entropy Gradients are Present, In Royal Society conference on internal aerodynamics (turbomachinery), pp.133-146
- Jansen, W., Carter, A. F., & Swarden, M. C. (1980), Improvements In Surge Margin For Centrifugal Compressors, AGARD Centrifugal Compressors, Flow Phenomena and Performance.
- Ji, C., Wang, Y., & Yao, L. (2007), Numerical Analysis and Optimization of the Volute in a Centrifugal Compressor, International Conference on Power Engineering, October 23-27, Hangzhou, (pp. 1352-1356), China.
- Jin, D., Haupt, U., Hasemann, H., & Rautenberg, M. (1992), Excitation of Blade Vibration Due to Surge of Centrifugal Compressors, In ASME 1992 International Gas Turbine and Aeroengine Congress and Exposition, Germany, ASME, No. 92-GT-139
- Jumonville, J. (2004), Tutorial on Cryogenic Turboexpanders, Proceedings of the Thirty-Third Turbomachinery Symposium, pp. 127-133, California.
- Kalinkevych, M., & Shcherbakov, O. (2013), Numerical Modeling of the Flow in a Vaneless Diffuser of Centrifugal Compressor Stage, Technical Thermophysics Department, Sumy State University, Article ID: 602384.
- Kalinkevych, M., & Skoryk, A. (2013), Design Method for Channel Diffusers of Centrifugal Compressors. International Journal of Rotating Machinery, Hindawi Publishing Corporation.
- Kalinkevych, M., Obukhov, O., Smirnov, A., and Skoryk, A., (2011), The Design of Vaned Diffusers of Centrifugal Compressors Based on the Given Velocity Distribution, in Proceedings of the 7th International Journal of Rotating Machinery, International Conference on Compressors and their Systems, pp. 61–69.
- Kammer, N. & Rautenberger, M. (1986), A Distinction Between Different Types of Stall in a Centrifugal Compressor Stage, Journal of Engineering for Gas Turbines and Power, 108(1), 83-92.
- Kerry, F. G. (2007), Industrial Gas Handbook: Gas Separation and Purification, 1th Edition, Taylor & Francis Group LLC, CRC Press.

- Kidnay, A. J., Parrish, W. R., & McCartney, D. G. (2011), Fundamentals of Natural Gas Processing (Vol. 218), Second Edition, CRC Press.
- Kim, Y., Engeda, A., Aungier, R., & Amineni, N. (2002), A Centrifugal Compressor Stage with Wide Flow Range Vaned Diffusers and Different Inlet Configurations, Proceedings of the Institution of Mechanical Engineers, Part A: Journal of Power and Energy, 216(4), 307-320.
- Kong, C., Ki, J., & Kang, M. (2002), A New Scaling Method for Component Maps of Gas Turbine using System Identification, Journal of Engineering for Gas turbines and Power, 125(4), 979-985.
- Koumoutsos, A., Tourlidakis, A., & Elder, R. L. (2000), Computational Studies of Unsteady Flows in a Centrifugal Compressor Stage, Proceedings of the Institution of Mechanical Engineers, Part A: Journal of Power and Energy, 214(6), 611-633.
- Kurz, R., Marechale, R. K., Fowler, E. J., Ji, M. & Cave, M. J. (2011), Operation of Centrifugal Compressors in Choke Conditions, Proceedings of the Fortieth Turbomachinery Symposium, Houston, Texas.
- Kurzke, J., & Riegler, C. (2000), A New Compressor Map Scaling Procedure for Preliminary Conceptual Design of Gas Turbines, In Proceedings of the ASME Turbo Expo 2000: Power for Land, Sea, and Air, Munich, Germany, 8–11 May 2000.
- Lapina, R. P. (1982), Estimating Centrifugal Compressor Performance, Gulf Publishing Company, New York, USA.
- Le Sausse, P., Fabrie, P., Arnou, D., & Clunet, F. (2013), CFD comparison with Centrifugal Compressor Measurements on a wide Operating Range, Johnson Controls Industries, In EPJ Web of Conferences, vol. 45, p. 01059.
- Li, J., Yin, Y., Li, S., & Zhang, J. (2013), Numerical Simulation Investigation on Centrifugal Compressor Performance of Turbocharger, Journal of Mechanical Science and Technology, 27(6), 1597-1601.
- Linder, P. (1983), Aerodynamic Tests on Centrifugal Compressors: Influence of Diffuser Diameter Ratio, Axial Stage Pitch and Impeller Cutback, ASME, Journals of Eng. For Power, 105 (4), pp. 910-919.
- Ling, K. (2010), Gas Viscosity At High Pressure and High Temperature, PhD Thesis, Texas A & M University
- Ljevar, S. (2007), Rotating Stall in Wide Vaneless Diffusers, Ph.D. thesis, Technische University, Eindhoven, The Netherlands.
- Ljevar, S. S., Lange, D. H., & Steenhoven, V. A. (2005), Rotating Stall in A Two-Dimensional Vaneless Diffuser Flow, Energy Technology Section, Department of Mechanical Engineering Eindhoven University of Technology, Eindhoven.
- Lüdtke, K. (1983), Aerodynamic Tests on Centrifugal Process Compressors: The Influence of the Vaneless Diffusor, Journal of engineering for power, 105 (4), pp. 902-909.
- Lüdtke, K. H. (2004), Process Centrifugal Compressors, Basics, Function, Operation, Design, Application, Springer-Verlag, 1st Edition, Berlin, Germany.
- Ma, Y., Fretheim, H., Persson, E., & Haugen, T. (2013), An Iterative Method Applied to Correct the Actual Compressor Performance to the Equivalent Performance under the Specified Reference Conditions, Department of Product and Technology for Oil, Division of Process Automation.
- Macdougal, I., & Elder, R. L. (1982), The Improvement of Operating Range in A Small High Speed Centrifugal Compressor using Casing Treatment, IMechE Conference, C32/82.
- Mallen, M. & Saville, G. (1977), Polytropic Processes in the Performance Prediction of Centrifugal Compressors, Institution of Mechanical Engineers, London, UK, pp. 89–96.

- Man Turbo (2009), Engineering the Future – Since 1758, Available at: http://www.mandieselturbo.com/files/news/filesof587/Gesch%C3%A4ftsbericht%20MAN%20Diesel%202009.pdf (Accessed on 14/01/2016).
- Maskell, E. C. (1955), Flow Separation in Three Dimensions, Ministry of Supply, Royal Aircraft Establishment, RAE Farnborough, England
- Mechanical Engineering in Process Equipment (2009), Centrifugal Compressor Basic Manual, Available at: http://jensapardi.files.wordpress.com/2009/12/centrifugal_compressor_manual1.pdf (Excessed on 27/12/2014).
- Meher-Homji, C. B., Focke, A. B., & Wooldridge, M. B. (1989), Fouling of Axial Flow Compressors- Causes, Effects, Detection and Control, In proceedings of the 18th Turbomachinery Symposium, pp.55-76, Texas.
- Mehra, Y. R., & Gaskin, T. K. (1999), Guidelines Offered for Choosing Cryogenics Or Absorption for Gas Processing, Oil & gas journal, 97(9).
- Miwa, J., Dou, C. H., Sawai, K., Namura, M., & Toriyama, T. (2009), Aerodynamic Consideration on Impeller, Diffuser and Volute for MEMS Centrifugal Compressor. Power MEMS 1-4.
- Mohtar, H., Chesse, P., Chalet, D., Hetet, J. F., & Yammine, A. (2011), Effect of Diffuser and Volute on Turbocharger Centrifugal Compressor Stability and Performance: Experimental Study, Oil & Gas Science and Technology–Revue d'IFP Energies Nouvelles, 66(5), 779-790.
- Motiee, M. (1991), Estimate Possibility of Hydrates, Hydrocarbon Processing, Vol. 70, No. 7, pp. 98-99
- Mund, F. C., & Pilidis, P. (2006), Gas Turbine Compressor Washing: Historical Developments, Trends and Main Design Parameters for Online Systems, Journal of engineering for gas turbines and power, 128(2), 344-353.
- Narayanan, K. V. (2011), A Textbook of Chemical Engineering Thermodynamics, Fifth edition, PHI Learning Prive Limited, New Delhi.
- Natural Gas STAR Partners (2006), Replacing Wet Seals with Dry Seals in Centrifugal Compressors, Washington, US, Available at: http://www3.epa.gov/gasstar/documents/ll_wetseals.pdf (Accessed on: 14/01/2016).
- Nelson, E. B., Paduano, J. D., & Epstein, A. H. (2000), Active Stabilization of Surge in an Axicentrifugal Turboshaft Engine, ASME J. Turbomachinery., 122, pp. 485–493.
- Niazi, S., Stein, A., & Sankar, L. N. (1998), Development and Application of a CFD Solver to the Simulation of Centrifugal Compressors, Washington, D.C, AIAA Paper 98-0934.
- Oakes, W. C., Lawless, P. B., & Fleeter, S. (1998), High-speed Centrifugal Compressor Instabilities During Speed Transients, Washington, AIAA-98/3307.
- Oh, H. W., Yoon, E. S., & Chung, M. K. (1997), An Optimum Set of Loss Models for Performance Prediction of Centrifugal Compressors, Proceedings of the Institution of Mechanical Engineers, Part A: Journal of Power and Energy, 211(4), 331-338.
- Okhuahesogie, O. F., Stewart, J., Heyes, F. J. G. & Roach, P.E. (2012), Design Optimization of Two-Stage Turbocharger Compressor Impeller, KTP Associates Conference.
- Osborne, C. & Sorokes, J. (1988), The Application of Low Solidity Diffusers in Centrifugal Compressor Flow in Non-Rotating Turbomachinery Component, Vol. 69, ASME, New York, pp. 89–101.
- Paduano, J. D., Greitzer, E. M., & Epstein, A. H. (2001), Compression System Stability and Active Control, Annual review of fluid mechanics, 33(1), 491-517.
- Pampreeen, R. C. (1993), Compressor Surge and Stall, First Edition, Norwich, Vermont: Concepts ETI
- Peng, D. Y., & Robinson, D. B. (1975), A New Two-Constant Equation of State, 15(1), 59-64.

- Petrofac (2009), Turbo-Expander & Re-Compressor Handout.
- Prasad, V. V., Kumar, M. L., & Reddy, B. M. (2011), Centrifugal Compressor Fluid Flow Analysis Using CFD, Science Insights: An International Journal, 1(1), 6-10.
- Rasmussen, P. C., & Kurz, R. (2009), Centrifugal Compressor Applications-Upstream and Midstream, In proceedings of the Thirty-Eight Turbomachinery Symposium, Houston, Texas, pp.169-186.
- Raw, J. (1986), Surge Margin Enhancement by A Porous Throat Diffuser, Canadian Aeronautics and Space Journal, 32(1), 54-61.
- Reddy, T. C. S., Murty, G. R., Mukkavilli, P., & Reddy, D. N. (2004), Effect of Settling Angle of a Low-Solidity Vaned Diffuser on the Performance of a Centrifugal Compressor Stage, Proceedings of the Institution of Mechanical Engineers, Part A: Journal of Power and Energy, 218(8), 637-646.
- Redlich, O., & Kwong, J. N. (1949), On the Thermodynamics of Solutions. V. An Equation of State. Fugacities of Gaseous Solutions. Chemical reviews, 44(1), 233-244.
- Rodgers, C. (1964), Typical Performance Characteristics of Gas Turbine Radial Compressors, ASME J. Eng. Power, 86, pp. 161–175.
- Rodgers, C. (1978), A Diffusion Factor Correlation for Centrifugal Impeller Stalling, Journal of Engineering for Gas Turbines and Power, 100(4), 592-601.
- Rodgers, C., & Langworthy, R. A. (1974), Design and Test of a Small Two Stage High Pressure Ratio Centrifugal Compressor, ASME, 74-GT-137.
- Rojey, A., & Jaffret, C. (1997), Natural Gas: Production, Processing and Transport, Paris: Editions Technip, USA
- Sable, M. J. and Ramgir, M. S. (2006), Gas Turbines & Jet Propulsion, 1st Edition, Technical Publications Pune, India.
- Salamat, R. (2012), Gas Path Diagnostics for Compressors, PhD Thesis, Cranfield University, UK.
- Sandberg, M. R. & Colby, G.M. (2013), Limitations of ASME PTC 10 in Accurately Evaluating Centrifugal Compressor Thermodynamic Performance, In Proceedings of the Forty-Second Turbomachinery Symposium, Houston, TX, USA.
- Santinelli, P. (2006), Centrifugal Compressor: Performances Simulation for Natural Gas Processing in the Oil and Gas Industry. Master's Thesis, Cranfield University, Bedford, UK.
- Savidge, J. L. (2000), Compressibility of Natural Gas, 78th Int. School for Hydrocarbon Measurement (Class 1040). CEESI.
- Schultz, J. M. (1962), The Polytropic Analysis of Centrifugal Compressors, Journal of Engineering for Gas Turbines and Power, 84(1), 69-82.
- Senoo, Y., & Ishida, M. (1986), Pressure Loss Due to the Tip Clearance of Impeller Blades in Centrifugal and Axial Blowers, Journal of Engineering for Gas Turbines and Power, 108(1), 32-37.
- Serovy, G. K. (1976), Compressor and Turbine Performance Prediction System Development- Lessons from Thirty Years of History, AGARD Lecture Series No. 83, pp 5-1 to 5-27
- Shell (2011), DEP 31.29.40.10; Compressors – Selection, Testing and Installation. Netherland, Available at: https://www.shelldeps.com (Accessed on 12/11/2013).
- Shell International Petroleum (1991), Facilities and Maintenance Production Handbook Volume 9, Maatschappij Hague, Netherland.
- Shepherd, D. G. (1956), Principles of Turbomachinery, Macmillan Co.
- Siemens (2016), Single Shaft Horizontal Split Turbocompressors, Available at: http://www.energy.siemens.com/mx/en/compression-expansion/product-lines/single-shaft-horizontal-split/stc-sh.htm (Accessed on 19/04/2016).
- Simmons, P., Nesbitt, B., & Searle, D. (2003), Guide to European Compressors and Their Applications: the Complete Practical Reference Guide to Compressors Design, Operation and Applications, vol. 2, Professional Engineering Publishing, London.

- Simms, J. (2009), Fundamentals of Turboexpanders: Basic Theory and Design, SIMMS Machinery International, INC., USA.
- Simon, H., Wallmann, T., & Monk, T. (1987), Improvements in Performance Characteristics of Single Stage and Multistage Centrifugal Compressors by Simultaneous Adjustments of Inlet Guide Vanes and Diffuser Vanes, Journal of turbomachinery, 109(1), 41-47.
- Sinnott, R.K. (2005), Coulson and Richardson's Chemical Engineering Volume 6 - Chemical Engineering Design, 4th Edition, Elsevier.
- Sishtla, V. (1996), Performance of Centrifugal Compressors with Variable Vaned Diffuser, International Compressor Engineering Conference, Purdue University
- Sitaram, N., & Swamy, S. M. (2012), Performance Improvement of a Centrifugal Compressor by Passive Means, International Journal of Rotating Machinery.
- Sixsmith, H. (1984), Miniature Cryogenic Expansion Turbines—A Review. In Advances in Cryogenic Engineering, pp.511-523, Springer US.
- Skoch, G. J. (2003), Experimental Investigation of Centrifugal Compressor Stabilization Techniques. In ASME Turbo Expo 2003, pp. 765-776, ASME.
- Sloan, E. D. (1998), Clathrates Hydrates of Natural Gas, 2nd edition, New York: Marcel Dekker Inc., p. 757.
- Soave, G. (1972), Equilibrium Constants from a Modified Redkh-Kwong Equation of State, Chemical Engineering Science, 27(6), pp. 1197-1203.
- Sood, V. K. (1979), Design and Full Load Testing of a High Pressure Centrifugal Natural Gas Injection Compressor, In Proceeding of Eighth Turbomachinery Symposium, pp. 35-42.
- Sorokes, J. M. (2013), Selecting A Centrifugal Compressor, Chemical Engineering Progress, AIChE and Dresser- Rand, 109(6), 44-51.
- Sorokes, J. M., & Kuzdzal, M. J. (2010). Centrifugal Compressor Evolution, In Turbomachinery Symposium Proceedings, Texas A&M.
- Sorokes, J. M., & Welch, J. P. (1992), Experimental Results on a Rotatable Low Solidity Vaned Diffuser, In ASME 1992 International Gas Turbine and Aeroengine Congress and Exposition, ASME, 92-GT-19.
- Sorokes, J. M., Miller, H. F., & Koch, J. M. (2006), The Consequences of Compressor Operation in Overload. In Proceedings of the 35th Turbomachinery Symposium, Turbomachinery Laboratory, Texas A&M University, College Station.
- Stanitz, J. D. (1952), Some Theoretical Aerodynamic Investigations of Impellers in Radial and Mixed-Flow Centrifugal Compressors, ASME, vol.74, pp.473- 476.
- Stebbins, W. L. (1994), Are You Certain You Understand The Economics For Applying ASD Systems to Centrifugal Loads?, In Textile, Fiber and Film Industry Technical Conference, 1994, IEEE 1994 Annual (pp. 1-8). IEEE.
- Stein, A., Niazi, S., & Sankar, L. N. (2000), Numerical Analysis of Stall and Surge in a High-Speed Centrifugal Compressor, In 38th Aerospace Sciences Meeting and Exhibit (pp. 2000-0226).
- Steinke, R. J. (1982), A Computer Code for Predicting Multistage Axial-Flow Compressor Performance by A Meanline Stage-Stacking Method, NASA-TP2020
- Strub, R. A., L. Bonciani, C. J. Borer, M. V. Casey, S. L. Cole, B. B. Cook, J. Kotzur, H. Simon, and M. A. Strite (1987), Influence of Reynolds Number on the Performance of Centrifugal Compressors, Final Report, ICAAMC, Journal of Turbomachinery, 109 (4), pp. 541-544.
- Svensson, M. (2014), Wet Gas Compression Effect of a Liquid Phase on Radial Compressor Performance, Master Thesis, Lund University, Sweden
- Swain, E. (1990), A Simple Method for Predicting Centrifugal Compressor Performance Characteristics, Proceedings of IMechE Conference, C405/040.

- Swain, E. (2005), Improving a One-Dimensional Centrifugal Compressor Performance Prediction Method, Proceedings of the Institution of Mechanical Engineers, Part A: Journal of Power and Energy, 219(8), 653-659.
- Tang, J., Turunen-Saaresti, T., & Larjola, J. (2008), Use of Partially Shrouded Impeller in A Small Centrifugal Compressor, Journal of Thermal Science, 17(1), 21-27.
- Taylor, B. (2009), RBI Centrifugal Compressors presentation, API Spring Refining meeting, Dresser-Rand, Denver, USA.
- Towler, B. F., & Mokhatab, S. (2005), Quickly Estimate Hydrate Formation Conditions in Natural Gases, Hydrocarbons Processing, 84(4), 61–62.
- Tsujimoto, Y., Yoshida, Y., & Mori, Y. (1996), Study of Vaneless Diffuser Rotating Stall Based on Two-Dimensional Inviscid Flow Analysis, Journal of fluids engineering, 118(1), 123-127.
- Turunen-Saaresti, T., Grönman, A. P., & Jaatinen, A. (2009), Experimental Study of Pinch in Vaneless Diffuser of Centrifugal Compressor, In ASME Turbo Expo 2009: Power for Land, Sea, and Air, pp.1427-1438, ASME.
- U.S. Energy Development Corporation (2013), Natural Gas: Dry vs. Wet, Mining Weekly Online. Feb. 2013, NewYork, Available at: http://www.usenergydevcorp.com/media_downloads/Natural%20Gas%20Dry%20Vs%20Wet_050913.pdf (Accessed on 26/12/2015)
- Uchida, H., Kashimoto, A., & Iwakiri, Y. (2006), Development of Wide Flow Range Compressor with Variable Inlet Guide Vane, Turbocharging Technologies, R &D Review of Toyota CRDL Vol.41, No.3, China.
- Van den Braembussche, R. A., Ayder, E., Hagelstein, D., Rautenberg, M., & Keiper, R. (1998), Improved Model for the Design and Analysis of Centrifugal Compressor Volutes, In ASME 1998 International Gas Turbine and Aeroengine Congress and Exhibition, 121(3), pp. 619-625, ASME/98-GT-187.
- Von Backström, T. W. (2006), A Unified Correlation for Slip Factor in Centrifugal Impellers, Journal of Turbomachinery, ASME, 128 (1), pp. 1-10.
- Von Backström, T. W. (2007), Relative-eddy Induced Slip in Centrifugal Impellers for Engineering Students, R & D Journal, 23(1).
- Walitt, L., Nguyen, C., & Nyquist, R. (1997), Unsteady Analysis and Re-Design of A Centrifugal Compressor Stage Using a CFD Optimizer, Washington, AIAA-97/3024
- Wang, Y., Lin, F., Nie, C., & Engeda, A. (2013), Design and Performance Evaluation of a Very Low Flow Coefficient Centrifugal Compressor, Hindawi Publishing Corporation International Journal of Rotating Machinery, Article ID 293486,
- Wharton, P. (2013), Compressor Design; Pumps and Compressor Selection, Cranfield University, Lecture Notes, UK.
- Whitfield, A. (1992), Conceptual Design of a Centrifugal Compressor Including Consideration of the Effect of Inlet Prewhirl, In ASME 1992 International Gas Turbine and Aeroengine Congress and Exposition, ASME Paper No. 92-GT-11.
- Whitfield, A. (2000), Review of Variable Geometry Techniques Applied to Enhance the Performance of Centrifugal Compressors, International Compressor Engineering Conference, Purdue University, Paper 1368.
- Whitfield, A., & Abdullah, A. H. (1994), The Potential of Variable Geometry Techniques for Broad Operating Range Centrifugal Compressors, Proc. IMECHE Euro Conf Developments in Industrial Compressors and their Systems, C477/006/94, IMECHE (ISBN 0 85298 904 0), Vol. 2, pp. 133-44.
- Whitfield, A., & Sutton, A. J. (1989), The Effect of Vaneless Diffuser Geometry on the Surge Margin of Turbocharger Compressors, IMechE, 203(2), 91-98.
- Whitfield, A., Wallace, F. J., & Atkey, R. C. (1976), The Effect of Variable Geometry on the Operating Range and Surge Margin of a Centrifugal Compressors, In International Gas Turbine and Fluids Engineering Conference, ASME, 76-GT-98

- Wiesner, F. J. (1967), A Review of Slip Factors for Centrifugal Impellers, Trans. ASME: J. Eng. Gas Turbines Power, 89 (4), pp. 558–566.
- Wu, G. (2010), Flow and Performance of Vaned Diffuser and its Impact on A Centrifugal Compressor, MSc Thesis, Cranfield University, England
- Xiao, J., Gu, C., Shu, X., & Gao, C. (2007), Performance Analysis of A Centrifugal Compressor with Variable Inlet Guide Vanes, Frontiers of Energy and Power Engineering in China, 1(4), 473-476.
- Xu, C., & Amano, R. S. (2012), Empirical Design Considerations for Industrial Centrifugal Compressors, International Journal of Rotating Machinery.
- Xu, W., Wang, T., & Gu, C. (2011), Performance of a Centrifugal Compressor with Holed Casing Treatment in the Large Flowrate Condition, Science China Technological Sciences, 54(9), 2483-2492.
- Yoshinaga, Y., Gyobu, I., Mishina, H., Koseki, F., & Nishida, H. (1980), Aerodynamic Performance of A Centrifugal Compressor with Vaned Diffusers, Journal of Fluids Engineering, 102(4), 486-493
- Yoshinaga, Y., Kaneki, T., Kobayashi, H., & Hoshino, M. (1987), A study of Performance Improvement for High Specific Speed Centrifugal Compressors by Using Diffusers with Half Guide Vanes, Journal of fluids engineering, 109(4), 359-366.
- Zemp, A. (2007), CFD Investigation on Inlet Flow Distortion in a Centrifugal Compressor, Swiss Federal Institute of Technology, ETH, Zurich Turbomachinery Laboratory, Master Thesis, Switzerland
- Zheng, Q., Sun, Y., Li, S., & Wang, Y. (2002), Thermodynamic Analysis of Wet Compression Process in the Compressor of a Gas Turbine, In ASME Turbo Expo 2002: Power for Land, Sea, and Air, pp. 487-496, ASME.
- Zheng, X. Q., Huenteler, J., Yang, M. Y., Zhang, Y. J., & Bamba, T. (2010), Influence of the Volute on the Flow in A Centrifugal Compressor of A High-Pressure Ratio Turbocharger, Institution of Mechanical Engineers, Part A: Journal of Power and Energy, 224(8), 1157-1169.
- Zohrabian, A. (2010), Offshore Department, Qatar Petroleum, Qatar.

Appendices

Appendix A : **List of Author Publications**

❖ Published Journals from the Thesis

1. Al-Busaidi, W., & Pilidis, P. (2016), A New Method for Reliable Performance Prediction of Multi-Stage Industrial Centrifugal Compressors Based on Stage Stacking Technique: Part I–Existing Models Evaluation, Applied Thermal Engineering, Elsevier, 98(1), pp 10–28.
2. Al-Busaidi, W., & Pilidis, P. (2015), A New Method for Reliable Performance Prediction of Multi-Stage Industrial Centrifugal Compressors Based on Stage Stacking Technique: Part II–New Integrated Model Verification, Applied Thermal Engineering, Elsevier, 90(1), pp 927-936.
3. Al-Busaidi, W., & Pilidis, P. (2015), An Iterative Method to Derive the Equivalent Centrifugal Compressor Performance at Various Operating Conditions: Part I: Modelling of Suction Parameters Impact, Energies, 8(8), pp 8497-8515.
4. Al-Busaidi, W., & Pilidis, P. (2015), An Iterative Method to Derive the Equivalent Centrifugal Compressor Performance at Various Operating Conditions: Part II: Modeling of Gas Properties Impact, Energies, 8(8), pp 8516-8536.
5. Al-Busaidi, W., & Pilidis, P. (2015), Review of Efficiency and Stable Operating Range Enhancements Options of Centrifugal Compressors, Journal of Applied Mechanical Engineering, 4(5), pp 1-12.
6. Al-Busaidi, W., & Pilidis, P. (2016), Modelling of the Non-Reactive Deposits Impact on Centrifugal Compressor Aerothermo Dynamic Performance, Engineering Failure Analysis, Elsevier, 60(1), pp 57-85.
7. Al-Busaidi, W., & Pilidis, P. (2016), Investigation of Efficiency Deterioration Causes in Process Centrifugal Compressor Operation, Journal of Failure Analysis and Prevention, Springer, 16(1), pp 19-36.
8. Al-Busaidi, W., & Pilidis, P. (2016), Modeling of Partially Shrouded Impellers' Effect on Operating Efficiency and Flow Range of Centrifugal Compressor, Journal of Energy Engineering, Accepted Article in Press
9. Al-Busaidi, W., & Pilidis, P. (2016), Techno-Economic Optimization of Diffuser Configuration Effect on Centrifugal Compressor Performance, American Journal of Energy Research, 3(2), 37-48.

Conference Papers from the Thesis

1. Al-Busaidi, W., & Pilidis, P. (2016), Empirical Approach to Model the Operating Conditions Impact on the Performance Characteristics of Process Centrifugal Compressor. In 18th International Conference on Turbomachinery and Fluid Dynamics. World Academy of Science, Engineering and Technology, International Journal of Mechanical and Mechatronics Engineering 3(2), Paris, Accepted Paper.

Other Publications

1. Al-Busaidi, W., & Pilidis, P. (2015), An Approach to Evaluate the Heat Exchanger Retrofit for Installed Gas Turbines: Part I- Technical Evaluation, International Journal of Research in Engineering & Technology, 4(9), pp 1-12.
2. Al-Busaidi, W., & Pilidis, P. (2015), An Approach to Evaluate the Heat Exchanger Retrofit for Installed Gas Turbines: Part II- Economic Evaluation, International Journal of Research in Engineering & Technology, 4(8), pp 392-399.
3. Al-Busaidi, W., & Pilidis, P. (2016, June), A Method to Evaluate the Heat Exchanger Retrofit for Industrial Gas Turbines Based on Technical and Economic Perspective. In ASME Turbo Expo 2016: Turbine Technical Conference and Exposition. American Society of Mechanical Engineers, Seoul**,** Accepted Paper.

Appendix B : Developed Approaches for Centrifugal Compressor Selection and Sizing

B1. Compressor Type Selection - Process Requirements Evaluation (Sub-Model A1)

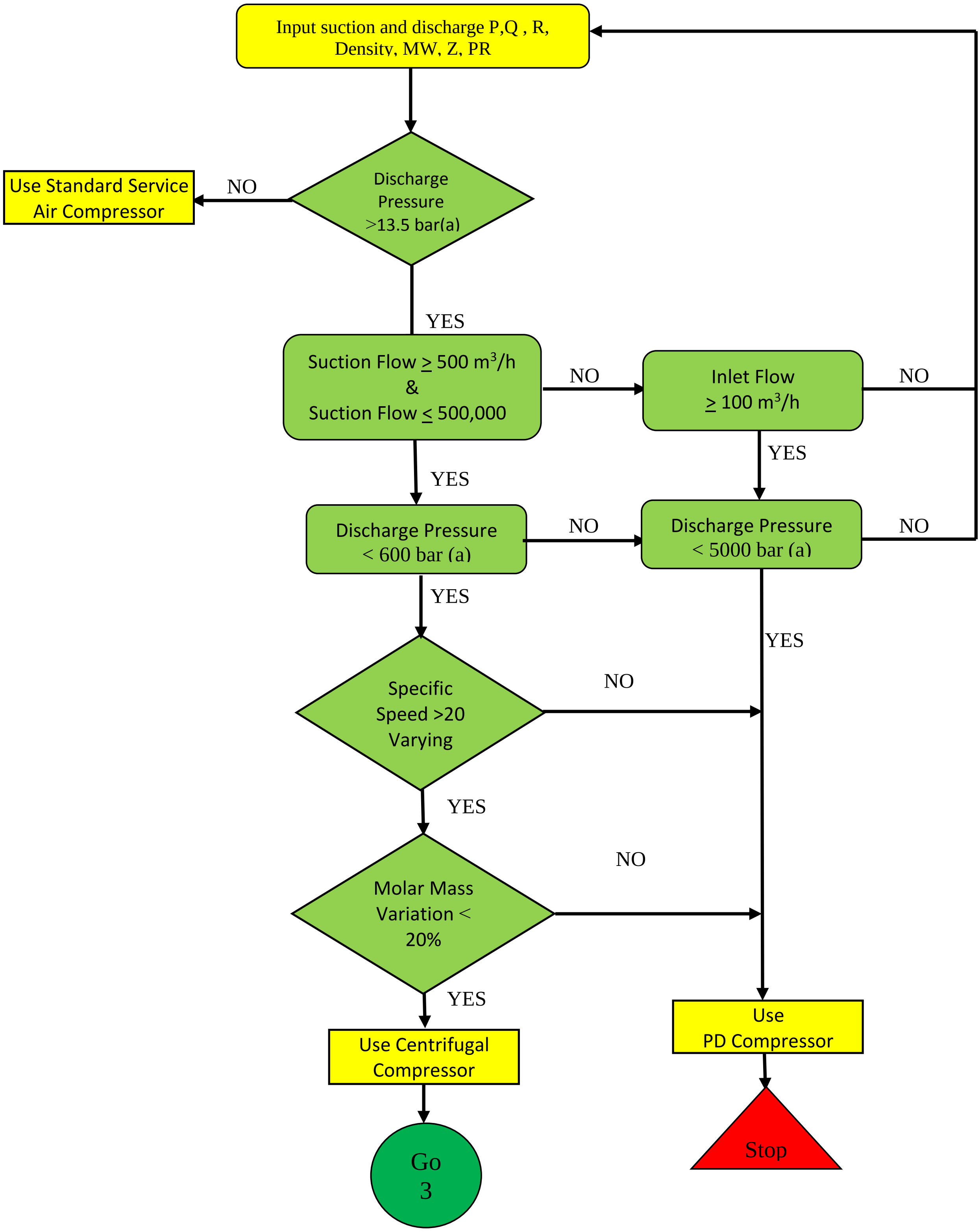

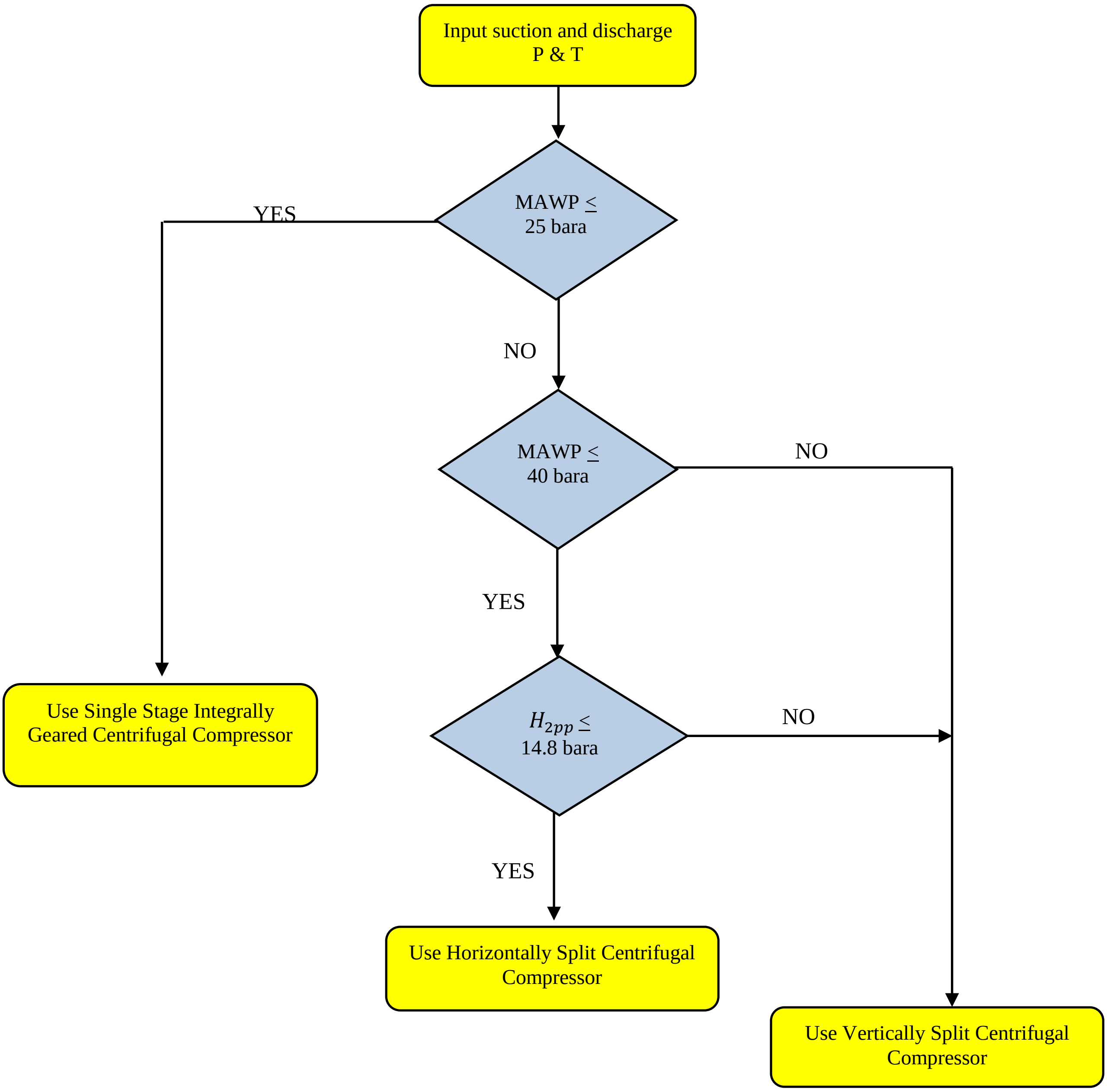

B2. Selection of Casing Structure for Centrifugal Compressor (Sub-Model B)

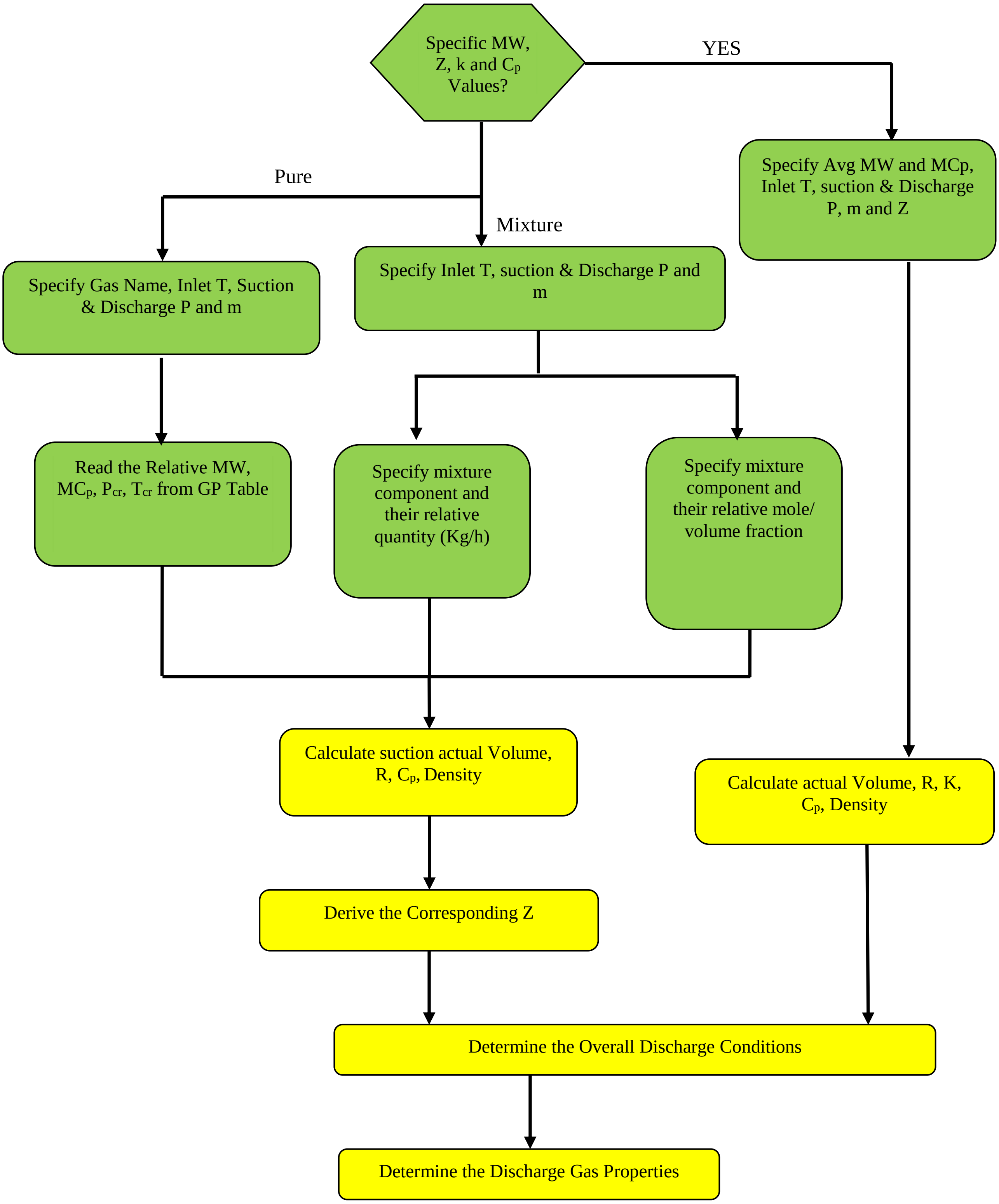

B3. Algorithm of Determination of Suction and Discharge Gas Properties (Sub Model C)

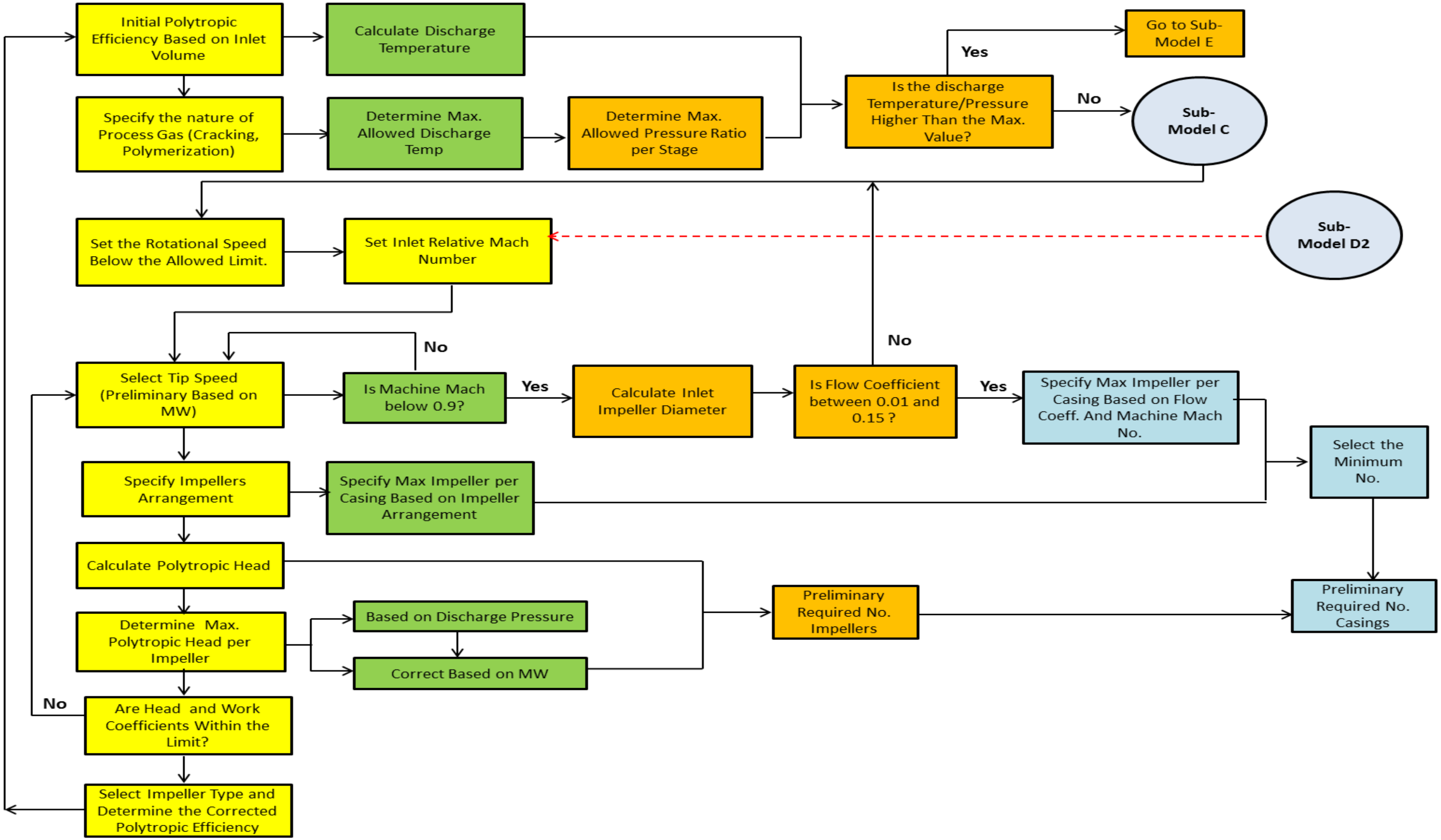

B4. Sizing and Aerodynamic Modelling Approach of Single Stage Centrifugal Compressor (Sub-Model D1)

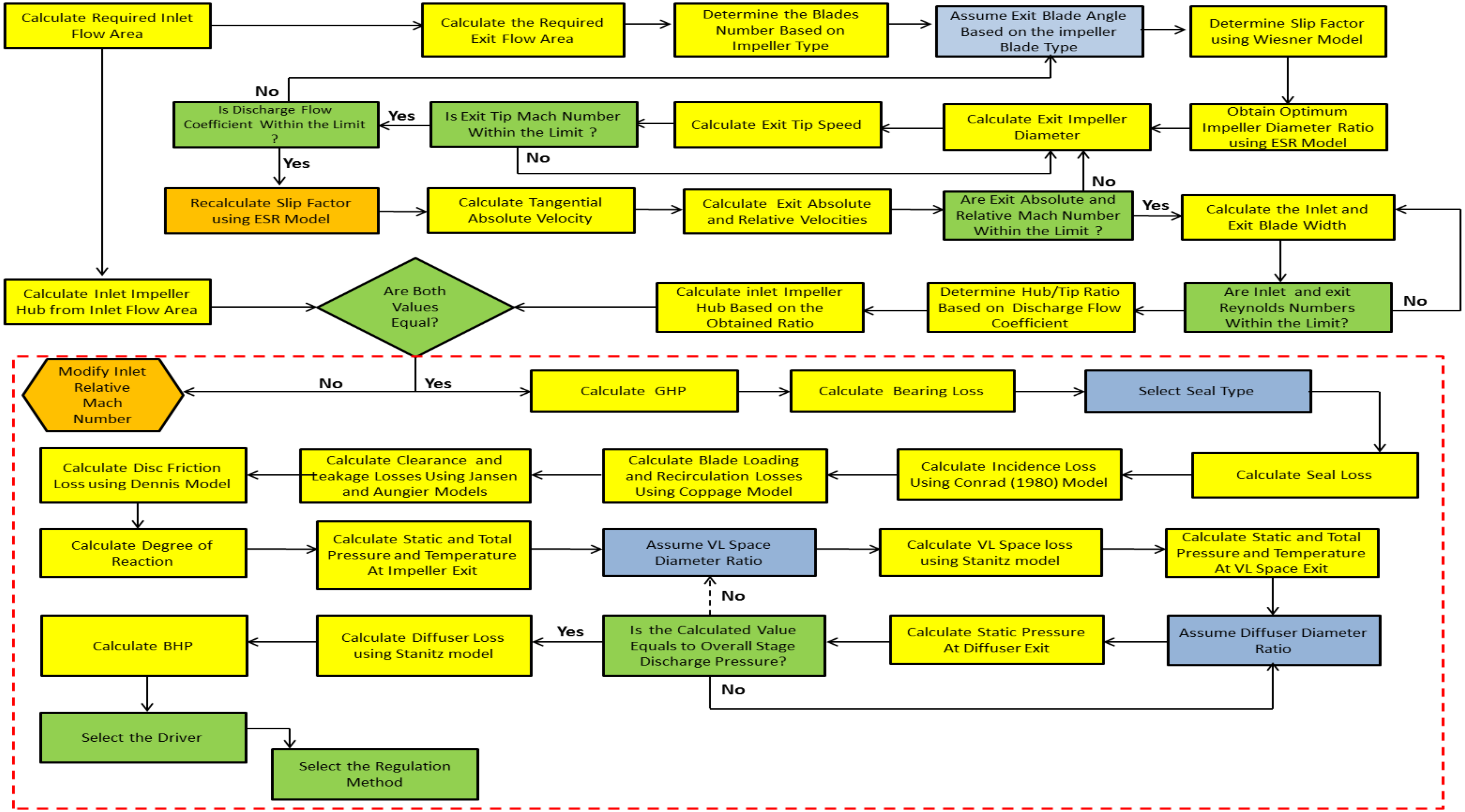

B4. Sizing and Aerodynamic Modelling Approach of Single Stage Centrifugal Compressor (Sub-Model D2)

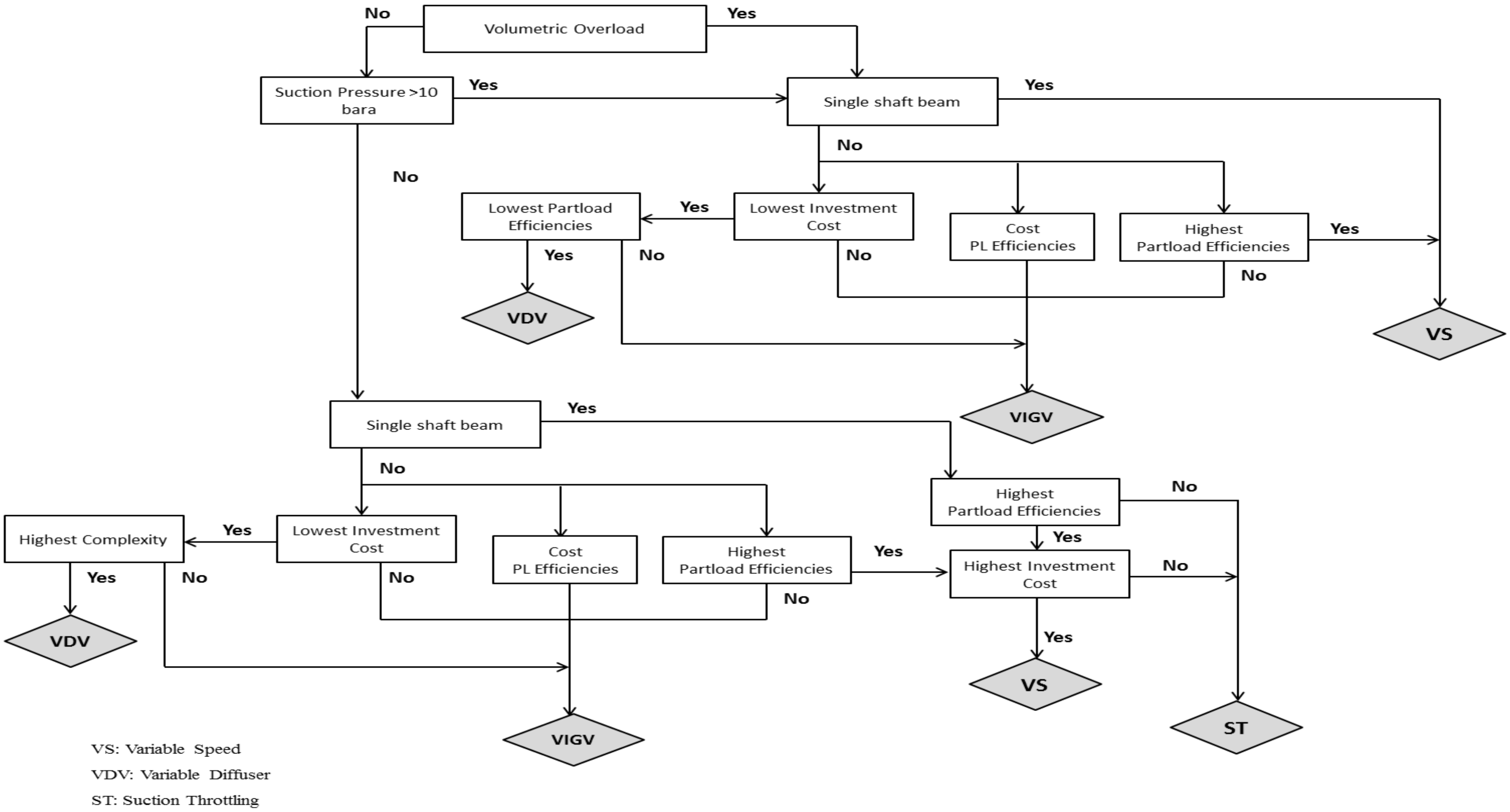

B5. Regulation Method Selection Approach

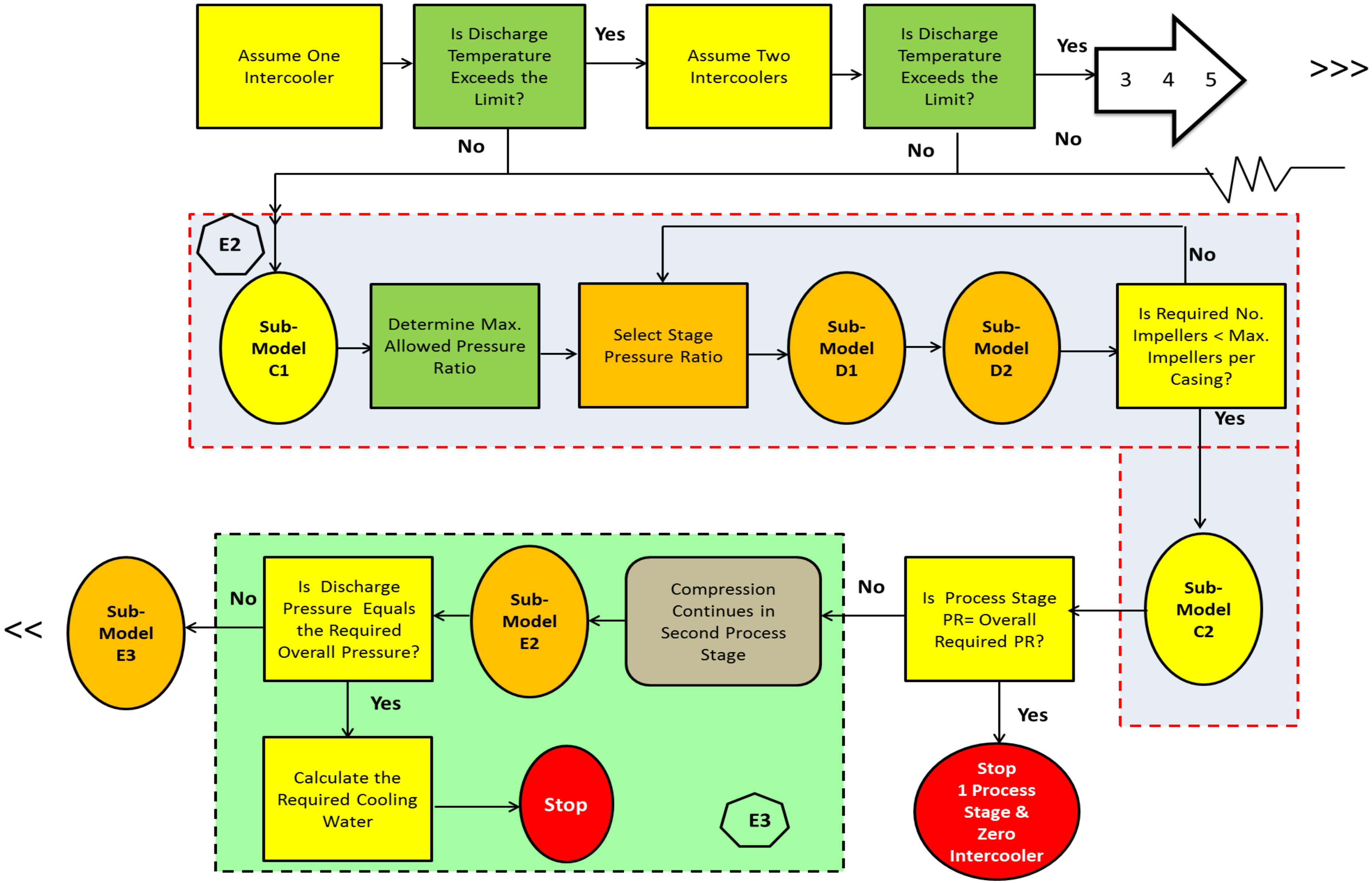

B6. Sizing and Aerodynamic Modelling Approach of Multi-Stage Centrifugal Compressor (E)

Appendix C : **Validation of Compressor Type and Casing Structure Selection**

The Use of Centrifugal Compressor is Recommanded

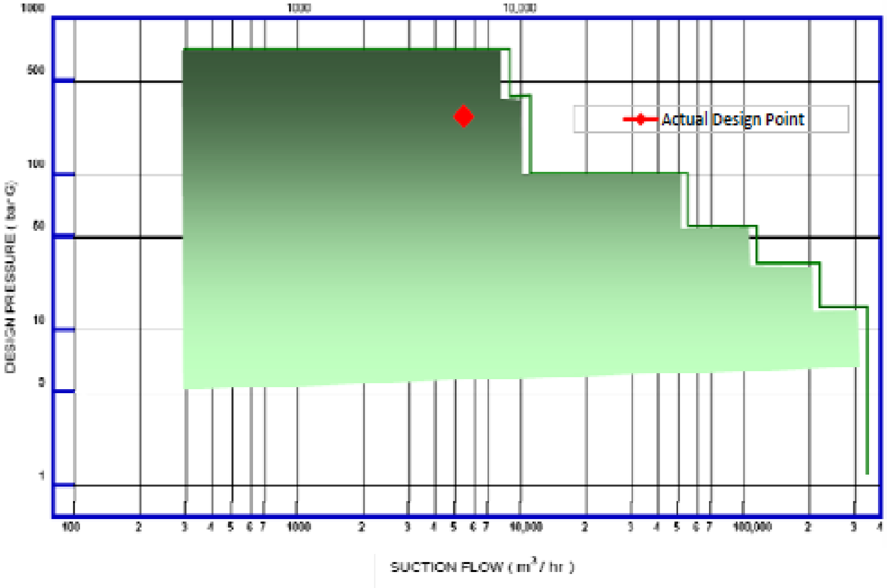

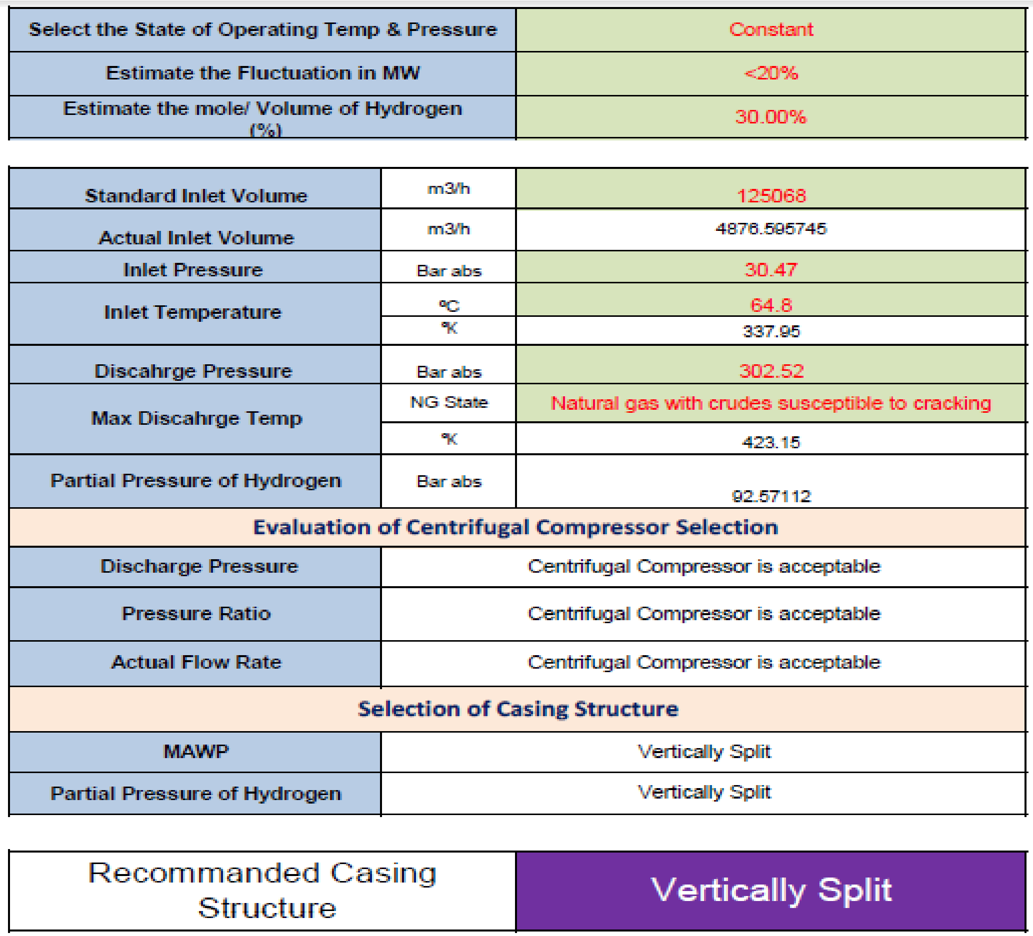

Select the State of Operating Temp & Pressure		Constant
Estimate the Fluctuation in MW		<20%
Estimate the mole/ Volume of Hydrogen (%)		30.00%
Standard Inlet Volume	m3/h	125068
Actual Inlet Volume	m3/h	4876.595745
Inlet Pressure	Bar abs	30.47
Inlet Temperature	ºC	64.8
	ºK	337.95
Discahrge Pressure	Bar abs	302.52
Max Discahrge Temp	NG State	Natural gas with crudes susceptible to cracking
	ºK	423.15
Partial Pressure of Hydrogen	Bar abs	92.57112
Evaluation of Centrifugal Compressor Selection		
Discharge Pressure	Centrifugal Compressor is acceptable	
Pressure Ratio	Centrifugal Compressor is acceptable	
Actual Flow Rate	Centrifugal Compressor is acceptable	
Selection of Casing Structure		
MAWP	Vertically Split	
Partial Pressure of Hydrogen	Vertically Split	

Recommanded Casing Structure	Vertically Split

C1. Velocity Triangles at the Inlet and Exit Impeller Diameter

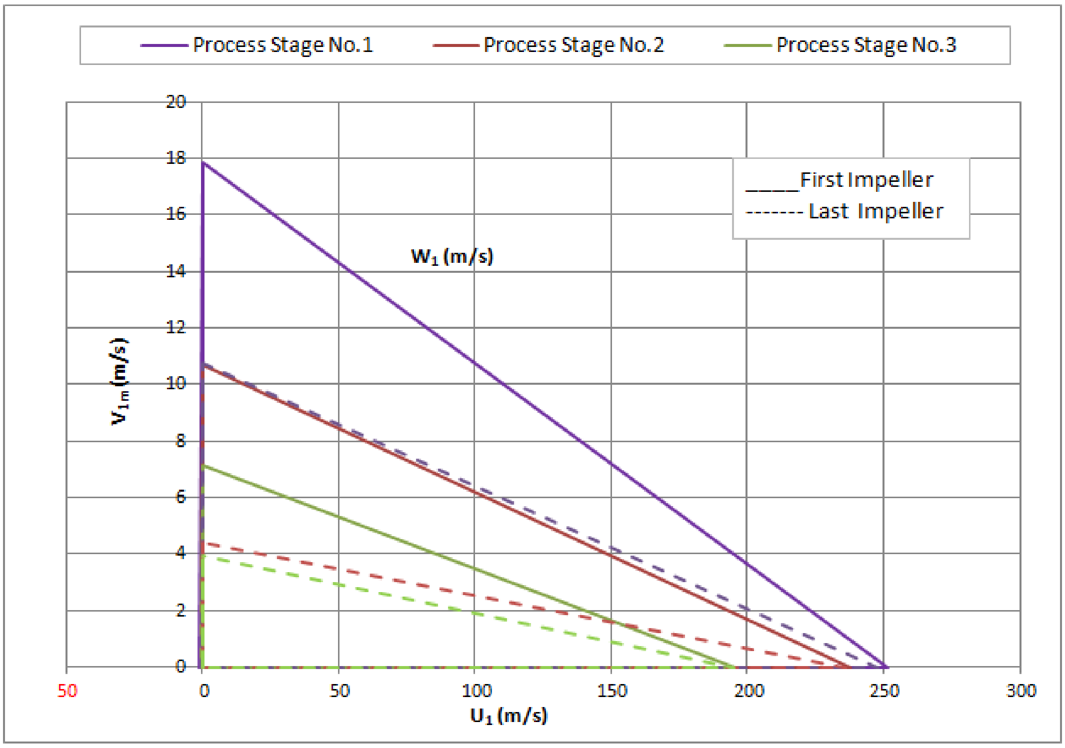

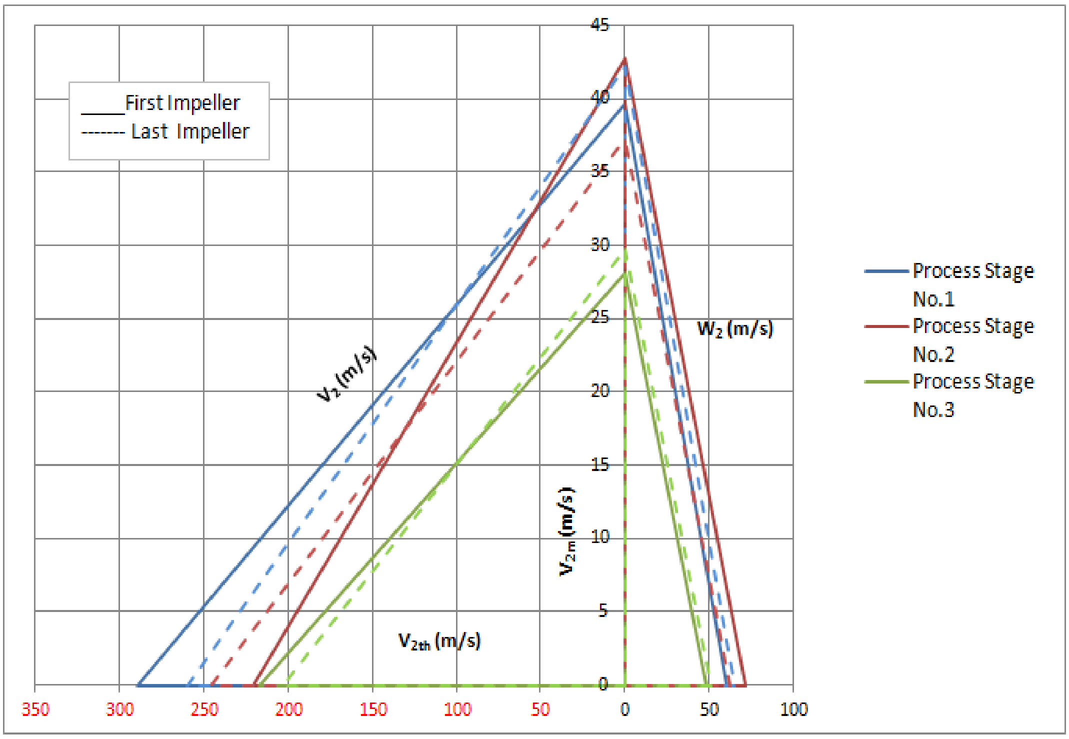

Appendix D : Dimensional Compressor Performance Curves using Casey Model

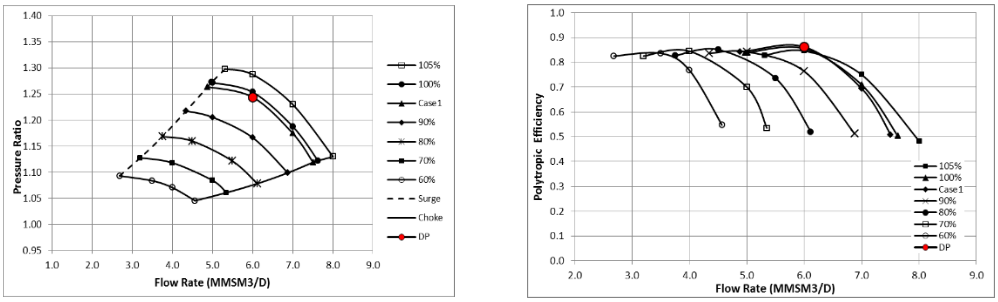

First Mechanical Stage

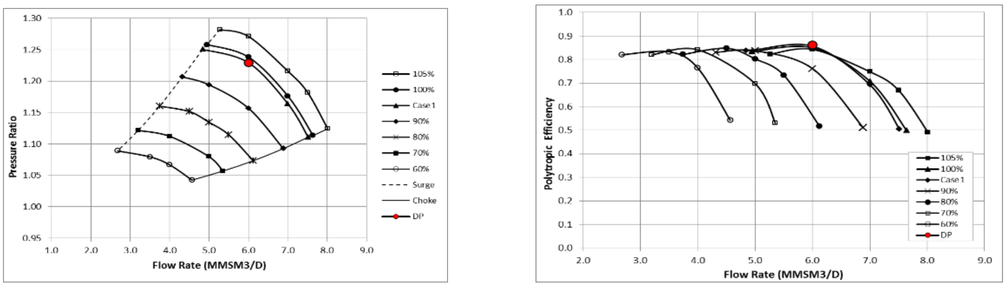

2nd Mechanical Stage

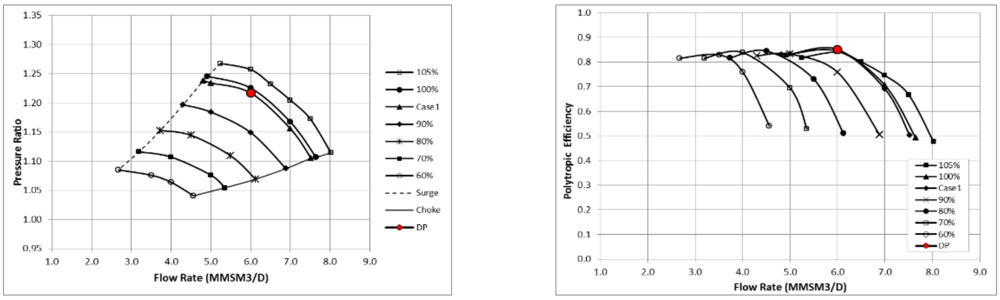

3rd Mechanical Stage

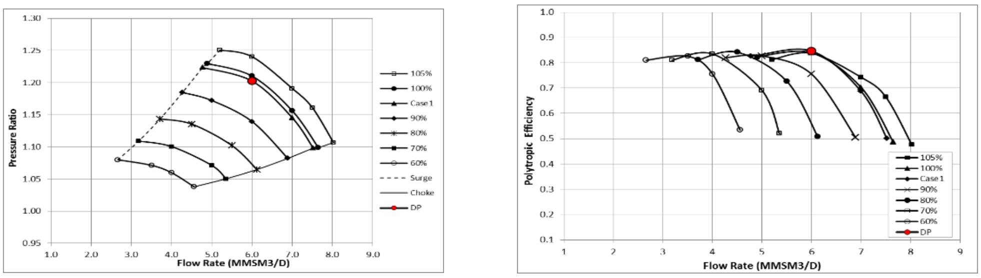

4th Mechanical Stage

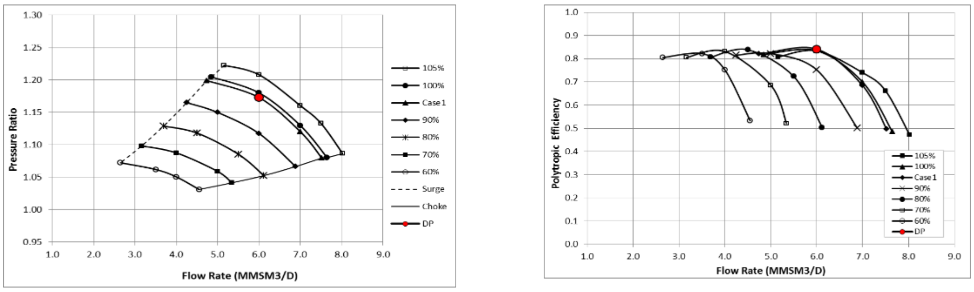

5th Mechanical Stage

Appendix E : Dimensionless Performance Curves of Second Case Study (section 6.7.2)

E1. First Mechanical Stage

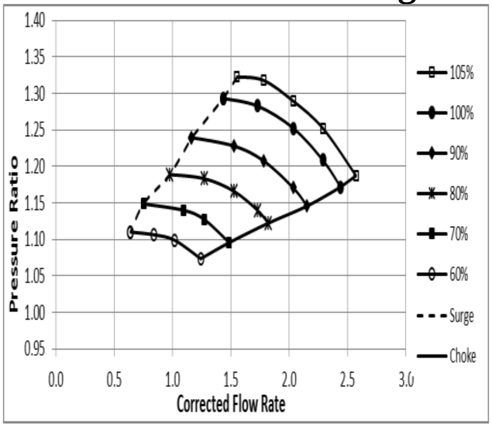

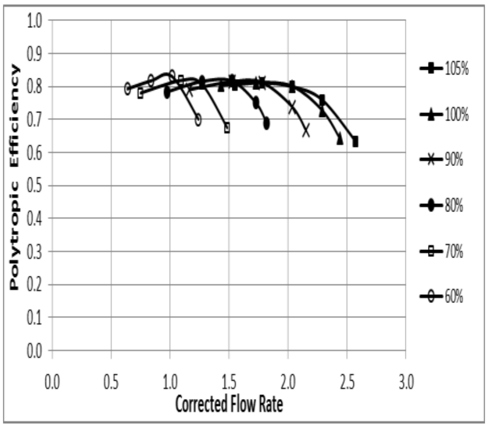

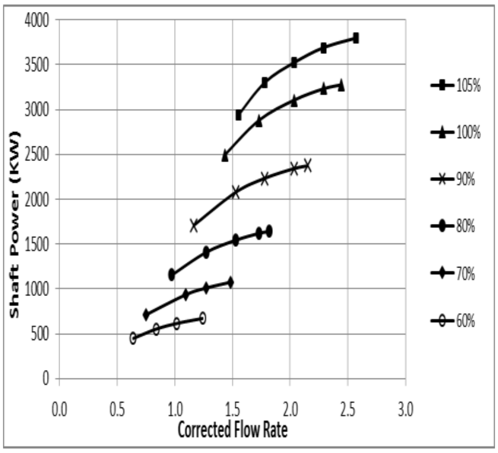

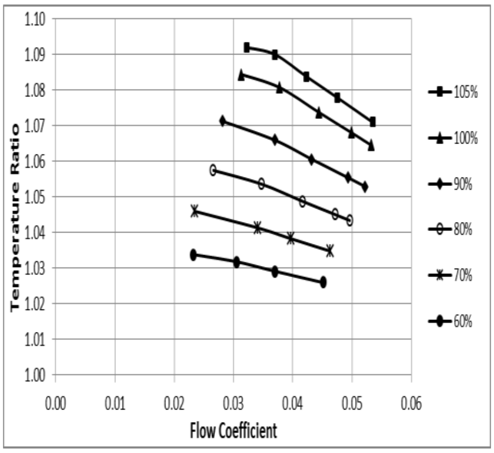

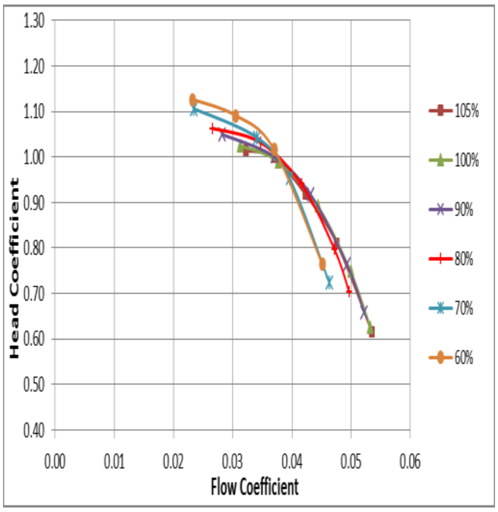

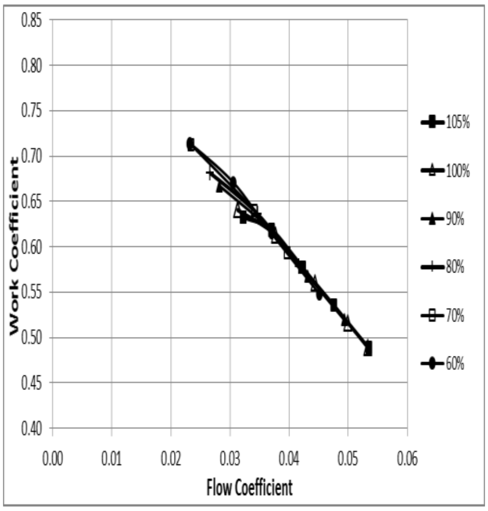

E2. 2nd Mechanical Stage

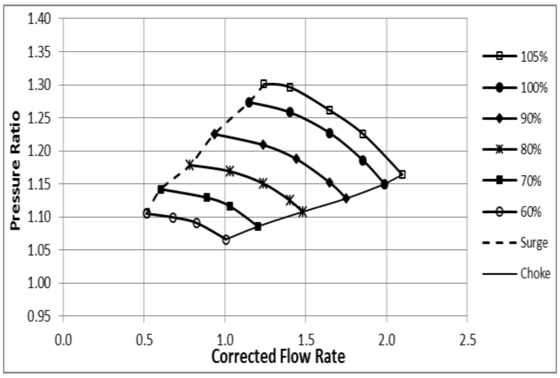

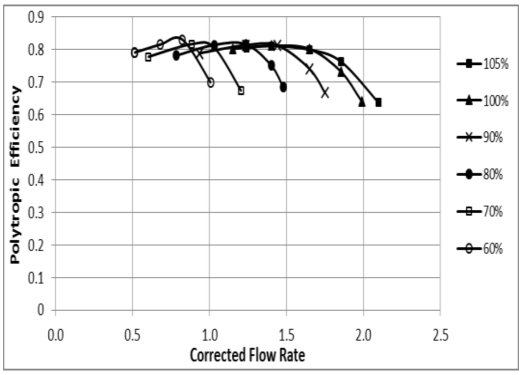

E3. 3rd Mechanical Stage

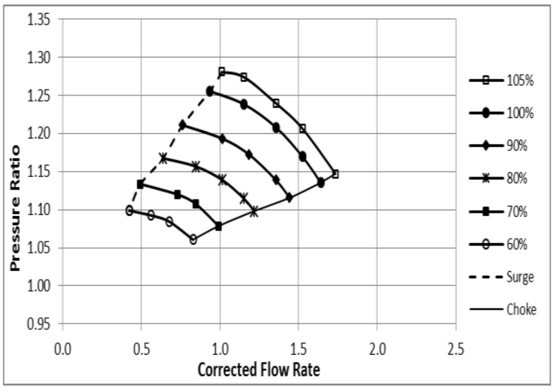

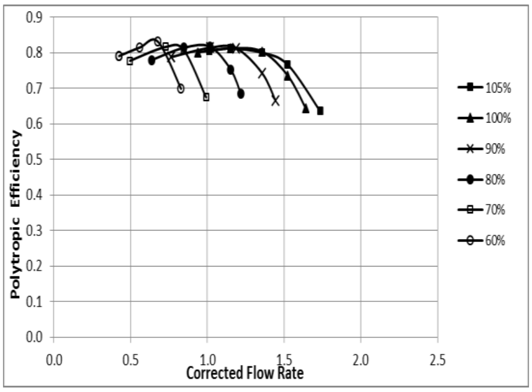

E4. 4th Mechanical Stage

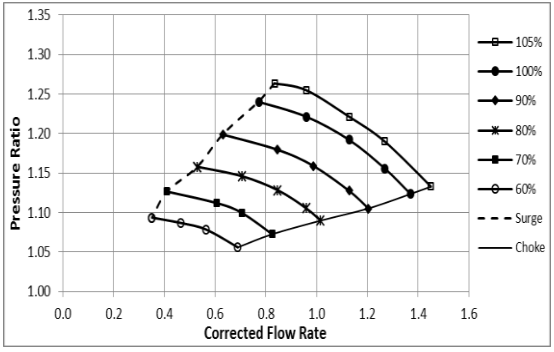

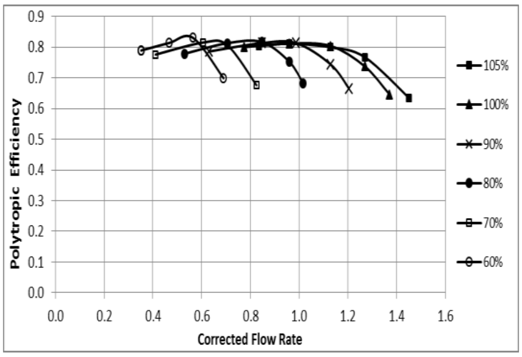

E5. 5th Mechanical Stage

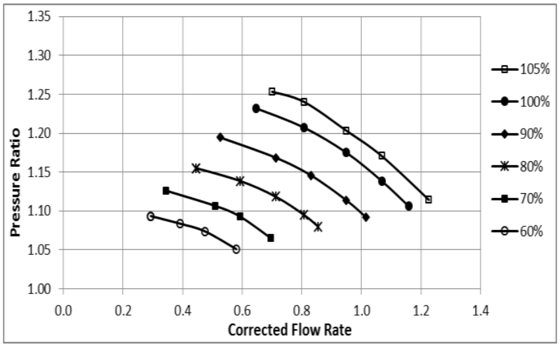

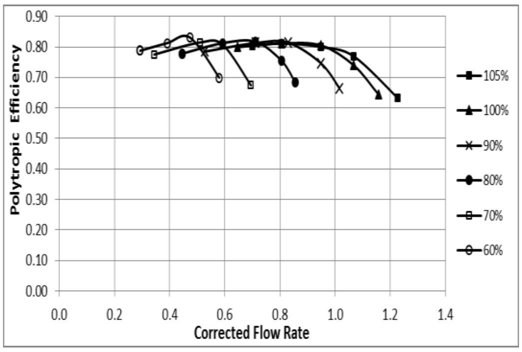

Appendix F : **Impact of Two-Phase Flow on Compressor Performance**

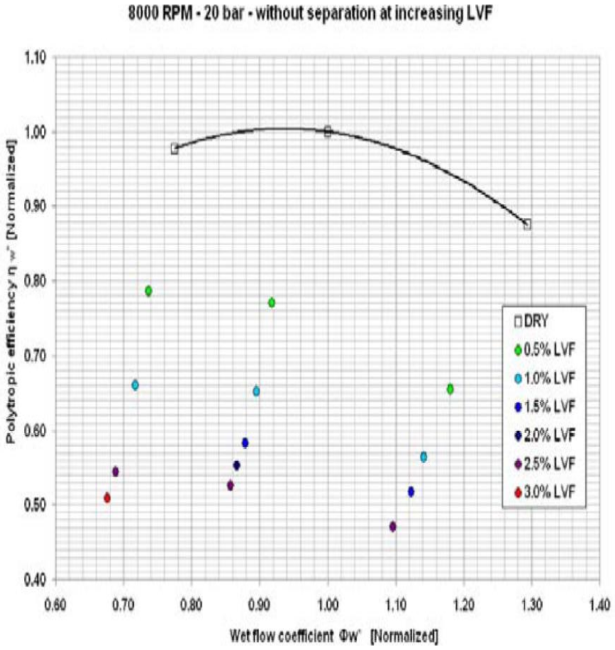

(A) Bertoneri et al. (2012)

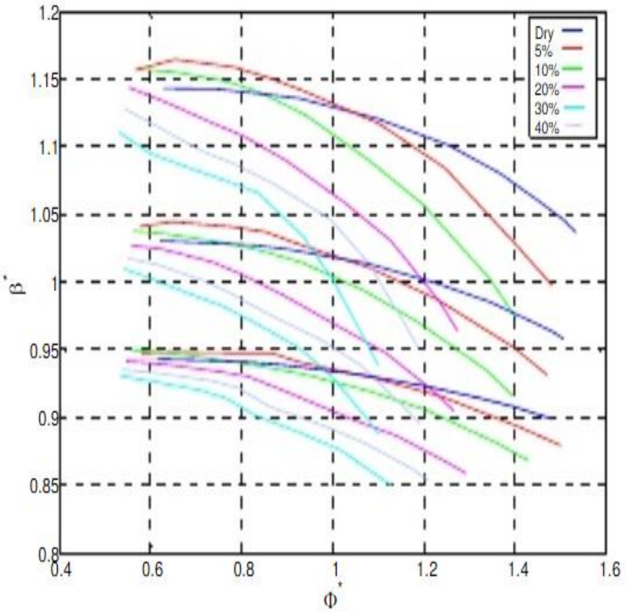

(B) Fabbrizzi et al. (2009)

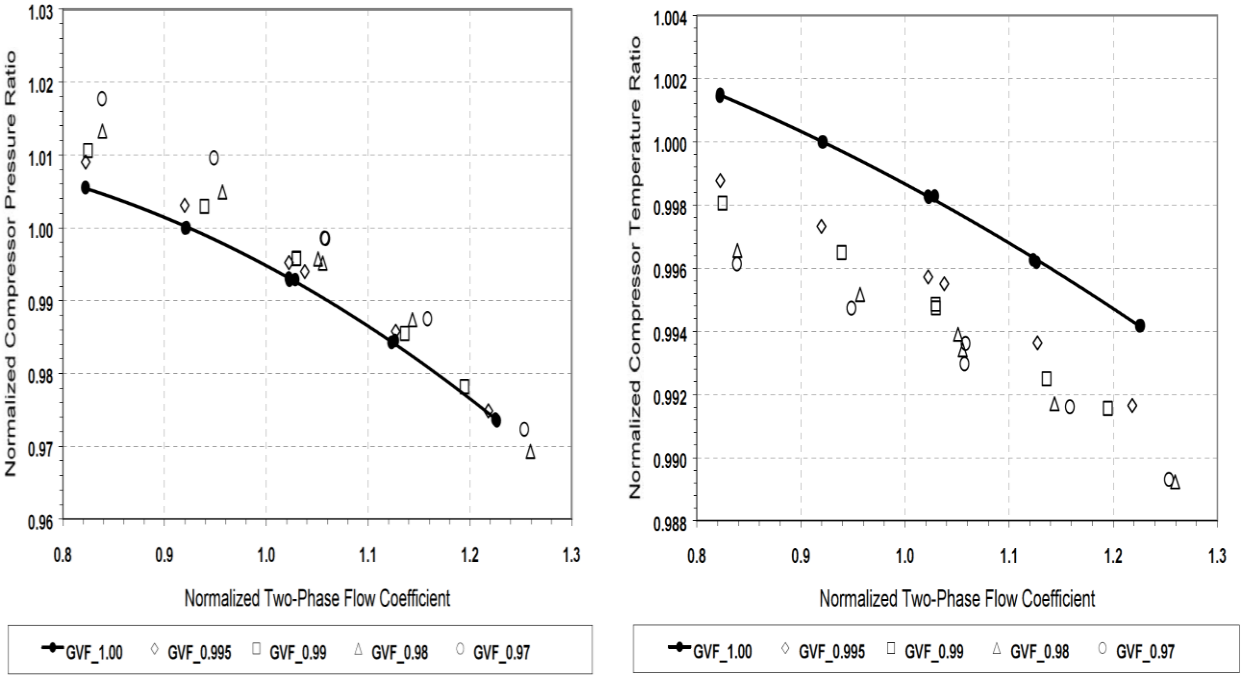

(C) Brenne et al. (2005)

Appendix G : **Hydrate Temperature Estimation Models**

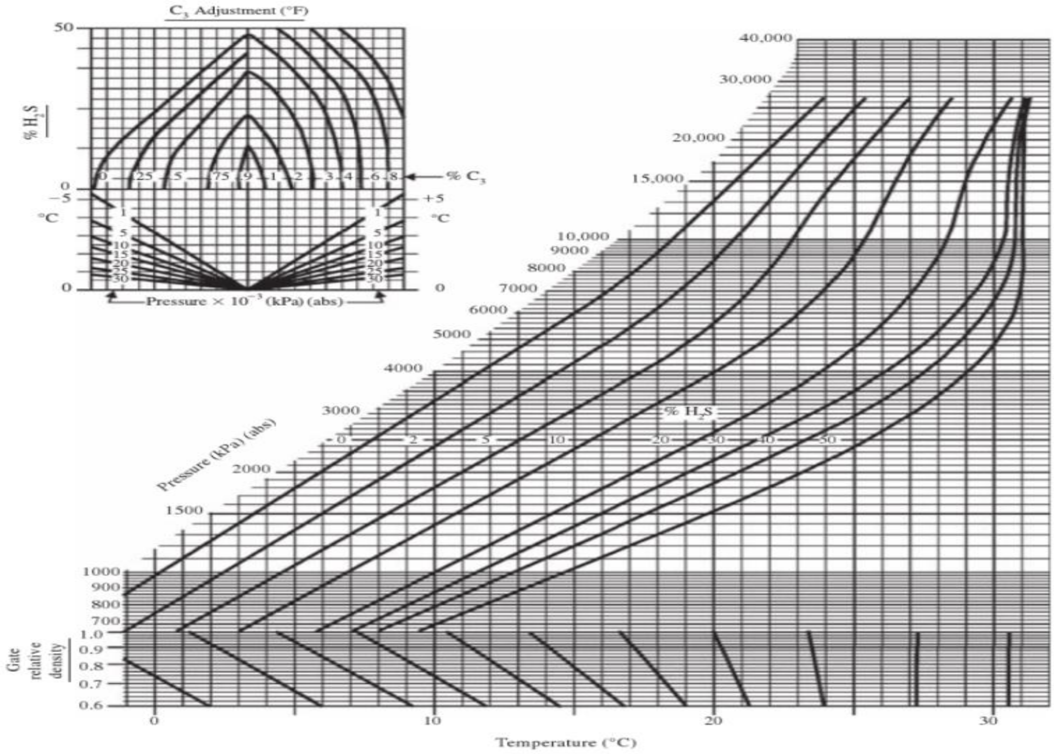

Baillie–Wichert Chart (Carroll, 2014)

Empirical Coefficients of Bahadori-Vuthaluru's Correlation (2009)

	MW<23 **1200< P< 5000**	**MW<23** **5000< P < 40,000**	**MW>23** **1200< P< 40,000**
A_1	-4.181213278	7.095970395	6.418507111
B_1	1.472639349	-0.218060301	-0.088017108
C_1	-0.072745386	0.011305933	0.003557343
D_1	0.00118978	-0.00019272	-4.74998E-05
A_2	45284.975	-125846.4942	-8642.628914
B_2	-6862.812445	18993.11177	1024.330785
C_2	342.4072186	-952.6005813	-40.96639255
D_2	-5.642533019	15.80682009	0.544500508
A_3	-83170750.73	921903822.8	11596430.3
B_3	12604810.25	-140304105.7	-1385902.777
C_3	-630185.7947	7082041.799	55353.14827
D_3	10408.84843	-118187.6347	-733.9994548
A_4	5858977399	-2.10535E+12	-4020095148
B_4	-966349625.4	3.21399E+11	479133183.3
C_4	51347314.22	-16274767263	-19036325.3
D_4	-887818.5865	272488432.5	251132.974

Appendix H : **Flow Chart of Operation Case Study in Section 8.3**

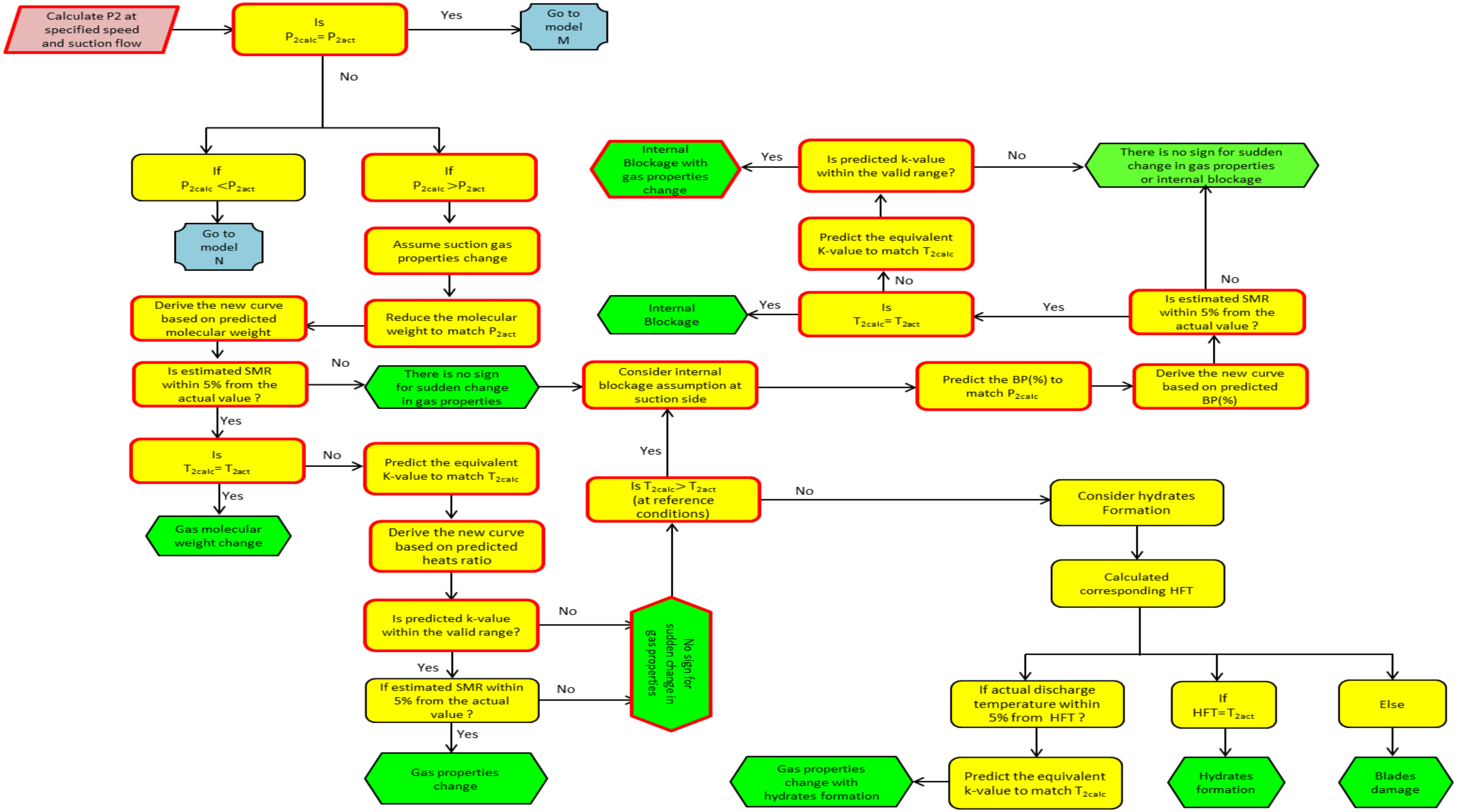

Appendix I : **Model (M) To evaluate Compressor Discharge Temperature**

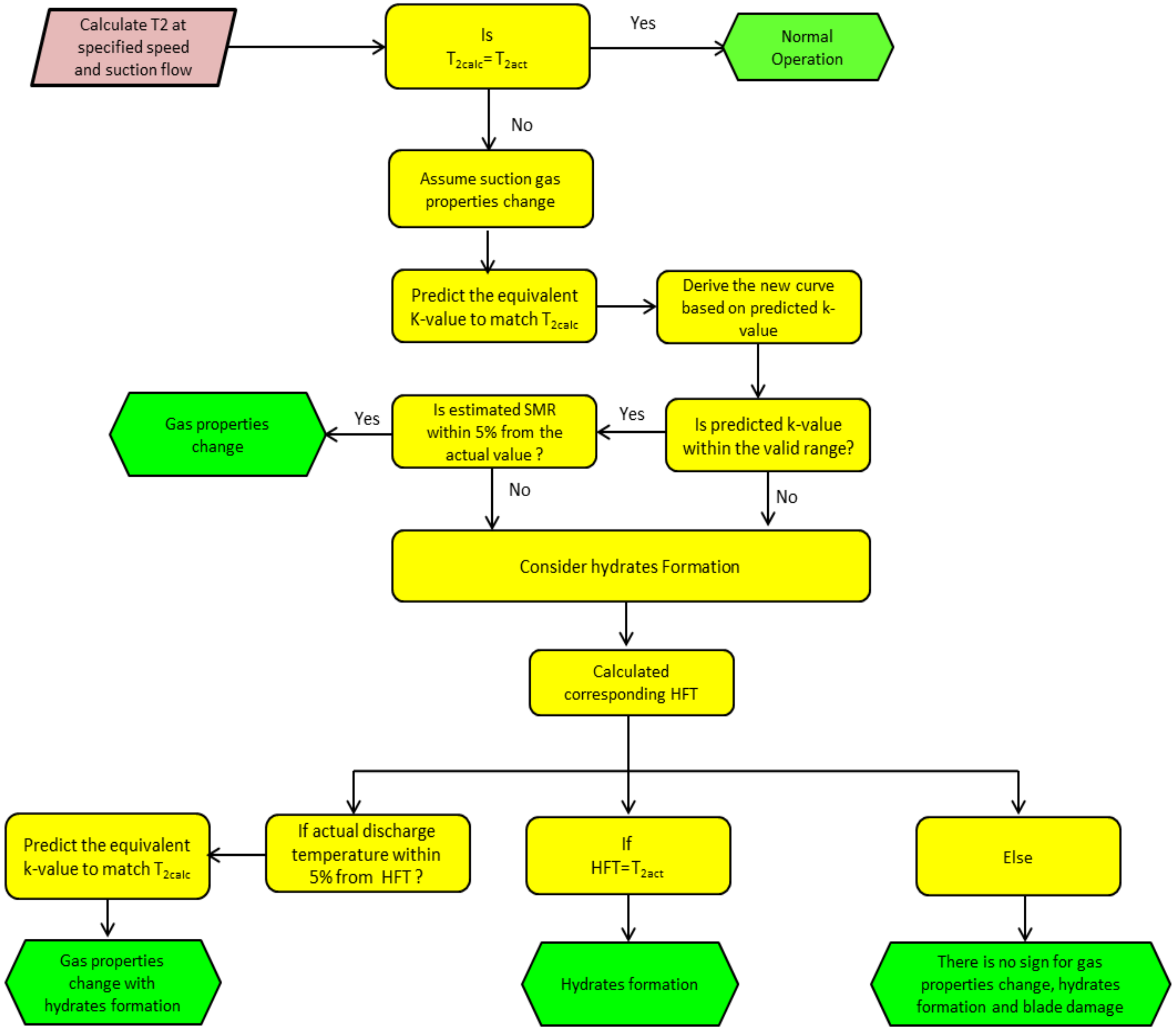

Appendix J : **Model (N) Flow Chart of Operation Case Study in Section 8.4**

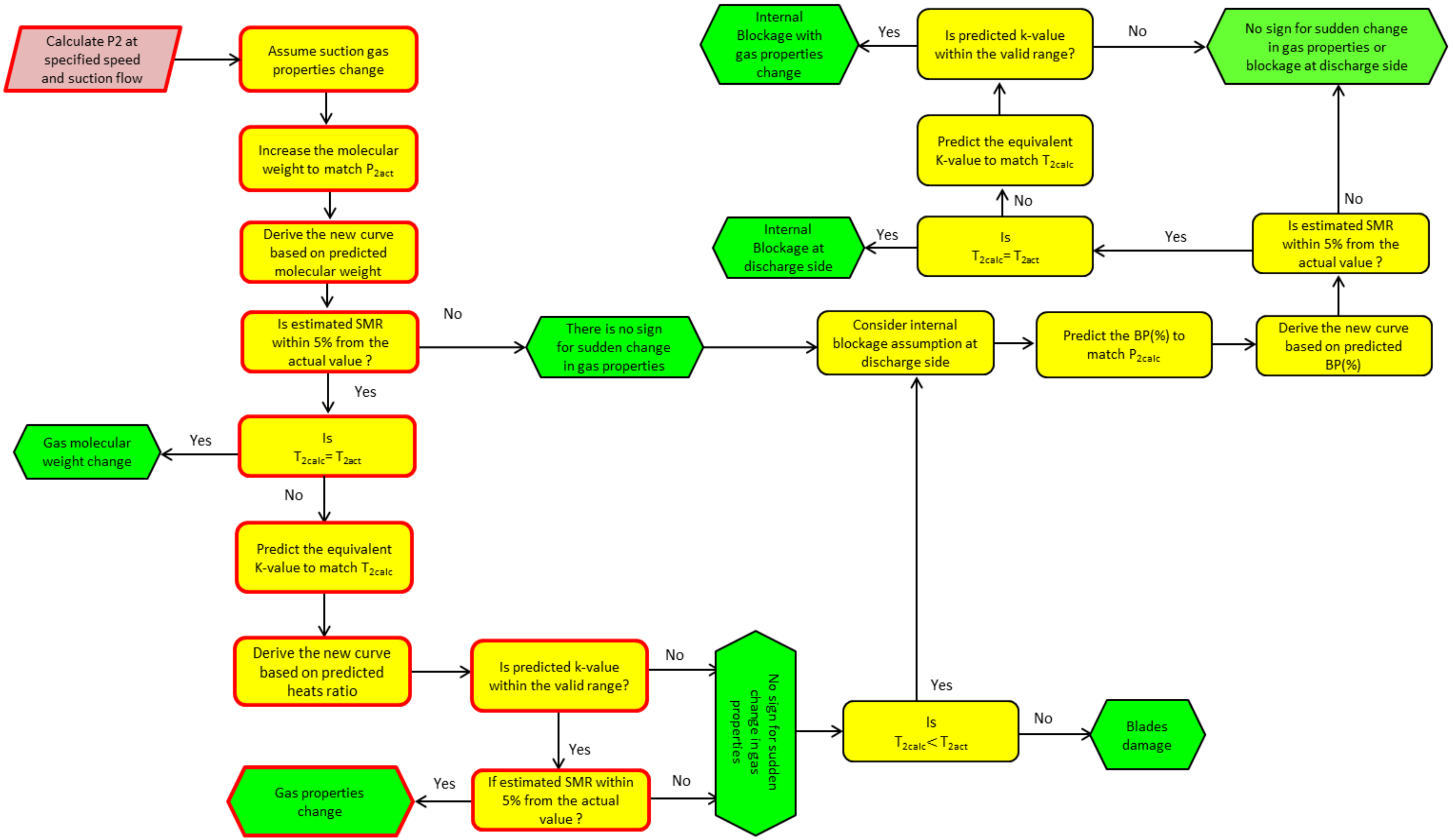

Appendix K : **Flow Chart of Operation Case Study in Section 8.5**